

## ABSTRACT

### MONOENERGETIC POSITRONS AND CORRELATED ELECTRONS FROM SUPERHEAVY NUCLEAR COLLISIONS

Thomas Edward Cowan  
Yale University  
1988

The origin of the narrow peaks in the energy distribution of positrons produced in superheavy ion-atom collisions has been experimentally investigated using the EPOS spectrometer at GSI Darmstadt. We systematically studied the dependence of monoenergetic positron emission on the combined charge of the colliding nuclei  $Z_U$ , and measured the velocity of the system emitting the peaks by their laboratory Doppler broadening. Motivated by the results of these studies, additional experiments designed to search for monoenergetic electrons emitted in coincidence with the positron peaks were performed.

In the first series of measurements, narrow positron peaks between 300 and 400 keV were detected in each of five supercritical (U+Cm, Th+Cm, U+U, Th+U, and Th+Th) and one subcritical (Th+Ta) collision systems studied. The structures were produced with similar cross section ( $\sim 10 \mu$  b/sr) in quasi-elastic collisions which differed slightly from Rutherford scattering. They cannot be attributed to nuclear conversion processes. The positron peak widths (each  $\sim 75$  keV) indicate that the emitting source lives for  $\geq 10^{-20}$ s, and has a mean laboratory velocity of  $\sim 0.05c$ , consistent with the center-of-mass velocity. Spontaneous positron emission from the decay of the QED vacuum is unable to explain the independence of the peak energies on  $Z_U$ .

The common energy of the positron lines led us to explore the possibility that the peaks are associated with the decay of an intermediate state. Using a modified configuration of the EPOS spectrometer, we discovered narrow electron lines, emitted in coincidence with positron peaks, in U+Th, Th+Cm, and Th+Th

collisions. In each case, the peak in the distribution of the sum of the positron and electron kinetic energies was much narrower than the individual lines, suggesting the correlated cancellation of their Doppler shifts. Three prominent sets of coincidence structures have been identified at sum energies of  $(E_{e^-} + E_{e^+}) \approx 610$ , 750, and 815 keV. Monte Carlo simulations have been used to rule out background radiations, instrumental effects, and all known nuclear conversion processes as possible origins for the coincidence lines. A kinematic analysis of the correlated peak widths implies that the positrons and electrons are emitted back-to-back in the rest frame of their source. One possible interpretation of these data is that we are observing the two-body decay of previously undetected neutral objects which have total energies between 1.5 and 2 MeV.

**Monoenergetic Positrons and Correlated Electrons  
from Superheavy Nuclear Collisions**

A Dissertation

Presented to the Faculty of the Graduate School

of

Yale University

in Candidacy for the Degree of

Doctor of Philosophy

by

Thomas Edward Cowan

May, 1988

## **ACKNOWLEDGEMENTS**

I would like to thank my advisor, Professor Jack S. Greenberg, who has been the guiding force behind these experiments, for his direction and numerous suggestions throughout the course of this dissertation research. I would also like to thank Professor D. Allan Bromley, director of the A. W. Wright Nuclear Structure Laboratory for his continued support, and the other members of my committee, Professors A. Chodos, E. Hinds, and V. Hughes, for their helpful comments and observations.

I would like to take this opportunity to thank the members of the EPOS Spectrometer group whose combined efforts have made for a very pleasurable and rewarding experimental collaboration. They have included: Hartmut Backe, Marie-Louise Begemann-Blaich, Klaus Bethge, Helmut Bokemeyer, Helmut Folger, J.S. Greenberg, Axel Gruppe, Yoshiaki Kido, Michaela Klüver, Kiyo Sakaguchi, Piotr Salabura, Roland Schulé, Dirk Schwalm, John Schweppe, Kurt Steibing, N. Trautmann, and Paul Vincent. I would like to single out John Schweppe, my predecessor, who lent considerable support and encouragement, and Werner Kreuzer, whose expert assistance with many technical aspects of the experiment has been invaluable.

I warmly acknowledge valuable discussions with Walter Greiner, Berndt Müller, J. Reinhardt, G. Soff, U. Müller, T. de Reus, A. Schäfer, P. Schlüter, and their co-workers at the Univ. Frankfurt Theory group. I am also grateful for the kind hospitality extended to me by the staff of GSI. I would like to thank R. Bock and W. Henning for their support, R. Kluber for handling numerous important details, and Isia Busch and Traudel Eisold who have been especially helpful.

On the other side of the Atlantic, I am grateful to the administrative and secretarial staffs of the A.W. Wright Nuclear Structure Laboratory and the Yale University Department of Physics for taking care of financial support and for handling foreign travel requests, reports, and many long-distance communications. I would particularly like to thank Mary Anne Schultz, Jean, Rita Bonito, and Sara Batter.

We are particularly grateful to the operating staff of the UNILAC who pushed the machine to its limits for our experiments. I also thank the GSI computer center staff, and especially Hans Grein, for assistance during several stages of the data acquisition and analysis. We thank the Transplutonium Program of the U.S. Department of

Energy for the loan of the  $^{248}\text{Cm}$  isotope material. This research has been supported in part by the U.S. Department of Energy Contract No. DE-AC02-76ER03074, and by the Bundesministerium für Forschung und Technologie of the Federal Republic of Germany.

On a personal note, I would like to thank my parents, Drs. John and Nancy Cowan, who passed on to me their joy of learning, and my grandparents, Justin and Anne Simpson. Their generosity and their many achievements have been a continual source of inspiration. Most of all, I would like to thank my wife, Rebecca. Without her steadfast love, help, and encouragement over the years, this dissertation could never have been completed. She is the "wind beneath my wings." It is to her that this work is dedicated.

# Table of Contents

<b>Chapter 1 Introduction</b> .....	<b>1</b>
Section 1.1 Motivation .....	1
Section 1.2 Present Work .....	4
Section 1.3 Organization .....	6
<b>PART I. ANOMALOUS POSITRON PEAKS FROM SUPERHEAVY COLLISIONS</b> .....	<b>8</b>
<b>Chapter 2 Experimental Apparatus</b> .....	<b>9</b>
Section 2.1 Overview of EPOS Spectrometer .....	9
Section 2.2 Positron Detection .....	14
Sec. 2.2.1 Solenoid Transport Field .....	15
Sec. 2.2.2 Spiral Baffle .....	21
Sec. 2.2.3 Positron Si(Li) Detector .....	28
Sec. 2.2.4 NaI Annihilation Radiation Detector .....	32
Sec. 2.2.5 Positron Detection Efficiency .....	34
Sec. 2.2.6 EPOS Spectrometer Performance .....	43
Sec. 2.2.7 Doppler-Broadened Positron Lineshape .....	51
Sec. 2.2.8 Summary .....	64
Section 2.3 Heavy-Ion Detection .....	65
Sec. 2.3.1 Physical Characteristics .....	65
Sec. 2.3.2 Heavy-Ion Kinematics .....	67
Sec. 2.3.3 Operation in Magnetic Field .....	70
Section 2.4 Gamma-Ray Detection .....	73
Section 2.5 Electron Detection .....	73
Section 2.6 Targets .....	78
Sec. 2.6.1 Curium Targets .....	78
Sec. 2.6.2 Proton Backscattering Measurements .....	81
Sec. 2.6.3 Development Efforts .....	85
Sec. 2.6.4 Summary .....	87
Section 2.7 Heavy-Ion Beam .....	88
Sec. 2.7.1 UNILAC Accelerator .....	88
Sec. 2.7.2 Beam Current, Focus, and Duty-Cycle .....	88
Sec. 2.7.3 Beam Energy and Isotopic Purity .....	91
Section 2.8 Data Acquisition System .....	93
Sec. 2.8.1 Experimental Electronics .....	93
Sec. 2.8.2 CAMAC Interface and Logic Trigger .....	95
<b>Chapter 3 Data and Analysis</b> .....	<b>98</b>
Section 3.1 Experiments .....	98
Sec. 3.1.1 Systems Measured .....	98
Sec. 3.1.2 Online Control .....	100
Section 3.2 Data Reduction .....	102
Sec. 3.2.1 Heavy-Ion Data .....	102
Sec. 3.2.2 $\gamma$ -Ray and Electron Events .....	104
Sec. 3.2.3 Positron Events .....	104
Sec. 3.2.4 Background Subtraction .....	107
Sec. 3.2.5 Time-of-Flight Corrections .....	108
Section 3.3 Total Positron Energy Distributions .....	110
Section 3.4 Narrow Positron Peaks .....	117
Sec. 3.4.1 Summary of Peak Characteristics .....	119
Sec. 3.4.2 Kinematic Cuts, Angular Distribution .....	122
Sec. 3.4.4 Beam-Energy Dependence .....	133
Sec. 3.4.5 Peak Cross-Sections .....	138
<b>Chapter 4 Discussion of Peak Origins</b> .....	<b>143</b>

Section 4.1 Instrumental Origins	143
Section 4.2 Nuclear Conversion Processes	150
Sec. 4.2.1 Conversion Processes and Coefficients	150
Sec. 4.2.2 Comparison with $\gamma$ -Ray Data	156
Sec. 4.2.3 Electron Data and E0 Transitions	159
Section 4.3 Measurement of Emitting System Velocity	167
Sec. 4.3.1 HI Scattering Angle Dependence of Peak Width	167
Sec. 4.3.2 Distribution of Velocities	171
Sec. 4.3.3 Angular Distribution	172
Sec. 4.3.4 Nuclear Level Lifetime	176
Sec. 4.3.5 Intrinsic Width	177
Section 4.4 Spontaneous Positron Emission	180
Sec. 4.4.1 Application to U + Cm Data.	180
Sec. 4.4.2 Z Dependence	184
Sec. 4.4.3 Isomeric Configurations	187
Sec. 4.4.4 Common Super-Nucleus	190
Sec. 4.4.5 Side Structures	194
Section 4.5 Other Effects	196
Sec. 4.5.1 Prolonged Nuclear Contact	196
Sec. 4.5.2 Multi-Electron Transitions	197
Sec. 4.5.3 Sudden Rearrangement of Atomic Shells	200
Sec. 4.5.4 Conversions in Super-Nucleus	201
Section 4.6 Summary of Hypothesized Origins	203
<b>PART II: POSITRON-ELECTRON COINCIDENCE MEASUREMENTS</b>	<b>205</b>
<b>Chapter 5 Experimental Design</b>	<b>206</b>
Section 5.1 Introduction	206
Sec. 5.1.2 Expected Signature	211
Section 5.2 EPOS Spectrometer	215
Sec. 5.2.1 Overview	215
Sec. 5.2.2 Electron Detection	216
Sec. 5.2.3 Experimental Electronics	224
Sec. 5.2.4 Data Reduction	226
Section 5.3 Detection Efficiency and Time-of-Flight	227
Section 5.4 Coincidence Detection	235
Sec. 5.4.1 Monte-Carlo Simulations	235
Sec. 5.4.2 Two-Body Decay Coincidence Detection	237
Sec. 5.4.3 Non-Correlated Coincidence Detection	240
Sec. 5.4.4 Continuous Pair Creation Detection	242
Section 5.5 Continuous Positron and Electron Backgrounds	248
Section 5.6 Importance of Various Projections	254
<b>Chapter 6 Data and Results</b>	<b>257</b>
Section 6.1 Measurements	257
Section 6.2 750 keV Structure in U + Th	258
Section 6.3 Additional Results	265
Section 6.4 Follow-up Experiments	266
Section 6.5 Correlations with Kinematic Parameters	270
Sec. 6.5.1 Projectile Energy	273
Sec. 6.5.2 Flight Time	275
Sec. 6.5.3 Heavy Ion Scattering Angle	280
Section 6.6 Other Structures	281
<b>Chapter 7 Discussion of Possible Origins</b>	<b>285</b>
Section 7.1 Instrumental Backgrounds	285
Section 7.2 Uncorrelated, Independent Peaks	289
Section 7.3 Correlated Positron/Electron Pair Creation	294

Sec. 7.3.1 Internal Pair Creation .....	294
Sec. 7.3.2 IPC in Nuclear Fragments or Clusters .....	300
Sec. 7.3.3 $^{90}\text{Zr}$ IPC .....	302
Sec. 7.3.4 External Pair Creation .....	302
Section 7.4 Sequential Positron-Electron Emission .....	304
Section 7.5 Two-Body Final States .....	307
Sec. 7.5.1 Theoretical Motivation .....	307
Sec. 7.5.2 Positron/Electron Lines from a Moving Source .....	311
Sec. 7.5.3 Multi-Body Final States .....	313
Sec. 7.5.4 Two-Body Decay from Rest in the Lab .....	316
Sec. 7.5.5 Emission Angle Correlation .....	317
Sec. 7.5.6 Emitter Velocity .....	326
Sec. 7.5.7 Multiple Structure .....	338
<b>Chapter 8 Summary and Outlook .....</b>	<b>342</b>
Section 8.1 Positron Peak Data .....	342
Section 8.2 Coincident Positron-Electron Peaks .....	342
Section 8.3 Open Questions .....	343
Section 8.4 Future Experiments .....	344
Sec. 8.4.1 Particle Experiments .....	344
Sec. 8.4.2 Heavy-Ion Experiments .....	345
<b>Appendix A Heavy-Ion Kinematic Relations .....</b>	<b>348</b>
Section A.1 Elastic Scattering .....	348
Section A.2 Inelastic Collisions .....	350
Section A.3 Heavy-Ion Energy-Loss .....	353
<b>Appendix B Ray-Tracing Calculations .....</b>	<b>355</b>
Section B.1 Equations of Motion .....	355
Section B.2 Magnetic Field and Vector Potential .....	356
Section B.3 Runga-Kutta Method .....	357
Section B.4 Milne Predictor-Corrector Method .....	359
Section B.5 Performance .....	359
<b>Appendix C Monte-Carlo Simulations of Positron-Electron Coincidences .....</b>	<b>361</b>
Section C.1 Event Generators .....	361
Section C.2 Efficiency Determination .....	362
Section C.3 Detector Response .....	362
Section C.4 Event Analysis .....	363
<b>Appendix D Abbreviations .....</b>	<b>364</b>
<b>References .....</b>	<b>365</b>

# Chapter 1 Introduction

## Section 1.1 Motivation

A narrow peak was recently discovered in the energy distribution of positrons emitted from collisions between uranium and curium nuclei at projectile energies close to the Coulomb barrier [Shw83]. The experiment was performed by the EPOS collaboration (Yale, GSI, Frankfurt, Heidelberg, Mainz, and BNL) using the *Electron-POsitrion Solenoid Spectrometer* at GSI, Darmstadt. The peak, shown in Fig. 1-1, is centered at a kinetic energy of  $316 \pm 10$  keV, and its intensity corresponds to a production cross-section of  $d\sigma_{e^+}/d\Omega_{HI} \sim 10 \mu\text{b}/\text{sr}$ , assuming that the yield is proportional to the target thickness. The narrow width of  $\sim 75$  keV implies from the uncertainty relation that the emitting source lives for  $\geq 10^{-20}$  sec, almost an order of magnitude longer than the duration of the heavy-ion collision. Similar but weaker lines were also observed in the U+U system [Shw85, Bok83], and by an independent group in U+U and U+Th collisions [Cle84].

One possible interpretation for the U+Cm positron peak is the spontaneous decay of the neutral quantum electrodynamic vacuum in the presence of a supercritical external electric field [Vor61, Ger69, Pie69, Raf71], the search for which originally motivated these experiments. This process is illustrated in Fig. 1-2a which shows the energy of the atomic 1s (and  $2p_{1/2}$ ) state in the Coulomb field of a static nuclear charge  $Z$ . For  $Z$  larger than a critical value,  $Z_{cr} \cong 173$ , the 1s state is bound with energy greater than  $2m_e c^2$  and enters the negative energy Dirac continuum as a resonance. It is then energetically favorable for a vacancy in the resonant 1s state to decay, with a lifetime  $\tau_{sp} \sim 10^{-19}$  sec, by binding the electron of a spontaneously created positron-electron pair [Mül72, Mül72b, Zel72]. The liberated positron has discrete energy,  $E_{e^+} = |E_{1s}| - 2m_e c^2$ , and the resulting ground state which includes two 1s electrons represents a new "charged" QED vacuum [Ful73, Raf74, Mül73].

The supercritical nuclear charge necessary to study this process experimentally can, in principle, be assembled transiently in very heavy ion-atom collisions [Ger69, Raf72]. As indicated in Fig. 1-2b, however, the energy distribution of emitted positrons is expected to be broad and structureless for the following reasons. First, the time during which the quasimolecular  $1\sigma$  state is supercritically bound,  $t_{cr} \cong 2 \times 10^{-21}$  sec, is short compared to the supercritical decay time  $\tau_{sp} \cong 10^{-19}$  sec, so very few quasimolecular vacancies decay by spontaneous emission. By the un-

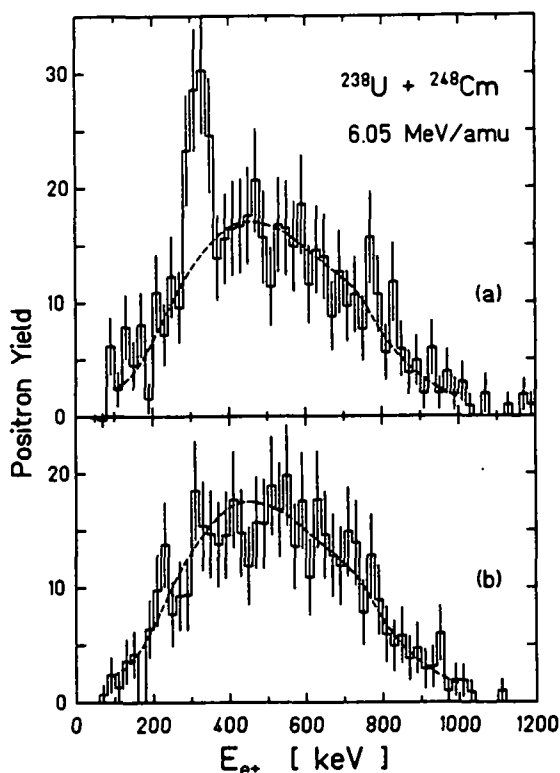


**Figure 1-1.** Positron energy spectra measured for U+Cm collisions at 6.05 MeV/u. Kinematic selections ( $28^\circ < \theta_{\text{rel}} < 40.5^\circ$ ) overlap preferentially with elastic scattering angle regions: (a)  $100^\circ < \theta_{\text{CM}} < 130^\circ$ , and (b)  $50^\circ < \theta_{\text{CM}} < 80^\circ$ . The dashed lines represent the continuous contributions from dynamic and nuclear processes, corrected for detection efficiency, and normalized to the data excluding the peak region. (Reproduced from [Shw83].)

certainly principle, the spontaneously emitted positrons are also distributed over  $\Delta E_{e^+} \geq 300$  keV so no narrow peak is expected. Next, the spontaneous amplitude adds coherently with a much larger "dynamic" positron contribution which is produced by the rapid time variation of the strong electric fields [Smi74, Sof77]. Finally, an additional broad positron background (indicated by the dashed line in Fig. 1-2b) arises from internal pair creation of transitions excited in the individual nuclei [Obe76, Obe76b]. In principle, if the collision time is prolonged by nuclear reactions, the spontaneous positron signal becomes larger and narrower [Rei81b], as indicated schematically in Fig. 1-2c. Perhaps coincidentally, the  $1\sigma$  binding energy calculated for the internuclear distance of closest approach achievable in central U+Cm collisions at the measured beam energy of  $\sim 6$  MeV/u corresponds closely to the energy of the positron peak in Fig. 1-1.

For an exhaustive list of references to this field as well as comprehensive discussions of the theoretical details of spontaneous positron emission and the experimental developments which led up to the present work, the reader is referred to the

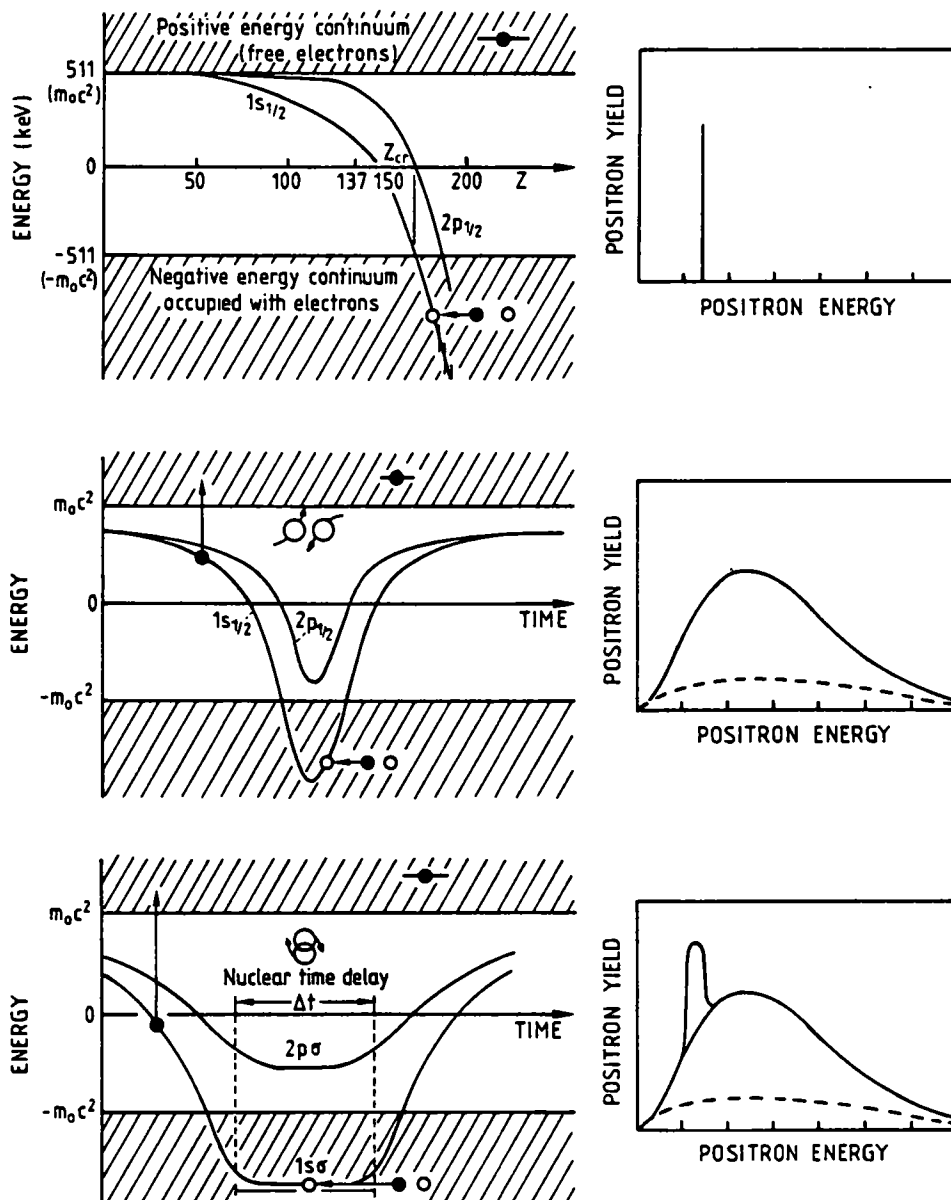


**Figure 1-2.** Binding energy of the  $1\sigma$  orbital versus a static nuclear charge,  $Z$  (top). For  $Z > 173$ , a vacancy decays spontaneously with a time,  $\tau_{sp} = 10^{-19}$  s, liberating a monoenergetic positron. Middle panel illustrates time evolution of the binding energy in a heavy-ion collision, which produces a broad distribution of spontaneous and dynamically induced positrons (solid curve). Internal pair creation from transitions in the Coulomb excited nuclei produces a nuclear positron background (dashed line). Emergence of a narrow spontaneous peak for collisions with prolonged nuclear contact is indicated schematically in the lower panel. (Reproduced from [Vin83].)

the Ph.D. dissertation of J. Schweppe [Shw85], and the review articles of Greenberg and Vincent [Gre85] and Reinhardt and Greiner [Rei85].<sup>1</sup>

## Section 1.2 Present Work

This dissertation reports on a continuation of the EPOS experiments mentioned above, with the goal of determining the source of the anomalous positron peak structures. Two investigations have been pursued towards this goal. First, the dependence of the peak production on the combined nuclear charge,  $Z_U$ , of the collision system is investigated. This is motivated by the unusual  $Z_U \sim 20$  power law dependence of the binding energy of the quasimolecular  $1s\sigma$  orbital expected from QED [Rei81]. For internuclear separations achievable for bombarding energies at the Coulomb barrier, spontaneous emission is predicted to occur above a threshold of  $Z_U \cong 178$ , and the positron peak energy should increase by  $\sim 30$  keV with each additional unit of charge. Positron emission has therefore been measured for several combinations of target and projectile nuclei chosen to cover a range extending throughout the supercritical range available from U+Cm ( $Z_U = 188$ ) to Th+Th ( $Z_U = 180$ ). The subcritical Th+Ta system ( $Z_U = 163$ ) was studied to examine positron emission well below the critical charge threshold.

The second investigation was directed toward establishing the identity of the system emitting the peaks by exploiting the Doppler broadening of the positron lines in order to measure the velocity of the source. An origin directly involving the quasimolecular system, such as spontaneous vacuum decay, is characterized by an emitter velocity equal to that of the heavy-ion center-of-mass system. Positrons from other sources could exhibit different emitter velocities and hence Doppler broadened linewidths. For example, the broadening of peaks emitted from the individual nuclei would vary with the recoil angle, and hence velocity, of the scattered ion. In order to further investigate the specific possibility that nuclear transitions produce the peaks, electrons and  $\gamma$ -rays were measured simultaneously with positrons in order to search for the competing internal conversion or  $\gamma$ -ray decay channels.

In order to perform the  $Z_U$  dependence and emitter velocity measurements, the EPOS Solenoid spectrometer required various modifications. For example, to trace the  $Z_U$  dependence of the positron peak energy throughout the range expected for spontaneous positron emission (from  $\sim 300$  keV at  $Z_U = 188$  to  $\sim 80$  keV at  $Z_U = 180$ ),

---

1

Other recent reviews include [Grn83, Bac85, Bos86, Kie86, Grn87] and references therein.

the positron detection efficiency had to be extended to lower energies. The magnetic field configuration was therefore rearranged, the spiral baffle redesigned, and the previous positron detector replaced with a new Si(Li) counter having a sensitive front surface. In addition to extending the spectrometer band-pass to below 100 keV, these improvements increased the absolute detection efficiency by more than a factor of-two. This provided higher data accumulation rates and greater sensitivity to the relatively small ( $\sim \mu\text{b/sr}$ ) peak signals. Insights into the detailed operation of the solenoid magnetic transport system gained while optimizing the efficiency led to substantially improved computational models of the spectrometer performance. This has, in turn, benefitted the emitter velocity measurement by making possible accurate calculations of the Doppler-broadened positron lineshape. Both the efficiency and lineshape response have been directly confirmed with a variety of radioactive source and in-beam measurements.

A detailed understanding of the EPOS spectrometer is very important from the additional point of view of investigating whether structure in the energy distribution of positrons emitted from the superheavy collisions can be produced by some purely instrumental means or as a trivial background. The eventual interpretation of the peak structures obviously depends on being able to predict the response of the spectrometer to positrons created in the collision and positrons of nuclear and other origins, as well as to other radiations (e.g.,  $\gamma$ -rays, neutrons, or electrons) interacting in the apparatus. A major portion of this dissertation has therefore entailed the analysis of the characteristics of the EPOS spectrometer and its response under a variety of conditions.

The results of this systematic study of positron peak production [Cow85] led to a second major experimental program – namely, the search for a correlated monoenergetic electron signal. In particular, in each collision system investigated, peaks were found which are emitted from a source moving with a mean laboratory velocity consistent with the velocity of the CMS, and which could not be attributed to nuclear transitions in the ejectiles. The nearly constant energy of the peaks observed throughout the range from subcritical to supercritical nuclear charges suggests a common source not associated with spontaneous positron emission. One possibility is the two-body decay of a previously undetected neutral object into a positron-electron pair. To investigate this possibility, we modified the EPOS spectrometer to search for a monoenergetic electron associated with each positron peak. The magnetic field configuration was again rearranged and a new large area

electron counter installed to detect, with high efficiency, electrons *in coincidence* with positrons.

Monoenergetic electron peaks in coincidence with narrow positron lines have been discovered in U+Th, Th+Th, and Th+Cm collisions [Cow86, Cow86b]. The corresponding peaks in the distribution of the sum of the electron and positron energies are narrower than the individual  $e^+$  or  $e^-$  lines, suggesting the correlated cancellation of Doppler shifts expected for back-to-back emission characteristic of a two-body final state. The feasibility of a variety of other sources for the positron-electron coincidence signal (e.g., nuclear conversions, atomic oscillations, or background radiations) have been investigated by simulating the response of the EPOS spectrometer to Monte-Carlo generated events. A kinematic analysis of the coincidence positron, electron, sum-energy and  $e^+e^-$  difference-energy peak shapes provides an indirect measurement of the angular correlation between the monoenergetic positron and electron in the rest frame of the emitter. Within the context of a two-body decay origin, Monte-Carlo simulations are also used to study the velocity and angular distributions of the emitting source.

### Section 1.3 Organization

Because of the significant changes in the experimental apparatus and differences in approach between the investigations of the single positron lines and the coincidence electron-positron structures, this dissertation is divided into two parts. Part I, consisting of chapters two through four, covers the investigation of the  $Z_U$  dependence of the positron peak structures and the measurement of the emitter velocity, including an evaluation of nuclear background processes. Chapter 2 describes the EPOS spectrometer, highlighting changes made to the pre-existing instrument which were necessary for the present experiments. As noted above, particular emphasis is placed on the operation of the positron detection system. Experimental contributions by other members of the EPOS collaboration – including improvements to the heavy-ion gas detectors, the design of the electron detector used in Part I of this thesis to search for internal conversion transitions, and the fabrication and independent study of the actinide targets – are also briefly described.

Chapter 3 reviews the data analysis procedures and presents the results of the measurements on six collision systems:  $^{238}\text{U} + ^{248}\text{Cm}$ ,  $^{232}\text{Th} + ^{248}\text{Cm}$ ,  $^{238}\text{U} + ^{238}\text{U}$ ,  $^{232}\text{Th} + ^{238}\text{U}$ ,  $^{232}\text{Th} + ^{232}\text{Th}$ , and  $^{232}\text{Th} + ^{181}\text{Ta}$ . The characteristics of the positron peaks

are described, as well as the dependence of their production on beam energy, HI scattering angle, and  $Z_U$ . The dynamic positron energy distribution is discussed insofar as it determines the background beneath the positron peaks. Chapter 4 presents an analysis of several possible origins for the positron lines including instrumental effects, nuclear conversions, spontaneous positron emission, and various interference effects. Although many of these have subsequently been ruled out by the existence of a correlated monoenergetic electron peak, they are discussed in the present work for completeness and because of their historical importance.

Part II of this dissertation describes the search for, and analysis of, coincident monoenergetic positron-electron emission in superheavy collisions. Chapter 5 begins with a discussion of some prerequisite considerations including the anticipated signal for two-body decay. Modifications to the EPOS spectrometer required for the coincidence experiment are then described. The spectrometer's performance, particularly regarding the coincidence detection of positrons and electrons, is analyzed using Monte-Carlo simulations and source measurements. Particular emphasis is again placed on understanding the detailed operation of the solenoid in order to assess various backgrounds and interpretations of the coincidence peak data.

Results of the search for a coincidence electron line are presented in Chapter 6. Measurements of the  $^{238}\text{U} + ^{232}\text{Th}$ ,  $^{232}\text{Th} + ^{232}\text{Th}$ , and  $^{232}\text{Th} + ^{248}\text{Cm}$  systems are described covering data from two different experiments. Chapter 7 presents an analysis of several possible origins for the coincidence signals. Monte-Carlo simulations are again used to compare various conventional and exotic nuclear, atomic, and background processes to the data. A kinematic analysis of the angular correlation between the emitted positron and electron is presented, and the momentum distribution of the neutral object is discussed.

Chapter 8 concludes this dissertation with a summary of the observations associated with the positron peaks and coincidence electron lines. Our present understanding of the data is reviewed in light of the current popular theoretical speculations regarding the origins of the peaks, and several remaining unanswered questions are addressed. Prospects for advancing the experimental situation in the near future are briefly discussed.

***Part I. Anomalous Positron Peaks from  
Superheavy Collisions***

# Chapter 2 Experimental Apparatus

## Section 2.1 Overview of EPOS Spectrometer

The first part of this dissertation describes an investigation of the  $Z_U$  dependence of monoenergetic positron production in superheavy collisions. In addition, the velocity of the source emitting the peaks is measured by the Doppler broadening, and peak origins involving nuclear transitions are studied. The data presented here were measured at the Gesellschaft für Schwerionenforschung in Darmstadt, West Germany, using the *Electron-POsitrone Solenoid (EPOS) Spectrometer*. The relevant configuration used for Part I of this work is shown in Fig. 2-1. The spectrometer and several additional aspects of the current work have evolved over the course of this thesis research from earlier experiments with the EPOS apparatus. The previous versions, described in detail in [Shw85, Gru85 and Gre85], were used to study dynamic positron production and to search for indications of spontaneous positron emission. These measurements culminated in the discovery of the narrow positron peak in the U + Cm system, presented in Fig. 1-1.

As discussed in [Shw85] and [Gre85], the EPOS spectrometer was designed primarily to address the principal difficulty associated with measuring positrons in the superheavy collision environment, namely the small size of the signal immersed in a large background of other radiations. This situation is summarized by Fig. 2-2 (adapted from [Shw85]) which shows that  $\gamma$ -rays and  $\delta$ -electrons are emitted in the HI collision with a factor of  $10^5$  to  $10^6$  larger probability than the positron peaks under investigation (denoted by shaded region). The EPOS solenoid deals with this problem by transporting positrons away from the high flux of neutral  $\gamma$ - and X-rays and heavy nuclear particles, which are localized near the target site, to a well shielded background-free region where their energy is measured in a solid-state detector. This technique was pioneered by Greenberg to measure rare internal pair creation in beta decay [Gre56] and later adapted for in-beam electron spectroscopy in HI collisions [Bur65, Kot69]. It exploits the axial focussing properties of the solenoid field in which a positron (or electron) emitted from a target placed on the axis of the magnetic field, traces out spiraling orbits which repeatedly return to the spectrometer axis. The helical trajectories are eventually intercepted by a thin pencil-like Si(Li) detector, where the positron energy is measured with  $\sim 12$  keV resolution.

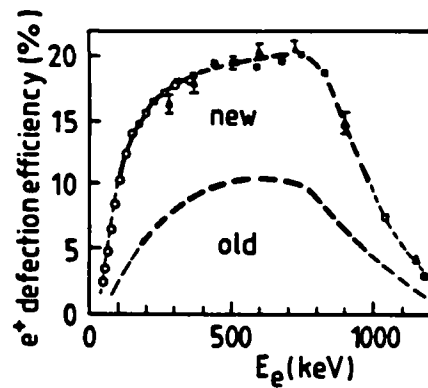
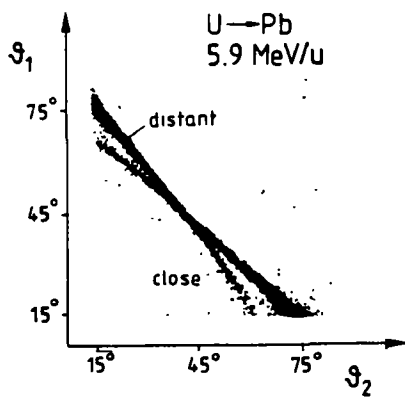
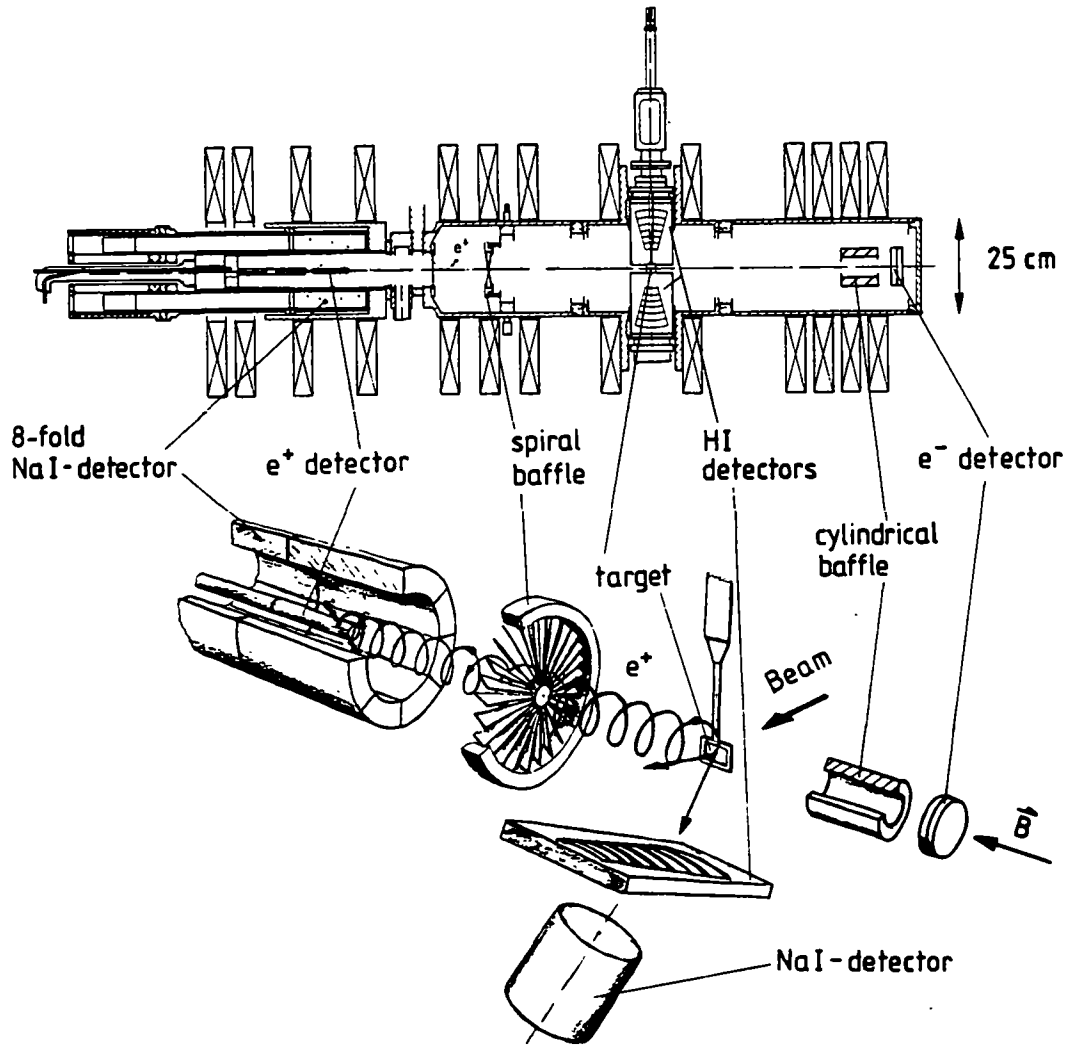


**Figure 2-1.** Schematic view of the EPOS spectrometer. Lower left illustrates detection of both scattered ions in kinematic coincidence. Positron detection efficiency (lower right) shown for present ("new") and previous ("old") EPOS configurations.

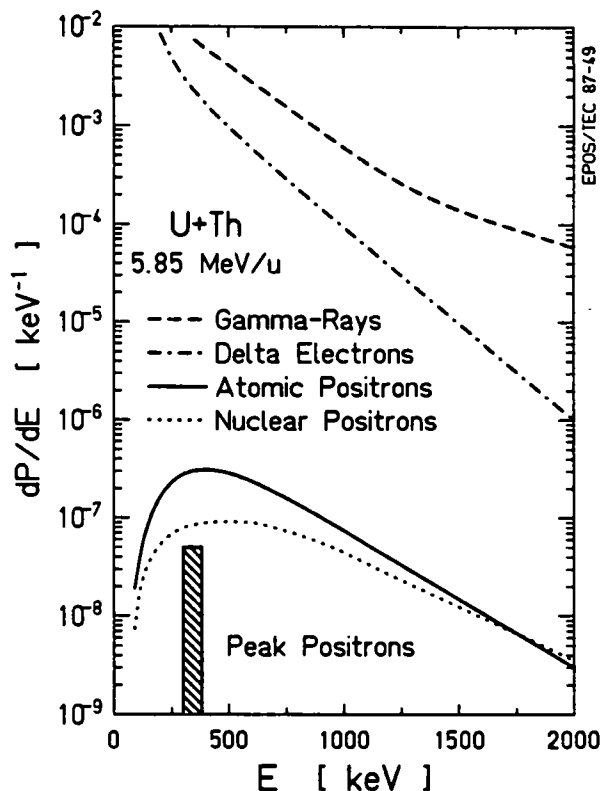


**Figure 2-2.** Production probability (per HI scattered into  $25^\circ < \theta_{lab} < 65^\circ$ ) of  $\gamma$ -rays,  $\delta$ -electrons, and dynamic and nuclear IPC positrons in 5.85 MeV/u U+Th collisions. Shaded region denotes the approximate size of the positron peaks under investigation. (Adapted from [Shw85].)

Positrons initially moving away from the Si(Li) detector enter a region of increased field strength, and those emitted with angles steeper than  $35^\circ$  with respect to the solenoid axis are reflected. About 90% of all positrons emitted isotropically over  $4\pi$  are therefore transported toward the Si(Li). The huge flux of electrons, which are also transported by the solenoid field, are mechanically blocked from reaching the detector by a fan-shaped spiral baffle which exploits the opposite spiralling direction of the positron and electron orbits. Positrons are unambiguously identified by the coincident measurement of their 511 keV annihilation radiation in a cylindrical array of eight NaI(Tl) crystals mounted around the Si(Li) detector. Improvements in the present apparatus include a redesigned magnetic field configuration, a new spiral baffle, and the addition of a sensitive front surface to the cylindrical positron detector. These combine to provide a factor of  $> 2$  increase in detection efficiency over the previous EPOS set-up [Shw85], as shown in Fig. 2-1d. A maximum positron detection probability of 20% is achieved, with  $\epsilon_{e^+} > 10\%$  over a broad range of ener-

gies extending from  $\sim 100$  keV to 1.0 MeV. Collection of positrons over nearly  $4\pi$  leads to the maximum Doppler broadening, measured in the laboratory, of intrinsically narrow peaks. For emission of 350 keV positrons from the CM system, this broadening amounts to  $\Delta E_{e^+} = 77.7$  keV (FWHM), with a shift of the peak centroid of  $\delta E_{e^+} = 1.3$  keV. As long as the intrinsic width is small, high resolution measurement of the positron linewidth provides direct information regarding the mean laboratory velocity of the source emitting the  $e^+$  peak.

The small cross-sectional area of the pencil-like Si(Li) detector perpendicular to the axis presents only a very small solid angle ( $10^{-5}$  of  $4\pi$ ) for  $\gamma$ -rays and neutrons emitted from the target. The direct flux of X- and  $\gamma$ -rays is further attenuated by a tantalum disk in the center of the spiral baffle. The axial arrangement of the positron detector ensures that particles created or scattered away from the solenoid axis have a significantly reduced probability for detection. In order to reduce the creation of secondary positrons from external conversion or beam activation, material near the solenoid axis is kept to a minimum. The necessary baffles and target frame are constructed of low-Z material, and the Ta baffle disk is encased in plexiglas to absorb externally converted pairs.

Positrons are detected in coincidence with the scattered projectile and target recoil ions which are measured in two Parallel Plate Avalanche Counters (PPAC's) equipped with continuous delay-line readouts. Detection of both nuclear ejectiles substantially determines the reaction kinematics over the full laboratory angular range of  $20^\circ < \theta_{HI} < 70^\circ$ . The good angular resolution ( $\sim 1^\circ$ ) achieved in the earlier experiments of [Shw85] proved to be very important in isolating the peak structure in the U+Cm system. For these experiments, the intrinsic scattering angle resolution has therefore been improved to  $\delta\theta_{lab} \sim 0.5^\circ$ , and the azimuthal angle of the scattering plane is now measured by a  $\phi$ -sensitive anode foil in order to further enhance the kinematic definition. Under typical in-beam conditions using  $\sim 300$   $\mu\text{g}/\text{cm}^2$  targets, the sum of the polar scattering angles measured in the upper and lower PPAC's,  $\Sigma\theta_{HI} = \theta_U + \theta_L$ , is determined with  $0.8^\circ$  resolution (FWHM). The  $\Sigma\theta_{HI}$  coordinate is directly related to the kinetic energy lost or transferred to excitation of the ions (Q-value) and also reflects the mass-ratio of the ejectiles. The equivalent resolution in Q-value is  $\delta Q = 20$  MeV (FWHM), with a mass resolution of  $\delta M \sim 10$  amu. For the slightly asymmetric Th+Cm collision system, the angular resolution is adequate to almost completely resolve forward from backward scattering.

Nuclear  $\gamma$  radiation is monitored with two 3"x3" NaI(Tl) detectors placed at  $45^\circ$  in the forward and backward direction with respect to the beam axis. As described in [Shw85], convolution of the observed  $\gamma$ -ray energy distribution with theoretical IPC coefficients gives the continuous positron contribution arising from nuclear internal pair creation. The detectors are operated in coincidence with the heavy-ion PPAC's, simultaneously with the positron measurement. Origins for the positron peaks involving nuclear transitions are investigated by searching the  $\gamma$ -ray energy distribution for competing conversion lines under conditions identical to those which yield the positron lines.

To extend the study of nuclear origins to non  $\gamma$ -ray emitting transitions (i.e., electric monopole), a Si(Li) detector to detect internal conversion (IC) electrons has been added to the apparatus for these measurements. It is placed on the axis beyond the magnetic mirror field so that it accepts electrons emitted at very flat angles with respect to the axis which are not reflected back toward the positron detector. A tubular baffle system reduces the angular acceptance to  $\theta_{e^-} \leq 10^\circ$ , which limits the Doppler broadening of electron energies above 1 MeV, where nuclear IC electron lines would be expected in competition with the positron peak, to  $\Delta E_{e^-} \sim 80$  keV. Because internal conversion normally exceeds positron emitting decays by several orders of magnitude, although the electron detection efficiency ( $\epsilon_{e^-} \sim 0.5\%$ ) is small compared to  $\epsilon_{e^+}$ , it provides sufficient sensitivity to investigate E0 transitions.

Earlier results from U + Cm collisions [Shw83] indicated that the observation of the positron line is associated with a narrow range of projectile energies, suggesting that resonant nuclear reactions may play an important role in peak production. It was also found that the curium targets used were non-uniform and changed their thickness profile rapidly during irradiation. In order to pursue a measurement of the beam-energy dependence of peak production, a program of improving target uniformity and stability, and of defining and measuring the beam energy, was undertaken. For the most recent experiments, this has culminated in the installation of a non-destructive beam time-of-flight probe in the EPOS beamline. The mean energy was maintained to within 0.02-0.03 MeV/u during an experiment. The thin targets used, typically  $\sim 250 \mu\text{g}/\text{cm}^2$ , were changed every  $\sim 1\frac{1}{2}$  hours, and the beam current was limited to  $\cong 1$  PnA (particle nanoampere), to reduce target deterioration. After irradiation, the thickness and uniformity were sampled for several targets by proton

backscattering measurements performed with the University of Frankfurt Van de Graaff accelerator.

Finally, as described in [Shw85], the time and energy information from the positron, annihilation radiation, heavy-ion,  $\gamma$ -ray, electron, and monitor detectors were read with a CAMAC based data-acquisition system and written event-by-event to magnetic tape. A preliminary on-line analysis of the data provided real-time monitoring of the status of the beam, targets, and detectors, as well as a check of the quality of the incoming data.

The following sections treat in greater detail each of the experimental components. Section 2.2 describes the positron detection system and its performance. Sections 2.3-2.5 discuss the PPAC's,  $\gamma$ -ray, and electron detectors. The fabrication, in-beam behavior, and post-irradiation measurements of the actinide targets are presented in Sec. 2.6, and Sec. 2.7 discusses the UNILAC beam characteristics. For simplicity, the developments in improving beam and target quality which chronologically belong to Part II of this dissertation are included here. Finally, the experimental electronics and data-acquisition system are summarized in Sec. 2.8.

## **Section 2.2 Positron Detection**

Detection of positrons in the EPOS spectrometer involves four principal components: the solenoid transport field, the spiral baffle, the positron Si(Li) detector, and the eight-fold NaI annihilation radiation detector (ARD). In this section, the physical characteristics and operation of each of these components are reviewed (for more details the reader is referred to [Shw85]). As mentioned in the introduction, it is particularly important in interpreting the data to understand the details of the transport efficiency of the spectrometer. One central question throughout this discussion is whether instrumental effects can produce structure in the positron energy distribution. The way in which these components combine to determine the positron detection efficiency is therefore studied, and the results of numerical calculations are compared to direct measurements involving radioactive sources. This section concludes with a derivation of the Doppler-broadened lineshape response of the EPOS spectrometer to a moving positron source. The effects on the lineshape and efficiency of a positron angular distribution, off-axis emission, source velocity, and emitter lifetime are discussed.

## Sec. 2.2.1 Solenoid Transport Field

**Sec. 2.2.1.1 Definition of Coordinates:** Throughout the following discussions of the solenoid transport system and detection efficiency, the following coordinate systems are used. The solenoid coordinate system is aligned with its Z-axis along the rotational-symmetry-axis of the EPOS-spectrometer. The origin is placed at the target position and the +Z direction is toward the positron detector. +X is in the beam direction (forward) and +Y is aligned vertically upward. The solenoid magnetic field vector points in the +Z direction, and the position of a positron or electron in the solenoid is described by the cylindrical coordinates  $(r, \phi, z)$ . The motion of the positron about its guiding center is denoted by radius  $\rho$ , and azimuthal angle,  $\psi$ . The polar angle between the positron path and the +Z direction is  $\theta$ . CGS units are used throughout and  $P_{e+}$  denotes momentum,  $\beta_{e+} = v_{e+}/c$  is velocity,  $m_e c^2$  is the positron (electron) mass, and  $B$  is the magnetic field strength. The quantity  $mc^2/e = 1705$  Gauss-cm is useful for numerical calculations of the positron orbit.

**Sec. 2.2.1.2 Positron Motion in the Magnetic Field:** Positrons and electrons move in the the solenoid magnetic field guided by the Lorentz force,

$$d\vec{p}^*/dt = e/c(\vec{v}^* \times \vec{B}^*), \quad (2.1)$$

with

$$dE/dt = 0.$$

As described in Sec. 12.3 of [Jac75], for a uniform magnetic field along the Z-axis, the longitudinal motion in the Z direction is completely decoupled from the cyclical transverse motion. A positron emitted at polar angle  $\theta_0$  traces out circular orbits of radius

$$\rho = (p_{\perp} c/eB) = (pc/eB) \sin\theta_0, \quad (2.2)$$

with a (counterclockwise) rotational frequency about the guiding center of

$$d\psi/dt = -\omega = -eB/\gamma mc, \quad (2.3)$$

where  $\gamma = (1 - \beta_{e+}^2)^{-1/2}$ . It completes one orbit in a time

$$T = |2\pi/(d\psi/dt)| = 2\pi/\omega = 2\pi(\gamma mc/eB). \quad (2.4)$$

The positron simultaneously drifts parallel to the field with constant velocity

$$v_{\parallel} = v_e + \cos(\theta_0). \quad (2.5)$$

The trajectory repeatedly crosses the field line which passes through the point of emission. The positron travels a distance of

$$L = v_{\parallel}T = 2\pi(pc/eB)\cos\theta_0 \quad (2.6)$$

along the Z-axis during each orbit. The trajectory resembles a helix of pitch angle  $\theta$  and pitch length L.

The EPOS magnetic field is not uniform (see Fig. 2-5). It varies slowly enough as a function of position along the Z-axis, compared to a single positron or electron orbit, however, that the positron and electron orbital motion remains adiabatic. As discussed in Sec. 12.6 of [Jac75], the magnetic flux linked by a given orbit,  $\pi\rho^2B$ , is therefore a constant of motion. From Eqn. 2.2, this gives  $v_{\perp}^2/B = \text{constant}$ . The radial velocity then depends on the field strength, and at any position along the axis,

$$v_{\perp}^2/B = v_{\perp 0}^2/B_0, \quad (2.7)$$

where the subscript "o" refers to the velocity or field strength at the initial position of the trajectory (usually the target site,  $Z = 0$ ). From conservation of energy,  $v_{\perp}^2 + v_{\parallel}^2 = v_0^2$ , the velocity in the Z direction is

$$v_{\parallel}^2 = v_0^2 - v_{\perp 0}^2 (B/B_0). \quad (2.8)$$

From Eqns. 2.7-2.8 and the definitions above, the trajectory parameters at any position Z are given by

$$\omega = eB/\gamma mc = \omega_0(B/B_0), \quad (2.9)$$

$$\theta = \sin^{-1}[(B/B_0)^{1/2} \sin\theta_0], \quad (2.10)$$

$$\rho = (pc/eB) \sin\theta = \rho_0(B_0/B)^{1/2}, \quad (2.11)$$

$$L = 2\pi(pc/eB) \cos\theta = 2\pi(pc/eB_0)(B_0/B)[1-(B/B_0)\sin^2\theta_0]^{1/2}. \quad (2.12)$$

The orbiting positron still repeatedly crosses the field-line which passes through the point of its emission. A positron emitted from the symmetry axis of the solenoid always returns to the axis. Similarly, a positron emitted away from the axis, or scattered from an object off-axis, generally does not pass through the z-axis. This property originally motivated the axial arrangement of the EPOS apparatus with target and detector placed on the solenoid symmetry axis [Gre56, Bur65, Kot70, Shw85, and Gru85].

Equations 2.7-2.12 indicate that as the positron drifts into a region of increased magnetic field strength ( $B > B_0$ ), the orbital radius  $\rho$  decreases, the pitch-angle  $\theta$  steepens, the rotation frequency  $\omega$  increases, the pitch-length  $L$  is reduced, and the velocity along the axis  $v_{\parallel}$  is decreased. The opposite occurs in a weaker field. These relationships are summarized graphically in Figs. 2-3(a-d). Finally, radial gradients of the solenoid field,  $B$ , cause the guiding center of the trajectory to precess slowly around the solenoid axis with a drift velocity (given by Eqn. 12.55 in [Jac75]) of

$$v_{\text{drift}} = \frac{1}{2} v_{\perp} \rho B^{-1} (\partial B / \partial r), \quad (2.13)$$

where  $v_{\perp}$  and  $\rho$  are given by Eqns. 2.7, 2.11.

**Sec. 2.2.1.3 Field Coils:** The EPOS magnetic field itself is produced by 15 pancake coils of 27 cm inner diameter, powered by two 200 kW power supplies. As shown in Fig. 2-4a, each coil consists of 4 planes of 18 windings of 1 cm square copper channel, with a center-to-center spacing of 1.1 cm. The resistance of each coil is  $\cong 0.025$  ohms. Cooling water flows through the center of the hollow channels at  $\sim 8$  bar. The magnetic field along the z-axis is given by superposition of the field strengths, given exactly by Biot-Savat's law,

$$B(z; l, r, z_0) = (2\pi l / c) r^2 [r^2 + (z - z_0)^2]^{-3/2}, \quad (2.14)$$

where  $l$  is the current and  $a$  the radius of the given loop centered at  $Z = z_0$ . The summation over the current loops in each coil is given explicitly by

$$B(z) = \sum_{i=1}^4 \sum_{j=1}^{18} \sum_{k=1}^8 (1/8) B(z; l, r_{ijk}, z_{ijk}), \quad (2.15)$$

with,

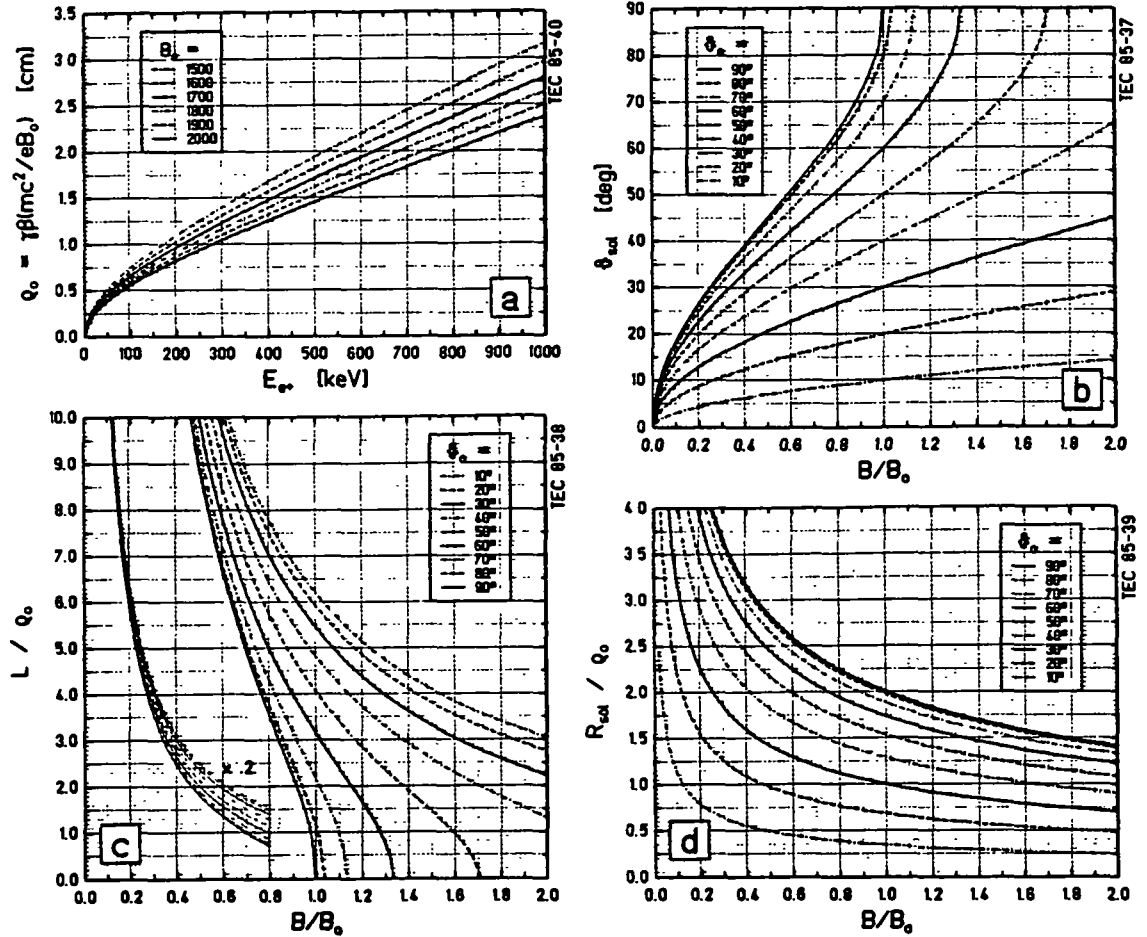


**Figure 2-3.** Adiabatic calculation of positron orbital parameters versus the solenoid magnetic field strength, relative to that at the target site. (a) Maximum gyration radius vs.  $E_{e^+}$ . (b) Pitch-angle, (c) Pitch-length, and (d) Orbital diameter.

$$r_{ijk} = 12.95 + 1.1 \cdot j + r_k,$$

$$z_{ijk} = 1.1 \cdot i - 2.75 + z_k,$$

where the  $r$  and  $z$  are in cm and the offsets  $(r_k, z_k)$  correspond to eight current loops at eight points equally spaced around each of the square copper windings  $[(r_k, z_k) = (+\frac{1}{2}, +\frac{1}{2}), (0, +\frac{1}{2}), (-\frac{1}{2}, +\frac{1}{2}), (-\frac{1}{2}, 0), (-\frac{1}{2}, -\frac{1}{2}), (0, -\frac{1}{2}), (+\frac{1}{2}, -\frac{1}{2}), (+\frac{1}{2}, 0)]$ . Figure 2-4b compares the calculated magnetic field using Eqn. 2.15 to the actual value measured for a prototype coil with a Hall probe. They agree to within 2%.

The positions of each of the 15 coils that produce the EPOS solenoid field are shown in Fig. 2-5. The coils on the  $-Z$  side of the target are powered with a single current supply at 495 amps. On the  $+Z$  side of the spectrometer, the coils are op-

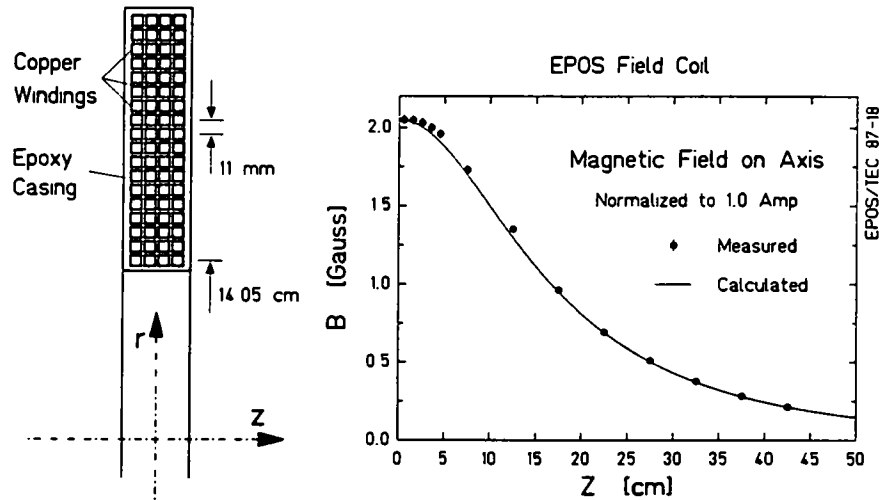


**Figure 2-4.** Cross-sectional view of an EPOS pancake coil showing dimensions of the  $1 \times 1 \text{ cm}^2$  Cu windings (left). Comparison of the calculated magnetic field strength along the solenoid axis to Hall probe measurements [Shu80] of a prototype coil (right).

erated with the second supply at 450 amps. The total power is  $\cong 80 \text{ kW}$ . At the target position the magnetic field strength is  $B_0 = 1872 \text{ Gauss}$ . A 350 keV positron or electron emitted at  $\theta_0 = 90^\circ$  therefore orbits with a gyration radius of  $\rho = 1.23 \text{ cm}$ , extending to a maximum 2.46 cm from the axis. It completes one orbit every  $T = 3.4 \times 10^{-10} \text{ sec}$ . The orbital pitch-length is  $L = 7.73 \cdot \cos\theta_0 \text{ cm}$ .

In the leg opposite the positron detector (i.e.,  $-Z$  direction), the magnetic field strength increases (six coils operating at 495 amps are placed close together) to a maximum of 5700 Gauss (at  $Z = -58 \text{ cm}$  from the target). As positrons which are emitted with  $\theta_0 > 90^\circ$  drift into this region of stronger field, their longitudinal velocity, given by Eqn. 2.8, is reduced until  $v_{\parallel}$  reaches zero and reverses direction at a position  $z$  such that,

$$\sin^2\theta_0 = B_0/B(z), \quad (2.16)$$

where the positron is "reflected." The steepest emission angle for which the positron penetrates the magnetic mirror, that is, the flattest emission angle which is reflected at the position of the maximum field strength, is

$$\begin{aligned} \theta_{\text{mir}} &= \sin^{-1}(B_0/B_{\text{max}})^{1/2} \\ &= \sin^{-1}(1872/5700)^{1/2} = 34.97^\circ. \end{aligned} \quad (2.17)$$

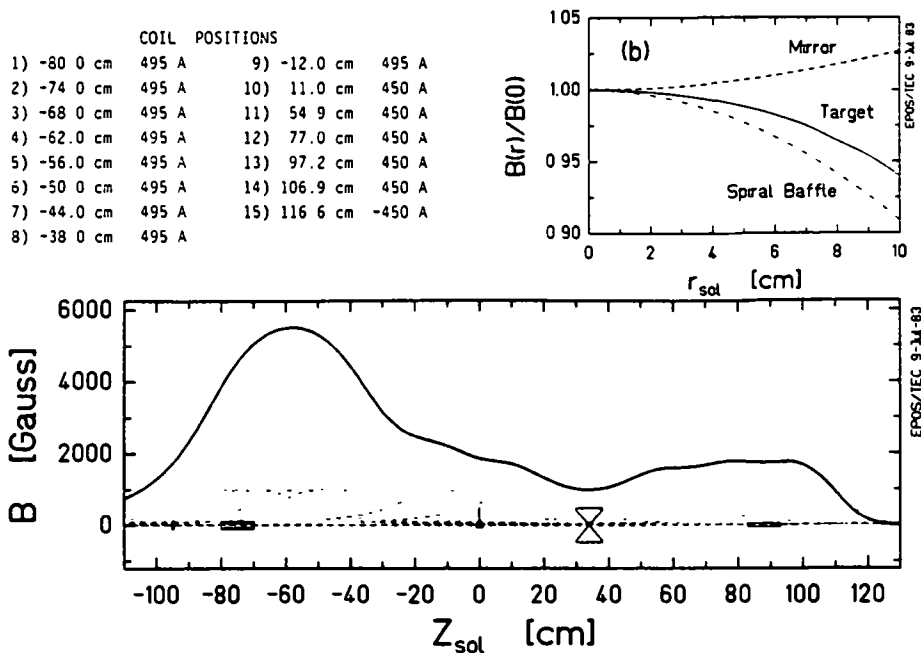


**Figure 2-5.** EPOS magnetic field along the solenoid axis (bottom) produced by the field coils operated at the currents and positions as marked (upper left). The inset (b) shows the radial dependence of the strength of the magnetic field at the position of the target, spiral baffle, and the maximum of the mirror field.

All positrons emitted from  $0^\circ$  to  $(\pi - \theta_{\text{mir}})$  are therefore transmitted toward the spiral baffle and positron detector. This amounts to a solid angle for collection of 91% of  $4\pi$ . As discussed in Sec. 2.5, electrons emitted with  $\theta_0 > (\pi - 35^\circ)$  may penetrate the magnetic mirror and are transported toward the electron detector positioned at  $Z = -96$  cm.

In order to maintain high positron collection efficiency, the magnetic field along the  $+Z$  axis is uniformly lower than at the target site. No magnetic mirrors then limit the transport efficiency of steeply emitted positrons on their way to the  $e^+$  detector. The dip in the magnetic field at the spiral baffle serves both to adjust the mean orbital pitch angle of positrons to the baffle acceptance, and to trap positrons or electrons scattered at the baffle in a magnetic bottle. Both of these effects are discussed more fully below. Finally, the last coil positioned at  $Z = +116$  cm is operated with reversed polarity (-450 amps) to reduce the magnetic field in the region beyond the positron detector to  $B \cong 0$  Gauss in order to provide a low-field environment for the ARD's photomultiplier tubes.

In previous experiments [Shw85], the mirror and target fields were  $B_{\text{mir}} = 3945$  and  $B_0 = 1835$  Gauss, respectively. The reflection angle was  $\theta_{\text{mir}} \cong 137^\circ$ . In addition, a shallow magnetic bottle centered at the target trapped positrons emitted with angles steeper than  $83.2^\circ$ . Positrons were therefore collected over only 74.8% of  $4\pi$ , so the present arrangement amounts to a 22% increase in detection efficiency over that of earlier measurements.

The radial dependence of the magnetic field strength at the target, magnetic mirror, and spiral baffle is shown in Fig. 2-5b. Averaged over the size ( $R = 2\rho$ ) of a 350 keV positron orbit, the variation in the magnetic field is on the order of

$$\Delta B/B = B^{-1} (\partial B/\partial r) \cdot 2\rho \cong \pm 2 \times 10^{-3}. \quad (2.18)$$

From Eqn. 2.13, the precession velocity of the guiding center about the solenoid axis is then

$$v_{\text{drift}} = v_{\perp} \cdot 5 \times 10^{-4} \cong 0.12 \text{ mm/ns}. \quad (2.19)$$

As shown below, the average positron flight time is  $\sim 10$  ns, so the guiding center typically shifts by less than 2 mm, or  $< 10^\circ$ , in the  $-\phi$  direction.

### **Sec. 2.2.2 Spiral Baffle**

The success of the magnetic transport system in providing a clean, background-free environment for positron identification and measurement depends critically on the efficient suppression of the huge flood of low energy  $\delta$ -electrons which are simultaneously transported from the target site. As shown in Fig. 2-2, production of electrons exceeds that of positrons by four to five orders of magnitude in the interesting range for studying peaks,  $E_{e^+} < 500$  keV. It is therefore necessary to suppress the detection of electrons relative to positrons by a factor of  $10^2$ - $10^3$  in order to limit pileup of electrons with the positrons to less than 10%.

As mentioned in Sec. 2.1, the operation of the spiral baffle exploits the opposite spiraling directions of positrons and electrons to mechanically block electrons from reaching the  $e^+$  detector. As viewed from the target toward the baffle, positrons orbit in a left-handed sense, and electrons with a right-handed helicity. The baffle therefore resembles a left-handed six-bladed propeller, as shown in Fig. 2-6. The

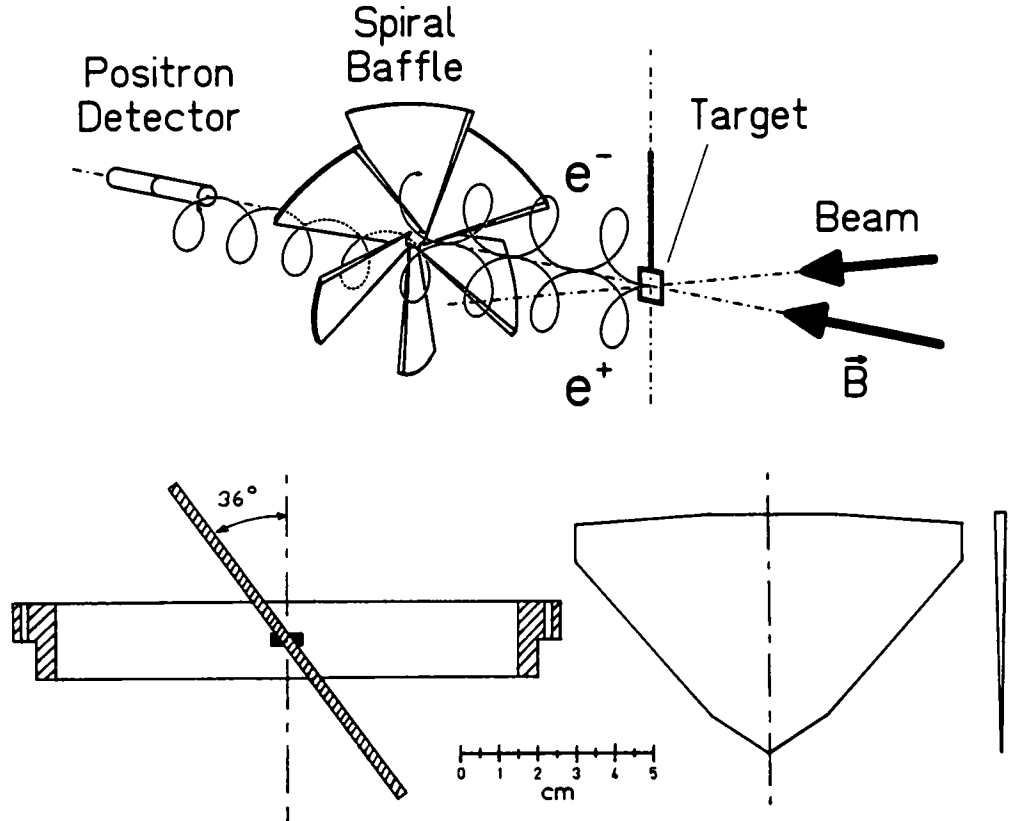


**Figure 2-6.** Diagram of the fan-shaped spiral baffle (top) illustrating how positrons pass between the blades while electrons, having opposite orbital helicity, are stopped by the blades. Dimensions and orientation of the six baffle blades are given in the lower panel.

present baffle is placed  $Z_{\text{baf}} = 34$  cm from the target. Each blade has a width  $w(R)$  and thickness  $t(R)$ , where  $R$  is the radial distance along its centerline, given by

$$w(R) = \begin{cases} 3 \cdot R & \text{cm, for } 0 < R < 1 \text{ cm,} \\ 1.25 + 1.75 \times R & \text{cm, for } 1 < R < 5 \text{ cm,} \end{cases} \quad (2.20)$$

$$t(R) = \begin{cases} 10 & \text{cm, for } 5 < R < 6 \text{ cm,} \\ 0.0318 + 0.0364 \times R & \text{cm,} \end{cases} \quad (2.21)$$

and is oriented at an angle of  $\Theta_{\text{baf}} = 36^\circ$  with respect to to the Z-axis.

The operation of the spiral baffle is most easily analyzed in the cylindrical coordinate system where the positron motion is particularly simple. Consider a positron orbit of radius  $\rho_0$  which passes through the origin and is centered around

$$x_0 = 0; y_0 = \rho_0. \quad (2.22)$$

In cartesian coordinates the trajectory is described by,

$$\begin{aligned} x(\psi) &= \rho_0 \cos\psi, \\ y(\psi) &= \rho_0 (1 + \sin\psi), \\ z(\psi) &= (L_0/2\pi)\psi, \end{aligned} \quad (2.23)$$

where  $L_0$  is the pitch-length defined in Eqn. 2.6. The radial distance of the positron from the Z-axis is

$$r = (x^2 + y^2)^{1/2} = \rho[2(1 + \sin\psi)]^{1/2}. \quad (2.24)$$

Using the simple geometric identity that an angle inscribed in a circle equals  $1/2$  of the central angle which sweeps out the same arc, i.e.,  $\Delta\phi = 1/2\Delta\psi$ , the solenoid angle  $\phi$  corresponding to  $\psi$  is

$$\begin{aligned} \phi &= \psi/2 + \pi/4, \text{ or} \\ \psi &= 2\phi - \pi/2. \end{aligned} \quad (2.25)$$

Inserting Eqns. 2.25 into 2.23,24 gives the positron motion in cylindrical coordinates:

$$r(\phi) = 2\rho_0|\sin(\phi)|, \quad (2.26a)$$

$$z(\phi) = (L_0/\pi)\phi, \quad (2.26b)$$

or,

$$r(z) = 2\rho_0|\sin(\pi z/L_0)|. \quad (2.26c)$$

Equations 2.26 are generalized to an arbitrary orbit centered at  $(\rho_0, \phi_0)$  which crosses the Z-axis at  $z_0$  by the substitutions

$$r(\phi) = 2\rho_0 |\sin(\phi - \phi_0 + \pi/2)|, \quad (2.27a)$$

$$z(\phi) = (L_0/\pi)(\phi - \phi_0 + \pi/2) + z_0. \quad (2.27b)$$

and,

$$r(z) = 2\rho_0 |\sin(\pi[z-z_0]/L_0)|. \quad (2.27c)$$

In the neighborhood around the spiral baffle (denoted below by the subscript "b"), the magnetic field,  $B_b$  is essentially constant so that the orbital parameters  $\omega_b$ ,  $\rho_b$ ,  $\theta_b$ , and  $L_b$ , are similarly constant. Of particular importance is the constant velocity along the Z-axis,  $v_{\parallel b}$ . Using the relation  $\Delta\phi = \frac{1}{2}\Delta\psi$  and the definition of  $\omega$ , the solenoid angle swept out by the orbit while traversing a given distance along the Z-axis,

$$d\phi/dz = \frac{1}{2}(d\psi/dt)/(dz/dt) = -\frac{1}{2}\omega_b/v_{\parallel b} = -\pi/L_b, \quad (2.28)$$

is negative and constant for positrons. In a two-dimensional  $\phi$  vs.  $z$  representation, the positron therefore traces out a straight-line trajectory having a slope given by Eqn. 2.28. This corresponds to the projection of the orbit onto a cylinder of constant radius about the solenoid axis. Electrons, by virtue of their opposite charge, trace out trajectories having opposite slope, i.e.,  $d\phi/dz$  is always positive. Because of these simple trajectories, the transmission of positrons or electrons through the baffle is easily calculated geometrically once the shape of the baffle blades in  $\phi$ -Z space is known.

As noted above, the individual baffle blades are planar and oriented at an angle  $\Theta_{\text{baf}}$  to the Z-axis. The equation of the plane of an ideal, thin blade, centered radially outward along the X-axis is

$$(z-Z_{\text{baf}}) = -y/\tan(\Theta_{\text{baf}}). \quad (2.29)$$

The intersection of this plane with a cylinder of radius  $r$  (using  $y = r \cdot \sin\phi$ ) is

$$z = Z_{\text{baf}} - r \cdot \sin(\phi)/\tan(\Theta_{\text{baf}}). \quad (2.30)$$

Instead of being straight in  $\phi$ -Z space, the baffle blades follow a sine curve as indicated in Fig. 2-7a. The shaded region includes the finite blade thickness  $t(x)$  as a function of the radial distance,

$$y = (Z_{\text{baf}} - Z)\tan(\Theta_{\text{baf}}) \pm \frac{1}{2}t(x)/\cos(\Theta_{\text{baf}}).$$

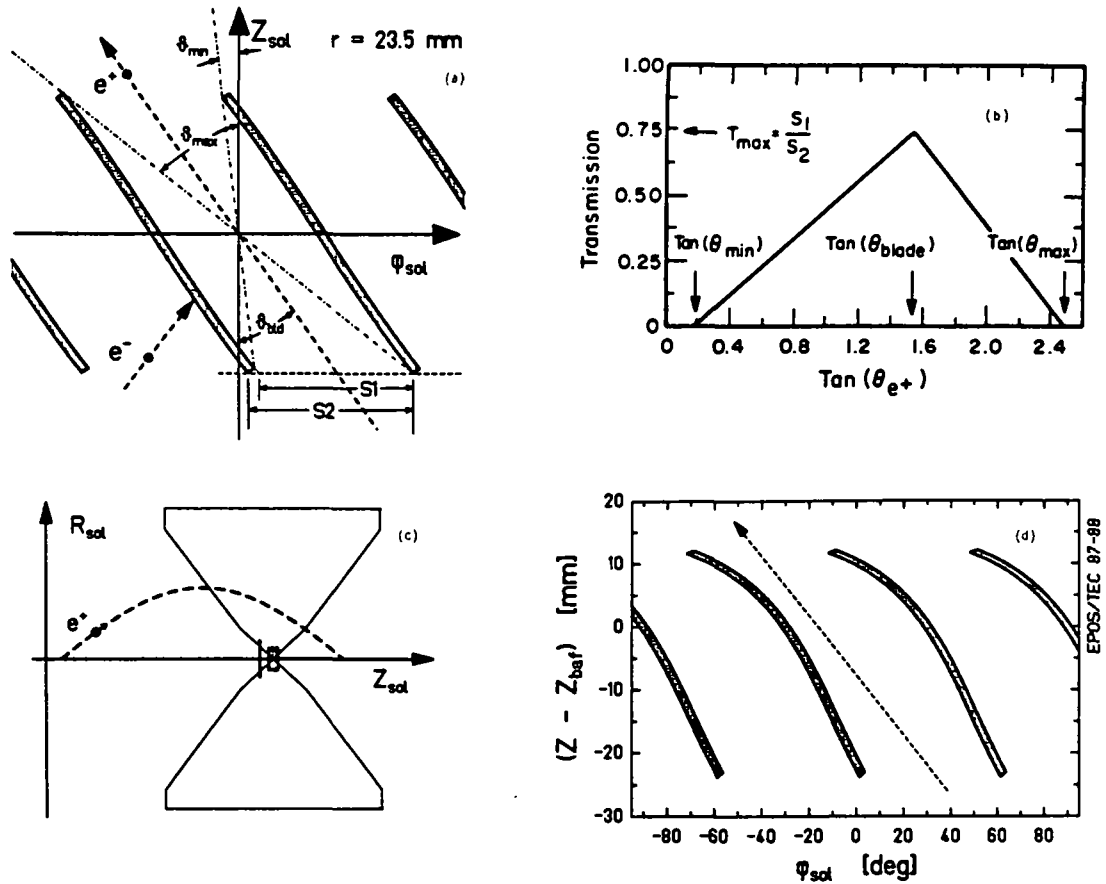


**Figure 2-7.** Diagram of baffle blades in  $\phi$ - $Z$  space (a) at a constant radius of 23.5 mm. Paths followed by positron or electron are indicated by dashed lines, and dot-dashed show the maximum and minimum slopes of the positron trajectory which can pass between the blades. The maximum of the transmission function (b, reproduced from [Shw85]) is determined from the portion of solid-angle not blocked by blades ( $S_1$  in a). Shape of blades encountered by realistic trajectory of 350 keV  $e^+$  emitted at  $\theta_0 = 70^\circ$  (indicated in c) is shown in (d).

In cylindrical coordinates, the azimuthal angular range subtended by a baffle blade at a given position ( $z, r$ ) along the positron orbit is

$$\varphi_{\pm} = \varphi_{bld} + \sin^{-1}\{r^{-1}[(Z_{baf}-z)\tan(\Theta_{baf}) \pm \frac{1}{2}t(x)/\cos(\Theta_{baf})]\}, \quad (2.31)$$

where the blade is centered about the solenoid angle  $\varphi_{bld}$ , and  $x = r \cdot \cos(\varphi - \varphi_{bld})$ .

As indicated by the dashed trajectory in Fig. 2-7a, positrons have the proper slope of  $\Delta z/\Delta \varphi$  to pass between the blades with large probability, while electrons strike the blades head-on. The actual  $\varphi$ - $Z$  profile of each blade "seen" by the positron

traversing the baffle depends on the solenoid radius,  $r(z)$ , of the trajectory at each position  $z$ . As noted in Eqn. 2-27c,  $r \propto \sin(z)$ , and as shown in Fig. 2-7c,d this tends to exaggerate the curvature of each blade. Positrons may pass between the blades if their slope,  $\Delta z/\Delta\phi = -L_b/\pi$ , is between the limiting values  $(\Delta z/\Delta\phi)_{\max}$  and  $(\Delta z/\Delta\phi)_{\min}$  defined by the blade surfaces.

Transmission varies linearly with  $d\phi/dz$  and is maximized for trajectories parallel to the tangent of the blade surface, as indicated in Fig. 2-7b. Whether a given positron is transmitted or stopped depends on the azimuthal emission angle,  $\phi_0$ , of its trajectory. The average probability of being transmitted is simply the  $\Delta\phi$  range *not* shadowed by the baffle (S1 in Fig. 2-7a),

$$\varepsilon_{\text{baf}}[(d\phi/dz)_{e+}] = 1 - \Delta\phi_{\text{shadowed}}/(2\pi/N_{\text{blades}}), \quad (2.32)$$

where  $N_{\text{blades}} = 6$ .

For high efficiency, the range of slopes  $(\Delta z/\Delta\phi)$  of the emitted positrons (from very short pitch-lengths for  $\theta_0 \sim 90^\circ$  to long pitch-lengths for  $\theta_0 \sim 0^\circ$ ) must be compressed to a small range which is then matched with the maximum transmission through the spiral baffle. This is achieved by depressing the magnetic field at the baffle to  $B_b = 999$  Gauss. Positrons emitted at  $\theta_0 = 90^\circ$  have a pitch angle at the baffle of  $\theta_b = 47^\circ$ . The range of positron slopes accepted and the maximum value of the transmission curve depend on the radius of the positron orbit, its pitch-angle, and its phase upon entering the baffle. For example, if the positron returns through the axis within the  $\Delta z$  range of the baffle, it strikes the central tantalum disk and is stopped. The baffle width in  $\Delta z_{\text{baf}}$  at radius  $r$  is designed to be smaller than the shortest pitch length  $L_b$  (for  $\theta_0 = 90^\circ$  emission) for positrons having a kinetic energy sufficient to reach that radius, i.e., for all positrons with  $2\rho_b > r$ .

Because electrons emitted at flat angles to the solenoid axis ( $\theta_0 \sim 0^\circ$ ) have very long pitch lengths and follow almost vertical paths in the  $\phi$ - $Z$  representation depicted in Fig. 2-7a,d, the width of the blades,  $w(R)$  in Eqn. 2.20, was chosen so that each blade is wider than  $\Delta\phi = 60^\circ$ . The blade edges therefore overlap, allowing no electrons to pass through unhindered. The thickness,  $t(R)$  in Eqn. 2.21, is tapered to reduce the material at small radii (thereby shadowing a smaller range of  $\phi$  to maintain large positron efficiency), but it is thick enough to absorb electrons with energies

large enough to reach  $2\rho = R$ . In cylindrical coordinates, the edges of a baffle blade are parameterized by

$$\begin{aligned} z(R) &= Z_{\text{baf}} \pm \frac{1}{2}[w(R)\cos(\Theta_{\text{baf}}) + t(R)\sin(\Theta_{\text{baf}})], \\ r(R) &= \frac{1}{2}\{4R^2 + [w(R)\sin(\Theta_{\text{baf}}) + t(R)\cos(\Theta_{\text{baf}})]^2\}^{1/2}, \\ \varphi(R) &= \varphi_{\text{bld}} \pm \tan^{-1}\{[w(R)\sin(\Theta_{\text{baf}}) + t(R)\cos(\Theta_{\text{baf}})]/2R\}, \end{aligned} \quad (2.33)$$

where the  $R$  is the distance from the solenoid axis along the centerline of the blade.

In addition to the considerations discussed above, the spiral baffle geometry is particularly well suited to reducing the flux of electrons which reach the Si(Li) detector because the blade area is large so that electrons which scatter from the surface tend to spiral back into the blades. Due to their orbital helicity, electrons migrate radially outward from the solenoid axis with each scattering process. Those which eventually do multiply scatter through the baffle are therefore further suppressed from returning through the solenoid axis to the positron detector. The rather large field depression, compared to the magnetic field strength at the Si(Li) detector ( $B_{\text{det}} = 1780$  Gauss), forms a magnetic bottle around the baffle which traps particles scattered with angles steeper than  $48.5^\circ$  relative to the Z-axis. Assuming an isotropic distribution of secondary emission angles, about 66% of the scattered positrons and electrons are prevented from reaching the Si(Li) detector. A 16 mm dia., 0.5 mm thick aluminum disk is attached to the front hub of the baffle to further reduce the transmission of low energy  $\delta$ -electrons having small orbital radii.

The suppression factor, defined by the transmission efficiency of positrons divided by that for electrons, is shown in Fig. 2-8. It was measured with different electron line sources by dividing the total counting rate of detected electrons for opposite polarities of the magnetic field, one time transmitting positrons (stopping electrons), and the next transmitting electrons. Some electrons multiply scatter between the blades and are detected, but the loss of kinetic energy shifts them out of the full-energy peak. As indicated by the dashed line in Fig. 2-8, the suppression of electrons in the full-energy peak is therefore a factor of  $\sim 20$  times larger, e.g.,  $(\epsilon_{e^-}/\epsilon_{e^+})_{\text{pk}} \cong 3 \times 10^{-4}$  at 364 keV (measured with a  $^{113}\text{Sn}$  source). If the source is positioned several mm off-axis, the electrons have an increased chance of passing through the baffle. At a distance  $d_{\perp} \cong 5$  mm, e.g., the suppression factor is reduced such that  $(\epsilon_{e^-}/\epsilon_{e^+}) \sim 0.01$  for 364 keV electrons.

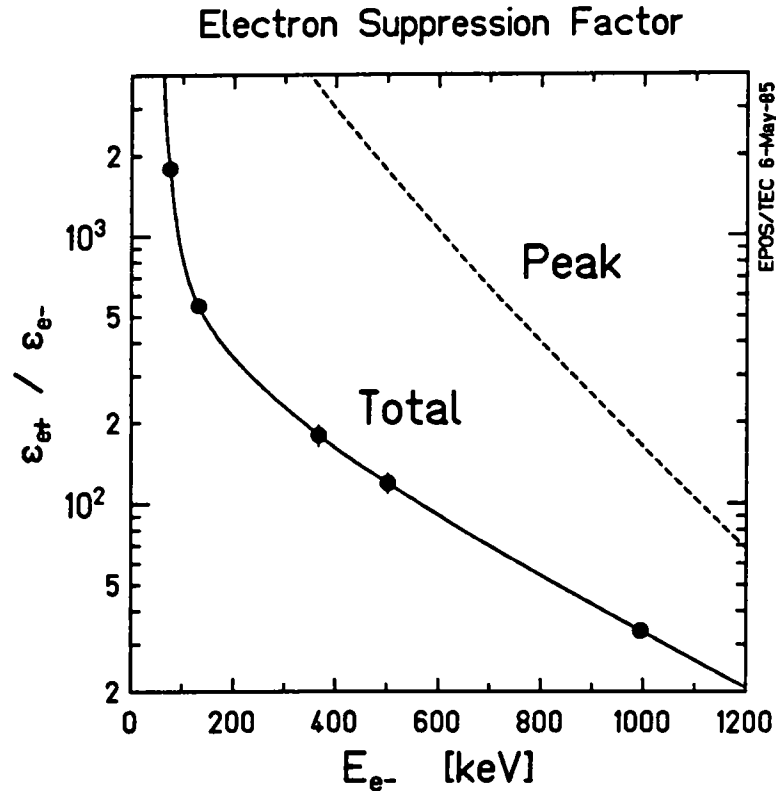


**Figure 2-8.** Suppression factor of electron transmission through the spiral baffle compared to the positron efficiency. Solid curve integrates total energy distribution of electrons transmitted through the baffle, which includes energy-loss due to scattering, while dashed line includes only energies within 50 keV around peak. Solid points present measurements with  $^{109}\text{Cd}$ ,  $^{139}\text{Ce}$ ,  $^{113}\text{Sn}$ , and  $^{207}\text{Bi}$  electron conversion line sources.

As mentioned above, the number of blades, their dimensions and pitch angle, and the magnetic dip field, were all chosen to optimize the transmission efficiency of positrons below 500 keV, while maintaining a wide band-pass for higher energies, as well as providing effective electron suppression. The transport efficiency was calculated interactively at each stage of the design process by a numerical integration within the adiabatic approximation, as described in Sec. 2.2.5. For each prototype baffle design, a full ray-tracing efficiency calculation was performed, as described in App. B.

### Sec. 2.2.3 Positron Si(Li) Detector

As discussed in [Gre85] and [Shw85], the axial focussing property of the solenoid magnetic field suggests a natural detector geometry for the positron energy measurement. This consists of a counter located on the EPOS solenoid axis, long

enough to intercept a large range of orbital pitch-lengths,  $L$ . Having a small radius, it simultaneously presents a small cross-sectional area to the direct flux of neutral radiation from the target, and suppresses the detection of secondary positrons and electrons emitted (created or scattered) away from the solenoid axis. The pencil-like lithium-drifted silicon [Si(Li)] positron detector employed in these measurements<sup>2</sup> is located on the solenoid axis 83.2 cm from the target. As shown in Fig. 2-9, it consists of two hollow cylindrical segments, with a 10.3 mm outer diameter and a 4.8 mm inner diameter. The rear portion is 43.8 mm long, with 1.8 mm and 1.3 mm dead zones at either end. The front segment is 41.2 mm long, with a 1.5 mm dead region at the rear end. The forward surface is sensitive, forming a rounded 60° cone.

The detector used previously [Shw85] had an insensitive Teflon disk on its front surface. As described in Sec. 2.2.5 below, such a passive element preferentially stops and absorbs positrons having small orbital radii, i.e., those with small energies or emitted at flat angles. The present detector was particularly designed to improve low energy detection efficiency. As shown by the comparison of the positron detection efficiency for the old and new arrangements in Fig. 2-1, between 200 and 800 keV the transport efficiency is increased by a factor of  $\cong 2$  due to the improved detector, baffle, and solenoid field. At  $E_{e^+} \cong 100$  keV, the efficiency is now larger by a factor of 4.8. This additional low energy-sensitivity is due almost entirely to the active snout on the present Si(Li) detector.

Lithium is drifted radially outward from the inner surface of the crystal upon which a nickel layer is plated for an electrical ground connection. The outer surface is implanted with boron and covered with a 50  $\mu\text{g}/\text{cm}^2$  evaporated gold contact. The active depletion depth of 2.75 mm is thick enough to completely stop positrons of up to 1200 keV, providing full energy measurement throughout the interesting spectral range.

The entire crystal assembly is mounted on an aluminum cold finger maintained at a temperature of -150° C through contact with a liquid nitrogen reservoir (150  $\text{cm}^3$ ). Each detector segment is connected to a cooled FET, placed directly behind the crystals on the cold-finger, whose outputs are fed into matched preamplifiers located

---

<sup>2</sup>

The Si(Li) detector was manufactured by Soci t  d'Etude Physique, Paris, France.

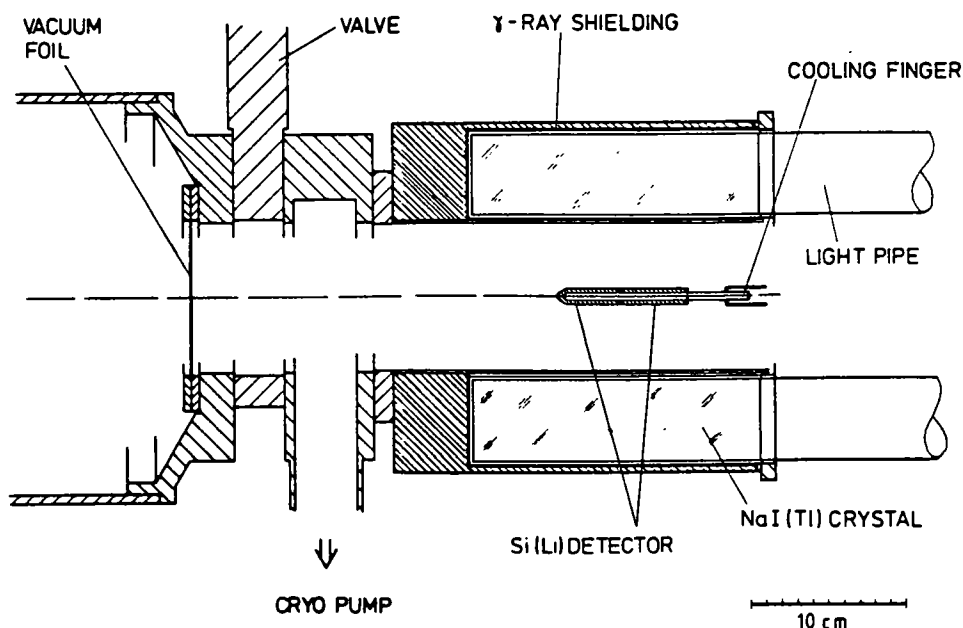


**Figure 2-9.** Cross sectional drawing of the pencil-like positron Si(Li) detector, showing its orientation within the vacuum chamber and with respect to the Annihilation Radiation Detector.

outside the vacuum chamber. The diode is operated at -250 volts bias. The small chamber surrounding the detector is electrically isolated from the spectrometer walls, pump, and vacuum measurement instruments. Condensation on the detector surfaces is reduced by maintaining a  $<10^{-7}$  Torr vacuum, sealed from the main spectrometer chamber (where typically  $P \cong 10^{-5}$  Torr) by a  $3.5 \mu\text{m}$  aluminized Mylar foil. Scattering in this vacuum foil produces, in effect, an extended source of positrons at the foil plane. The root mean square deflection angle,  $\langle \delta\theta \rangle \sim 6^\circ$  [Kno68], is small enough, however, that almost all positrons return to within a few mm of the spectrometer axis and are detected in the Si(Li). No reduction in the transport efficiency has been observed. The small energy loss,  $\delta E_{e^+} \cong (1 \text{ keV})/\cos\theta_{e^+}$ , and straggling in the vacuum foil only slightly degrade the measured positron energy resolution by  $\leq 3 \text{ keV}$ .

The axial orientation of the Si(Li) detector presents only a small surface area to the target, subtending a solid angle of  $1.2 \times 10^{-4}$  sr. Only  $9.6 \times 10^{-6}$  of the direct flux of  $\gamma$ -rays and neutrons emitted isotropically from the target is intercepted. The detector is shadowed by an 8 mm dia.  $\times$  3 mm thick tantalum disk in the center of the spiral baffle which further attenuates low energy  $\gamma$ - and X-rays by a factor ranging

from  $10^9$  at 100 keV to  $\cong 5$  at 300 keV. The disk is encased in 2 mm of plexiglas to absorb positron-electron pairs externally converted in the Ta material.

The energy resolution of the detector is  $\Delta E \sim 10$  keV (FWHM) at 350 keV. The timing resolution, measured against the fast ( $\sim 1$  ns) PPAC's, is  $\Delta t = 7.5$  ns (FWHM). The pulse-height response of each Si(Li) segment is separately calibrated with K and L conversion lines from radioactive  $^{109}\text{Cd}$ ,  $^{139}\text{Ce}$ ,  $^{113}\text{Sn}$ , and  $^{207}\text{Bi}$  sources. Periodic checks during each beamtime showed that the calibration generally remained stable to within  $\sim 3$  keV ( $1\sigma$  level) throughout an experiment.

The detector response to electrons exhibits, in addition to the full energy peak, a broad low-energy tail which arises from out-scattering from the silicon material. The lineshape is parameterized as an asymmetric gaussian peak, polynomial tail, and a low-energy cutoff from the constant fraction discriminator threshold.

$$\begin{aligned}
 F(E, E_0) &= F_{\text{cfd}} (F_{\text{peak}} + F_{\text{tail}}), & (2.34) \\
 F_{\text{peak}} &= \exp[-(E-E_0)^2/2\sigma^2] \\
 F_{\text{tail}} &= \text{erfc}[(E-E_0)/\sigma] \{a + b \cdot E + c \cdot \exp[(E-E_0)/\tau]\} \\
 F_{\text{cfd}} &= \text{erf}[(E-E_{\text{cfd}})/\Gamma_{\text{cfd}}]
 \end{aligned}$$

Figure 2-10 shows fits of Eqn 2.34 to several source spectra. The steep exponential portion of the lineshape just below the peak is due to energy-loss straggling in the source and vacuum foil, incomplete charge collection, and, at higher incident energies, to brehmstrahlung.

Positrons which strike the Si(Li) are detected in coincidence with their 511 keV annihilation radiation, giving rise to a somewhat different lineshape. As discussed in [Shw85], only those scattered positrons which eventually stop in the detector or cold finger annihilate and emit a photon to trigger the ARD array. The magnitude of the broad out-scattered low-energy tail is therefore significantly reduced. One or both of the annihilation quanta may, however, Compton scatter in the silicon detector material before being absorbed in the ARD. A resulting continuous smooth distribution extending to the 341 keV Compton edge, adds as pileup to the positron signal (see Fig. 2-11). A comparison of the  $\beta^+$  energy spectra from a  $^{22}\text{Na}$  source (see, e.g., Fig. 4.3 in [Shw85]) requiring the full absorption of either both, or at least one, 511 keV quanta in the ARD, indicated that in the present configuration the Compton pileup occurs with  $\cong 8\%$  probability.

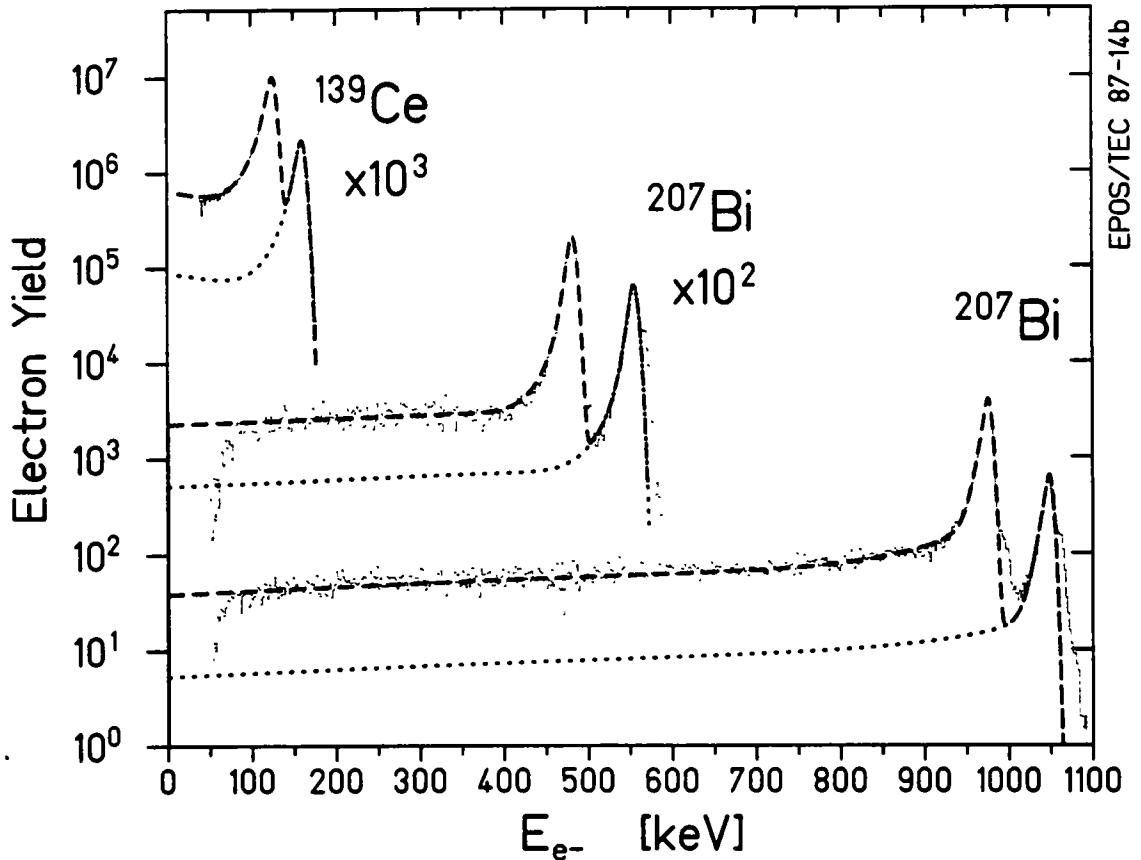


**Figure 2-10.** Plot of the response of the Si(Li) detector to conversion electron line sources. Dashed and dotted curves show fits of the experimental data using Eqn. 2.34 for the K and L lines, respectively.

As described in Secs. 4.1 and 6.4 of [Shw85], the size of the low energy positron tail is determined by iteratively unfolding a continuous  $\beta^+$  spectrum, correcting for transport efficiency, and comparing to the theoretical  $\beta$  decay energy distribution. It is reduced compared to electron detection by a factor of 0.6-0.8. The resulting peak-to-total ratio for 350 keV positrons is  $\cong 80\%$  (see Fig. 2-11c).

#### **Sec. 2.2.4 NaI Annihilation Radiation Detector**

Unambiguous identification of positrons is provided by a coincident measurement of their back-to-back 511 keV annihilation quanta in the Annihilation Radiation Detector (ARD). This detector consists of an array of eight NaI(Tl) crystals, each 51 mm thick by 200 mm long, forming a cylinder with an inner diameter of 106.5 mm (see Fig. 2-12). The geometric solid angle subtended is 70% of  $4\pi$  for  $\gamma$ -rays emitted from the axis at the midpoint of the cylinder. Each crystal is connected by a 43 cm

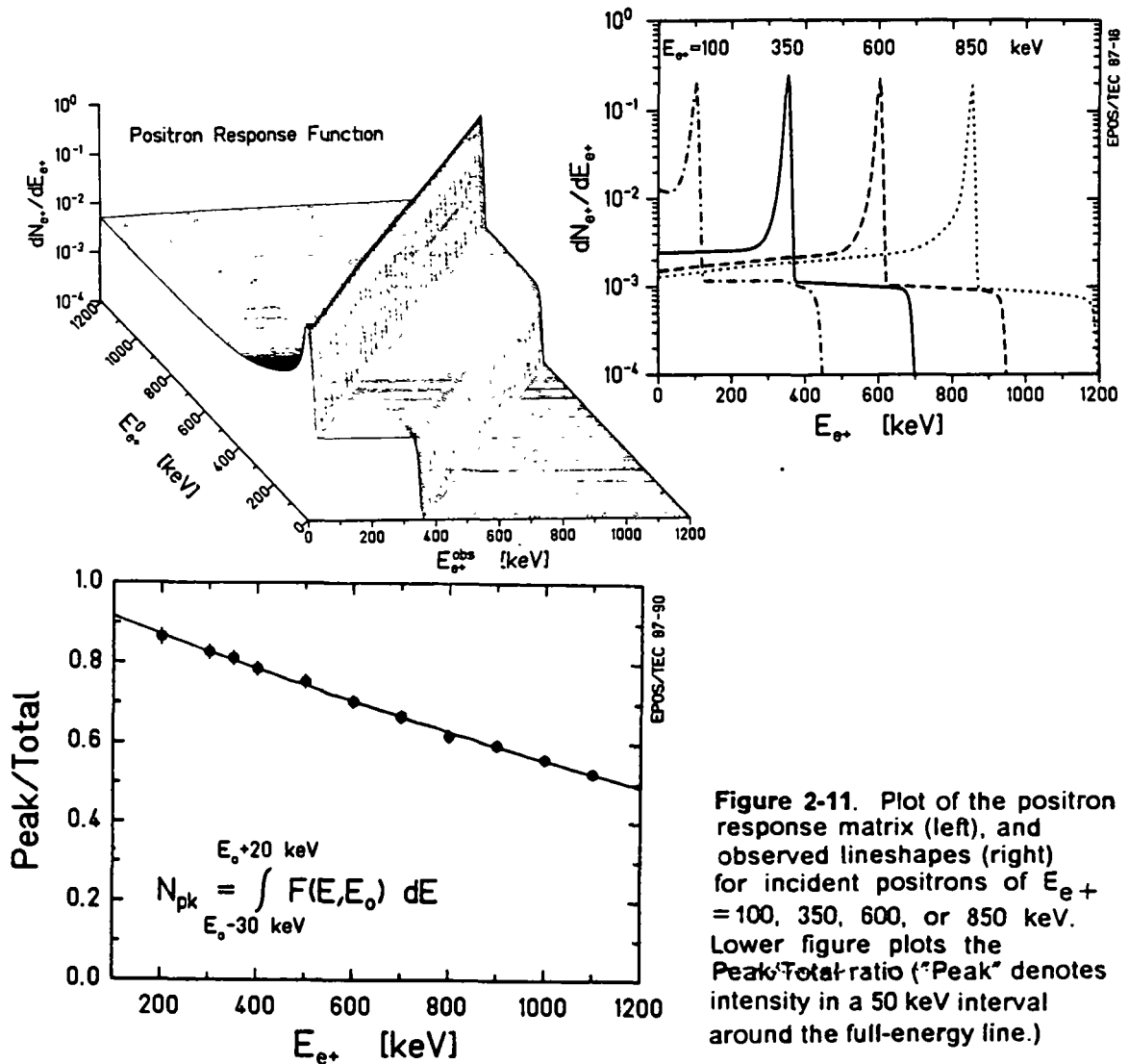
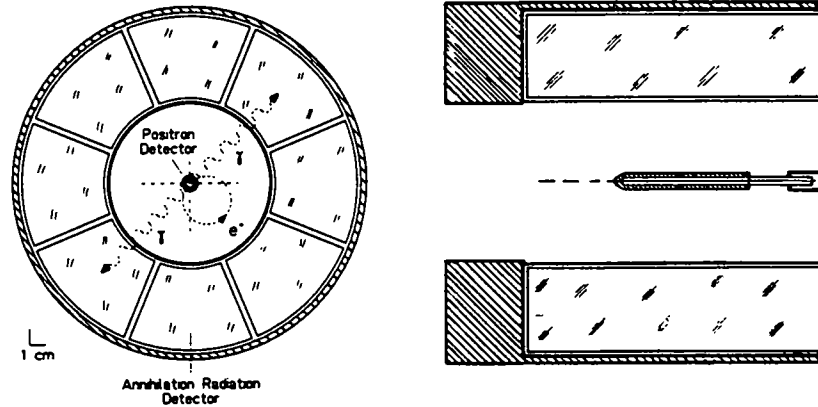


Figure 2-11. Plot of the positron response matrix (left), and observed lineshapes (right) for incident positrons of  $E_{e+} = 100, 350, 600, \text{ or } 850$  keV. Lower figure plots the Peak/Total ratio ("Peak" denotes intensity in a 50 keV interval around the full-energy line.)

light pipe to a photomultiplier tube (PMT) located beyond the bucking coil of the solenoid. To further reduce stray magnetic fields, each PMT is wrapped in a 2 mm thick  $\mu$ -metal sleeve, and an 8 mm thick  $\mu$ -metal cylinder surrounds the set of eight phototubes. The PMT's are operated at -1400 volts. A fast time pick-off signal is taken from the anode, and one dynode signal is integrated in a charge-sensitive preamp for the energy measurement. Because of the long lightpipe, an energy resolution of only  $\Delta E_{\gamma} \cong 70$  keV (FWHM) is achieved at  $E_{\gamma} = 511$  keV. The time resolution [Si(Li)-ARD] is  $\Delta t \cong 15$  ns (FWHM).

The detector system is heavily shielded from  $\gamma$ - and X-radiation emerging from the target. A graded absorber consisting of 50 mm Pb and 2 mm each of Cu, Sn, and Al, placed at the front end of the cylindrical array, as shown in Fig. 2-12, attenuates the direct  $\gamma$ -ray flux by  $\sim 10^4$  at 511 keV (including the steel vacuum isolation valve



**Figure 2-12.** Front and Side views of the 8-fold Annihilation Radiation Detector (ARD) NaI(Tl) crystal array.

and aluminum chamber shown in Fig. 2-9 which further shadow the ARD). In-scattering from the spectrometer coils is reduced by a layer of 6 mm Pb, 2 mm Sn, and 1 mm Cu wrapped around the outside of the crystal array.

The energy signals of the photons detected in prompt time coincidence with positrons in the Si(Li) are added together. As shown in Fig. 2-13 for a measurement of  $\beta$  decay positrons from  $^{58}\text{Co}$ , the sum-energy spectrum exhibits prominent peaks at 511 keV and 1022 keV, corresponding to the full-energy absorption of one or both annihilation quanta. Compton scattering of one or both photons in the ARD contributes to a smooth continuum at energies below 400 keV. The full absorption of one, and Compton scattering of the second photon, leads to a similar distribution between 600 and 900 keV. By selecting only the 1022 keV ARD sum-energy peak, the 8% Compton positron tail discussed above is eliminated. This, however, does not offset the factor of  $\sim 3$  lost in ARD positron identification efficiency. In practice, a sum-energy above 420 keV is taken to signal the arrival of a positron in the Si(Li) detector. As described in [Shw85], the net ARD detection efficiency is  $\cong 60\%$ , and it is essentially independent of positron energy.

### **Sec. 2.2.5 Positron Detection Efficiency**

The positron detection efficiency of the EPOS spectrometer depends on the three independent factors introduced above: the transport efficiency, the ARD annihilation

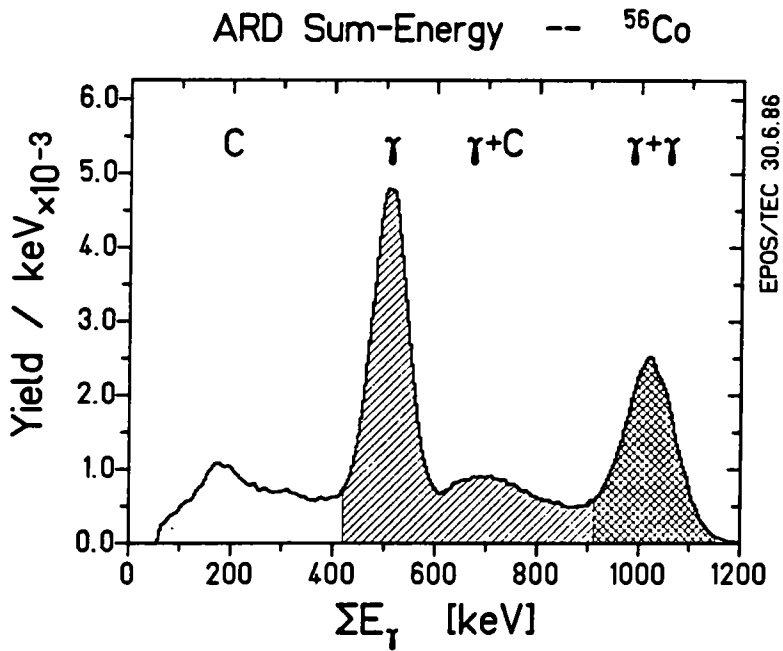


**Figure 2-13.** Distribution of the sum of NaI-segment energies in the Annihilation Radiation Detector measured for positrons from  $^{56}\text{Co}$   $\beta^+$  source. One and two 511 keV photon peaks, and Compton continua are marked. Shaded region denotes software selection for identification of positron events.

photon identification efficiency, and for positron peak detection efficiency, on the Si(Li) peak/total lineshape ratio,

$$\epsilon_{\text{C}^+}^{\text{pk}} = \epsilon_{\text{trans}} \cdot \epsilon_{\text{ARD}} \cdot (P/T)_{\text{e}^+}. \quad (2.35)$$

In principle, each of these components is a function of the kinetic energy of the positron,  $E_{\text{e}^+}$ , and its emission angles,  $\theta_{\text{e}^+}$ ,  $\varphi_{\text{e}^+}$ . As mentioned above, the probability of detecting at least one annihilation photon is essentially independent of positron energy and emission angle, and can be taken as a constant  $\epsilon_{\text{ARD}} = 0.60$ . The peak-to-total ratio depends in principle on the emission angle via the stop position of the positron in the Si(Li) and its entrance angle. This is contained, in an average way, in Eqn. 2.34 and is assumed to depend only on energy, as shown in Fig. 2-11c. Almost the entire energy dependence of the positron detection efficiency is therefore given by the transport probability,  $\epsilon_{\text{trans}}$ .

**Sec. 2.2.5.1 Adiabatic Transport Efficiency:** Two different methods are used to calculate the transport efficiency – a semi-analytical approach using the adiabatic ap-

proximation, and a ray-tracing technique which numerically integrates the equations of motion. The former has proven to be computationally much faster and more efficient, and it provides a general understanding of the effect on the transmission efficiency of the various individual components in the spectrometer.

The adiabatic method involves calculating the positron transmission probability past each of the individual elements in the spectrometer separately. The total transport efficiency for a given emission angle  $\theta_0$  and energy  $E_{e^+}$  is taken as the product of the efficiencies for the individual components (vacuum chamber, magnetic mirror, target frame, baffle, detector), where each is averaged over the relative phase of the orbit and over the azimuthal emission direction  $\varphi_0$ ,

$$\varepsilon_{\text{trans}}(\theta_0, E_{e^+}) = \langle \varepsilon_{\text{cham}} \rangle \cdot \langle \varepsilon_{\text{mir}} \rangle \cdot \langle \varepsilon_{\text{tar}} \rangle \cdot \langle \varepsilon_{\text{baf}} \rangle \cdot \langle \varepsilon_{\text{det}} \rangle. \quad (2.36)$$

These averaged efficiencies,  $\langle \varepsilon_i \rangle$ , are calculated either geometrically or numerically in the following manner. At each position along the Z-axis, the orbital radius, pitch-angle, and pitch-length, for the appropriate magnetic field strength, are given by the adiabatic approximation (Eqns. 2.9-2.12). The path is described in solenoid coordinates by Eqn. 2.27c,

$$\begin{aligned} r(z) &= 2\rho_0 | \sin[(z-z_0)\pi/L] |, \text{ and} \\ \varphi(z) &= \varphi_0 - (z-z_0)\pi/L, \end{aligned} \quad (2.37)$$

where  $z_0$  is the last position where the positron orbit crossed the solenoid axis.

This adiabatic description of the orbit is used only at the particular element under consideration, positioned at  $z_i$ , and the previous history of the trajectory is ignored. In particular, the "phase" of the orbit, i.e., where the  $e^+$  last crossed the axis, is not known, so we assume a uniform probability for  $z_0$  between  $(z_i-l) \leq z_0 \leq z_i$ . The efficiency, averaged over  $\varphi_0$  and phase, is then

$$\langle \varepsilon_i(E_{e^+}, \theta_0) \rangle = (1/L) \int_{z_i-l}^{z_i} dz_0 (1/2\pi) \int d\varphi_0 \varepsilon_i(E_{e^+}, \theta_0, \varphi_0, z_0). \quad (2.38)$$

The angle-integrated energy-dependent transmission efficiency is

$$\varepsilon_{e^+}(E_{e^+}) = \frac{1}{2} \int_0^\pi \sin\theta_0 d\theta_0 \Pi_i \langle \varepsilon_i \rangle. \quad (2.39)$$

Since the detailed history of the positron is not calculated (e.g., by ray-tracing), this method is very fast [an entire efficiency curve  $\varepsilon_{e^+}(E_{e^+})$  requires only a few cpu seconds on an IBM 3090 computer] and was therefore used to interactively design and optimize each of the components of the EPOS spectrometer modified for these experiments. For more accurate calculations, Eqn. 2.38 can be modified to retain the  $\varphi_0$  dependence of transmission,  $\langle \varepsilon_i(E_{e^+}, \theta_0, \varphi_0) \rangle = \int dz_0 \varepsilon_i$ .

**Magnetic Mirror Field.** As mentioned above, several of the components have very simple analytical expressions for the average efficiency,  $\langle \varepsilon_i \rangle$ . The dependence of each on  $E_{e^+}$  and  $\theta_0$  provides a very useful "feel" for the operation of this instrument. For example, the magnetic mirror efficiency is simply,

$$\varepsilon_{\text{mir}} = \begin{cases} 1 & \text{for } \theta_0 < (\pi - \theta_{\text{mir}}), \\ 0 & \text{for } \theta_0 > (\pi - \theta_{\text{mir}}) \end{cases} \quad (2.40)$$

with  $\theta_{\text{mir}} = \sin^{-1}(B_0/B_{\text{mir}})^{1/2}$ .

**Vacuum Chamber Geometry.** Transmission through the vacuum chamber is unity unless the radial extent of the orbit ( $2\rho$ ) exceeds the chamber inner radius which is smallest,  $R_{\text{cham}} = 5.0$  cm, for  $Z > 59.2$  cm (see Fig. 2-9). Thus,

$$\varepsilon_{\text{cham}} = \begin{cases} 1 & \text{for } \theta_0 < \theta_{\text{max}} \\ 0 & \text{for } \theta_0 > \theta_{\text{max}} \end{cases} \quad (2.41)$$

with,

$$\theta_{\text{max}} = \sin^{-1}\left\{\frac{1}{2}R_{\text{cham}}(eB_{\text{cham}}/pc)(B_0/B_{\text{cham}})^{1/2}\right\},$$

where  $B_{\text{cham}}$  is the minimum magnetic field strength (giving the maximum orbital radius) between  $Z = 59.2$  cm and the detector at  $Z = 83.2$  cm.

**Spiral Baffle.** The average transmission past the spiral baffle is given by the integral of Eqn. 2.38 where the integrand includes the effect of the baffle blades (see Fig. 2-7) and the 16 mm dia. central disk.

$$\langle \varepsilon_{\text{baf}} \rangle = (1/2\pi L) \int_{Z_{\text{baf-L}}}^{Z_{\text{baf}}} dz_0 \int d\varphi_0 \varepsilon_{\text{bld}}(E_{e^+}, \theta_0, \varphi_0, z_0) \cdot \varepsilon_{\text{disk}}(E_{e^+}, \theta_0, z_0) \quad (2.42)$$

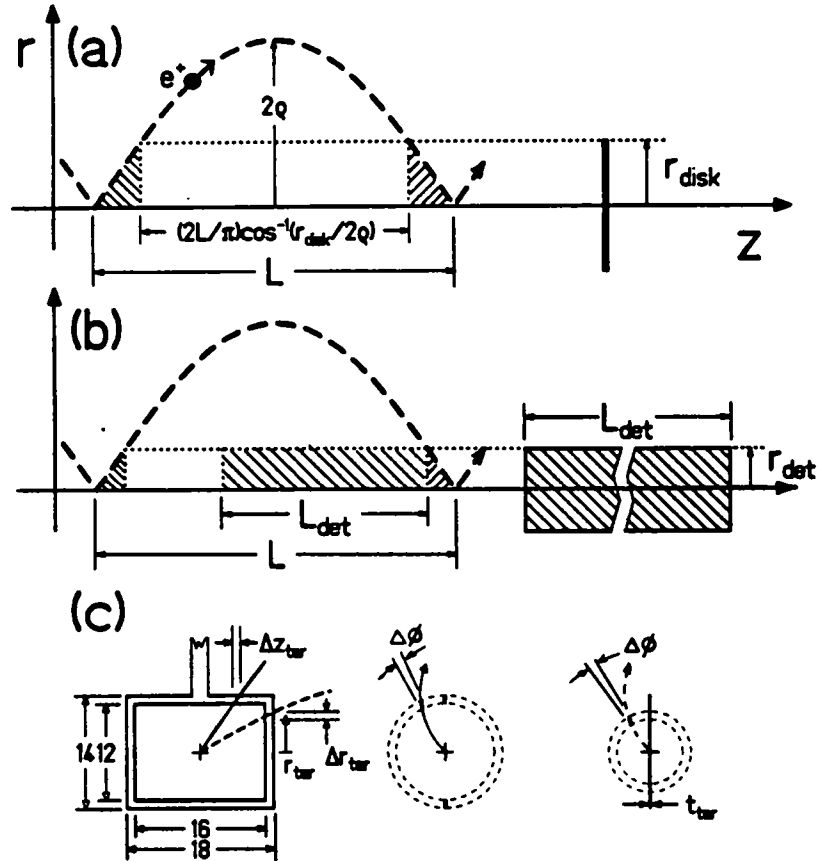


**Figure 2-14.** Diagram indicating average fraction of positrons stopped by passive disk (a), and Si(Li) detector (b), calculated in adiabatic approximation. Shaded portions of pitch-length  $L$  indicate relative position of trajectory, with respect to disk or front edge of detector, at which positron is stopped. Efficiency of target frame (c) calculated, as described in text, from the azimuthal range  $\Delta\phi$  swept out by the positron orbit as it passes the horizontal cross-pieces (solid line and middle figure) or the vertical sections (dashed orbit and right figure).

As shown in Fig. 2-14a, the positron is not stopped in the disk for a given phase  $z_0$  if  $r(Z_{\text{baf}}) > R_{\text{disk}}$ . This limits the  $z_0$  integration to

$$\sin^{-1}(R_{\text{disk}}/2\rho) < (Z_{\text{baf}}z_0)\pi/L < [\pi - \sin^{-1}(R_{\text{disk}}/2\rho)]$$

that is,

$$\begin{aligned} \varepsilon_{\text{disk}} &= 1 \text{ for } [(Z_{\text{baf}}L) + (L/\pi)\sin^{-1}(R/2\rho)] < z_0 < [Z_{\text{baf}}L/\pi\sin^{-1}(R/2\rho)], \\ &= 0 \text{ otherwise, or if } 2\rho < R. \end{aligned} \quad (2.43)$$

**Positron Detector.** The probability that a positron hits the Si(Li) detector combines the probability of hitting the front surface at  $Z_{\text{det}} = 83.2$  cm, or of striking the cylindrical surface at  $R_{\text{det}} = 5.15$  mm. As indicated in Fig. 2-14b, the fraction of trajectories striking the front (for an idealized flat front face) is

$$P_{\text{front}} = (2/\pi) \sin^{-1}(R_{\text{det}}/2\rho).$$

If the remaining portion of the pitch-length of the trajectory,  $L \cdot (1 - P_{\text{front}})$ , is less than the length of the detector,  $L_{\text{det}}$ , the detection efficiency is  $\epsilon_{\text{det}} \equiv 1$ . Otherwise,

$$\langle \epsilon_{\text{det}}(E_{e^+}, \theta_0) \rangle = L_{\text{det}}/L + (2/\pi) \sin^{-1}(R_{\text{det}}/2\rho). \quad (2.44)$$

**Target Frame.** Finally, the chance that the positron hits the target frame,  $P_{\text{hit}} = (1 - \langle \epsilon_{\text{tar}} \rangle)$ , averaged over  $\phi_0$ , is given geometrically by the angle swept out by the positron  $\Delta\phi_{e^+}$ , as it passes across the cylinder of rotation of the target frame about the solenoid axis. Including the  $t_{\text{tar}} = 0.3$  mm frame thickness, the positron which crosses the frame boundary at radius  $r$  gives,

$$\langle \epsilon_{\text{tar}} \rangle = 1 - (1/\pi)[|\Delta\phi| + t_{\text{tar}}/r].$$

If the positron exits through the cylindrical surface ( $r = R_{\text{tar}}$  for  $|z| < Z_{\text{tar}}$ ),  $\Delta\phi = (d\phi/dr)\Delta r$ , evaluated at  $R_{\text{tar}} = 2\rho \sin\phi$ . This gives,

$$|\Delta\phi| = \Delta r (4\rho^2 - R_{\text{tar}}^2)^{-1/2}.$$

If the positron exits in the direction of the axis through one of the ends of the target frame ( $|z| = Z_{\text{tar}}$  for  $r < R_{\text{tar}}$ ), then  $\Delta\phi = (d\phi/dz)\Delta Z_{\text{tar}} = (\pi/L)\Delta Z_{\text{tar}}$ . The radius is  $r = 2\rho \sin[(Z_{\text{tar}} - z_0)\pi/L]$ . Combining these,

$$\langle \epsilon_{\text{tar}} \rangle = 1 - [\Delta R_{\text{tar}}/(4\rho^2 - R_{\text{tar}}^2)^{1/2} + t_{\text{tar}}/R_{\text{tar}}] \quad (2.45a)$$

or,

$$= 1 - \{\Delta Z_{\text{tar}}\pi/L + t_{\text{tar}}[2\rho \sin\{(Z_{\text{tar}} - z_0)\pi/L}\}^{-1}\}. \quad (2.45b)$$

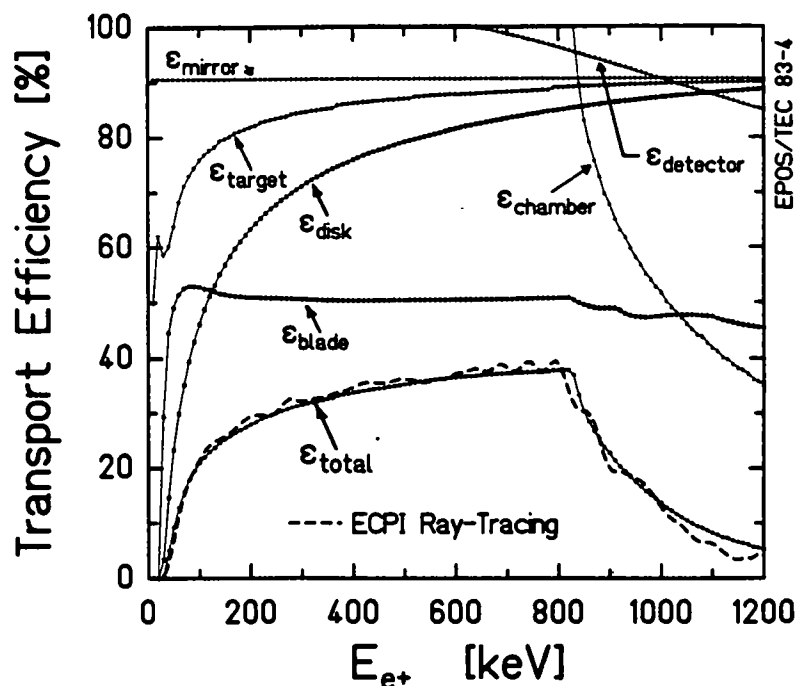


**Figure 2-15.** Energy differential transport efficiency calculated within adiabatic approximation showing individual contributions of the magnetic mirror, chamber geometry, target frame, baffle disk, baffle blades, and Si(Li) detector as marked. Dashed line compares ray-tracing calculation.

Figure 2-15 presents the energy-dependence of the transport efficiency (Eqn. 2.39) using the adiabatic approximation for each of the spectrometer elements. The shape of the efficiency is determined at low energies mainly by the disk at the center of the baffle, and at high energies ( $E_{e+} > 800$  keV), by the cut-off of steeply emitted positrons by the inner radius of the vacuum chamber surrounding the Si(Li) detector. The spiral baffle blade acceptance and the magnetic mirror reflection angle do not depend sensitively on  $E_{e+}$ .

**Sec. 2.2.5.2 Ray-Tracing Calculations:** More accurate calculations of the efficiency which include the full azimuthal dependence of transmission and the correct phase of the positron orbits along the entire trajectory are required for differential estimations of the positron detection efficiency, e.g., as a function of  $\theta_0$  and  $\phi_0$ . A ray-tracing code, ECPI (Efficiency Calculation by Path Integration [Lia82], see App. B for details), was developed by E. Liarokapis (Yale) and R. Schule (Frankfurt) which integrates the Lorentz equations of motion, Eqn. 2.1, and iteratively traces the path

through the EPOS spectrometer. The equations of motion separate in cylindrical coordinates [God44] giving

$$d^2z/dt^2 = -(e/\gamma mc)^2 A_\phi \partial A_\phi / \partial z, \quad (2.46a)$$

$$d^2r/dt^2 = -(e/\gamma mc)^2 A_\phi \partial A_\phi / \partial r, \quad (2.46b)$$

$$d\phi/dt = -(e/\gamma mc) A_\phi / r. \quad (2.46c)$$

The vector potential  $A_\phi$  is obtained from the magnetic field strength along the axis (Eqns. 2.14,2.15) by the expansion,

$$A_\phi = \sum_n \{(-1)^n [n!(n+1)!]^{-1} B_z^{(2n)} (r/2)^{2n+1}\}, \quad (2.47)$$

calculated to order  $r^7$ . The first four steps of the trajectory are integrated with a Runge-Kutta method. Thereafter, for each additional step along the path, the preceding four points are used to extrapolate a fifth point using a Milne Predictor-Corrector algorithm. As described in App. B, the optimal step size leads to an accuracy of  $< 0.1 \mu\text{m}$  for each  $\cong 0.8 \text{ mm}$  step. The original ECPI program was modified by the author to properly include the spiral baffle, target frame, the full  $\phi$ -dependence of transmission, and the modifications to the present apparatus discussed above (magnetic field, baffle geometry, and Si(Li) detector).

**Sec. 2.2.5.3 Transport Efficiency:** The EPOS positron transport efficiency calculated with the ECPI ray-tracing program is shown in Fig. 2-16a as a function of energy. The points represent measurements with electron line sources with the polarity of the magnetic field reversed. Each source is used to trace out a large portion of the energy-dependent transmission by scaling the magnetic field and noting that the simulated electron momentum changes adiabatically with the field strength,

$$p_{sim}^{e+} = p_0^{e+} (B_0/B_{sim})^{1/2}. \quad (2.48)$$

Table 2-1 summarizes the places in the solenoid where positrons are stopped. As indicated above, the positron detection efficiency (Fig. 2-16b) is a nearly constant factor of 0.6 times the transport efficiency, giving a value at the plateau of  $\epsilon_{e+} \cong 20\%$ . The positron peak efficiency, including the additional energy-dependent peak/total ratio, achieves a value at 350 keV of  $\epsilon_{e+}^{pk} \cong 16\%$ , a factor of more than 2 larger than the 7% positron peak efficiency in the previous EPOS arrangement [Shw85].

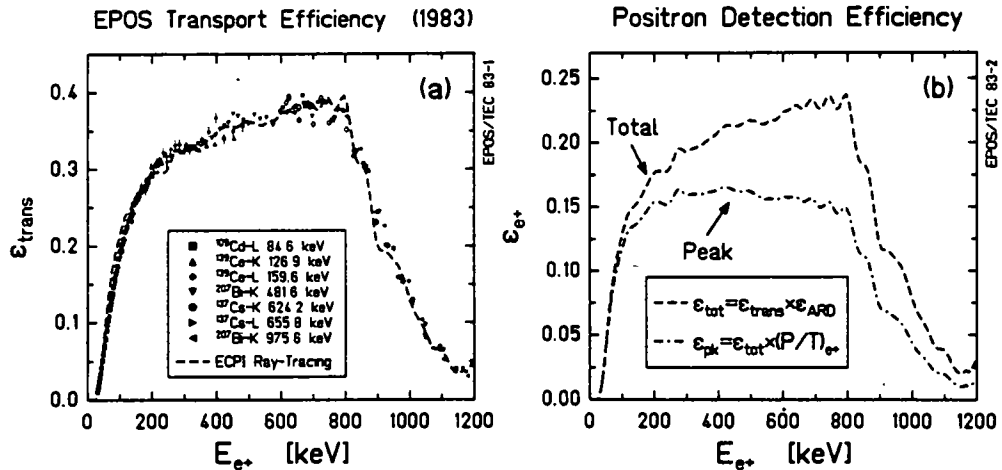


**Figure 2-16.** (a) Energy dependence of the EPOS positron transport efficiency measured with several electron conversion line sources using reversed polarity of the magnetic field. The entire range of energies is simulated by varying the field strength, as described in text. (b) Calculated total and peak positron detection efficiencies.

Figure 2-17 illustrates the transport efficiency of 350 keV positrons as a function of polar and azimuthal emission angles. Several features are clearly evident, such as detection of trajectories only for angles smaller than the critical magnetic mirror emission angle (Eqn. 2.17). The six-fold periodicity in  $\varphi$  corresponds to passage through the gaps in the six-bladed spiral baffle. An oscillatory structure in  $\cos\theta_0$  arises from the orbital phase at the central hub of the spiral baffle. Those trajectories, for which the target-baffle distance is divisible by an integral number of pitch-lengths, cross through the solenoid axis close to the baffle and are absorbed by the central hub. Orbits with a half-integral divisor, on the other hand, achieve their maximum solenoid radius at the baffle and have a large probability of transmission. The thin horizontal gaps in detection near  $\varphi = 80^\circ$  and  $260^\circ$  are those trajectories which strike the target frame. The triangular-shaped gap at  $\cos\theta_0 \cong 0$  arises from the very steeply emitted positrons that strike the 2 mm wide stem which supports the target frame.

Figure 2-18 presents the relation between the positron energy, emission angle  $\theta_0$ , and detection efficiency. The efficiency is shown integrated over azimuthal angle. The oscillations in  $\theta_0$  apparent in Fig. 2-17 are clearly evident in Fig. 2-18 as well. The positions of the maxima, however, vary with positron energy in the same way as the pitch-lengths vary, i.e., proportionally to  $P_{e^+} \cos(\theta_{e^+})$ . In addition, the

Table 2-1: Stop Positions in EPOS Spectrometer

Position\Energy	200 keV	350 keV	500 keV	800 keV	1000 keV
Detector	30.09%	33.40%	36.16%	40.11%	12.31%
Baffle Blades	23.46%	29.81%	28.38%	30.99%	25.97%
Baffle Disk	23.60%	17.82%	18.30%	12.64%	39.94%
Target Frame	13.73%	9.80%	7.96%	5.65%	4.50%
Vacuum Chamber	0.00%	0.00%	0.00%	1.49%	8.14%
Mirror	9.21%	9.26%	9.29%	9.22%	9.23%

cutoff at high energies for steep emission angles which strike the inner radius of the Si(Li) vacuum chamber is visible. As noted above, positrons emitted with angles larger than

$$\sin\theta_{e^+} > \frac{1}{2}(eB/pc)R_{\text{cham}} \quad (2.49)$$

are prevented from reaching the detector. Similarly the low-energy cutoff from the baffle hub stops positrons with emission angles flatter than

$$\sin\theta_{e^+} < \frac{1}{2}(eB/pc)r_{\text{baf}} \quad (2.50)$$

The fine-structures superimposed on the gently oscillating efficiency surface correspond to positrons which strike the target frame.

### Sec. 2.2.6 EPOS Spectrometer Performance

It was mentioned earlier that these experiments focussed on investigating the production and characteristics of positron peaks in superheavy collisions. It is therefore crucial to understand whether the response of the EPOS spectrometer can artificially produce structure in the positron energy distribution. Generally the oscillating dependence of detection efficiency on positron energy and emission angle does not lead to narrow structures in the energy spectrum of positrons from a continuous source. In reality, the calculated patterns of Figs. 2-17,2-18 overestimate the extent of the oscillatory behavior because they correspond to emission from a point source in an ideal spectrometer whose components are perfectly

$$E_{e^+} = 350 \text{ keV} \quad (1983)$$

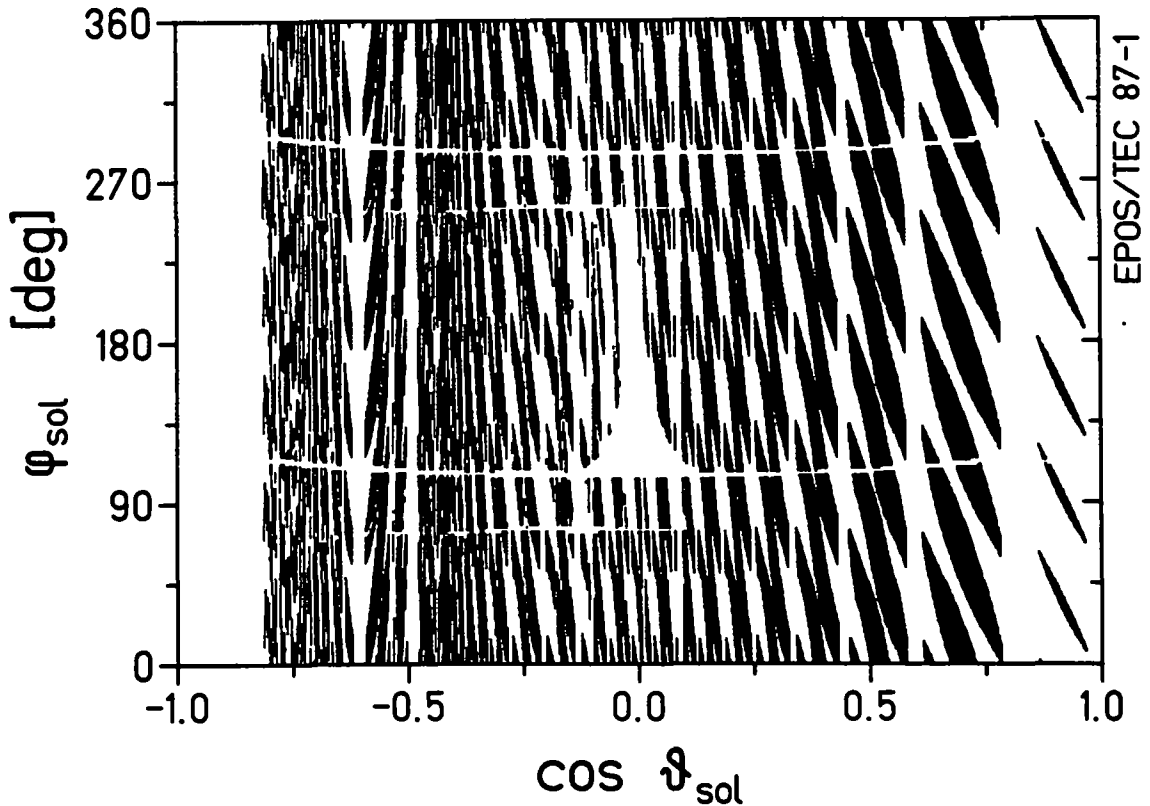


**Figure 2-17.** Transport efficiency for 350 keV positrons emitted from a point target with angles  $\theta$ ,  $\phi$  w.r.t. the solenoid axis. Dark (light) regions denote hits (misses) in Si(Li) detector. Evident features include the six-fold periodicity of  $e^+$  detection in  $\phi$  from the spiral baffle, gaps in efficiency caused by target frame at  $\cos\theta \cong 0$  and  $\phi \cong 90^\circ$  and  $270^\circ$ , and the oscillatory structure in  $\cos\theta$  when, after an integral number of orbits, the positron hits the central disk of the spiral baffle.

aligned. Averaging over the typical beam-spot size (5 mm dia.) substantially smooths out the acceptance of Fig. 2-17.

As can be seen from the adiabatic parameterization of the positron orbit given by Eqn. 2.37, a finite source size,  $\Delta z$ ,  $\Delta r$ , is equivalent to integrating over a range of phases (i.e., a range of  $z_0$ ) at the oscillation-producing baffle. The orbital parameters of a 350 keV positron, emitted at a typical angle of  $\theta_0 = 70^\circ$ , are  $L_b = 10.5$  cm,  $2\rho_b = 3.16$  cm, and  $\theta_b = 43.4^\circ$  at the baffle position. The smearing in the phase of the positron trajectory due to the horizontal width of the beam spot ( $\Delta z$ ) is  $(\Delta z/L_b) \cong 5\%$ , or about  $9^\circ$  out of the  $180^\circ$  orbital period. The vertical width of the beam ef-

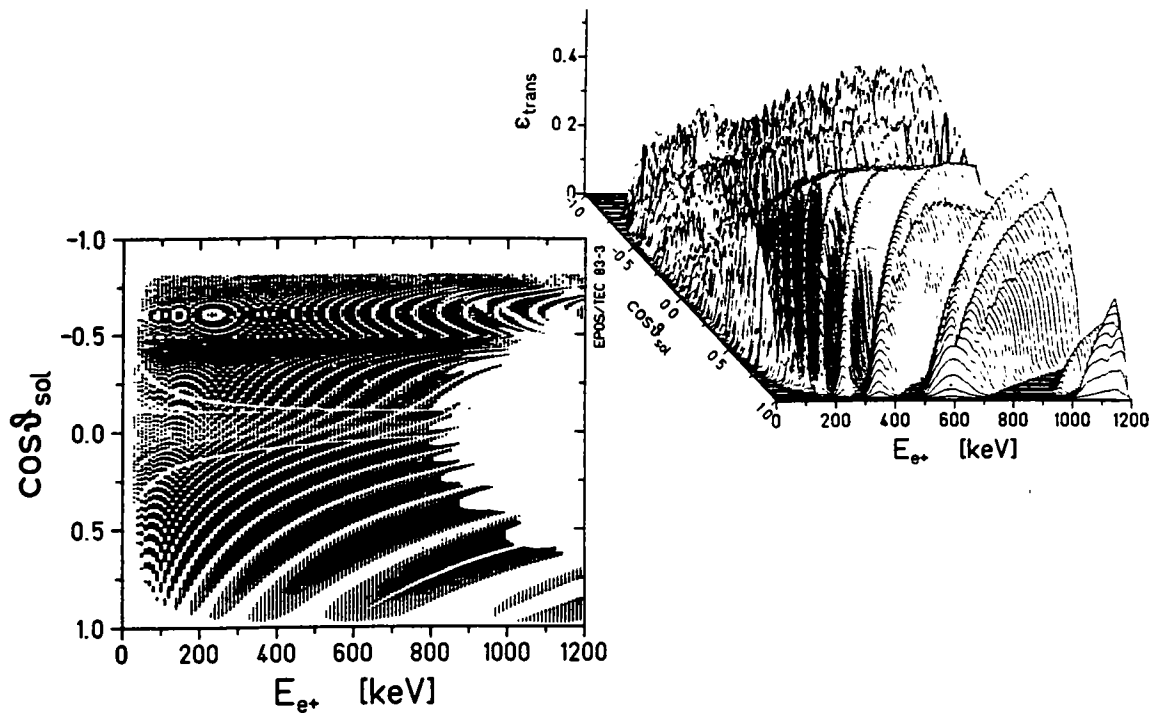


**Figure 2-18.** Contours of constant positron detection efficiency (integrated over  $\phi$ ) plotted versus kinetic energy and solenoid emission angle (right), and an isomeric representation (left). Undulatory structures are produced by spiral baffle transmission, with finer structures produced by the target frame.

fectively averages over both radial and azimuthal coordinates. The effective size of the variation is magnified at the baffle because the magnetic field line passing through an off-axis point of emission of a positron ( $r_0$ ) diffuses outward in the reduced field region around the baffle by an extra factor  $(B_0/B_{baf})^{1/2} = 1.37$ . The appropriate radial spread in the orbital phase is therefore  $(\Delta z_0)_{rad} = (1.37r_0)(dz/dr)_{avg}$ , which amounts to  $\cong 25^\circ$  out of the  $180^\circ$  period. Finally, the spread in the azimuthal coordinate depends on the solenoid angle  $\phi$  at which the positron passes through the baffle and is approximately  $(1.37r_0 \cos \phi)$  divided by the mean distance of the positron from the solenoid axis. This amounts to an  $\cong 13^\circ$  spread.

Together these shifts can be simulated by averaging the detection efficiency over a large range of initial momenta,  $\Delta P/P \cong 10\%$ . This is equivalent to averaging over the corresponding energy range,  $\Delta E_{e^+} = [P/(E + 2m_e c^2)] \Delta P \cong 60$  keV. This smooths out sharp features in the efficiency curve, e.g., the high-energy cutoff at 800 keV, and produces better agreement with the measured transport efficiency (see

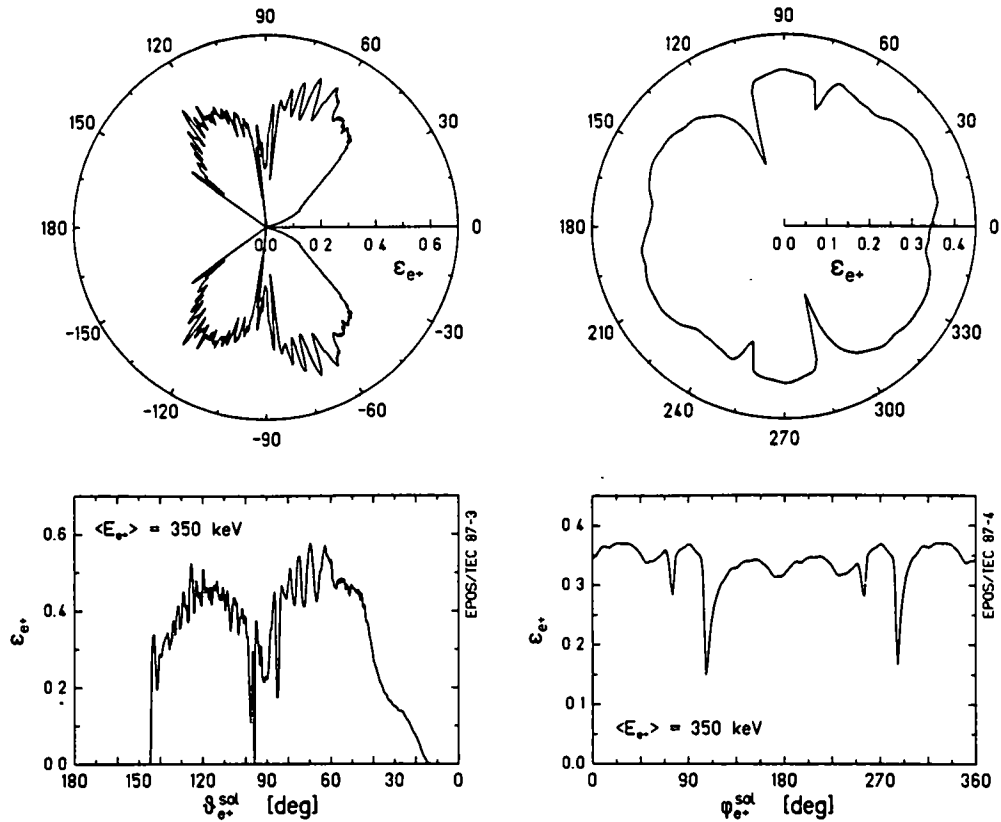


**Figure 2-19.** EPOS transport probability for  $300 < E_{e+} < 400$  keV, shown as a function of: polar emission angle  $\theta$  (left) w.r.t. the solenoid axis (integrated over  $\phi$ ), and azimuthal angle  $\phi$  (right, integrated over  $\theta$ ).

Fig. 2-16). Figure 2-19 presents polar plots of the detection efficiency, averaged over  $300 < E_{e+} < 400$  keV, as a function of the emission angles  $\theta_{e+}$  and  $\phi_{e+}$ . In each case, the detection probability is fairly uniform. A direct verification that the detection efficiency is a smooth function of the positron emission angles and energy is shown in Fig. 2-20. The energy distribution of positrons detected from the  $\beta^+$  decay of a  $^{56}\text{Co}$  source placed at the target position is smooth and structureless. All of this clearly shows that peaks are *not* produced by the transport and detection efficiencies of the EPOS spectrometer.

**Sec. 2.2.6.2 Positron Hit Position in Si(Li) Detector:** The position along the Si(Li) detector where a positron actually is stopped can, in principle, slightly affect both the probability of detecting the 511 keV annihilation radiation in the ARD NaI crystal array and the charge collection in the Si(Li) detector, and thereby the measured linesh-

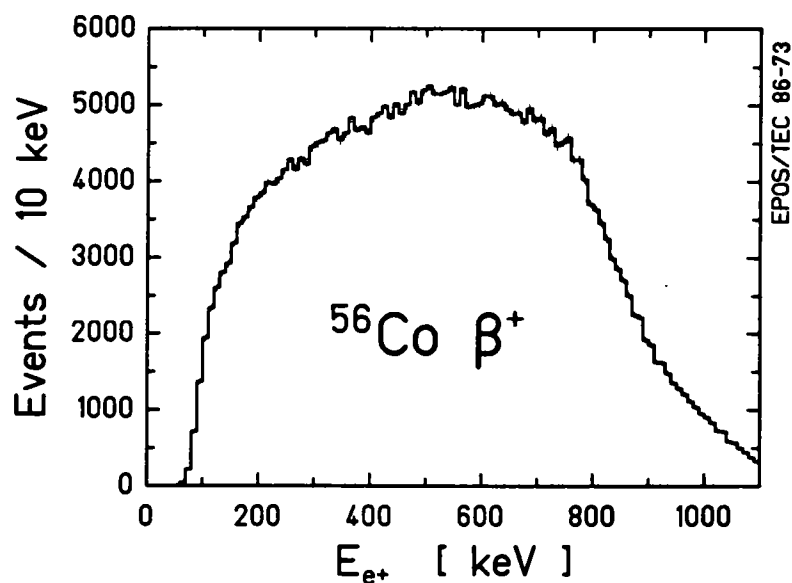


**Figure 2-20.** Measured energy distribution of positrons from a  $^{56}\text{Co}$   $\beta^+$  source, illustrating smoothness of positron detection efficiency.

ape. Positron trajectories having longer pitch-length obviously have the largest probability of striking the rear portions of the counter. Low energy positrons, or steeper emission angles, having small pitch-lengths, primarily strike the forward portion of the detector. Figure 2-21 presents the stop position along the Si(Li) of positrons of fixed energy, as calculated with the ray-tracing code. An integration over the dynamic positron energy spectrum shows that only 15.5% of the positrons are incident in the rear Si(Li) segment. However, about 4.3% of positrons striking the front segment outscatter and are eventually stopped in the rear crystal. When this type of prompt coincidence between the Si(Li) segments is recorded, their energy signals are added together to give the total positron kinetic energy.

**Sec. 2.2.6.3 Off-Axis Detection Efficiency:** As described above, the axial arrangement of the positron detector was motivated by the reduced efficiency of detecting positrons created or scattered away from the solenoid axis. In addition to verifying this feature quantitatively, it is necessary to study the detection efficiency for positrons emitted off-axis in order to understand, for example, the response of the solenoid to a long-lived source. This could be particularly important in understanding the width and intensities of the positron peaks. Moreover, one must again be certain that a broad distribution of emitted positron energies from a long-lived source, e.g., internal

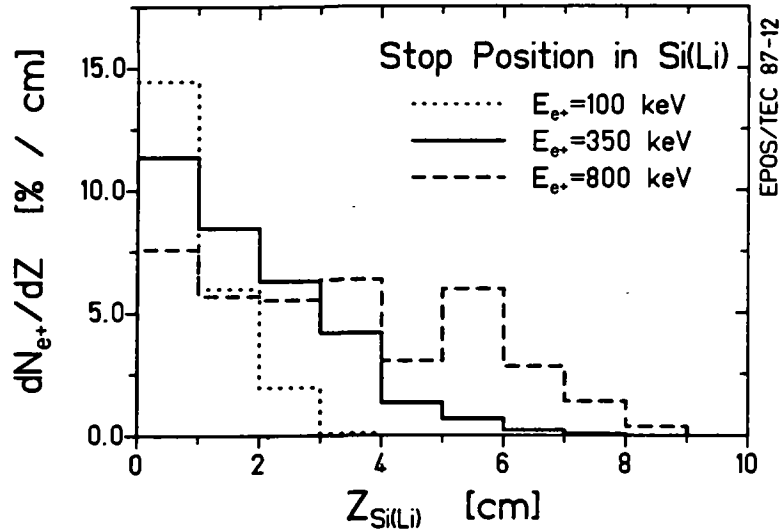


**Figure 2-21.** Histogram of the position along the Z-axis where positrons are incident in the pencil-like Si(Li) detector.

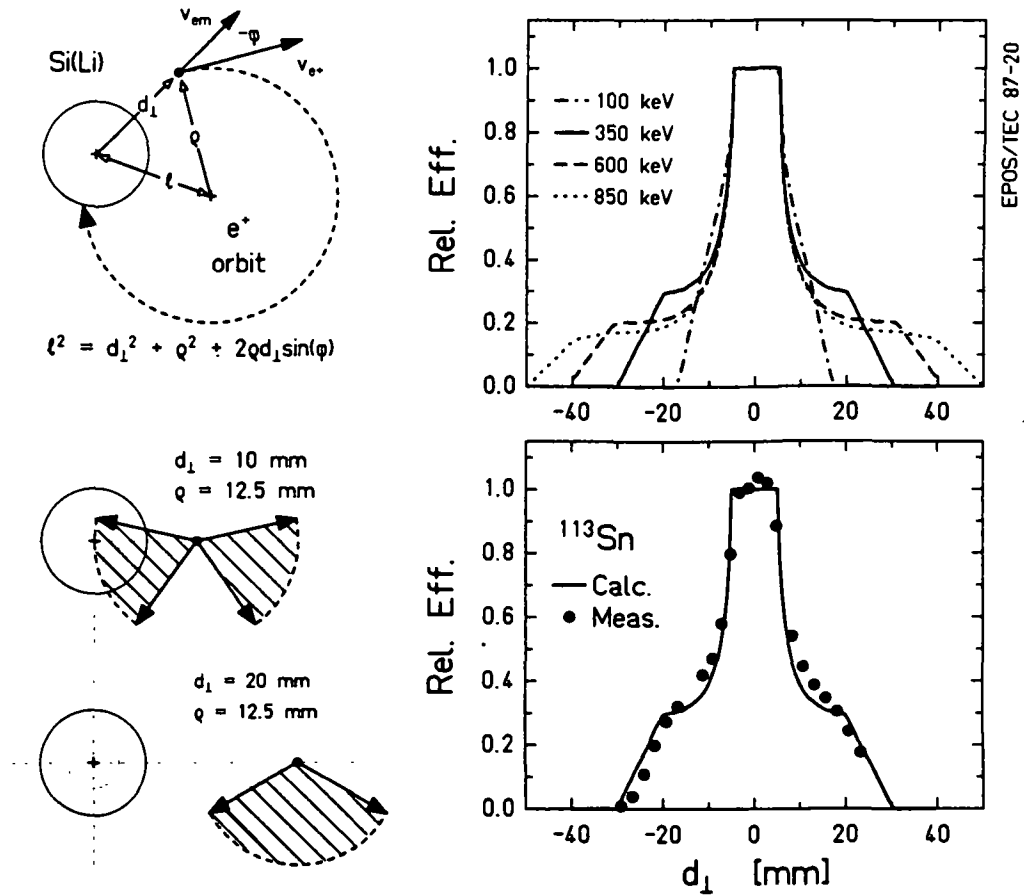
pair creation in the separated nuclei, cannot produce the narrow structures observed in these experiments.

Figure 2-22 shows schematically how the efficiency for detection varies for positrons emitted at a distance,  $d_{\perp}$ , perpendicularly off-axis. For positron energies around 350 keV, the change in the transmission efficiency through the baffle for off-axis emission with  $d_{\perp} \leq 15$  mm is, in first order, rather small. This is because the distance  $d_{\perp}$  mostly simulates a change in the radial position  $R_{\text{baf}}$  where the positron passes through the baffle, which in turn simulates a somewhat different positron energy. Over this range of effective emission energies, the transport efficiency is rather flat in Fig. 2-16, which indicates that the baffle acceptance remains fairly constant. The major difference in off-axis transport efficiency is therefore the proportion of trajectories which strike the Si(Li) detector. As is evident from Fig. 2-22, for  $d_{\perp} < R_{\text{det}}$ , almost no change in efficiency is expected. For larger distances, however, the orbit does not intersect the Si(Li) for all azimuthal emission angles  $\phi$ . Noting that the distance  $\ell$  between the guiding center of the orbit and the sole-noid axis is

$$\ell = [d^2 + \rho^2 + 2d\rho \sin\phi]^{1/2}, \quad (2.51)$$

the probability of striking the detector is

## Off-Axis Detection Efficiency



**Figure 2-22.** Sketch of a positron emitted from a source positioned  $d_{\perp}$  off-axis with an orbital radius of  $\rho$  (upper left). Range of azimuthal emission angles for which the positrons are detected denoted by shaded regions for two off-axis distances (lower left). Upper right shows relative detection efficiency versus off-axis distance calculated for several energies, and compared to source measurements with 364 keV  $^{113}\text{Sn}$  K-line (lower right).

$$\begin{aligned} \varepsilon_{\text{det}} &= 1 \text{ if } |\rho - \ell| < R_{\text{det}} \text{ and } (\rho + \ell) < R_{\text{cham}}, \\ &= 0 \text{ if } |\rho - \ell| > R_{\text{det}} \text{ or } (\rho + \ell) > R_{\text{cham}}. \end{aligned} \quad (2.52)$$

Figure 2-22b plots the off-axis detection efficiency calculated for  $E_{e^+} = 100, 350, 600, 850$  keV. Figure 2-22c compares the calculated off-axis positron efficiency for 350 keV to a measurement with a  $^{113}\text{Sn}$  source ( $E_K^{e^-} = 364$  keV). The FWHM of the off-axis efficiency is about 10 mm, which reflects the diameter of the Si(Li) detector. This represents the approximate fiducial volume of the EPOS spectrometer.

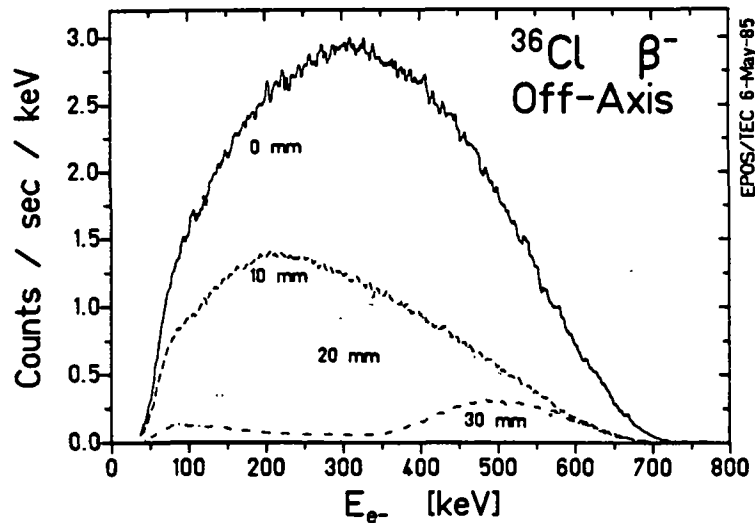


**Figure 2-23.** Energy distributions of electrons detected (using reversed magnetic field polarity) from a  $^{36}\text{Cl}$   $\beta^-$  source positioned 0, 10, 20, and 30 mm perpendicularly away from the solenoid axis.

Figure 2-23 presents energy spectra for electrons (detected with reversed magnetic field polarity) from a  $^{36}\text{Cl}$   $\beta^-$  source. As the source is moved away from the solenoid axis, the low-energy electrons are attenuated more quickly than for higher energies, as is evident from Fig. 2-22b. Lineshape tailing prevents the spectrum near  $E_{e^-} < 100$  keV from going to zero. No narrow structures emerge, however. The change in  $\epsilon_{e^-}(E_{e^-})$  is a smooth function of  $d_{\perp}$ . The possibility of producing a peak by this type of effect is discussed further in Sec. 4.1.

The suppression of electrons by the baffle, however, does change with emission away from the axis. For on-axis emission the change in solenoid angle,  $\phi$ , varies monotonically with motion in the Z-direction, and  $d\phi/dz > 0$  (for  $e^-$ ) is opposite that of the spiral baffle blades. For off-axis emission with  $\ell > \rho$ , the portion of the trajectory nearest to the axis has a reversed rotational sense, and therefore simulates the motion of a positron at small values of  $r$ . The suppression of electrons is therefore decreased. At  $d_{\perp} \cong 10$  mm, the suppression factor (Fig. 2-8) is reduced by a factor of  $\sim 10$  at 350 keV, compared to the on-axis value of  $\sim 10^3$ .

**Sec. 2.2.6.4 Positron Time-of-Flight:** The nature of the EPOS magnetic spectrometer as a transport system, rather than an analyzing spectrograph, is not optimally suited for direct measurements of the emission angles of the detected positrons. An ap-

proximate determination of the polar angle  $\theta_{e+}$ , however, is in principle possible by measuring the time-of-flight (TOF) of the positron from the target to the Si(Li) detector. It might therefore be possible to extract an emission angular distribution for the peak positrons from their distribution of flight-times.

In a uniform field, positrons emitted toward the detector located a distance  $Z_{\text{det}}$  away from the target have a TOF given by

$$\text{TOF} = Z_{\text{det}}/v_z = Z_{\text{det}}/[(pc/eB) \cos\theta_{e+}]. \quad (2.53a)$$

In the nonuniform EPOS field, the parallel velocity depends on  $B(z)$ , and the TOF must be integrated over the trajectory,

$$\text{TOF} = \int_0^{Z_{\text{det}}} dz / \{(pc/eB) [1-(B(z)/B_0)\sin^2\theta_0]^{1/2}\}. \quad (2.53b)$$

For steeply emitted positrons,  $\cos\theta_0 \cong 0$ , or positrons reflected from the magnetic mirror, the flight time is rather large. Figure 2-24a presents the positron TOF as a function of  $E_{e+}$  and  $\theta_0$ , as calculated with the ray-tracing code described in App. C. The TOF as a function of emission angle is shown for 350 keV positrons in Fig. 2-23b. The range in flight-time between positrons emitted at flat angles and those at steep angles or reflected by the mirror is from TOF  $\sim 4$  ns to  $\sim 13$  ns. Since the trajectory only strikes the positron detector when it returns to the solenoid axis, the TOF reflects integral multiples of the  $\sim 340$  ps period of a single positron orbit, leading to the step-like appearance in Fig. 2-24b. Figure 2-24c gives the TOF integrated over  $d(\cos\theta_0)$  as a function of  $E_{e+}$ . The inverse dependence on momentum,  $\propto 1/P_{e+}$ , is evident in the increased mean TOF at low energies. For  $E_{e+} > 800$  keV, the reduction of transmission for steep emission angles with  $2\rho > R_{\text{cham}}$  is apparent. The flatter mean detected emission angles have larger longitudinal velocities, with consequently smaller flight times. As discussed below, the poor separation of flight times for  $-1 < \cos\theta_0 < +0.1$  makes it difficult in this set-up to differentiate positrons emitted with  $\theta_0 \cong 90^\circ$  from those emitted at flatter angles,  $\theta_0 \sim 0^\circ$ , or  $180^\circ$ .

### **Sec. 2.2.7 Doppler-Broadened Positron Lineshape**

A major portion of Part I of this dissertation reports the determination of the mean velocity of the source emitting the positron peaks by measuring the Doppler-broa-

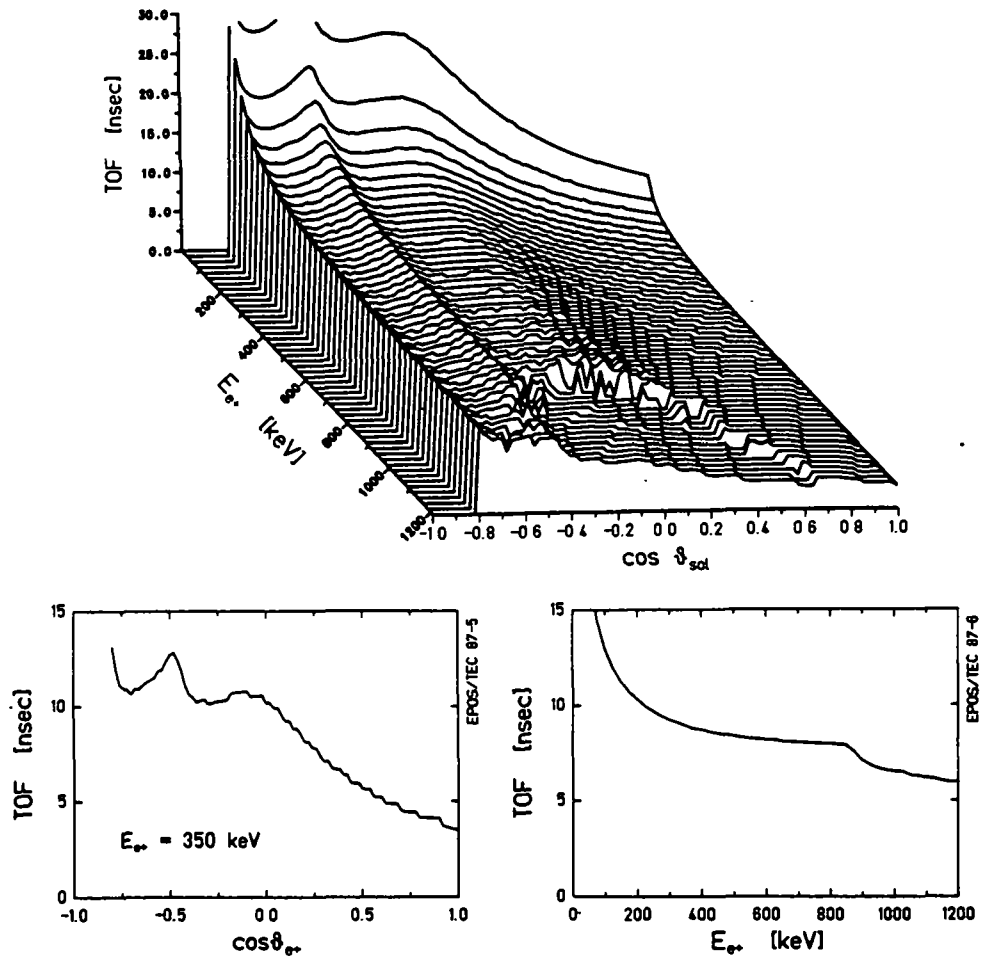


**Figure 2-24.** Calculated flight time of positrons from the target to the Si(Li) detector as a function of the energy and polar emission angle  $\theta_{sol}$  (top). Lower left shows the emission angle dependence for 350 keV positrons, and lower right presents the mean TOF versus energy, averaged over all emission directions.

dening of the positron line in the laboratory. To extract the source velocity from the positron linewidth, the response of the EPOS spectrometer to a moving emitter must be known. Moreover, an understanding of the detailed shape of the expected positron peak is required simply to determine the important parameters of the positron lines, namely their mean energy in the rest frame of the source, the intrinsic width (and hence, source lifetime), and the production cross-section. This section presents a general derivation of the EPOS lineshape, discusses some important special cases, and addresses several effects which alter the laboratory linewidth, such as positron emission angular distribution, intrinsic width, range of emitter velocities, off-axis emission, and source lifetimes. Finally, the calculated lineshape is compared to a

direct measurement of monoenergetic electron emission from a source formed in a HI fusion reaction.

**Sec. 2.2.7.1 Coordinates:** Throughout this discussion the following definitions, coordinate systems, and variables are used. Positron motion in the solenoid coordinate system (e.g., for detection efficiency) is described by the polar and azimuthal angles  $(\theta, \phi)$  introduced in Sec. 2.2.1 and shown in Fig. 2-25a. In the frame  $S^*$  of the emitting source, the emission direction of the positron is denoted by the polar angle  $\psi^*$  and azimuthal angle  $\Phi^*$ , where  $z^*$  is taken in the direction of the source velocity (see Fig. 2-25b). The  $x^*$  axis is in the vertical plane which passes through the  $z^*$  axis (and the solenoid Y axis), oriented toward the upward half-plane. In the lab frame, the positron is described by  $(\psi, \Phi)$  relative to the coordinate system  $^{\circ}$ , which is oriented in the same way as  $S^*$ . The velocity of  $S^*$  in the lab is  $\beta_{em} = v_{em}/c$  along the  $z^*$  direction, which forms an angle  $(\theta_{em}, \phi_{em})$  with respect to the solenoid axis.

In keeping with the convention used elsewhere in this dissertation, where  $E_{e^+}$  and  $P_{e^+}$  denote kinetic energy and momentum, respectively, the symbol  $W$  is adopted here for total energy. For simplicity, the subscripts "e+" and "e-" are dropped. That is,

$$W^* = (E^* + m_e c^2) = [P^{*2} + m_e^2 c^4]^{1/2},$$

where  $m_e$  is the electron rest mass. Finally, distributions are denoted by,

$$d^3N^*/dE^*d\Omega^* = \omega^*(E^*, \Omega^*),$$

where  $d\Omega^* = d(\cos\psi^*)d\Phi^*$ .

**Sec. 2.2.7.2 Kinematic Relations:** A positron (or electron) emitted from the source,  $S^*$ , moving with velocity  $\beta_{em}$ , has energy and momentum in the laboratory given by the Lorentz transformations,

$$W = \gamma_{em}(W^* + \beta_{em}P^* \cos\psi^*), \quad (2.54a)$$

$$P \cos\psi = \gamma_{em}(P^* \cos\psi^* + \beta_{em}W^*), \quad (2.54b)$$

$$P \sin\psi = P^* \sin\psi^*. \quad (2.54c)$$

The laboratory polar angle with respect to the direction of motion is given by

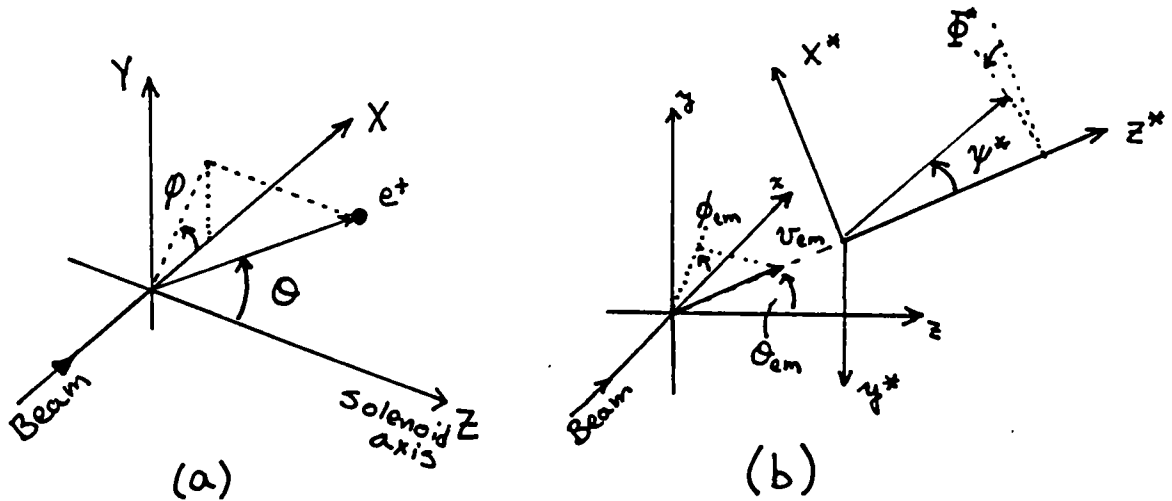


**Figure 2-25.** (A) Solenoid coordinate system used to express detection efficiencies. (B) Coordinate system of emitting source.

$$\tan\psi = \sin\psi^* [\gamma_{em}(\cos\psi^* + \beta_{em}/\beta^*)]^{-1}, \quad (2.54d)$$

where  $\beta^* = P^*/(E^* + m)$  is the velocity of the positron in  $S^*$ . The emitted energy and momentum in  $S^*$  are expressed in terms of the laboratory values by interchanging starred and unstarred quantities in Eqns. 2.54 and reversing the sign of  $\beta_{em}$ .

A distribution of positrons emitted from  $S^*$  is transformed to the laboratory system by

$$\omega(E, \Omega) = [\partial(E, \Omega)/\partial(E^*, \Omega^*)] \omega^*(E^*, \Omega^*). \quad (2.55)$$

The Jacobian is found from the Lorentz invariant quantities,

$$d^3P/(E + m) = P^2(E + m)^{-1} dP d\Omega = P dE d\Omega = P^* dE^* d\Omega^*, \quad (2.56)$$

which indicate that  $P^{-1}\omega(E, \Omega)$  is also a Lorentz invariant. The laboratory distribution is therefore given by,

$$\omega(E, \Omega) = (P/P^*) \omega^*(E^*, \Omega^*). \quad (2.57)$$

**Sec. 2.2.7.3 Laboratory Lineshape:** The spectrometer lineshape is defined as the energy distribution of positrons detected in the lab,  $dN/dE$ . It is obtained from Eqn. 2.57 by multiplying the emitted distribution by the positron detection efficiency and integrating over laboratory solid angle,

$$dN/dE = \int d\Omega (P/P^*) \omega^*(E^*, \Omega^*) \varepsilon_{e^+}(E, \theta, \varphi). \quad (2.58)$$

For a given laboratory energy bin,  $E$  is fixed in Eqn. 2.58, and the inverse of the Lorentz relation 2.54a gives,

$$dE^* = -\gamma\beta P d(\cos\psi). \quad (2.59)$$

The  $d(\cos\psi)$  integration in (2.58) can therefore be replaced by an integration over  $(\gamma\beta P)^{-1} dE^*$  between the limits

$$\gamma_{em}(W - \beta_{em}P) < (E^* + m_e c^2) < \gamma_{em}(W + \beta_{em}P).$$

That is, for  $\cos\psi = +1$  to  $\cos\psi = -1$ . Substitution into Eqn. 2.58 gives the Doppler-broadened laboratory positron lineshape,

$$dN/dE = \int dE^* (\gamma\beta P^*)^{-1} \int_0^{2\pi} d\Phi \omega^*(E^*, \Omega^*) \varepsilon_{e^+}(E, \theta, \varphi). \quad (2.60)$$

If the source is emitted with a range of laboratory velocities, the entire expression (2.60) must be integrated over the source velocity distribution,

$$dN/dE = \int d^3\beta_{em} \omega(\beta_{em}) \int dE^* (\gamma\beta P^*)^{-1} \times \int_0^{2\pi} d\Phi \omega^*(E^*, \Omega^*) \varepsilon_{e^+}(E, \theta, \varphi). \quad (2.61)$$

The positron detection efficiency,  $\varepsilon_{e^+}(E, \theta, \varphi)$ , in Eqn. 2.61 is a function of the laboratory energy and emission direction (expressed as a function of the polar coordinates  $\theta, \varphi$ , with respect to the solenoid axis, as shown in Sec. 2.2.5). The angular integration in 2.61, on the other hand, is performed azimuthally around a cone of fixed polar angle  $\psi$  given by  $W^*, \psi = \cos^{-1}[(W - W^*)/\gamma_{em}]/\gamma\beta$ ; coaxial about the laboratory direction of the emitting system. The respective solenoid angles  $\theta, \varphi$  are given as a function of  $\psi, \Phi$ , by an Euler rotation matrix,  $n = R \bullet n'$ ,

$$R = \begin{bmatrix} \cos\theta_{em}\cos\varphi_{em} & -\sin\varphi_{em} & \sin\theta_{em}\cos\varphi_{em} \\ \cos\theta_{em}\sin\varphi_{em} & \cos\varphi_{em} & \sin\theta_{em}\sin\varphi_{em} \\ -\sin\theta_{em} & 0 & \cos\theta_{em} \end{bmatrix}, \quad (2.62a)$$

with,

$$n = \begin{bmatrix} \sin\theta \cos\varphi \\ \sin\theta \sin\varphi \\ \cos\theta \end{bmatrix}, \quad n' = \begin{bmatrix} \sin\psi \cos\Phi \\ \sin\psi \sin\Phi \\ \cos\psi \end{bmatrix}, \quad (2.62b)$$

where  $\theta_{em}$ ,  $\varphi_{em}$ , denote the direction of the emitter velocity in the laboratory. The specific definition of Euler angles employed in Eqn. 2.62 ensures that a null rotation,  $\theta_{em} = \varphi_{em} = 0$ , gives the identity matrix.

For certain very simple positron emission distributions and source velocities, the coordinate transformation can recast the  $\Phi$  integration in Eqn. 2.61, using  $d\Phi/d\theta d\varphi$ , into an angular integral which may be performed numerically, taking advantage of the near rotational symmetry of the positron detection efficiency,  $\varepsilon_{e^+}(E, \theta, \varphi) \cong (2\pi)^{-1} \varepsilon_{e^+}(E, \theta)$ . Calculations along these lines were performed using the adiabatic approximation of  $\varepsilon_{e^+}(E, \theta)$  discussed in Sec. 2.2.5, for the lineshape analyses presented in [Sch83, Cow85]. More accurate evaluation of Eqn. 2.61, incorporating Eqn. 2.62 and using the full EPOS detection efficiency, requires a Monte-Carlo approach. The calculations presented in this section were performed with the MCSPEC program described in App. C.

**Sec. 2.2.7.4 Monoenergetic CM Emission:** One very important application of the Doppler lineshape analysis concerns a monoenergetic positron peak emitted isotropically from the CM system, as would be expected for spontaneous positron emission. The velocity and positron angular distributions are given by:

$$\omega^*(E^*, \Omega^*) = (1/4\pi) \delta(E^* - E_o^*), \quad (2.63a)$$

$$\omega(\beta_{em}) = \delta(\beta_{em} - \beta_{cm}). \quad (2.63b)$$

Since  $\theta_{em} = \pi/2$  and  $\varphi_{em} = 0$ , the coordinate transformation of Eqns. 2.62 give

$$\cos\theta = -\sin\psi \cos\Phi,$$

$$\tan\varphi = \tan\psi \sin\Phi,$$

and the lineshape integral 2.61 reduces to

$$dN/dE = (2\gamma\beta P_0^*)^{-1} (1/2\pi) \int_0^{2\pi} d\Phi \epsilon_{e^+}(E, \theta, \phi), \quad (2.64)$$

between the lab energies,

$$\gamma_{em}(W_0^* - \beta_{em} P_0^*) < (E + m) < \gamma_{em}(W_0^* + \beta_{em} P_0^*). \quad (2.65)$$

For the special case of uniform detection (i.e.,  $\epsilon_{e^+} \equiv 1$ ), the laboratory distribution of positrons is a constant equal to  $(2\gamma\beta P_0^*)^{-1}$  between the limits  $\gamma_{em}(W_0^* \pm \beta_{em} P_0^*)$ . As shown by the dashed line in Fig. 2-26, the rectangular peak has a width of  $\Delta E = 2\gamma\beta P_0^*$ , and the centroid of the laboratory distribution is shifted from the emitted mean energy  $E_0^*$  by  $\delta E = (\gamma_{em} - 1)W_0^*$ . For a 320 keV positron emitted from the CM system of Th+Cm at 6.0 MeV/u ( $v_{CM} = .056c$ ), the lab lineshape has a FWHM of  $\Delta E = 73.5$  keV, and is centered at 321.3 keV ( $\delta E = 1.3$  keV).

The EPOS detection efficiency modifies the emitted laboratory distribution (Eqn. 2.64) as shown by the shaded histogram in Fig. 2-26a. The characteristic dip in the central portion of the positron lineshape arises due to the orientation of the source velocity perpendicular to the solenoid axis. The acceptance of the EPOS spectrometer is rather broad, but it vanishes for very flat emission angles along the solenoid axis, as shown in Fig. 2-19. Those positrons exhibiting maximum Doppler shift, i.e., emitted parallel or anti-parallel to  $v_{CM}$ , travel with steep pitch angles with respect to the solenoid axis and are detected with large probability. Positrons exhibiting small Doppler shifts, however (those emitted close to the vertical plane through the solenoid axis), are detected with smaller efficiency because of the large fraction which fall within the regions of reduced transport probability. The slightly asymmetric shape of the positron line reflects the relativistic solid angle transformation which sweeps the isotropically (in  $S^*$ ) emitted positrons to more forward angles in the lab so that relatively more intensity is shifted to higher energies.

A fine structure is also apparent in the laboratory positron lineshape of Fig. 2-26. It is produced because for neighboring energies, the azimuthal integration  $d\Phi$  about the cone of constant  $\psi$  cuts differently across the  $\phi$ -dependence of the spiral-baffle transmission efficiency. The oscillatory structures, of order  $\sim 4$

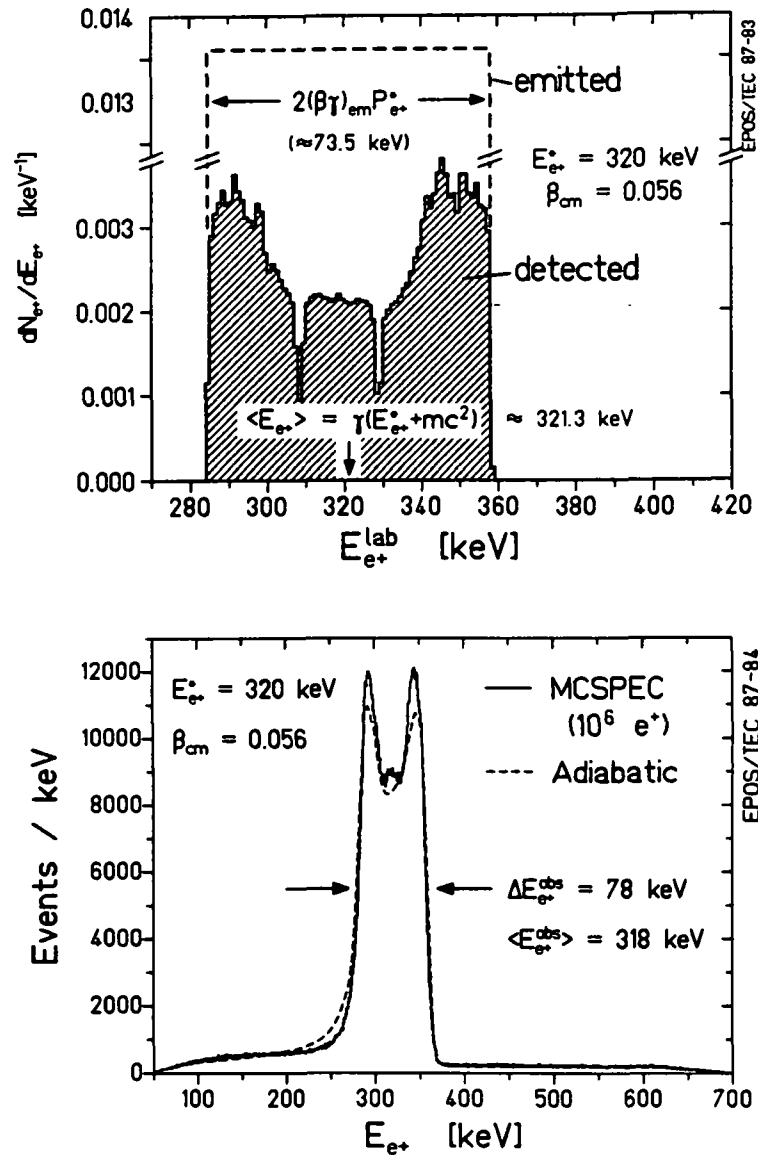


**Figure 2-26.** Dashed line (top) presents the laboratory energy-differential probability distribution of 320 keV positrons emitted isotropically from the HI center-of-mass system ( $v_{CM} = 0.056c$ ). Shaded histogram is the detected distribution, including EPOS transport efficiency and ARD annihilation photon detection probability, but excluding the resolution and tailing of the Si(Li) detector response. Lower figure includes the detector response (histogram), and compares with results of previous calculations using an adiabatic efficiency approximation (dashed curve).

keV wide, are however smaller than the energy resolution of the Si(Li) detector. Figure 2-26b includes the experimental detector response.

$$(dN/dE)_{obs} = \int_0^{E_0} F(E, E_0) \cdot (dN/dE_0) dE_0 \quad (2.66)$$

The finite energy resolution smears out the narrow fine-structure, and the low-energy tail partly fills in the central dip, giving a more symmetric profile to the laboratory lineshape.

Also shown in Fig. 2-26b by the dashed curve is the numerically integrated lineshape calculated within the adiabatic approximation, which was used in the analysis of [Sch83, Cow85]. As mentioned above, the efficiency was assumed to be azimuthally symmetric, depending only on  $\theta$  and  $E$ , and the integral of Eqn. 2.64 was simplified by the change of coordinates,

$$d\Phi = -\sin\theta \cdot [\sin^2\psi - \cos^2\theta]^{-1/2} d\theta. \quad (2.67)$$

The range of integration extends from  $(\pi/2 - \psi) < \theta < \pi/2$ . The good agreement between the adiabatic calculation and the full Monte-Carlo lineshape emphasizes the relative unimportance, when dealing with broad distributions, of the detailed  $\theta$ - $\psi$ - $E$  dependence of the EPOS transport efficiency.

The width and detailed shape of the Doppler broadened lineshape is also very insensitive to the direction of the emitter velocity, as long as it is roughly perpendicular to the solenoid axis. The lineshape presented in Fig. 2-26 very nearly gives the profile expected for monoenergetic positron emission from the separated nuclei, with the stipulation that the emitter velocity, or range of velocities  $\omega(\beta_{em})$ , which is typically larger than  $v_{CM}$ , adjusts the width of the lineshape,  $\Delta E \cong 2(\gamma\beta)_{em}P^*$ , accordingly (see, e.g., Fig. 4-16).

In addition to the emitter velocity distribution, the other aspects of the positron lineshape already built into Eqn. 2.61 can affect the laboratory positron linewidth. These include non-isotropic angular distributions for the emitted positrons, a distribution of emitted energies (e.g., intrinsic width due to short source lifetime), or off-axis emission associated with a long lifetime for the positron peak source.

**Sec. 2.2.7.5 Angular Distribution:** If monoenergetic positrons are emitted with a distribution of emission angles  $\psi^*$ , from a system moving with fixed velocity  $\beta_{em}$ , Eqn. 2.63 becomes

$$\omega^*(E^*, \Omega^*) = (2\pi)^{-1} \delta(E^* - E_0^*) \cdot dN^*/d(\cos\psi^*). \quad (2.68)$$

Since the azimuthal integration in 2.60 is over a cone of constant  $\psi^*$  for fixed laboratory energy,  $dN^*/d(\cos\psi^*)$  factors out of the integral, and enters Eqn. 2.64 as a multiplicative factor,

$$dN/dE = (\gamma\beta P_0^*)^{-1} \cdot dN^*/d(\cos\psi^*) \cdot (1/2\pi) \int_0^{2\pi} d\Phi \epsilon_{e^+}(E, \theta, \phi). \quad (2.69)$$

From the Lorentz transformation in Eqn. 2.54a, the lab energy  $E$ , is linearly proportional to  $\cos\psi^*$ , so the net effect of an angular distribution on the Doppler-broadened linewidth is simply to replace the original rectangular form of Fig. 2-24a with the distribution versus  $\cos\psi^*$ ,

$$dN/dE \sim dN^*/d(\cos\psi^*), \quad (2.70a)$$

where

$$\cos\psi^* = (\beta_{em} P^*)^{-1} \cdot (W^* - \gamma_{em}^{-1} W). \quad (2.70b)$$

The maximum linewidth is therefore directly determined by the range of positron emission angles detected. An emission angle distribution which enhances or suppresses positrons emitted parallel and antiparallel to the direction of  $v_{em}$  would increase or decrease the linewidth, respectively.

The lineshape would be similarly affected if the acceptance of the EPOS spectrometer were to limit the detection of maximally Doppler-shifted positrons. Figure 2-27 addresses the possibility that the calculated Doppler-broadened lineshape may be in error due to incorrect assumptions about the EPOS acceptance. Figure 2-27b plots the positron lineshape assuming that positrons emitted at angles steeper than some cut-off,  $\theta_{cut}$ , with respect to the solenoid axis are not detected. This scenario was motivated by the presence of a magnetic bottle surrounding the target in the 1981 field configuration [Shw85] which trapped steeply emitted positrons, and by the fact that positrons produced in the CMS have maximum Doppler shifts for emission angles perpendicular to the solenoid axis. Cut-off angles of  $\theta_{cut} \leq 65^\circ$  are required to substantially reduce the measured linewidth. The positron transport efficiency, shown in Fig. 2-27a calculated for  $\theta_{cut}$  in the adiabatic approximation, would however also be greatly reduced because the steep angles correspond to the region of largest solid-angle. Source measurements, indicated by the points in Fig. 2-27a, limit the minimum possible  $\theta_{cut}$  to  $\theta_{cut} \approx 75^\circ$  in a direct, nearly model-independent fashion.

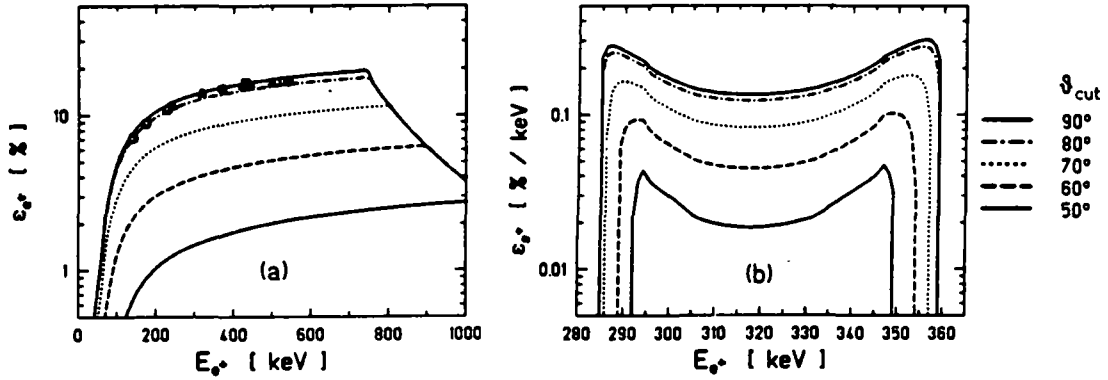


**Figure 2-27.** Adiabatic transport efficiency (a) and Doppler-broadened positron lineshape (b) calculated for maximum detected emission angle,  $\theta_{\text{cut}}$  with respect to solenoid axis, as marked.

**Sec. 2.2.7.6 Intrinsic Energy Distribution:** If positrons are emitted isotropically from  $S^+$  with a distribution of energies,  $\omega^+(E^+) = dN^+/dE^+$ , then Eqn. 2.63 becomes,

$$\omega^+(E^+, \Omega^+) = (4\pi)^{-1} \omega^+(E^+), \quad (2.71)$$

and Eqn. 2.60 reduces to,

$$dN/dE = (2\gamma\beta)^{-1} \int dE^+ P^{*-1} \omega^+(E^+) (1/2\pi) \int_0^{2\pi} d\Phi \varepsilon_{e^+}(E, \theta, \phi). \quad (2.72)$$

Equation 2.72 represents a simple convolution integral of the energy distribution  $\omega^+(E^+)$  with the energy-dependent positron lineshape given by Eqn. 2.64.

The distribution of positrons may have any form ranging from a collection of discrete energies, as might occur for transitions between a collection of different states, to the broad bell-shaped continuum of induced positrons emitted dynamically from the CM system. Two particularly important examples which are discussed later in this dissertation concern nuclear conversions and emitter lifetime. Nuclear internal pair creation (IPC) transitions entail folding the Doppler-broadened laboratory lineshape with the almost triangular spectrum of positrons given by the differential conversion coefficient,  $d\beta/dE^+$  (see Sec. 4.2). A source lifetime  $\tau$  produces, from the uncertainty principle, a distribution of energies with width  $\Gamma = \hbar\tau$ , which typically yields a Breit-Wigner shape,

$$\omega^*(E^*) = (\Gamma/2\pi) [(E^* - E_0^*)^2 + (\Gamma/2)^2]^{-1}. \quad (2.73)$$

**Sec. 2.2.7.7 Off-Axis Lineshape:** As discussed in Sec. 2.2.5, if the positrons are emitted from a source removed perpendicularly away from the solenoid axis by a distance  $d_{\perp}$  greater than  $R_{\text{det}}$ , the detection efficiency is decreased, and in Eqn. 2.61  $\epsilon_{e^+}$  is then a function of  $d_{\perp}$ , as well as  $E^*$ ,  $\theta$ , and  $\phi$ . The range of azimuthal emission angles,  $\phi$ , intercepted by the Si(Li) is indicated in Fig. 2-22 for two off-axis distances,  $d_{\perp} = d(\sin\theta)$ . For  $R_{\text{det}} < d_{\perp} < (2\rho - R_{\text{det}})$ , detection is limited to positrons emitted preferentially forward and backward, emphasizing the maximum doppler-shifts, as illustrated in Fig. 2-28 for a source moving in the CM direction. If  $d_{\perp} \geq (2\rho - R_{\text{det}})$ , only positrons emitted downward which spiral back through the detector are measured, and the lineshape becomes narrow, emphasizing the unshifted central portion. For  $d_{\perp} > (2\rho + R_{\text{det}})$ , the detection probability is zero.

**Sec. 2.2.7.8 Long Source Lifetimes:** If the source of the positrons has a lifetime long enough that emission occurs off axis, then the lineshape integral 2.61 must include not only the proper off-axis detection efficiency, for time  $t$ ,  $d_{\perp} = (\beta_{\text{em}} ct) \sin\theta$ , but also the  $e^{-t/\tau}$  decay-time distribution of the source,

$$\begin{aligned} dN/dE = & \int_0^{\infty} dt \tau^{-1} e^{-t/\tau} \int d^3\beta_{\text{em}} \omega(\beta_{\text{em}}) \int dE^* [(\gamma\beta)_{\text{em}} P^*]^{-1} \\ & \times \int_0^{2\pi} d\phi \omega^*(E^*, \Omega^*) \epsilon_{e^+}(E, \theta, \phi, d_{\perp} = d_{\perp 0} + v_{\perp} t). \end{aligned} \quad (2.74)$$

The exponential distribution of decay times, together with the rapid decrease in detection efficiency for large  $d_{\perp}$ , heavily weights the superposition of off-axis lineshapes in favor of those emitted near the axis. Nearly the full Doppler-broadened width is expected, as shown in Fig. 2-28b, where the direction of motion is taken as  $\beta_{\text{cm}}$  in the beam direction.

The preferential detection of positrons emitted near the axis, for a given lifetime  $\tau$ , changes if the transition emitting the positron line is populated from higher states characterized by a feeding time  $\tau'$ . The time integrand in Eqn. 2.74 becomes,

$$dN/dt = A_0 (1 - e^{-t/\tau'}) e^{-t/\tau},$$

which increases the mean distance at which the positrons are emitted. For times  $\geq 10^{-9}$  sec, the source travels well outside of the fiducial volume of the spectrometer

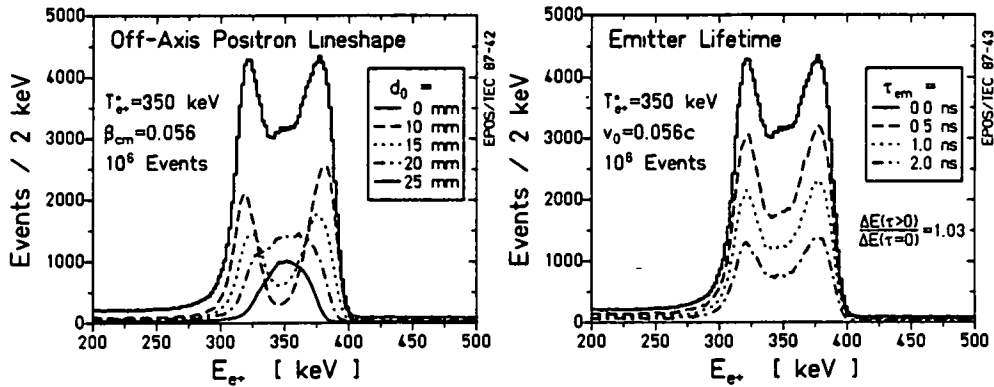


**Figure 2-28.** MCSPEC calculation of Doppler-broadened lineshape for 350 keV positrons emitted, from a source moving with  $v_{CM}$ , at discrete distances off-axis (left). After folding in source lifetime (right), the detection efficiency decreases but the linewidth remains constant.

and the detection efficiency is very small. For a sufficiently long lifetime,  $\tau$  or  $\tau' > 10^{-10}$  sec, this effectively suppresses the detection of fast moving positron sources, while relatively enhancing the observation of slowly moving emitters. This "velocity filter" effect [Cow85, Cow86] is discussed in greater detail in Chap. 5 in the context of a very broad distribution of velocities for the source of the positron peaks.

**Sec. 2.2.7.9 Experimental Verification:** The width and shape of the Doppler-broadened positron peak has been verified experimentally by reversing the polarity of the magnetic field and measuring internal conversion electrons from  $^{126}\text{Ba}$  nuclei formed in  $^{12}\text{C}(^{118}\text{Sn}, 4n)^{126}\text{Ba}$  reactions at 5.86 MeV/u. The five lowest lying rotational states are listed in Table 2-2 [Sei79]. The  $2^+ \rightarrow 0^+$  transition has a lifetime of 188 ps. At the emitter velocity,  $v_{CM} = 0.1013c$ , the  $^{126}\text{Ba}$  nucleus therefore travels on the order of  $\cong 5$  mm before it decays. To compare the expected lineshape to this measurement, the  $2^+ \rightarrow 0^+$  conversions are appropriately calculated using Eqn. 2.74.

Figure 2-29a presents the measured energy distribution of electrons detected in coincidence with  $\gamma$ -rays for the target positioned on the solenoid axis. The Doppler-shifted lobes of the K and L conversion lines for the  $2^+ \rightarrow 0^+$ ,  $4^+ \rightarrow 2^+$ , and  $6^+ \rightarrow 4^+$  transitions are clearly visible. The measured width of the  $2^+ \rightarrow 0^+$  K-line,  $\Delta E_{e^+} = 107 \pm 3$  keV, is in excellent agreement with the calculated FWHM of 109 keV. The reduction of the  $^{126}\text{Ba}$  velocity as it loses energy traversing the target foil decreases this calculated value by up to 2 keV.

Table 2-2  $^{126}\text{Ba}$  Internal Conversion Lines

Transition	$E_\gamma$	$\tau$	$E_{e^-}^*$	$\Delta E_{e^-}$
$2^+ \rightarrow 0^+$	256 keV	$188_{-30}^{+10}$ ps	K: 218.56 keV	106.05 keV
			L: 250.2 keV	114.91 keV
$4^+ \rightarrow 2^+$	455 keV	$9.3_{-1.1}^{+1.0}$ ps	K: 417.56 keV	157.90 keV
			L: 449.2 keV	165.57 keV
$6^+ \rightarrow 4^+$	622 keV	$1.62_{-0.5}^{+1.0}$ ps	K: 584.56 keV	197.37 keV
			L: 616.2 keV	204.63 keV
$8^+ \rightarrow 6^+$	757 keV	$2.14_{-0.25}^{+0.35}$ ps	K: 719.56 keV	227.99 keV
			L: 751.2 keV	235.06 keV

In order to investigate the off-axis lineshape, the target was also placed 10 mm downstream of the solenoid axis. The corresponding electron spectrum, in coincidence with  $\gamma$ -rays, is shown in Fig. 2-29b. Each of the expected lineshapes is calculated for a discrete offset,  $d_\perp = 10$  mm, plus the associated lifetime. The  $2^+ \rightarrow 0^+$  transition converts at an average distance of  $d_\perp = 15$  mm off-axis. Its observed width is  $\cong 10\%$  smaller than in Fig. 2-29a, in excellent agreement with the calculated shape. The higher energy  $4^+ \rightarrow 2^+$  line is only  $\leq 2\%$  narrower, also in agreement with the expectations of Eqn. 2.74. The accuracy of these Doppler-broadened positron lineshape calculations is confirmed. Its shape, and in particular its width, appear to be very well understood.

### Sec. 2.2.8 Summary

As a whole, the efficiency and lineshape measurements of Figs. 2-16, 2-20, and 2-29 demonstrate that the response of the solenoid transport system and positron detector apparatus is very well understood, and can be accurately calculated. Several features of the EPOS spectrometer are of particular note. By using the solenoid magnetic field as a transport system, a broad-band pass for positron transmission is achieved together with high efficiency. At the same time, a suppression of electrons of the order of  $10^3$  is provided in the low-energy region where the flux of  $\delta$ -electrons is most intense. The oscillating structures in the angle-energy dependence of transport efficiency caused by the spiral baffle, are averaged out for any physically reasonable positron emission angle distribution. They cause no structure

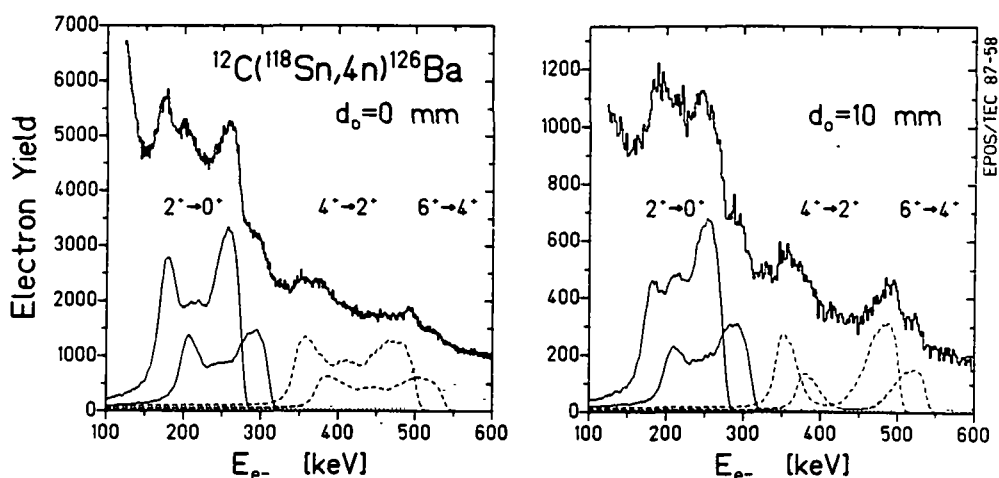


**Figure 2-29.** Energy distribution of electrons (transported to the  $e^+$  detector with reversed magnetic field) from 5.86 MeV/u  $^{118}\text{Sn} \rightarrow ^{12}\text{C}$  collisions, measured in coincidence with  $\gamma$ -rays, with target placed on solenoid axis (a), and 10 mm downstream in beam direction (b). Lines present MCSPEC calculations of Doppler-broadened K and L internal conversion lines from  $^{126}\text{Ba}$  ( $v_{\text{CM}} = .101c$ ).

in the continuous distribution of  $\beta$  decay positrons, nor do they produce an observable fine-structure in the Doppler-broadened positron lineshape. Positrons (or electrons) emitted away from the axis have a significantly reduced chance of striking the Si(Li) detector, and the fiducial volume of the EPOS spectrometer is therefore limited to an  $\cong 1$  cm radius perpendicularly around the solenoid axis. The Doppler-broadened lineshape is well understood for emission on and off the symmetry axis, and its dependence on emitter velocity provides a measure of the velocity of the source of the monoenergetic positron peaks. Finally, a rough measure of the emission angle of the positrons is provided by the positron TOF. Those features which are central to certain aspects of the interpretation of the positron lines will be discussed in more detail in later sections of this dissertation.

## Section 2.3 Heavy-Ion Detection

### Sec. 2.3.1 Physical Characteristics

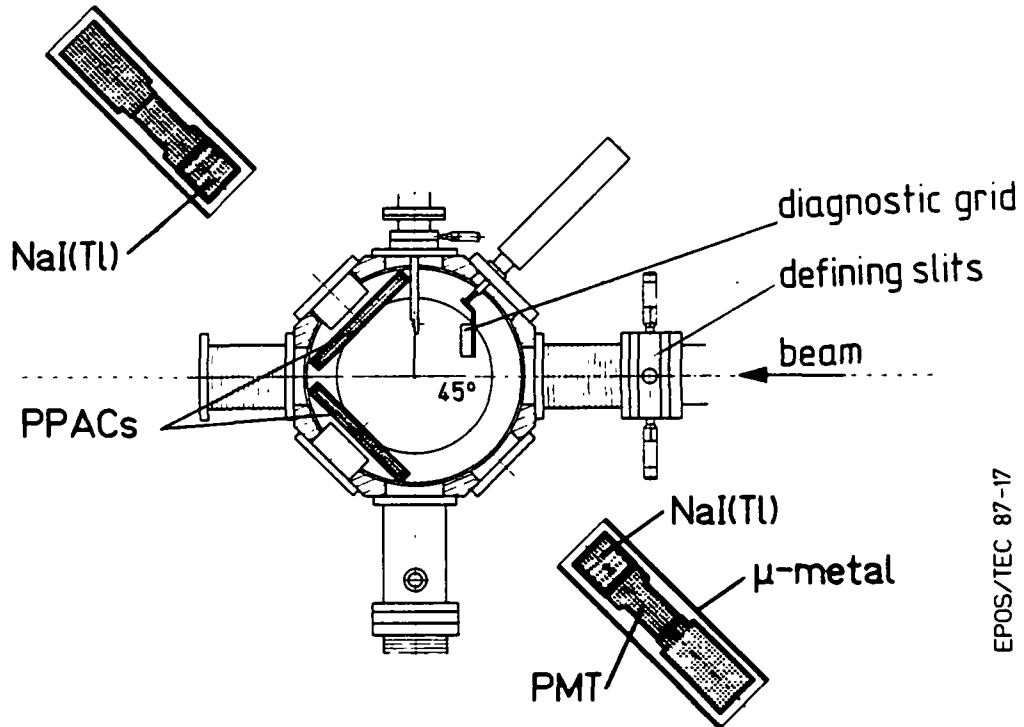
As mentioned in Sec. 2.1, it was found in previous experiments that determining the heavy-ion (HI) scattering kinematics is very important in isolating the positron peak in U+Cm collisions [Shw83]. In particular, the peak positrons are associated with binary HI scattering events whose angle-angle correlation differs slightly from that

characteristic of elastic Rutherford collisions. For the present experiments, the angular resolution of the HI Parallel Plate Avalanche Counter (PPAC) detectors has been improved in order to exploit more fully the special nature of the peak-producing events. This should improve both the peak-to-background ratio of the positron signal and the study of the collision process responsible for producing the lines. With the  $\sim 0.5^\circ$  resolution achieved, the deviations from elastic scattering associated with nuclear reaction energy-loss, nucleon evaporation, and mass-transfer between the collision partners, are in principle measurable.

Scattered projectile-like and recoiling target-like nuclei are detected in kinematic coincidence in two gas-filled PPAC's. The PPAC's have continuous delay line readouts which determine the laboratory scattering angle,  $\theta_p$  or  $\theta_r$ , respectively. The PPAC's, provided by our Univ. of Frankfurt collaborators, were originally designed by A. Gruppe [Gru85, see also Ste82], and later improved and further developed by K.E. Stiebing. They are mounted at  $45^\circ$  symmetrically above and below the beam axis and positioned 14.4 cm from the target (measured to the delay-line plane at  $\theta_{lab} = 45^\circ$ ), as shown in Fig. 2-30. Precision aluminum masks define the angular range subtended by each detector,  $20^\circ < \theta_{lab} < 70^\circ$ . In the 1983 U+Cm experiments, the azimuthal acceptance was a constant  $-18^\circ < \varphi < +18^\circ$ , which was enlarged for later experiments to  $-28^\circ < \varphi < +28^\circ$  at  $\theta_{lab} = 45^\circ$  tapering to  $-18^\circ < \varphi < +18^\circ$  at  $\theta_{lab} = 20^\circ, 70^\circ$ , as shown in Fig. 2-31a.

The delay-line structure, which is etched onto both sides (relatively shifted to one another) of a copper-plated fiberglass-reinforced printed circuit sheet, is operated at ground potential as an anode toward which the electron avalanche in the gas multiplies. Its pattern meanders back and forth along lines of constant  $\theta_{lab}$  with path-lengths designed to provide a constant pulse propagation time of 2.9 ns/degree. As shown in Fig. 2-31b, the 1.5  $\mu\text{m}$  silvered Hostafion cathode foil, held at -520 Volts, is placed 2 mm above the delay-line plane. Contacts of constant  $\varphi$  ( $6^\circ$  wide) are evaporated on a second 1.5  $\mu\text{m}$  anode foil placed 2 mm above the cathode. In order to maintain a stable cathode-anode separation (and hence constant gas amplification and timing response) the vacuum seal is provided by a third 3  $\mu\text{m}$  aluminized Mylar foil. Each PPAC detector is encased in a heavy aluminum housing which is electrically isolated from the rest of the EPOS spectrometer.

The HI detectors are operated with  $\cong 13$  mbar of isobutane gas and draw  $\leq 0.5$   $\mu\text{A}$  at an average scattering rate of  $10^4$  Hz (i.e.,  $\sim 50$  kHz, instantaneous). The



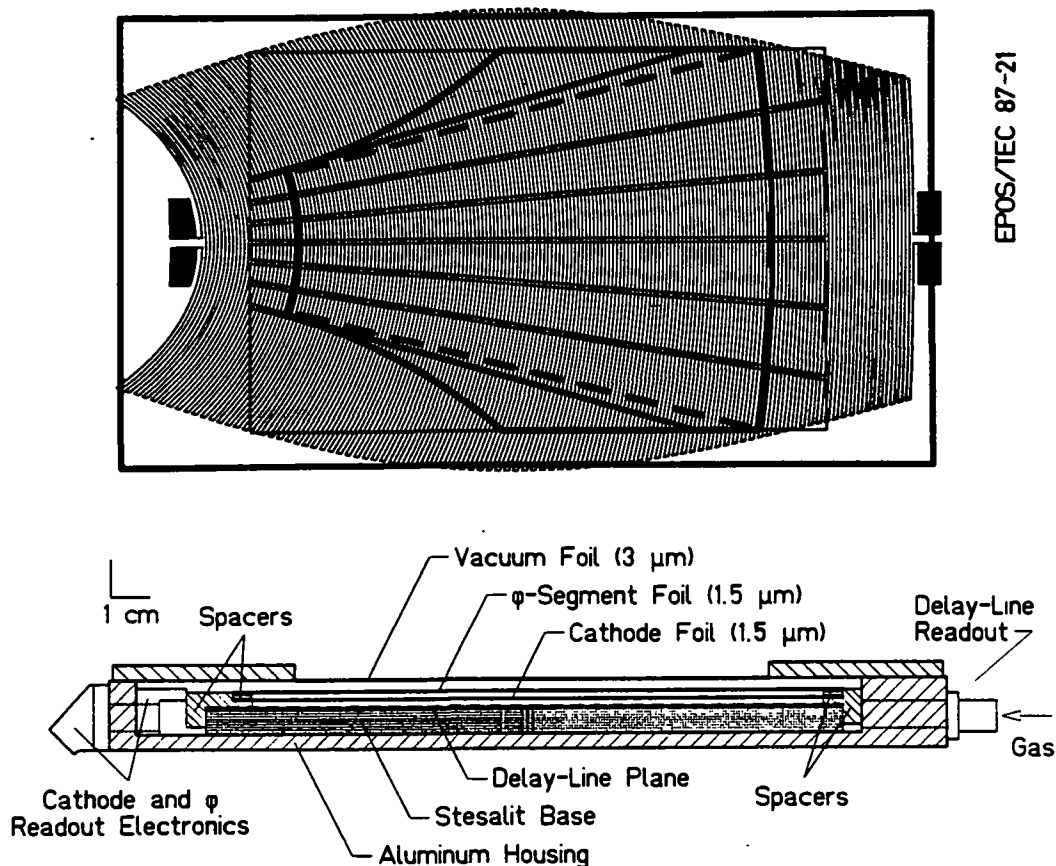
EPOS/TEC 87-17

**Figure 2-30.** Side view of EPOS target chamber showing the position of the heavy-ion PPAC detectors and  $\gamma$ -ray NaI(Tl) detectors. The solenoid axis is perpendicular to the page.

$\phi$  foil and cathode signals are shaped with fast timing amplifiers and have pulse rise times of  $t_r \cong 1$  ns. The two shifted delay-line segments (top and bottom surface of the circuit sheet) are terminated at the small lab-angle end and are read out at the large angle end of the detectors using matched differencing preamps ( $t_r \cong 3$  ns). The time difference between the delay-line and the cathode is linearly proportional to lab angle. The net time resolution of  $\Delta t \cong 1$  ns provides an intrinsic angular resolution of  $\delta\theta_{lab} \cong 0.5^\circ$ . A  $\cong 10\%$  resolution (FWHM) HI energy measurement is made by integrating the charge of the cathode and delay-line signals.

### Sec. 2.3.2 Heavy-Ion Kinematics

As discussed in App. A, a nonrelativistic description of the HI scattering kinematics is sufficient for the beam energies of interest in these experiments. The laboratory angle and kinetic energy of a projectile of mass  $M_p$  and target recoil of mass  $M_t$  are related for scattering through a center-of-mass angle  $\theta_p^{cm}$  by



EPOS/TEC 87-21

**Figure 2-31.** Cross-sectional view of the heavy-ion PPAC detectors (bottom). The delay-line pattern and  $\phi$ -segment foil are shown at the top. The angular acceptance of the defining masks are indicated by the dashed (for 1983) and thick (1984-1985) lines.

$$\theta_p^{cm} = \pi - 2\theta_t = \theta_p + \sin^{-1}[(M_p/M_t) \sin\theta_p] \quad (2.75)$$

$$E_t = E_o - E_p = [2M_p M_t / (M_p + M_t)^2] (1 - \cos\theta_{CM}) E_o. \quad (2.76)$$

It was previously found [Shw85, Gru85] that the analysis of HI scattering data is simplified by plotting the sum of the scattering angles in the upper and lower detectors,  $\Sigma\theta_{HI} = \theta_U + \theta_L$ , versus their difference,  $\Delta\theta_{HI} = \theta_U - \theta_L$ , which is the equivalent (to within a factor of  $\sqrt{2}$ ) of a rotation of the plane by  $45^\circ$ , indicated by Fig. 2-32a. A mirror symmetry is expected about  $\Delta\theta_{HI} = 0^\circ$ . For symmetric collisions,  $M_p = M_t$ , the lab angles  $\theta_p, \theta_t$ , are each equal to one half the CM angles  $\theta_p^{cm}, \theta_t^{cm}$  and add to a constant  $\Sigma\theta_{HI} = 90^\circ$ . If  $M_p > M_t$ , the angle-angle correlation lies below  $\Sigma\theta_{HI} = 90^\circ$ , and for  $M_p < M_t$ ,  $\Sigma\theta_{HI} > 90^\circ$ . The decreased angular range covered by the  $\Delta\theta_{HI} - \Sigma\theta_{HI}$  parameterization allows higher resolution binning and eliminates from the analysis pri-

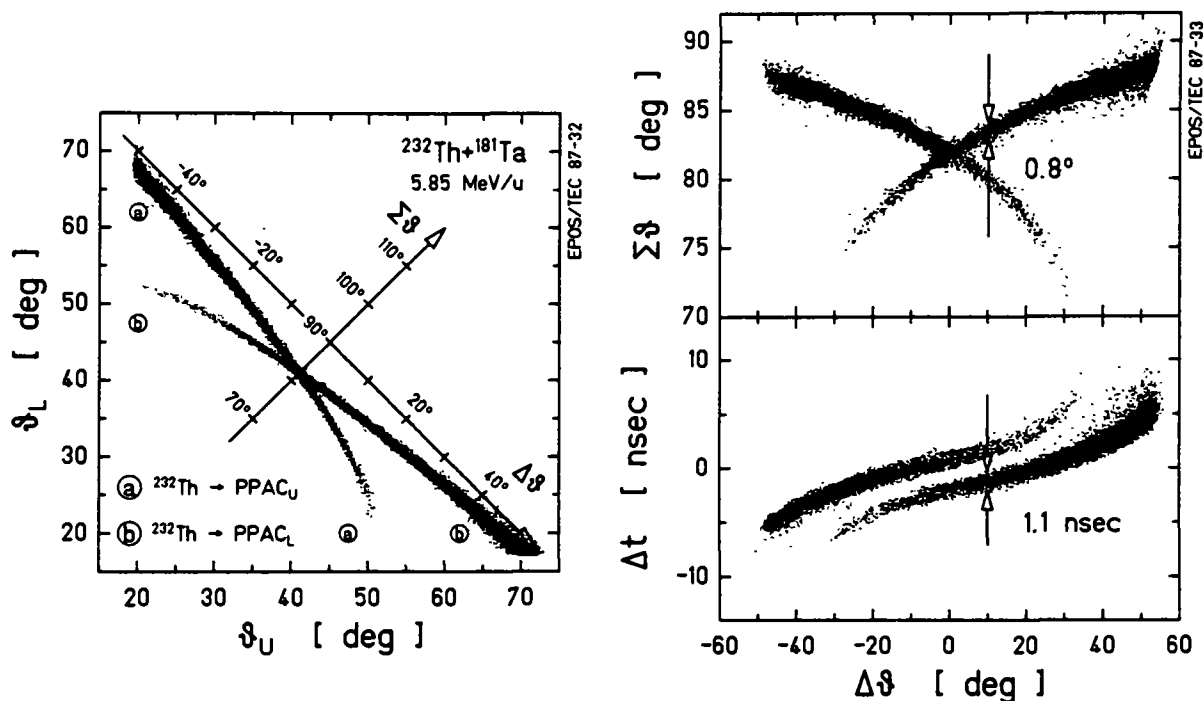


**Figure 2-32.** Angle-angle correlation of ions scattered into the upper and lower PPAC's in Th+Ta collisions (left). Rotated axes indicate the  $\Sigma\theta_{\text{HI}}$  and  $\Delta\theta_{\text{HI}}$  coordinates used in the upper right. Typical  $\Sigma\theta_{\text{HI}}$  angular resolution is  $\delta\theta_{\text{HI}} = 0.8^\circ$ , and the resolution of the flight-time difference between the detectors is  $\delta t \sim 1 \text{ ns}$  (lower right).

mary collisions between beam ions and low-Z elements in the target. It has the added advantage that the  $\Sigma\theta_{\text{HI}}$  coordinate is directly related to the physically important Q-values and the relative masses of the ejectiles.

The angular calibration was determined relatively to within  $\leq 0.5^\circ$  by the fixed mask acceptance of  $20^\circ$ - $70^\circ$ . It was absolutely fixed by adjusting the linear offsets so that the measured mean value of  $\Sigma\theta_{\text{HI}}$  matches the value expected for elastic collisions. Figure 2-32b illustrates the typical in-beam resolution, measured with 5.8 MeV/u  $^{232}\text{Th}$  incident on a sputtered  $\sim 300 \mu\text{g}/\text{cm}^2$   $^{181}\text{Ta}$  target. The resolution in the sum of the two scattering angles,  $\Sigma\theta_{\text{HI}} = \theta_U + \theta_L$ , is  $\delta(\Sigma\theta_{\text{HI}}) \cong 0.8^\circ$  (FWHM). The two branches of the angle-angle correlation plot correspond to the projectile nucleus scattered into either the upper or lower PPAC, respectively.

The time-of-flight difference between the arrival of ions at the PPAC cathodes depends on the velocity of the ejectiles, and hence on their laboratory scattering angles and energies. Like the  $\Delta\theta_{\text{HI}}$ - $\Sigma\theta_{\text{HI}}$  pattern, it is unique for a particular combina-

tion of HI masses. For an ion velocity  $v_{HI} \cong 2v_{CM}\cos\theta_{HI}$ , the flight time to the PPAC is

$$t_{HI} = d(\theta_{HI}, \phi_{HI})/v_{HI}, \quad (2.77)$$

where  $d(\theta, \phi)$  is the distance to the PPAC detector plane,

$$d(\theta, \phi) = \sqrt{2} (14.4 \text{ cm}) / (\cos\theta + \sin\theta\cos\phi) \quad (2.78)$$

Figure 2-32b indicates that the typical experimental time difference resolution is  $\Delta t \cong 1 \text{ ns}$ .

Figure 2-33a illustrates the effect of Q-loss on the kinematic  $\Delta\theta_{HI}-\Sigma\theta_{HI}$  pattern of Fig. 2-32, calculated for Th+Cm collisions. A 25 MeV loss leads to a negative shift in  $\Sigma\theta_{HI}$  of  $1^\circ$ . The  $0.8^\circ \Sigma\theta_{HI}$  angular resolution therefore provides a 20 MeV resolution in Q. The width of the bow-tie pattern of the angle-angle correlation depends on the ejectile masses. Mass transfer between a Th projectile and Cm target nucleus is illustrated in Fig. 2-32b. A  $1^\circ \Sigma\theta_{HI}$  separation between the branches at  $|\Delta\theta_{HI}|=25^\circ$  corresponds to a scattered-recoil mass asymmetry of  $|M_S-M_R|=10 \text{ amu}$ . Mass drifts are therefore observable in the kinematic correlation with a resolution of  $\Delta M \sim 10 \text{ amu}$ . As described in App. A, nucleon evaporation can be expressed in terms of Q. The experimental resolution of  $\Delta Q < 20 \text{ MeV}$  is equivalent to an observable limit of 2 neutrons or 1 proton ejected from the combined system. By combining the HI TOF difference with the  $\Sigma\theta_{HI}-\Delta\theta_{HI}$  correlation, the kinematic branches of the slightly asymmetric Th+Cm system are almost completely resolved.

### Sec. 2.3.3 Operation in Magnetic Field

In the solenoid magnetic field, the operation of the PPAC detectors is slightly modified, as described in [Gru85]. Briefly, the charged heavy ions are deflected from their trajectories with a radius of curvature,  $Mvc/qB$ . The charge,  $q$ , of an ion depends on its velocity through the target backing material. The semi-empirical formula of [Nik68] gives the mean of the equilibrium charge distribution as

$$\langle q \rangle / Z = [1 + (v/Z^{\alpha} v')^{-1/k}]^{-k}, \quad (2.79a)$$

with a width,

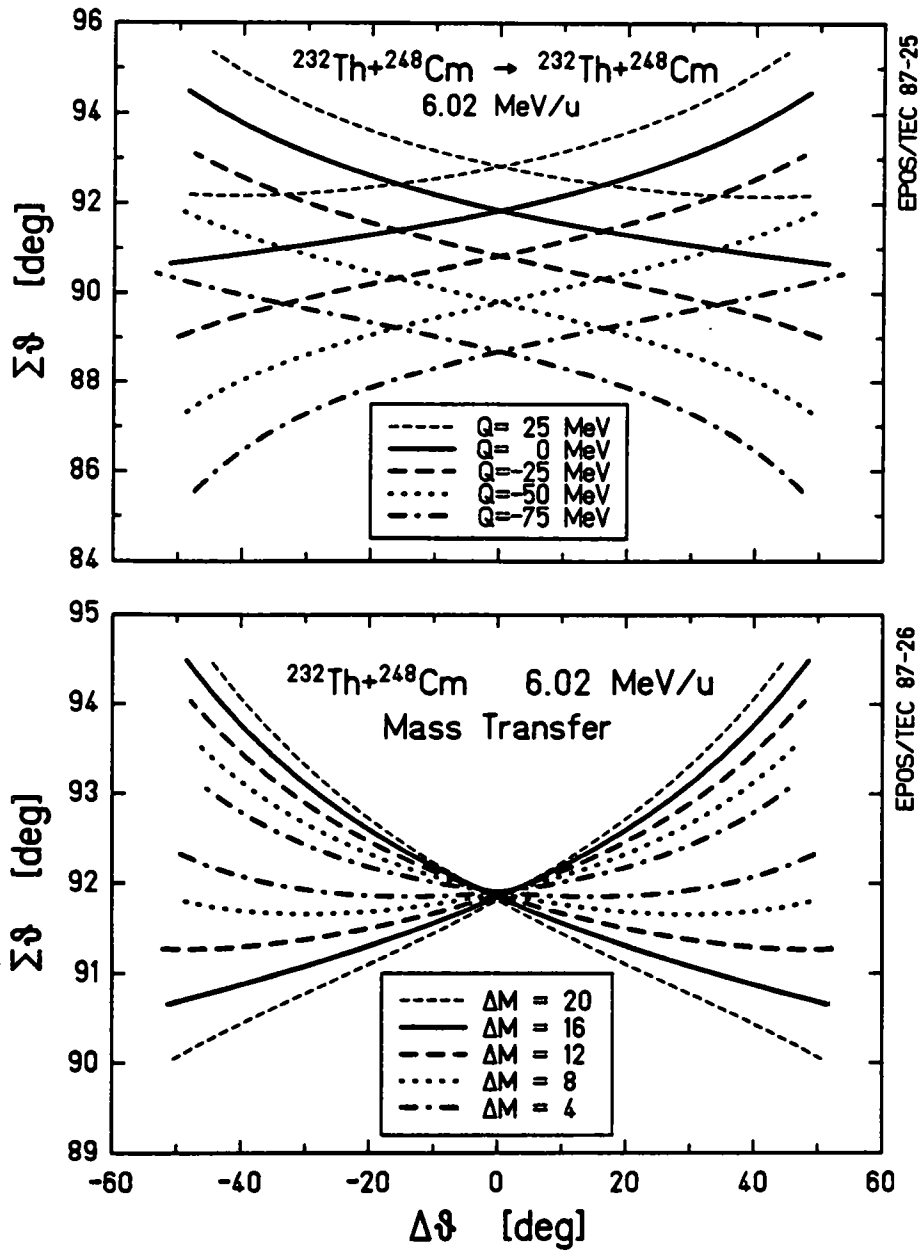


**Figure 2-33.**  $\Sigma\theta_{H_1}-\Delta\theta_{H_1}$  scattering angle correlations calculated for Th + Cm collisions with several values of  $Q$  (top) and exit channel masses (bottom).

$$d = 0.5 \{ \langle q \rangle [1 - (\langle q \rangle / Z)^{1/k}] \}^{1/2}, \quad (2.79b)$$

where  $\alpha = 0.45$ ,  $k = 0.6$ , and  $v' \cong 3.6 \times 10^8 \text{ cm/sec}$ . Recent charge state measurements are given in [Mao82, Sti86]. As shown in Fig. 2-34a, the mean charge depends on scattering angle and varies from  $\sim 65^+$  at  $\theta = 20^\circ$  to  $\sim 35^+$  at  $70^\circ$ . The

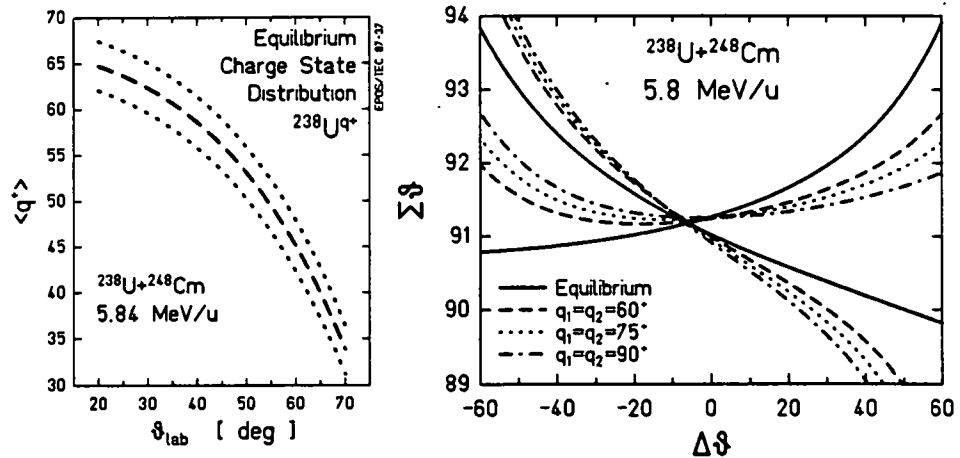


**Figure 2-34.** Equilibrium ionic charge states (left) lead to a rotation of scattering angle correlation pattern (right side, solid line). Patterns for equal, velocity-independent charges for both ejectiles are shown by the dashed, dotted, and dot-dashed lines. (Reproduced from [Gru85].)

net effect is an average downward rotation of both scattered heavy-ions in the spectrometer by about  $1^\circ$ .

A similar deflection of the electron avalanche inside the PPAC's, described in [Gru85, and Shw85], is negligible in the present arrangement because of the smaller cathode-anode separation (2 mm vs. 5mm) and the reversed direction of the PPAC electric field.

The HI deflection results in a negative angular deviation in the upper PPAC, and a positive shift in the lower PPAC. The magnitude of each depends on the angle,  $\theta_U$ ,  $\theta_L$ . This produces a  $\Delta\theta_{HI}$  translation and a slight clockwise rotation of the angle-angle correlation pattern, relative to the unperturbed elastic scattering pattern, which is shown by the solid line in Fig. 2-34b which plots the  $\Sigma\theta_{HI} - \Delta\theta_{HI}$  pattern for equilibrium charge states in U + Cm collisions, calculated by [Gru85]. Deviations of the mean ionic charge state from Eqn. 2.79, either to larger values or to charges independent of nuclear velocity, result in larger rotations. This is illustrated in Fig. 2-34b by the broken lines which assume equal, velocity-independent ionic charges,  $q_1 = q_2 = 60^+$ ,  $75^+$  or  $90^+$ . The average rotation for elastic collisions is approximately corrected for in the angular calibration. As discussed below, abnor-

mal ionic charge states may be responsible for the deviations of the positron peak events from the elastic scattering kinematics.

## Section 2.4 Gamma-Ray Detection

Gamma-rays are detected in these experiments in coincidence with scattered H<sup>+</sup>'s, and simultaneously with the positron measurement, in order to search for strong nuclear transitions which might be responsible for the positron peaks. The two 3" × 3" NaI detectors mounted at 45° and -135° with respect to the beam axis, are shown in Fig. 2-30. These were previously used to determine the continuous nuclear internal pair creation (IPC) background in the total positron distributions. Details of their operation, shielding, and lineshape response are found in [Shw85].

For the subsequent analysis (see Sec. 5.2), only the rear detector was used. It was positioned at  $408 \pm 2$  mm from the target in the 1983 and February 1984 beam-times, and  $430 \pm 2$  mm from July 1984 to the present. The peak detection efficiency, which is necessary in order to calculate the nuclear transition strengths required to produce the positron peaks by pair creation (and to compare these to the measured  $\gamma$ -ray yields), is shown in Fig. 2-35 for  $d_0 = 430$  mm. Its absolute shape and magnitude agree with the calculated efficiency given in [Hea64]. At  $E_\gamma = 1270$  keV, the peak efficiency is  $\epsilon_\gamma^{\text{pk}} \cong 4 \times 10^{-4}$ , and the energy resolution is  $\Delta E_\gamma \cong 85$  keV (FWHM).

## Section 2.5 Electron Detection

To search for strong non- $\gamma$ -ray emitting nuclear transitions (i.e., electric monopole) which may be a source of positron structures, internal conversion lines are sought in the energy distribution of electrons emitted from the heavy-ion collisions. The electron detector system, provided by our Univ. of Mainz collaborators, was set up in the leg of the spectrometer opposite the positron counter, placed beyond the magnetic mirror [Beg83, Beg87]. The 1" dia. (500 mm<sup>2</sup>) Si(Li) detector was centered on, and normal to, the solenoid axis, 94.6 cm away from the target. Its active depth of 5.5 mm is sufficient to stop electrons of up to  $\sim 3$  MeV. The detector was operated at +900 Volts bias and cooled to -30° C. The resulting intrinsic energy resolution was  $\sim 9$  keV at 1 MeV with a time resolution of  $\sim 10$  ns. Electrons emitted at flat angles within 35° of the EPOS axis ( $145^\circ < \theta_{e^-} < 180^\circ$ , corresponding to 9% of  $4\pi$ ) pass through the magnetic mirror field and are transported toward the detector. A copper absorber foil was placed directly in front of the detector in order stop the large flux

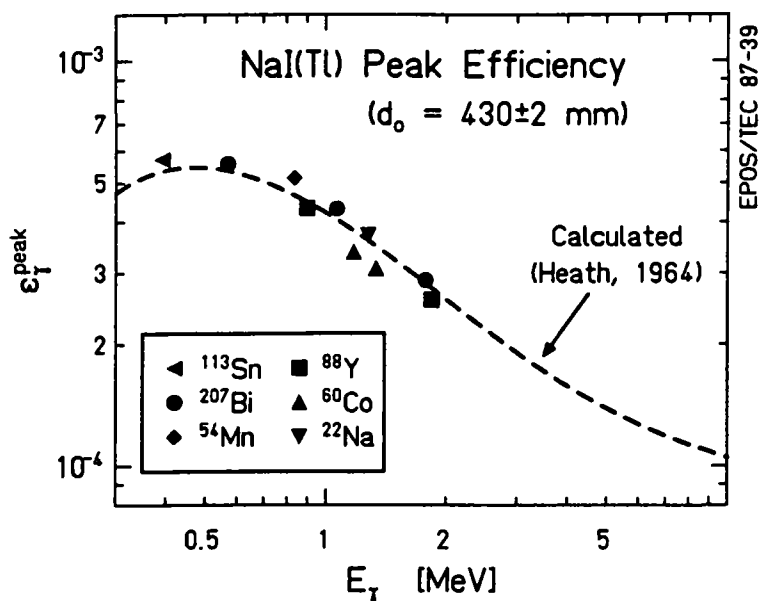


**Figure 2-35.** Peak detection efficiency of  $\gamma$ -rays in the backward NaI(Tl) detector. Source measurements are compared to the calculated efficiency [Hea64], including absorbers.

of low energy  $\delta$ -electrons. Its thickness was changed from  $40.2 \text{ mg/cm}^2$  used in 1983, to  $20.9 \text{ mg/cm}^2$  in February 1984, to  $20 \text{ mg/cm}^2$  for the July and September 1984 experiments. Energy-loss straggling in the foil degraded the electron energy resolution at 1 MeV to  $\Delta E_{e^-} \cong 26 \text{ keV}$  (FWHM).

The electron detector response was parameterized, in the same way as for the pencil-like positron detector, by Eqn. 2.34. Figure 2-36 shows a fit to the K and L conversion lines from the 1065 keV transition in  $^{207}\text{Bi}$ . The peak-to-total ratio for incident energies above 1 MeV is nearly constant,  $(P/T) \cong 0.5$ . An increase in exponential tailing below the full-energy peak arises from the straggling in the Cu absorber foil. Incomplete  $\delta$ -electron suppression led to an additional electron pileup occurring with  $\cong 6\%$  probability, whose energy distribution follows the exponential shape of the  $\delta$ -ray spectrum.

In order to limit the Doppler-broadening associated with an internal conversion line in the interesting energy region above 1 MeV, the emission angular acceptance of electrons was limited to a  $\sim 10^\circ$  cone about the axis by placing a 10 cm long cylindrical tube baffle at 69.9 cm from the target, 12 cm beyond the position of the maximum of the magnetic mirror field. The tube baffle had an inner diameter of 15

## Electron Detector Response

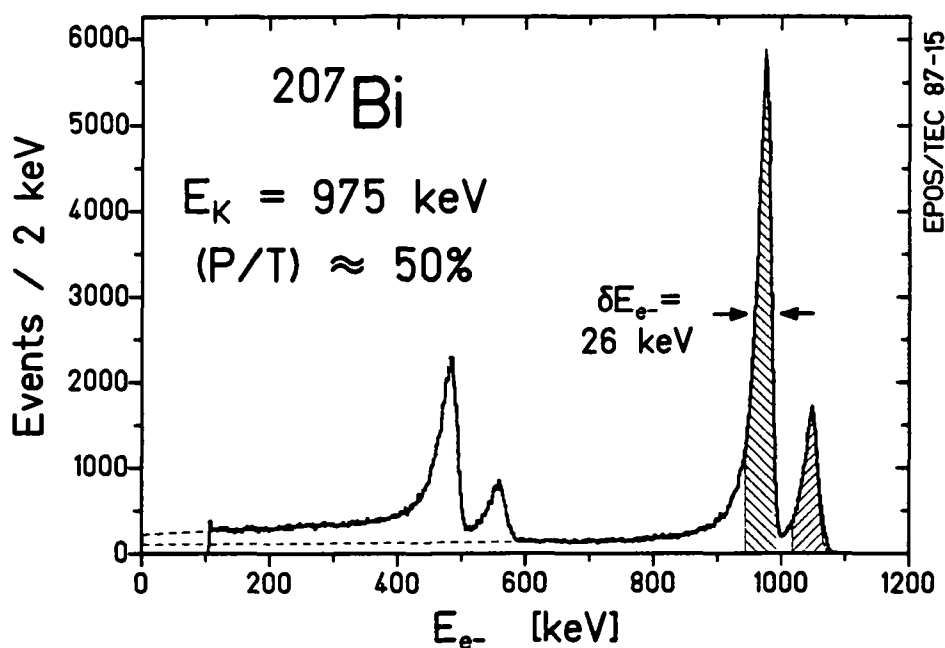


**Figure 2-36.** Energy spectrum of  $^{207}\text{Bi}$  conversion electrons measured in the 1" dia. electron Si(Li) detector. Energy resolution and Peak/Total ratio as marked.

mm, and a 5 mm wall thickness. Its operation is illustrated in Fig. 2-37. The angle between the electron and the emitting nucleus includes the azimuthal angular range of the PPAC's,  $\theta_{\text{HI}/e^-} = \theta_{e^-} + \Phi_{\text{HI}}$ . Folding the  $\theta_{e^-}$  acceptance of the tube baffle with the  $\Phi_{\text{HI}}$  range produces a final electron peak width of  $\cong 70 \text{ keV}$  at  $E_{e^-} \cong 1400 \text{ keV}$ . In order to reduce the chance that  $\delta$ -electrons backscatter from the tube baffle and pass back through the mirror field on toward the positron detector, a deep groove is machined in the front rim of the aluminum cylinder to trap electrons which scatter from the end of the tube. Electrons which scatter from the inner or outer walls of the baffle spiral back into that surface and are stopped with large probability.

A measurement of the detection efficiency of the electron counter and baffle system is shown in Fig. 2-38. The data points simulate different energies using a  $^{207}\text{Bi}$  source by scaling the EPOS magnetic field. The falloff of the transport efficiency with increasing electron kinetic energy reflects the correspondingly smaller range of emission angles for which the electron passes through the cylindrical baffle. For the idealized situation of a very long tube in a constant magnetic field,  $B_{\text{tube}}$ , electrons emitted from the target ( $z_0 = 0$ ) on the solenoid axis are stopped if

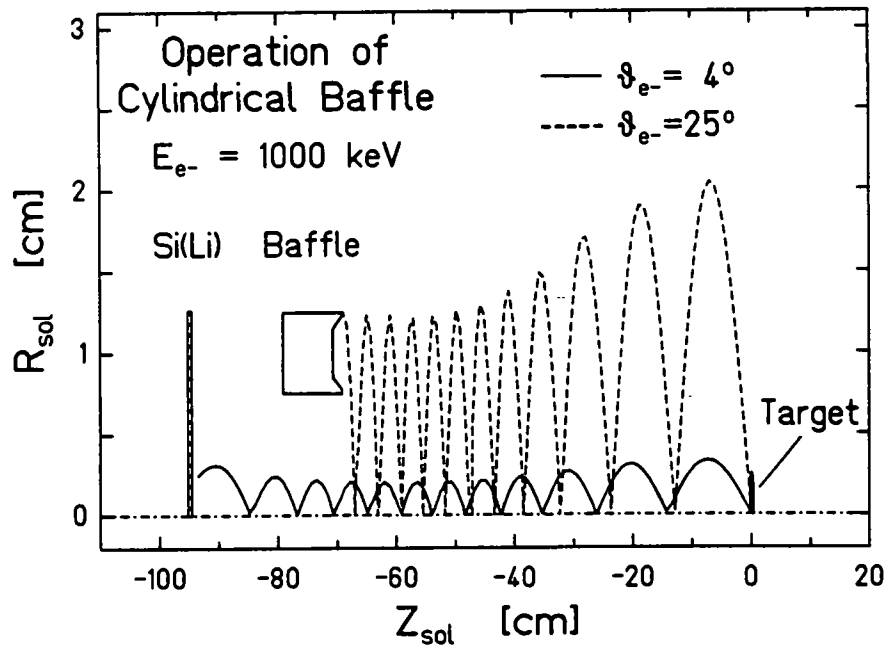


**Figure 2-37.** Illustration of how the cylindrical tube baffle absorbs electrons emitted at steep angles ( $\geq 10^\circ$ ) with respect to the solenoid axis. (Adapted from [Beg87].)

$$r_{\text{tube}} < 2\rho = 2(pc/eB_0)(B_0/B_{\text{tube}})^{1/2} \sin\theta_0, \quad (2.80)$$

where  $r_{\text{tube}}$  is the inner radius of the cylindrical baffle. The orbital parameters are taken from Eqns. 2.9-12. The range of emission angles transmitted through the baffle is simply

$$\pi > \theta_0 > \pi - \sin^{-1}\left[\frac{1}{2}r_{\text{tube}}(eB_0/pc)(B_{\text{tube}}/B_0)^{1/2}\right]. \quad (2.81)$$

If all electrons not stopped in the baffle are detected, the efficiency is  $\varepsilon_{e^-} = \frac{1}{2}(1 - \cos\theta_{\text{max}})$ .

In the experimental arrangement, the position and length of the tube are chosen so that all electrons which pass through strike the Si(Li) detector and are registered. The magnetic field is, however, not constant over the length of the baffle. At the entrance,  $z \cong -70$  cm,  $B \cong 5000$  G, and at the exit,  $B \cong 3000$  G. This variation gives rise to the oscillatory structure apparent in Fig. 2-38. For example, if the orbit of a 1400 keV electron reaches its maximum excursion from the solenoid axis at the entrance of the baffle, the steepest emission angle accepted is

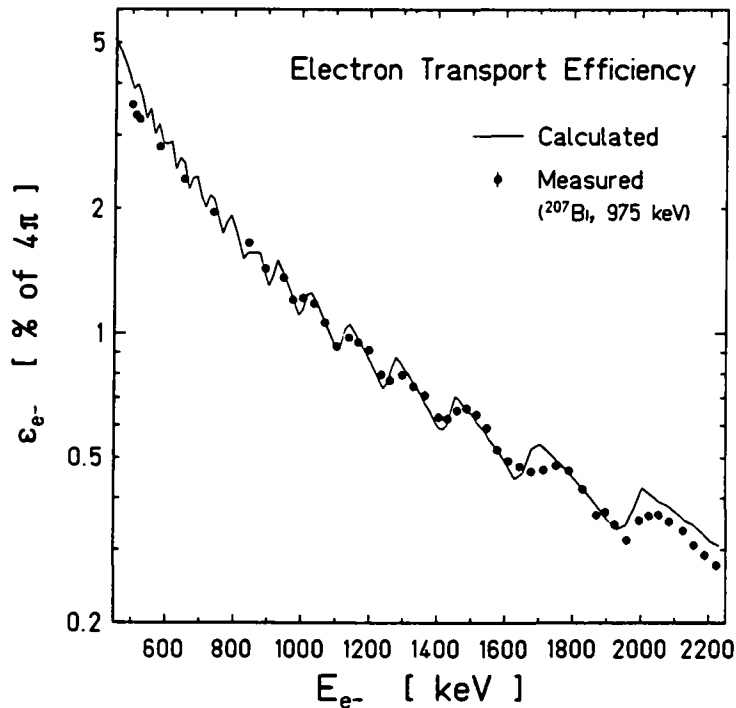


**Figure 2-38.** Transport efficiency of electrons from the target to the  $e^-$  Si(Li) detector as a function of electron energy. Oscillatory structure calculated with the ECPI ray-tracing program (App. B) is compared to measurements with a  $^{207}\text{Bi}$  source. (Reproduced from [Beg87].)

$$\theta_{\max}(B = 5000 \text{ G}) = 10.76^\circ,$$

with a corresponding efficiency,  $\varepsilon_{e^-} = 0.88\%$ . On the other hand, if the orbit is limited by the exit end of the baffle,

$$\theta_{\max}(B = 3000 \text{ G}) = 8.32^\circ,$$

yielding  $\varepsilon_{e^-} = 0.53\%$ , a factor of 0.6 times  $\varepsilon_{e^-}(B = 5000 \text{ G})$ .

The cutoff angle  $\theta_0$  for a given energy therefore depends sensitively on exactly where the corresponding trajectory reaches its maximum excursion within the length of the baffle. Because of the flat emission angles accepted, and hence long orbital pitch-lengths involved, only a few orbits are traced out between the target and baffle and the efficiency curve retains the oscillatory phase sensitivity. From Fig. 2-37 it is apparent that 1000 keV electrons are limited during their 11th orbit at the entrance of the baffle. The valley at  $E_{e^+} = 1400 \text{ keV}$  in Fig. 2-38 therefore corresponds to the

maximum of the 9th orbit, occurring near the exit of the tube, and of the 8th orbit at its entrance.

This sensitivity to the exact phase of the limiting electron trajectory at the baffle precludes an adiabatic calculation of the efficiency (Sec. 2.2.5). The solid line in Fig. 2-38 therefore shows the expected efficiency calculated with the ECPI ray-tracing program. The measured oscillations are somewhat smoother than calculated because the finite source size effectively averages over a distribution of baffle inner radii.

A measurement verifying the sensitivity of the Si(Li) and cylindrical baffle detection geometry is shown in Fig. 2-39. The weak  $0^+ \rightarrow 0^+$  (E0) transition in  $^{238}\text{U}$  is excited in collisions with  $^{136}\text{Xe}$  at 3.6 MeV/u. The FWHM of the  $\sim 870$  keV K-line is  $\cong 70$  keV, in good agreement with that expected from the angular acceptance of the baffle and PPAC detectors.

## Section 2.6 Targets

### Sec. 2.6.1 Curium Targets

One of the most important and sensitive aspects of these experiments is the stability of the targets. As mentioned above, early experiments [Shw83] indicated that production of the positron peak in U+Cm collisions may be associated with a resonant scattering process. To optimize peak-to-background, subsequent measurements required good definition of the collision energy in the CMS. The small positron peak cross-section simultaneously requires that sufficient target material and beam currents be available for reasonable event rates. On the other hand, the good HI scattering angle resolution necessary for enhancing the positron peak over background by angle cuts suffers, because of straggling, if a target foil is too thick. To accommodate these disparate requirements, relatively thin and uniform target foils are important. Using the heaviest elements available (Cm, U, and Th) complicates the situation because of their natural radioactivity and, for  $^{248}\text{Cm}$ , the limited supply of isotope material. Target fabrication sometimes involved less than optimum techniques, which were studied and substantially improved by H. Folger over the course of this thesis research. Special attention to the content and quality of the targets gave rise to dedicated monitor systems and additional measurement programs. To

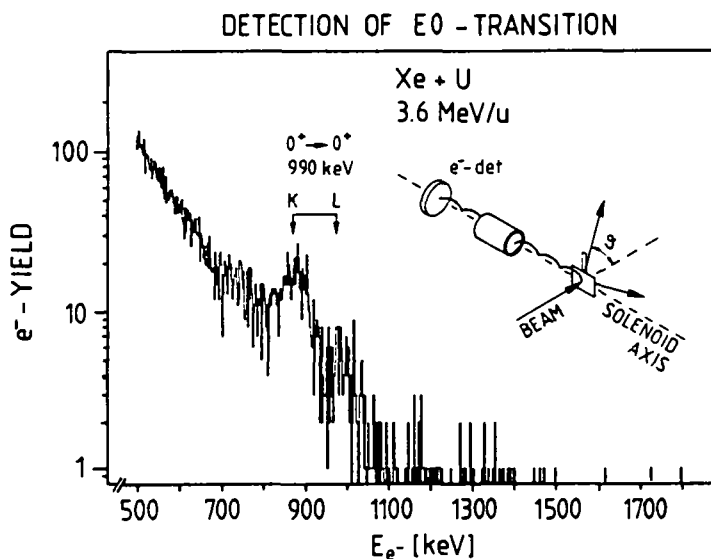


**Figure 2-39.** Energy spectrum of electrons emitted in 3.6 MeV/u Xe + U collisions. The width of the 990 keV E0 K-conversion line from  $^{238}\text{U}$  agrees with the expected Doppler broadening. (Reproduced from [Bok84].)

provide an overview of the target situation, the various EPOS target studies and development projects are collected here and presented chronologically.

The targets employed in the 1983 experiments, aimed at reproducing and extending the results of [Shw83], consisted of layers of curium oxide sandwiched between two carbon foils. Five mg of  $^{248}\text{Cm}$  isotope material was borrowed from the U.S. Department of Energy Transplutonium Committee. The curium was processed at the Univ. Mainz Nuclear Chemistry lab by N. Trautmann, in collaboration with H. Folger, head of the GSI target lab.  $\text{Cm}_2\text{O}_3$  compound was dissolved in a carrier solution and was deposited in  $\sim 200\text{-}400 \mu\text{g}/\text{cm}^2$  layers onto  $140 \mu\text{g}/\text{cm}^2$  C backings in 5 mm dia. spots by molecular plating (see [Tra82] and [Fol84]). The target material was then covered with  $\sim 40 \mu\text{g}/\text{cm}^2$  thick C foils to reduce material loss due to sputtering and evaporation. With this technique, several targets ( $\sim 50$ ) were fabricated from the limited supply of curium. In addition to conserving Cm material, the 5 mm spot centered on the  $14 \times 18 \text{ mm}^2$  backing avoided situations where a misaligned HI beam could strike the 2 mm wide by 0.3 mm thick Al target frame. Direct irradiation of the frame would swamp the detectors in a flood of  $\delta$ -electrons and excite long half-life  $\beta^+$  active backgrounds.

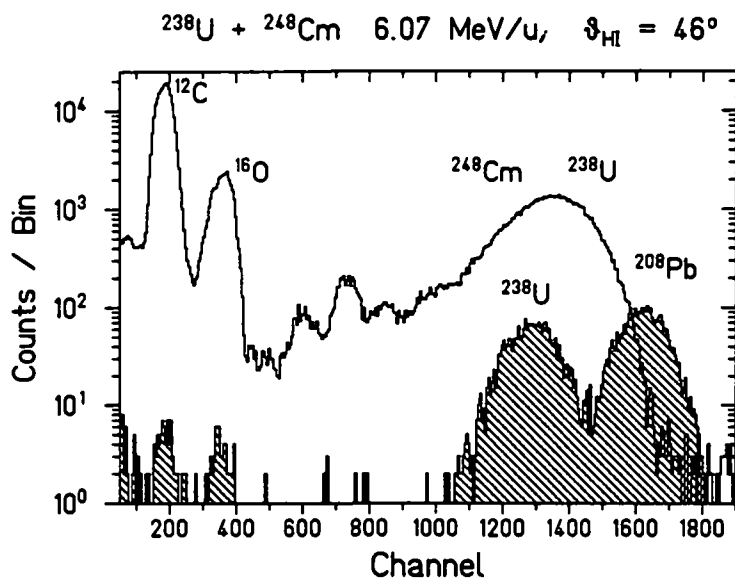


**Figure 2-40.** Energy distribution of heavy ions scattered into the 50 mm<sup>2</sup> surface barrier monitor detector at  $\theta_{\text{lab}} = 45^\circ$  from U+Cm and U+Pb collisions. Concentrations of various elements in the target are determined by relative scattering yields. (Reproduced from [KlÜ84].)

Measurements using these targets, discussed in Chap. 3, indicated that the production of  $\approx 320$  keV peak positrons is largest for incident uranium beam energies between 6.0 and 6.2 MeV/u. Of course projectile ions traversing the target material lose energy. The  $\sim 350$   $\mu\text{g}/\text{cm}^2$  nominal  $\text{Cm}_2\text{O}_3$  thickness translates to a 0.07 MeV/u spread in the incident beam energy. During the experiment the target condition was monitored in two ways. First, the average thickness of curium was checked by normalizing the scattering rate of U+Cm collisions into the PPAC's to the beam current measured in a Faraday cup in the beam stop. Second, a small surface barrier Si detector (50 mm<sup>2</sup>), mounted at  $45^\circ$  to the beam and cooled to  $5^\circ$  C, measured the energies and relative intensities of the scattered U and recoiling Cm ions, as well as C and O nuclei scattered from the backing and target compound. Figure 2-40 shows an energy spectrum of the monitor counter for a typical  $\text{Cm}_2\text{O}_3$  target in a 6.07 MeV/u U beam. Throughout the irradiation, the beam current was limited to 0.5 PnA (particle-nA) to reduce thermal damage.

Rather drastic changes in the ratio of oxygen to curium content (by as much as a factor of 3 to 5) were observed over the course of an  $\sim 8$  hr target irradiation. This was accompanied by the integral loss of only  $\sim 20\%$  of the Cm in the beam-spot. Together with difficulties in maintaining a constant positron peak production

rate over the course of several days, despite using the same nominal  $^{238}\text{U}$  beam energy and nominal target thickness, it seemed likely that the composition or distribution of material in the targets was changing during the HI irradiation. This has serious implications for understanding the apparent peak excitation function. The energy-loss thickness (relevant for beam energy determination) of the Cm targets was measured by a standard Rutherford backscattering technique.

### Sec. 2.6.2 Proton Backscattering Measurements

The Cm target thicknesses were measured after the 1983 beamtime, by M. Klüver, M. Begemann, and K.E. Stiebing [Klü84],<sup>3</sup> at the Univ. Frankfurt Institut für Kernphysik Tandem Accelerator using a 2.0 MeV proton beam collimated to  $0.2 \times 0.2$  mm<sup>2</sup>. The protons were scattered from the target foils through  $\theta = 165^\circ$  into a Si surface barrier detector where they were measured with 13 keV (FWHM) resolution (including kinematic broadening). The maximum energy of protons backscattered from a pure homogeneous target of mass  $M \gg M_p$  is

$$E_p \cong f \cdot E_0, \text{ with } f \equiv [(M - M_p)/(M + M_p)]^2, \quad (2.82)$$

where  $E_0$  is the incident energy. For a thick target, protons which scatter from a layer of depth  $\Delta x$  lose energy  $\Delta E = (dE/dx) \cdot \Delta x$  while penetrating the target. They scatter with energy  $E' = f \cdot [E_0 - (dE/dx) \cdot \Delta x]$ , and lose an additional  $(dE/dx) \cdot (\Delta x / \cos \theta_p)$  on the way out of the target. If  $(dE/dx)$  is approximately constant over the energy range of interest, the detected protons have energy

$$E_p = f \cdot E_0 - (dE/dx)(f + 1/\cos \theta) \Delta x. \quad (2.83)$$

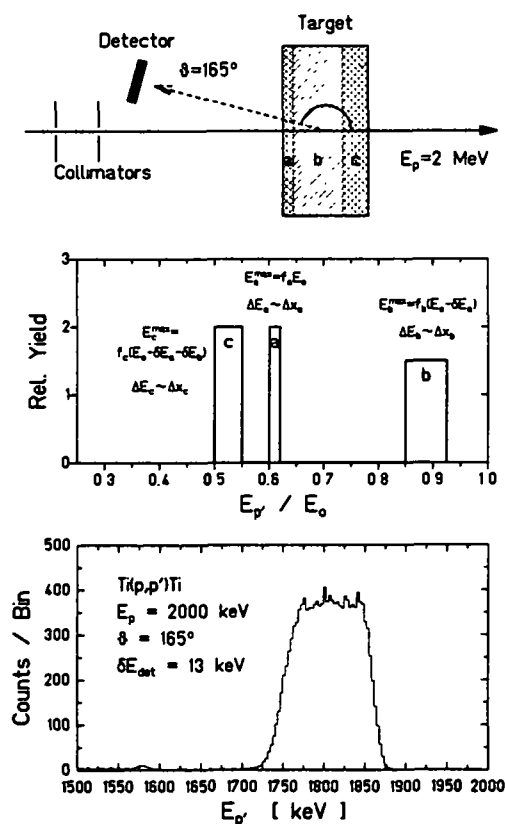
As shown in Fig. 2-41, an ideal target with uniform layers of different elements leads to an energy spectrum consisting of several rectangular distributions whose widths linearly reflect the energy-loss throughout that layer ( $\Delta x$  of Eqn. 2.83). This relationship is verified by scattering from a uniform metallic titanium foil (Fig. 2-41c).

Figure 2-42a shows the backscattered proton energy spectrum comparing an irradiated molecular-plated  $\text{Cm}_2\text{O}_3$  sandwich target with an evaporated

<sup>3</sup>

These measurements were subsequently extended and improved by [Kra87].

## Proton Backscatter Measurements



**Figure 2-41.** Schematic diagram of the experimental set-up for measurements of the target thickness by proton backscattering (top). The rectangular energy distribution expected for scattering from a target with uniform layers (middle) is verified with a metallic Ti calibration foil (bottom). (Adapted from [Klü84].)

$^{238}\text{U}$  target. The  $^{12}\text{C}$  and  $^{16}\text{O}$  peaks are clearly resolved, but the  $^{248}\text{Cm}$  target is dominated by large tails to low proton energies. The obvious interpretation is that the  $\text{Cm}_2\text{O}_3$  material is nonuniformly distributed, e.g., in layers of varying thickness, each of which contributes to a rectangular form of different width. An alternative explanation, that the Cm targets may contain large levels of isotopic contaminants which are not individually resolved in the p backscattering measurements, was ruled out by the negative result of a search for characteristic X-rays not belonging to  $^{12}\text{C}$ ,  $^{16}\text{O}$ , or  $^{248}\text{Cm}$  following proton excitation (PIXE).

Measurements with non-irradiated foils showed that the Cm material clumps in some non-uniform manner as it is initially deposited on the C backing foil. The structure does not appear to become more uniform after HI irradiation, as shown in Fig. 2-43 which presents the  $E_p$  spectra for a target with beam positioned on the Cm spot (a) and away from the spot on the bare  $^{12}\text{C}$  backing foil (b). From Eqn. 2.83, the  $^{12}\text{C}$  backscatter peak should be shifted between the two spectra by an amount,

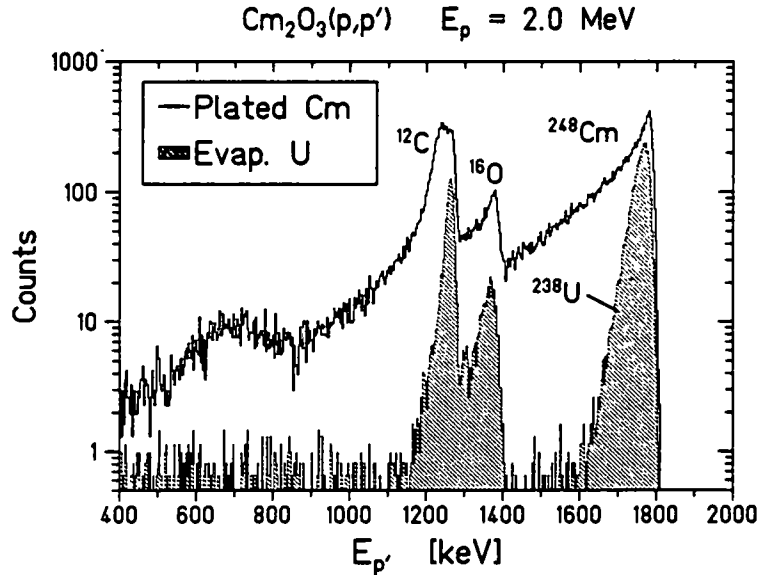


**Figure 2-42.** Backscattered proton energy distributions for a  $\text{Cm}_2\text{O}_3$  and an evaporated  $^{238}\text{U}$  target. Extensive tailing indicates a very non-uniform distribution of the curium material. (Reproduced from [Klü84].)

$$\Delta E_p^C = (1 + 1/\cos\theta)(dE/dx)_{\text{Cm}_2\text{O}_3}(\Delta x)_{\text{Cm}_2\text{O}_3} \quad (2.84)$$

However, curve (a) shows that less than 50% of the  $^{12}\text{C}$  peak intensity is shifted as expected by energy-loss of the beam passing through the  $\text{Cm}_2\text{O}_3$  target layer. This implies that the proton beam has  $\sim 50\%$  probability of encountering no  $^{248}\text{Cm}$  material, before first striking the  $^{12}\text{C}$  backing foil. Clearly, the  $\sim 300 \mu\text{g}/\text{cm}^2$   $\text{Cm}_2\text{O}_3$  must be distributed non-uniformly with an average thickness of  $\geq 600 \mu\text{g}/\text{cm}^2$  covering less than half the geometric target area. The suggestion of Figs. 2-42,41 is that large clumps form, perhaps resembling peaks and valleys on the target surface. Instead of an average  $0.07 \text{ MeV}/\text{u}$  energy loss of the HI beam traversing the  $300 \mu\text{g}/\text{cm}^2$  targets,  $\sim 0.15 \text{ MeV}/\text{u}$  is implied by the measurements. This represents the limiting resolution which can be assigned to the U+Cm excitation function measurement.

**Composition Measurements:** The proton measurements also give the quantity of each isotope in the target by comparing the  $^{12}\text{C}$ ,  $^{16}\text{O}$ , and  $^{248}\text{Cm}$  peak intensities, for a given accumulated beam current, to the known scattering cross-section. For  $^{248}\text{Cm}$  and other heavy elements, Rutherford scattering is sufficient, but at 2 MeV, protons are resonantly scattered from  $^{12}\text{C}$  and  $^{16}\text{O}$ . At  $\theta = 165^\circ$ ,  $^{12}\text{C}(p,p')^{12}\text{C}$  and

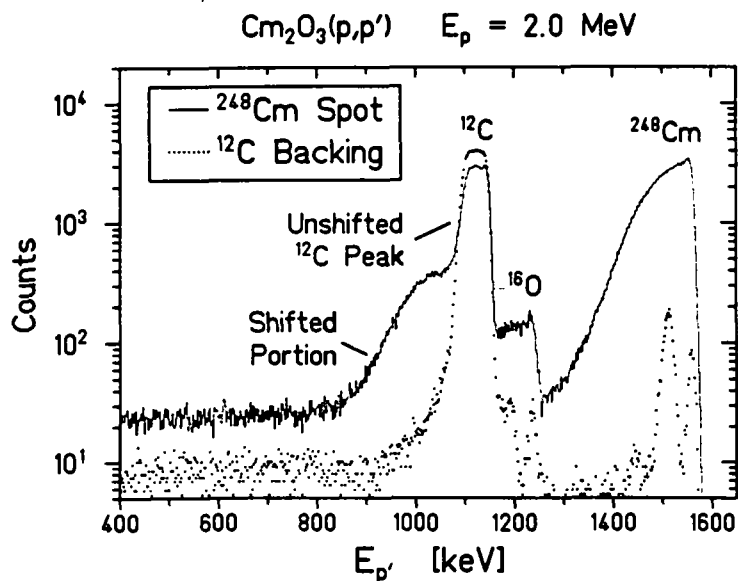


**Figure 2-43.** Comparison of backscattered energy spectra for protons incident on a  $\text{Cm}_2\text{O}_3$  target (solid histogram) and on the carbon target backing (dotted). (Reproduced from [KlÜ84].)

$^{16}\text{O}(p,p')^{16}\text{O}$  cross-sections exceed  $(d\sigma/d\Omega)_{\text{ruth}}$  by factors of 9.6 and 3.5 respectively [KlÜ84]. Taking this into account, an X-Y scan of the collimated proton beam across the target surface provides a thickness profile of the beam spot. Figure 2-44 presents horizontal scans across a Cm target both before (left) and after irradiation in the UNILAC beam. The integral thickness of  $^{12}\text{C}$ ,  $^{16}\text{O}$ , and  $^{248}\text{Cm}$  is plotted at each point, as well as the  $dE/dx$  thickness for  $^{248}\text{Cm}$ . Of particular note is the large concentration of  $^{16}\text{O}$  before, and its drastic decrease after irradiation. The  $^{16}\text{O}$  thickness expected in the  $\text{Cm}_2\text{O}_3$  compound is only 9.7% of the Cm thickness, when expressed in  $\mu\text{g}/\text{cm}^2$ . Initially then, the target has an overabundance of  $\sim 100 \mu\text{g}/\text{cm}^2$   $^{16}\text{O}$ . After irradiation it is more in line with the chemical concentration of  $\text{Cm}_2\text{O}_3$ . A similar  $\sim 100 \mu\text{g}/\text{cm}^2$  excess in  $^{12}\text{C}$  is also initially present. Sputtering of the thick C backing placed downstream of the  $\text{Cm}_2\text{O}_3$  layer in the UNILAC beam results in a dip in the  $^{12}\text{C}$  yield within the beam spot. H. Folger interpreted these initial excesses of  $^{12}\text{C}$  and  $^{16}\text{O}$  as the presence of traces in the target of the alcohol carrier solution used in the molecular plating process. These contaminants would be driven away in-beam, leaving  $\text{Cm}_2\text{O}_3$  in some crystalline form. Interestingly, the factor of 3 larger energy-loss thickness remains roughly constant throughout the HI irradiation.

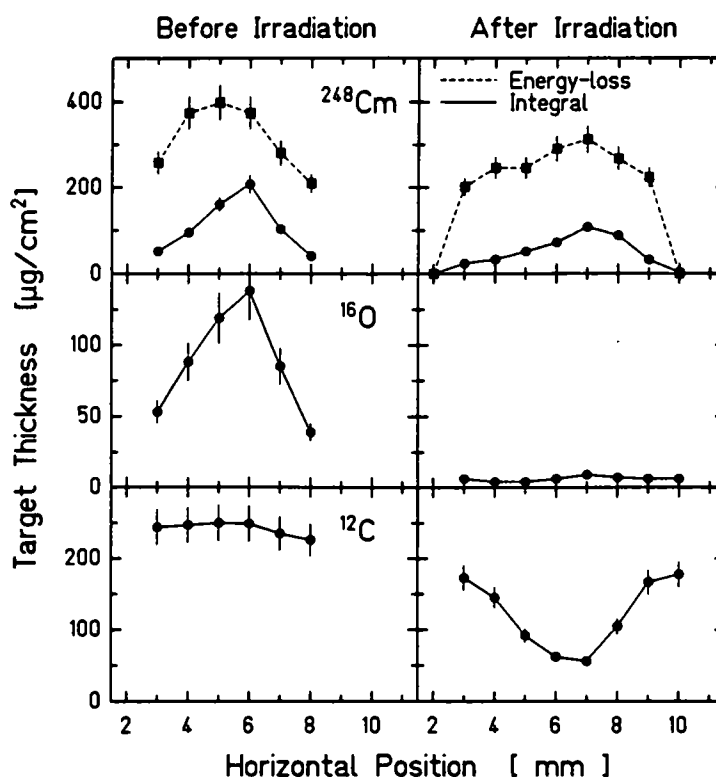


**Figure 2-44.** Yield of  $^{12}\text{C}$ ,  $^{16}\text{O}$ , and  $^{248}\text{Cm}$ , plotted versus the horizontal position of the proton beam, in a  $\text{Cm}_2\text{O}_3$  target before (left) and after (right) irradiation in the UNILAC beam. Concentrations of each element are given by the solid lines, energy-loss thickness of the curium layer by the dashed lines. (Reproduced from [Klü84].)

### Sec. 2.6.3 Development Efforts

Possibilities to improve of the quality of plated curium targets were studied in a series of test measurements using uranium and gadolinium (a chemical equivalent to curium) targets fabricated by different techniques. For example, N. Trautmann modified the plating method to deposit several thinner layers of  $\text{Gd}_2\text{O}_3$  to build up a  $300 \mu\text{g}/\text{cm}^2$  target, the idea being that perhaps a more uniform deposition could be attained by driving off the carrier solvent between layers. Although initially more uniform, the layered target still lost  $^{16}\text{O}$  and its  $\Delta E$  thickness increased during irradiation to the same level as for a target made in a single layer. Different compounds were also investigated, but the only positive advance was made by evaporating the Gd and U material directly on to the C backing foil. The evaporated U target maintained much better homogeneity than the plated Cm targets. For measurements of Th + Th and Th + U, therefore, we used  $\text{ThF}_4$  targets evaporated in  $\sim 250 \mu\text{g}/\text{cm}^2$  layers of  $\sim 40 \mu\text{g}/\text{cm}^2$   $^{12}\text{C}$  backings, and covered with  $5\text{-}10 \mu\text{g}/\text{cm}^2$  layers of C evaporated over

the target spot. The fluoride compound was chosen over the oxide because it formed more uniform layers. On the other hand, it appeared that the oxide targets tested lost material less rapidly in beam. It was furthermore found that without the thin  $^{12}\text{C}$  coverings, the targets lost material from backward angle sputtering very quickly (as much as 30% per hour in UNILAC beam).

In order to extend its useful data-taking lifetime, we adopted a policy of conditioning each target very carefully in-beam. To avoid sudden thermal shocks with uncontrolled rearrangement of the microscopic structure, each fresh target was initially irradiated with a very low beam current,  $< 0.05$  PnA, for a few minutes. After this gentle warming period, the current was steadily increased to  $\cong 1$  PnA over  $\sim 10$  minutes. Throughout its irradiation, the thickness was monitored by comparing the HI scattering rate to the beam current. The thickness typically remained constant for  $\sim 1$  hour, after which it began to decrease. When the target had lost  $\sim 10\%$  integral thickness, i.e., after  $1\frac{1}{2}$  to 2 hours, it was replaced. Using higher beam currents significantly accelerated deterioration. For example, at  $\sim 2$  PnA a  $\text{ThF}_4$  target lost 10% in about 15 minutes.

Tantalum targets were fabricated by sputtering Ta metal onto the  $^{12}\text{C}$  backings, again in a 5 mm dia. spot. They were covered with  $\sim 5$   $\mu\text{g}/\text{cm}^2$  evaporated  $^{12}\text{C}$ . Their in-beam stability was comparable to or better than the evaporated  $\text{ThF}_4$  targets.

For the most recent Th + Cm measurements which are discussed in Part II of this dissertation, evaporated  $\text{CmF}_3$  targets were purchased from Oak Ridge National Laboratory. Although their stability seemed comparable to the  $\text{ThF}_4$  targets, only a limited number were available and each was therefore irradiated for a very long time ( $\sim 12$ -20 hours). As a result, the energy-loss thickness was close to a factor of two larger than the nominal thickness, and the effective beam-energy dependence of the data is in question. Figure 2-45 presents energy spectra of protons backscattered from  $\text{CmF}_3$  and  $\text{ThF}_4$  targets, measured at points inside and outside the irradiated beam spot. Although both sets of spectra exhibit narrower backscatter peaks than for the earlier plated targets, tailing to low energies, indicating non-uniform density distributions, remains problematic with the Cm targets. The relative intensities of the shifted to unshifted  $^{12}\text{C}$  components further implies that the  $\text{CmF}_3$  material again clumped in such a way as to leave much of the backing foil exposed. The  $\text{ThF}_4$  target material seems to have adequately covered the backing.

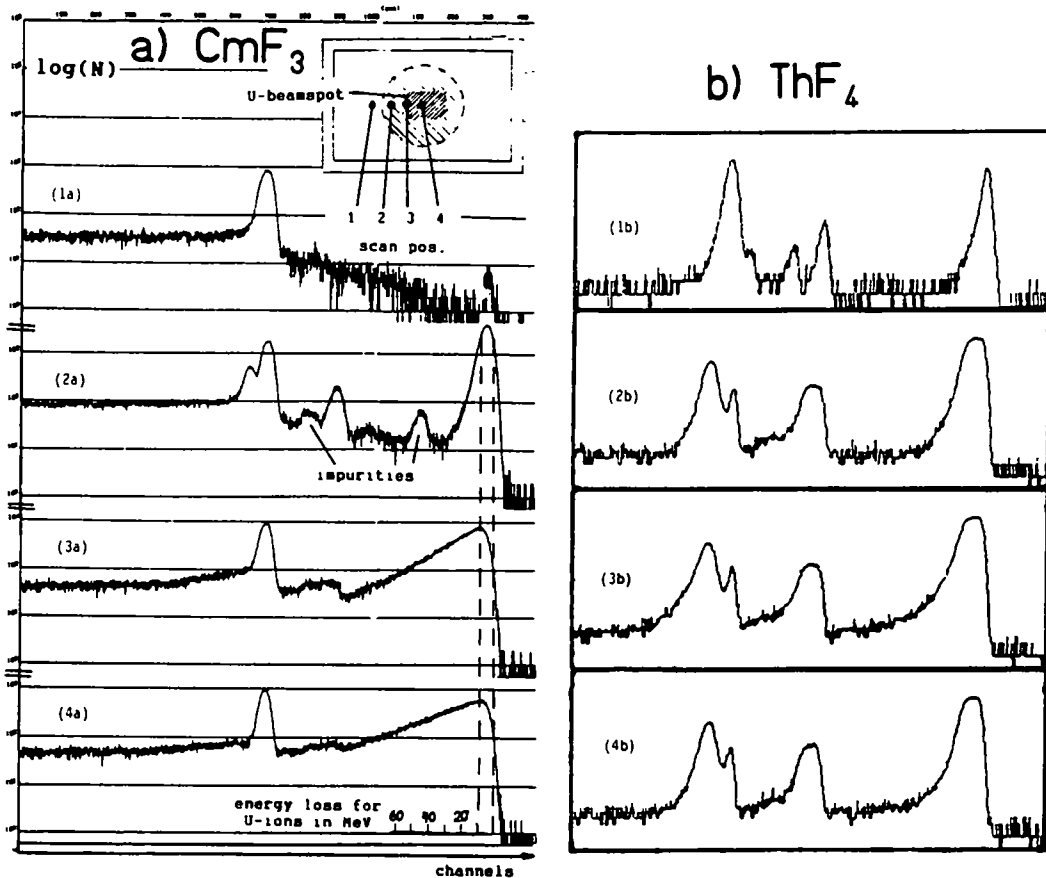


**Figure 2-45.** Backscattered proton energy spectra measured at four positions on an ORNL  $\text{CmF}_3$  target (left), and a GSI  $\text{ThF}_4$  target (right), after irradiation in the UNILAC beam. (Adapted from [Sti86] and [Kra87].)

### Sec. 2.6.4 Summary

The experience gained in working with heavy actinide targets over the years of the EPOS experiments has revealed several difficulties for maintaining target homogeneity and stability. Of the various fabrication techniques investigated by H. Folger and N. Trautmann, evaporated targets of fluoride compounds appear to provide the most uniform layers. However, these targets appear to deteriorate rapidly and have lifetimes of only 1-2 PnA-hours in  $^{238}\text{U}$  and  $^{232}\text{Th}$  beams at  $\sim 6$  MeV/u. The energy-loss thickness exceeds the nominal thickness (assuming a uniform layer) by up to a factor of  $\sim 1.5$ , with small excursions to twice the  $\text{ThF}_4$  target thickness. The consequences of these results for measuring an excitation function of the positron peak are that not only is a beam energy definition better than 0.05-0.07 MeV/u very difficult to achieve, but the reproducibility and stability of measurements involving

resonant scattering processes is non-trivial. The amount of target material within a given narrow collision-energy range depends sensitively on the thickness profile of the particular target, which probably changes during the measurement due to clumping and rapid target deterioration.

## **Section 2.7 Heavy-Ion Beam**

### ***Sec. 2.7.1 UNILAC Accelerator***

The experiments described in this thesis used beams of U and Th ions accelerated to energies of  $\sim 6$  MeV/u (1.4 GeV) by the UNILAC accelerator of the Gesellschaft für Schwerionenforschung in Darmstadt, West Germany. When the investigations of positron production in heavy-ion collisions began in 1976, the UNILAC was the only machine in the world capable of accelerating beams of U to energies near the Coulomb barrier, as required to generate the highest possible combined nuclear charges. Figure 2-46 shows the layout of the accelerator and the target hall. The EPOS spectrometer is set up at the Z2 experiment site.

The UNILAC (UNiversal Linear ACcelerator, cf. [Ang77]) is a pulsed machine (50 Hz), delivering a  $\sim 4$  ms long beam pulse every 20 ms for a net duty cycle of  $\sim 20\%$ . The beam particles are produced in a Penning-type positive-ion source by sputtering a uranium (or thorium) electrode in an argon atmosphere. The entire source is maintained at -300 kV potential, and  $\mu\text{A}$  currents of charge  $10+$  ions are extracted and then bunched (with a 1 ns pulse width and 37 ns separation) prior to injection into a series of four Wideröe drift tube acceleration tanks (operated at 27.04 MHz). The 1.4 MeV/u beam is then stripped to a higher mean charge state of  $28+$  by passage through a supersonic  $\text{N}_2$  gas jet. Two of four available Alvarez tanks (operated at 108 MHz) further accelerate the beam to 5.9 MeV/u. The final energy is tuned over a range of  $\pm 0.3$  MeV/u by accelerating or decelerating the beam with single RF-cavity resonators.

### ***Sec. 2.7.2 Beam Current, Focus, and Duty-Cycle***

As mentioned above, two of the experimental parameters which seem to play an important role in isolating the narrow positron peaks are their correlations with incident projectile energy and associated heavy-ion scattering-angle kinematics. Both of these variables depend sensitively on the quality of the heavy-ion beam, and, as de-

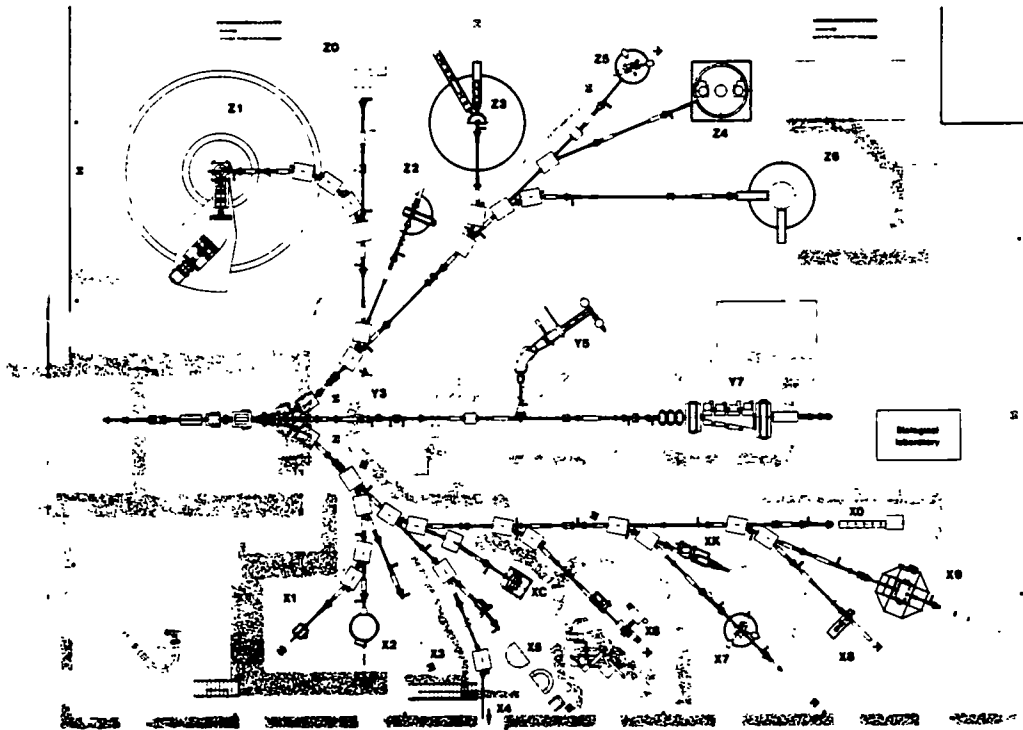
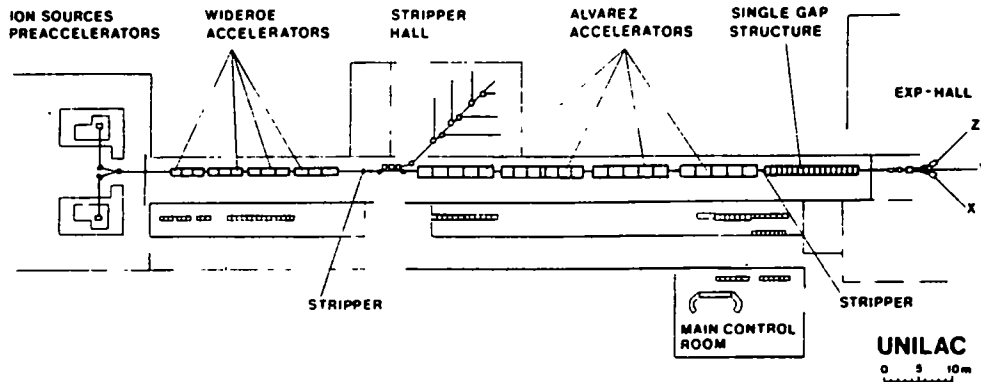


**Figure 2-46.** Diagram of the UNILAC accelerator (top) and experimental hall (bottom) at GSI, Darmstadt, West Germany. The EPOS spectrometer is installed at the Z2 experimental site. (Reproduced from [Ang77].)

scribed in Sec. 2.6, on the stability and thickness of the targets. As a consequence, over the span of the EPOS experiments the UNILAC has been progressively pushed to the limits of its energy resolution, stability, and duty-cycle.

As discussed in the preceding section, the actinide targets are subject to rapid deterioration in the heavy uranium and thorium beams. The beam current was

therefore limited, from the available  $\sim 5$  PnA at the exit of the UNILAC, to  $\cong 1$  PnA on target. Above this current the target material was found to evaporate very quickly. By operating the Penning source below its maximum current output, the life of the sputter electrodes was also prolonged (typically 12 to 30 hours), and the frequency of source changes reduced. The beam current was measured in a Faraday cup, which served as the EPOS beam dump, about 2 m downstream of the target. The beam ions were stripped by passage through the target to  $\cong 60^+$ . The electrical current was averaged with an  $\sim 1$  sec time constant in a current digitizer and then integrated in a scaler which was read out and reset with each EPOS event trigger. This provided a running record of the beam on target.

The beam focus on the target was measured by means of retractable diagnostic grids [Str86] located directly in front of the target and  $\sim 60$  cm behind the target in the beam dump. The X-Y spacial profile provided by ions hitting the  $1.5 \text{ mm} \times 1.5 \text{ mm}$  mesh of sense wires was checked during each target change. The beam dump grid remained in the beam continuously to provide an on-line control of the beam position. Gamma-rays emitted from the activated grid wires were shielded from the positron and electron detectors by 2 cm of Pb placed around the beam dump. In order to maintain optimal scattering-angle resolution in the PPAC's, and to reduce the flux of  $\delta$ -electrons emitted slightly away from the solenoid axis, the size of the beam spot was kept small. It could not be too small, however, or else too much energy would be deposited in a small area of the target, increasing deterioration. We typically focussed the beam to a 3 mm high by 5 mm wide spot.

The pulsed nature of the beam is a disadvantage for a multi-coincidence experiment such as EPOS. Accidental background coincidences due to unrelated scattering events from the same beam-pulse increase with the square of the instantaneous counting rate, while prompt events increase only linearly with counting rate. With a 20% duty-cycle, the typical chance rates in the positron channel are  $\sim 5\%$  (at 1 PnA). Plasma oscillations in the ion source occasionally led to uneven extraction, sometimes with only every tenth micro-pulse having a significant number of beam particles. Under these conditions, an average beam current of 1 PnA led to very large instantaneous currents and problematic chance background rates. The duty-cycle was therefore monitored with oscilloscope displays of the time-structure of the beam current, measured by capacitive probes at the Penning ion source and at the output of the UNILAC. In addition, the timing signals of the PPAC's and posi-

tron detector were often checked for unusually high instantaneous rates, and the analyzed data inspected for large chance rates.

### **Sec. 2.7.3 Beam Energy and Isotopic Purity**

The energy spread of the UNILAC beam is limited by the phase-space acceptance of the Widerøe and Alvarez accelerating structures. Under optimum conditions, the energy resolution is  $\Delta E/E \sim 0.3\%$ , or  $\Delta E \cong 0.02$  MeV/u at 6 MeV/u. We tried to maintain this accuracy in each experiment. The UNILAC beam energy was measured by time-of-flight between two non-destructive capacitive phase probes. Throughout Part I of this thesis research, we used TOF pickoff probes separated by 3.5 m. The  $\sim 100$  ps TOF resolution allowed a determination of the mean energy to 0.02 MeV/u. The width of the time structure of the signals induced on the probes reflects the spread in beam energies by their spacial dispersion over the flight path. As discussed below, the absolute mean beam energy was not easily reproduced between experiments. As evidence accumulated for a resonance-like origin for the positron peak, it became necessary to better control the beam energy. Recently, we used probes separated by  $\cong 8$  m so that the readout of the mean beam energy was accurate to  $\sim 3$  keV/u.

The beam transport line to Z2 also provided a rough magnetic momentum analysis. On its way to the experimental site, the beam was deflected through an arc of  $70^\circ$  by a beam-switching "kicker" magnet and by three dipole bending magnets. The transverse position of the beam was measured in several diagnostic grids located at selected points along the beam line. Together with a set of slits placed after the second dipole, this partially constrained the beam path, limiting the beam-spot size on target. Assuming stable emittance from the UNILAC, the transmitted beam is limited to a constant energy interval. Measurements of the beam intensity on target while scanning the dipole magnet currents indicated that the momentum acceptance was  $\Delta P/P \cong 0.5\text{-}1\%$ .

In a preliminary measurement just completed, satellite components having different energies from the main  $^{238}\text{U}$  beam were also identified. Depending on a variety of conditions, up to a few percent of the beam particles having an ionic charge state of other than  $28^+$  can be accelerated in the Alvarez. Those with the same magnetic rigidity ( $\propto Mv/q$ ) can be transported through the beam-line to the target. Percent-level satellites with energies of  $\sim 5\%$  larger than the main beam were iden-

tified in the GSI magnetic spectrometer [Shü87]. Trace contaminations of other elements, e.g., Mo and Zr, were also observed at the  $10^{-3}$  level.

Unfortunately, the exact mean energy of the beam and its energy spread, as well as the sizes of the satellite components and contaminants, all depend sensitively on the emittance of the accelerated beam at various points along the UNILAC. For example, by changing the aperture of slits in the injection region of the Wideröe in order to control the intensity of the beam on the target at Z2, the mean energy spread and focus of the beam at Z2 can be altered. The same is true of slightly resteeing the beam into the Wideröe, or after the stripper region into the Alvarez. Moreover, as the sputter electrodes in the Penning source age, the burning mode of the plasma itself changes, altering the beam's spacial and momentum distribution after extraction. All of these variations affect the acceleration of the ion bunches and their entrance into the Z-branch. Although slight drifts in the transmitted beam energy and intensity result, they are generally  $\leq 0.02$  MeV/u over the lifetime of a single source. When a source was replaced, however, the new extraction characteristics altered the beam profile and energy. Shifts of up to 0.05 MeV/u were observed between consecutive source changes. After every source change, therefore, the beam energy was checked, and if necessary, re-tuned by adjusting the single cavity resonators. Residual variations in the spacial profile affect beam transport through the Z-line bending magnets, at least marginally changing the beam-on-target energy. The relative concentrations of contaminant elements were also observed to vary by up to an order of magnitude depending on the particular source and its age.

These inherent instabilities in the UNILAC emittance limited the effective resolution of the beam over the course of an experiment. This was further compounded by the accumulation of many small steering and focussing adjustments over a several day run or the major retuning frequently required after repairs to UNILAC components which occasionally broke down during an experiment. Very different beam-paths through the accelerator invariably evolved during an experiment. Maintaining beam stability (even relatively) to 0.02 MeV/u, long enough to accumulate several thousand total positrons, proved to be difficult. Absolute reproducibility in beam energy from experiment to experiment was further limited by changes and drifts in the TOF read-out, the different initial tuning of the machine, and on one occasion, a poorly documented change in the capacitive TOF probe calibrations. From a practical point of view, beam energies used in different experiments cannot be directly compared to

better than  $\sim 0.05$  MeV/u. Over a few day period within a single run, a given mean energy could not be reproduced with better than  $\cong 0.02$  MeV/u accuracy.

## Section 2.8 Data Acquisition System

### *Sec. 2.8.1 Experimental Electronics*

The energy and timing signals from each of the detector components were stored event-by-event on magnetic tape for subsequent off-line analysis. Figure 2-47 summarizes the EPOS experimental electronics. (Table 2-3 lists the abbreviations used in Fig. 2-47.) A more complete description is given in [Shw85]. Very briefly, a standard fast/slow multi-parameter coincidence technique was used, employing commercially available NIM electronic components. The data were digitized in gated ADC's and TDC's which were read out by a dedicated PDP-11/45 computer through a CAMAC interface. Each event buffer was then transferred to the GSI IBM mainframe computer where an online analysis was performed and the data were written to high density magnetic tape. Data conversion and readout were triggered for positron-HI coincidence events,  $\gamma$ -HI events, electron-HI events, Si Monitor singles, and HI collisions for normalization.

For the semi-conductor and NaI detectors, the HV bias supplies, preamplifiers, timing filter amplifiers, constant fraction discriminators, and test pulsers were located at the Z2 experimental site, while main amplifiers and all logic and CAMAC electronics were situated in a shielded data acquisition room which housed the PDP-11/45 computers. Amplifier gains and timing delays were adjusted with radioactive sources. Of the PPAC electronics, only the preamps were situated at the spectrometer as all other adjustments (HV, timing delays, and CFD thresholds) were optimized with the beam. As indicated in Fig. 2-47, the energy output from each detector was amplified and fed directly into a gated ADC. The fast time outputs were amplified (the anode signal is taken for NaI's) and fed into constant fraction discriminators. The negative NIM logic outputs were split in the data-acquisition room into a time signal which stopped the respective TDC, and a logic signal used for trigger processing. Each of these were shaped and adjusted by gate and delay generators. The logic outputs of the two positron Si(Li) segments, as well as the eight ARD NaI crystals, were "OR"-ed to provide a single "system" logic signal.

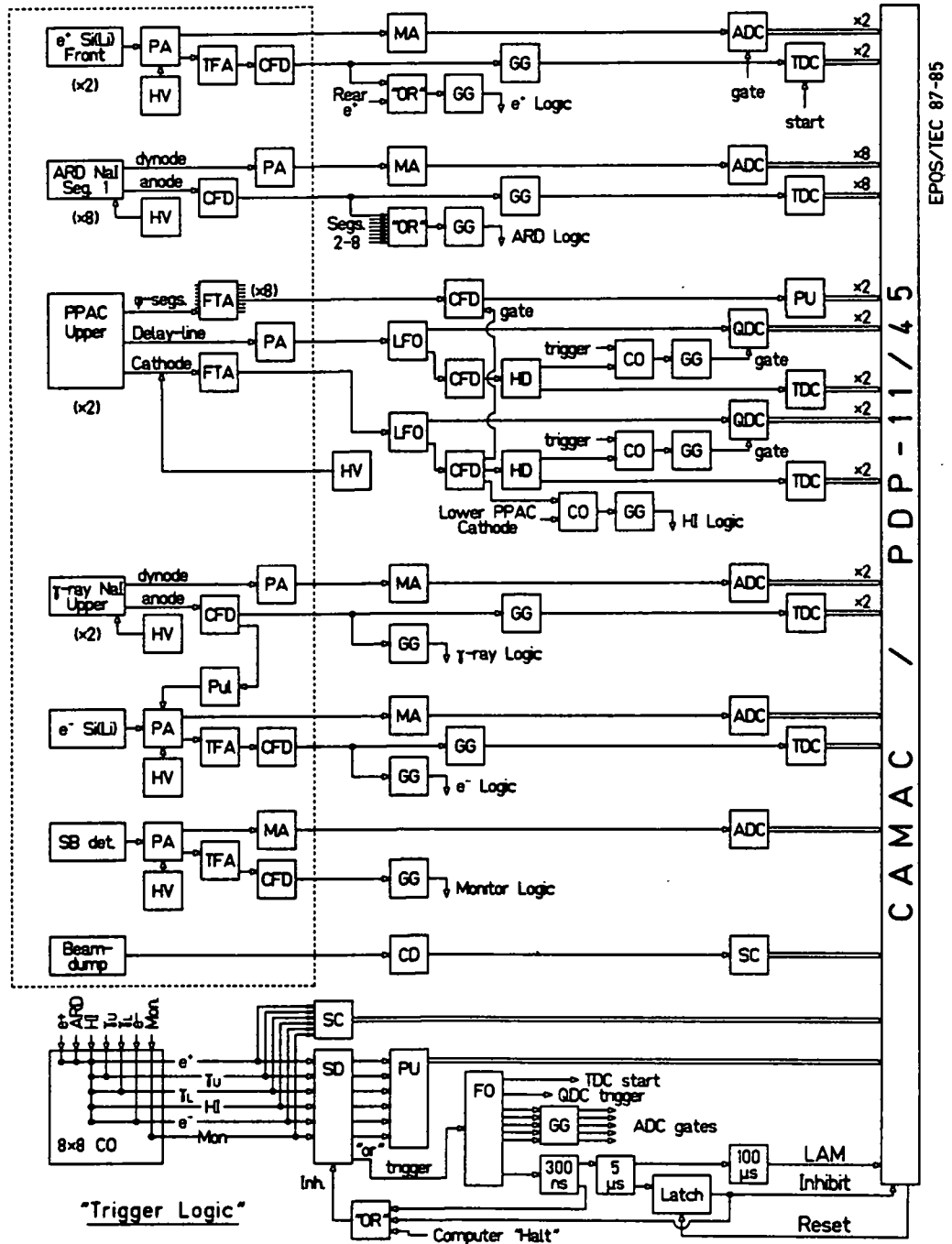


**Figure 2-47.** Block diagram of the experimental data acquisition electronics. Electronic components for the segmented detectors occur twice for the  $e^+$  Si(Li), eight times for the ARD, twice for the PPAC's, and twice for the  $\gamma$ -ray NaI's. Gates and start signals for each ADC and TDC are shown explicitly only for the  $e^+$  Si(Li) detector. Components inside the dotted rectangle are situated at the Z2 experimental site. Abbreviations are defined in Table 2-3.

The signals from the PPAC's had rise-times of order  $\sim 1-3$  ns (cathode or delay respectively), with an amplitude of order 0.3 to 1 Volt depending on gas-pressure and HV bias. They were therefore routed directly from the timing preamps to the data acquisition room, where they were split in linear fanouts into timing, energy, and logic signals. An overlap between the CFD outputs of the cathode foils from each detector formed the HI coincidence logic signal. TDC stop signals were appropriately delayed ( $\sim 300$  ns) using low dead-time hybrid delay units. Gate and delay generators were not used because of the large  $\sim 5-10\%$  deadtime which would result from the high instantaneous counting rates ( $\sim 50-100$  kHz). The  $\phi$ -segment signals were discriminated and the outputs used only to set a bit which marked the  $\phi$  segment that fired. To ensure that the  $\phi$  for the correct HI scattering was registered, this CFD was gated by an overlap of the event trigger and the prompt cathode logic signal. In the same way, charge digitizers (QDC's), which integrated the cathode and delay-line signal outputs, were gated by an overlap of the event trigger with the respective prompt PPAC timing signal.

Also read out with each event were the average beam current integrated in a CAMAC scaler, and in recent experiments, measures of the beam energy by TOF probe pick-off times. An additional bit in the event bit-pattern unit identified whether the 4 ms beam "macro-pulse" was present, distinguishing beam-on from beam-off events.

### ***Sec. 2.8.2 CAMAC Interface and Logic Trigger***

The types of events recorded by the EPOS spectrometer were chosen by an overlap coincidence of appropriate combinations of detector logic signals. For example, positron events were defined by the three-fold overlap of the Si(Li) (forward or rear segment), ARD (at least one of eight segments), and HI (both PPAC's) logic signals. The other event types recorded were  $\gamma$ -ray-HI coincidences with either the front or rear NaI detector, electron-HI coincidences, monitor detector singles (only the energy signal was read out), and for normalization, HI PPAC-PPAC coincidences alone. Each logic signal was 150 ns wide providing a total 300 ns coincident resolving time. The delays were adjusted to provide maximum overlap for prompt coincidences, so a 150 ns shift of any logic signal provided an accumulation of chance coincidences over about four beam-pulses either before or after the prompt event. The HI, Monitor, electron, and  $\gamma$ -ray events, which arrive many times faster than the positron events, were scaled down in rate dividers to prevent excessive dead-

Table 2-3: Abbreviations Used in Figure 2-47

ADC	Analog to Digital Converter
CD	Beam Current Digitizer
CFD	Constant Fraction Discriminator
CO	Overlap Coincidence Unit
FTA	Fast Timing Amplifier
FO	Logical Fan-Out
GG	Gate and Delay Generator
HD	Hybrid Delay
HV	High Voltage Supply
LFO	Linear Fan-Out
MA	Main Amplifier (Linear Energy Signals)
"OR"	Logical "OR" (Fan-In)
PA	Pre-amplifier
PU	Bit Pattern Unit
Pul	Pulser
QDC	Charge to Digital Converter
SC	CAMAC Scalers
SD	Scale Down Unit
TDC	Time to Digital Converter
TFA	Timing Filter Amplifier
5 $\mu$ s	Delay as marked

---

time. Both the trigger coincidence box and scaledown unit were custom-built at GSI and provided eight event channels. The rate-divider unit accepted every  $2^n$ -th pulse and was vetoed by the system-wide inhibit. An "OR" of the accepted events formed the system trigger. Outputs from the rate-divider box were routed to a bit-pattern unit to identify which event types triggered the system and to rate meters. The non-inhibited non-scaled-down coincidence box outputs were also integrated in CAMAC scalars, which were read out and written to tape for each tape file. The quotient of the integrated overlap coincidence rate,  $N_{\text{coinc}}^i$ , to the recorded number of event triggers,  $N_{\text{trig}}^i$ , gives the scaledown, SD, times the live-time,  $1-\tau_{\text{dead}}$ , for a given event type  $i$ :

$$SD_i \cdot (1-\tau_{\text{dead}}) = N_{\text{coinc}}^i / N_{\text{trig}}^i \quad (2.85)$$

The total number of parameters written to tape per event was approximately 45: time and energy signals for each of the two positron Si(Li) segments, the eight ARD NaI segments, the two  $\gamma$ -ray detectors, the electron Si(Li), each PPAC delay-line and cathode foil, and the Si monitor counter; bit patterns for each PPAC  $\phi$ -foil and for the event-type trigger; time signals for the beam energy probes and the UNILAC  $\mu$ -pulse; and a scaler for the integrated beam current. A Ge(Li) detector positioned

at 45° below the beam line was also operated and read out, but its data were not analyzed in connection with the positron production measurements and have been excluded from this dissertation.

The sequence of processes following each event trigger was as follows: Upon generation of a trigger, gates were simultaneously generated for all ADC's, QDC's, and bit pattern units, and start signals were sent to the TDC's. After a 300 ns delay to allow for the resolving time of the overlap logic coincidences, the decision electronics (rate-divider box) were inhibited until the accepted event was processed. An event trigger was sent to CAMAC four  $\mu\text{sec}$  after the initial overlap coincidence in order to allow all analog signals to fully reach their peak voltages, and a latch was set inhibiting the inputs to all CAMAC modules. The PDP computer then initiated digitalization of the ADC, QDC and TDC inputs. A fixed 100  $\mu\text{sec}$  conversion time was allowed to ensure complete processing of the 8-fold TDC and ADC 2048 channel range. A LAM ("Look-At-Me") pulse was then sent to the computer, through CAMAC, beginning data transfer. Each event parameter required a readout time of 7  $\mu\text{sec}$ . The last ADC dumped returned a ready signal which reset the inhibit latch and enabled further data accumulation. The entire busy time per event was the sum of the logic resolving time (300 ns), analog "coincidence" time (4  $\mu\text{sec}$ ), conversion time (100  $\mu\text{sec}$ ), and data transfer time ( $\sim 45 \text{ events} \times 7 \mu\text{sec}$ ) for a total of  $\cong 400 \mu\text{sec}$ . In order to maintain small dead times (e.g.,  $\tau_{\text{dead}} < 10\%$ ), the average event rate was limited to  $\leq 50 \text{ Hz}$ . The HI events were scaled down by a factor of  $\sim 2048$ ,  $\gamma$ -ray events by  $\cong 2$ , electron events by  $\sim 8$ , and monitor events by  $\sim 64$ . Positron triple-coincidences arrived at an average  $\cong 0.4 \text{ Hz}$ , about half of which were chance events and  $\sim 25\%$  identified as clean positron events. During a typical 7 day run in which  $\sim 15,000$  positrons were measured, approximately  $2 \times 10^6$  events of all kinds were recorded on  $\sim$ ten 6250 bpi computer tapes. More information regarding the GSI On-line Data Acquisition System and computer facilities is found in [Bus83].

## Chapter 3 Data and Analysis

As discussed in Chap. 1, the first part of this dissertation research focused on searching for and studying the properties of positron peaks in superheavy collision systems. This investigation involved five separate beamtimes (each  $\sim 5$  days long) over the period from June 1983 to September 1984. One subcritical collision and five supercritical systems were measured, ranging from  $^{232}\text{Th} + ^{181}\text{Ta}$  ( $Z_U = 163$ ), to  $^{238}\text{U} + ^{248}\text{Cm}$  ( $Z_U = 188$ ), using UNILAC beams of  $^{238}\text{U}$  and  $^{232}\text{Th}$  of 5.65 to 6.24 MeV/u. In this chapter, following a brief overview of the systems measured in each experiment, the reduction of the data is discussed. The continuous dynamic and nuclear positron energy distributions are evaluated, and the experimental results for the positron energy spectra under selected kinematic conditions are presented. The discussion which follows in Chap. 4 also includes some data measured earlier [Shw85] for  $^{238}\text{U} + ^{248}\text{Cm}$  and  $^{238}\text{U} + ^{238}\text{U}$ .

### Section 3.1 Experiments

#### Sec. 3.1.1 Systems Measured

In the first two experiments in June and July 1983,  $^{238}\text{U} + ^{248}\text{Cm}$  ( $Z_U = 188$ ) collisions were studied at beam energies between 5.92 and 6.24 MeV/u. The aim of these measurements was first to reproduce the original narrow positron peak structure discovered in January 1981 [Shw83], and then to improve its statistical accuracy. The electron detector was added to EPOS to investigate possible nuclear electric monopole transition origins for the narrow positron peaks by searching for competing internal conversion lines. As described in Chap. 2, the EPOS detection efficiency was increased by a factor of  $\sim 2$ , and extended to below 100 keV in order to increase the data accumulation rate and provide sensitivity to lower energy structures. The PPAC angular resolution was improved to  $\sim 0.5^\circ$  in order to gather better information concerning the apparent rotation of the associated HI scattering kinematics in the solenoid field.

As mentioned in Sec. 2.6, the targets were molecular plated  $\text{Cm}_2\text{O}_3$  layers on titanium and then carbon backings. Their nominal thickness ( $\cong 300 \mu\text{g}/\text{cm}^2$ ) corresponds to a beam energy-loss of 0.07 MeV/u. However subsequent measurement of the targets by proton backscattering revealed a  $\Delta E$  thickness of  $\cong 0.15$  MeV/u. The beam energy was originally chosen at 6.13 MeV/u to correspond to the same mean

energy in the target (accounting for loss in the backing foil) as in the January 1981 measurement. During the experiment we noticed an apparent dependence of peak production on beam energy. An excitation function measurement was therefore attempted with 0.02 MeV/u steps between 6.02 and 6.13 MeV/u, with additional points 0.1 MeV/u above and below this range at 5.92 and 6.24 MeV/u. As discussed below, the positron peak was detected for  $6.04 \leq E_{\text{beam}} \leq 6.13$  MeV/u. During an apparatus set-up period, we also measured  $^{238}\text{U} + ^{238}\text{U}$  ( $Z_{\text{U}} = 184$ ) and found a narrow positron peak there as well.

The next experiment, in February 1984, was intended as a search for the spontaneous positron line in  $^{232}\text{Th} + ^{248}\text{Cm}$  ( $Z_{\text{U}} = 186$ ) collisions, predicted to occur at  $\cong 250$  keV, which should be observable assuming that the U + Cm peak is associated with QED vacuum decay. During an initial set-up period with U + Cm we discovered stability problems with the  $^{248}\text{Cm}$  targets, but during the Th + Cm measurement, evidence was found for a positron peak which appeared at an energy similar to that of the U + Cm structure. Because of target problems, no excitation function was attempted and we concentrated our search at beam energies of 6.00, 6.02, and 6.04 MeV/u, using a total of five Cm targets of which two turned out to be extremely thin ( $\sim 100 \mu\text{g}/\text{cm}^2$ ) and were therefore discarded. The chosen beam energy was scaled from the mean "resonance" energy in U + Cm ( $\cong 6.07$  MeV/u), assuming a constant overlap of the nuclear surfaces. Very preliminary test measurements of Th + Th and Th + Ta were also attempted.

Having ruled out nuclear processes and having cast doubt on spontaneous positron emission as possible explanations for the positron peaks at similar energies in U + U, Th + Cm, and U + Cm, the next step was to extend the systematic  $Z_{\text{U}}$  dependence to lower systems. In July 1984, the  $^{232}\text{Th} + ^{232}\text{Th}$  ( $Z_{\text{U}} = 180$ ) system was measured at beam energies of 5.68, 5.72, 5.75, 5.78, and 5.82 MeV/u. Getting away from Cm targets opened the possibility of again measuring a beam energy dependence of peak production. Evaporated targets of  $\text{ThF}_4$ ,  $\cong 250 \mu\text{g}/\text{cm}^2$  thick, were employed. They exhibited good uniformity but tended to lose material at a rate of  $\sim 5\%$  per hour at  $\cong 1$  PnA beam currents. At the highest and lowest beam energies little structure was observed, while at 5.75 MeV/u, large pronounced structures were discovered. At 5.73 and 5.78 MeV/u, a broad enhancement at  $E_{e^+} \sim 400$  keV emerged which obscured the narrow line at  $E_{e^+} \cong 330$  keV. As discussed in Part II of this dissertation, it was not understood until the positron-electron coincidence experiment was completed that this reflected the presence of more than one positron

structure which, due to Doppler broadening, cannot be resolved. Only the 5.75 MeV/u data are therefore presented in detail in the following discussion.

A truly subcritical system,  $^{232}\text{Th} + ^{181}\text{Ta}$  ( $Z_U = 163$ ), was measured in September 1984. The targets consisted of  $\cong 250 \mu\text{g}/\text{cm}^2$  layers of Ta metal sputtered onto  $\sim 40 \mu\text{g}/\text{cm}^2$  C backings. M. Waldschmidt and K.E. Stiebing of Univ. Frankfurt assisted H. Folger of GSI in fabricating some of the targets. Beam energies in 0.05 MeV/u steps were sampled, bracketing the energy of constant nuclear overlap scaled from the supercritical systems. Evidence for both the  $\cong 320$  keV and  $\cong 380$  keV lines were found at 5.75 and 5.80 MeV/u. Very little peak data was observed in 5.85 MeV/u collisions. To round out the supercritical  $Z_U$  dependence,  $^{232}\text{Th} + ^{238}\text{U}$  ( $Z_U = 184$ ) collisions were also measured at 5.80 and 5.85 MeV/u. The  $\text{UF}_3$  targets were  $\cong 250 \mu\text{g}/\text{cm}^2$  thick.

Table 3-1 lists the nuclide combinations measured, the average target thicknesses, beam energies, and mean distances of closest approach in each of the systems. In each case the internuclear separation was larger than the nuclear interaction distances of [Wil80],  $R_{\text{int}} \sim 16$  fm, and the "safe" distances of [Nee82], below which the reaction cross-section rapidly increases.

Table 3-1 Collision Systems

System	$E_{\text{beam}}$	mg/cm <sup>2</sup>	$\Delta E_{\text{beam}}$	$R_{\text{min}}$	$N_{\text{et}}$
U+Cm	5.92-6.24	$\sim 350$	0.16	16.8 - 18.2	$\sim 20,000$
Th+Cm	6.00-6.04	$\sim 250$	0.11	17.2 - 17.6	$\sim 12,000$
Th+U	5.80-5.85	$\sim 250$	0.07	17.3 - 17.7	$\sim 5,000$
Th+Th	5.68-5.83	$\sim 270$	0.08	17.2 - 18.0	$\sim 15,000$
Th+Ta	5.75-5.85	$\sim 350$	0.07	15.9 - 16.4	$\sim 13,000$

### Sec. 3.1.2 Online Control

To ensure proper operation of the EPOS spectrometer and to maintain acceptable data-taking conditions, several aspects of the experiment were monitored online. The event-by-event data were analyzed in real time with a streamlined version of the main analysis program discussed in Sec. 3.2. In particular, raw spectra were

accumulated for each ADC, QDC, TDC, and pattern unit to check the operation of the data acquisition electronics. Energy and time spectra were generated for each detector for the appropriate event-type triggers to check for gain shifts or unusual counting rates. As noted in Sec. 2.8, the PPAC's were set up in-beam which required online calibration of the HI scattering angles. During the beam time, the angle-angle correlation plot was periodically examined, as were plots of  $\theta_{HI}$  vs.  $\phi_{HI}$  and  $\theta_{HI}$  vs.  $E_{HI}$ . In addition to monitoring the PPAC's, the angular resolution determined from the correlation plot also gave indications of the formation of thick clumps in the target. The target condition was also monitored by noting the relative scattering rates of C, O or F, and Ta, Th, U, or Cm, into the surface barrier detector. Its average thickness was determined by dividing the HI scattering rate into the PPAC's by the average beam current in the beam dump. As noted in Sec. 2.6, when material began to evaporate (> 10-20% loss) the targets were changed. The beam focus was also monitored continuously with an X-Y diagnostic grid in the beam stop.

The ARD NaI array was checked for uniform performance by histogramming the yield of annihilation photons incident in each NaI crystal segment. Time-difference spectra between appropriate pairs of detectors (e.g., PPAC-Si(Li) and Si(Li)-ARD) were periodically monitored for excessive chance coincidence rates which occasionally arose due to a decrease in UNILAC duty cycle because of plasma oscillations in the Penning ion source. Usually this was first noticed by an increase of very low energy  $\delta$ -electron events contaminating the total positron spectrum. The ARD sum energy spectrum then exhibited increased low energy backgrounds as well. The energy spectra of pulsers in the positron and electron Si(Li)'s provided online indications of the degree of  $\delta$ -electron pileup. As noted below, pileup seldom exceeded 3% in the positron, and 6% in the electron detectors, respectively.

An online analysis running on the GSI mainframe IBM computer monitored the status of the incoming positron data. Total positron spectra were continually updated for the beam energy run, target, and magnetic tape file in progress. A three dimensional  $\Sigma\theta_{HI}-\Delta\theta_{HI}-E_{e+}$  analyzer was accumulated and preliminary HI angle-angle cuts were periodically made to search for structure. This differential analysis was, of course, severely limited by the available online statistics. Interestingly, the shape of the total positron energy distribution proved to be a good indicator of the presence of peak intensity. When a shoulder in the distribution developed at energies between  $\sim 250$  and  $\sim 400$  keV, it was usually possible to isolate a narrow posi-

tron peak in certain HI scattering regions offline. A similar online analysis for the other detector systems was also performed.

As noted in Sec. 2.8, the average event rate was 20-50 Hz, depending on the HI,  $\gamma$ -ray, and electron event scaledowns. These were normally  $SD_{HI} = 2048$ ,  $SD_{\gamma} = 2$ , and  $SD_{e^-} = 8$ . The UNILAC was typically down for source changes, energy changes, beam optimization, and repairs for 20-50% of each beamtime. Target changes and slow target warm-up added an additional  $\sim 10\%$  experiment down-time. The positron accumulation rate during beam on target was 300-400 positrons per hour. In a typical 2-3 day run at a single energy,  $\sim 5000$  positrons were detected. The total number of positrons accumulated for each system is listed in Table 3-1.

## Section 3.2 Data Reduction

Because of the large quantity of data accumulated in these experiments ( $\sim 10^7$  events per beamtime), and the relative complexity of the analysis, data reduction is divided into several stages. In the first stage, the event-mode data were sorted by event type; energy, time, and angle calibrations were performed; true and chance coincidences were evaluated; and reduced parameter lists for subsets of the data (e.g., HI- $\gamma$ , HI- $e^+$ , and HI- $e^-$ ) were written to magnetic tape. In the second stage, faster individualized programs were used to study correlations between the data, e.g., positron energy distributions as a function of HI scattering angle. For either the total data or for specific kinematic selections, the more complex ARD background subtraction was then performed. In a final stage, absolute spectra were constructed after unfolding the detector responses, normalizing to the scattered HI yield and adjusting for scaledowns and deadtime. In order to simultaneously examine the  $\gamma$ -ray and electron spectra under identical conditions as the positron events, the run number, target, and magnetic tape file were identified, and HI scattering data were included with each subset for absolute normalization. Most of the techniques and procedures used in the data reduction were developed by J. Schweppe and A. Gruppe. A very detailed description is found in [Shw85], so only selected aspects of the data analysis are reviewed here.

### Sec. 3.2.1 Heavy-Ion Data

Since the positrons, electrons, and  $\gamma$ -rays were all measured in coincidence with scattered heavy ions, the PPAC data were analyzed in an identical way for all ev-

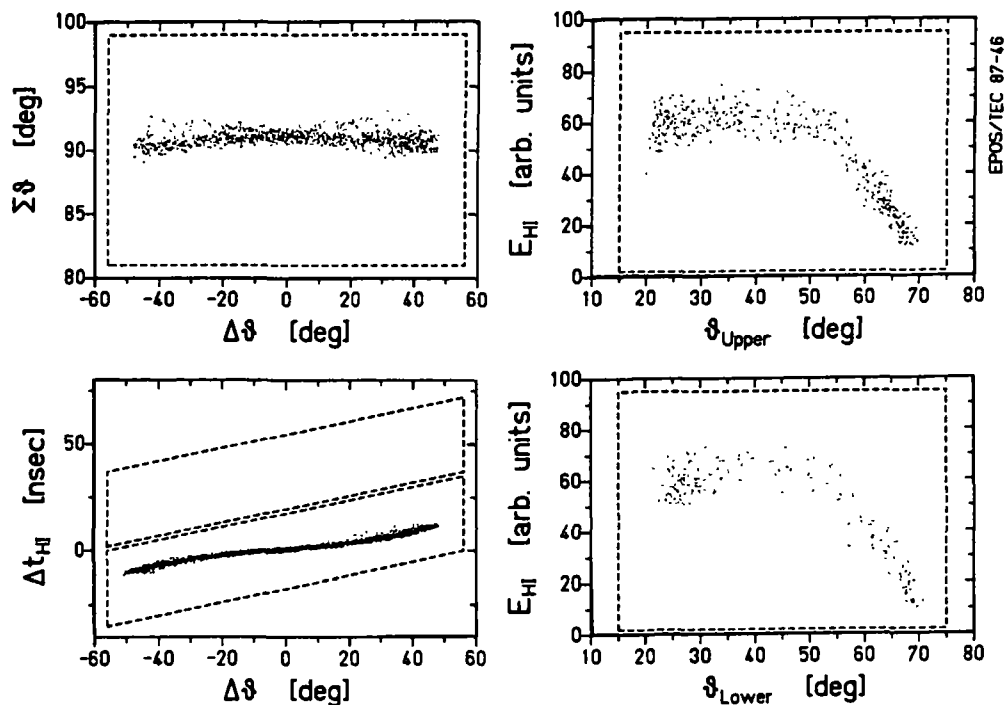


**Figure 3-1.** Data analysis gates for reduction of Th + Cm Heavy-ion scattering events. Dashed curves indicated windows on  $\Sigma\theta_{HI}$  vs.  $\Delta\theta_{HI}$  (upper left), kinetic energy vs.  $\Delta\theta_{HI}$  (right), and prompt and chance windows on the TOF difference between the PPAC's versus  $\Delta\theta_{HI}$  (lower left).

ent-type triggers. As noted previously, prompt coincidences between the PPAC cathode signals defined true events. The HI scattering angle was calculated for each detector from the difference between the delay-line and cathode TDC singles, using a linear calibration. The  $\phi$  segment information was simply passed on to the next stage of the analysis as a logic bit. Figure 3-1 illustrates the coincidence gates set in this first stage of the analysis, using the Th + Cm system as an example. The HI scattering-angle distribution was constrained (Fig. 3-1a) to accept quasi-elastic collisions of Th projectile and Cm target atoms. This excluded all events involving scattering from the low-Z  $^{12}\text{C}$ ,  $^{16}\text{O}$ , or  $^{19}\text{F}$  target atoms. Virtually no inelastic events (with  $Q \geq 50$  MeV, e.g., from fission) were observed in these collisions.

The time-of-flight difference between the arrival times of the heavy-ions in the PPAC cathodes ( $t_U - t_L$ ) depends on  $\theta_{HI}$  and is plotted versus  $\Delta\theta_{HI}$  in Fig. 3-1b. It exhibits a negligible accidental background rate ( $\leq 0.05\%$  in neighboring beam pulses), which allowed the PPAC pair to be treated as a single detector unit in subsequent coincidence analyses with other counters. As described in [Shw85], this is

because the PPAC's sampled complementary regions of laboratory solid angle and nearly 100% HI coincident detection efficiency was achieved over almost the entire range. The HI spectra appear cleaner than in previous measurements [Shw85] because thinner, lower-Z carbon target backings were used in place of titanium. This prevented elastically scattered projectile-backing events from triggering the PPAC's in kinematic coincidence. Gates on HI energy were left almost completely open (Figs. 3-1c,d).

### **Sec. 3.2.2 $\gamma$ -Ray and Electron Events**

The  $\gamma$ -ray and electron event types were identified by appropriate bits set in the event pattern word by the hardware coincidence. Since the PPAC's were treated as a unit, the HI- $\gamma$ -ray and HI- $e^-$  analyses used standard single coincidence techniques. Prompt time windows are shown in Fig. 3-2a,b (dashed polygons). The time-difference, formed from the upper PPAC cathode time minus the  $\gamma$ -ray or electron detector time signals, depends on  $\Delta t_{HI}$  because of the flight-time of the scattered HI to the PPAC. The gate therefore followed the contour of the prompt peak ensuring that no artificial scattering angle dependences were introduced. Accidental coincidences were removed by subtracting the data of a neighboring beam-pulse, using an identical contour displaced by 37 ns (dotted polygon). The time calibration was corrected for slow drifts by calculating the centroid of the prompt peak for every  $\sim 500$  events and modifying the calibration to return it to  $\Delta t = 0$ . The TOF resolution for  $\gamma$ -ray and electron events was 4 ns and 10 ns, respectively. The resulting total  $\gamma$ -ray and electron spectra are shown in Fig. 3-2c,d. The forward NaI intercepted neutrons emitted in the collision as well as  $\gamma$ -rays. Although their longer flight-time allowed a partial separation from prompt  $\gamma$ -rays with a sharp time gate, for subsequent analysis, only the rear NaI was considered. PPAC-PPAC, HI- $\gamma$ , and HI- $e^-$  data, were written to tape with reduced parameter lists which included the HI angles  $\theta_U, \theta_L$ ;  $\phi_{HI}$ -pattern bits; the PPAC TOF difference  $\Delta t_{HI}$ ; the HI- $\gamma$ (or  $e^-$ ) TOF;  $\gamma$ -ray (or  $e^-$ ) energy; and finally, a logic word which flagged true and chance coincidence events.

### **Sec. 3.2.3 Positron Events**

Figure 3-3 summarizes similar timing gates used in the positron analysis. A PPAC-Si(Li) time difference was formed for both the front and rear segments of the positron detector (front segment shown in Fig. 3-3a). If both segments registered a

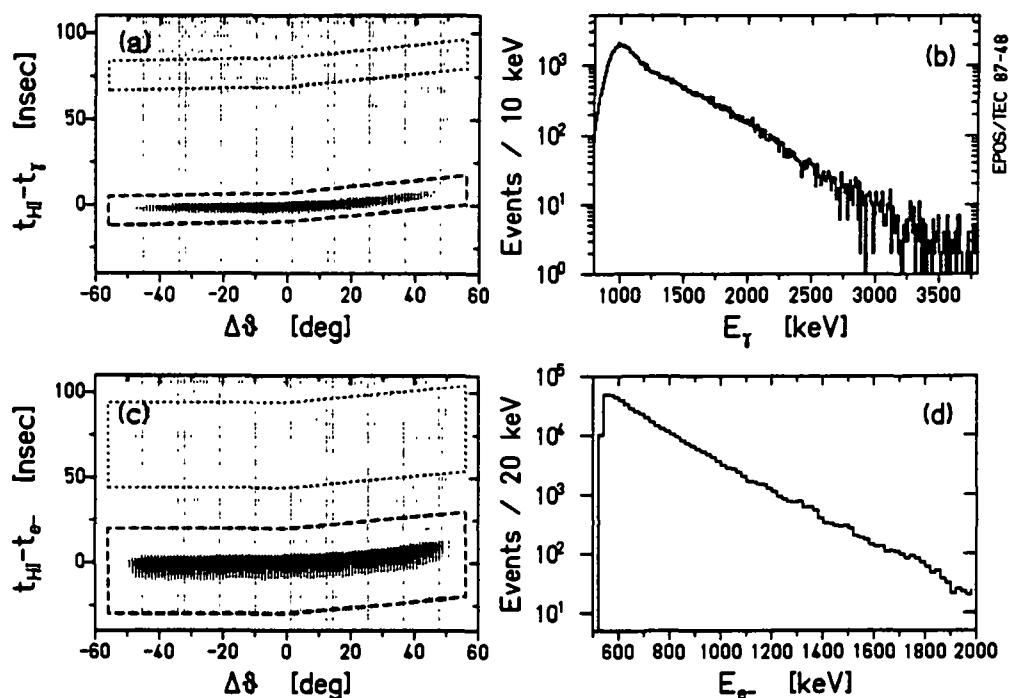


**Figure 3-2.** Prompt (dashed) and chance (dotted) timing gates on HI vs.  $\gamma$ -ray and electron time spectra (a,c). Corresponding total energy distributions are shown in (b,d) for Th + Cm collisions.

hit, their time difference was formed (Fig. 3b), and when in prompt coincidence (hatched region), the sum of the two energy signals was taken as  $E_{e^+}$ . The time signal of the appropriate Si(Li) detector segment was used in forming time differences with each of the eight ARD crystals. (If both segments fired, it was assumed that a positron scattered from the front to the rear segments, so the forward detector time pulse was used.) Figure 3-3c illustrates this distribution for one combination. The width of the prompt "true" gate (marked "T") was chosen to fully accept the 511 keV photopeak counts, while suppressing low energy (long rise time) Compton scattered photons. All time-difference distributions and ARD NaI energy spectra (e.g., Fig. 3-3d) were stabilized against time and gain drifts.

Adding the energies of the prompt ARD segments gave the characteristic sum spectrum of Fig. 3-3e. Comparison with the distribution obtained using  $\beta^+$  sources (cf. Fig. 2-13) reveals that in addition to the one- and two-photon full energy peaks and associated Compton continua, there is a steep low energy background. The associated positron spectrum increases rapidly at low energies, and the PPAC-Si(Li) time difference exhibits the flight-time expected for low energy leptons. This indi-

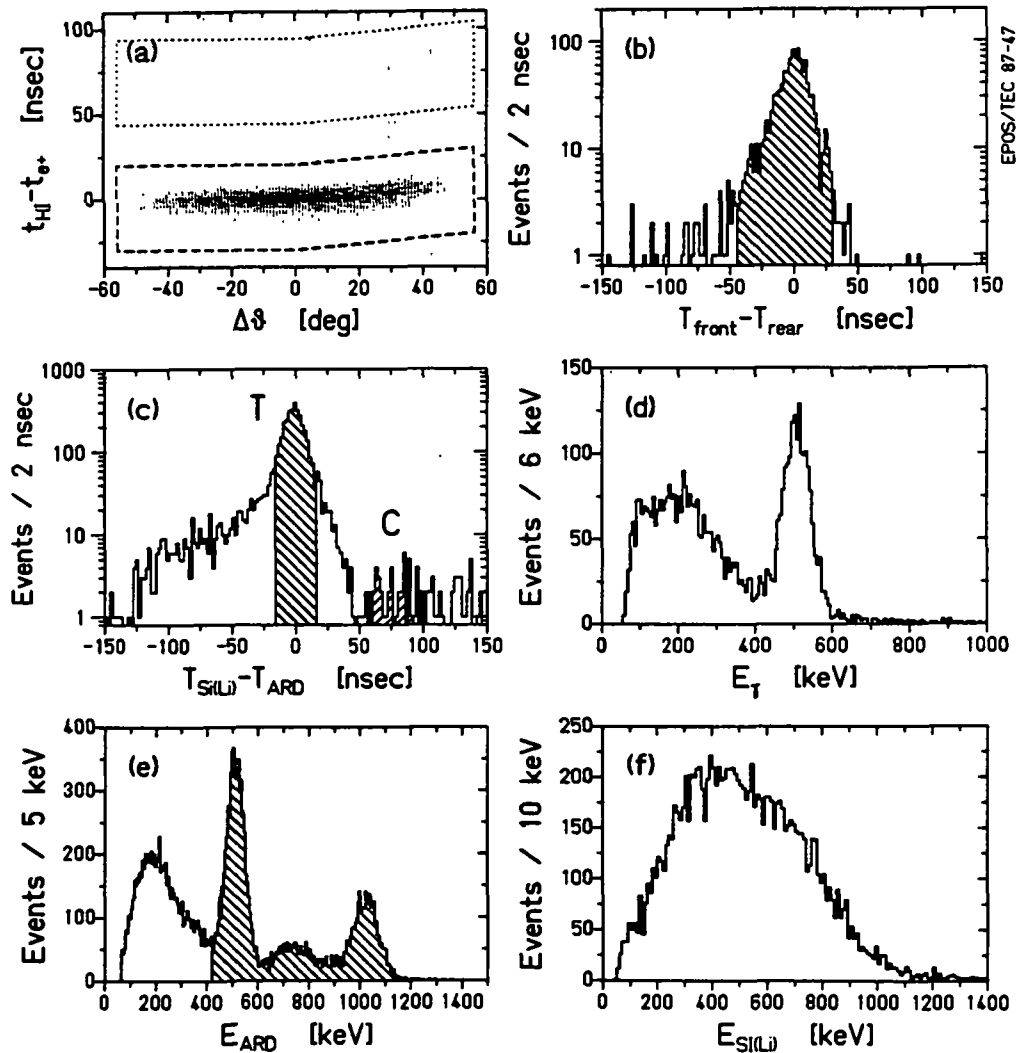


**Figure 3-3.** Gates for positron analysis. (a) Prompt and chance windows on HI- $e^+$  time difference spectrum, (b) time difference for front-rear Si(Li) segment coincidences, (c) typical Si(Li)-ARD timing spectrum for one segment with true and chance windows as marked, (d) energy distributions of  $\gamma$ -rays in typical ARD segment, (e) spectrum of the sum of energies for ARD segments in prompt coincidence with positrons, and (f) total Th + Cm positron energy spectrum in coincidence with  $\geq 1$  annihilation photon in ARD.

cates that these events are delta electrons which were detected in the Si(Li) in coincidence with  $\gamma$ -rays from the target which were scattered into the ARD array. No evidence was found in the improved set-up for direct scattering of  $\gamma$ -rays from the Si(Li) to the ARD, as previously discussed in [Shw85] and [Gru85]. The shaded region of Fig. 3-3e denotes the window used to select positrons ( $420 < E_{ARD} < 1150$

keV, window A in Fig. 3-4a). The total corresponding positron energy spectrum is shown in Fig. 3-3f.

As discussed in [Shw85], the excess in the ARD energy spectrum is described by an exponential which, taken together with the distribution derived from  $\beta^+$  source measurements, provides a good fit to the in-beam spectrum for sum energies above the  $\sim 200$  keV NaI constant fraction discriminator thresholds. This is shown for Th+Cm in Fig. 3-4a. The low energy contamination was removed by scaling the Si(Li) energy distribution measured in coincidence with window B ( $200 < E_{ARD} < 400$  keV) by the ratio of the areas of the exponential fit in windows A and B respectively, and subtracting this from the positron distribution of window A. Figure 3-4b summarizes this procedure. Superimposed on the histogram associated with window A is the scaled distribution for window B (hatched). Even though this correction amounts to only  $\sim 8\%$  of the total positron yield, it significantly improves the spectral shape since  $\delta$ -electrons are concentrated at low energies where the positron emission probability is small. All events surviving the time analysis were written to tape with a reduced event list which included the PPAC angles, energies,  $\phi$ 's, and TOF; the positron energy; ARD sum energy; HI- $e^+$  TOF; and a true/chance logic flag.

#### **Sec. 3.2.4 Background Subtraction**

Chance background events under the prompt time peaks in the HI- $e^+$  and  $e^+$ -ARD time difference spectra were subtracted using a 2-dimensional method described in [Shw85]. Each event in either the true or chance windows of both Fig. 3-3a and Fig. 3-3c were assigned a weight,  $w_{HI}$  or  $w_{ARD}$ , for the corresponding time difference equal to +1 if it was a prompt event, or -1 for chance events. The weight for the positron event is the product of these individual weights,

$$w_{e^+} = w_{HI} \cdot w_{ARD} = \pm 1. \quad (3.1)$$

The net positron spectrum therefore consists of events that appear in both prompt time coincidence windows, minus those in one prompt and one chance window, plus those in both chance gates.

As noted above, the PPAC-PPAC chance rate was negligible. The time analysis of Eqn. 3.1 corrects for a chance coincidence background which amounts to  $\sim 5\%$  of the total positron yield in Th+Cm. As already mentioned, subtraction of the low energy  $\delta$ -electron ARD background amounts to  $\leq 5\%$ . The subtracted rates for the

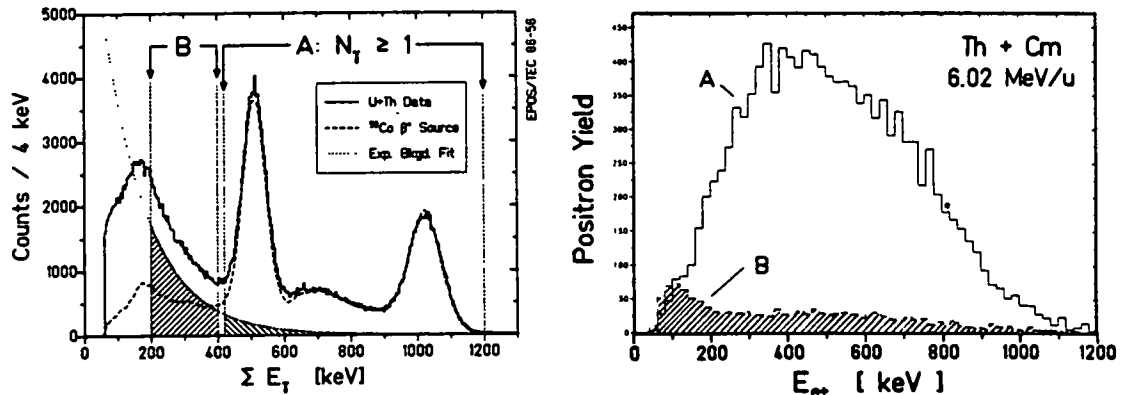


**Figure 3-4.** ARD sum-energy spectrum (left) measured for U+Th collisions (histogram) compared to distribution measured with  $^{56}\text{Co}$  source (dashed curve). Excess exponential background (dotted line) in positron gate (A) is subtracted by scaling background cut (B) by ratio of shaded areas. Positron energy distribution (right) shown for Th + Cm collisions gated on ARD window A, and scaled background from window B (shaded).

other systems are listed in Table 3-2. Similar rates were found for all supercritical systems. (The larger  $e^+$ -ARD background in the 1981 U+U experiment was due to the less selective positron detection system used.) For the subcritical Th+Ta system, the total positron production cross-section is smaller, so the  $\delta$ -electron background was relatively enhanced, amounting to  $\sim 9\%$ . For each system, the subtracted energy distribution was inspected and found to be smooth and structureless.

### Sec. 3.2.5 Time-of-Flight Corrections

A recent innovation motivated by results of the positron-electron coincidence experiments discussed in Part II of this dissertation involved an investigation of the intensity of the peak as a function of the positron TOF from target to detector. If the lifetime of the source of the peak positrons is short ( $\leq 10^{-9}$  s) and the positrons are emitted close the solenoid axis, the flight time then reflects the emission angle  $\theta_0$  with respect to the Z-axis as discussed in Sec. 2.2.6. In order to extract such emission angle information, however, the HI- $e^+$  TOF must be corrected for its systematic dependence on  $\theta_{\text{HI}}$  and  $E_{e^+}$ .

The HI- $e^+$  time difference was formed from the upper PPAC cathode signal minus the appropriate Si(Li) detector segment time. The PPAC timing includes the HI

Table 3-2 Summary of Background Rates

System	PPAC-PPAC	HI-e <sup>+</sup>	e <sup>+</sup> -ARD	ARD- $\delta e^-$
U+Cm	0.218%	4.55%	0.83%	2.69%
Th+Cm	0.097%	4.37%	0.93%	3.65%
U+U	0.074%	12.23%	1.24%	4.56%
Th+U	0.117%	5.86%	1.06%	5.53%
Th+Th	0.196%	5.56%	1.68%	6.72%
Th+Ta	0.107%	6.94%	1.08%	7.74%

flight-time from the target to the PPAC detector. This depends on ion velocity and PPAC distance, and hence on scattering angle, as given by Eqns. 2.77,78,

$$t_{HI} = (d_0/\sqrt{2} v_{HI})[\cos\theta_{HI} + \sin\theta_{HI}\cos\phi_{HI}]^{-1}, \quad (3.2)$$

where  $v_{HI} \cong 2v_{CM}\cos\theta_{HI}$ , correct for elastic scattering of nearly symmetric partners, is used. Subtracting  $(t_{HI}-t_{e+})$  from Eqn. 3.2 leaves only the TOF of the positron to the Si(Li) detector.

As described in Sec. 2.2.6, the positron flight time from the target depends on both the momentum of the positron and its emission angle,  $\theta_0$ ,

$$t_{e+}(P_{e+}, \theta_0) = P_{e+}^{-1} \int_0^{Z_{det}} \{(c/eB)[1-(B/B_0)\sin^2\theta_0]^{1/2}\}^{-1} dz. \quad (3.3)$$

The path length along the axis is longer than  $Z_{det}$  if the positron is emitted with  $\theta_0 > 90^\circ$  and reflected by the mirror field. However, because of lineshape tailing in the Si(Li) detector, the TOF distribution measured at a given  $E_{e+}$  includes contributions from several other energies. The energy (momentum) dependence can therefore not be completely compensated. Only an average correction is performed by subtracting from the measured distribution the mean flight-time expected as a function of energy, assuming isotropic positron emission. A corrected positron TOF variable,  $t_{corr}$  is thereby constructed which, on the average, depends only on  $\theta_0$ ,

$$t_{corr}(\theta_0) = t_{HI}(\theta_{HI}, \phi_{HI}) - (t_{HI}-t_{e+})_{meas} - \langle t_{e+}(E_{e+}) \rangle, \quad (3.4)$$

where,

$$\langle t_{e^+}(E_{e^+}) \rangle = [\int t_{e^+}(E_{e^+}, \theta_0) d(\cos\theta_0)] / [\int d(\cos\theta_0)]. \quad (3.5)$$

The resulting distribution of  $t_{\text{corr}}$  depends primarily on  $\theta_0$  and mirrors the  $\sim 1/\cos\theta_0$  dependence shown in Fig. 2-24b. Unfortunately, with the magnetic field configuration used in Part I of this thesis, all positrons emitted with  $\cos\theta_0 < 0.1$  have  $t_{\text{corr}} \sim 10\text{-}13$  ns. Positrons emitted near  $\theta_0 \sim 90^\circ$  (i.e., in the plane of HI scattering), therefore could not be distinguished from positrons emitted with flatter angles,  $\theta_0 > 120^\circ$  (i.e., those perpendicular to the scattering plane). Shorter flight-times are expected for  $0^\circ < \theta_0 < 70^\circ$ , but the  $\cong 8$  ns detector time resolution tended to obscure this. Very little emission angle information could be gained with the present set-up. As discussed in Part II, the absence of the mirror field for the positron-electron coincidence experiment eliminated the problem of flat emission angles with  $\theta_0 > 90^\circ$  arriving simultaneously with the steeply emitted positrons. Some angular information may, with the coincidence arrangement, be extractable.

### Section 3.3 Total Positron Energy Distributions

Absolute total positron production rates were determined previously by J. Schweppe for collisions of U+Sm, U+Pb, U+U, and U+Cm [Shw85]. As shown in Fig. 3-5, the absolute size and shape of the positron yields are in good agreement with the continuous distributions expected from dynamic positron production added to the nuclear internal pair creation contribution (dashed line). An identical analysis for the present data is not yet completed. However, for the subsequent investigation of the positron peak structures, it is only necessary to understand the shape of the continuum positron background and to verify that the production probability is consistent with theoretical expectations and with that measured previously.

The analysis leading to Fig. 3-5 is described in detail by [Shw85] and involved several steps. These included: correcting the measured positron and  $\gamma$ -ray spectra for lineshape response, detection efficiency, scaledown, and deadtime; normalizing each to the number of heavy-ions scattered into the corresponding PPAC angular range; calculating the nuclear positron IPC contribution from the corrected  $\gamma$ -ray energy distribution; and finally, comparing the theoretical dynamic, plus nuclear, positron distributions to the corrected experimental yields. Because only the

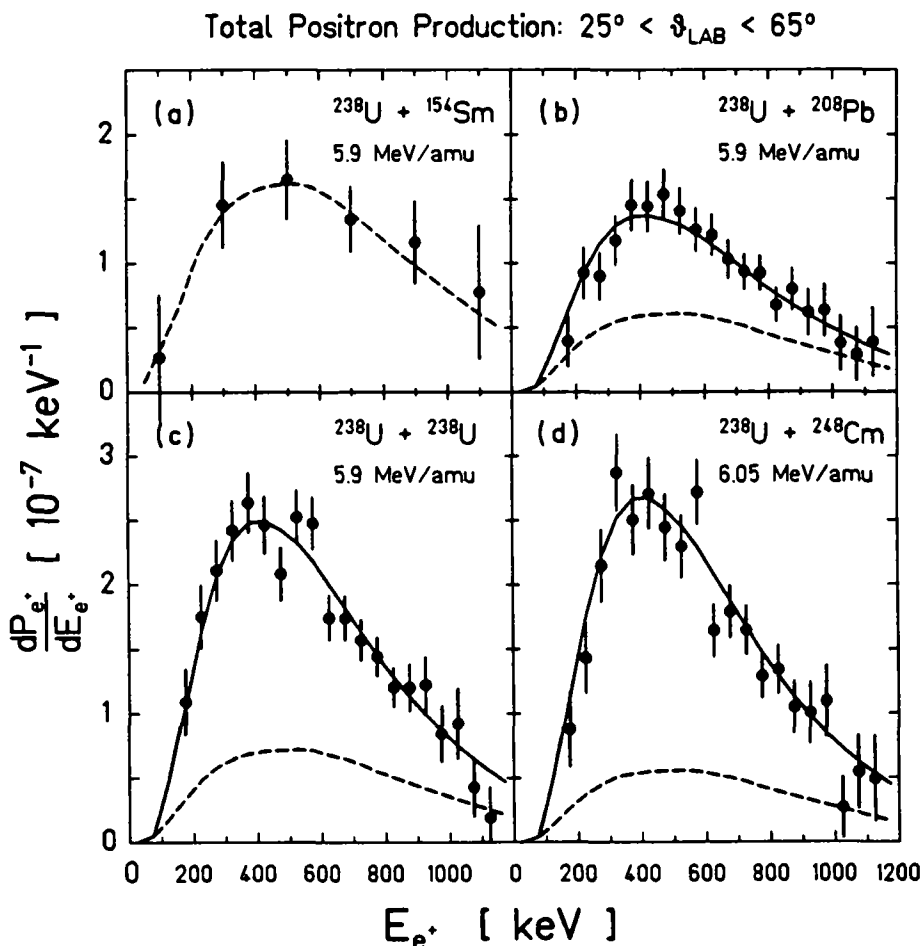


**Figure 3-5.** Measured absolute energy-differential positron production probabilities for U+Sm, U+Pb, U+U, and U+Cm collisions [Shw85]. Data are selected for  $25^\circ < \theta_{\text{HL}} < 65^\circ$ , and corrected for detector response, transport efficiency, and dead-time. Dashed curves denote nuclear positron IPC background calculated from simultaneously measured  $\gamma$ -rays. Solid curves include theoretical predictions of dynamic positron production [MüU83].

size and shape of the measured positron energy distributions are relevant to the analysis of peak structures in the data, the above program was abbreviated. The  $\gamma$ -ray distribution was used to construct the nuclear IPC background and then the sum of dynamic plus nuclear contributions were corrected for the positron detection efficiency and lineshape and directly compared to the total observed positron energy distribution. This was originally performed for the Th+Ta system by J. Schweppe, and has been subsequently improved and extended by K. Sakaguchi for both Th+Ta and, from Part II of this dissertation, U+Th collisions [Sak88]. The results are briefly described below.

The  $\gamma$ -ray energy distribution was first unfolded by stripping the tails of the NaI detector lineshape response using standard techniques. The standard deviations for each energy bin in the unfolded result, which are overestimated by simple propagation of errors, were evaluated using a Monte-Carlo technique developed (by J. Schweppe) which consists of the following steps. First several  $\gamma$ -ray energy spectra are artificially generated by simultaneously varying the contents of each bin about the measured number of counts according to Poisson statistics. This simulates the effects of statistical fluctuations in the data. Next, each spectrum is unfolded by stripping the lineshape tails. The statistical error for each channel is then taken as the standard deviation of the distribution of unfolded contents for the several simulated spectra. Systematic errors, such as from uncertainties in the lineshape peak to total ratio, were estimated to be much smaller than the statistical errors determined by the Monte-Carlo method. The unfolded  $\gamma$ -ray distribution was finally divided by the  $\gamma$ -ray peak detection efficiency,  $\epsilon_{\gamma}^{\text{pk}}(E_{\gamma})$ , given in Fig. 2-35, and multiplied by the appropriate scaledown,  $SD_{\gamma}$ , given by Eqn. 2.85.

These corrections give the emitted  $\gamma$ -ray energy distribution in the laboratory frame. As described in [Shw85], the lab distribution is transformed into the frame of the emitting nucleus by including the relativistic correction for the solid angle of the NaI detector and the Doppler shift of the  $\gamma$ -ray energy, both of which assume that, on the average, half the observed counts come from one ejectile and half from the other scattered nucleus. This assumption was sufficient for U+Th and the other supercritical systems measured because the experimental  $\gamma$ -ray distributions had a smooth exponential shape like that of Fig. 3-2b. However, in the Th+Ta system shown in Fig. 3-6, three strong  $\gamma$ -ray lines in excess of the smooth continuum were observed at 1250, 1400, and 1550 keV. The PPAC angular resolution allowed full separation of the Th+Ta kinematics (see Fig. 2-32) and an analysis of the Doppler shift of these lines as a function of HI scattering angle identified the target recoil nucleus as the emitter of the peaks. These lines were therefore Doppler corrected for emission from the  $^{181}\text{Ta}$  nucleus, while the underlying continuum was treated separately in the average way mentioned above.

Following the method of [Mey77], the nuclear positron contribution  $(dN_{e^+}/dE_{e^+})_{\text{nuc}}$  was calculated from the unfolded absolute  $\gamma$ -ray yield,  $dN_{\gamma}/dE_{\gamma}$ , by convolution with the differential internal pair creation coefficient  $d\beta(E_{\gamma}, M\lambda)/dE_{\gamma}$ , where  $M\lambda$  represents the transition multipolarity.

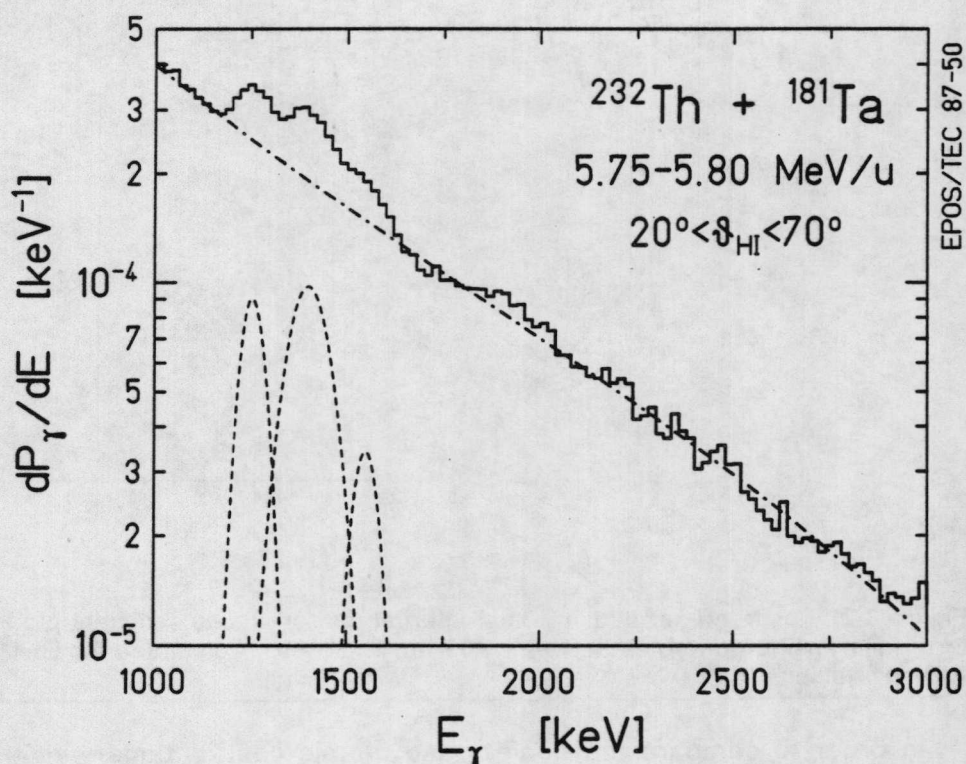


**Figure 3-6.** Absolute  $\gamma$ -ray energy spectra from Th + Ta collisions, corrected for Doppler shifts, lineshape tailing, and peak detection efficiency. Three structures are observed above the smooth exponential continuum at  $E_\gamma \cong 1250, 1400,$  and  $1550$  keV. The widths of the 1250 and 1550 keV lines are consistent with detector resolution, while the broad 1400 keV line suggests the contribution of two or more unresolved peaks.

$$(dN_{e^+}/dE_{e^+})_{nuc} = \int_0^\infty m_e c^2 (dN_\gamma/dE_\gamma) \cdot [d\beta(E_\gamma, M\lambda)/dE_{e^+}] dE_\gamma \quad (3.6)$$

This is equivalent to multiplying the corrected  $\gamma$ -ray energy spectrum (e.g., of Fig. 3-6) by a conversion coefficient matrix, an example of which is shown in Fig. 3-7 for electric dipole transitions in a  $Z=91$  nucleus (average of Th and U). The energy distribution of dynamically created positrons  $(dN_{e^+}/dE_{e^+})_{dyn}$  was obtained from the theoretical production probability per collision,  $(dP/dE_{e^+})_{the}$ , by multiplying by the observed number of heavy-ions scattered into the PPAC angular range and correcting for the HI event type scaledown,

$$(dN_{e^+}/dE_{e^+})_{dyn} = (dP/dE_{e^+})_{the} \cdot N_{HI} \cdot SD_{HI} \quad (3.7)$$

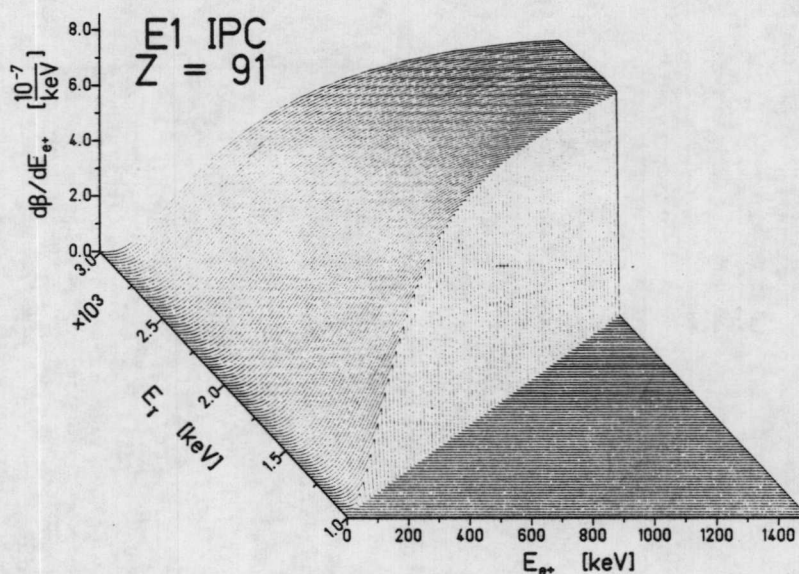


**Figure 3-7.** Positron energy-differential internal pair creation coefficient plotted in matrix form for transition energies between  $1.0 < E_{\gamma} < 3.0$  MeV. Calculated for E1 transitions in a  $Z=91$  nucleus [Shl81].

In order to compare the nuclear and atomic contributions with the measured positron energy spectrum, the calculated distributions first had to be corrected for a variety of effects. The positron energies were Doppler-shifted appropriately for emission from either the CMS or separated nuclei, after which the laboratory spectrum was multiplied by the detection efficiency,  $\epsilon_{e+}(E_{e+})$ . Folding in the response of the Si(Li) detector lineshape,  $F(E_{e+}^{obs}, E_{e+}^0)$  from Eqn. 2.34, and correcting for deadtime, the expected distribution is

$$(dN/dE_{e+})_{obs} = S D_{e+}^{-1} \int_0^{\infty} F(E_{e+}, E_{e+}^0) \cdot (dN/dE_{e+})_{nuc} \cdot \epsilon_{e+}(E_{e+}^0) dE_{e+}^0.$$

This quantity may be compared directly to the measured positron energy distribution.

The only free parameter in this entire analysis is the distribution of  $\gamma$ -ray multiplicities,  $\omega(M\lambda, E_{\gamma})$ , which affects the shape and magnitude of the calculated nuclear IPC background in Eqn. 3.6. In order to approximately remove this uncertainty and obtain an absolute comparison between experiment and theory,  $\omega(M\lambda, E_{\gamma})$  was assumed to remain constant for all target-projectile combinations and was determined empirically from low- $Z_U$  collision systems (such as Th+Ta), where the positron yield is largely of nuclear origin. Figure 3-8b presents the measured

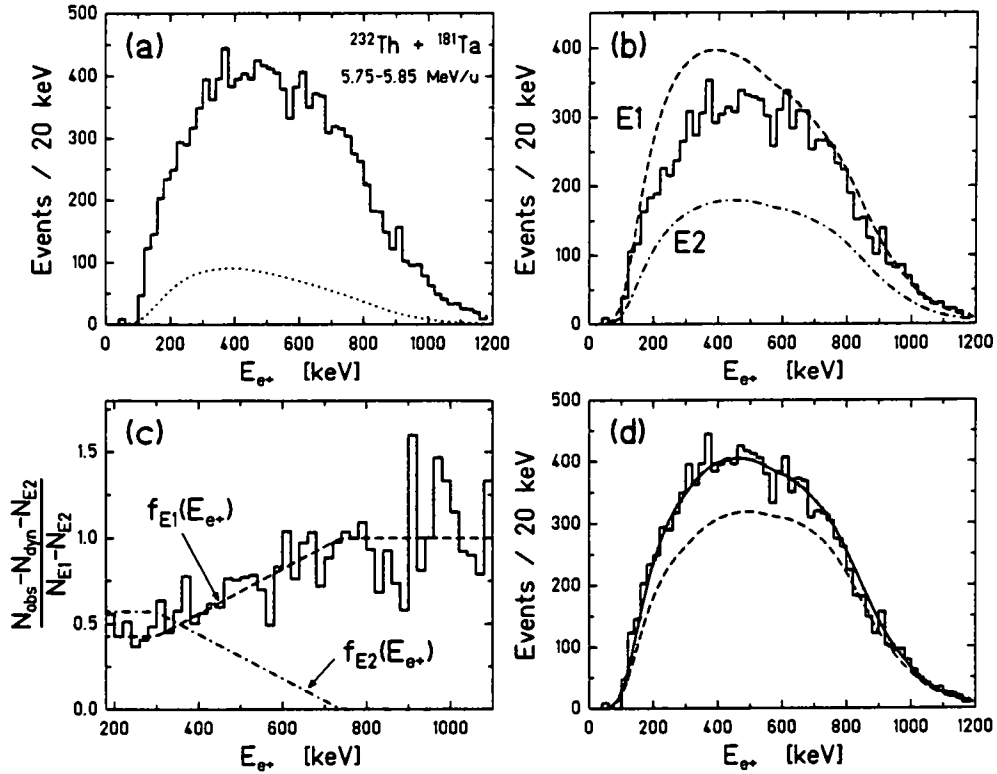


**Figure 3-8.** Comparison of the calculated nuclear and dynamic positron contributions to the total measured Th+Ta positron energy distribution. (a) Total measured  $e^+$  spectrum with the predicted dynamic distribution [Reu87] (dotted curve, corrected for efficiency and folded with detector lineshape as described in text). (b) Measured  $e^+$  distribution minus calculated dynamic contribution, compared to nuclear IPC distributions calculated from data of Fig. 3-6 assuming entirely E1 (dashed) or E2 (dot-dashed)  $\gamma$ -ray multipolarity. (c) Empirical multipolarity distributions,  $f_{E1}(E_{e^+})$  and  $f_{E2}(E_{e^+})$  ( $f_{E2} \equiv 1 - f_{E1}$ ), determined from data as described in text. (d) Total measured Th+Ta positron spectrum with nuclear IPC contribution (dashed curve) calculated using (c). Solid curve includes dynamic contribution. (Adapted from [Sak88].)

Th + Ta positron energy distribution, after subtracting the calculated dynamic positron contribution (dotted curve in Fig. 3-8a). The dashed and dot-dashed curves show the calculated IPC positron contribution, assuming either pure E1 or E2 multipolarity for the entire measured  $\gamma$ -ray energy spectrum, respectively. While E1 appears to describe the observed yield for  $E_{e^+} \geq 700$  keV, some admixture of E2 or other  $\lambda > 1$  multipolarity is required to fit the positron distribution at lower energies.

We empirically described the nuclear IPC contribution as a mixture of the calculated pure E1 and E2 components,

$$\begin{aligned}
N_{\text{obs}}(E_{e+}) &= N_{\text{dyn}}(E_{e+}) + N_{\text{IPC}}(E_{e+}), \\
N_{\text{IPC}}(E_{e+}) &= f_{E1}(E_{e+}) \cdot N_{E1}(E_{e+}) + f_{E2}(E_{e+}) \cdot N_{E2}(E_{e+}),
\end{aligned}
\tag{3.9}$$

where  $f_{E2}(E_{e+}) + f_{E1}(E_{e+}) \equiv 1$ . To solve for  $f_{E1}(E_{e+})$ , the quantity  $[N_{\text{obs}}(E_{e+}) - N_{\text{dyn}}(E_{e+}) - N_{E2}(E_{e+})] / [N_{E1}(E_{e+}) - N_{E2}(E_{e+})]$  was plotted in Fig. 3-8c. The simple parameterization for  $f_{E1}(E_{e+})$  and  $f_{E2}(E_{e+})$  indicated by the dashed and dot-dashed lines in Fig. 3-8c, combined with Eqn. 3.9, yielded the dashed curve in Fig. 3-8d for the total IPC positron background. Adding the dynamic contribution gave the total expected positron yield (solid curve) which agrees with the total measured Th + Ta positron energy distribution (histogram) [Sak88].

The validity of this technique hinges on the extrapolation of the  $f_{E1}(E_{e+})/f_{E2}(E_{e+})$   $\gamma$ -ray multipolarity parameterization to high  $Z_U$  collision systems. Figure 3-9 presents the results of a similar analysis for 5.81 MeV/u U + Th collisions measured during Part II of this dissertation. (Very little peak structure was discovered at this beam energy, suggesting that deviations in the total distribution from dynamic plus nuclear IPC contributions should be small.) The multipolarity distribution used in obtaining the dashed IPC background curve in Fig. 3-9 was exactly that derived in Fig. 3-8c for Th + Ta collisions. Adding the relatively much larger theoretical dynamic positron contribution gave the solid curve, whose shape and magnitude are in excellent agreement with the experimentally measured U + Th positron yield. The positron detection efficiency used in this calculation was taken from Part II of this dissertation. It should be emphasized that this calculation is absolute, i.e., no overall normalization has been included. The only free parameter (namely, the  $\gamma$ -ray multipolarity) was taken directly from the Th + Ta system.

Similar good agreement between the measured and expected total positron energy distribution was also found for Th + Cm collisions and subsets of the Th + Th and U + Cm data presented in this chapter [Sak88]. Although the analysis of the total positron spectra is not yet complete, and has not yet proceeded to unfold the measured data and compare it *directly* to the theoretical expectations as in Fig. 3-5, it is clear that the previous results of [Shw85] have been substantially corroborated. Moreover, it is clear that the Univ. of Frankfurt calculations of dynamic positron production [Rei81, Reu87], assuming Rutherford trajectories only, agree with the observed yields at the level of any experimental systematic errors (estimated to be  $\leq 10\%$ ). Most importantly, at least for the analysis presented in Sec. 3.4, the shape and the magnitude of the continuous dynamic and nuclear positron energy distribu-

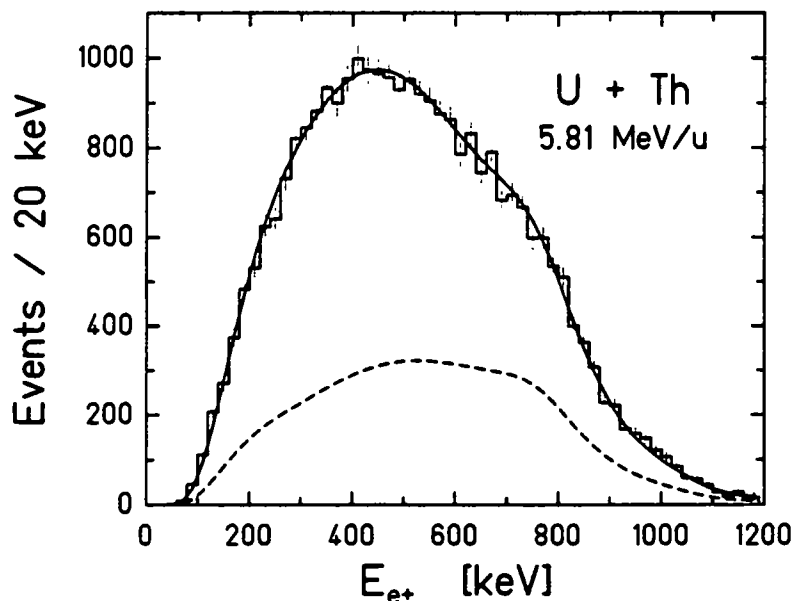


**Figure 3-9.** Energy distribution of positrons measured in 5.81 MeV/u U+Th collisions (from Chap. 6), compared to nuclear IPC background (dashed curve), and sum of IPC and predicted dynamic positrons (solid curve). IPC contribution is calculated from simultaneously measured  $\gamma$ -rays using multipolarity distribution derived in Fig. 3-8.

tions are very well understood and can be used as a smooth background with respect to which we may study the appearance of narrow positron peaks.

### Section 3.4 Narrow Positron Peaks

As mentioned in Chapter 1, peaks have been found in the energy distribution of positrons from each of the five supercritical and the subcritical collision systems measured in Part I of this dissertation. The search for these structures involved constructing a three dimensional  $\Delta\theta_{HI}-\Sigma\theta_{HI}-E_{e+}$  matrix, using the positron data analyzed as described in Sec. 3.2, out of which positron energy spectra were projected for chosen HI scattering angle ranges. The angle-angle parameter space was explored by subdividing the data into  $\Delta\theta_{HI}-\Sigma\theta_{HI}$  sections, examining the corresponding positron distribution, and successively concentrating the search in the regions which exhibit structure above the smooth dynamic positron background. Data at projectile energies which contain peaks in the data were added together and the entire sample was reanalyzed to find the HI angular condition which enhanced the size of the positron line over the continuous dynamic plus nuclear IPC background.

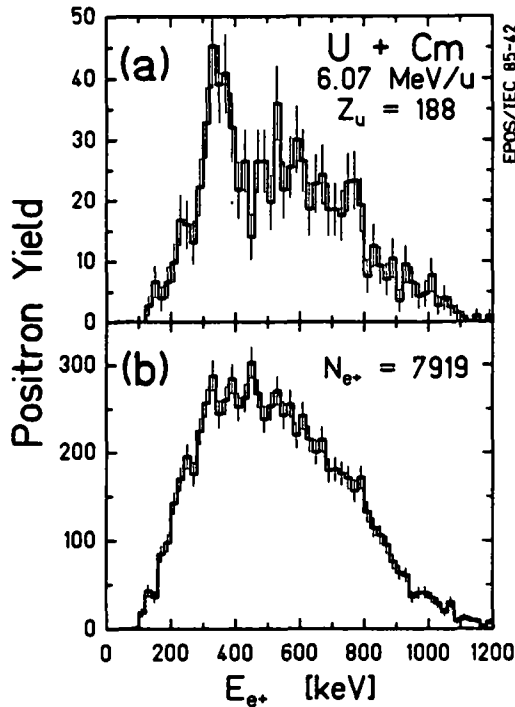


**Figure 3-10.** Energy distribution of positrons measured in U+Cm collisions between 6.04 and 6.13 MeV/u. Lower spectrum presents total spectrum, while upper figure corresponds to a HI scattering angle region ( $41.5^\circ < \theta_{HI} < 56^\circ$ ) which prominently displays the  $\sim 330$  keV peak.

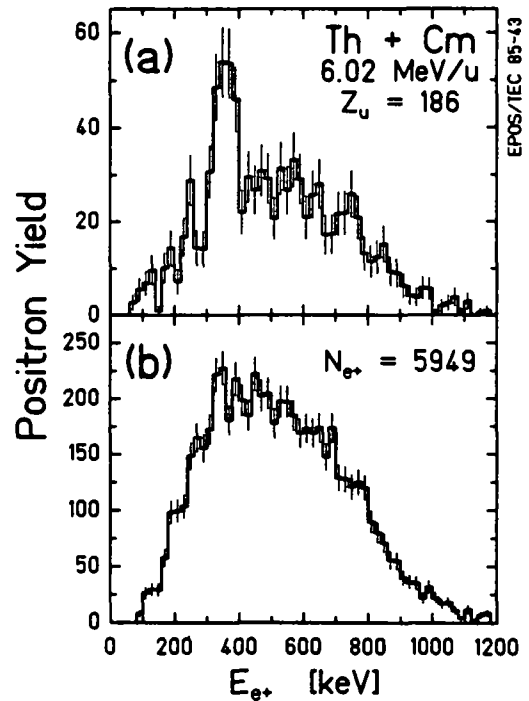


**Figure 3-11.** Same as Fig. 3-10 for Th+Cm collisions between 6.00 and 6.04 MeV/u. Upper figure corresponds to  $35^\circ < \theta_{HI} < 57^\circ$ .

Parts (b) of Figs. 3-10 to 3-15 present the total positron energy distributions used in the peak analysis for each of the six collision systems studied in these experiments. As mentioned in Sec. 3.1, most of the data for each system were used. As discussed in Sec. 3.4.4, U+Cm data collected below 6.02 MeV/u and at 6.24 MeV/u exhibited little evidence of structure, so Fig. 3-10 contains positrons collected only between 6.04 and 6.13 MeV/u. Figure 3-11 includes Th+Cm data between 6.00 and 6.04 MeV/u. Figure 3-12 presents a reanalysis of 5.8 MeV/u U+U data measured in January 1981, and borrows from [Kid83]. Data collected between 5.80 and 5.85 MeV/u for Th+U are included in Fig. 3-13, and Th+Th data measured at 5.75 MeV/u only are presented in Fig. 3-14. Figure 3-15 combines Th+Ta runs at 5.75 and 5.80 MeV/u. (In this particular case, the peak was associated with different angular regions for the two beam energies, so these were individually added to obtain Fig. 3-15a.)

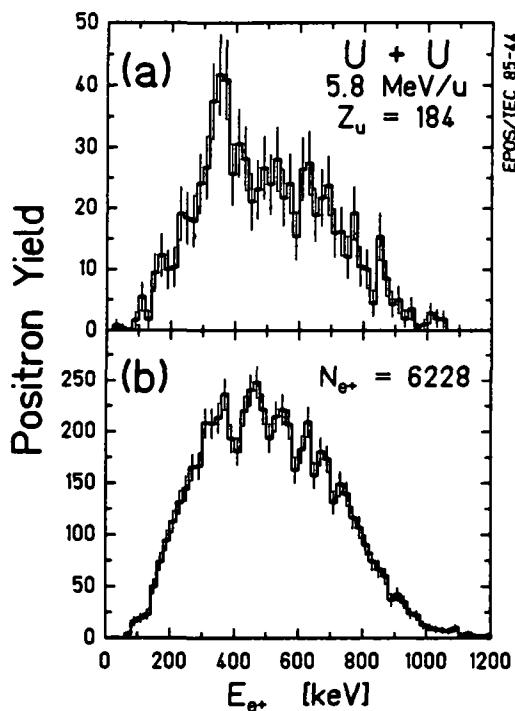


**Figure 3-12.** Same as Fig. 3-10 for U+U collisions at  $\sim 5.8$  MeV/u (1981). Upper figure corresponds to  $30^\circ < \theta_{HI} < 35^\circ$  plus  $48^\circ < \theta_{HI} < 53^\circ$ .

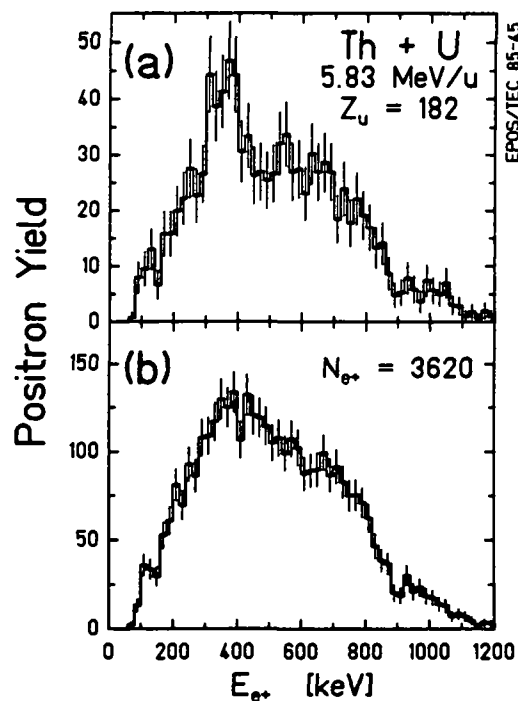


**Figure 3-13.** Same as Fig. 3-10 for Th+U collisions at 5.80 and 5.85 MeV/u. Upper figure corresponds to  $20^\circ < \theta_{HI} < 42^\circ$ .

In most of these total spectra, deviations are visible above the smooth dynamic and nuclear continuum discussed in Sec. 3.3, at energies around the positron peak region. Part (a) of each figure presents the energy spectrum for the HI scattering angle window chosen to enhance the size of the positron line over the background. For each system, the characteristics of the HI scattering events associated with the positron lines were studied by analyzing the PPAC energy signals, angle-angle correlation, and HI and positron TOF with a gate on the positron peak energy. As discussed further in the following sections, the exit channels of the collisions appear to be binary and very close to elastic.

### Sec. 3.4.1 Summary of Peak Characteristics

The peak-containing spectra are compared in Fig. 3-16. The striking feature in all of these data is the presence of a narrow peak between 300 and 360 keV. The lines have similar widths of  $\sim 75$  keV, and as discussed in Sec. 3.4.5, similar cross-sections. Table 3-3 lists the mean positron peak energy, width, intensity, mean beam

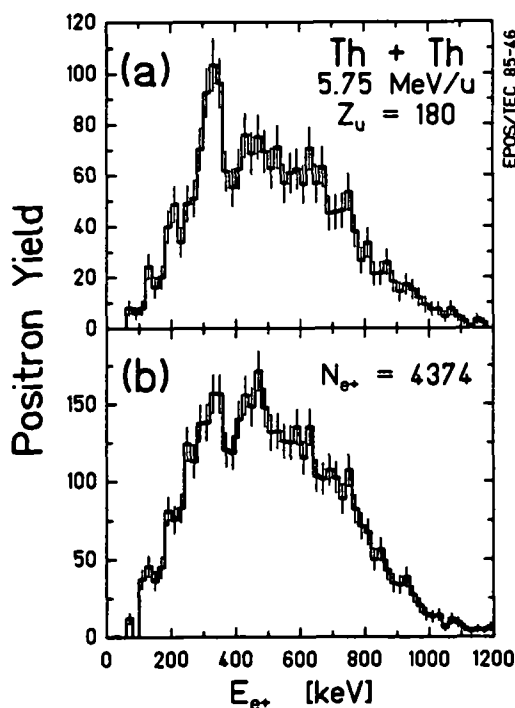


**Figure 3-14.** Same as Fig. 3-10 for Th+Th collisions at 5.75 MeV/u. Upper figure corresponds to  $20^\circ < \theta_{HI} < 46^\circ$  plus  $51^\circ < \theta_{HI} < 70^\circ$ .

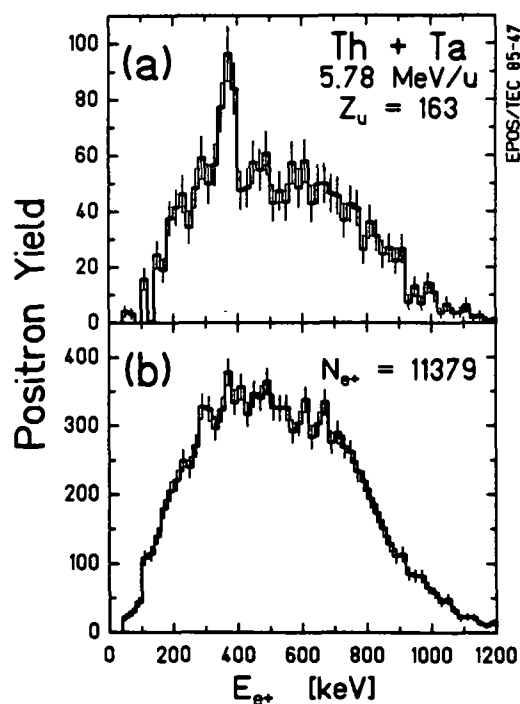


**Figure 3-15.** Same as Fig. 3-10 for Th+Ta collisions at 5.75 and 5.80 MeV/u. Upper figure corresponds to  $45.5^\circ < \theta_{HI} < 52.5^\circ$  for 5.75 MeV/u, plus  $52^\circ < \theta_{HI} < 70^\circ$  for 5.80 MeV/u collisions.

energy, and the HI angular window for each line. The errors quoted are statistical only.

Each of these structures appears at the  $4\sigma$  to  $6\sigma$  level of confidence. A Monte-Carlo study which randomly generated positron spectra with  $\sim 500$  total counts from an underlying smooth probability distribution showed that peaks at this level of significance occur with much less than 1% probability. For example, out of 600 trials, only 3 spectra exhibited lines at any energy with a  $3\sigma$  deviation, and none of these was as large as any of the measured peaks. The compound probability of observing deviations around 300 keV in several independent experiments is vanishingly small. Including additional data from Part II of this thesis, all but the Th+Ta line have been observed in at least two different experiments, and Th+Ta structure was discovered at two beam energies. The existence of structure in this energy range is therefore well established on statistical grounds. This result justifies a more critical test which considers the possibility that a fluctuation of the continuous background produces a peak in this physically predetermined region. For example,

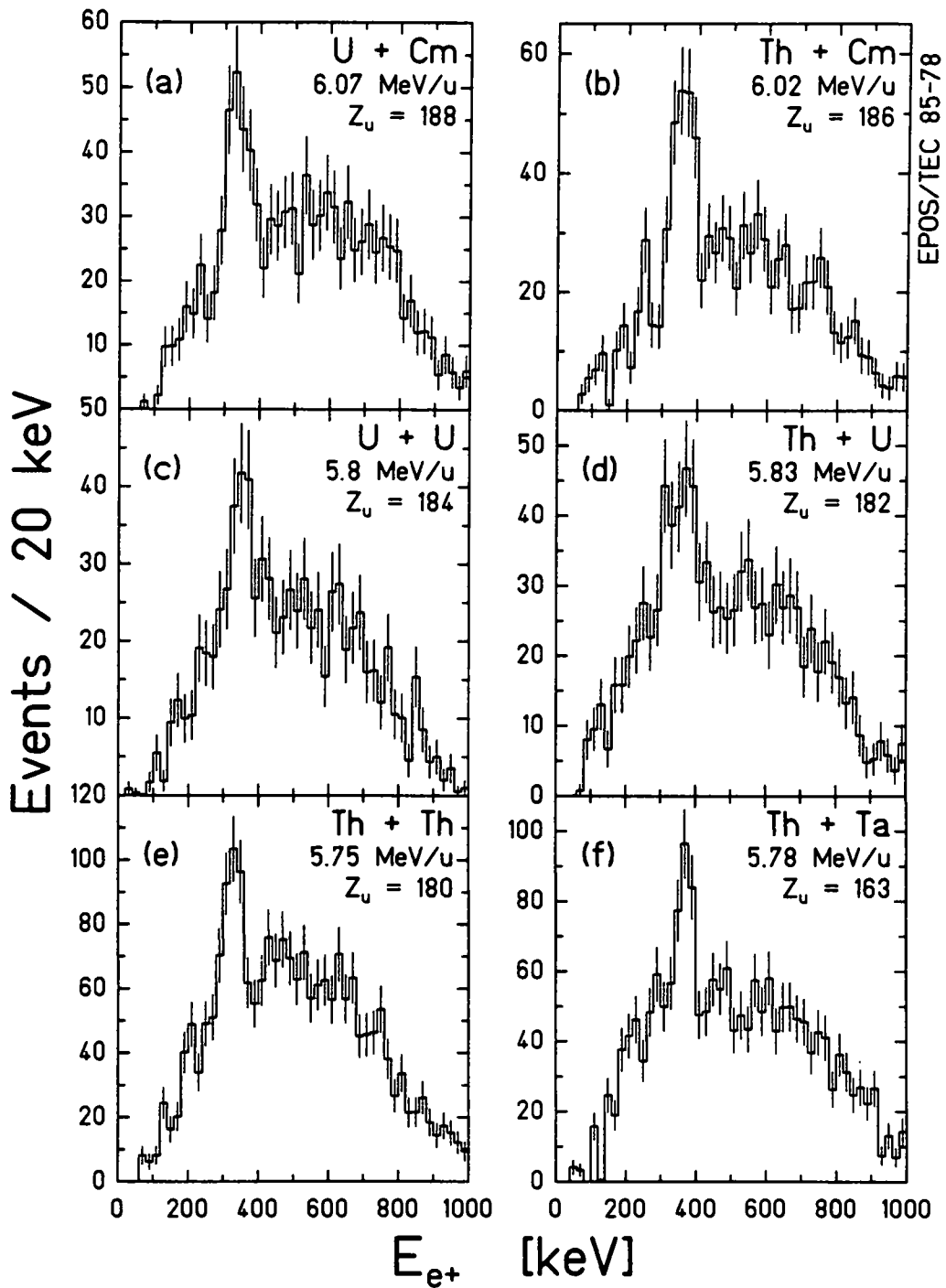


**Figure 3-16.** Positron energy spectra for the six collision systems and bombarding energies as indicated, from Figs. 3-10a to 3-15a, associated with HI scattering angle regions which prominently display the presence of the peak structures, as described in the text.

the U+Cm peak contains  $69.2 \pm 15.8$  counts above a background of  $112.8 \pm 10.6$ . The 183 positrons observed in this energy range therefore would require a

Table 3-3 Peak Characteristics

	$Z_U$	$E_{pk}$	$N_{pk}$	$\Delta E_{pk}(FWHM)$	$E_{beam}$	$\theta_U$ cut
U+Cm	188	$334.2 \pm 6.8$	$69.2 \pm 15.8$	$73.3 \pm 12.4$	6.04-6.13	( $41.5^\circ$ - $56^\circ$ )
U+Cm <sup>a</sup>	188	$320.9 \pm 5.4$	$50.0 \pm 10.0$	$70.6 \pm 7.8$	6.05	( $28^\circ$ - $40.5^\circ$ )
Th+Cm	186	$354.2 \pm 4.4$	$89.9 \pm 16.1$	$74.5 \pm 7.8$	6.00-6.04	( $35^\circ$ - $57^\circ$ )
U+U	184	$343.7 \pm 7.3$	$57.1 \pm 13.1$	$70.9 \pm 9.4$	5.8	( $30^\circ$ - $35^\circ$ ) + ( $48^\circ$ - $53^\circ$ )
U+U <sup>b</sup>	184	$312.9 \pm 7.8$	$45.0 \pm 10.0$	$75.1 \pm 8.2$	5.9	( $35.5^\circ$ - $39.5^\circ$ ) + ( $50.5^\circ$ - $54.5^\circ$ )
Th+U	182	$348.9 \pm 7.1$	$63.1 \pm 15.6$	$87.6 \pm 9.6$	5.80-5.85	( $20^\circ$ - $42^\circ$ )
Th+Th	180	$326.8 \pm 4.5$	$103.3 \pm 20.0$	$66.0 \pm 7.7$	5.75	( $20^\circ$ - $46^\circ$ ) + ( $51^\circ$ - $70^\circ$ )
Th+Ta	163	$375.2 \pm 6.8$	$97.2 \pm 17.8$	$65.0 \pm 10.1$	5.75 5.80	( $45.5^\circ$ - $52.5^\circ$ ) ( $52^\circ$ - $70^\circ$ )
	a) [Shw83]		b) [Bok83]			

6.5 $\sigma$  deviation of the background in order to explain the peak as a statistical fluke. The unlikelihood of an explanation in terms of a statistical deviation is once again compounded by the existence of lines in each system measured.

### Sec. 3.4.2 Kinematic Cuts, Angular Distribution

The peak spectra of Fig. 3-16 were all projected out of the corresponding total positron energy distribution by gating on a particular heavy-ion scattering angle region (listed in the last column in Table 3-3). This technique was developed in the previous work of [Shw83] and [Shw85]. It relies on and is associated with several very important experimental observations. First and foremost is the fact that the peak events can be enhanced relative to the bulk of the continuous dynamic and nuclear background by HI angle cuts. This suggests that the peak production is correlated with some specific aspect of the HI collision. It was pointed out in [Shw83] that the particular window employed in enhancing the U+Cm line does not directly reflect a HI scattering angle distribution for the peak events, but rather may be associated with a "redistribution of the kinematic correlations" in the magnetic field. This relates to the second major observation that the positron peak events are often asymmetrically

distributed in their HI angle correlations on either side of  $\Delta\theta_{\text{HI}} = 0^\circ$ , about which mirror symmetry is expected (see Sec. 2.3).

Two types of asymmetries were observed: 1) a clockwise rotation of the peak-related HI events about the  $\Delta\theta_{\text{HI}}-\Sigma\theta_{\text{HI}}$  pattern characteristic of elastic scattering; and 2) an unequal distribution of the positron peak intensity between the negative and positive sides of  $\Delta\theta_{\text{HI}} = 0^\circ$ , which would correspond to a preferred scattering direction for the projectile nucleus, either into the upper or lower PPAC in the laboratory, respectively. We further observed that overall, the peak-related scattering events lie close to the elastic kinematic branches, suggesting that the HI exit channels are nearly binary and are associated with small total kinetic energy loss.

With the larger data sample available from these measurements, several of these features have been more fully investigated than was possible in [Shw83] and [Shw85]. For example, while the HI scattering angle cuts employed to enhance the positron peak signal-to-background were very wide (usually  $\geq 10^\circ$  out of the  $50^\circ$  PPAC range), in many cases there were no observable peak events in the remaining regions, indicating that the cuts in fact reflect a non-isotropic angular distribution. The rotation of the peak-related HI scattering angle pattern first observed in [Shw83] was also reproduced in three systems, and may possibly be understood in terms of a deviation of the heavy-ion charge states from those associated with pure Rutherford collisions. Although the up-down asymmetry of the peak related scatterings is not understood, the HI cuts which enhance the peaks may be connected with the incident beam energy or the centroid of the positron lines. Despite the remaining uncertainties, we have continued with our previous approach of exploiting the the apparent differences in the HI scattering correlations between peak and dynamic positron events to enhance the peak signal by "cutting away" the continuous backgrounds, in order to more easily study the positron peak structures.

Before discussing the HI angular correlations, on the quasi-elastic nature of the peak-producing collisions is elaborated and the very important question of the extent to which the specific choice of the HI angular cut affects the measured positron peak characteristics is addressed.

**Sec. 3.4.2.1 Elasticity of Peak-Related Collisions:** In each case, the HI angular cuts used to enhance the peaks of Fig. 3-16 lie very close to the Rutherford scattering kinematics. The centroids of the angular cuts, in the  $\Sigma\theta_{\text{HI}}$  direction, are usually less

than  $0.5^\circ$  away from the mean of the elastically scattered events. As noted in App. A, a  $1^\circ \Sigma\theta_{HI}$  shift corresponds to  $\Delta Q = 25$  MeV of total kinetic energy loss in the collision. The collisions giving rise to the positron lines therefore exhibit Q-values of  $\leq 15$  MeV, relative to the mean of the dynamic positron producing HI collisions. In terms of nucleon evaporation, possibly combined with mass transfer, the calculations of Sec. 2.3 imply that at most two neutrons or one proton are ejected from the combined system. The possible participation of very inelastic collisions (e.g., with  $|Q| > 50$  MeV or fission of the ejectiles) in producing the peaks was checked by projecting out the positron energy distribution for the entire angular region with  $E_\Sigma$  less than  $2^\circ$  below the elastic kinematic branches. In addition to there being very few total positrons ( $\approx 100$  counts for all systems), there was no evidence of peak structure. This verifies that the peak-producing collisions are therefore largely binary, and at most, only slightly inelastic.

**Sec. 3.4.2.2 Affect of HI Cut on Peak Characteristics:** Obviously, the exact angular region chosen to enhance the appearance of the structure is somewhat subjective. It is important to note, however, that the centroids and widths of the peaks are not affected, within statistical uncertainties, by slightly altering the angular selections. Figure 3-17, for example, compares the peak in the Th + Cm system for the cut of Fig. 3-11 with similar spectra obtained from the same data sample by shifting the angular window in different directions by  $0.5^\circ$  in  $\Sigma\theta_{HI}$  and  $5^\circ$  in  $\Delta\theta_{HI}$ . As kinematic regions of higher dynamic positron production cross-section are included, the relative size of the peak above the continuous background changes, but in each case, the peak remains clearly visible. Despite a variation of the peak intensity from  $\cong 110$  down to  $\cong 40$  counts, the root mean square deviation of the centroid of the peak, above a fit of the smooth dynamic shape (dashed line) to the continuum background, remains constant to within  $\pm 3$  keV. The FWHM of the peak moreover varies by only  $\sigma_{\Delta E}/\Delta E \cong 12\%$ . The influence of the particular angular cut on the existence of a peak or on certain relevant parameters (mean energy and width) is obviously rather weak. On the other hand, the size of the signal can depend sensitively on the HI scattering angle region chosen.

It bears emphasis that in analyzing these data, only the unambiguous appearance of a narrow structure above the dynamic continuum was identified as a "peak." Smaller fluctuations, e.g., on the scale of those measured by [Cle84] and [Tse85] whose identification often relies on an accurate fit of the background curve, are also

## $\Delta\delta, \Sigma\delta$ Sensitivity of Th+ Cm $e^+$ Peak

$\Delta\delta$  shifted by  $\pm 5^\circ$   
 $\Sigma\delta$  shifted by  $\pm 0.5^\circ$

$\Rightarrow$  70% Range of  $N_{e^+}^{\text{peak}}$   
 12.5% RMS variation of  $\Delta E_{e^+}$   
 0.9% RMS variation of  $\langle E_{e^+} \rangle$

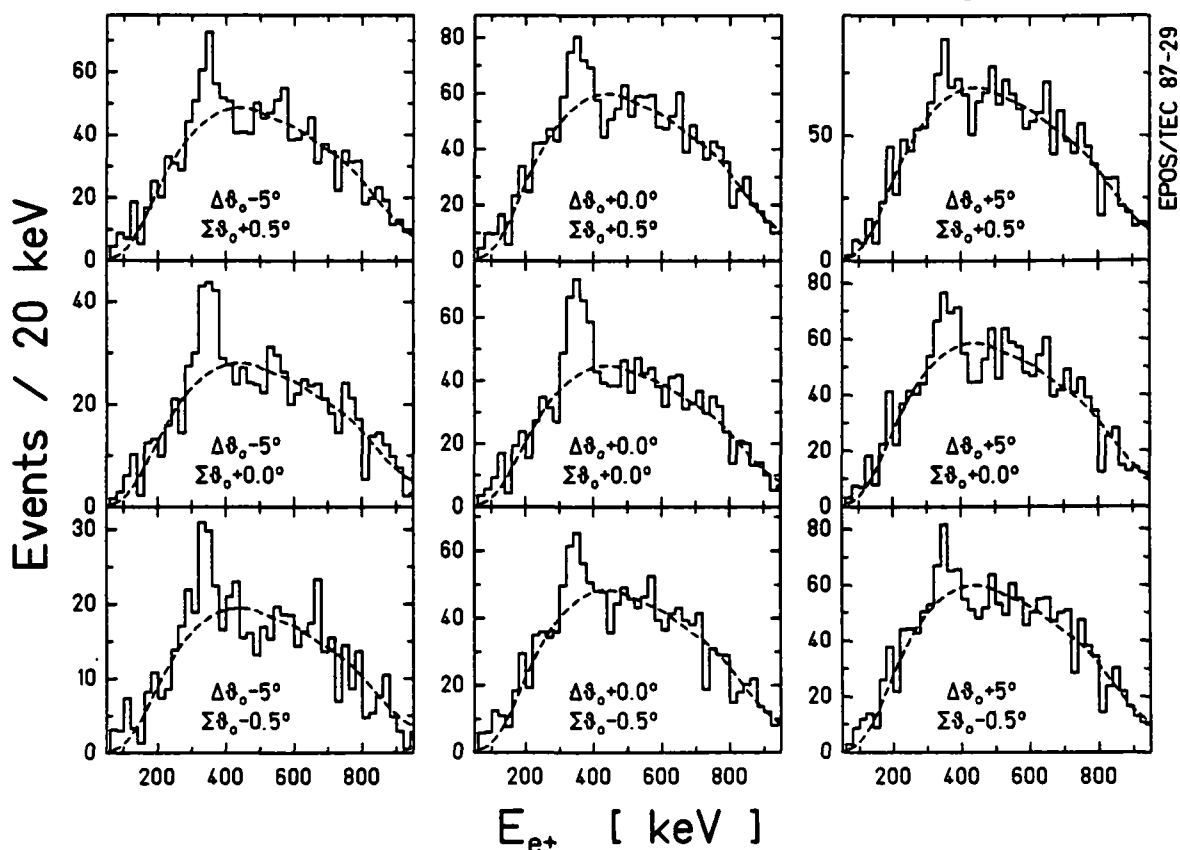
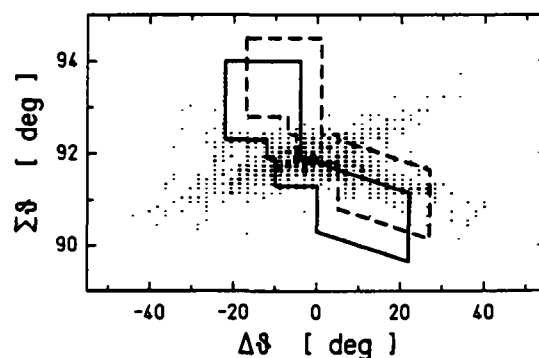


**Figure 3-17.** Array of positron spectra for Th + Cm data, obtained by shifting the HI kinematic "peak" window (solid polygon in upper right) by  $\pm 0.5^\circ$  or  $0^\circ$  in the  $\Sigma\theta_{\text{HI}}$  direction, and  $\pm 5.0^\circ$  or  $0^\circ$  in the  $\Delta\theta_{\text{HI}}$  direction (dashed window shown for  $+0.5^\circ/+5.0^\circ$  shift). Although peak intensity varies between 30 to 110 counts, the centroid and width remain fairly constant independent of the HI window.

observed but are not discussed below. This introduces a bias of sorts which should be noted when comparing our results to those of other groups.

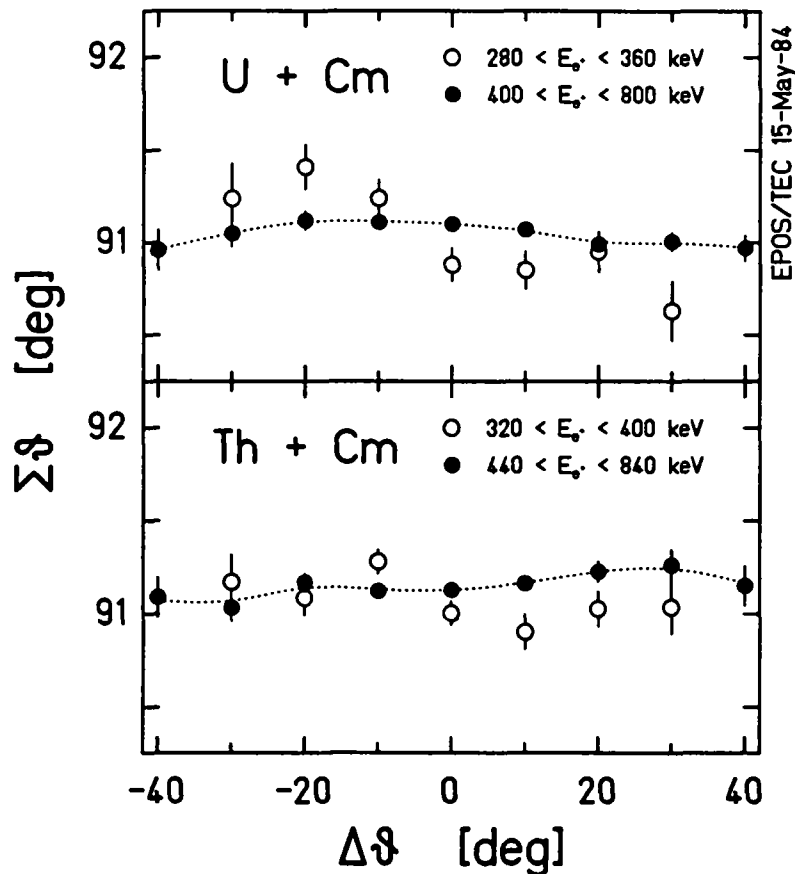


**Figure 3-18.** Plot of  $\Sigma\theta_{HI}$  centroids (as a function of  $\Delta\theta_{HI}$ ) of heavy-ion scattering events associated with positron energies containing the peak region (open circles) or the continuous dynamic distribution (solid points), for U+Cm and Th+Cm collisions.

**Sec. 3.4.2.3 Rotation of Kinematic Correlation Pattern:** The selection of HI scattering regions which enhance the positron lines is possible here because the good HI angular resolution of the PPAC detectors allows us to take advantage of apparent deviations of the peak scattering events from pure elastic kinematics to improve the signal to background. As mentioned above, the slight clockwise rotation of the pattern of HI scattering-angle correlations found previously in the U+Cm system [Shw83] is reproduced in the 1983 experiments presented here, and a similar effect is observed in Th+Cm collisions. Figure 3-18 presents the pattern of HI angle-angle correlation associated with positron peak events compared to scattering which produces dynamic positrons. The centroids of the HI  $\Sigma\theta_{HI}$  distribution for windows of  $\Delta\theta_{HI}$  are plotted, which are in coincidence with positrons in two energy intervals for U+Cm and Th+Cm collisions. Open circles denote positron energies including the peaks (U+Cm:  $280 < E_{e^+} < 360$  keV, Th+Cm:  $300 < E_{e^+} < 400$  keV), and the solid

points are gated on the smooth dynamic and nuclear IPC positron background ( $400 < E_{e^+} < 800$  keV). The  $\Delta\theta_{HI}$  ranges are each  $\pm 10^\circ$  about the respective center which slightly smooths the curves to make the systematic dependence more clear (for a justification of this procedure, see Sec. 4.1.3 of [Fri74]). The pattern of the HI events associated with the positron peaks in these two systems appears to be rotated in a clockwise direction with respect to the mean scattering angle correlation of the continuum positrons.

In order to compare the earlier U+Cm measurement to the present data, Figure 3-19 removes biases arising from systematic differences in the HI scattering angle calibration between the several experiments by plotting the difference between the  $\Sigma\theta_{HI}$  centroids for the gate on the peak positron energies minus that for the continuum background ( $\langle \Sigma\theta_{HI}^{pk} \rangle - \langle \Sigma\theta_{HI}^{bk} \rangle$ ). It is evident that a similarly rotated kinematic pattern is found in the present U+Cm measurements and in the Th+Cm and U+U (5.8 MeV/u) data. This effect may also be present in the U+U data of [Shw85] measured at 5.9 MeV/u, as shown in Fig. 3-20 which presents the positron energy spectra for two selections of the HI scattering angle regions as indicated. Although no narrow peak is clearly observed, the rotated HI window is associated with an excess of positrons between 300 and 400 keV. In the heaviest systems, this empirical shift seems to single out the peak producing scattering events as somehow different from normal Rutherford collisions.

A similar deviation in the HI kinematics associated with the positron peaks is not clearly evident in the lighter Th+U, Th+Th, or Th+Ta systems. As discussed below, one possible explanation for the absence of a rotation may be that thinner targets and backing layers were used in each of these experiments.

**Sec. 3.4.2.4 Asymmetric Intensity Distributions:** As mentioned above, there are additional asymmetries in the HI angular distribution of the peak events. As listed in Table 3-3, for example, the Th+Ta and Th+U peaks in these data are enhanced relative to the continuous background by choosing angular regions on the positive side of  $\Delta\theta_{HI}=0$ . A similar effect was observed in the earlier U+Cm measurement [Shw83] where the positron peak was most easily enhanced for a HI region with  $\Delta\theta_{HI} < 0$  [Shw85]. The intensity of the line, however, was approximately evenly divided between the two sides of the kinematic plot, as shown by the bimodal distribution in Fig. 3-21, which plots the number of positrons in the energy range centered on the peak,  $N_{e^+}(280 < E_{e^+} < 360$  keV), divided by the total positron yield,

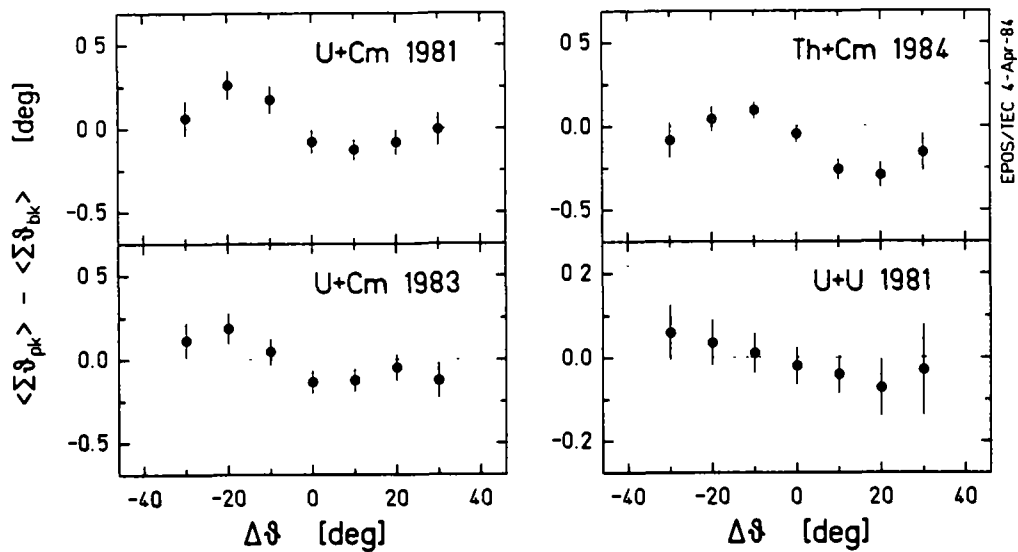


**Figure 3-19.** Relative deviations from the dynamic background (dotted line) of the centroid in the  $\Sigma\theta_{HI}$  direction for peak-related HI scattering events, plotted for overlapping  $\pm 10^\circ$  wide windows in  $\Delta\theta_{HI}$ . The upper-left/lower-right clockwise rotation of peak events is reproduced for two U+Cm experiments and in Th+Cm and U+U collisions.

$N_{e+}$  ( $100 < E_{e+} < 1000$  keV), for ranges of  $\Delta\theta_{HI}$ . Despite this apparent symmetry of the peak intensity, only a weak line could be identified for  $\Delta\theta_{HI} > 0$  presumably because the  $\Sigma\theta_{HI}$  rotation moved the structure into a region of greater dynamic positron cross-section. It must therefore be emphasized that the emergence of structure with a large size over background is primarily a function of the extent to which its HI angular correlation is separated from the regions of large dynamic positron intensity. It should also be noted that the position in the HI scattering angle plane of the maximum positron peak intensity may vary between experiments. Figure 3-21b, for example, shows the net peak intensity versus  $\Delta\theta_{HI}$  for the U+Cm and Th+Cm measurements from the present work. The values plotted are calculated from the number of counts in the peak positron energy region minus the expected number of counts in the continuous background expected from the total number of remaining positrons in the cut,

$$N_{net} = N_{e+}(280 < E_{e+} < 380 \text{ keV}) - f \cdot [N_{e+}(0-280) + N_{e+}(400-1200)], \quad (3.10)$$

where  $f \cong 0.13$ . Both the U+Cm and Th+Cm data in the present measurements appear to be centered around  $\theta_{lab} \cong 45^\circ$ .

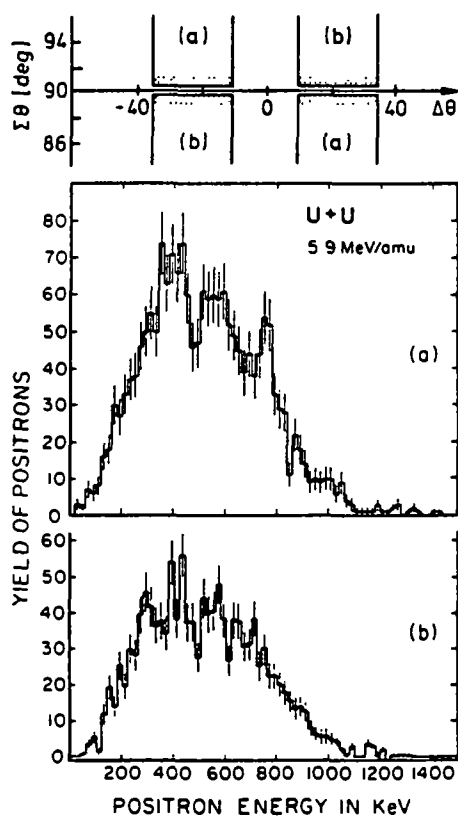


**Figure 3-20.** Positron energy spectra exhibiting structure for 5.9 MeV/u U+U collisions for HI scattering angle regions rotated clockwise (a) about the elastic kinematic branches. Similar structure is not observed in counterclockwise rotated window (b). (Reproduced from [Shw85].)

Under certain conditions, the asymmetry of the positron peak intensity can be striking. For example, Fig. 3-22 shows that an excess of positrons is observed with ( $300 < E_{e^+} < 400$  keV) for  $\Delta\theta_{HI} > 0$  in Th+Th collisions at 5.73 and 5.78 MeV/u. The solid histogram plots the positron energy distribution for  $\Delta\theta_{HI} > 0$ , and the dashed curve for  $\Delta\theta_{HI} < 0$ . The excess of events on the positive side of  $\Delta\theta_{HI} = 0$  cannot be explained by a nonuniform efficiency response of the PPAC detectors because no corresponding imbalance is found in the simultaneously measured  $\gamma$ -ray and electron yields as a function of  $\Delta\theta_{HI}$ . As was also demonstrated in Sec. 2.2, the detection efficiency of the EPOS spectrometer is also largely azimuthally symmetric about the solenoid axis. It has been verified by Monte-Carlo calculations that neither the detected intensity nor shape of either positron peaks or continuum distributions, emitted from an ejectile nucleus, depends on whether that nucleus is scattered into the upper or lower PPAC. In any case, it is clear from Figs. 3-17, 3-21, and

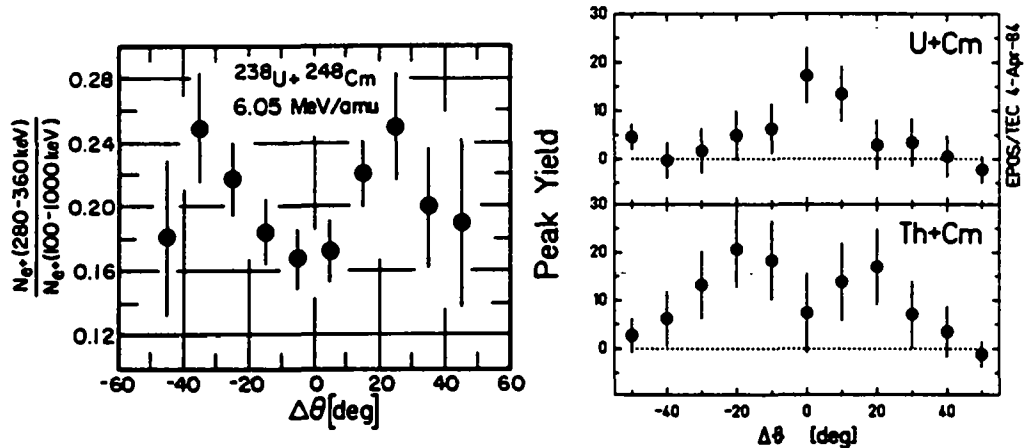


**Figure 3-21.** Ratio of number of positrons in peak energy interval to total positrons (left, reproduced from [Shw85]) plotted versus  $\Delta\theta_{\text{HI}}$ , compared to net positron peak yields above background from U+Cm and Th+Cm collisions.

3-22 that the intensity of the positron peaks are not necessarily evenly distributed over the entire angular range of the PPAC acceptance. In at least one system, Th+Ta, we also have an indication that the peak production shifts to smaller CM scattering angles with increasing beam energy.

**Sec. 3.4.2.5 Ionic Charge States:** Viewed separately, it is tempting to treat each of these deviations from elastic scattering kinematics in the heavy-ion angle correlation associated with the positron peaks as a statistical clustering of events in the two-dimensional angle-angle plane. However, certain features are obviously common to much of the data. Although the up-down asymmetry in the peak intensity distributions is difficult to explain, the rotation of the peak-related ion-angle correlation pattern may be related to the physical handedness of the EPOS spectrometer introduced by the direction of the solenoid transport field. As discussed in Sec. 2.3.3, in the 1872 G magnetic field at the target site, the positively charged positrons and scattered nuclei are deflected downwards with radius of curvature  $r = P_{\perp}c/qB$ . One explanation for the rotation may therefore be a deviation from the typical charge state distribution for the ions.

Charge-state measurements with very thin targets show that immediately after a nuclear collision, the electrons shared by the quasimolecular system are distributed roughly equally between the ejectiles. Equilibrium ionic charges ([Nik68] and Fig. 2-34) are approached as the nuclei exit through the target material and gather

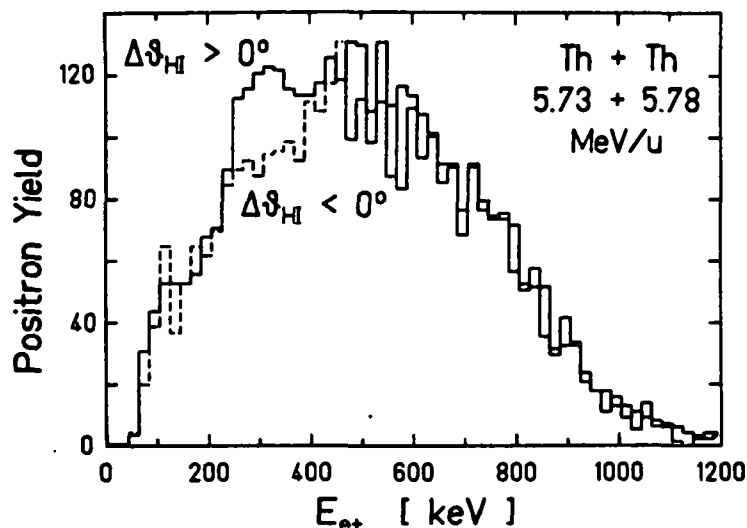


**Figure 3-22.** Positron energy spectra from Th + Th collisions for heavy-ions scattered into  $\Delta\theta_{HI} > 0^\circ$  region (solid curve), compared to  $\Delta\theta_{HI} < 0^\circ$  (dashed histogram).

electrons at different rates, with probability inversely proportional to velocity. As noted in Sec. 2.3.3, the mean rotation of the elastically scattered heavy-ions is partially corrected by the PPAC angular calibration. If both scattered ions associated with the positron peak exhibit nearly equal, velocity-independent charges, an additional rotation could be observed. As shown in Fig. 3-23, the rotation in the present U + Cm measurement could be explained if  $q_p \cong q_t \cong 60^+$ .

One unlikely possibility for the formation of equal, or unusually high charge states could involve the formation of a compound system which survives  $\geq 10^{-13}$  sec, long enough to exit the target foil. Upon dissociation, the heavy fragments would carry similar ionic charge, independent of their laboratory velocity. Another scenario might involve particularly high levels of excitation of those scattered nuclei associated with the collisions which produce the positron peaks. A series of Auger cascades after the ejectiles leave the target (on the time scale of  $\geq 10^{-14}$  sec) could then lead to anomalously large ionic charges.

Alternatively, the peak-producing collisions could occur predominantly in thin layers of a very clumpy target, or in the last layer of a thick target. The peak related scattered ions would therefore traverse less target and backing material after the collision. As shown in Fig. 3-24, which plots the distribution of Pb charge states observed after  $5^\circ$  and  $35^\circ$  scattering from Au targets of various thicknesses [Sti86],

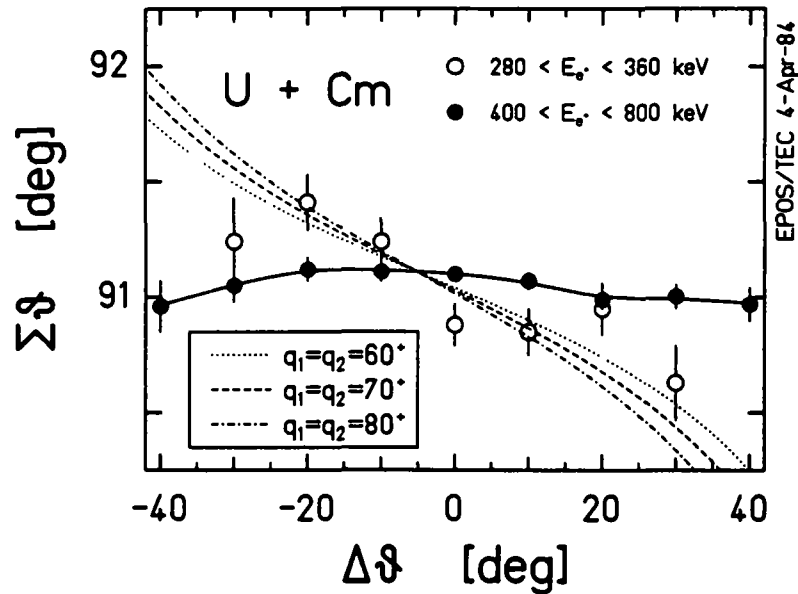


**Figure 3-23.** Plot of  $\Sigma\theta_{HI}$  centroids (as a function of  $\Delta\theta_{HI}$ ) of heavy-ion scattering events associated with positron energies containing the peak region (open circles) or the continuous dynamic distribution (solid points), for U+Cm collisions. Dotted, dashed, and dot-dashed curves present calculations [Gru85] of expected kinematic pattern for equal, velocity-independent ionic charge states of  $60^+$ ,  $70^+$ , and  $80^+$ .

equilibrium charges are first approached for targets  $> 100 \mu\text{g}/\text{cm}^2$  thick. The peak events would then be associated with large values of  $q_{iON}$ , while the bulk of dynamic positron producing events – uniformly distributed over the depth of the target material with consequently much more intensity from thick clumpy portions – would more closely approach equilibrium charge states.

Within this context, the absence of an apparent rotation connected with the positron peaks in the Th+U, Th+Th, and Th+Ta collisions is explained quite naturally. As mentioned in Sec. 3.1, the Th, U, and Ta targets were somewhat thinner and much more uniform than the Cm foils, and these newer targets used very thin  $\sim 40 \mu\text{g}/\text{cm}^2$   $^{12}\text{C}$  backings. In these measurements, elastically scattered ions (associated with dynamic positrons) traverse on the average  $\sim 150 \mu\text{g}/\text{cm}^2$  of material and do not yet approach the lower equilibrium charges typical of thick target measurements, as indicated in Fig. 3-24. The mean Rutherford collision charge state could be as much as 8-10 units higher at a given scattering angle, than that produced in the U+Cm and Th+Cm collisions. The rotation of the peak positrons, while possibly the same in absolute terms in all the systems measured, is then masked by the dy-

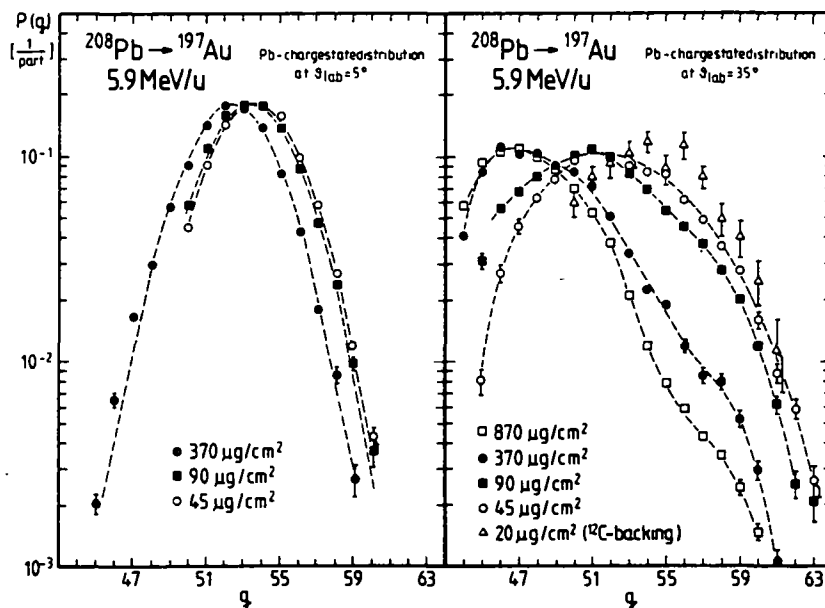


**Figure 3-24.** Charge-state distributions for Pb ions scattered at an angle of  $5^\circ$  (left) or  $35^\circ$  (right) from Au targets of various thickness as marked.

namic background in the thin target measurements which is rotated farther in the magnetic field and falls on top of the peak event angle-angle correlation pattern.

Although attractive, this explanation is still speculative. A satisfactory resolution of the HI scattering-angle asymmetries and positron peak related kinematic rotation requires further measurements gathering substantially greater statistics for a variety of target backings and thicknesses. Given the small positron production cross-sections and difficulties with in-beam target deterioration, this program was not feasible as part of the present dissertation research. In the meantime, we have exploited the empirical differences between peak producing collisions and Rutherford scattering in order to study the characteristics of the positron lines.

#### **Sec. 3.4.4 Beam-Energy Dependence**

As described previously [Shw83], the appearance of the narrow positron peak in U + Cm collisions seems to be correlated with bombarding energies between 6.0 and 6.2 MeV/u. This corresponds, in head-on encounters, to marginally touching collision partners. Figure 3-25 presents spectra from three ranges of beam energy measured for the U + Cm system. Identical HI scattering angle windows are used

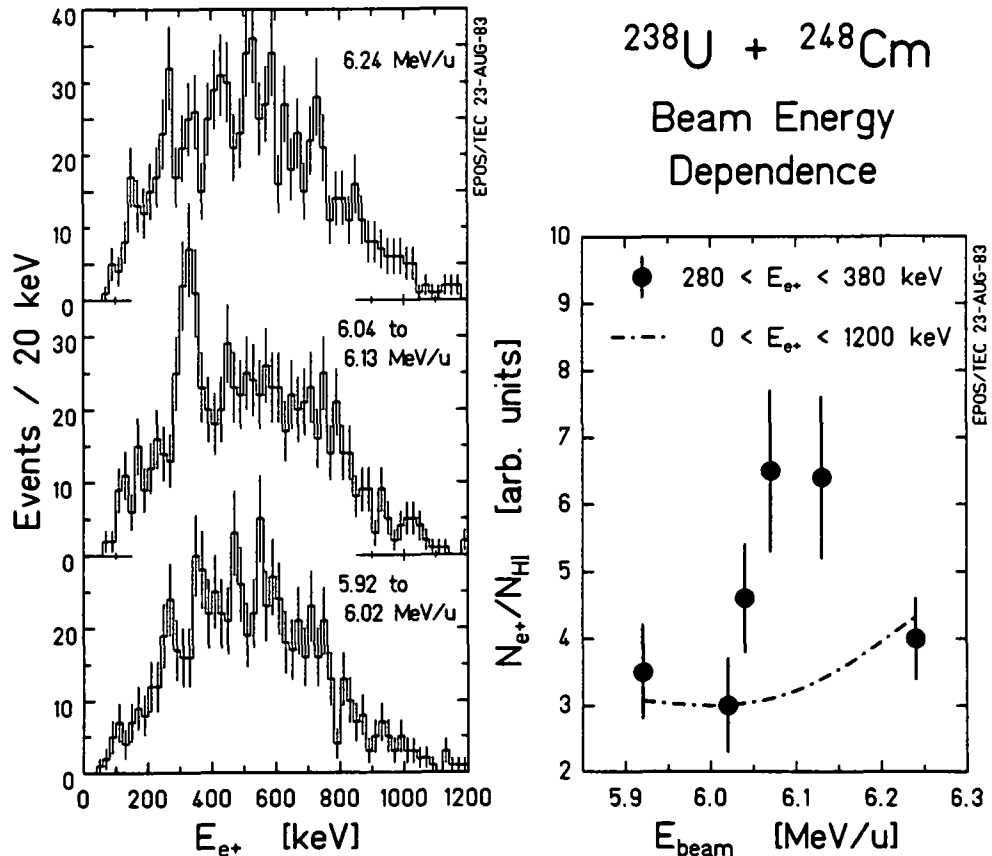


**Figure 3-25.** Beam energy dependence of production of the U+Cm  $\sim 330$  keV positron peak. Left panel shows positron spectra for three beam energy intervals, gated on  $42^\circ < \theta_{\text{HI}} < 51^\circ$  which enhances the peak for 6.04-6.13 MeV/u collisions. Right presents relative yield of positrons with  $280 < E_{e^+} < 360$  keV, compared to total  $e^+$  production, as a function of beam energy.

( $41^\circ < \theta_{\text{HI}} < 51^\circ$ ), which optimizes the positron peak for  $6.04 \leq E_{\text{beam}} \leq 6.13$  MeV/u. As noted above, the peak angular distribution is not well known, so comparison of similar cuts for different beam energies may have limited meaning. Empirically, however, no clear evidence for the positron peak was found for any angular region in the data measured at 5.92, 6.02, and 6.24 MeV/u. Figure 3-25b attempts to quantify the appearance of the line by plotting the peak intensity divided by scattered particle yield for smaller steps of beam energy. The solid circles present the positron yield for  $280 < E_{e^+} < 360$  keV, and the dotted curve for  $400 < E_{e^+} < 480$  keV.

Taken at face value, the absence of positron peak intensity for 5.92 - 6.02 MeV/u suggests a dependence on projectile energy which exhibits a threshold-like behavior

at  $E_{\text{beam}} \geq 6.02$  MeV/u. The relatively small rise in dynamic positron production with beam energy further suggests that the peak's disappearance at 6.24 MeV/u is not simply due to an increase in the continuous backgrounds, but rather points to a resonance-like behavior bounded above by 6.24 MeV/u minus the target thickness. As discussed in Sec. 2.6, clumping of the  $\text{Cm}_2\text{O}_3$  material produced a mean target energy-loss thickness of  $\sim 0.15$  MeV/u. Target deterioration may also have been responsible for the null measurements above and below the central energies. An additional run at 6.11 MeV/u measured in July, 1983, with the target previously used for the 6.13 MeV/u measurement in June 1983, also showed little indication of peak intensity. The target was irradiated for a cumulative  $\sim 40$  hours, and was the only instance that a Cm target was reused. Post-irradiation studies revealed an especially large energy-loss thickness. This data point was therefore considered highly suspect and was not included in Fig. 3-25. If a nuclear scattering resonance is involved in this energy range, it is centered between  $\cong 6.04$  to  $\cong 6.07$  MeV/u.

In head-on collisions at the "resonance" energy, the deformed U and Cm nuclei, when oriented end-to-end, overlap by  $\sim 0.1$  fm assuming uniformly distributed nuclear matter. Marginal overlap suggests that nuclear contact may play some role in producing the peak, either by causing a time delay via resonant nuclear reactions, or by the onset of strong interactions. This empirical "resonant-energy" was extrapolated to other collision systems by calculating the nuclear overlap,  $\delta_{\text{nuc}} = R_{\text{min}} - (R_{\text{p}} + R_{\text{t}})$ , as a function of beam energy. The experimental search for positron structures in each combination of target and projectile nuclei was concentrated in those energy regions which provide similar overlap.

Using available estimates of nuclear deformation coefficients [Göt72, Bem73, Ron81, Zum84], the maximum radii for various target and projectile nuclei (listed in Table 3-4) are given by

$$R_{\text{p,t}} = R_0 \cdot [1 + \beta_2 Y_{20} + \beta_4 Y_{40} + \beta_6 Y_{60}] \quad (3.11)$$

evaluated at  $\theta=0$ , with  $R_0 = 1.2 \cdot A^{1/3}$  fm.  $\delta_{\text{nuc}}$  is calculated using

$$R_{\text{min}} = (A_{\text{p}} + A_{\text{t}}) Z_{\text{p}} Z_{\text{t}} e^2 / (A_{\text{p}} A_{\text{t}} E_0). \quad (3.12)$$

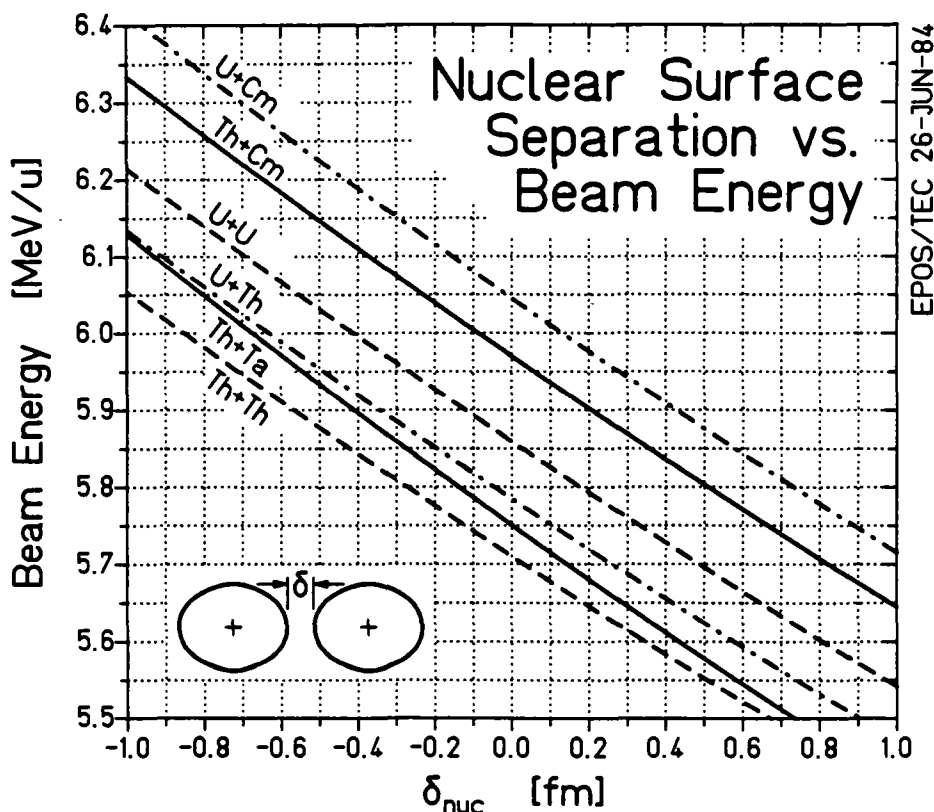


**Figure 3-26.** Plot of the separation between the nuclear surfaces (calculated assuming uniform density and deformed shapes in the orientation of greatest overlap, as described in text), as a function of projectile energy.

with  $e^2 = 1.44 \text{ MeV}\cdot\text{fm}$ , and  $E_0$  is the beam energy in  $\text{MeV}/u$ . Figure 3-26a plots curves of surface separation  $\delta_{\text{nuc}}$  versus  $E_{\text{beam}}$  for the collision systems measured. In Fig. 3-27, the beam energy at which the collision partners are just touching ( $\delta_{\text{nuc}} = 0$ ) for each system is indicated by the horizontal bar. The solid points represent incident projectile energies at which the peaks of Fig. 3-16 are observed, and open circles denote those where no clear evidence for a positron peak was found. The half-filled points indicate energies with ambiguous results for different runs. The vertical bars indicate the nominal target thickness, representing the energy interval spanned in each case. Due to rapid target deterioration, the actual energy range sampled maybe up to twice as large. Although these data do not constitute a systematic excitation function, the similar scaling in the beam energy for which the narrow lines are observed suggests that nuclear contact may play some role in the peak production.

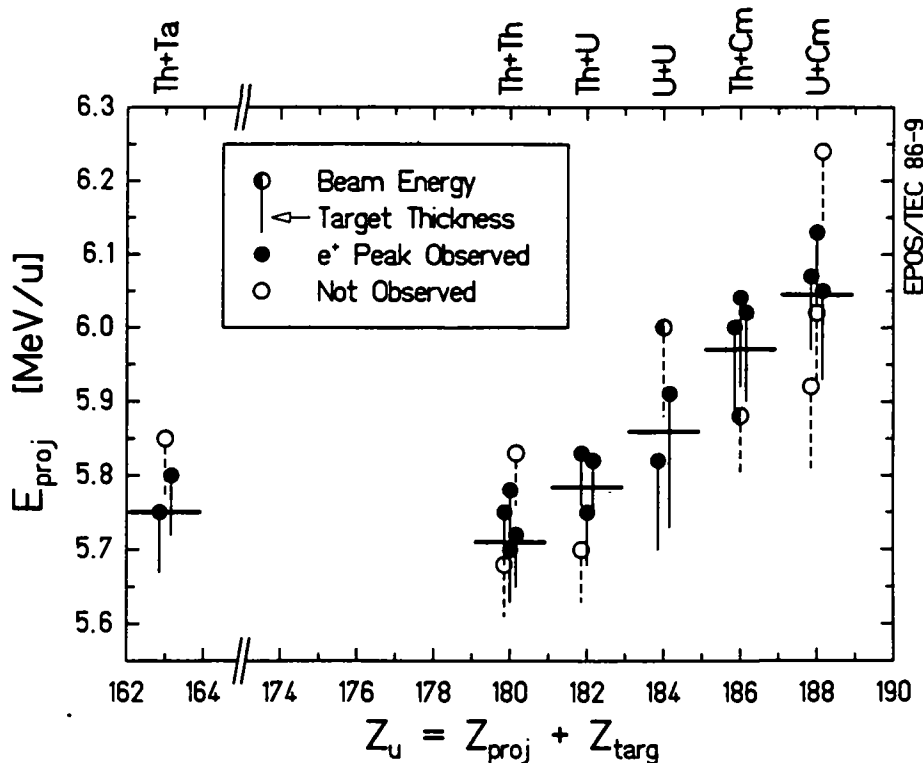


**Figure 3-27.** Projectile energies at which positron peaks have been unambiguously observed (solid points), or not observed (open circles), plotted versus combined nuclear charge. Vertical lines denote the energy range spanned by the nominal target thickness. Horizontal bars indicate energies for which  $\delta_{\text{nuc}} = 0$  calculated in Fig. 3-26.

A further indication of a projectile energy dependence is the observation that the positron peak production rate is not constant for all targets measured. As noted above, proton backscattering measurements showed that actinide targets clump and their composition changes on a short time scale, leading to variations in the effective energy-loss thickness. If the positron lines were produced over a broad range of incident energies, the target thickness would play no role in the peak yield. All targets would equally produce a uniform intensity signal.

On the other hand, a sharp beam-energy dependence would imply that only a small portion of each target, in the proper  $\Delta E_{\text{beam}}$  interval, would produce peak events. The remaining material would add only to the continuous dynamic and nuclear positron backgrounds. If stable conditions could be maintained with thin targets, the peak would in this case be considerably enhanced. Figure 3-28 presents a total positron spectrum for 5.72 MeV/u Th+Th collisions (i.e., no cuts on the HI scattering angles) where data accumulated only with thin  $\sim 200 \mu\text{g}/\text{cm}^2$  ThF<sub>4</sub> targets have been

Table 3-4 Projectile and Target Nuclear Deformations

Nuclide	$R_0$ [fm]	$\beta_2$	$\beta_4$	$\beta_6$	$R(r=0)$ [fm]
$^{248}\text{Cm}$	7.539	0.285(14)	-0.049(60)	---	8.582
$^{238}\text{U}$	7.437	0.226(1)	0.052(1)	-0.011(12)	8.741
$^{232}\text{Th}$	7.374	0.202(2)	0.068(1)	0.009(2)	8.805
$^{181}\text{Ta}$	6.788	0.245	-0.08	---	7.377

included. To reduce clumping, each target was irradiated for only short times ( $\sim 1$  hr). The emergence of a large peak in this *total* spectrum again argues for just such an energy dependence. Moreover, these data prove that the existence of the positron peak, and its narrow width, are in no way artifacts of the kinematic analysis leading to the spectra of Fig. 3-16.

As was mentioned in Sec. 2.7, as the target quality was improved over the course of these experiments, we began to concentrate more on the stability of the UNILAC beam. For measurements with thin, stable targets having energy-loss thicknesses as low as 0.05 MeV/u, the spread in the beam energy could affect the production of peak events if they are created in a resonant process. Using Monte-Carlo simulations, we studied the effect of production rate on the identification of line structures and found that a change of the peak cross-section by a factor of 2-3 could make these lines indistinguishable from the continuous background. A variation of this size in the rate could result transiently either from 1) beam energy shifts if the resonant energy is close to the edge of the range sampled by beam energy spread and target thickness, or 2) target thickness variations which change the amount of material within the resonant energy-loss window. Obviously this entire discussion is considerably complicated if the positron peaks are in any way associated with satellite components or contaminants in the beam.

### Sec. 3.4.5 Peak Cross-Sections

A description of the observed peak intensities in terms of a production probability, i.e., emitted positrons per scattered HI, is not particularly meaningful in this experiment. Because both the scattered projectile and target recoil ions are detected with good angular resolution, we exploit the empirical differences between Rutherford

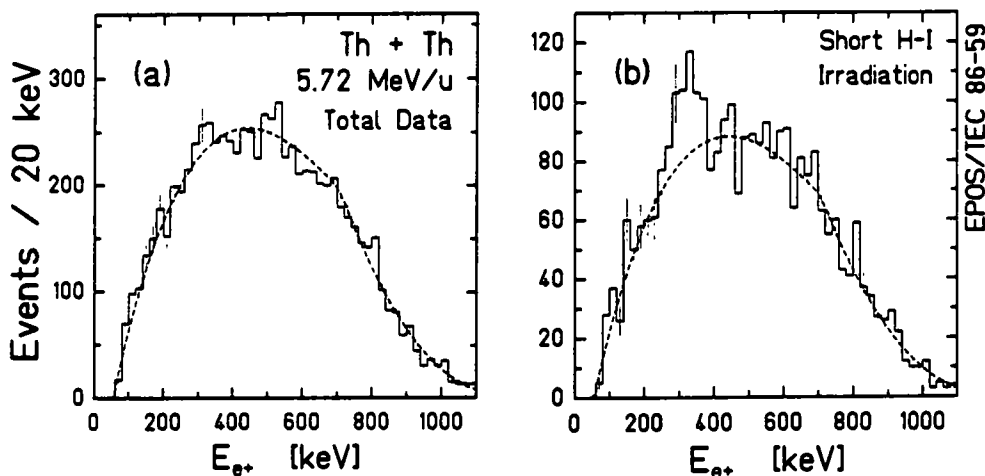


**Figure 3-28.** (a) Total positron energy distribution ( $20^\circ < \theta_{HI} < 70^\circ$ ) for Th+Th collisions at 5.75 and 5.70 MeV/u, July 1985. (b) Subset of data selecting approximately the first hour of heavy-ion irradiation on each target.

collisions and the peak-related events. The peaks are enhanced by making cuts in the  $\Sigma\theta_{HI}$  coordinate to "cut away" dynamic positron background. Where the selected region lies on the tail of the elastic distribution, the number of ions scattered into the angular window is small and the normalization gives anomalously large values of  $P_{e+}$ . A physically more reasonable measure of the absolute size of the peak signals is the production cross-section. This ignores the  $\Sigma\theta_{HI}$  selection by normalizing the positron peak intensity to the HI yield in the entire corresponding  $\Delta\theta_{HI}$  interval. Quoting a cross-section also facilitates comparison with other experiments [Cle84, Tse85] which do not have the advantage of detecting both scattered ions over their full angular acceptance, and therefore cannot make similar kinematic cuts. For example, the 316 keV U+Cm peak of [Shw83] appears with a probability of  $P_{e+} = (2.5 \pm 0.5) \times 10^{-5}$  and a cross-section of  $d\sigma_{e+}/d\Omega_{HI} \cong 12.9 \pm 2.5 \mu\text{b/sr}$ . The ORANGE collaboration reports [Cle84] a probability of only  $P_{e+} = 1.0 \times 10^{-5}$  for a similar peak in the U+U system, whose cross-section is  $\cong 9 \mu\text{b/sr}$ . Although these structures are produced with similar cross-sections, the extra factor of 2.5 in the production probability reflects the fact that the  $\Sigma\theta_{HI}$  window used in the U+Cm analysis includes only  $\sim 40\%$  of the HI's scattered into that  $\Delta\theta_{HI}$  region.

The production probability and cross-section of each observed peak is calculated by comparing the peak intensity to the yield of scattered ions integrated over

the same  $\Delta\theta_{HI}$  regions. The positron peak detection efficiency,  $\epsilon_{e^+}^{pk}$ , the CMS solid angle of the cut,  $\Omega_{HI}$ , and the Rutherford cross-section,  $\sigma_R$ , combine to give the differential CM peak cross-section,

$$d\sigma_{e^+}/d\Omega_{HI} = (\Delta\Omega_{HI})^{-1} [N_{e^+} SD_{e^+} / \epsilon_{e^+}^{pk}] [(N_{HI} SD_{HI})^{-1} \int_{\Delta\Omega} (d\sigma_R/d\Omega)]. \quad (3.13)$$

These cross-sections are plotted in Fig. 3-29a, for the data of Fig. 3-16, versus  $Z_U$  of the combined system. The error bars reflect the statistical uncertainty in the peak intensity only. They do not include either the uncertainty in the underlying peak angular distribution, or the projectile energy range sampled by the target thickness and beam spread.

The target thickness is potentially a very important consideration in evaluating the cross-section if positron peak production is resonant. Only a very limited portion of the target may be irradiated in the proper energy interval to create peak positrons. The rest produces background positrons, diluting the average measured peak cross-sections. Figure 3-29b plots the data of 3-29a normalized to a consistent beam energy spread by multiplying  $d\sigma_{e^+}/d\Omega_{HI}$  by the appropriate mean target energy-loss thickness. The peaks appear to be produced with roughly constant cross-section ( $\sim 10 \mu\text{b/sr}$ ), with no clear systematic variation over the large range of  $Z_U$ . In principle, this dependence reflects the role played by the Coulomb field in the positron peak production mechanism. A straightforward experimental limit on the fall-off of  $\sigma_{e^+}$  over the range  $163 \leq Z_U \leq 188$  is a factor of 2 to 3. In terms of a power law dependence of the cross-section on  $Z_U$ ,

$$\sigma_{e^+} \propto Z_U^n, \quad (3.14)$$

this places an upper limit on the exponent of  $n \leq 8$ . Production mechanisms in which the electric field enters the amplitude with larger powers (e.g., with  $Z_U \sim 20$  as expected for certain quasiatonic processes) therefore appear unlikely.

This result, based on the near constancy of  $d\sigma_{e^+}/d\Omega_{HI}$ , obviously depends sensitively on the details of the production mechanism. If resonant, it assumes that the effects of target thickness and beam energy, as mentioned above, are corrected for in a consistent way for each of the systems. Moreover, because of peak events are distributed over  $\Delta\theta_{HI}$  differently from system to system, it is not even clear whether the differential or the total cross-section,  $\sigma_{e^+} = \int_{4\pi} (d\sigma_{e^+}/d\Omega_{HI})$ , is more

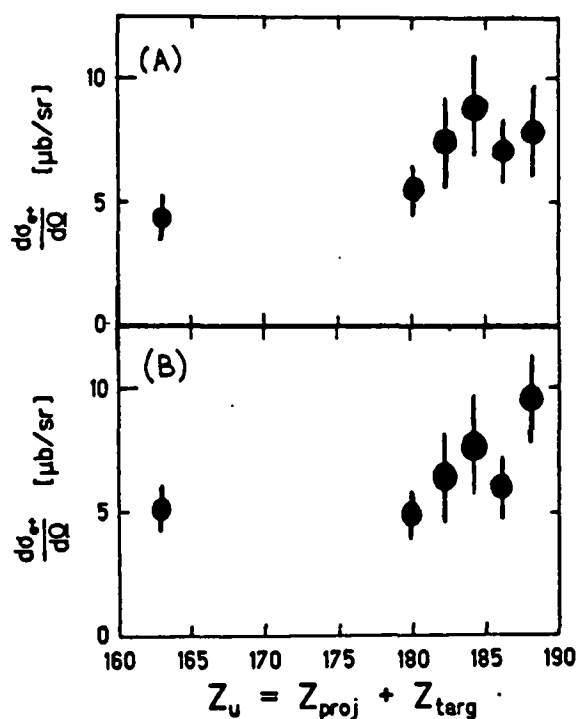


**Figure 3-29.** Differential positron peak production cross-sections (a), calculated for the heavy-ion scattering angle regions displayed in Fig. 3-16, plotted versus combined nuclear charge. Part (b) adjusts cross-sections for energy range spanned by target thickness.

appropriate to describe the production process. A convenient approximation of the peak size provided by the empirical observation that in each collision system, the peak intensity amounts to 1-2% of the entire positron yield. If the peak production is associated in a detailed way with the UNILAC performance (e.g., distribution of beam energies, satellites, contaminants), the difficulty of extracting a sensible cross-section is compounded. However, it should be noted that a mechanism involving the  $\sim 0.1\text{-}1\%$  beam contaminants would require a much larger production cross-section (at least  $\sigma \sim \text{mb}$ ), and would be difficult to accommodate in light of the quasi-elastic nature of the observed exit channel.

In light of the uncertainties cited above, only certain of the more general features of the positron peaks should be considered as firmly established: 1) narrow peaks are observed in each system measured,  $163 \leq Z_u \leq 188$ , at energies between  $E_{e^+} = 310$  to  $380$  keV. 2) They have similar widths, of order  $\Delta E_{e^+} \cong 70$  keV (FWHM). And 3) the production cross-sections are on the order of  $d\sigma_{e^+}/d\Omega_{HI} \sim 10$

$\mu\text{b}/\text{sr}$ . Although not experimentally proven, the beam energy data suggest that the peaks may be produced in association with nuclear contact or resonant reactions. The HI scattering angle-angle correlations of the peak-related events appear to differ from that of Rutherford scattering. More thorough conclusions await further systematic investigations.

## Chapter 4 Discussion of Peak Origins

Several of the observations described in the preceding chapter are particularly relevant to an analysis of the origin of the positron peaks. Foremost among these are the nearly common peak energies and similar production cross-sections which appear to be nearly independent of  $Z_U$ . The peak lineshapes, which seem to be dominated by Doppler broadening, are all  $\sim 75$  keV wide and suggest a common source created in the collision with a mean velocity of  $\sim 0.05c$ . Moreover, the narrow peak widths imply, from the uncertainty principle, that the source lifetime is  $\tau > 10^{-20}$  sec, an order of magnitude longer than the Rutherford scattering time,  $T = 2a/v_\infty = 2 \times 10^{-21}$  sec. In addition, the pattern of ion angle-angle correlations and the observation that the production rate is not constant for all beam energies suggest that the associated heavy-ion collision differs from simple elastic scattering.

In this chapter, several of the origins which have been hypothesized for the positron peaks are discussed in light of the experimental findings. The topics include: positron emitting transitions, both conventional and exotic, in the separated final state nuclei; a discussion of the emitting source velocity deduced from measurements of the positron linewidth; spontaneous positron emission from the decay of the neutral QED vacuum, and constraints on the peak-producing HI reaction from the collision kinematics; atomic interference phenomena; and conversions in a giant super-nucleus. Before assigning the peaks to a new phenomenon, however, the possibility of a purely instrumental origin or trivial secondary background is first addressed.

### Section 4.1 Instrumental Origins

Various aspects of the EPOS spectrometer preclude the possibility that a trivial mechanism is responsible for the positron peaks. As discussed in Chap. 2, neutral radiations are suppressed by the small geometric cross-section of the positron detector and additional absorbers, while electrons are blocked by the spiral baffle. In the data reduction, positrons are selected by their TOF from the target and by the coincident detection of 511 keV annihilation radiation. The detailed efficiency response of the detector system is well understood, including the energy versus emission-angle dependence of transport efficiency, the Doppler-broadened lineshape from moving sources, and the detection of positrons and electrons emitted off-axis.

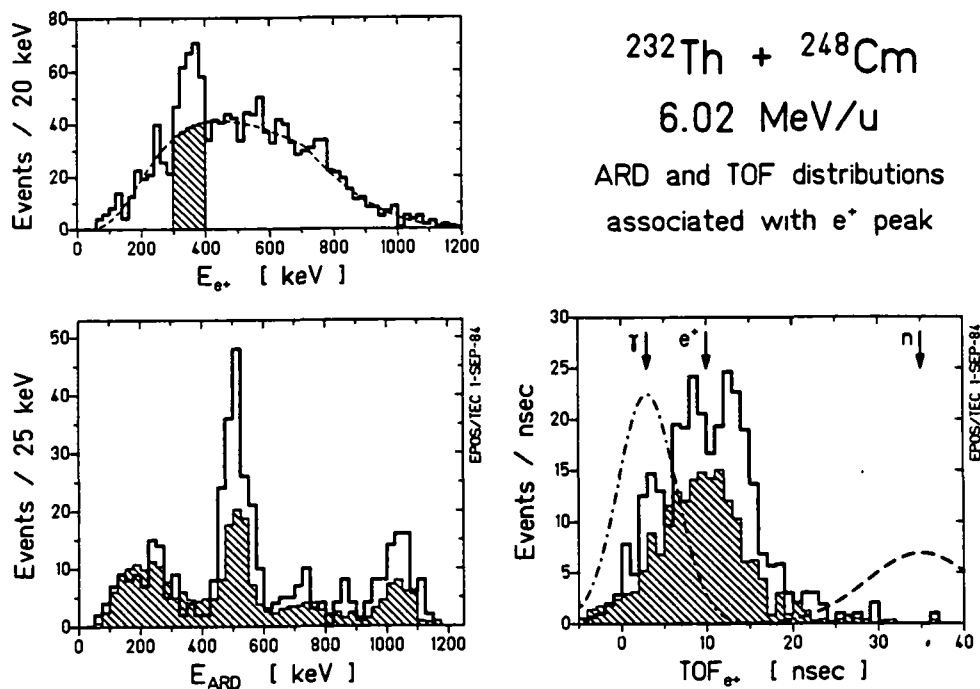


**Figure 4-1.** Time-of-Flight (lower right) and ARD energy distributions (lower left) for Th+Cm data associated with positron peak (upper left). Solid curves gated on  $300 < E_{e^+} < 400$  keV. shaded histograms correspond to dynamic positron distribution normalized to background under the peak. Dashed and dot-dashed curves indicate expected flight times for a  $\gamma$ -ray or neutron induced positron peak (including  $\sim 10$  ns experimental time resolution).

Two direct indications that the narrow peaks in the positron energy distribution actually represent positrons, and are *not* due to a background radiation, are their coincident detection with annihilation radiation in the ARD (ruling out electrons) and the target-detector TOF difference consistent with the average positron flight-time (precluding neutral radiations). Figures 4-1b,c present an example of the ARD energy distribution and HI-positron TOF spectrum for events gated on the positron peak in Th+Cm collisions. In each plot, the solid line presents the data for energies between  $300 < E_{e^+} < 400$  keV, as denoted in Fig. 4-1a, and the shaded histogram is an average of data at energies above and below this window, normalized to the continuous background under the peak.

The ARD spectrum of Fig. 4-1b in coincidence with the peak counts exhibits photon peaks at 511 keV and 1022 keV, clearly signaling the annihilation of a positron in the fiducial region sampled by the NaI crystal array. The relative intensities of the one and two annihilation photon peaks and the Compton continua are in excellent

agreement with the known distribution for positrons incident in the Si(Li), measured with  $^{22}\text{Na}$  and  $^{56}\text{Co}$   $\beta^+$  decay sources (see e.g., Fig. 2-13). The clear detection of both annihilation photons is particularly important because it rules out the possibility that the positron line arises from the scattering of one 511 keV photon in the Si(Li) detector, leaving a Compton edge at  $E_{e^+} \cong 341$  keV. In principle, if the positron annihilates in the vacuum chamber wall or cold-finger and one annihilation photon registers in the ARD while the second scatters in the Si(Li), a peak near 340 keV could be simulated. In experimental arrangements where the annihilation quanta are not measured [Cle84, Tse85, Erb86, Pec87], this effect is particularly dangerous and may trivially produce narrow structure near the Compton-edge energy which is misidentified as a monoenergetic positron line. Any mechanism proposed to explain the positron structure in the present experiments must therefore also explain the coincident detection in the ARD array of the clear 511 + 511 keV signature for positron annihilation in the Si(Li).

The HI-positron TOF spectrum in Fig. 4-1c further indicates that the signal in the Si(Li) detector is produced at a time following the HI collision which mirrors the known  $\sim 5$  to  $\sim 15$  ns flight-time observed for the continuous distribution of dynamic positrons. The arrows mark the expected mean TOF if the peak were associated with either prompt  $\gamma$ -rays ( $\Delta t = c/83 \text{ cm} \cong 3 \text{ ns}$ ) or evaporation neutrons ( $\Delta t \cong 35 \text{ ns}$ , for  $E_n \sim 3 \text{ MeV}$ ) which interact near the positron detector. The disparity with the expected  $\gamma$ -ray TOF argues against processes which involve, for example, the external positron-electron pair conversion of  $\gamma$ -rays near or in the Si detector material, the vacuum chamber walls, or the NaI crystals, with the subsequent detection of either the positron, electron, or a Compton scattered annihilation photon in the Si(Li). Direct measurements with intense  $\gamma$ -ray sources placed near the target also showed no evidence for this  $\gamma$ -ray induced background process.

The long neutron TOF further rules out  $(n,n')$  or similar reactions in the Si(Li) detector or immediate surroundings, which, with energy  $> 2m_e c^2$ , could lead to a similar "positron" signal. Measurements with a strong Pu-Be neutron source placed outside the solenoid,  $\sim 50$  cm away from the Si(Li) detector, also showed no hint of structure in the positron energy distribution. Direct interaction of neutral radiation in the Si(Li) detector is, of course, very unlikely because of its small solid angle ( $10^{-5}$  of  $4\pi$ ) viewed from the target. As a final test of such processes, a Cm target was bombarded with a 1 PnA 6.0 MeV/u  $^{232}\text{Th}$  beam for  $\sim 2$  hours with the gate valve to the Si(Li) detector closed. Although at least  $\cong 350$  positrons would otherwise have

been detected, no positrons, defined by the standard PPAC-Si(Li)-ARD coincidence, were identified. (In fact, there were no hardware positron triggers.) If due to neutral radiations, about six peak counts should have been recorded with that integrated beam current. On several separate occasions, the magnetic transport field was switched off (for purposes of PPAC calibrations) and similarly no positron events were ever identified.

The TOF arguments could be mitigated if  $\gamma$  or neutron radiation interacted in a region close to the target so that created positrons would be transported to the Si(Li), thereby exhibiting the usual flight-time to the detector. The probability per  $\gamma$ -ray of creating an electron-positron pair in a material with thickness  $t$ , subtending solid angle  $\Delta\Omega$ , is

$$P_{e^+e^-} = (\Delta\Omega/4\pi) (\sigma t \rho N_0/A), \quad (4.1)$$

where  $N_0$  is Avogadro's constant,  $A$  is the target mass number, and  $\rho$  is its density. Using pair production cross-sections  $\sigma$  of [Sto70], a 1500 keV  $\gamma$ -ray produces  $4 \times 10^{-6}$  pairs in a typical  $250 \mu\text{g}/\text{cm}^2$   $\text{ThF}_4$  sandwich target (including the Al frame), and  $1.2 \times 10^{-6}$  pairs in the spiral baffle (which subtends  $9 \times 10^{-3}$  of  $4\pi$  sr). By comparison, internal pair creation (IPC) in the target produces about  $2 \times 10^{-4}$  pairs per  $\gamma$ -ray. Positrons produced elsewhere, e.g., in the vacuum chamber walls or PPAC's, are emitted off-axis and spiral back into the spectrometer wall and are thus prevented from reaching the detector. External pair creation (EPC) is smaller by a factor of  $\sim 50$  than IPC (which accounts for  $\sim 25\%$  of the positron yield in Th+Cm). It can therefore account for at most 0.5% of the total positron yield. Moreover, the continuous  $\gamma$ -ray energy distribution leads to a broad positron spectrum of which only  $\sim 15\%$  of the intensity is between  $300 < E_{e^+} < 400$  keV. This is further distributed throughout the HI scattering angle range, which reduces the EPC portion in the peak energy region by a factor of  $\sim 10$ . The expected contribution to the positron peak intensity from external conversion in each of the spectra of Fig. 3-16 is therefore  $N_{\text{EPC}} \leq 1$  count. Similar arguments rule out prompt neutron reactions in the target and baffle material as well.

The prompt relationship between the positron arrival time in the Si(Li) and the heavy-ion collision also precludes an explanation for the peaks involving steady-state backgrounds or very long source lifetimes ( $> 10^{-8}$  sec). For example, if natural room backgrounds or cosmic rays were to produce monoenergetic positrons, their

contribution would be evenly distributed in arrival time and would therefore be eliminated from the net positron yield by the chance coincidence subtraction. Positrons emitted from  $\beta^+$  decay of the radioactive Cm target or from material near the target activated by the heavy-ion beam (e.g., diagnostic grid, target frame, or PPAC's) also exhibit long decay times (on the order of seconds to years) and are similarly subtracted. Beam-off measurements of Si(Li)-ARD coincidences indicate that these backgrounds are detected with a  $\sim 30$  Hz rate. (The PPAC-Si(Li)-ARD rate is zero.) Within the prompt  $\sim 20$  ns HI-positron coincidence time,  $\sim 6$  chance coincidence events are expected per 10,000 total positrons (including the  $\cong 20\%$  UNILAC duty cycle.) The yield for  $300 < E_{e^+} < 400$  keV is therefore  $< 1$  event, distributed over the entire PPAC angular range, per experiment. As mentioned above, this chance background is, on the average, properly subtracted. In any case, the energy distribution (which is dominated by  $^{248}\text{Cm}$   $\beta^+$  decay) is broad and structureless near 350 keV.

Together with the prompt time relationship between the arrival of a signal in the Si(Li) detector and the detection of 511 keV photons in the ARD (see Fig. 3-3c), Fig. 4-1 constitutes convincing proof that the observed peak events actually represent positrons, incident in the Si(Li) detector, which are emitted from or near the target in prompt time coincidence with the HI collision. The correlations of positron peak production with the HI scattering angle and projectile energy all argue against a simple explanation of the positron peak in terms of a pathological response of the EPOS solenoid to the continuous distribution of dynamic positrons. From the discussion of Chap. 2.2.5, it is clear that the continuous dynamic and nuclear positron backgrounds do not produce narrow structure as a result of the spectrometer acceptance. Measurements of  $\beta^+$  decay sources, e.g., Fig. 2-20, exhibit smooth structureless spectra. Even the Doppler broadened lineshape, which integrates the oscillating detection efficiency of Fig. 2-17 over a range of correlated energies and emission angles, shows no measurable fine structure beyond the central-dip of Fig. 2-26 which is understood simply from the broad features of the EPOS acceptance. Unless dynamic positrons are emitted with a strong and unusually sharp correlation between energy and angle, the continuous distributions cannot produce peak-like structures in the data. The original monopole calculations of the Frankfurt group showed that atomic positrons are emitted isotropically. More recent calculations [Gra87] indicate that there is a  $(1 + \alpha \cos \theta_{e^+}^*)$  distribution between positrons and electrons emitted in coincidence from HI collisions, but positron emission is still presumably nearly isotropic with respect to the CMS motion. Various positron

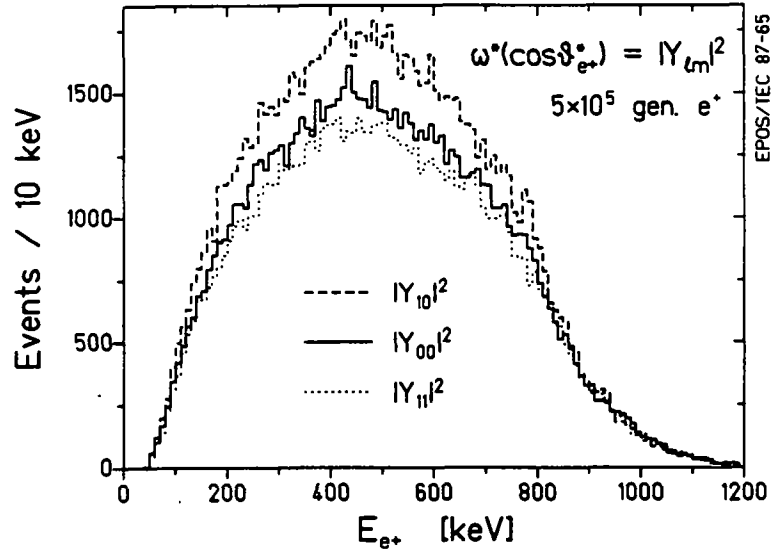


**Figure 4-2.** MCSPEC calculations of dynamic positron energy distributions assuming emission from CMS either isotropically (solid curve), or with  $\omega(\theta_{e+}^{cm}) = |Y_{10}|^2 = \cos^2\theta_{e+}$  (dashed) or  $|Y_{11}|^2 = \sin^2\theta_{e+}$  (dotted) angular distributions.

emission distributions have been modelled with the MCSPEC code described in App. C. Figure 4-2 presents Monte-Carlo simulations of dynamic positron emission assuming angular distributions of the form  $\omega(\cos\theta_{e+}^*) \propto |Y_{\ell m}|^2$  with respect to the beam direction. If dynamic positrons are not emitted isotropically from the CMS, Fig. 4-2 indicates that the absolute detection efficiency may vary by up to  $\sim 20\%$ . However, as long as the distribution  $\omega(\cos\theta_{e+}^*)$  is independent of, or varies smoothly with,  $E_{e+}^*$ , no significant structures in the positron energy distribution are produced.

Emission of a continuous distribution of positrons away from the solenoid axis also does not produce narrow structure. Figure 4-3 presents a direct measurement of positrons detected for various off-axis positions of a  $^{22}\text{Na}$   $\beta^+$  source. As described in Sec. 2.2.6, the detection efficiency for low energy positrons decreases more quickly than for higher energies, and only certain ranges of emission angles are accepted. For distances of  $\cong 25$  mm off axis, the low energies are suppressed such that a small enhancement near 350 keV remains. However, the detection efficiency also decreases by an order of magnitude compared to emission from the target. If off-axis emission of continuous positrons is associated with a moving source of life-

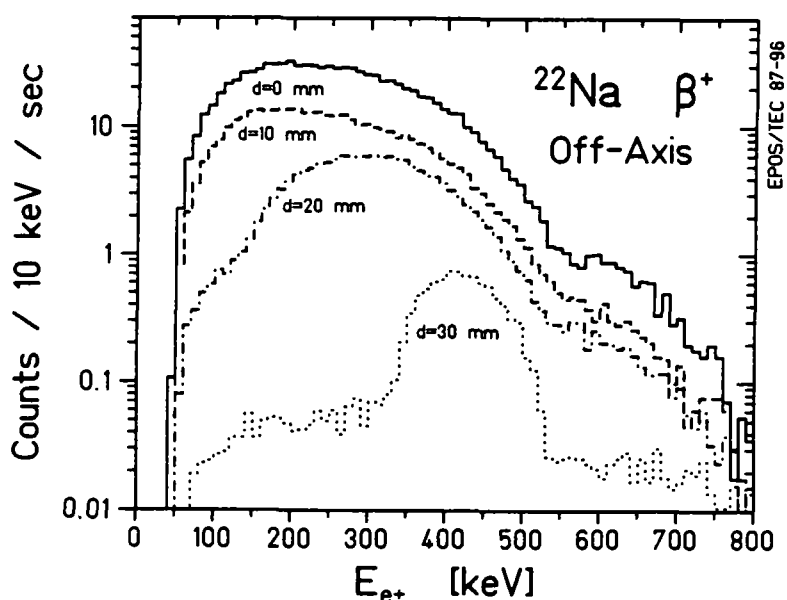


**Figure 4-3.** Measured positron energy spectra for  $^{22}\text{Na}$  source positioned  $d_{\perp} = 0, 10, 20,$  or  $30$  mm off-axis as marked.

time  $\tau \geq (25 \text{ mm}/v_{em})$ , folding the decay probability,  $e^{-t/\tau}$ , with the spectra of Fig. 4-3 results in a broad distribution with a negligible bump near  $E_{e+}^{\text{max}}$ .

Finally it should be noted that the positron peaks have been observed over a period of six years with different configurations of the EPOS spectrometer. The first peak was detected in U+Cm collisions with a completely different spiral baffle (22 blades oriented at  $57^{\circ}$ ), Si(Li) detector (not front sensitive), and magnetic field ( $\theta_{\text{mir}} = 137^{\circ}$ ). These combined to produce a factor of two lower detection efficiency and, because of the large number of baffle blades, a more uniform acceptance in  $\phi$ . Including Part II of this thesis, measurements with the present baffle and detector have revealed peaks for two different magnetic field configurations. Similar peaks have also been observed in U+U and U+Th collisions in an apparatus using a completely different detection technique and beset with different instrumental backgrounds [Cle84, Tse85]. With the exception of Th+Ta, all the structures have been reproduced in subsequent EPOS beamtimes, and the Th+Ta peak was observed separately at two different beam energies. In the most recent positron-electron coincidence experiments, discussed in Part II of this dissertation, the  $\cong 320$  keV peak in Th+Th collisions has even been detected in the total positron distribution accumulated with thin targets – independent of kinematic cuts on the HI scattering an-

gles. Clearly the positron peak structures of Fig. 3-16 are not attributable to any known background process, nor are they connected with a trivial instrumental effect.

## Section 4.2 Nuclear Conversion Processes

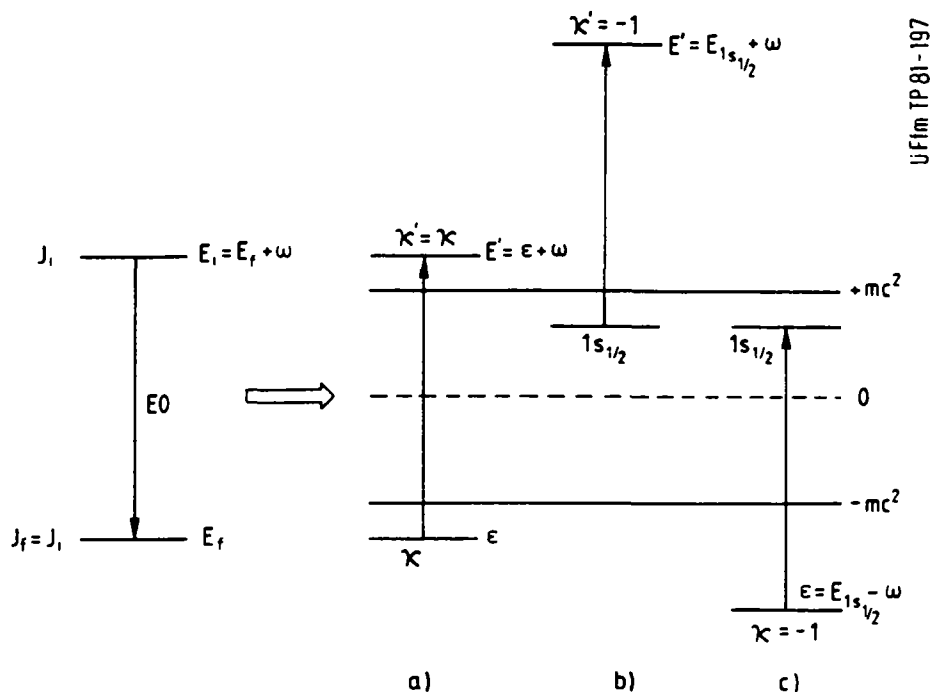
### Sec. 4.2.1 Conversion Processes and Coefficients

The only conventional source of structure in the energy distribution of positrons from HI collisions is Internal Pair Creation (IPC) from transitions between excited states in either the scattered projectile or target recoil nuclei. As shown in Fig. 4-4, which summarizes the various decay modes of a nuclear transition of energy  $W$ , the energy spectrum of IPC positrons is broad and continuous up to a maximum value,  $E_{\max}^{e^+} = W - 2m_e c^2$ . The positron spectrum is roughly triangular, peaking at higher energies due to Coulomb suppression of low energy positron emission in the field of the  $Z \cong 92$  nucleus. Figure 4-5 presents the shape of the IPC distribution after correcting for the response of the EPOS spectrometer including Doppler broadening associated with the velocity of the emitting nucleus. An IPC "peak" centered at  $\cong 320$  keV has a FWHM of  $\cong 230$  keV, which is far in excess of the  $\sim 70 \pm 10$  keV widths measured in the superheavy collision systems.

Figure 4-6a presents a quantitative comparison of the IPC positron lineshape to the peak at  $316 \pm 10$  keV observed in U + Cm collisions [Shw83]. The dashed background curve is determined by correcting the continuous dynamic and nuclear contributions for transport efficiency and detector response. It is normalized to the data excluding an energy region around the peak ( $200 \leq E_{e^+} < 400$  keV). The positron spectrum for the individual nuclear IPC transition, corrected for Doppler broadening and EPOS response, is then added to the background, and its position and intensity was varied to maximize the log-likelihood function, equivalent to maximizing

$$\ln(L) = \sum_i [n_i \cdot \ln(f_i) - f_i], \quad (4.2)$$

where  $n_i$  and  $f_i$  denote the number of measured and predicted positrons in the  $i^{\text{th}}$  energy bin, respectively. A Pearson goodness-of-fit test within the 200 keV "peak" interval yields a reduced  $\chi^2$  of 19.92/8 d.o.f., evaluated for the best-fit transition energy using  $E_{\max} = 383$  keV. The low statistical probability of this fit, 1.06%, corroborates the visual impression that the IPC lineshape is a poor match to the



UFlm TP 81-197

**Figure 4-4.** Diagram of possible electromagnetic decay modes of nuclear transitions. (A) Internal pair creation, (B) internal K-shell electron conversion, and (C) monoenergetic positron creation. (Reproduced from [Shi81].)

data. Similar results are obtained for each of the positron peaks presented in Chapter 3. It is apparent that conventional internal pair creation, an inherently 3-body process, leads to energy distributions too broad to explain the observed positron lines.

A related conversion process, Monoenergetic Positron Creation (MPC), first proposed by L.A. Sliv [Sliv49], however, leads to a two-body final state, producing monoenergetic positrons. As indicated in Fig. 4-4, in MPC the electron of an internally created pair is bound in an empty atomic  $1s$  orbital. The liberated positron is emitted with fixed energy,  $E_{e^+} = W - 2m_e c^2 + |E_K^B|$ , i.e., shifted above  $E_{\max}^{IPC}$  by the K-shell binding energy. This rare process has been observed following K capture in decays of  $^{205,206}\text{Bi}$  [Bru59, Lei61, Per62, Per62b, Wie63] and  $^{152}\text{Eu}$  [Vas60, Per62c, Shi64], with total probabilities of  $\sim 10^{-5}$ . In HI collisions, the short K-vacancy lifetime,  $\sim 10^{-17}$  sec, compared to typically longer nuclear transition times  $\sim 10^{-13}$  sec, and the low K-hole production probability  $P_K \leq 10\%$ , combine to suppress this decay mode by an additional factor of  $\sim 10^5$ , or in total by about  $10^9$  compared to  $\gamma$ -ray emission.

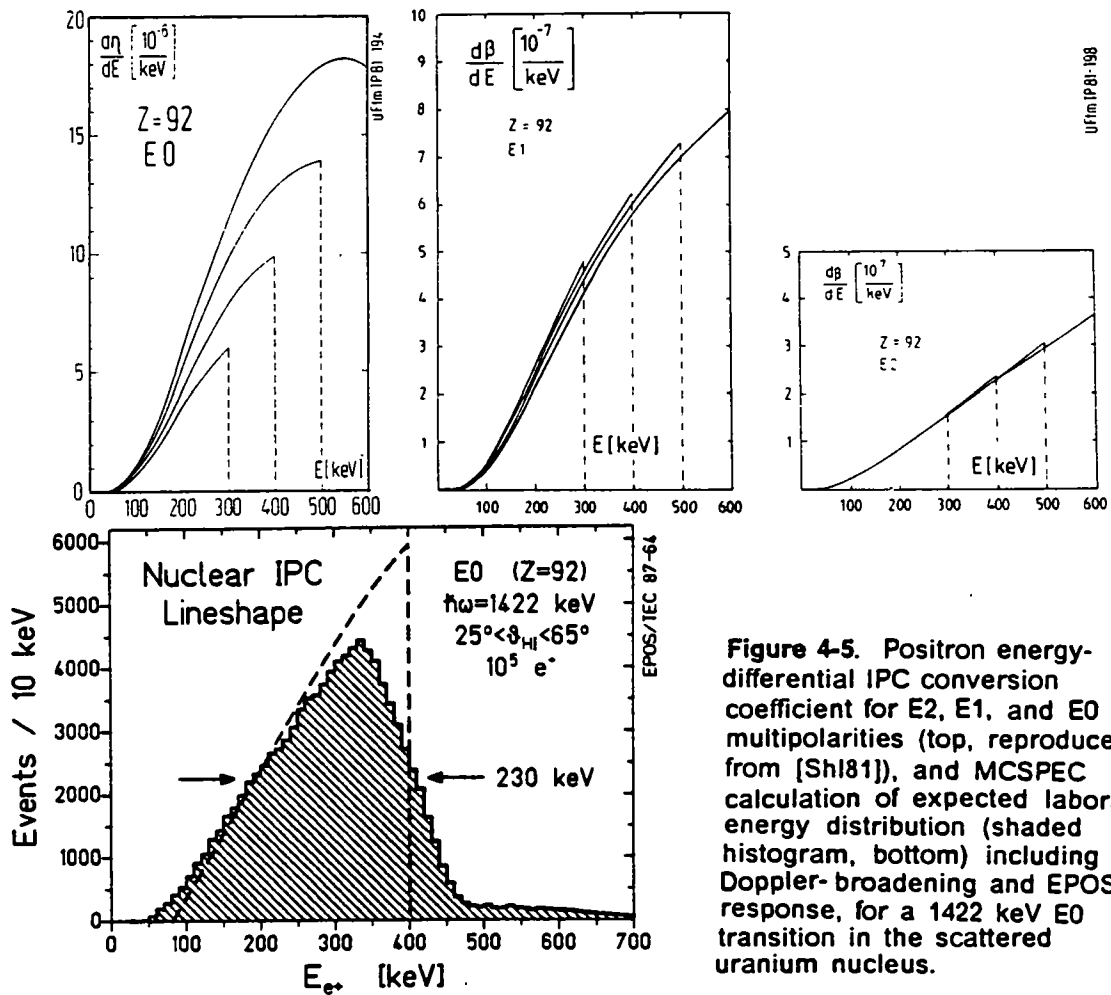


**Figure 4-5.** Positron energy-differential IPC conversion coefficient for E2, E1, and E0 multiplicities (top, reproduced from [Sh181]), and MCSPEC calculation of expected laboratory energy distribution (shaded histogram, bottom) including Doppler-broadening and EPOS response, for a 1422 keV E0 transition in the scattered uranium nucleus.

In the laboratory, the width of an MPC positron line is given by kinematic Doppler broadening associated with the velocity of the emitting nucleus. In the example of Fig. 4-6a, the positron peak is observed between  $28^\circ \leq \theta_{HI} \leq 40.5^\circ$ , corresponding to a mean emitter velocity of either  $0.063c$  or  $0.093c$  for the projectile-like or target-like nucleus respectively. Figure 4-6b,c compares these possibilities with the data, again with transition energy and intensity taken as fit parameters. The  $\chi^2$  and corresponding probability for each possibility are:  $\chi_{fast}^2 = 2.15$  ( $P_{\chi^2} = 0.035$ ), and  $\chi_{slow}^2 = 1.38$  ( $P_{\chi^2} = 0.21$ ), respectively. Although the large linewidth associated with emission from the faster ejectile does not appear to match the data, emission from the slower nucleus cannot be ruled out. This rare process is therefore a possible candidate explanation for the positron peaks. A comparison of the expected line width with the other measured positron peaks, and a detailed analysis of their Doppler lineshape, are presented in Sec. 4.3.

Apart from the positron peak linewidths, the suitability of IPC and MPC nuclear decays in describing the observed lines can be investigated by searching for the

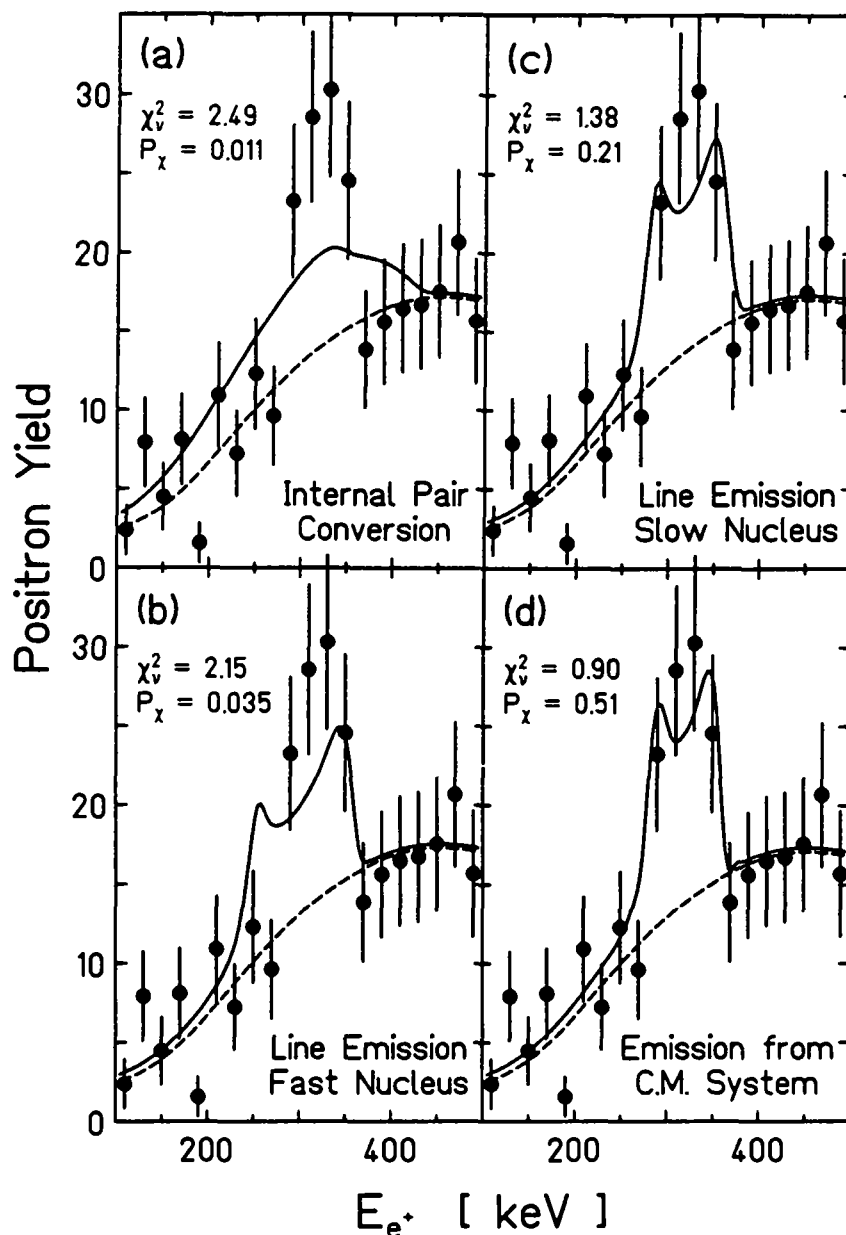


**Figure 4-6.** Maximum-likelihood fits, to the U+Cm data of [Shw83], of the lineshapes expected from IPC and monoenergetic  $e^+$  emission from the scattered nuclei of CM system. The peak intensity, position, and the magnitude of the continuous background (dashed lines) are simultaneously fit to the energy range  $100 < E_{e^+} < 1000$  keV. Pearson  $\chi^2$  is quoted for a 200 keV region around the peak.

competing  $\gamma$ -ray or Internal Conversion (IC) electron peaks which must accompany the positron emitting transition. The expected  $\gamma$ -ray or electron peak intensities are related to the observed positron line by the relative transition mode branching ratios, and their respective detection efficiencies. The absolute transition rate, from

Fermi's Golden Rule, is proportional to the square of an integral of the transition operator times the overlap of the well-known electron or positron wavefunctions and the initial and final state, model-dependent nuclear wavefunctions. Most of the nuclear structure dependence approximately drops out by taking ratios of the competing transition probabilities, leaving well-defined and, for the most part, experimentally verified relations of conversion coefficients.

Usually, the transition probabilities are normalized to the probability of the  $\gamma$ -ray decay mode,  $P_\gamma$ . The relative probability of internal pair creation is denoted by  $\beta$  which is the integral of the differential pair creation coefficient in Eqn. 3.6,

$$\beta = \int_0^{E_{\max}} (d\beta/dE_{e^+}) dE_{e^+}. \quad (4.3)$$

The probability of internally converting a K-shell electron (assuming a filled 1s orbital) is

$$P_{IC} = \alpha_K \cdot P_\gamma, \quad (4.4)$$

while the transition probability for monoenergetic positron creation associated with binding the electron in an empty K-orbital is

$$P_{MPC} = \alpha_K^{e^+} \cdot P_\gamma. \quad (4.5)$$

In addition, as pointed out in [Sh183], the MPC process is proportional to the number of K-shell vacancies,  $x$  ( $0 \leq x \leq 2$ ), into which the created electron can be bound, while Internal Conversion (IC) is proportional to the number of K-electrons,  $(2-x)$ , which can be ejected. The positron and electron emitting transition probabilities are therefore

$$P_{IPC} = \beta \cdot P_\gamma, \quad (4.6a)$$

$$P_{MPC} = (x/2)\alpha_K^{e^+} \cdot P_\gamma, \text{ and} \quad (4.6b)$$

$$P_{IC} = (1-x/2)\alpha_K \cdot P_\gamma. \quad (4.6c)$$

Each of these conversion coefficients depends on the transition energy and multipolarity. The shape of  $d\beta/dE_{e^+}$  and the magnitudes of  $\beta$  and  $\alpha_K^{e^+}$  are shown in Fig. 4-7 [Sh183] for transition energies of  $W \cong 1340$  or  $1450$  keV, appropriate to explain a 320 keV positron peak by either IPC or MPC, respectively.

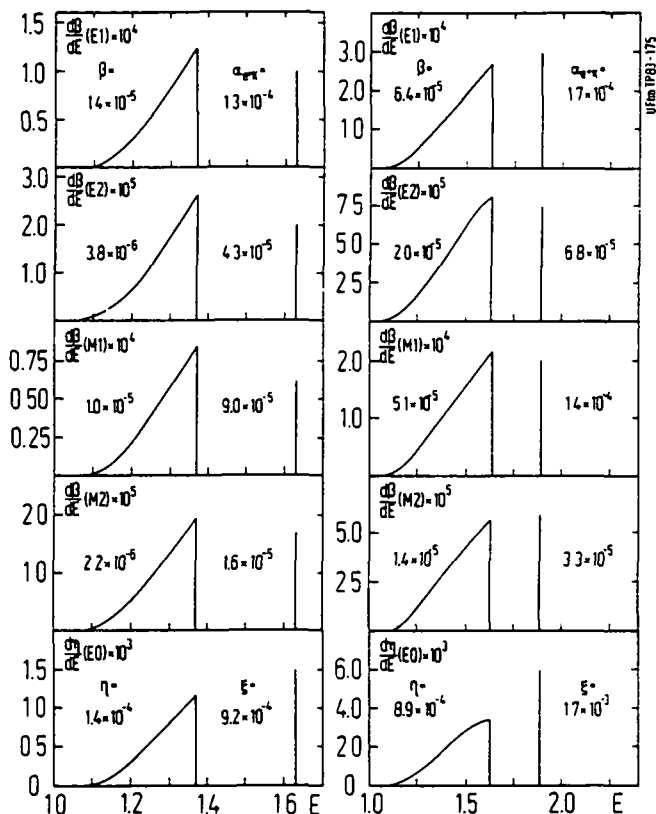


**Figure 4-7.** Theoretical conversion coefficients  $d\beta/dE_{e^+}$ ,  $d\eta/dE_{e^+}$ ,  $\alpha_K^{e^+}$ , and  $\xi$ , for E1, E2, M1, M2, and E0 multipolarities, assuming a 320 keV positron peak is produced by IPC (left) or MPC (right). (Reproduced from [Shl83].)

In the special case of Electric Monopole transitions (e.g.,  $0^+ \rightarrow 0^+$ ), where there is no change in total angular momentum or parity between the initial and final nuclear states, nuclear decay by single photon emission is forbidden because a  $\gamma$ -ray carries one unit of angular momentum. The second-order two-photon decay process is suppressed by order  $\alpha^2$ , and IC normally dominates the transition. Schlüter et al. [Shl83], normalize the positron emitting transition probabilities to internal conversion,

$$P_{IPC} = (1-x/2)^{-1} \eta P_{IC}, \text{ and} \quad (4.7a)$$

$$P_{MPC} = (2/x-1)^{-1} \xi P_{IC}. \quad (4.7b)$$

In the following discussion, interaction with the atomic electrons is limited to the K-shell. IC of higher shells (usually occurring with  $< 10\%$  of the neutral atom K-shell

rate) becomes important only for extreme cases when the 1s orbital is almost completely ionized.

### Sec. 4.2.2 Comparison with $\gamma$ -Ray Data

For  $N_O$  decays of a particular nuclear transition, the number of observed peak positrons and  $\gamma$ -rays, given the emission probabilities  $P_{e+}$  and  $P_\gamma$ , are

$$N_{e+} = N_O \cdot P_{e+} \cdot \epsilon_{e+}^{pk} / SD_{e+}, \text{ and} \quad (4.8a)$$

$$N_\gamma = N_O \cdot P_\gamma \cdot \epsilon_\gamma^{pk} / SD_\gamma, \quad (4.8b)$$

where  $\epsilon_{e+}^{pk}$  and  $\epsilon_\gamma^{pk}$  denote the positron and  $\gamma$ -ray peak detection efficiencies and  $SD_i$  are the event-type scaledowns including deadtime, as defined in Eqn. 2.85. If a peak due to a nuclear conversion were found in the positron energy distribution under certain kinematic conditions (e.g., HI angle cuts), the  $\gamma$ -ray energy spectrum, under identical conditions, should then exhibit a conversion line having an intensity

$$N_\gamma = (\epsilon_\gamma^{pk}/SD_\gamma) \cdot (SD_{e+}/\epsilon_{e+}^{pk}) \cdot (P_\gamma/P_{e+}) \cdot N_{e+}, \quad (4.9)$$

where  $P_{e+}$  denotes either  $P_{IPC}$  or  $P_{MPC}$ . The negative result of a search in the simultaneously measured  $\gamma$ -ray energy spectrum for a peak of sufficient intensity to account for the corresponding positron line would therefore constitute evidence against a positron peak origin based on nuclear conversions.

In the U+Cm system reported by [Shw83], a clear positron peak is observed at  $E_{e+} = 316 \pm 10$  keV with  $N_{e+} = 50 \pm 10$  counts. Figure 4-8a shows the corresponding  $\gamma$ -ray energy distribution for identical runs and HI scattering angle cuts. Inserting the appropriate efficiencies and coefficients, Eqn. 4.9 predicts  $\cong 5300 \pm 1060$   $\gamma$ -ray peak counts for an electric dipole (E1) IPC process. Since it is not *a priori* known which nuclide emits the positron line, a worst case is assumed by dividing the intensity equally between the U-like and the Cm-like ejectiles. These are scattered into different lab angles, with differing velocities and orientations with respect to the  $\gamma$ -ray detector. The energy distribution for each is Doppler shifted by

$$E_\gamma^{lab} = \hbar\omega[\gamma_{em}(1 - \beta_{em}\cos\theta_{\gamma p})]^{-1}, \quad (4.10)$$

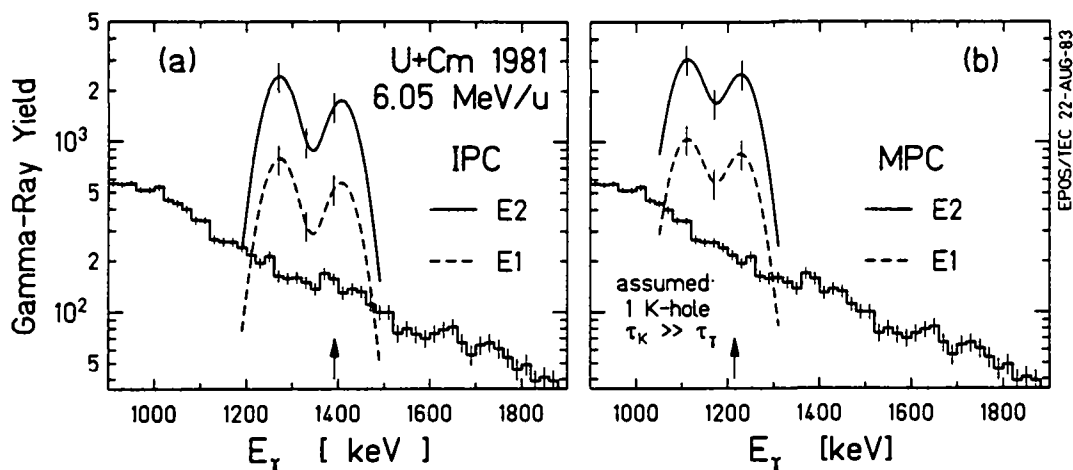


**Figure 4-8.** Simultaneously measured U+Cm  $\gamma$ -ray energy distribution under identical kinematic conditions as the peak in Fig. 1-1a. Solid and dashed curves present the absolute  $\gamma$ -ray intensity required to explain the  $e^+$  peak by IPC or MPC.

and broadened by the detector resolution ( $\Delta E \sim 90$  keV), leading to the double-humped shape shown in Fig. 4-8. The transition energy is taken from the fit of Fig. 4-6a,  $\hbar\omega = 1405$  keV. The structure is not added to the continuous  $\gamma$ -ray distribution but plotted over it in absolute scale. Clearly, for E1 and all higher multiplicities, the  $\gamma$ -ray intensity required to explain the positron line in terms of IPC exceeds the measured yield by an order of magnitude. The IPC process is therefore ruled out as a possible origin. A statistical comparison of the required  $\gamma$ -ray line to the structureless measured spectrum yields a reduced- $\chi^2$  of  $\sim 19$ .

Part (b) of Fig. 4-8 shows the same data assuming MPC as the positron line origin. The  $\gamma$ -ray energy necessary to produce the positron peak is reduced relative to that of part (a) by the K-shell binding energy ( $E_B \cong 115$  keV, or  $\hbar\omega \cong 1290$  keV). The expected  $\gamma$ -ray intensity is

$$N_{\gamma} = (\epsilon_{\gamma}^{\text{pk}} / \text{SD}_{\gamma}) \cdot (\text{SD}_{e^+} / \epsilon_{e^+}^{\text{pk}}) \cdot (2/x \alpha_K^{e^+}) \cdot N_{e^+}, \quad (4.11)$$

inversely proportional to the number of K-holes. The lines are drawn in absolute scale for  $x=1$  K-hole. As mentioned above, K-vacancy production probabilities ( $P_K \sim 10^{-1}$ ) and lifetimes ( $\tau < 10^{-15}$  s) consistent with existing atomic physics data imply  $x \leq 10^{-5}$ , leading to an expected  $\gamma$ -ray peak  $10^6$  larger than the measured intensity. In the extreme case that two K-holes are present, the plotted line is reduced

by a factor of two, but is still inconsistent with the data (reduced  $\chi^2 = 19$ ). Independent of the K-vacancy probability or lifetime, IPC and MPC are therefore completely ruled out as possible explanations for the observed positron peaks for nuclear transition multipolarities of E1, M1 and higher.

The other supercritical collision systems exhibit similarly smooth  $\gamma$ -ray spectra. As discussed in Sec. 3.3, only for Th+Ta collisions have significant structures been observed in the  $\gamma$ -ray energy distribution. Figure 4-9 compares the analysis of the expected dynamic plus nuclear continuum distribution described in Sec. 3.3 for the total PPAC angular range (a,b) to that for the positron peak cut of Fig. 3-15 (c,d) for 5.75 + 5.80 MeV/u Th+Ta collisions. The  $\gamma$ -ray energy distributions (b,d) have been unfolded, divided by detection efficiency (including scaledown and deadtime), transformed to the emitting frame, and normalized to the number of scattered ions in the angular region. As described in Sec. 3.3, the  $\gamma$ -ray peaks at 1250, 1400, and 1550 keV were Doppler corrected for emission from  $^{181}\text{Ta}$ , and the underlying continuum was averaged for equal emission from the Ta and Th ejectiles.

The  $\gamma$ -ray lines are equally intense in both spectra while the positron peak is only observed in part (c). The curves through the positron spectra represent the dynamic plus nuclear pair creation yields calculated by Schweppe [Shw85b] from the corresponding  $\gamma$ -ray distributions. The  $\gamma$ -ray continuum and the peaks were treated separately assuming a "worst case" E1 multipolarity for the latter (i.e., maximum  $e^+$  yield). The shaded portion of the positron distribution denotes the contribution from the  $\gamma$ -ray lines alone. The empirical continuum E1/E2  $\gamma$ -ray multipolarity (see Fig. 3-8c) was adjusted to fit the total spectrum. The multipolarity parameterization and absolute normalization are identical for both Figs. 4-9(a) and (c).

Clearly, neither the narrow width nor the intensity of the positron line can be explained by the  $\gamma$ -ray structures. Figure 4-10 extends this result to MPC transitions with an analysis similar to that in Fig. 4-8. Because the source is known, the expected  $\gamma$ -ray intensity is properly Doppler shifted and the peak is not double-humped. The presence of the necessary  $\gamma$ -ray peak intensity is completely excluded for all but E1 multipolarity. Quantitatively, at most  $25 \pm 10\%$  of the positron peak area could be accounted for by an E1 nuclear conversion. This analysis therefore safely rules out  $\lambda \geq 1$  nuclear transitions as the origin for the narrow positron peaks for each of the supercritical, as well as the subcritical Th+Ta, systems measured.

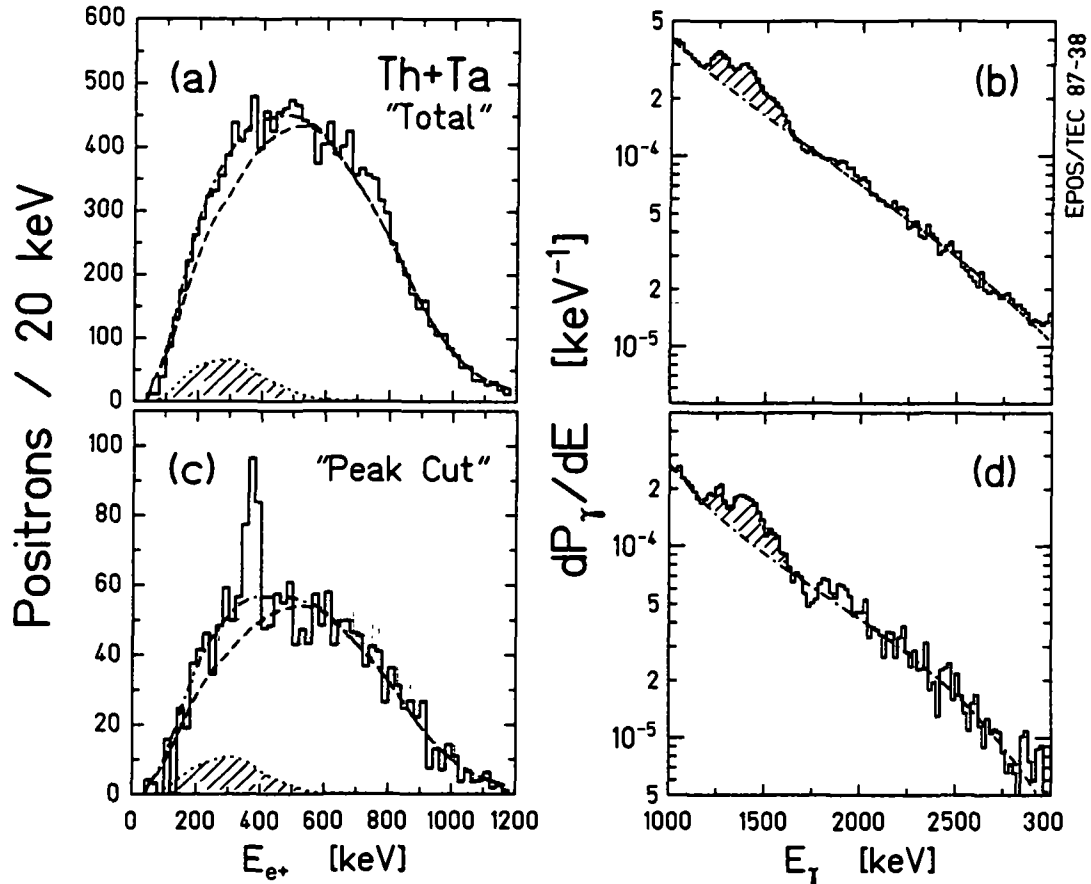


**Figure 4-9.** Positron and  $\gamma$ -ray energy spectra from Th+Ta collisions for total detected scattering angle range (a,b) and kinematic region which reveals the peak of Fig. 3-15 (c,d). Curves through the positron data represent the dynamic plus nuclear IPC yields, calculated from the simultaneously measured  $\gamma$ -rays. The shaded region denotes the contribution from the  $\gamma$ -ray line structures.

### Sec. 4.2.3 Electron Data and E0 Transitions

As noted above, for E0 transitions the  $\gamma$ -decay channel is inhibited so one must search for the associated internal conversion electron line which competes with the hypothetical positron emitting nuclear transition. For either IPC or MPC, the kinetic energy of the ejected K-electron is the nuclear transition energy minus the K-shell binding energy,  $E_{e^-} = \hbar\omega - |E_B|$ . As discussed in Sec. 2.5, the FWHM of the expected electron peak is  $\Delta E_{e^-} \sim 90$  keV, including the acceptance of the cylindrical baffle, the detector resolution, and the azimuthal range of scattered nuclei. The number of expected peak electrons is

$$N_{e^-} = (\epsilon_{e^-}^{pk} SD_{e^-}) \cdot (SD_{e^+} / \epsilon_{e^+}^{pk}) \cdot (P_{IC} / P_{e^+}) \cdot N_{e^+} \quad (4.12)$$

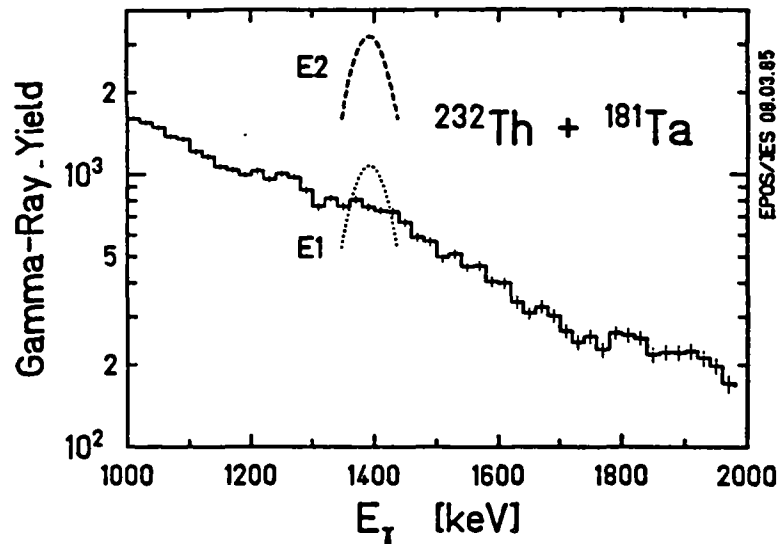


**Figure 4-10.**  $\gamma$ -Ray energy distribution measured simultaneously under identical kinematic conditions as the Th+Ta positron peak, not corrected for Doppler shifts, efficiencies, or detector response. Solid and dashed curves present the absolute  $\gamma$ -ray intensity required to explain the  $e^+$  peak by an IPC transition in the tantalum nucleus.

For both the IPC and MPC mechanisms, the IC channel represents a competing transition mode, so the corresponding peak intensities vary inversely with the number of available K-vacancies:

$$N_{e^-}^{\text{IPC}} = N_{e^+} \cdot (\epsilon_{e^-}^{\text{pk}} y_{\text{SD}_{e^-}}) \cdot (\text{SD}_{e^+} / \epsilon_{e^+}^{\text{pk}}) \cdot (1-x/2) / \eta \quad (4.13)$$

$$N_{e^-}^{\text{MPC}} = N_{e^+} \cdot (\epsilon_{e^-}^{\text{pk}} y_{\text{SD}_{e^-}}) \cdot (\text{SD}_{e^+} / \epsilon_{e^+}^{\text{pk}}) \cdot (2/x-1) / \xi. \quad (4.14)$$

For the unlikely case that two K-holes survive until the E0 transition occurs, the IC electron peak vanishes completely.

Figure 4-11 presents the simultaneously measured electron spectrum corresponding to the HI angular cut associated with the positron peak in U+Cm of Fig. 3-16 [Cow85]. Shown superimposed, not added to the data, are the IC electron peaks expected for an IPC or MPC positron peak origin, plotted for  $x = 1$  K-hole present when the transition occurs. The observed structureless spectrum places a limit on the possible intensity of the competing electron peak,  $N_{e^-}$ , determined by a  $\chi^2$  comparison of the underlying continuous electron spectrum ( $n_{\text{obs}}(E_{e^-})$ ) to the expected ( $n_{\text{exp}}(E_{e^-}) = \text{peak} + \text{continuum}$ ),

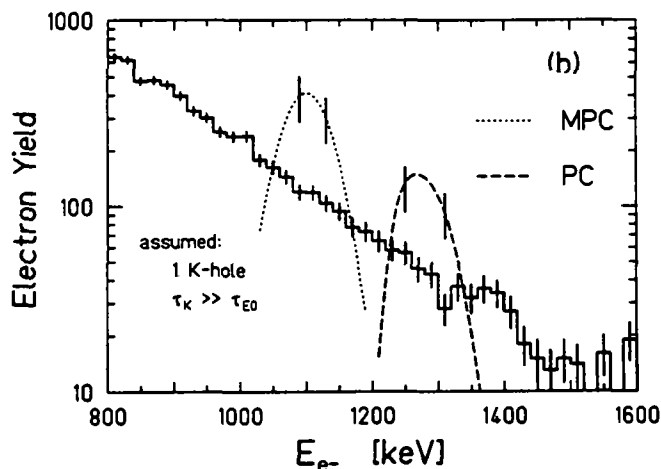


**Figure 4-11.** Electron energy distribution from 6.04-6.13 MeV/u U+Cm collisions measured simultaneously under identical kinematic conditions which produce the positron peak. Dashed and dotted curves present the absolute IC electron peak intensity, plotted for  $x=1$  K-hole, required to explain the  $e^+$  line by nuclear IPC or MPC transitions.

$$\begin{aligned}\chi^2 &= \sum_i (n_{\text{exp}} - n_{\text{obs}})^2 / n_{\text{exp}} \\ &= \sum_i (N_{e^-} \cdot f_i)^2 / (n_i + N_{e^-} \cdot f_i).\end{aligned}\quad (4.15)$$

In Eqn. 4.15,  $n_i$  denotes the contents of each  $E_{e^-}$  bin,  $f_i$  is the spectral shape of the electron line ( $\sum f_i = 1$ ), and  $N_{e^-}$  is its intensity. Allowing an upper limit on  $\chi^2$  of  $\chi^2(N_{e^-}) \leq 2$ , provides an upper limit on  $P_{e^-}$  ( $\equiv N_{e^-}/N_{\text{HI}}$ ) of  $P_{e^-} \leq 10^{-3}$  per scattered HI (95% C.L.), which from Eqns. 4.13,14 translates into a lower limit on the average number of K-holes required during the transition ( $x_{\text{av}} > 1.9$  at 95% C.L.). This is related to vacancy production and K-hole and E0 transition lifetimes by

$$x_{\text{av}} = x(t=0) \tau_K / (\tau_{E0} + \tau_K). \quad (4.16)$$

Assuming that the K-shell is completely stripped in the collision,  $x(t=0) = 2$ , the K-hole lifetime must still exceed the nuclear decay time by an order of magnitude. Normally, K-vacancies are filled by X-ray cascades from higher shells with a typical lifetime,  $\tau_K \sim 10^{-17}$  sec [Anh75], while the E0 transition decays on a time scale,  $\tau_{E0} \sim 10^{-12}$  sec.

In the case of extreme K-shell ionization, as required above, internal conversion of higher shell electrons represents an important new channel for the nuclear transi-

tion. It occurs at  $\sim 10\%$  of the neutral atom K-conversion rate, i.e., approximately  $10^{-3}$ , which is just the limit on  $P_{e^-}$  extracted from the data. One therefore expects slightly higher deduced  $x_{av}$  values in order to account for the measured positron peaks. Figure 4-12 leads to a somewhat less stringent limit on  $x$  for the Th + Ta system.

**Confidence Intervals and Interpretation.:** The preceding relationship between  $x$ , the number of K-holes at the time of the transition, and the ratio of the K-vacancy to E0 lifetimes, while making clear the need for extreme states of ionization to satisfy the MPC hypothesis, masks one of the striking features of this decay process because it tacitly assumes that all HI scatterings lead to the same degree of ionization. For the extreme case of a completely stripped ion, the IC channel vanishes as illustrated by Fig. 4-13 which traces  $x$  dependence of various decay probabilities relative to  $P_{E0} = 1$ . MPC would then account for most of the total transition probability, and only a small probability for exciting this particular E0 transition ( $P_{E0} \cong P_{MPC} = P_{e^+} \sim 10^{-5}$ ) would be required to account for the positron peak. In principle, at least, excitation of the E0 transition may be correlated to the production of long-living stripped ions, possibly requiring an exotic collision in only a small fraction of scattering processes.

In order to explore this possibility quantitatively, the explicit time dependence of the competing decay modes must be considered. In terms of the total E0 transition probability,

$$\begin{aligned} P_{E0} &= P_{IC} + P_{MPC} + P_{IPC} \\ &= [1 + \eta + (\xi-1)x/2](1-x/2)^{-1} P_{IC}, \end{aligned} \quad (4.17)$$

where 2-photon decay and IC of higher shells are ignored. The individual decay modes are:

$$P_{IC} = P_{E0} (1-x/2) [1 + \eta + (\xi-1)x/2]^{-1}, \quad (4.18)$$

$$P_{IPC} = P_{E0} \eta [1 + \eta + (\xi-1)x/2]^{-1}, \quad (4.19)$$

$$P_{MPC} = P_{E0} \xi [1 + \eta + (\xi-1)x/2]^{-1}. \quad (4.20)$$

The number of nuclear transitions occurring per unit time is

$$dN_{E0}/dt = -(P_{E0}/\tau_{E0}) e^{-t/\tau_{E0}}, \quad (4.21)$$

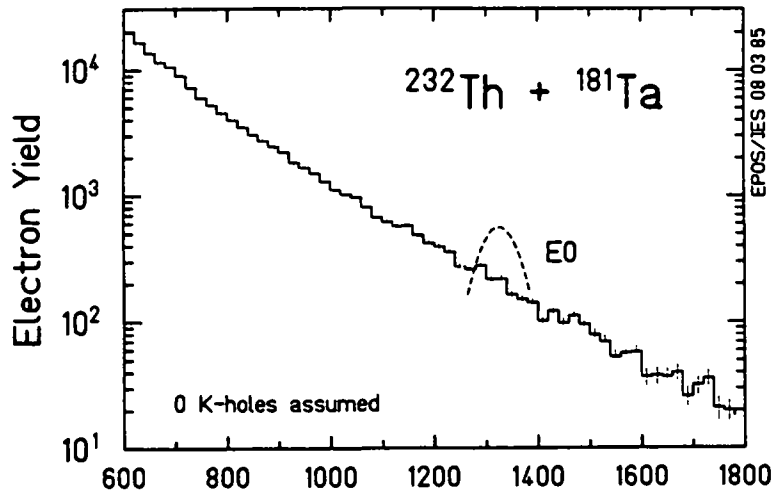


**Figure 4-12.** Same as Fig. 4-11 for Th + Ta electrons, comparing the required IC peak intensity associated with an IPC origin for the positron line.

and the number of available K-holes for the various processes at time  $t$  is

$$x(t) = 2P_K e^{-t/\tau_K}. \quad (4.22)$$

Assuming a distribution of ionic charge states with weight  $w_i$  and corresponding K-shell ionization probabilities  $P_{Ki}$  and lifetimes  $\tau_{Ki}$ , the total Internal Conversion electron production probability is explicitly

$$P_{IC} = \sum_i w_i \int_0^\infty (1 - P_{Ki} e^{-t/\tau_{Ki}}) [1 + \eta + (\xi - 1) P_{Ki} e^{-t/\tau_{Ki}}]^{-1} \cdot (P_{E0}/\tau_{E0}) e^{-t/\tau_{E0}} dt, \quad (4.23)$$

with similar expressions for  $P_{MPC}$  and  $P_{IPC}$ . Letting  $z = e^{-t/\tau_{Ki}}$  and  $a_i = \tau_{E0}/\tau_{Ki}$ , and defining the integrals

$$I_1(P_{Ki}, a_i) = \int_0^1 [1 + \eta + (\xi - 1) P_{Ki} z]^{-1} dz, \quad (4.24)$$

$$I_2(P_{Ki}, a_i) = \int_0^1 P_{Ki} z^{a_i} [1 + \eta + (\xi - 1) P_{Ki} z]^{-1} dz, \quad (4.25)$$

the conversion probabilities for each decay channel are given by

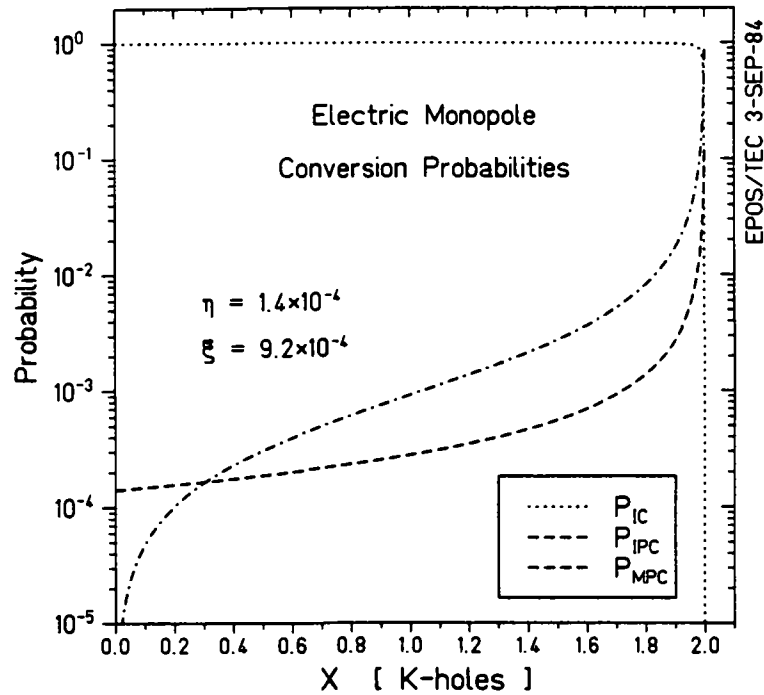


**Figure 4-13.** Branching fractions for IC, IPC, and MPC decay modes of a 1.4 MeV E0 transition in uranium, versus the number of K-shell vacancies present when the transition occurs.

$$P_{IC} = P_{E0} \sum_i [w_i \bullet \{I_1(P_{K_i, \alpha_i}) - I_2(P_{K_i, \alpha_i})\}], \quad (4.26)$$

$$P_{IPC} = P_{E0} \sum_i [w_i \bullet \eta \bullet I_1(P_{K_i, \alpha_i})], \quad (4.27)$$

$$P_{MPC} = P_{E0} \sum_i [w_i \bullet \xi \bullet I_2(P_{K_i, \alpha_i})]. \quad (4.28)$$

To evaluated confidence levels for E0 conversions, we must first consider the attributes of a physically reasonable model. The neutral atom K-vacancy lifetime for  $Z \cong 92$  is  $\tau_K \sim 10^{-17}$  sec [Anh75], falling far short of the typical nuclear electric monopole lifetimes of  $\tau_{E0} \sim 10^{-12} - 10^{-13}$  sec. Atoms with only upper shell electrons (e.g.,  $\geq M$  shell) fill the 1s orbital in  $\leq 10^{-14}$  sec by X-ray cascades [Mok87]. This disparity in lifetime implies that all usual combinations of ionic charge state and K-hole lifetime, e.g., from equilibrium calculations [Nik68], provide filled K-shells within a fraction of the E0 transition time and can be safely treated as approximately neutral atoms for the present analysis. Since even in highly ionized atoms the presence of higher shell electrons still offers a competing IC mode (which should occur on at least the same level as MPC), it is clear that the only scattering events that might

significantly contribute to the MPC or IPC positron yield, while exhibiting no IC electron line ( $P_{e^-}^C < 10^{-3}$ ), are those which produce essentially fully stripped ions.

A physically reasonable, though not necessarily plausible, model therefore consists of a charge distribution with effectively only two components: a fraction,  $f$ , of completely stripped ions, and  $(1-f)$  effectively neutral atoms (which includes all normal atomic ionization processes). Under these assumptions, the transition probabilities become,

$$P_{IC} = P_{E0} [(1-f)/(1+\eta) + f \cdot \{I_1(1,\alpha) - I_2(1,\alpha)\}] , \quad (4.29)$$

$$P_{MPC} = P_{E0} [f \cdot \xi \cdot I_2(1,\alpha)] , \quad (4.30)$$

$$P_{IPC} = P_{E0} [(1-f)\eta/(1+\eta) + f \cdot I_1(1,\alpha)] . \quad (4.31)$$

Inserting the observed magnitude of the positron peak  $P_{e^+}$  in the U+Cm system, and the upper limit (95% C.L.) of  $P_{e^-}$  for the existence of a corresponding K-electron conversion peak, provides a relationship between the necessary fraction of stripped ions and the K-shell lifetime relative to the transition lifetime. As shown in Fig. 4-14, for all levels of ionization a greatly extended K-lifetime, still an order of magnitude larger than  $\tau_{E0}$ , is required. The large fraction of stripped ions ( $f \geq 1.5\%$ ), which given  $\tau_{E0} \sim 10^{-12}$  sec must survive while traversing the target foil, would have been easily detected in previous charge-state measurements [Mao82, Sti86].

The combination of large  $\tau_K$  and large  $f$ , outside the present experience of atomic physics, strongly argues against this very specialized positron emission process. Even if stripped ions were formed, it should be noted that the scattered ion exits through the target material and backing foil characterized by a mean time between atomic collisions of  $10^{-17}$  sec. It is unlikely that a fully stripped ion could traverse  $\sim 100 \mu\text{g}/\text{cm}^2$  of material without capturing several electrons in higher orbitals, which would then radiatively fill the K-shell. Within the context of a nuclear origin, the fact that positron peaks are observed with several combinations of target and projectile nuclei further necessitates the presence of a strong E0 transition of appropriate energy in more than one nuclide, or conversely, that one common nuclear species is created with significant probability via mass transfer in all these collision systems. Finally, the result of the positron-electron coincidence experiment described in Part II of this dissertation indicates that the positron peaks are accompanied by a correlated monoenergetic electron, which does not occur naturally in the context of IPC or MPC processes.

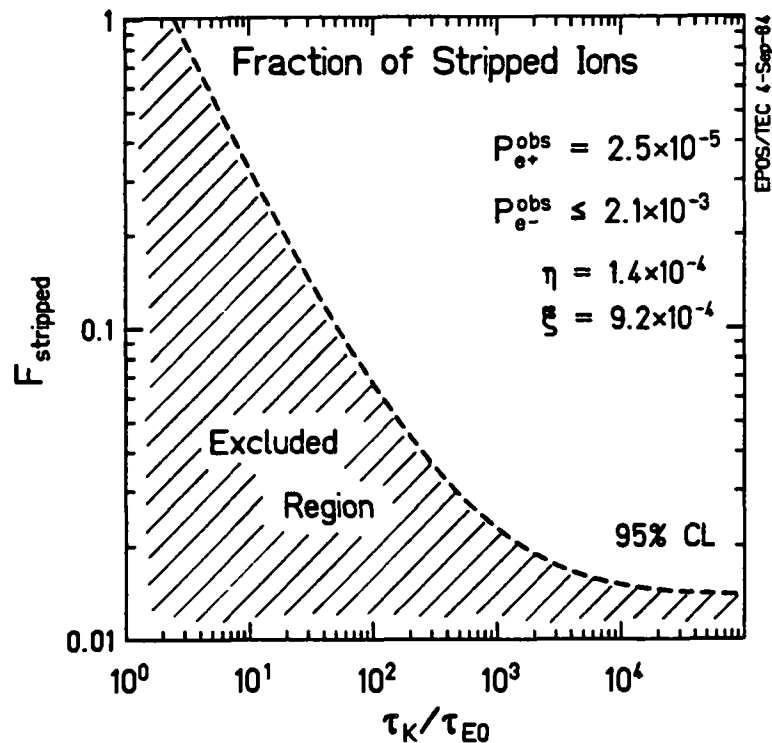


**Figure 4-14.** 95% C.L. limits on minimum fraction of completely stripped ions produced in U+Cm collisions, for a given ratio of K-shell to E0 transition lifetimes, for which the positron peak can be explained as nuclear MPC, in light of the structureless measured electron spectrum.

In conclusion, this investigation of the possibility of a nuclear origin for the observed narrow positron peaks from superheavy collisions has focussed on a search for the  $\gamma$ -ray and internal conversion electron decays which must accompany either an IPC or MPC conversion process. Comparison of the required  $\gamma$ -ray line, based only on the positron peak intensity and known conversion coefficients, to the simultaneously measured structureless photon spectrum completely rules out both of these mechanisms for transitions with multipolarity  $\lambda \geq 1$ . The absence of structure in the simultaneously measured electron spectrum provides a lower limit on the necessary ionic charge and K-hole lifetime necessary to reproduce the positron intensity associated with an E0 transition. The production of significant fractions ( $\geq 1.5\%$ ) of effectively fully stripped  $Z \sim 90$  ions at these beam energies is outside the present experience of atomic physics, and the existence of very long K-vacancy lifetimes,  $\geq 100$  ps, has not been previously observed. On the basis of intensity alone, it therefore appears that no nuclear Internal Pair Creation or Monoenergetic Positron

Conversion process is able to account for the positron lines presented in this dissertation.

### Section 4.3 Measurement of Emitting System Velocity

As described in Chapter 1, one of the principal goals of Part I of this dissertation has been a determination of the velocity of the source emitting the narrow positron peaks, which could provide considerable information regarding their origin. A central portion of Chapter 2 therefore was devoted to understanding the details of the Doppler broadened positron lineshape in the EPOS spectrometer. Its width,  $\Delta E_{e^+} \cong 2(\gamma\beta)_{em} P_{e^+}$  (not including detector resolution), is almost linearly proportional to the mean laboratory velocity of the emitter. An accurate determination of the observed positron peak widths therefore provides an independent discrimination between the specific sources commonly under discussion involving the scattered nuclei or emission from the heavy-ion CMS. Center-of-mass emission would point toward a process involving the quasimolecule, for example, Spontaneous Positron Emission following supercritical binding. An analysis of the widths of the positron peaks presented in Chap. 3, and particularly their dependence on the scattering angle of the heavy-ions, is presented in this section.

As was indicated in Fig. 4-6, fits of the Doppler-broadened lineshape to the positron peak from previous U + Cm experiments [Shw83] already effectively rule out an Internal Pair Creation origin, while allowing for MPC from the slowly moving HI ejectile. An even better fit to the data, however, is provided by assuming that the peak positrons are emitted from the CM system. As shown in Fig. 4-6d, under this assumption, the fit (described in Sec. 4.2.1) yields a  $\chi^2 = 0.90$  and a statistical probability  $P_{\chi^2}$  of 51%. A more effective discrimination between the CM emission and emission from the slow recoiling ion can be attained in the data presented in this work where the line is observed over a wide range of HI scattering angles, including around  $\theta_{lab} \sim 45^\circ$  where the velocities of both recoil nuclei are unambiguously much larger than  $v_{CM}$ .

#### Sec. 4.3.1 HI Scattering Angle Dependence of Peak Width

In addition to the generally larger velocity of the recoiling nuclei compared to  $v_{CM}$ , emission of positrons from the separated nuclei must reflect the characteristic variation of the nuclear velocity as a function of the HI scattering angle. For the nearly

symmetric supercritical collision systems,  $v_{\text{nuc}}$  depends on the cosine of the laboratory scattering angle,

$$v_{\text{nuc}} = 2v_{\text{CM}} \cos\theta_{\text{nuc}} = (2E_0/M_{\text{proj}}c^2)^{1/2} \cos\theta_{\text{nuc}}. \quad (4.32)$$

On the other hand, emission from the CM system exhibits an emitter velocity which is independent of nuclear scattering angle.

Figure 4-15 plots the widths of the positron peaks presented in Chap. 3 versus the mean HI scattering angle in the given kinematic window. The  $\Delta\theta_{\text{HI}}$  range of each HI angle cut is denoted by the horizontal bars. In order to facilitate comparison of the several measurements to the expected width of a monoenergetic positron line emitted from one of the scattered nuclei, the dependence of the Doppler broadening on the mean energy of the emitted positrons and on the masses of the collision partners has been approximately removed. This is accomplished by dividing the experimentally measured positron linewidth by the Doppler-broadened peak width expected for monoenergetic positron emission isotropically from the center-of-mass system. The expected CM lineshape is calculated by the Monte-Carlo program described in App. C, using the measured peak centroid as the energy of the positrons in the CMS. Using this procedure, positron peaks having different mean energies and observed in different collision systems at different bombarding energies may be directly compared because both the positron momentum dependence,  $P_{e^+}^*$ , of the Doppler broadening,  $\Delta E_{\text{Dop}} = 2(\gamma\beta)_{\text{em}} P_{e^+}^*$ , and the dependence of  $\beta_{\text{cm}}$  on the details of the HI collision, have been divided out. The ratio plotted in Fig. 4-15 therefore provides a relative measure of the mean laboratory velocity of the source,

$$\Delta E_{e^+}^{\text{obs}}/\Delta E_{\text{cm}}^{\text{calc}} = \langle (\gamma\beta)_{\text{em}} \rangle / (\gamma\beta)_{\text{cm}},$$

which over the range of interest reduces to the non-relativistic limit,

$$\Delta E_{e^+}^{\text{obs}}/\Delta E_{\text{cm}}^{\text{calc}} \cong \langle v_{\text{em}} \rangle / v_{\text{CM}}. \quad (4.33)$$

The curves in Fig. 4-15 present the expected linewidths for emission from either the fast or slow scattered heavy-ion, normalized to the expected CM Doppler broadening, i.e.,  $v_{\text{nuc}}/v_{\text{CM}} \cong 2 \cos\theta_{\text{nuc}}$ .

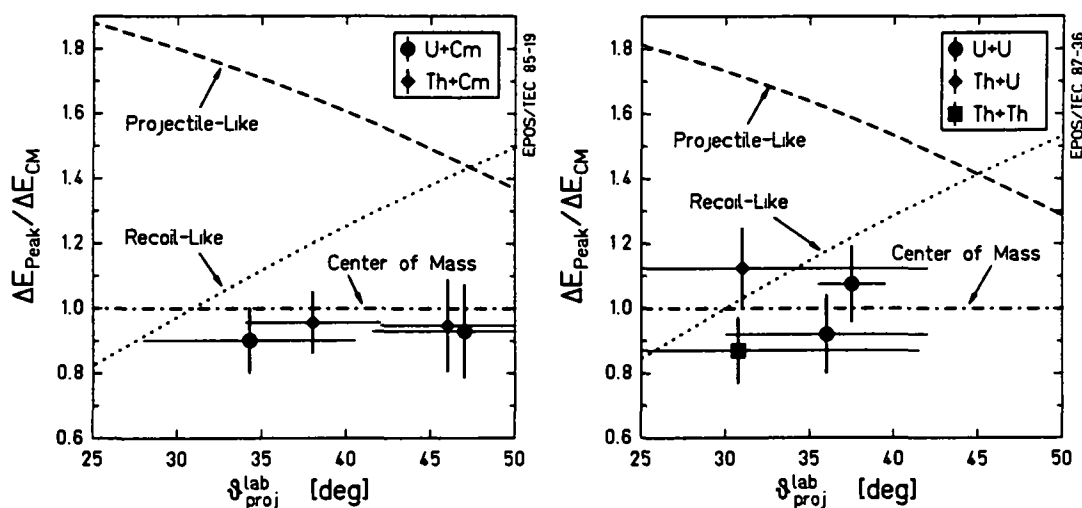


**Figure 4-15.** Plots of the positron peak widths versus the laboratory HI scattering angle. Widths normalized to the  $\cong 2\gamma\beta_{e^+}$  width predicted for emission from the CM system. Dashed, dotted, and dot-dashed curves compare the expected widths for monoenergetic  $e^+$  emission from either the projectile or recoil nucleus, or from the CMS.

The experimental linewidths of the positron peaks were extracted from the measured energy spectra of Fig. 3-16 in a well-defined statistical manner. This involved first fitting the background under the peak by normalizing the continuous dynamic plus nuclear background distribution (whose shape was determined in Sec. 3.3) to the data, excluding a  $\sim 150$  keV wide region centered around the mean peak energy. Within this "peak" interval, the width was then calculated from the standard deviation (equal to the square root of the variance,  $S.D. = V^{1/2}$ ) of the data above the background curve. The variance is defined in the usual way as the mean-square deviation of the positron energies about the mean energy. Including a correction for the bin-width,  $\Delta$ , of the histogrammed data, it is given by,

$$V = \{ \Sigma [(N_i - B_i) \cdot (E_i - \langle E \rangle)^2] / N_{\text{pk}} + \Delta^2 / 12. \quad (4.34)$$

The standard  $1\sigma$  error of the variance,  $\sigma_V$ , is given by

$$\sigma_V^2 = N_{\text{pk}}^{-2} \cdot \Sigma \{ (N_i + \sigma_B^2) \cdot [ (E_i - \langle E \rangle)^2 - V ]^2 + \Delta^2 (\Delta^2 / 80 + (E_i - \langle E \rangle)^2 / 2 - V / 6) \}, \quad (4.35)$$

where the first terms in the summation (top line) consist of the usual expression (see, e.g., [Pel82]), and the later terms involving  $\Delta$  account for the finite bin size. In Eqns. 4.34 and 4.35,  $N_i$ ,  $B_i$ , and  $\sigma_B$  denote the measured number of positrons in the  $i^{\text{th}}$  energy bin,  $E_i$ , the corresponding intensity of the background fit, and the fit error, respectively.  $N_{pk}$  is the net number of peak positrons above background, and  $\langle E \rangle$  is the mean peak energy.

The statistical width defined by Eqns. 4.34 and 4.35 is directly related to the peak FWHM. For example, for the simple case of an underlying gaussian distribution, the peak FWHM is given by  $\Delta E = (8 \ln 2)^{1/2} V^{1/2}$ , or for a rectangular distribution,  $\Delta E = \sqrt{12} V^{1/2}$ . The relationship between the FWHM and variance appropriate for the Doppler-broadened positron lineshape,  $\Delta E_{e^+} = 2(\gamma\beta)_{em} P_{e^+}^*$ , is

$$(\Delta E_{e^+})_{Dop} \cong 3.06 \times V^{1/2}. \quad (4.36)$$

The multiplicative constant was determined numerically from Monte-Carlo calculations of the lineshape. It varies slightly as a function of mean positron energy and average emitter velocity (by as much as  $\sim 4\%$  for the different peaks presented here). The experimental FWHM's for each peak listed in Table 3-3 were calculated with the factor appropriate for monoenergetic emission isotropically from the CMS of that collision system.

The ratios plotted in Fig. 4-15,  $\Delta E_{e^+}^{obs}/\Delta E_{cm}^{calc}$ , do not involve the intermediate calculation of the FWHM as described by Eqn. 4.36. They were determined directly from the standard deviations extracted from the measured peak data and the expected CMS lineshapes calculated for the appropriate mean positron energy and CM velocity (i.e.,  $S.D._{e^+}^{obs}/S.D._{cm}^{calc}$ ). For each system, the peak intensity above background is well localized so the statistical width and its error are largely insensitive to the size of the fit window, as long as it includes the entire peak intensity. In each case a 100 to 120 keV energy range centered around the peak was used. (For evaluating the expected width of nuclear-emission peaks, the window was appropriately increased as a function of scattering angle for wider structures.) The vertical error bars for each point in Fig. 4-15 represent the  $1\sigma$  error in the standard deviation of the peak data ( $\sigma_{SD} = \frac{1}{2} V^{-1/2} \sigma_V$ ), only. As noted in Fig. 3-17, the systematic error introduced by the exact choice of the HI angular cut is rather small,  $\leq 5\%$ .

As noted above, the principal advantage of using the well-defined statistical width of Eqn. 4.36 is that it provides an essentially model-independent comparison between data of different systems with slightly different mean peak energies and CM velocities. Moreover, because the lineshape is dominated by Doppler broadening and the detection efficiency is smooth and structureless, most of the information regarding the details of any peak-producing process under consideration is summarized simply by the linewidth. For a given assumed positron emission-angle distribution, intrinsic width, or source lifetime, the statistical line width is approximately linearly proportional to the source velocity  $(\gamma\beta)_{em}$ , and only the overall absolute normalization of the calculated CM and nuclear linewidths changes.

The supercritical peak data are separated between Figs. 4-15a and b into the asymmetric U + Cm and Th + Cm collision systems, which exhibit a crossing point in the scattering kinematics near  $\theta_{HI} = 47^\circ$ , and the symmetric U + U and Th + Th, and nearly symmetric Th + U systems, whose ejectile velocities are symmetric in  $\theta_{HI}$  about  $45^\circ$ . The two points for the U + Cm system at  $\langle \theta_{HI} \rangle \cong 34^\circ$  and  $46^\circ$  represent the measurements of [Shw83] and [Cow85], respectively. The Th + Cm peak data of [Cow85] are distributed over a large PPAC angular range and is divided into two subsets for the comparison of Fig. 4-15a. The U + U point at  $\langle \theta_{HI} \rangle = 37.5^\circ$  is the  $\cong 310$  keV peak presented in [Bok83], and the remaining data are taken from Fig. 3-16. Although emission from the slow nucleus cannot be excluded for positron peaks detected with  $\theta_{HI} < 40^\circ$ , the U + Cm and Th + Cm peaks near  $45^\circ$  are each  $\sim 3.2\sigma$  narrower than the expected nuclear MPC linewidth. Emission from the fast ejectile is ruled out throughout the angular range. Moreover, the positron peak widths for all the systems cluster around approximately the width expected for  $v_{em} = v_{CM}$ . At face value, these data indicate (independent of the intensity arguments of Sec. 4.2) that the separated nuclei are not the source of the narrow positron peaks. Within statistical uncertainty, the peak widths are independent of HI scattering angle, and are consistent with a source moving with the velocity of the HI center-of-mass system.

### **Sec. 4.3.2 Distribution of Velocities**

As discussed in Sec. 2.2.7, the EPOS linewidth depends on the details of the distribution of emitted positrons. Some of the conclusions implied by Fig. 4-15 are therefore model-dependent. One parameter important to nuclear emission is the distribution of source velocities. For the nearly symmetric Th + Th, U + U, and Th + U

systems presented in this dissertation, the PPAC resolution is not adequate to separate forward from backward collisions (in the U+Cm system separation is also only partial). For a given HI angular region, both kinematic branches are therefore sampled and the distinction between projectile-like and target-like emission is artificial. Instead of separating the two nuclear curves in Fig. 4-15 at a given  $\theta_{HI}$ , the peak intensity probably includes both fast and slow components. For a peak-emitting process which is rather insensitive to the distance of closest approach, the relative weighting follows the Rutherford cross-section and most of the observed intensity comes from distant collisions, exhibiting primarily either a fast (transition in the projectile nucleus) or slow (target nucleus) character. If the mechanism depends sensitively on  $R_0$ , e.g., involving Coulomb excitation or nuclear reactions, this tends to balance the Rutherford cross-section and an average of fast and slow components is likely observed.

Figure 4-16 shows the effect on the calculated EPOS positron lineshape of an equal admixture between fast and slow nuclear velocities. At each HI laboratory scattering angle, approximately the same effective statistical FWHM is observed, always  $\cong 39\%$  larger than for CM emission. The appropriate comparison in Fig. 4-15 would then be two parallel lines at  $\Delta E_{\text{peak}} = 1.0$  and  $1.39$  times  $\Delta E_{\text{cm}}$ . The weighted average of all the experimental data in Figs. 4-15,

$$\langle (\Delta E_{\text{peak}}/\Delta E_{\text{cm}}) \rangle_{\text{exp}} = 0.96 \pm 0.04, \quad (4.37)$$

is then a suitable test between these possibilities. It is consistent with  $\langle v_{\text{em}} \rangle = v_{\text{CM}}$ , but represents a  $10\sigma$  deviation from  $(\Delta E_{\text{peak}}/\Delta E_{\text{cm}}) = 1.39$ , as expected for nuclear emission.

### Sec. 4.3.3 Angular Distribution

The absolute value of the Doppler-broadened positron linewidth, and the subsequent determination of the suitability of the separated nuclei as emitting sources, depends on the angular distribution of the emitted positrons. In order for the measured linewidths to be statistically consistent with emission from the separated nuclei, the absolute nuclear linewidth must be  $\Delta E_{\text{nuc}} \leq 1.05 \cdot \Delta E_{\text{cm}}$  (90% C.L. from Eqn. 4.37), or about 25% narrower than  $1.39 \cdot \Delta E_{\text{cm}}$ . As mentioned in Sec. 2.2.7, for monoenergetic emission (appropriate for nuclear MPC), the laboratory energy distribution is proportional to

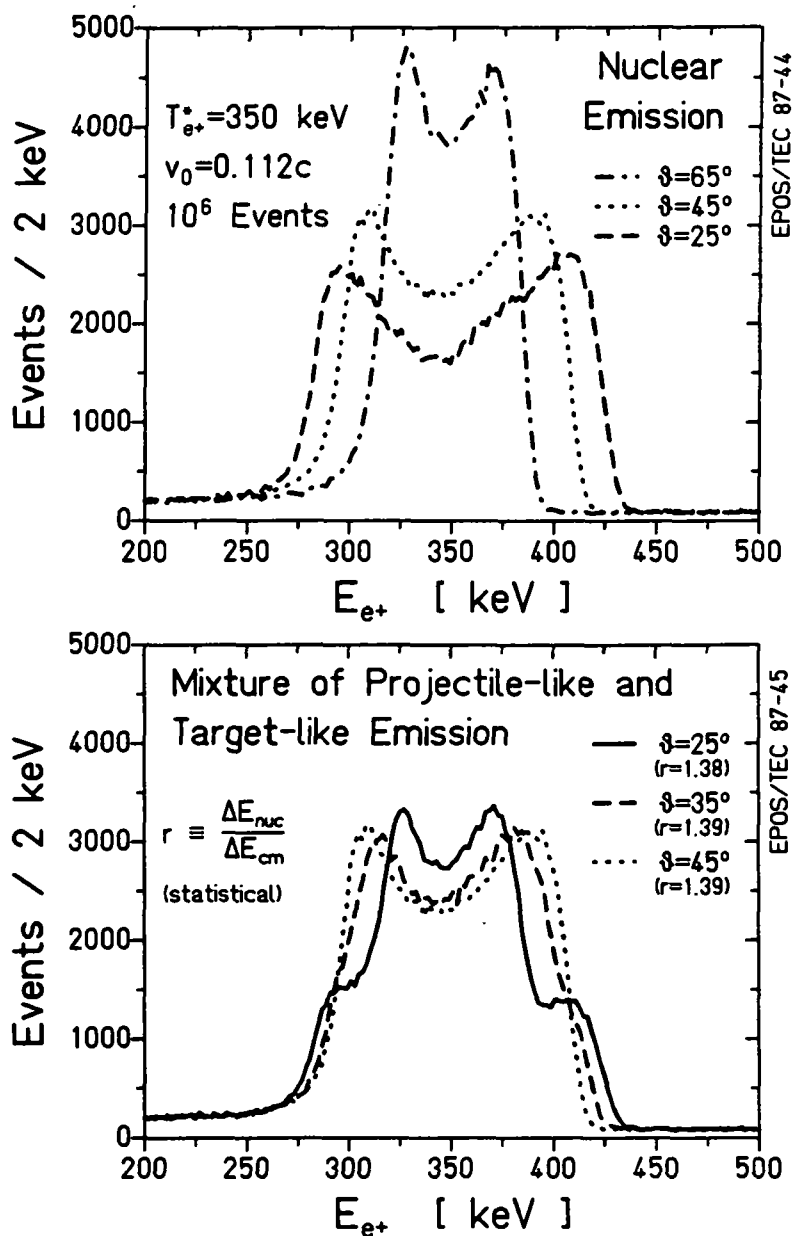


**Figure 4-16.** Doppler-broadened positron lineshapes calculated for monoenergetic positron emission from a nucleus scattered at a laboratory angle of  $25^\circ$ ,  $24^\circ$ , or  $65^\circ$  (top). Lower figure presents expected line profile assuming equal admixtures at each lab angle of projectile and recoil nucleus emission. The statistical peak width then equals  $1.39 \cdot \Delta E_{CM}$ , independent of  $\theta_{HI}$ .

$$dN/dE_{e^+} \propto dN^*/d\cos\theta_{e^+}^*, \quad (4.38)$$

with  $\cos\theta_{e^+}^* = \beta^{-1}[(E_{e^+} + m)/\gamma - (E_{e^+}^* + m)]$ . Only those distributions which suppress emission in the forward and backward directions (large Doppler shifts) effec-

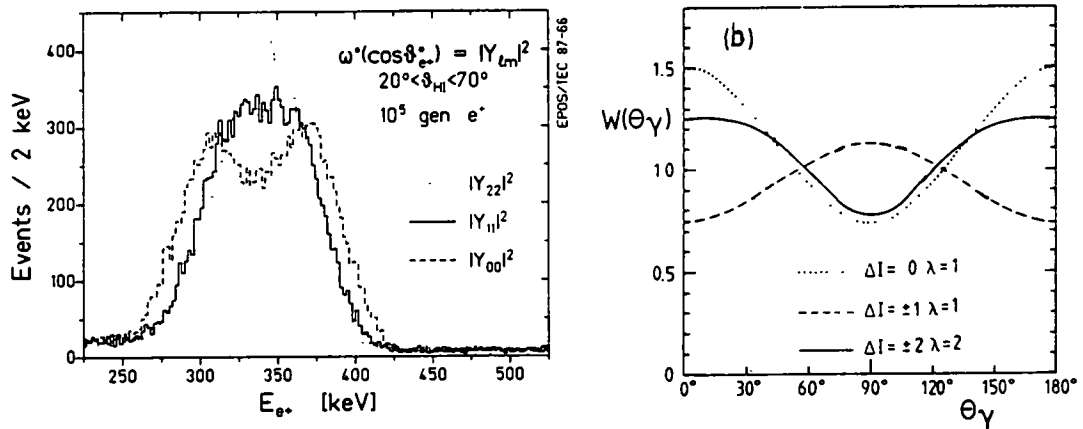


**Figure 4-17.** Doppler-broadened positron lineshape calculated for monoenergetic emission from the scattered nuclei (left). Dashed curve represents isotropic, solid shows  $\sin^2\theta_{e+}$ , and dotted presents  $\sin^4\theta_{e+}$  emission angle distributions for the positron w.r.t. the nuclear velocity. (B) presents  $\gamma$ -ray angular distributions from E1 (dotted and dashed) and E2 (solid) transitions in high-spin limit (reproduced from [Pel82]).

tively reduce the linewidth. Figure 4-17a illustrates the effect of different emission angle distributions  $dN^*/d\cos\theta_{e+}^* \propto |Y_{\ell m}|^2$  for  $m=\ell=0,1,2$ , with respect to the emitter velocity. For both  $m=\ell=1$  (solid) and  $m=\ell=2$  (dotted) distributions, the linewidth is narrower than for isotropic positron emission (dashed curve). For  $m=0$  ( $\ell=1,2$ ), forward and backward emission are favored and the statistical width of the lineshape is actually increased as compared to isotropic emission.

It is evident from Fig. 4-17a that for pure  $Y_{\ell m}$  distributions, the expected nuclear width can be consistent with the measured data. It should be noted however that after the collision, the heavy nuclei are generally not polarized or strongly aligned, so a broad range of orientations must be averaged over. The measured emission angle distributions in known nuclear conversions are nearly isotropic (exactly isotropic for E0 transitions). This follows from the  $\gamma$ -ray angular distribution which can in general be expressed [Pel82] by the expansion,

$$dN^*/d\cos\theta_{e+}^* = \sum_{\ell=0}^{\infty} a_{\ell} P_{\ell}(\cos\theta), \quad (4.39)$$

where, for parity conservation, only even values of  $\ell$  contribute. The coefficients  $a_{\ell}$  depend on the transition multipolarity and nuclear alignment, but they are generally dominated by the leading  $\ell=0$  term,  $a_0 \cong 1$ .

Figure 4-17b shows that the  $\gamma$ -ray angular distributions for stretched E1 and E2 transitions, common in HI collisions, are so broad that no decrease in the positron linewidth is expected. Moreover,  $\omega(\theta_\gamma)$  must be multiplied by the so-called particle parameters [Bie53, Chu64] to obtain  $\omega(\theta_{e^+})$ , which tends to further smooth out the angular correlation.

An interesting semi-classical argument provides an order of magnitude estimate of the relative importance of the various  $\ell$  components in the expansion 4.39. The positron wave function which enters the description of the emission process,  $e^{ik \cdot r}$ , can be expanded in the long wavelength limit,

$$e^{ik \cdot r} = 1 + ik \cdot r - \frac{1}{2}(k \cdot r)^2 \dots \quad (4.40)$$

The successive terms entering (4.40) are analogous to the higher angular momentum values  $\ell$  in (4.39). An estimate of the maximum contributing exponent of  $(k \cdot r)$  or value of  $\ell$ , and the relative importance of each succeeding term, is given by the maximum classical angular momentum which can be carried away by the positron when it is emitted from the maximum radius of the system,

$$L_{\max}^{\text{clas}} \cong P_{e^+} \cdot R_{\text{em}} \cong \ell_{\max} \hbar \quad (4.41)$$

For a 350 keV positron ( $P_{e^+} = 692 \text{ keV}/c$ ),

$$\ell_{\max} \cong 3.5 \times 10^{-3} R_{\text{em}}, \quad (4.42)$$

with  $R_{\text{em}}$  expressed in fm ( $\hbar c = 197.3 \text{ MeV}\cdot\text{fm}$ ).

Table 4-1 lists this semiclassical estimate of  $\ell_{\max}$  for emission from the separated nuclei, the quasi-molecular system, or from an outer-shell atomic effect. Because of parity conservation, even values of  $\ell$  contribute successively with a magnitude relative to the previous term of  $(p \cdot r / \hbar)^2 \cong \ell_{\max}^2$ . Unless the leading  $\ell = 0$  component is quantum mechanically forbidden, the angular distribution of positrons, emitted from either a nucleus or from the quasi-molecule, must be nearly isotropic since  $\ell = 2$  terms enter with magnitudes of  $10^{-3}$  to  $10^{-1}$ , respectively. Because of the very broad range of momenta available for atomic emission, one expects that several components contribute to the angular distribution, tending to smear out the well-defined correlations which could arise for fairly low

$\ell$ 's. In principle, the  $\ell=0$  term could be forbidden, or a suitable distribution of  $a_\ell$ 's may lead to a narrow emission angle distribution. It should again be noted, however, that experimentally we integrate over many of the physical degrees of freedom (positron polarization and emission direction, source velocity and orientation, and the momentum and spin of the associated electron discovered in Part II of this dissertation) so that even a narrow emission angle distribution should not usually lead to peak width noticeably smaller than the maximum possible Doppler broadening,  $2\gamma\beta_e^*$ .

It therefore seems unlikely that a conventional pair creation mechanism in the separated nuclei can explain the positron peak widths. Of course the IPC and MPC processes already appear to be ruled out on the basis of the intensity arguments of Sec. 4.2. It cannot be entirely excluded, however, that some unknown process associated with the scattered nuclei, which preferentially emits positrons perpendicular to their direction of motion, is the source of the narrow peaks.

#### **Sec. 4.3.4 Nuclear Level Lifetime**

As discussed in Sec. 2.2.7, if the source of positrons is more than  $\sim 20$  mm away from the solenoid axis, the Doppler-broadened lineshape width is also reduced because of the axial geometry of the positron detector. Low-lying nuclear levels occasionally have lifetimes  $> 100$  ps so off-axis emission is not impossible for high energy positron-emitting transitions. Figure 4-18 repeats Fig. 2-28 which plots the EPOS lineshape for various off-axis distances  $d_0$ , and source lifetimes,  $\tau_{em}$ , assuming  $v_{em} = v_{CM}$ . To use these peak shapes for emission from a nucleus of velocity  $v_{nuc}$  with a level lifetime of  $\tau_{nuc}$ , the appropriate CMS lifetime is  $\tau_{em} = (v_{nuc}/v_{CM})\tau_{nuc}$ . For a typical nuclear velocity,  $v_{nuc}/c \sim 0.10$ , and lifetime,  $\tau > 200$  ps, a reasonable fraction of the positrons are emitted more than 2 cm off axis. Because of the rapid fall-off of detection efficiency with  $d_0$ , a convolution with emission time (hence  $d_0$ ) yields lineshapes weighted heavily with the maximum width, as indicated in Fig. 4-18b. This obviously does not provide for narrow nuclear emission peaks of the order of Eqn. 4.37.

In principle, the different velocities associated with scattered fast and slow nuclei would change the equal admixture assumed in Fig. 4-16. For example with a transition lifetime  $\tau_{nuc} > 1$  ns, emission from the slow ejectiles would be detected with greater probability than that from the fast ejectiles, and the average nuclear peak width would converge to the "recoil-like" curve in Fig. 4-15. Nuclear emission is still

Table 4-1 Semi-Classical Estimate of  $\ell_{\max}$ 

Emitter	$R_{\text{em}}$	$\ell_{\max}$
Nucleus ( $^{238}\text{U}$ )	$1.2 \cdot A^{1/3} \cong 7.5 \text{ fm}$	0.026
Quasimolecule	$\langle r_{1s}^2 \rangle^{1/2} \cong 120 \text{ fm}$	0.42
Atom	$r_{\text{Bohr}} \cong 53000 \text{ fm}$	186

substantially ruled out by the data at  $\theta_{\text{HI}} \cong 45^\circ$  and by the intensity arguments of Sec. 4.2.

The positron linewidth for a nuclear transition could be smaller if the decay is fed from a very long-lived higher state, so that the positrons are first emitted with the nucleus is off-axis. From Fig. 4-18a, a distance of at least  $d_0 \cong 20 \text{ mm}$  is required. A correspondingly long feeding time of  $\tau_{\text{feed}} \geq 1 \text{ ns}$  is necessary to ensure that the transition does not emit positrons for  $d_0 = v_{\perp} t < 20 \text{ mm}$ .

#### Sec. 4.3.5 Intrinsic Width

From the preceding discussion, it is clear that on the basis of the linewidth alone, emission of positrons from the separated nuclei is substantially excluded as a source for the observed narrow peaks, *unless* the positrons are emitted preferentially perpendicular to the direction of motion or from a state which is populated with a very long feeding time. Conventional IPC and the rare MPC pair conversions do not meet these criteria and are largely precluded based on the intensity arguments of Sec. 4.2. In fact, nuclear processes involving off-axis emission have a smaller positron detection efficiency, so the required size of the competing  $\gamma$ -ray line would be even larger than shown in Figs. 4-8,4-9. The IC electron line, however, may be attenuated for a state fed with  $\tau > 1 \text{ ns}$ , because of the smaller fiducial volume of electron detection due to the cylindrical baffle ( $\Delta r_{e^-} \sim 5\text{-}10 \text{ mm}$ ). The limits extracted from this lineshape analysis also provide constraints on the required characteristics of unknown exotic peak producing processes.

For isotropic emission close to the solenoid axis (a condition which appears reasonable in the absence of evidence to the contrary), Fig. 4-15 implies that the peak positrons are emitted from a source moving with a velocity  $< 0.06c$  which is inde-

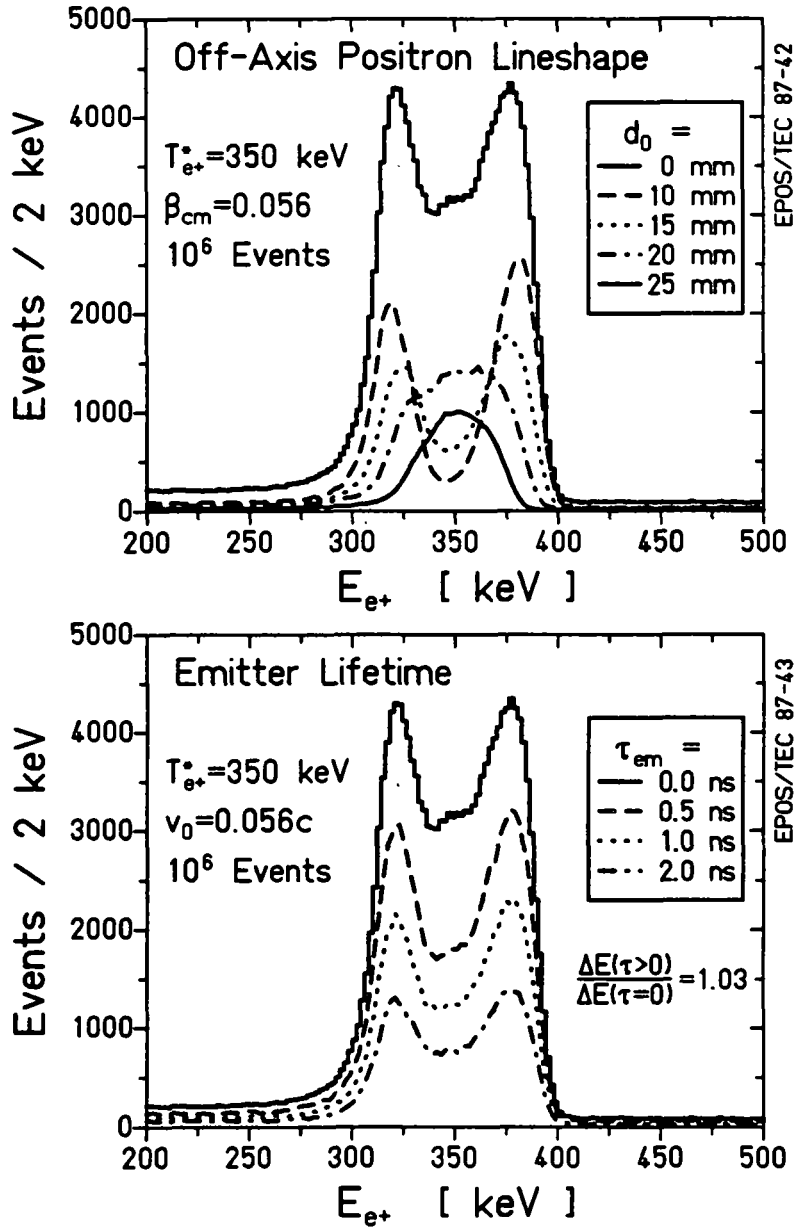


**Figure 4-18.** Doppler-broadened lineshape calculated for an emitter (moving with  $v_{CM}$ ) located a distance  $d_0$  perpendicularly off-axis (top). Long emitter lifetimes (bottom) reduce the efficiency but not the effective linewidth.

pendent of HI scattering angle. One obvious possibility is that the peaks are emitted from the CM system. If this is the case, it is interesting to determine the intrinsic width of the lines in order to estimate the lifetime of the compound system. Figure 4-19 presents the Doppler-broadened lineshape assuming a Lorentzian distribution of emitted positron energies with different widths  $\Gamma$  (FWHM), associated with a

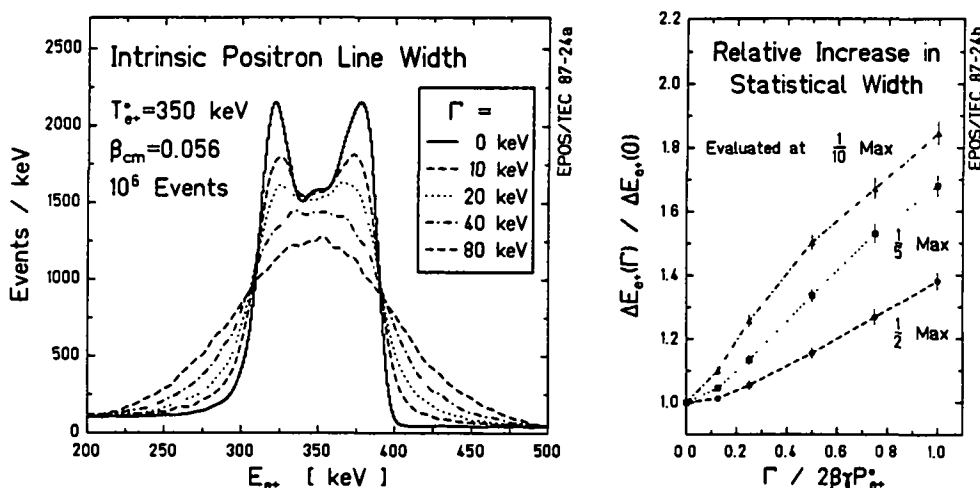


**Figure 4-19.** Doppler-broadened positron lineshape for  $\beta_{CM}$  calculated assuming an intrinsic Breit-Wigner distribution having FWHM  $\Gamma$  (left). Relative increase of the statistically determined width versus  $\Gamma$  (right), evaluated at  $1/2$ ,  $1/5$ , or  $1/10$  max.

source lifetime of  $\tau = \hbar/\Gamma$ . For small  $\Gamma$ , the central portion of the lineshape tends to fill in slowly until, at  $\Gamma \sim \Delta E_0$ , the entire laboratory distribution is significantly broadened. As illustrated in Fig. 4-19b, the measured peak FWHM ( $\Delta E_{e^+}$ ) which one determines statistically from the data by Eqns. 4.34 and 4.36, would depend on how wide an energy range is considered because of the broad tails (evident in Fig. 4-19a) which accompany a large intrinsic width. Tails on the experimental peaks could be reasonably identified above the smooth background at a height of  $\sim 25\%$  of the peak maximum. For comparison to the peak FWHM's (Eqn. 4.36) extracted from the measured data, the calculated widths of Fig. 4-19 should be evaluated at  $\sim 1/4$  max. The expected statistical FWHM is then approximately,

$$\Delta E_{e^+} \cong [(\Delta E_0)^2 + \Gamma^2]^{1/2}, \quad (4.43)$$

where  $\Delta E_0 \cong 2(\gamma\beta)_{em}P_{e^+}^*$  is the FWHM for a monoenergetic line.

The weighted average of the data of Fig. 4-15 gives an upper limit on the positron linewidth of  $\Delta E_{e^+}/\Delta E_{cm} < 1.04$  at a 95% confidence level (Eqn. 4.37), which implies from Fig. 4-19b that  $\Gamma/\Delta E_{cm} \leq 0.2$ . That is,  $\Gamma \leq 15$  keV (95% C.L.), which requires that the CM system must live for  $\tau \geq 4 \cdot 10^{-20}$  sec. Previously [Shw83], we obtained an upper limit (FWHM  $< 40$  keV, 95% C.L.) on the intrinsic width of a positron line emitted from the CM system for the U+Cm data of Fig. 4-6. This was

determined by including a gaussian intrinsic peak shape before correcting for Doppler broadening and detector lineshape response in the maximum likelihood fits described in Sec. 4.2.1. Using a Lorentzian intrinsic distribution gave an upper limit of  $\Gamma < 25$  keV (95% C.L.), comparable to that determined here for the average of all the peak data.

Of course, the measured width of the lines could be dominated by a large  $\Gamma$  associated with significantly smaller source velocities. In the limiting case of emission from rest in the lab,  $v_{em} = 0$ ,  $\Delta E_{e^+} \sim 75$  keV (FWHM), or  $\tau = \hbar \Delta E_{e^+} \cong 9 \times 10^{-21}$  sec. It should be noted that this short source lifetime is marginally longer than the HI collision time. It is very difficult to imagine how a source created in the collision, as is clearly indicated by the TOF arguments of Sec. 4.1, could come to rest in the target before decaying, especially since the travel time to the next atom in the target is  $\sim 10^{-17}$  sec. If a stationary source in the lab is somehow excited by the beam ions, the short observed lifetime makes it difficult to attribute the positron emitting process to atomic mechanisms (which are characterized by a typical time scale  $\geq 10^{-17}$  sec) or nuclear transitions (with times  $> 10^{-15}$  sec). Based on the arguments presented in this section, it would appear that the source of the positron peaks is either the CM system, or a secondary object traveling in the laboratory with a mean velocity whose magnitude is approximately equal to  $v_{CM}$ . The consequences of a secondary source on the Doppler-broadened positron lineshape is addressed in more detail in Chapter 5.

## Section 4.4 Spontaneous Positron Emission

### Sec. 4.4.1 Application to U+Cm Data.

Due in part to the inability of instrumental or nuclear mechanisms to explain the lines, and to the correspondence between the mean emitter velocity and  $v_{CM}$ , spontaneous positron emission has been widely discussed as a possible explanation for the narrow positron lines observed in superheavy collisions. As described in Chap. 1, the search for this process originally motivated these experiments, but the short collision times involved implied that no clear signature should be observed. Serious speculation [Rei81b, MüU83, Grn83b, Mül84, Hes84] was fueled primarily by the unexpected discovery of the narrow peak in the U + Cm system [Shw83] whose energy of  $316 \pm 10$  keV agrees with the predicted  $1\sigma$  binding energy for U and Cm nuclei separated by  $\cong 17$  fm, approximately the distance of closest approach in 6.05 MeV/u collisions. As

noted above, the narrow width of the positron line implies a source lifetime of  $\tau > 5 \times 10^{-20}$  sec, requiring, in this context, the formation of a long-lived compound nuclear system, which in itself would be of great interest to nuclear physics.

The theoretical formalism of dynamic and spontaneous positron production has been discussed many times and will not be repeated here. Many of the quantitative contributions in the literature were made by the Univ. Frankfurt theory group under the direction of W. Greiner. For theoretical details, the reader is therefore referred to the review of Reinhardt and Greiner [Grn85], and the many excellent references in [Grn83] and [Grn87]. Other calculations along these lines have been made by [Tom82, Tom82b, Tom83, Bot85, Hir86]. Only those aspects of the Frankfurt treatment germane to the present analysis of the positron peak structures are discussed below.

As mentioned in Chap. 1, only a broad, smooth distribution of energies is expected for positron emission from supercritical collisions. No monoenergetic spontaneous positron signal is anticipated mainly because of the short time during which the  $1s\sigma$  orbital is supercritically bound ( $t_{cr} \cong 2 \times 10^{-21}$  s). Due to the much longer spontaneous decay time ( $\tau_{sp} = \hbar\Gamma_{1s} \cong 10^{-19}$  s), very few of the  $1s\sigma$  vacancies, which are produced with probability  $P_{1s\sigma} \sim 5\%$  along the incoming path of the HI trajectory, have a chance to decay. Moreover, the energy distribution of the spontaneous positrons is spread over  $\Delta E_{e^+} \cong \hbar t_{cr} \cong 300$  keV by the uncertainty relation. Spontaneous vacuum decay can therefore form narrow peaks *only* if the collision time is substantially prolonged. For  $t_{cr}$  approaching  $\tau_{sp}$ , both the decay probability of the  $1s\sigma$  vacancy increases, and the width of the resulting line becomes narrower.

Following a suggestion by [Raf78], Reinhardt et al. [Rei81b] calculated the effect on the positron energy distribution of a fixed nuclear delay time,  $T$ , occurring at the distance of closest approach between the heavy ions. Using first order time-dependent perturbation theory they obtained,

$$dP_{e^+}/dE_{e^+} \sim P_{1s\sigma}(t=0) \cdot (\Gamma_{1s\sigma}/2\pi T^2) \cdot [\sin(x)/x]^2, \quad (4.44)$$

where  $x = (E_{e^+} - E_{1s\sigma})T/2\hbar$ . As shown in Fig. 4-20, in subcritical collision systems (left side) this results in an oscillatory pattern in the positron energy which has a period  $\Delta E = \hbar/T$ . As discussed in Sec. 4.5, the oscillations are quickly averaged out for

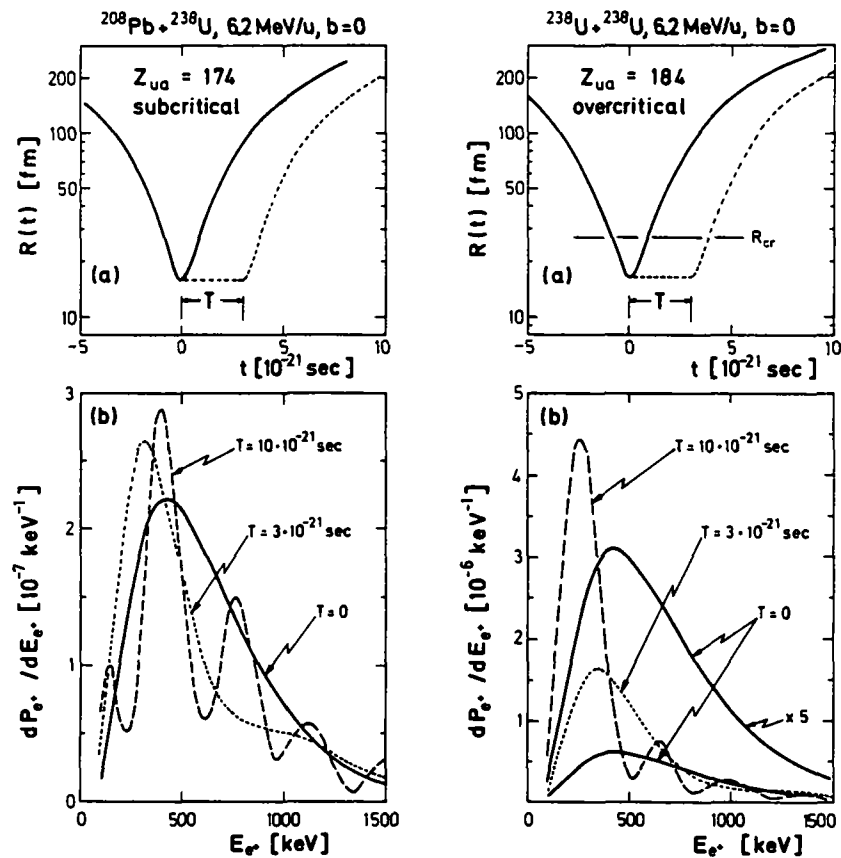


**Figure 4-20.** Predicted positron energy distributions for subcritical U+Pb (left) and supercritical U+U systems (right), calculated for discrete nuclear contact times,  $T$ . (Reproduced from [Shm83].)

a distribution of delay times, and the resulting smooth spectrum is not easily distinguishable from dynamic positron production.

In supercritical collisions (right), however, the spontaneous component emerges above the fluctuating continuum, and a peak-like structure develops which has a width,  $\Delta E_{e^+} = 5.56\hbar T$  [Rei81b]. As shown in Fig. 4-21, the magnitude of the spontaneous component, given by

$$P_{e^+}^{\text{spont}} \sim P_{1s\sigma^+}(t=0) \cdot \Gamma_{1s\sigma} T/\hbar \quad (4.45)$$

increases almost linearly with  $T$ , and quickly dominates the total positron production cross-section. U. Müller et al. [MüU83] demonstrated that the U+Cm peak of [Shw83] could be fit within this schematic model, by assuming a fixed time delay of

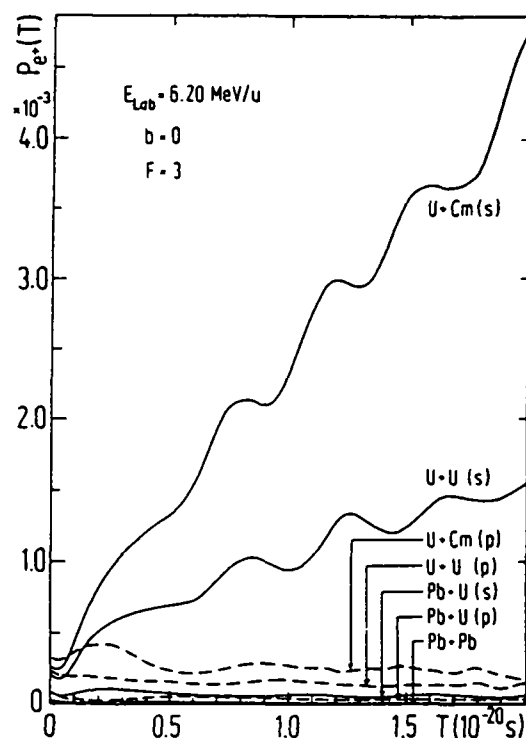


**Figure 4-21.** Production probability of positrons from pure  $s_{1/2}$  or  $p_{1/2}$  states shown for various systems as a function of nuclear delay time. Dynamic production slightly decreases with  $T$ , while spontaneous  $1\sigma$  decay increases almost linearly. (Reproduced from [MüU83].)

$T = 6.5 \times 10^{-20}$  sec, as shown in Fig. 4-22. Because of the correspondingly large production probability, such a di-nuclear complex (living for  $\sim 30$  times the Rutherford collision time) must be formed in only  $\sim 2$  out of every 1000 HI collisions, i.e., with a reaction cross-section of  $\sigma_{\eta} \sim 30$  mb. Similar results have also been obtained by other groups [Tom83, Bot85].

The formation of superheavy compound systems with lifetimes long enough to produce visible spontaneous positron peaks has never been independently observed experimentally, nor was it generally considered possible with mb cross-sections. Motivated by the existence of the narrow positron peaks presented in [Shw83, Cle84, Cow85, and Tse85] and Chap. 3, however, several models for forming a "pocket" in the HI scattering potential, which could possibly produce long-lived di-nuclear resonances, have been investigated theoretically. These include the use of double-folding models [Rho83, Str83, Hes84], folding-models plus a liquid-drop potential at small separations [Sei85], proximity potentials [Sei84, Mal85], and energy-

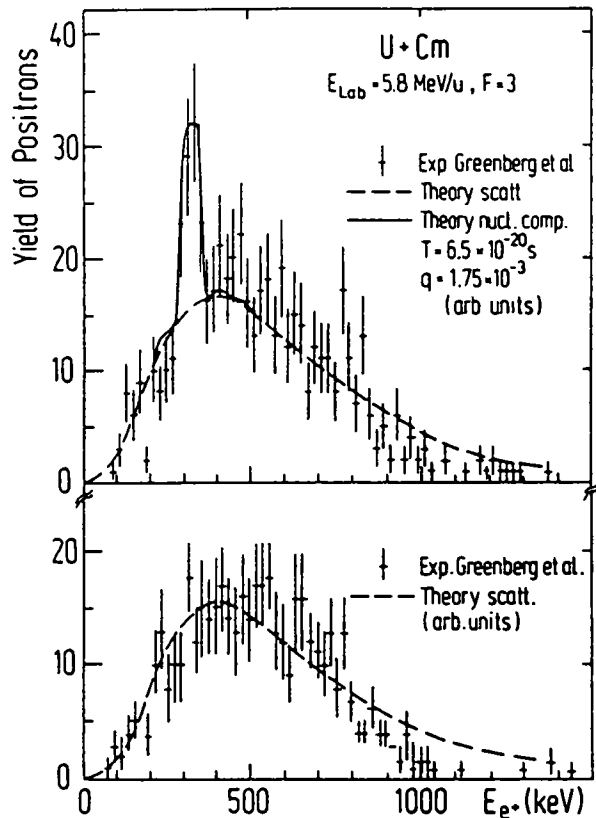


**Figure 4-22.** A fit by the Frankfurt group of spontaneous positron emission to the EPOS peak observed in U+Cm collisions. A fixed nuclear sticking time of  $6.5 \times 10^{-20}$  is assumed to occur in 1.75 out of  $10^3$  collisions. (Reproduced from [MüU83].)

density formalisms [Man86, Fin86, Fae87]. Quantum mechanical treatments of the interaction between nuclear resonances and spontaneous positron creation have also been performed [Hei83a,b, Hei84a,b]. As of this writing, the present state-of-the-art theories involving a semi-microscopic description of the HI environment [Kat86], or Hartree-Fock and shell-model calculations [Nei86], however, are pessimistic about the formation of potential pockets at beam energies relevant to this experiment [Obe86].

#### **Sec. 4.4.2 Z Dependence**

Assuming for the sake of argument that pockets exist in the nuclear scattering potential so that spontaneous positrons may be emitted with sufficient probability to be experimentally detected, the energy of the bound  $1s\sigma$  state, and hence the liberated monoenergetic positron, depends on the strength of the Coulomb field. For static

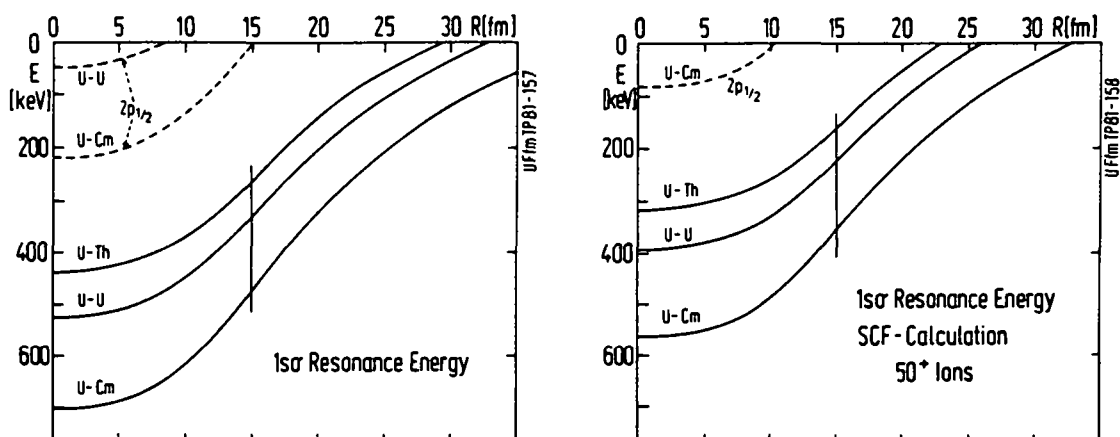


**Figure 4-23.** Expected energy of the spontaneous positron peak versus internuclear separation for U + Cm, U + U, and U + Th collisions. Calculations include finite nuclear size, assuming normal nuclear density, and are presented for inclusion (right) or exclusion (left) of electron screening. (Reproduced from [Rei81b].)

configurations of the di-nuclear complex, the positron peak energy is expected to vary as  $E_{e^+} \sim Z_U^{20}$  [Rei81b], i.e., changing by  $\cong 30$  keV with each unit of  $Z$  between  $180 \leq Z_U \leq 188$ . By the same token, the  $1s$  binding energy depends sensitively on the nuclear charge distribution and on electron screening effects. Figure 4-23 presents the expected spontaneous positron peak energies as a function of the internuclear distance  $R$ , for several systems [Rei81b]. Parts a and b compare the calculations without and with electron screening.

The experimentally observed positron peak energies (of Fig. 3-16) for each system are plotted in Fig. 4-24 versus the combined nuclear charge [Cow85]. The nearly flat dependence on  $Z_U$  obviously contradicts the straightforward theoretical predictions of spontaneous vacuum decay, represented by the lines in Fig. 4-24. Line (a) indicates the predicted spontaneous positron peak energy for the anticipated situation of a di-nuclear system fixed at an internuclear separation of 17 fm, the average distance of closest approach achieved in head-on collisions at the experimental beam energies. Electron screening is included. For systems lighter than U + Cm, the data clearly disagree with the QED calculations. For example, the predicted line energies in each system [Mül86] are  $E_{e^+} \cong 315$  keV (U + Cm),  $\cong 250$  keV (Th + Cm),  $\cong 170$  keV (U + U),  $\cong 115$  keV (U + Th), and  $\cong 60$  keV (Th + Th). Instead

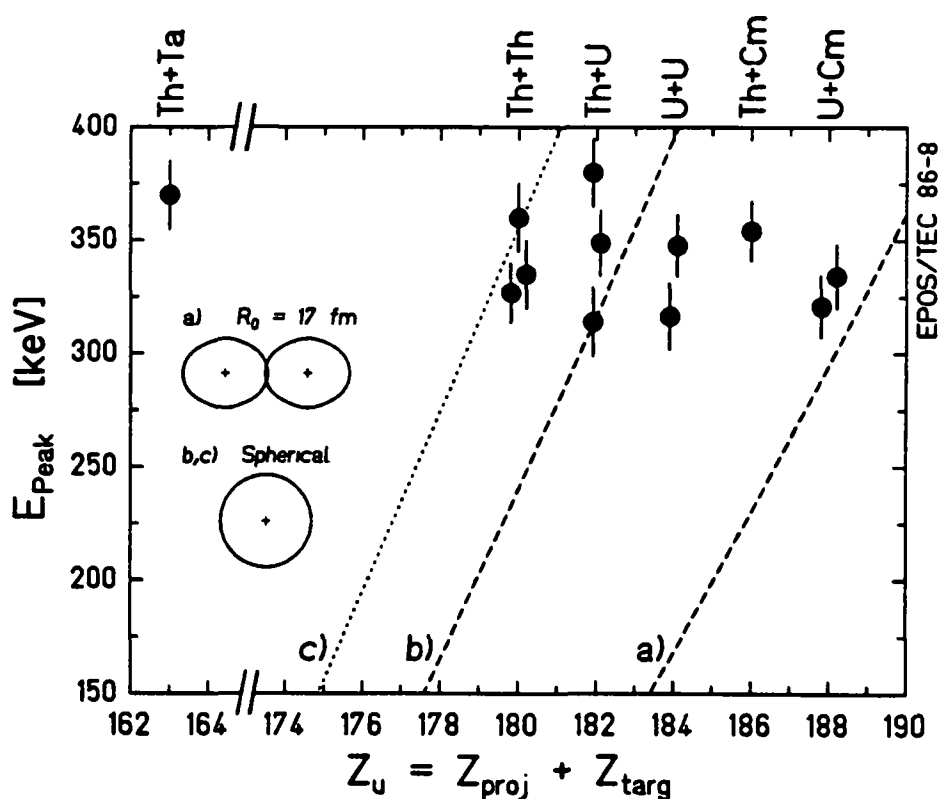


**Figure 4-24.** Mean energies of positron peaks presented in Fig. 3-16 as a function of  $Z_U$ . Curves present calculations of the expected spontaneous positron energies for emission from static complexes with internuclear separations fixed at  $R \cong 17$  fm (a), or from a spherical configuration (b,c). Electron screening is included in (a) and (b), but a stripped compound system is assumed in (c).

of such a sloping dependence on  $Z_U$ , a fit to the experimental peak positions is independent of combined charge, and their mean energy is  $E_{e^+} = 336 \pm 6$  keV.

From Fig. 4-23 it is evident that more spherical nuclear charge distributions (i.e.,  $R \rightarrow 0$ ) lead to higher spontaneous positron peak energies. Line (b) of Fig. 4-24 illustrates a limiting case assuming a screened configuration where the entire nuclear charge is uniformly distributed throughout a sphere whose radius is chosen to maintain normal nuclear density,  $R(Z_U) \propto R_0(A_p + A_t)^{1/3}$ . This configuration corresponds to the well-known supercritical charge threshold of  $Z_{cr} = 173$  (at which  $E_{1s\sigma} = 2m_e c^2$ ). The role played by electron screening is indicated by line (c) which presents the peak position for a spherical super-nucleus completely stripped of atomic electrons.

Any accommodation of the measured peak energies within the context of spontaneous positron emission must clearly involve systematic changes in the di-nuclear charge distribution, or in the degree of atomic ionization, which track with  $Z_U$  in such a way as to maintain a constant  $1s\sigma$  binding energy [Cow85]. Since atomic ionization processes appear to be theoretically understood, and only extreme states of ionization (e.g.,  $< 10$  remaining atomic electrons [Wei79]) lead to significant increases in  $E_{1s\sigma}$ , it appears that the Th + Th system already represents an effectively sub-critical combined nuclear charge. Similarly, the positron peak in Th + Ta, with  $Z_U = 163$  well below the supercritical threshold, is very difficult to incorporate into any model involving spontaneous decay.

#### **Sec. 4.4.3 Isomeric Configurations**

The Frankfurt theory group has investigated various mechanisms by which the di-nuclear charge configuration could scale with  $Z_U$  in such a way as to produce a nearly constant peak energy. The magnitude of the variation required is illustrated in Fig. 4-25 [MüU86] which compares the expected positron distributions for quasi-static configurations with the nuclear centers separated by a constant  $\sim 16.5$  fm (left panel) to the measured positron peaks (right). The required compound system shape for each  $Z_U$  is shown schematically with the experimental spectra. The inset of Fig. 4-26 sketches the nuclear scattering potential required to lead to such a di-nuclear system in U + U collisions [Shm86]. Instead of an increasing Coulomb potential beyond the hypothesized pocket at  $\cong 16$  fm, [Grn83b] suggested that a shape isomer may exist at small internuclear distance (similar to fission isomers in actinide nuclei located at the minimum within the double-humped fission barrier, see e.g., [Met80]). A double peaked positron spectrum, corresponding to the two values of  $R_{\min}$  for the different configurations, could in principle be produced (Fig. 4-26). In order to describe the Th + Th line at  $\cong 335$  keV in terms of spontaneous positron emission, however, de Reus et al. [Reu87] point out that a spherical  $Z_U = 180$  complex must be compressed  $\sim 50\%$  above the normal nuclear density ( $\rho_0 = 0.138$  fm $^{-3}$ ). The Th + Ta advantageously system stripped of electrons would still require a compound nuclear radius of  $\cong 3$  fm, having a density  $\rho \cong 17\rho_0$ .

Calculations by J. Maruhn et al. [cf. Mü186] were unsuccessful in constructing such isomers (which require a 180 MeV decrease of the interaction potential for spherical configurations) by extrapolating accepted nuclear physics to superheavy  $Z \cong 184$  and  $A \cong 480$  systems. A modification of the mass formula to include the re-

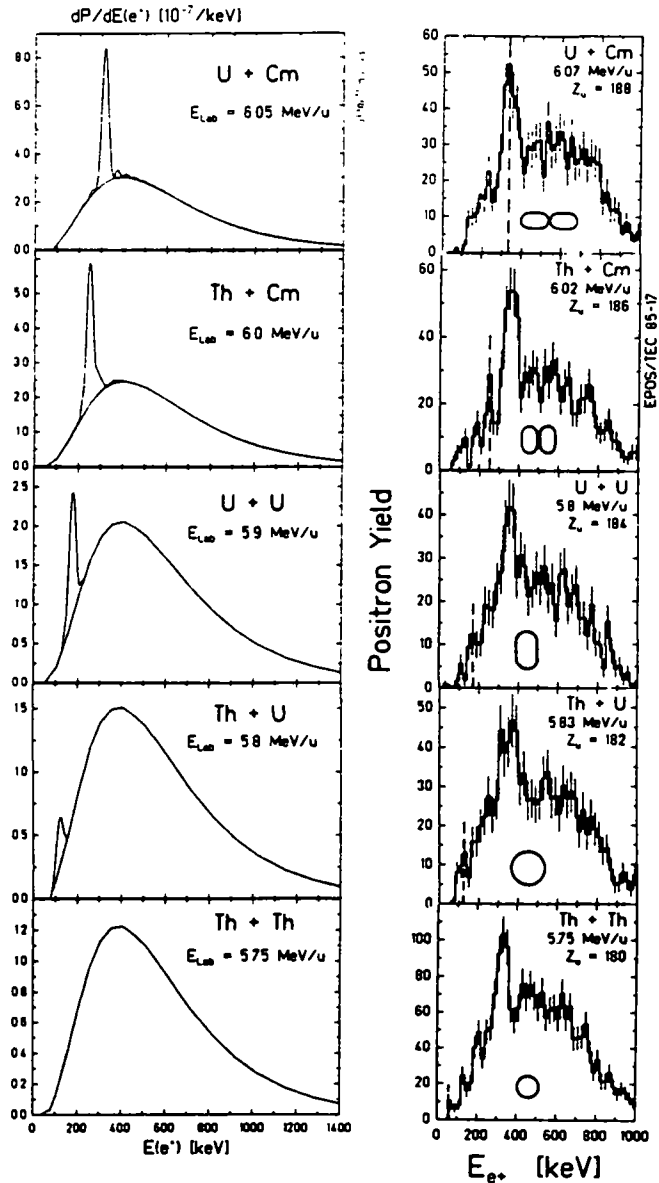


**Figure 4-25.** Calculated positron energy spectra illustrating the position and magnitude expected for the spontaneous peak (left) assuming that a similar static di-nuclear complex is formed at  $R \sim 16 \text{ fm}$  for each system. Insets in the measured data (right) show the di-nuclear configurations necessary to produced a spontaneous positron line at the observed peak energy. (Reproduced from [MüU86].)

quired binding in the superheavy domain [Sei85b] was able to obtain a good fit to the body of conventional nuclear physics data below  $Z = 100$  by reversing the sign of the surface contribution to nuclear compressibility. The authors suggested that this could involve a dissolution of the individual nucleon quark bags in superheavy nuclei [Vas85] with crucial implications for the search for the quark-gluon plasma phase

Independent of the measured positron peaks, the kinematics of the HI scattering provide an experimental constraint for the Frankfurt hypothesis of condensed and compressed superheavy compound systems. In particular, it is difficult to understand how two heavy nuclei enter into a nearly spherical conglomeration and then separate, with almost no loss of kinetic energy, into a nearly symmetric binary exit channel. As discussed in Chap. 3, the positron peaks are associated with HI collisions which differ from Rutherford scattering by a mean  $Q$ -loss of less than 20 MeV. This places a limit on the number of evaporated nucleons of  $\leq 2n$  or  $1p$ . Within the limits of the PPAC angular resolution, the exit channel masses appear identical to the entrance channel, placing a limit on possible mass drift of  $\Delta M \leq 10$  nucleons. In the fully resolved Th+Ta collisions,  $\Delta M \leq 5$  amu. Although detection efficiency remains high for 3-body events, no evidence is found for fission of either heavy partner. Based on all the kinematic parameters experimentally determined, the peak-related collision process appears to be quasi-elastic.

It seems very unlikely that a compound system could be formed with small internuclear separation, and hence large density overlap, neck formation, or fusion, without transferring large amounts of kinetic energy to the exit products. Such configurations are typical of deep inelastic collisions and, unless the hypothesized entrance channel is very gentle, imply a comparatively violent nuclear environment. The positron data, on the other hand, indicate that the HI ejectiles associated with peak events have excitation energies below the  $\sim 6$  MeV threshold (in  $^{238}\text{U}$ ) for fission and nucleon evaporation. It therefore appears improbable that a nuclear mechanism exists by which  $E_{1s\sigma}$  changes with  $Z_U$  so as to produce nearly constant spontaneous positron peak energies throughout the measured range.

#### **Sec. 4.4.4 Common Super-Nucleus**

A different explanation for the nearly constant measured positron peak energies within the context of spontaneous vacuum decay involves the formation, in each collision system, of a single common nuclear complex. This obviously would entail the emission of several nuclear charges in forming, e.g., a  $Z_U = 180$  complex in U+Cm ( $Z_U = 188$ ) collisions. Of course the formation time of the common nucleus must be short compared to the spontaneous decay time,  $\tau_{sp} \sim 10^{-19}$  sec, so charged fragments, for which emission is suppressed by the Coulomb barrier, must be ejected with rather large energies. Energy carried away from the combined system, both kinetic energy of the evaporation products and the difference in binding energy be-

tween parents and daughters, adds to an effective Q-value for the reaction which must be compared to the observed limit of  $|Q| < 20$  MeV, derived from the scattering angle correlation associated with positron peak events.

The laboratory HI scattering angles are determined by the vector sum of the CM velocity and the velocity (hence kinetic energy) of the heavy fragments in the CM frame. Defining Q as the final available HI kinetic energy minus that initially available ( $Q < 0$  is dissipative), conservation of energy and nucleon number gives

$$Q = (\Delta M_{HI} - \Sigma m_i - \Sigma t_i), \text{ with} \\ \Delta M_{HI} = (M_1 + M_2)_i - (M'_1 + M'_2)_f, \quad (4.46)$$

where M denotes the mass excess of each heavy fragment (mass excess  $M = \text{experimental mass} - A \cdot 931.51 \text{ MeV}/c^2$ , see [Mye77]), and  $m_i$  and  $t_i$  are the mass excess and kinetic energy of the evaporation products. Because  $m_n \cong 8$  MeV is lost in binding energy for each ejected neutron ( $m_p \cong 7.3$  MeV per proton), nucleons must be emitted in bound clusters to achieve small Q values. An alpha particle, for example, costs the combined system only  $m_\alpha = 2.425$  MeV. The difference in mass between entrance and exit heavy ions is generally not very large. For example,  $^{238}\text{U} + ^{248}\text{Cm} \rightarrow ^{238}\text{U} + ^{244}\text{Pu} + \alpha$ , corresponds to  $\Delta M = 8.13$  MeV [Mye77]. Including  $m_\alpha$  gives a total  $Q = (5.7 - t_\alpha)$  MeV.

The large kinetic energy required by the ejected cluster to tunnel through the Coulomb barrier represents the major contribution to the reaction Q value. For a given potential  $V(r)$ , the decay probability is given, in analogy with one-particle  $\alpha$ -decay theory (see, e.g., [Seg77]), by the WKB barrier penetration factor  $e^{-2G}$  times a repetition frequency  $(v/R_0)$

$$\lambda = (v_i/R_0) \exp[-2/\hbar \int_{R_0}^{R'} (2M_i t_i - V(r))^{1/2} dr] \quad (4.47)$$

The integration extends from the radius of contact,  $R_0 = R_{HI} + R_\alpha$ , to the outer turning point where  $2M_i t_i = V(R')$ . The Coulomb potential barrier against  $\alpha$  decay  $V_\alpha(r)$ , is shown in Fig. 4-27 for emission (a) perpendicularly from the neck of a dumbbell shaped di-nuclear complex, (b) from its end along the internuclear axis, or (c) from a spherical configuration. Fast emission,  $\tau_{\text{decay}} \cong 1/\lambda \leq 10^{-19}$  sec, requires kinetic energies just below the maximum of the potential,  $t_\alpha \cong 30$  MeV for the example indicated in Fig. 4-27. Proton emission requires  $t_p \cong 15$  MeV. Taking into account

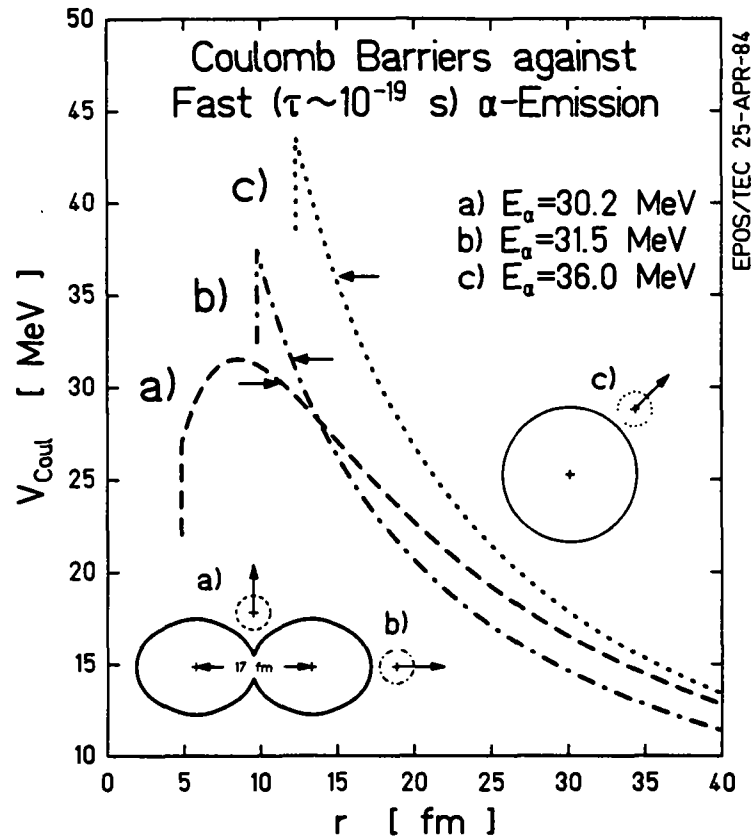


**Figure 4-27.** Coulomb barriers against  $\alpha$  emission from either (a) the neck or (b) the end of a di-nuclear complex with  $R=17$  fm, or (c) from a spherical compound nucleus. Energies for fast ( $\tau \sim 10^{-19}$  s) emission, calculated from one-body WKB barrier penetration model, as marked.

the average  $\Delta M_{HI}$ , each  $\alpha$  particle therefore costs a net  $Q_\alpha \cong -25$  MeV, a proton  $Q_p \cong -22$  MeV, or a neutron (assuming a Maxwellian energy distribution with  $\langle t_n \rangle \sim 2.5$  MeV)  $Q_n \cong -9$  MeV.

If the evaporation products are emitted, on the average, isotropically in the CM frame, the mean velocity of the CM of the remaining heavy ions equals  $v_{CM}$ . The momenta of the heavy fragments are reduced, thus leading to smaller lab scattering angles. As discussed in App. A,  $Q = -25$  MeV corresponds to a shift in  $\Sigma\theta_{HI}$  of  $-1^\circ$ . The effect on the HI scattering angle kinematics of neutron and  $\alpha$  particle emission is shown in Fig. 4-28. Evaporation of three neutrons, or one proton shifts  $\Sigma\theta_{HI}$  by  $\sim 1^\circ$ . Within this very simple model, one may already rule out the possibility that the U+Cm peak is related to a  $Z_{ij}^* = 186$  complex (i.e.,  $U+Cm \rightarrow [186] + \alpha$ ). The

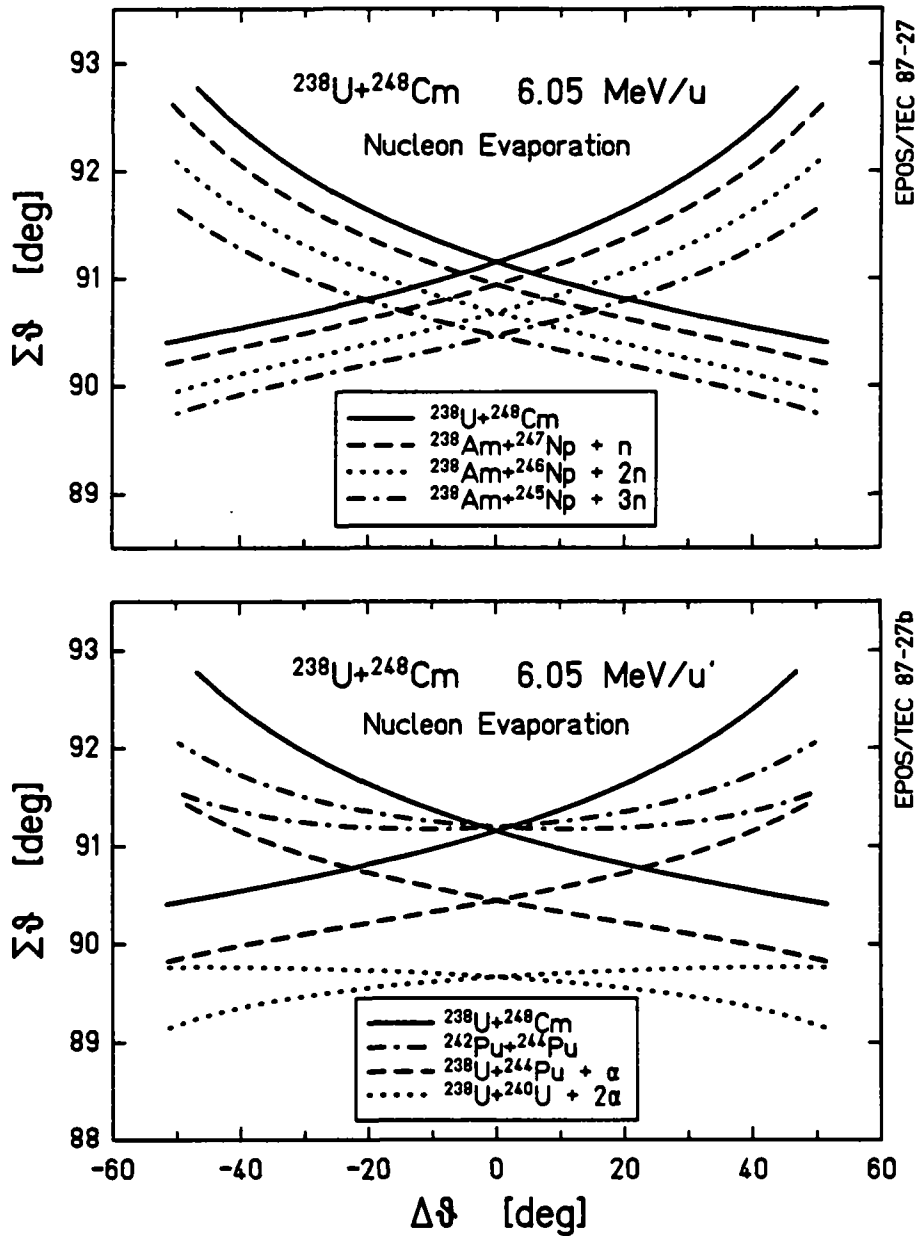


**Figure 4-28.** Kinematic plots of the HI  $\Delta\theta_{\text{HI}}-\Sigma\theta_{\text{HI}}$  correlation patterns for neutron evaporation (top) or  $\alpha$  particle emission (bottom) following U+Cm collisions. Energetically most favorable exit channel nuclei are assumed.

required 4  $\alpha$ 's (or, e.g.,  $^{16}\text{O}$ ) emitted in going from U+Cm to Th+Th ( $Z_{\text{U}} = 180$ ) would require  $Q \cong -100$  MeV with a mean  $\cong 4^\circ$  downward shift of the kinematic branches. If the evaporation products are emitted in the direction of  $v_{\text{CM}}$ , then the velocity of the remaining HI complex is reduced and almost no shift in  $\Sigma\theta_{\text{HI}}$  occurs. On the other hand, emission in the backward direction increases the HI  $v_{\text{CM}}$ , decreasing  $\Sigma\theta_{\text{HI}}$  by

up to  $7^\circ$  for  $4\alpha$  emission. The spread in the resulting kinematic correlation pattern for isotropic emission should therefore be on the order of  $\Delta(\Sigma\theta_{HI}) \sim 2^\circ$  (FWHM). This is obviously not observed in the HI angular correlations associated with the positron peaks of Fig. 3-16.

Finally it should be noted that the required kinetic energy for the fast emission of the given fragment depends only weakly on details of the model. The probability of forming an  $\alpha$  particle (or appropriate heavier cluster) and the repetition frequency ( $v_i/R_0$ ) are both dwarfed by the WKB barrier penetration factor. For any fast decay, the required kinetic energy is within a few MeV of the potential maximum,  $t_i \sim V_{\max}$ . Since the positron peaks observed in supercritical collisions appear to be associated with nearly symmetric, relatively stable final state nuclei where the nuclear mass excesses vary slowly with  $Z$  and  $A$ , the mass excess calculation ( $\Delta M - \Sigma m_i$ ) generally amounts to 1-2 MeV per proton in the cluster. The inescapable conclusion, therefore, is that unless the evaporation products are focussed in a very tight cone about the beam direction, the fast emission of an  $\alpha$  particle or more than 1 proton or 2 neutrons, associated with the narrow positron peaks, is ruled out based on the quasi-elastic nature of the observed HI angle-angle correlations. No common super-nucleus is formed in these collisions. (This model would still also require above normal nuclear density for a common super-nucleus of  $Z_U < 182$ .)

#### Sec. 4.4.5 Side Structures

From the above discussion, it is clear that spontaneous positron emission is unable to suitably describe the narrow positron peaks in the effectively subcritical Th + Th or Th + Ta systems. It has been pointed in [Grn83, MüU83, and Mü184] that an interplay between spontaneous positron production and the nuclear motion can lead to additional structures in the positron spectrum. For example, [MüU83] discusses the effect that a periodic radial oscillation of the di-nuclear separation has on the energy distribution of spontaneously emitted positrons. Parameterizing  $R(t)$  as

$$R(t) = R_0 [1 - \alpha_0 \sin(2\pi\nu t)] \quad (4.48)$$

with amplitude  $\alpha_0$  and frequency  $\nu$ , a second positron peak develops at an energy,  $E_{e^+} = E_{1s\sigma} \pm h\nu$ , for long contact times. An example in U + U collisions is shown in Fig. 4-29. A similar mechanism involving the direct transfer from a nuclear transition in the compound system to the spontaneous positron leads to very similar re-

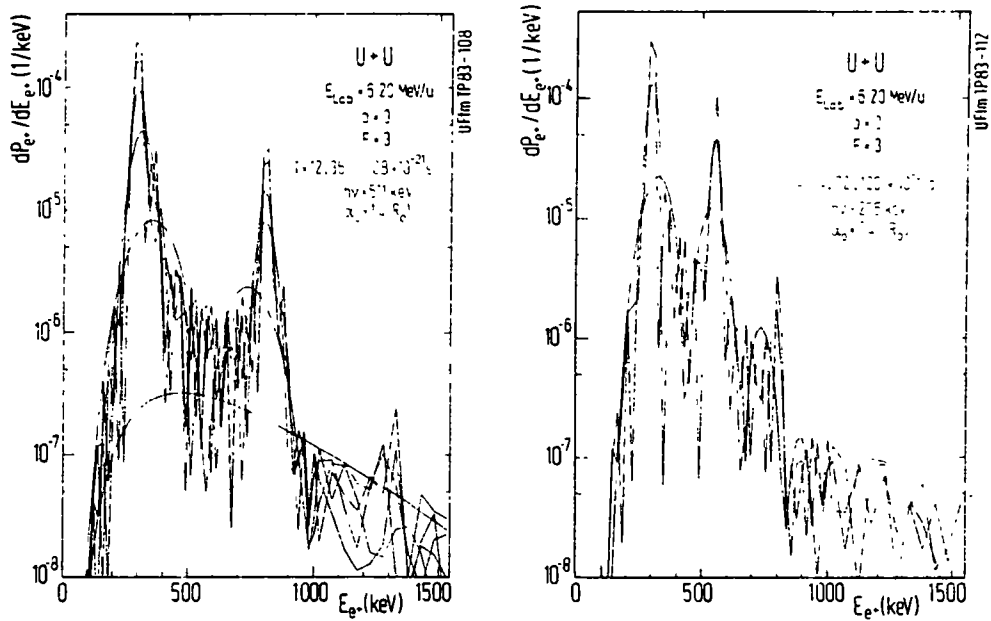


**Figure 4-29.** Spontaneous positron energy distributions modified by radial vibrations in U+U di-nuclear system, as described in text. Frequencies of  $\hbar\omega=511$  keV (left) and  $\hbar\omega=255$  keV (right) are considered. (Reproduced from [MüU83].)

suits. In both cases, structures reminiscent of Raman or anti-Stokes lines from molecular physics can, in principle, appear.

In the case of low- $Z_U$  collisions, this opens the possibility that a physically reasonable di-nuclear charge configuration (e.g., with  $R_0=17$  fm), could exhibit oscillatory motion and produce a positron peak above 300 keV. The expected 60 keV Th+Th spontaneous line could be boosted to 330 keV by a frequency of  $h\nu=270$  keV. If the dominant radial frequency in each supercritical system scales appropriately with  $Z_U$ , the measured positron lines in Th+U and U+U could also be explained by these side-band structures. In Th+Cm collisions, however, the EPOS detection efficiency is sufficiently large at  $E_{e^+}=250$  keV to have observed the associated unshifted spontaneous positron peak. Of course, this type of model still is unable to satisfactorily explain peaks in systems far below the supercritical charge threshold,  $Z_{cr}=173$ , such as Th+Ta. Finally, it should be mentioned that none of these mechanisms involving spontaneous positron emission accommodates, in a natural way, the observation discussed in Part II of this dissertation that a monoenergetic electron line is associated with the narrow positron peaks.

## Section 4.5 Other Effects

### Sec. 4.5.1 Prolonged Nuclear Contact

As noted above, prolonged nuclear contact is the essential ingredient in producing a narrow spontaneous positron peak in superheavy collisions. In addition to the enhancement in vacuum decay, however, Fig. 4-20 showed that for discrete delay times,  $T$ , oscillations develop in the dynamic positron distribution for both subcritical and supercritical values of  $Z_U$ . One might imagine that a suitable superposition of various nuclear contact times could therefore produce a narrow peak near 350 keV in all the collision systems.

The oscillatory structure is a quantum interference effect which can be qualitatively understood most simply with first order time-dependent perturbation theory. The amplitude for exciting an electron from a state in the negative energy continuum at  $E_i$  to a bound or positive energy state at  $E_f$  is given by,

$$a_{i \rightarrow f}(t = -\infty, t = +\infty) = \int_{-\infty}^{+\infty} \langle f | \partial/\partial t | i \rangle \exp[(i/\hbar) \int_{-\infty}^t (E_f - E_i) dt'] dt. \quad (4.49)$$

As described, e.g., in [Rei81b], the dynamic positron transition matrix element is proportional to

$$\langle f | \partial/\partial t | i \rangle \sim (dR/dt) \langle f | \partial V / \partial R | i \rangle. \quad (4.50)$$

During time  $T$  when the nuclei are assumed to remain at a fixed separation,  $R_0$ ,  $(dR/dt) = 0$  and the dynamic production is zero. For nearly quasi-elastic collisions, the excitation amplitudes are symmetric for the in-coming and out-going paths of the trajectory  $a(0, +\infty) = a(-\infty, 0)$ , and the delay-time  $T$  then introduces an extra phase between these components,

$$a_{i \rightarrow f}(t = -\infty, t = +\infty) = a_{i \rightarrow f}(-\infty, 0) + \exp[i(E_f - E_i)T/\hbar] a_{i \rightarrow f}(T, +\infty). \quad (4.51)$$

The production probability includes a quantum mechanical interference term,

$$dP_{e^+}/dE_{e^+} \sim |a_{i \rightarrow f}|^2 \sim |a|^2 [1 + \cos\{(E_f - E_i)T/\hbar\}], \quad (4.52)$$

which produces modulations with the period  $\Delta E = 2\pi\hbar/T$ , exhibited in Fig. 4-20. A more complete derivation which involves the coupled-channel formalism of [Rei81b] yields similar results.

The difficulty of this interpretation for the observed positron peaks is that for a distribution of delay-times,  $f(T)$ , the oscillations from transitions to subcritically bound orbitals are smeared out very quickly. This is shown in Fig. 4-30a,b for a gaussian distribution of delay-times centered at  $\langle T \rangle = 1.5 \times 10^{-20}$  sec with a width  $2.5 \times 10^{-21}$  sec. The subcritical positron spectrum, calculated within the coupled channel formalism, becomes completely smooth, while in supercritical collisions the spontaneous peak emerges as described in Sec. 4.4. Figure 4-30c,d presents  $dP_{e^+}/dE_{e^+}$  expected for U+Cm collisions assuming either a fixed delay time,  $T = \hbar\Gamma$  (thin lines), or an exponential distribution,  $f(t) \sim \exp(-T\Gamma/\hbar)$  (thick curves), which would be appropriate for a Breit-Wigner nuclear resonance of width  $\Gamma$ . Once again, no structure is expected.

Since the energy of the measured positron peaks does not vary systematically with  $Z_U$  as expected for spontaneous positron emission, the nuclear contact times for the supercritical systems must also be short enough (e.g.,  $\langle T \rangle \ll 10^{-20}$  sec from Fig. 4-20) so that the  $1\sigma$  resonance decay peak does not develop and dominate the spectrum. The periods of oscillation associated with this time scale, however, are  $\Delta E_{e^+} > 500$  keV, which are too broad to produce narrow structures only  $\sim 80$  keV wide. Since the time scale necessary to produce narrow peaks would lead to a large spontaneous positron component, and physically reasonable delay-time distributions smear out the underlying dynamically produced oscillations, it appears that atomic interference caused by prolonged nuclear contact cannot explain the measured positron data.

### **Sec. 4.5.2 Multi-Electron Transitions**

Lichten and Robatino [Lic85a] have pointed out that multi-electron transitions during a quasi-elastic collision involving Rutherford trajectories may be important for positron emission and could in principle produce structure in the positron energy distribution. They argue that the multiple application of the one-body electron excitation operator, used in the Frankfurt coupled-channel formalism [Rei85b and refs. therein] and which appears in Eqn. 4.49, cannot describe certain types of two-electron transitions which have been previously observed [Lic85b].

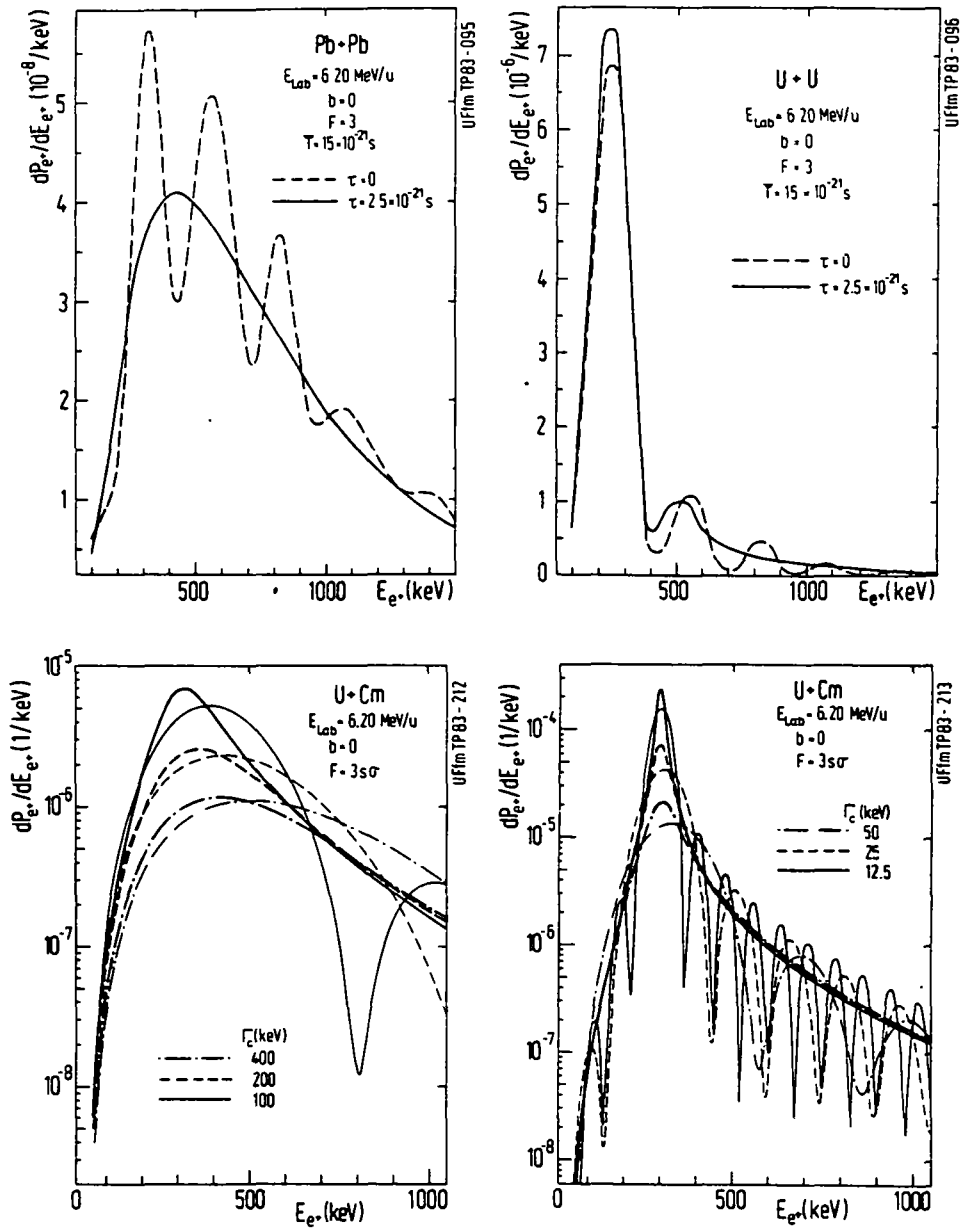


**Figure 4-30.** Influence of a distribution of contact times on the positron energy spectrum. Gaussian distribution of sticking times assumed for Pb+Pb and U+U collisions (top, reproduced from [MüU83]), and U+Cm spectra (bottom, reproduced from [Rei83]) for discrete (thin lines) and exponential distributions (thick curves).

Two-electron transitions could involve spontaneous or dynamic (induced) positron production. An example of the former is indicated in Fig. 4-31a which plots the binding energy associated with multiple-vacancy configurations of the quasi-molecular  $1s\sigma$  and  $2p\frac{1}{2}\sigma$  states. According to [Lic85a], a double vacancy in the  $1s$  shell

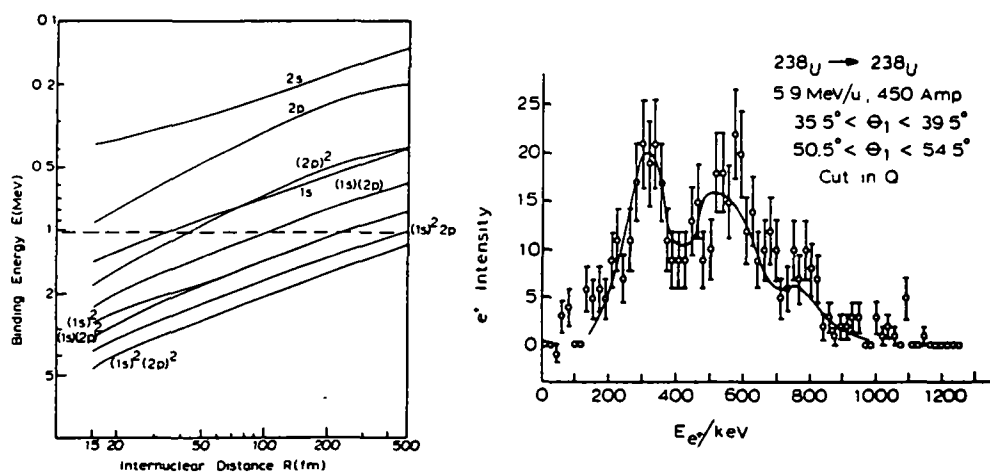


**Figure 4-31.** Binding energy of several multi-electron configurations of U + U quasimolecular orbitals (left). Model calculation of interference pattern generated in U + U collisions (right) assuming dynamic positron emission localized at  $R \cong R_{\min}$  and  $R \cong 500 \text{ fm}$  along the Rutherford trajectory, compared to data of [Bok83]. (Reproduced from [Lic85].)

could decay spontaneously by the simultaneous transitions of an electron from the  $2s$  orbital plus and electron from the negative energy continuum. The positron is liberated with energy,  $E_{e^+} \cong 2(E_{1s}) - E_{2s} - 2m_e c^2$ , and the double vacancy associated with this channel is supercritically bound, ( $2E_{1s} - E_{2s} > 2m_e c^2$ ) for larger internuclear separations ( $R_{cr} = 150 \text{ fm}$ ) than the  $1s\sigma$  state alone. The longer period of critical binding,  $t_{cr} \sim 10^{-20} \text{ s}$ , however should not directly lead to narrow spontaneous positron peaks because the change in the binding energy with inter-nuclear separation  $R$ , distributes the created positrons over a large energy interval.

The result of a model calculation [Lic85a] involving a two-electron transition with induced positron creation which leads to an oscillatory structure in the positron energy distribution is shown in Fig. 4-31b. Lichten and Robatino consider induced creation by electron excitations from the negative continuum to the  $2p_{1/2}$  orbital, coupled with transitions between the  $2p_{1/2}$  and  $2p_{3/2}$  levels. The amplitude for induced positron production involving the  $2p_{1/2}$  level is concentrated for internuclear separations  $R$  near the distance of closest approach,  $R_{\min}$ . In addition to this, an avoided crossing at  $R_0 \cong 500 \text{ fm}$  causes a very large transition matrix element between the  $2p_{1/2}$  and  $2p_{3/2}$  orbitals which produces vacancies in the  $2p_{1/2}$  shell which can be filled by induced emission from the negative continuum. [Lic85a] suggests that positron production is therefore also concentrated at  $R = 500 \text{ fm}$ . The oscillations

in Fig. 4-31b arise from the interference between positron creation at  $R = 500$  fm and  $R = R_{\min} \cong 20$  fm. The appropriate time interval between positron emission at these positions is  $\Delta T \cong (R_0 - R_{\min})/v_{\text{HI}}$ , where  $v_{\text{HI}} = 0.11c$ . The associated modulations in the positron energy distribution have a period

$$\Delta E_{e^+} = h\nu_{\text{HI}}/(R - R_{\min}) \cong 250 \text{ keV}, \quad (4.52)$$

approximately that of the structure observed in the preliminary U+U spectrum presented in [Bok83].

Several additional points must be considered before accepting this as the origin for the peaks presented above. First, although weak oscillatory structures at higher positron energies have been observed from time to time in the experimental data, they do not seem to be associated with the narrow peaks discussed in Chap. 4 which are much larger and which seem to be distinguished from the bulk of dynamic positrons by their HI angle-angle correlation. In addition, the two-electron excitation amplitude from the  $2p_{1/2}$  to  $2p_{3/2}$  states discussed by [Lic85a] must be added coherently to all other multi-electron transitions involving the  $2p_{1/2}$  level, as well as to the amplitudes of all first order excitations from the negative continuum to the  $2p_{1/2}$  orbital, which tends to smooth out the oscillations [Rei85b]. Perhaps more importantly, the suggestion by [Lic85a, Lic85b] that the single body operator used with the molecular-orbital basis by the Frankfurt group breaks down in the transition region between quasi-molecular and separated-atom behavior must be thoroughly investigated because it could have many far-reaching consequences in understanding these and other HI atomic physics experiments.

### **Sec. 4.5.3 Sudden Rearrangement of Atomic Shells**

The method of producing oscillatory structure suggested by [Lic85a] has recently been reintroduced by de Reus et al. [Reu87] using a different mechanism for concentrating positron production at large  $R$ . Although they claim that multi-electron effects are treated properly in their coupled channel formalism, the Frankfurt group suggests that a sudden rearrangement of the atomic orbitals could occur at  $R_0 \sim 1000$  fm, which would introduce a discontinuity in the potential felt by the inner shell electrons, either by a change in the total ionization state of the complex, or in the electron screening which enters self-consistently in the two-centered Coulomb potential [Reu84].

The transition matrix element for exciting electrons from the negative continuum (liberating positrons) is very large at  $R_0$  by virtue of its dependence on  $\partial V/\partial R$  (see Eqn. 4.50). The period of oscillation is once again given by Eqn. 4.52. In principle, a suitable combination of sudden jumps in the electron potential could be constructed to produce a single narrow peak. The calculations of [Reu87] indicate that unnaturally large changes in  $V(R)$  are required [ $\Delta V \sim 0.1 \cdot V(R_{\min})$ ], which moreover affect the electron ionization probabilities  $P_{e^-}(R)$ . A further analysis of this process in [Reu87b] indicates that the positron data presented in this work cannot be explained by this process without contradicting established experimental  $P_{e^-}(R)$  data. This process does, however, produce correlated electrons, and will be discussed again in Chap. 7.

#### **Sec. 4.5.4 Conversions in Super-Nucleus**

A non-atomic mechanism associated with the HI center-of-mass involves nuclear transitions in a long-lived compound system. It is motivated by the failure of conventional nuclear decays to explain the measured positron peaks because of the large expected linewidths proportional to the nuclear velocity, and the presence of large competing  $\gamma$ -ray and internal conversion (IC) electron decay modes. Transitions between nuclear levels of a long-lived compound system alleviate these difficulties because (1) the emitter velocity is  $v_{\text{CM}}$ , and (2) the relativistic increase of electron density at the origin decreases the  $\gamma$ -ray branching ratio. In supercritical systems, the presence of the  $1s\sigma$  orbital in the negative continuum alters the resulting positron spectra from nuclear conversions. Figure 4-32 presents the positron distribution resulting from a 2 MeV IPC transition in a spherical U+U nuclear complex. The sharp cusp corresponds to the  $1s\sigma$  resonance energy. The relativistically enhanced M1 conversion coefficient (up to  $10^2$ ) is five orders of magnitude larger than in  $Z=92$ , and completely dominates over  $\gamma$ -ray decay. Fast IPC transitions in a di-nuclear complex therefore contribute positron intensity at the usual spontaneous peak energy, but cannot be detected in the simultaneously measured  $\gamma$ -ray energy distribution. On the other hand, the peak energy varies in the usual way with  $Z_U^{20}$  and cannot be easily accommodated to the measured positron line energies.

Monoenergetic positron creation in a super-nucleus is also increased by orders of magnitude over  $Z=92$  because of the increased localization of atomic orbitals in which the created electron is bound. In order to explain the nearly constant line energy without invoking a di-nuclear structure which *a priori* scales properly with

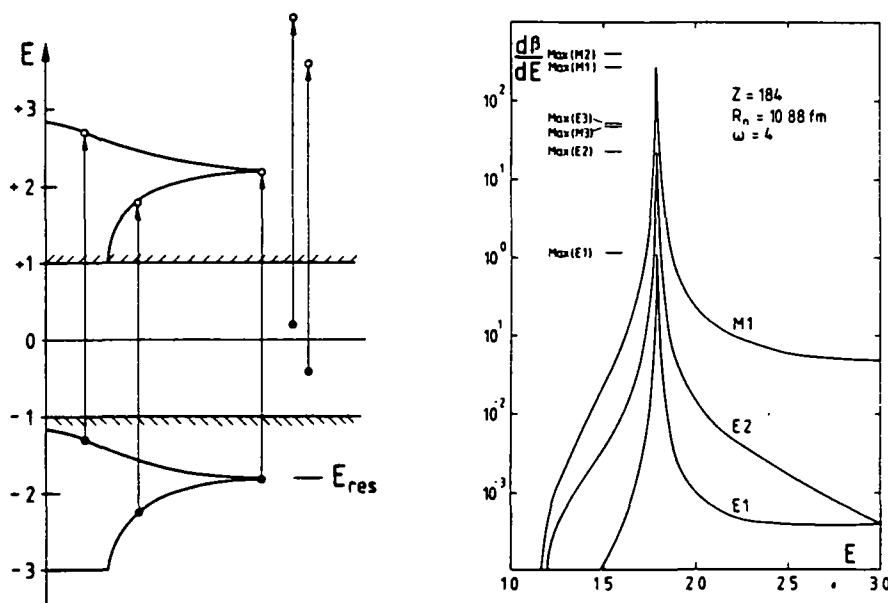


**Figure 4-32.** IPC positron energy distributions expected for various multipolarities in a  $Z = 184$  nucleus (right). Peak structure corresponds to  $1\sigma$  resonance embedded in negative Dirac continuum (left). (Reproduced from [Shl86].)

$Z_U$ . [Shl86] suggested that MPC probably would involve very similar nuclear transitions ( $\hbar\omega \sim 2 \text{ MeV}$ ) in each system, with capture of the electron into the M shell where the binding energy is fairly constant versus  $Z_U$ . Figure 4-33 illustrates schematically the resulting spectra for subcritical Pb+Cm and supercritical U+Cm collisions. In order to obtain an observable MPC peak, the combined system must be formed in  $\cong 1\%$  of HI collisions, with a lifetime longer than the atomic transition times,  $10^{-18}$  to  $10^{-17}$  sec [Shl86]. In addition to the stationary peak associated with MPC into the 3s shell, capture in the 1s, 2s, and 2p orbitals occurs with even larger probability, leading to large side-peaks which have not been unambiguously observed in these experiments. Furthermore, the long di-nuclear lifetimes imply that in supercritical systems, spontaneous positron emission should exceed MPC by a factor of  $\sim 30$  [Sof86]. Particularly because of the predicted observable presence of spontaneous emission in both the IPC and MPC processes, it appears unlikely that nuclear conversions in a long-lived di-nuclear complex adequately describes the narrow positron peaks presented in Fig. 3-16.

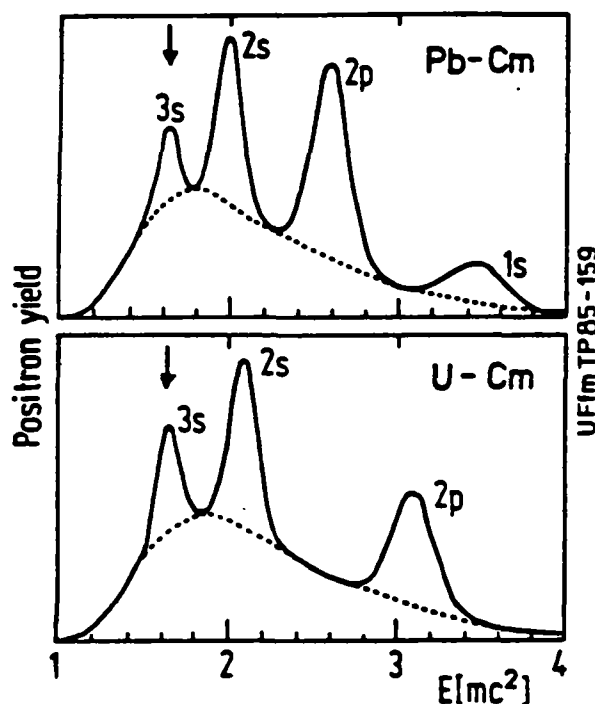


**Figure 4-33.** Model calculation of monoenergetic positron creation transitions involving capture of the electron into 3s, 2s, 2p, or 1s quasi-atomic orbitals in Pb+ Cm and U+ Cm collisions. (Reproduced from [Sof86].)

## Section 4.6 Summary of Hypothesized Origins

From the discussions of this chapter, it appears that the narrow positron peaks observed in U+ Cm, Th+ Cm, U+ U, U+ Th, Th+ Th, and Th+ Ta collisions cannot be easily explained by any of several effects considered. The response of the EPOS spectrometer to positrons and other radiations, as well as the dependence of peak production on details of the HI collision, convincingly rule out instrumental or background origins. The absence of competing  $\gamma$ -ray or internal conversion electron lines under kinematic conditions identical to those which enhance the positron peak similarly preclude origins involving the conventional internal pair creation or exotic monoenergetic positron creation transitions in the separated nuclei. An analysis of the width of the positron lines moreover argues against a source whose velocity depends on the nuclear scattering angle, but suggests that the mean laboratory velocity of the emitter is  $\langle v_{em} \rangle \leq 0.06c$ .

Although spontaneous positron emission is able to fit the peak in the U+Cm system by postulating the formation a long living nuclear molecule, it fails to reproduce the nearly constant energy of the peaks over a wide range of  $Z_U$  from 163 to 188. Attempts to accommodate spontaneous theory to the experimental energies requires implausible assumptions regarding the ionic charge distribution of the di-nuclear complex, and, for the effectively subcritical Th+Th and Th+Ta systems, significantly increased nuclear densities. Interference effects in the combined quasi-atomic system similarly have difficulty in fitting the data without arbitrary assumptions about the distribution of nuclear contact times or multi-electron transitions including discontinuities in the electronic potential. Nuclear transitions in the giant combined systems again reflect the  $Z_U$  dependent binding energies of the atomic orbitals and the  $1s\sigma$  resonance state, in contradiction with the observed data. Any scenario involving prolonged nuclear contact further is constrained by the small observed Q-loss and nearly symmetric binary HI exit channel associated with the positron peak events.

***Part II: Positron-Electron Coincidence  
Measurements***

# Chapter 5 Experimental Design

## Section 5.1 Introduction

The inability of instrumental, nuclear, or atomic processes to explain the narrow positron peaks observed in superheavy collisions described in Part I of this dissertation led us to consider other unorthodox possibilities. The very similar mean energies of all the lines suggested a single source common to all the collision systems, and the narrow peak widths suggested the possibility that the positrons are emitted in a two-body final state. One obvious possibility for the source of the peaks is the two-body decay of a previously undetected neutral particle-like object into a positron and electron pair. The search for the monoenergetic electron which must accompany the narrow positron peak therefore motivated the experiments described in Part II of this dissertation. Following a brief introduction and discussion of some preliminary considerations, this chapter describes the modifications to the EPOS spectrometer required for these measurements and an analysis of its performance. Chapter 6 presents the experimental results, and Chap. 7 discusses several possible interpretations of the data.

We first began to discuss particle-like origins for the positron peaks in the Spring of 1984 when the Th + Cm peak was discovered. In August 1984, after extending the  $Z_U$ -dependence measurement down to Th + Th ( $Z_U = 180$ ), serious work began on the design of an apparatus for the coincident detection of positrons and electrons. (The first public mention of a possible new particle was by J.S. Greenberg, Nashville, October 1984.) Some of the characteristics of the proposed neutral object,  $X^0$ , which have a bearing on the experiment, are already determined by the existing data. To decay into a positron-electron pair where  $E_{e^+} \cong 340$  keV, the total energy of the object must be  $M_X \cong 1.7$  MeV/c<sup>2</sup>. It could be formed either directly in the collision, or in competition with the conventional decay of an excited state in the exit nuclei or compound system. If such an object exists, its lifetime is bounded on the one hand by the positron peak widths,  $\tau_X \geq \hbar \Delta E_{e^+} \sim 10^{-19}$  sec, and on the other by the fiducial volume of the EPOS spectrometer,  $\tau_X < (\sim 1 \text{ cm})/v_X \sim 10^{-8}$  sec.

In principle, the decay partner could also be a  $\gamma$ -ray or neutrino, implying a charged object  $\phi^+$  with mass  $M_\phi \sim 1.5$  MeV/c<sup>2</sup>, or a heavier object, e.g., pion or nuclear fragment, which decays to a positron plus other heavy object. This experiment

focussed, however, on searching for a monoenergetic electron, at an energy  $E_{e^-} \sim E_{e^+}$ , appearing in coincidence with the positron line.

During the early stages of this experiment, before results were published in [Cow86], several theoretical papers discussed various versions of a particle-like interpretation for the positron peak data. For example, Schäfer et al. [Shä84] considered the effect of a strong external electric field on the Higgs vacuum and calculated that, in analogy with QED, a negatively charged Goldstone boson could be created to partially shield a supercritical nuclear charge. An accompanying positively charged "vacuum excitation" is then freed to decay to  $e^+v$ . Balantekin et al. [Bal85], and independently Schäfer et al. [Shä85], discussed the possibility that the positron peaks are due to the  $e^+e^-$  decay of an elementary particle. Of spin-parity assignments  $0^\pm, 1^\pm$ , [Shä85] rules out all but a pseudoscalar particle as contradicting high precision QED data. Balantekin et al. [Bal85] identify the  $0^-$  particle as a short-lived ( $\tau = 1.3 \times 10^{-13}$  sec) pseudoscalar axion [Wei78, Wil78], which should accompany the U(1) Peccei-Quinn symmetry [Pec77] postulated to remove the CP-violation predicted to occur in strong interactions by Quantum Chromodynamics. Although previous searches for the axion in nuclear transitions [Cal79], beam-dump experiments [Fai80], and heavy quarkonium decays [Edw82] had been negative, this mass-lifetime combination could have evaded detection [Muk86].

A very different mechanism to explain the narrow positron peaks was proposed by Wong [Won86]. He suggests that a loosely bound ( $e^+e^-e^+$ ) complex could be formed in the HI collision, which subsequently decays into  $e^+\gamma$  with  $E_{e^+} = 340$  keV. Later calculations [Chu86] showed, however, that the branching ratio for  $(e^+e^-e^+) \rightarrow e^+\gamma$ , as compared to the dominant  $(e^+e^-e^+) \rightarrow e^+\gamma\gamma$ , is only  $\sim 4 \times 10^{-11}$ . Approximately  $10^6$  b/sr production cross-sections would be required to fit the measured positron peak intensities. Other more serious models based on composite objects with internal structure [Won86, Bat86, Mül86, Gei87, Won87] have been proposed since the coincidence results were published. These are discussed in Chap. 7.

A rather novel process was proposed by Chodos and Wijewardhana [Cho86] to explain the lower energy positron peaks observed in [Tse85, Kön87] as well as those presented in this work [Cow85]. They suggest that a particle of mass just greater than  $2m_e c^2$  is produced in the collision,  $M_x c^2 \cong 2m_e c^2$ , which receives energy from the rotating compound system. It is then "spun-off" from the combined system with

discrete energies in increments of the HI rotational frequency,  $\hbar\omega$ . Since very little transverse momentum is imparted to the positron from the two-body decay of the light object at the mass threshold, the positron peak widths are given by the CM motion only. Multiple peaks in the positron spectrum may be explained with  $\hbar\omega \sim 100$  keV.

Neither the  $(e^+e^-e^+)$  nor the  $M_X \sim 2m_e c^2$  processes outlined above lead to detectable monoenergetic electrons emitted in coincidence with positrons, although both can, at least in principle, explain the observed narrow positron peak widths. On the other hand, while the production and  $e^+e^-$  decay of a neutral object with  $M_X \sim 1.7$  MeV/ $c^2$  provides a very natural explanation for the positron peaks, the calculations of [Bal85], [Cho86], and more recently, [Mül86] and [Rei86a], indicate that the axion, or other light particle which is created in the strong collisional electromagnetic field, is emitted with velocities much larger than  $v_{CM}$ . The positron peaks are therefore expected to be much wider than the measured  $\sim 80$  keV. This is also true if production competes with nuclear decays since all transitions above the  $\hbar\omega = M_X c^2$  threshold produce  $X^0$ 's with finite kinetic energies. An important consideration before searching for the accompanying electron is therefore whether it is possible for such a broad range of emission velocities to produce a narrow positron peak.

In addressing this question, we first note from Sec. 2.2.7 that the Doppler broadening of positrons isotropically emitted with energy  $E_{e^+}$  from a system traveling with velocity  $\beta$ , produces an energy distribution in the lab which resembles a rectangle of width  $2\gamma\beta P^+ c$ , centered at an energy  $(E + m_e c^2) = \gamma(E^+ + m_e c^2)$ . For creation and decay of an object  $X^0$ , the Doppler broadening is proportional to the laboratory source velocity,  $(\gamma\beta)_{em} = P_X^{lab}/M_X c$ . The most useful form of the source velocity distribution in the lineshape integral (Eqn. 2.74) is therefore in terms of the laboratory momentum of the source,  $\omega(P_X, \Omega_X) = dN_X/dP_X d\Omega_X$ . For illustration, the case of an  $X^0$  created in the CMS of a heavy-ion collision (e.g., Th+Cm at 6.02 MeV/u,  $v_{CM} = .056c$ ), with a constant distribution of velocities from  $\beta_X = 0$  to  $\beta_X = 1$ , is considered.

Combining the Lorentz invariant quantity,  $d^3P/(E + m_e c^2) = \text{constant}$ , with  $d^3P = P^2 dP d\Omega$  shows that  $[(E + m_e c^2)/P^2] \omega(P)$  is also Lorentz invariant. The laboratory distribution of  $X^0$  momenta is therefore related to its distribution in the center-of-mass system by

$$\omega(P_x, \Omega) = (P_x^2 W_x^* / P_x^{*2} W_x) \omega^*(P_x^*, \Omega^*). \quad (5.1)$$

The energy of the  $X^0$  object in the CM is given by the Lorentz transformation,

$$W_x^* = \gamma_{cm} [W_x - \beta_{cm} P_x \cos \theta_x]. \quad (5.2)$$

For this example, after integrating over the emission direction of the  $X^0$  in the lab,

$$\omega(P_x) = \int d\Omega_x (P_x^2 W_x^* / P_x^{*2} W_x) w^*(P_x^*, \Omega^*),$$

and using (from Eqn. 2.59),  $d(\cos \theta_x) = -dW_x^* / [(\gamma\beta)_{em} P_x]$ , and the identity  $dW^* = (P^*/W^*) dP^*$ ,

$$\omega(P_x) = (P_x / 2\gamma\beta W_x) \int_{P_x^* -}^{P_x^* +} w^*(P^*) / P^* \bullet dP^*, \quad (5.3)$$

The limits of integration are,

$$P_{\pm}^* = \gamma(P_x \pm \beta W_x). \quad (5.4)$$

For this particular choice of emitter distribution,  $dN/d\beta_x^* d\Omega_x^* = (4\pi)^{-1}$ ,

$$\omega(P_x^*) = (dN/d\beta_x^*) \bullet (d\beta_x^*/dP_x^*) = M_x^2 / W_x^{*3}, \quad (5.5)$$

and Eqn. 5.3 is,

$$\omega(P_x) = (M_x^2 P_x) / [2(\gamma\beta)_{cm} W_x] \int_{P_x^* -}^{P_x^* +} [P_x^* (P_x^{*2} + M_x^2)^{3/2}]^{-1} dP_x^*. \quad (5.6)$$

As shown in Fig. 5-1a, the laboratory momentum distribution is smooth except for a sharp Jacobian peak at  $\beta_x^{lab} = \beta_{CM}$  which reflects the singularity,  $1/P_x^*$ , in the integrand of Eqn. 5.6 and corresponds to the boost of slowly emitted particles up to the CM velocity.

The associated positron energy spectrum is calculated by superimposing appropriately shifted and broadened laboratory lineshapes, weighted by the momentum distribution of Fig. 5-1a. As seen in Fig. 5-1b, the concentration of  $X^0$  velocities in the Jacobian peak leads to a narrow positron peak with a width of  $\leq 100$  keV, only

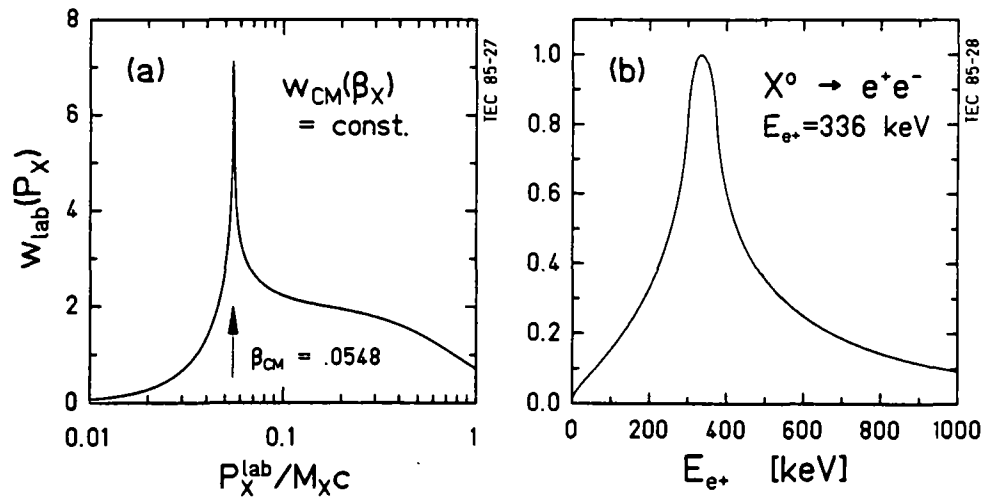


**Figure 5-1.** (a) Laboratory momentum distribution of a 1.8 MeV/c<sup>2</sup> object emitted isotropically from the CM system with a constant velocity distribution from  $v_x = 0$  to  $c$ . The Jacobian peak at  $v_{CM}$  produces a narrow line in the  $e^+$  energy spectrum (b), which has a width  $\leq 100$  keV (FWHM).

$\sim 10\%$  larger than that expected for a fixed lab velocity equal to  $v_{CM}$  [Cow85]. Neutral objects created with larger velocities produce much wider positron distributions shifted to higher energy. These form the broad continuum contribution of positron energies beneath the narrow peak.

Although the CM velocity distribution considered is not physically expected, this example demonstrates schematically that, despite a large range of emitted momenta, the peaks in the positron spectrum of heavy-ion collisions could be consistent with  $X^0$  creation if sufficient probability exists for the source to be created with low  $P_x$ . The tailing to high energy from fast objects would be hard to differentiate from the contribution of nuclear and dynamic positrons.

As discussed in Sec. 2.2.7, if the  $X^0$  lifetime is greater than  $\sim 10^{-10}$  sec, many of the high-momentum objects escape the  $\sim 2$  cm fiducial volume of the EPOS spectrometer before decaying. This velocity filter effect (see Sec. 2.2.6 and [Cow85, Cow86]) reduces detection of the high energy positron component and enhances the appearance of a narrow peak. It is illustrated quantitatively in Fig. 5-2 where the momentum distribution  $\omega(P_x^*) = \text{constant}$  is assumed for the emitted  $X^0$  particles. Although no peak is apparent for short lifetimes where the decays are centered near the solenoid axis, for  $\tau_x > 10^{-10}$  sec a narrow positron peak emerges

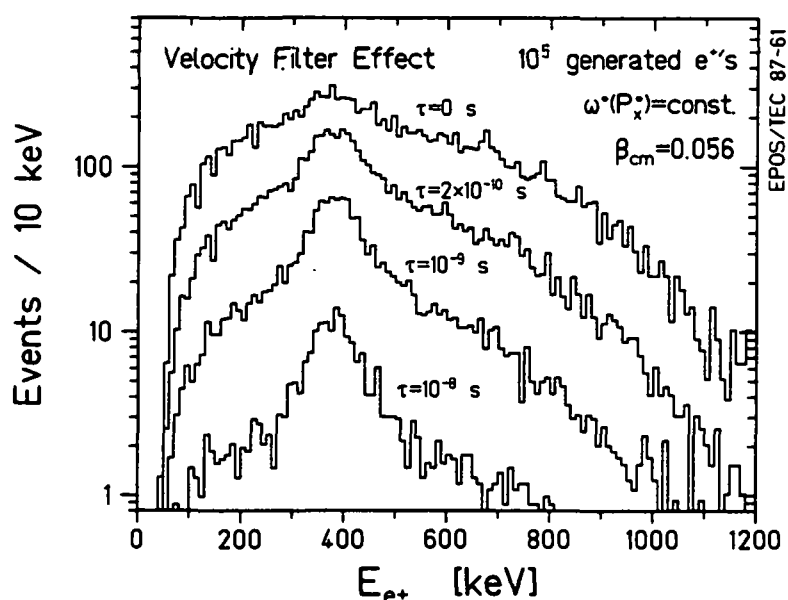


**Figure 5-2.** MCSPEC calculations of positron energy spectra from the two-body decay of a neutral object created isotropically in the CMS with a constant distribution of momenta ( $10^5$   $X^0$ 's generated per simulation). Curves reflect different assumed  $X^0$  lifetimes as marked.

because of the suppressed detection efficiency for high velocity  $X^0$ 's decaying off-axis. Based on these considerations, it is in principle possible that the emission of a monoenergetic positron in the two-body decay of a particle-like object is consistent with the observation of narrow positron peaks from superheavy collisions.

### **Sec. 5.1.2 Expected Signature**

The experimental signature for the two-body decay of a neutral object is the back-to-back emission of equal energy positrons and electrons in the rest frame of the emitter. If the source lives long enough to move away from the influence of the Coulomb field of the heavy ions, the mean positron and electron energies will be approximately equal in the lab (e.g.,  $|E_{e^+} - E_{e^-}| < 20$  keV requires  $r > 2 \times 10^4$  fm, or  $\tau_X \geq 10^{-18}$  sec). In the laboratory system, the kinetic energy distributions of the positron and electron will of course be Doppler broadened, and the opening angle between their momentum vectors reduced from  $180^\circ$ . The ideal experiment would involve measuring the energy and angle of the coincidentally emitted positrons and electrons, reconstructing their center-of-mass, and searching for resonances in the invariant  $e^+e^-$  mass spectrum.

As described in the next section, the salient aspects of such an experiment can be carried out with a modified version of the EPOS spectrometer based on the premise that the source is slowly moving. The relatively small emitter velocities ( $v_{em} \leq 0.1c$ ) deduced from the narrow positron peaks imply that the positron-electron opening angle in the laboratory remains large,  $\theta_{e^+e^-} \gg 90^\circ$ . This property can be exploited by redistributing the solenoid magnetic field to separate the EPOS spectrometer into two solenoid detection systems, transporting positrons to one side and electrons to the other. Detection of back-to-back, relative to isotropically emitted positrons and electrons, is thus enhanced. A search is then made for monoenergetic electron peaks which are coincident with the previously observed narrow positron structures.

Although only a very approximate measurement of the positron and electron emission angles is provided by their time-of-flight (TOF), high resolution  $e^+$  and  $e^-$  energy measurement substantially determines the positron-electron kinematics. In the lab, the positron and electron energies are given by the Lorentz transformations,

$$W_{e^+}^{lab} = \gamma_X(W_{e^+}^* + \beta_X P_{e^+}^* \cos \theta_{e^+}^*), \quad (5.7a)$$

$$W_{e^-}^{lab} = \gamma_X(W_{e^-}^* + \beta_X P_{e^-}^* \cos \theta_{e^-}^*). \quad (5.7b)$$

By adding the total energy of the coincident positron and electron, the emission-angle dependent parts of their Doppler shifts cancel (since  $P_{e^+}^* = P_{e^-}^*$  and  $\theta_{e^-}^* = \pi - \theta_{e^+}^*$ ), yielding

$$E_{e^+}^{lab} + E_{e^-}^{lab} = \gamma(E_{e^+}^* + E_{e^-}^*) = \gamma M_X c^2. \quad (5.8)$$

Since  $\beta$  and  $\gamma$  refer here to the laboratory velocity of the source, Eqn. 5.8 gives the total laboratory energy of the neutral object which is very nearly its rest mass for a considerable range of small  $X^0$  momenta. A characteristic signature of a two-body final state is then a sharp peak in the distribution of the sum of positron and electron energies, whose width (determined primarily by intrinsic detector resolution) is smaller than the Doppler-broadened energy distribution of the individual coincident positron and electron peaks, as illustrated in Fig. 5-3.

If the positron peaks are associated with a pair of charge conjugate particles (e.g.,  $\phi^+ \phi^-$  or  $(e^+ e^- e^+)$  and  $(e^- e^+ e^-)$ ), no such cancellation of the Doppler shifts oc-

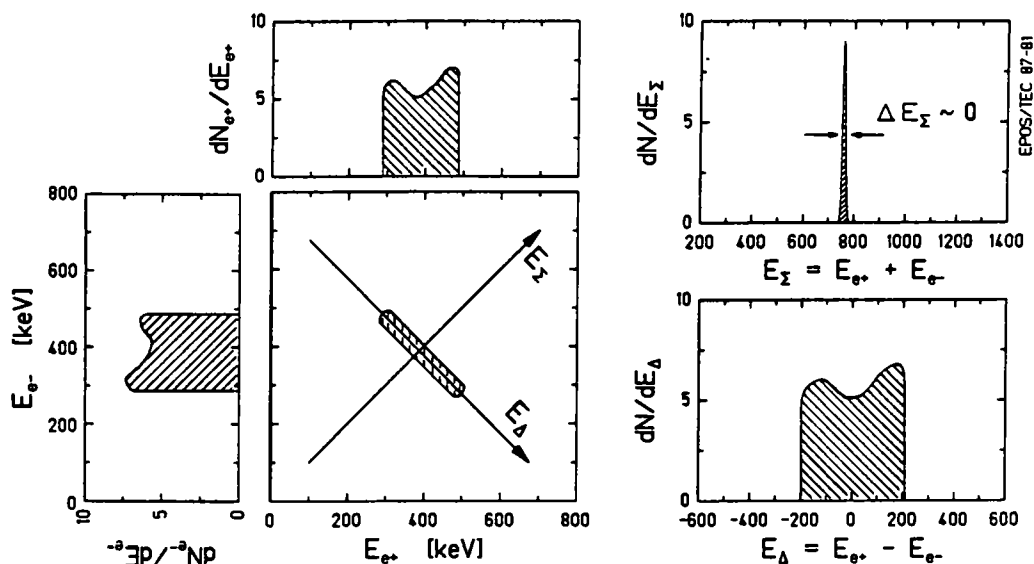


**Figure 5-3.** Correlation of measured positron versus electron energies from the two-body decay of a neutral object, and projections of the coincidence yield on the  $E_{e^+}$ ,  $E_{e^-}$ ,  $E_{\Sigma} \equiv E_{e^+} + E_{e^-}$ , and  $E_{\Delta} \equiv E_{e^+} - E_{e^-}$  axes.

curs. Identifying the decay electron which corresponds to the conjugate-partner decay positron is even more difficult because the kinetic energies of the positive and negatively charged parents will be shifted in opposite directions by the influence of the Coulomb field of the heavy ions. The associated electron should have a mean energy lower than the positron, and is therefore further obscured by the large background of low energy  $\delta$ -electrons. Different broadenings from the uncorrelated parent source velocities further complicates identification because the large intensity of the tails of each energy distribution reduces the ratio of peak electron to peak positron coincidences. Within the Chodos model mentioned above,  $M_x \cong 2m_e c^2$ , the positron and electron are emitted in almost the same laboratory direction and therefore have very little chance of being detected in the opposite sides of the EPOS solenoid. Of the various particle-related processes described previously, only the two-body decay of a neutral particle has a plausible chance of being identified.

EPOS Spectrometer

EPOS/IES 86-28

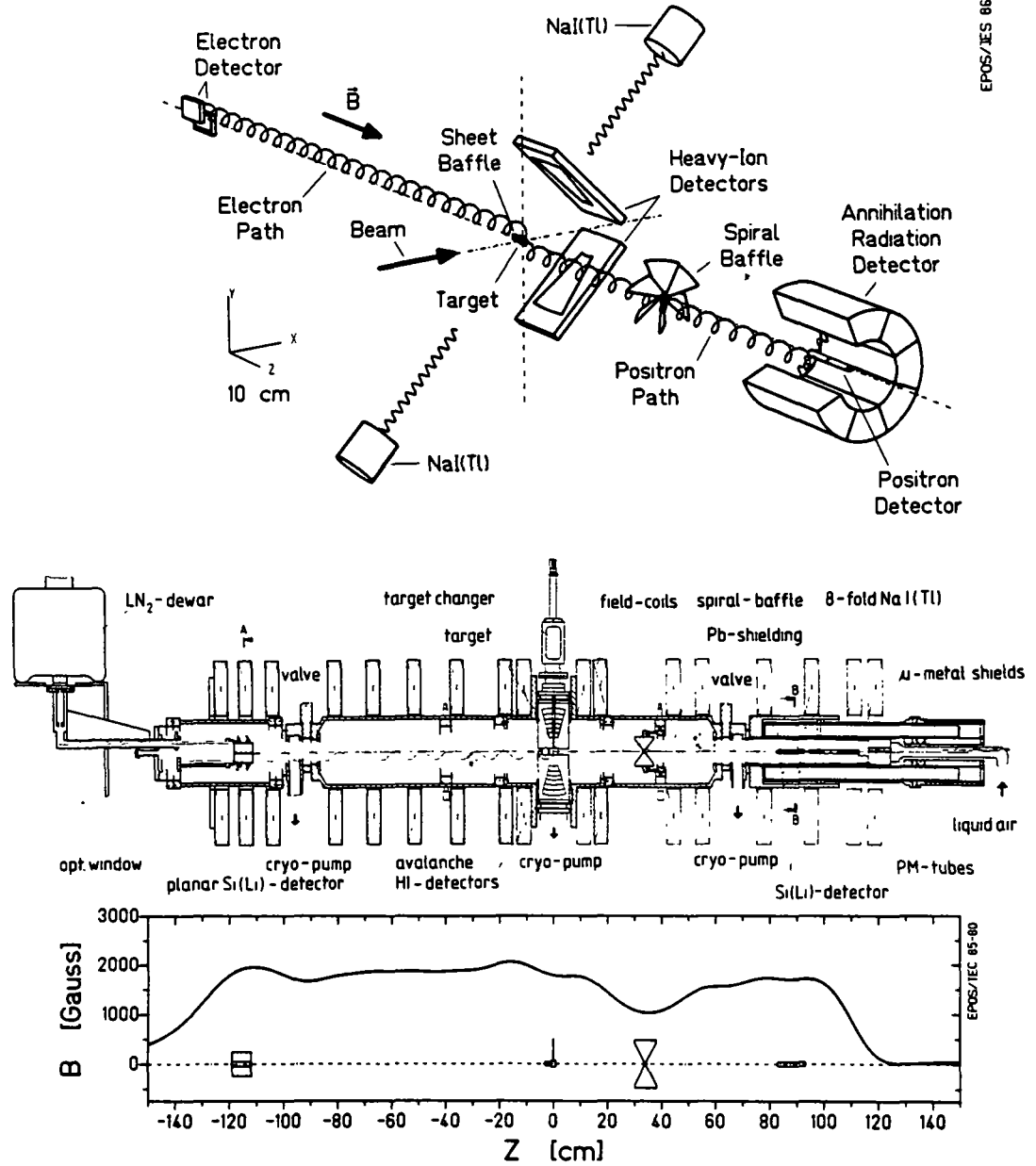


**Figure 5-4.** A perspective drawing of the EPOS spectrometer (upper panel), a schematic view (middle), and the magnetic field configuration (lower panel). Polar coordinates, with +Z along the solenoid axis and +X in the beam direction (noted in upper panel), are used to describe transport efficiency.

## Section 5.2 EPOS Spectrometer

### Sec. 5.2.1 Overview

In order to search for correlated positron and electron emission, the EPOS spectrometer was modified to increase the detection efficiency of electrons in coincidence with positrons. As shown in Fig. 5-4, the electron detector has been replaced and the pancake coils rearranged to produce a nearly uniform magnetic field configuration. The spectrometer is thereby divided into two essentially independent transport systems, one to detect positrons ( $Z > 0$ ) and the other electrons ( $Z < 0$ ).

For the first measurement in June/July 1985, the detection of scattered heavy-ions and  $\gamma$ -rays remained unchanged from that described in Chapter 2. In subsequent experiments (February/March and June 1986), a larger set of heavy-ion PPAC detectors was installed, shown in Fig. 5-5. The new counters subtend an angular range of  $25^\circ < \theta_{HI} < 65^\circ$  in theta, and  $-68^\circ < \phi_{HI} < +68^\circ$  in phi. In order to achieve this  $\sim 2.5$  gain in solid angle, the PPAC's were positioned somewhat closer to the target, which decreased the intrinsic polar angle resolution from  $\cong 0.5^\circ$  to  $\sim 1.2^\circ$ .

The positron detector and spiral baffle were unchanged from the configuration described in Sec. 2.2 although the ARD NaI crystal array was positioned  $\cong 1$  cm closer to the target in order to improve the positron identification efficiency. In exchange, the 5 cm Pb shielding in front of the ARD was reduced to 4 cm, and the suppression of  $\cong 500$  keV photons direct from the target is reduced from  $10^4$  to  $\cong 2 \times 10^3$ . The low-energy exponential background was slightly reduced relative to the previous measurements, and accounts for only 5.3% of the  $N_\gamma \geq 1$  positron-ARD intensity.

In order to avoid a magnetic bottle around the target site, a small magnetic mirror was retained on the electron side corresponding to  $\theta_{mir} = \pi - 68^\circ$ . Together with an aluminum sheet baffle placed next to the target to suppress low-energy  $\delta$ -electrons, this limits the maximum emission angle for which positrons are transported toward the Si(Li) detector to  $\theta_{e^+}^{max} \cong 110^\circ$ . As shown in Fig. 5-6a, the positron detection efficiency (including  $\epsilon_{ARD}$ ) reaches a maximum of  $\cong 12\%$  (a 40% reduction from Part I). The calculated efficiency is once again in good agreement with source measurements throughout the interesting range.

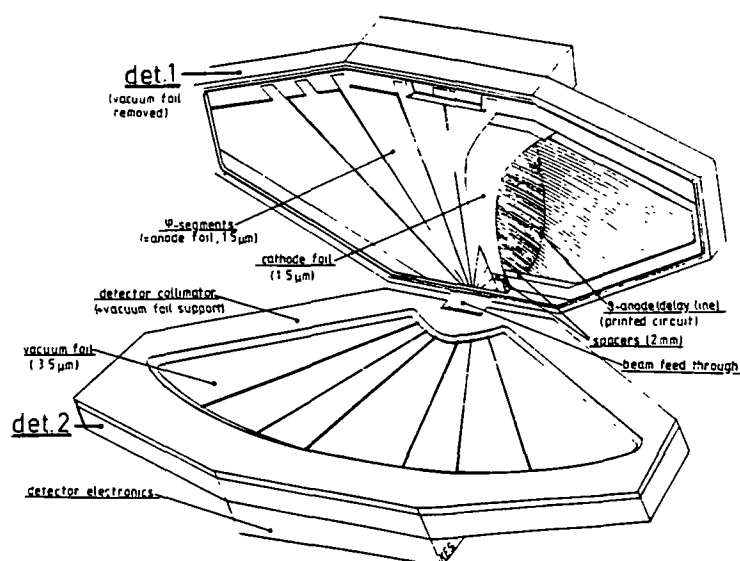


**Figure 5-5.** Diagram of the large area PPAC detectors used in 1986-87 coincidence measurements. Azimuthal angular range is  $-68^\circ < \phi < 68^\circ$  in  $12^\circ$  bins, with a  $\delta\theta_{\text{HI}} \sim 1.2^\circ$  polar angle resolution.

## Sec. 5.2.2 Electron Detection

**Sec. 5.2.2.1  $\delta$ -Electron Suppression:** As mentioned in Chapter 2, a very high flux of low-energy  $\delta$ -electrons is one of the dominant features of superheavy collision systems. Dealing with this situation presents the principal difficulty in carrying out coincidence measurements of electrons with positrons. In addition to the usual problems of measuring with high counting rates while maintaining good energy resolution, the presence of a high multiplicity of  $\delta$ -electrons, together with high efficiency, compounds the problem of detecting  $\delta$ -electrons simultaneously with the interesting monoenergetic electron signal. Because of the very steep exponential character of the  $\delta$ -electron energy distribution, this problem was addressed by maintaining high detection efficiency above the interesting energy range of  $E_{e^-} > 300$  keV, while striving for a very sharp cut-off in detection efficiency below this threshold. The method chosen employed a geometry similar to that used previously by Backe et al. [Bac83]. It adds a further feature to exclude the low energy part of the spectrum.

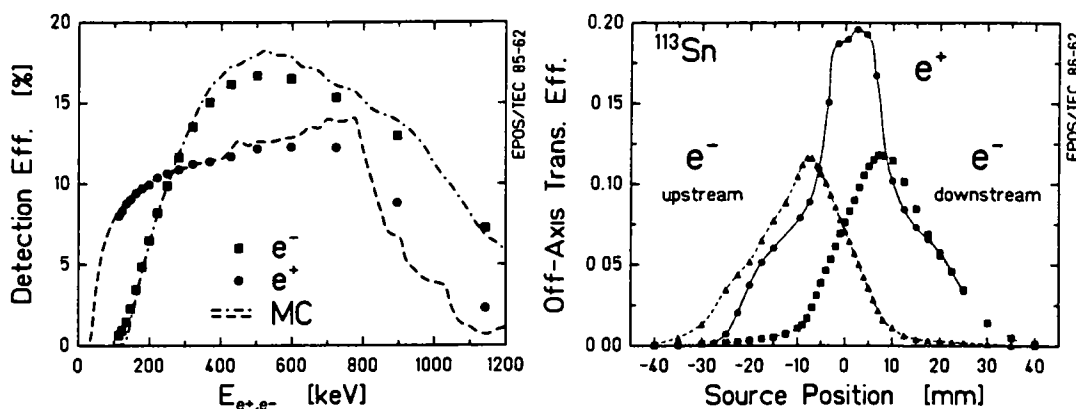


**Figure 5-6:** Energy dependence of  $e^+$  and  $e^-$  detection efficiencies (left). Dashed, dotted curves calculated with ECPI (App. B),  $\epsilon_{e^+}$  includes 60% detection efficiency of NaI array. Measured transport efficiency for  $e^+$  or  $e^-$  emission off-axis (right). Upstream and downstream  $e^-$  detectors are plotted separately.

Electrons are detected in two planar Si(Li) detectors ( $32 \times 65 \text{ mm}^2 \times 3 \text{ mm}$  thick) which are vertically oriented parallel to the solenoid axis at a distance of 112 cm (to  $\sim 119 \text{ cm}$ ) from the target. As shown in Fig. 5-7, the counters face each other and are removed a distance  $\ell = 9 \text{ mm}$  from the axis. The detector positioned upstream along the beam direction is displaced upward and the other symmetrically downward from the axis. Their active surfaces "overlap" in the vertical direction by  $\pm 4 \text{ mm}$  on either side of the solenoid axis. The horizontal separation,  $\ell$ , is chosen so that low-energy  $\delta$ -electrons having orbital radii,

$$2p = 2(pc/eB) \sin\theta_{e^-},$$

smaller than  $\ell = 9 \text{ mm}$  may then spiral between the counters unhindered. Detection is thereby suppressed for low electron energies (small  $P_{e^-}$ ) and flat emission angles with respect to the solenoid axis (i.e.,  $\theta_{e^-}$  near  $180^\circ$ ). Figure 5-7d illustrates the detection efficiency around this low energy threshold, showing that electrons emitted with  $P_{e^-} < \ell(eB/2c)/\sin\theta_{e^-}$  are not detected.

Simply increasing the inter-detector separation to exclude the entire range of undesired  $\delta$ -electron energies, however, leads to a smooth decrease in efficiency (i.e., for steeper emission angles) for the interesting energy range as well. A complementary, second-stage, low-energy suppression consists of a small sheet of alu-

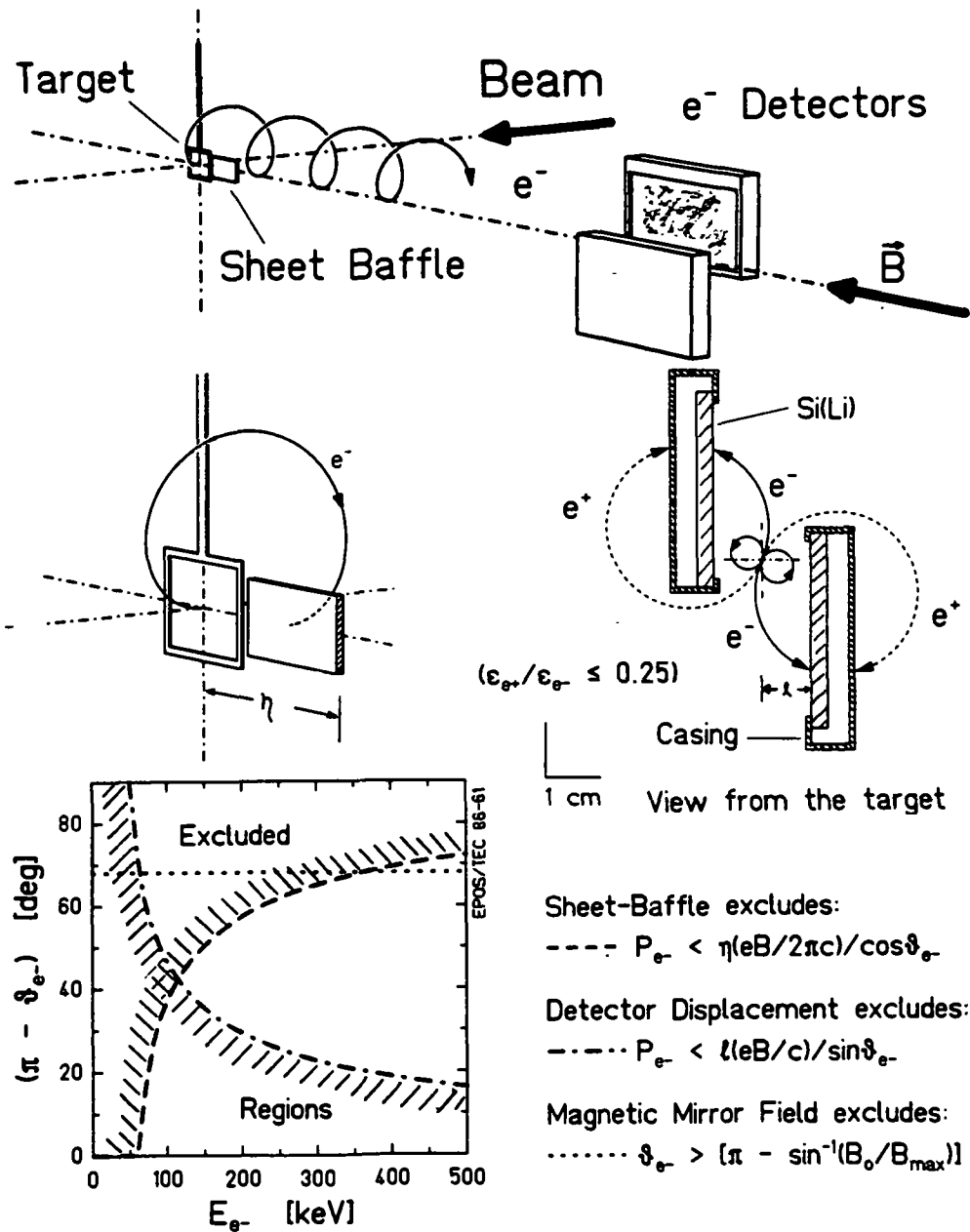


**Figure 5-7.** Suppression of intense low-energy  $\delta$ -electron flux by: 1) Off-axis arrangement of the  $32 \times 65 \text{ mm}^2$  (3 mm thick) Si(Li) detectors (middle-right). Low-energy electrons emitted at flat angles spiral between the counters. Positrons of opposite orbital helicity have a reduced probability ( $\times 0.25$ ) for detection. 2) A sheet baffle (middle-left) absorbs low-energy electrons emitted at steep angles (i.e., short pitch lengths).

minum (10 mm  $\times$  20 mm  $\times$  1 mm) placed beside the target. Its edges are positioned at  $Z = -31 \text{ mm}$  and  $Z = -11 \text{ mm}$  from the center of the beam spot, respectively. This "sheet" baffle is suspended between two 0.150 mm thick Cu-Be wires

(running in grooves along the two vertical edges) which are attached to brass supports  $\sim 10$  cm above and below the solenoid axis.

Low energy electrons which are emitted at angles steep enough such that their orbital radii are sufficient to reach the off-axis Si(Li) detectors (i.e.,  $\sin\theta_{e^-} > \frac{1}{2}\ell(eB/\rho c)$ ) have correspondingly shorter pitch-lengths, given by

$$L_o = 2\pi(P_{e^-c}/eB)\cos\theta_{e^-}.$$

Those with  $L_o$  shorter than the length of the sheet baffle,  $\eta = 31$  mm, are stopped in the baffle, leading to a suppression of electrons for  $P_{e^-} < \eta(eB/2\pi c)/\cos\theta_{e^-}$  (see Fig. 5-7d). This complements the  $1/\sin\theta_{e^-}$  dependence provided by the off-axis displacement of the detectors. A small magnetic mirror field was constructed on the electron side of the spectrometer to avoid the formation of a magnetic bottle around the target site. This further limits the range of emission angles for which the electrons are transported to the electron detectors to  $\theta_{e^-} > [\pi - \theta_{\text{mir}}] = 112^\circ$ . The sheet-baffle length,  $\eta$ , was chosen as the pitch-length of a 300 keV electron emitted at  $112^\circ$  ( $L_o = 31$  mm). The detection efficiency for "interesting" electron events above  $E_{e^-} \geq 300$  keV is therefore not significantly reduced by the sheet baffle.

The spectrometer acceptance as a function of electron energy and emission-angle was optimized by choosing the sheet baffle dimensions and detector geometry which best suppress the detection of electrons with  $E_{e^-} < 300$  keV, while simultaneously optimizing the detection efficiency for  $E_{e^-} > 300$  keV. The transport efficiency was calculated, during the design stage, by a hybrid adiabatic ray-tracing Monte-Carlo technique [Cow85a] which traced the electron orbits only in the target region and near the detectors, using the adiabatic gyration radius and pitch-angle calculated from Eqns. 2.9-2.12. The phase relationship between target and detector orbits for a given emitted electron energy and angle was ignored, as described in Sec. 2.2.5. Full ray-tracing calculations with the ECPI program described in App. B, verified that this approach is extremely accurate.

**Sec. 5.2.2.2 Detector Characteristics:** Each of the electron detector Si(Li) crystals is divided into two 32.5 mm  $\times$  32.0 mm active segments, as shown in Fig. 5-8. The halves share a common ground contact ( $40 \mu\text{g}/\text{cm}^2$  Au), but are read out by separate preamplifiers providing a total of four time and energy signals. The  $\cong 3$ mm active depth stops electrons with energy up to 1.8 MeV. Each detector is covered with a

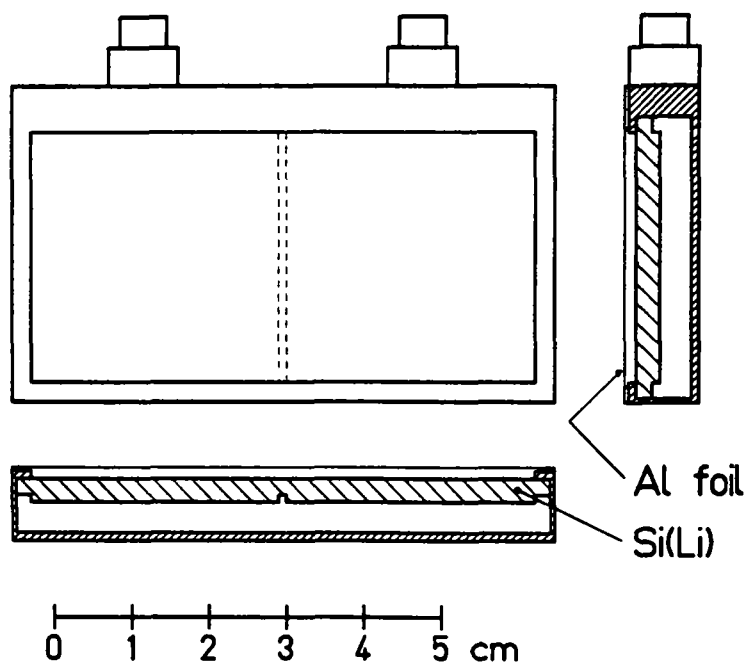


**Figure 5-8.** Diagram of one electron detector showing the orientation of the subdivided Si(Li) crystal within the detector housing and the light-tight aluminum covering foil.

light-tight  $3 \text{ mg/cm}^2$  ( $10 \text{ }\mu\text{m}$ ) Al foil, and cooled to  $-30^\circ \text{ C}$  (in 1985 experiment). This provided an energy resolution of  $\leq 30 \text{ keV}$  (FWHM) at  $E_{e^-} = 350 \text{ keV}$ . For subsequent measurements (1986) the counters were cooled with  $\text{LN}_2$  and achieved an  $\cong 10 \text{ keV}$  energy resolution. The detectors were operated at  $+200 \text{ V}$  bias and exhibited a  $\Delta t \cong 4 \text{ ns}$  time resolution (FWHM) measured versus the PPAC start signals. The line-shape response to electrons incident in the counters is parameterized as in Eqn. 2.34. Figure 5-9a presents fits to conversion electron lines from a  $^{207}\text{Bi}$  source. Backscattering from the counters leads to a peak-to-total ratio at  $350 \text{ keV}$  of  $\cong 60\%$ , as shown by the solid curve in Fig. 5-9b. Energy-loss straggling in the Al foil was small and did not significantly add to the electron tailing. Since it was mounted  $\cong 1 \text{ mm}$  directly above the crystal surface, the relatively large mean angular deviation from multiple scattering,  $\langle \delta\theta_{e^-} \rangle \sim 30^\circ$ , did not affect the detection efficiency.

The counters present a small geometric cross-section to the target ( $1.9 \times 10^{-4}$  of  $4\pi \text{ sr}$ ) reducing the intercepted flux of direct  $\gamma$ -rays and neutrons. Although the detector casings and cooling apparatus (consisting of a plastic mount  $3.2 \text{ cm}$  radius by  $15 \text{ mm}$  wide, and a  $3 \text{ mm}$  thick by  $1.5 \text{ cm} \times 1.5 \text{ cm}$  copper angle "heat-sink" to which

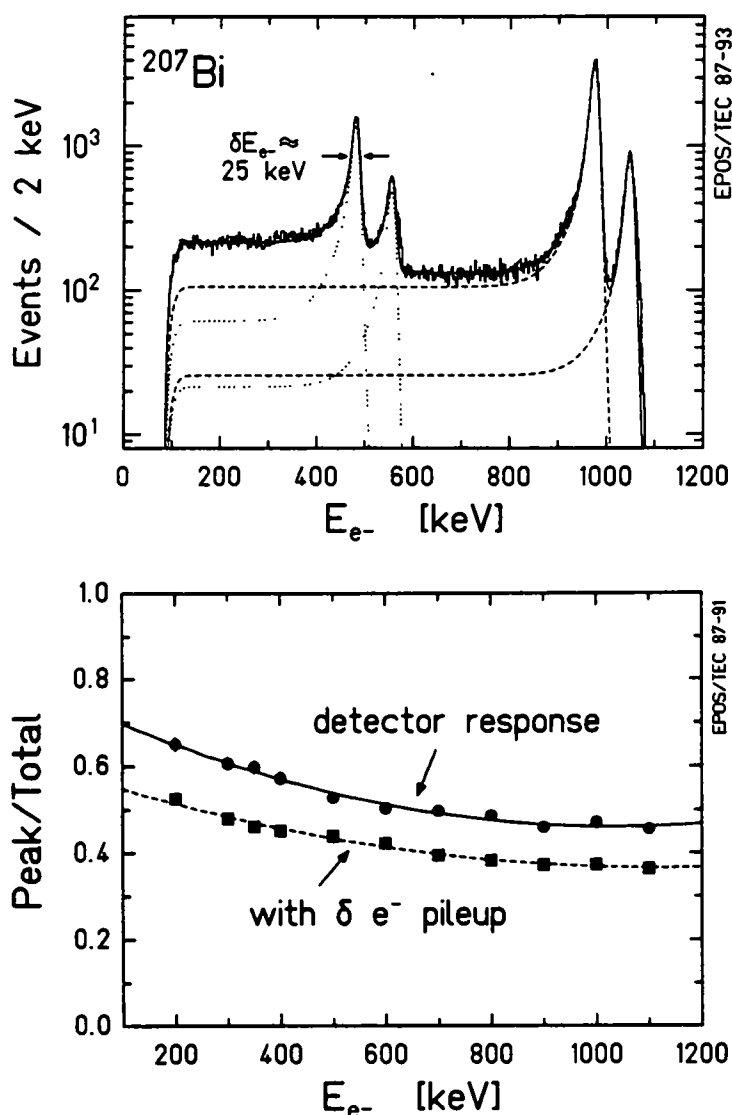


**Figure 5-9.** Response of the electron Si(Li) detectors to  $^{207}\text{Bi}$  electron source (top). Dotted and dashed curves show lineshape fits (Eqn. 2.34) to K and L conversion lines from the 570 and 1064 keV transitions, respectively. At  $E_{e^-} = 300$  keV, the energy resolution is  $\approx 30$  keV (FWHM). Lower figure plots the Peak/Total ratio from the lineshape response alone (solid line). Dashed curve includes  $\delta$ -electron pileup (see Fig. 5-10). ("Peak" denotes intensity in a 50 keV interval around the full-energy line.)

each detector is attached) subtend a much larger solid angle ( $\sim 2 \times 10^{-3}$  of  $4\pi$  sr), the increased probability for in-scattering of  $\gamma$ -rays is still negligible. To reduce electron scattering in the detector region, the space around the solenoid axis, out to a radius of 3.2 cm, was kept clear of material (except of course for the Si(Li) detectors them-

selves), and the end flange of the spectrometer was equipped with a cone-shaped aluminum baffle to trap electrons which spiral past the counters.

**Sec. 5.2.2.3 Performance In-Beam:** Under typical in-beam conditions (1 PnA on a  $\sim 300 \mu\text{g}/\text{cm}^2$  target), the instantaneous counting rate in the individual detector segments was  $\cong 100$  kHz. As discussed below, the rate of accidental coincidences, between HI's in the PPAC's and electrons from other beam pulses which are subtracted from the prompt HI- $e^-$  data, was  $\cong 10\%$ . We checked the influence of the high counting rate on the detector energy resolution by measuring the K-conversion lines of a  $^{207}\text{Bi}$  source accumulated simultaneously with beam incident on a  $300 \mu\text{g}/\text{cm}^2$  gold target. For instantaneous rates as high as 300 kHz, no shift in the amplification or degradation in electron energy resolution occurred. During actual measurement conditions, the beam current was limited to 1 PnA ( $R_{e^-} \cong 100$  kHz) because of target deterioration problems discussed in Sec. 2.6. The segments of each detector furthest from the target received only about 10% of the counting rate of the forward segments.

For the particular detection geometry used, about 20% of the measured positrons (from U+Th collisions) were detected in coincidence with electrons. The average multiplicity of electrons emitted in each collision,  $M$ , was deduced from the electron counting rate divided by the mean electron detection efficiency which is weighted over the  $\delta$ -electron energy distribution,

$$M \cong R_{e^-} / \langle \varepsilon_{e^-} \rangle, \quad (5.9)$$

$$\langle \varepsilon_{e^-} \rangle = [\int (dP_{e^-}/dE_{e^-}) \cdot \varepsilon_{e^-}(E_{e^-}) dE_{e^-}] / [\int (dP_{e^-}/dE_{e^-}) dE_{e^-}] \cong 5\%.$$

Inserting  $R_{e^-} \cong R_{e^+e^-}/R_{e^+} = 20\%$  yields an average multiplicity of  $M \sim 4$  electrons per collision, integrated for  $E_{e^-} > 100$  keV.

The pile-up rate, i.e., the probability of observing two or more electrons in a single detector segment, was determined from the rate of coincidences between the two forward electron detector segments. Since each forward detector (upstream and downstream along the beam direction) accounts for about one-half of the total detection efficiency,  $\varepsilon_{e^-}$ , the coincident rate between them (divided by the singles electron rate) should approximately equal the chance that a second electron is incident in one segment. Assuming that  $m$  electrons are emitted in a given collision, one therefore expects that the relative probability of detecting a second electron is

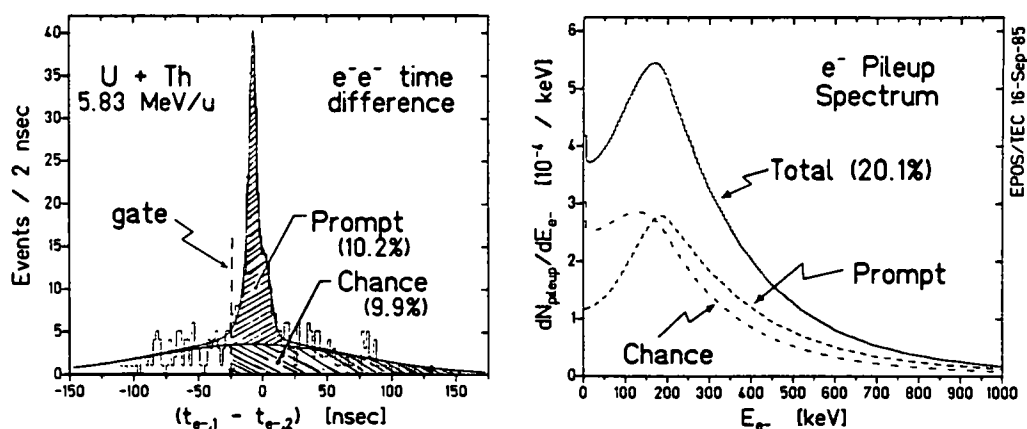


**Figure 5-10.** Analysis of electron pileup. Left: Time difference spectrum of electron events coincident in both the upstream and downstream (w.r.t. the beam direction) Si(Li) detectors. Prompt events from the high multiplicity of electrons in each collision produce dashed energy spectrum (right). Chance events arriving after the prompt electron produce distribution shifted to lower energies (dot-dashed), as described in the text.

approximately  $\frac{1}{2}(m-1)\langle\varepsilon_{e^-}\rangle$ . Including a Poisson distribution of  $m$  emitted electrons (given an average multiplicity,  $M$ ) yields a pileup rate of

$$\text{Pileup} = \sum_m (m^M e^{-M}/m!) \frac{1}{2}(m-1)\langle\varepsilon_{e^-}\rangle \cong 8\%, \quad (5.10)$$

due to the multiplicity of prompt electrons from the same collision. Figure 5-10a presents the time-difference spectrum between the forward segments. The prompt coincident rate between them is 10.2% of the electron counting rate in each segment alone, in accordance with Eqn. 5.10. The energy distribution of the pileup electrons simply reflects the shape of the total  $\delta$ -electron spectrum (corrected for the detection efficiency and lineshape tailing) as indicated by the dotted "prompt" curve in Fig. 5-10b.

An additional  $\cong 10\%$  pileup in the energy signal arises from chance coincidences between the primary electron and electrons from subsequent beam pulses. These events constitute the smooth continuum of upstream-segment/downstream-segment coincidences under the prompt peak in Fig. 5-10a. They can not be distinguished from the prompt electron when both electrons are incident in the same detector segment, however, because only the first time pulse is accepted as the electron stop signal in the TDC's and no hardware

pileup-rejection circuitry was employed. If the chance event arrives before the prompt electron (i.e., from an earlier beam pulse), only its time signal is recorded, and since it is not prompt, the event is discarded. For this reason, the magnitude of the chance pileup rate is calculated from Fig. 5-10a by integrating the background starting at the prompt peak and extending to later times. The 9.9% rate measured for U + Th collisions by this method was quantitatively verified by integrating the pileup tails of a test pulser energy signal which was externally triggered on close HI collisions using high-energy ( $> 1$  MeV)  $\gamma$ -rays detected in the NaI crystal (see Sec. 2.4).

The physical energy distribution of chance pileup events also reflects the  $\delta$ -electron spectrum. In the gated ADC's, however, the measured energies are distorted because the semi-gaussian shaped amplifier signal from a chance electron is shifted in time relative to the prompt pulse. For much later chance events, only the tail of the pulse adds to the prompt signal, altering the maximum signal voltage during the  $\cong 0.5$   $\mu$ sec ADC gate. The chance pileup electron energy spectrum is therefore shifted to lower energies, as indicated by the dot-dashed "chance" curve in Fig. 5-10b. The total pileup energy distribution, denoted by the solid curve, adds to the measured energy of any given prompt electron with about 20% probability. The electron lineshape of Fig. 5-9 must be folded with this pileup contribution (independent of incident energy) to give the effective in-beam electron detector response. As indicated by the dashed curve in Fig. 5-9b, the effective lineshape peak-to-total ratio (defined as the relative number of events within a 50 keV window about the incident energy) is decreased by the pileup tailing to  $\sim 47\%$  at  $E_{e^-} = 350$  keV.

### **Sec. 5.2.3 Experimental Electronics**

Figure 5-11 summarizes the experimental electronics for the planar pair of Si(Li) detectors. Two sets of constant fraction discriminators were used to provide two trigger levels. The low-energy threshold, set to  $E_{e^-} \sim 80$  keV, generated the TDC stop signals and was used for various ratemeters and scalers. A HI-electron coincidence event-type triggered with this low threshold was used to measure the detailed shape of the  $\delta$ -electron energy distribution, but because of the high counting rate, it was operated with a large scaledown ( $SD_{low} \cong 1024$ ). The high-energy threshold,  $E_{e^-} \geq 500$  keV, was used only for a separate HI-electron trigger which operated with a small scaledown ( $SD_{high} \cong 32$ ) in order to search for high-energy internal con-

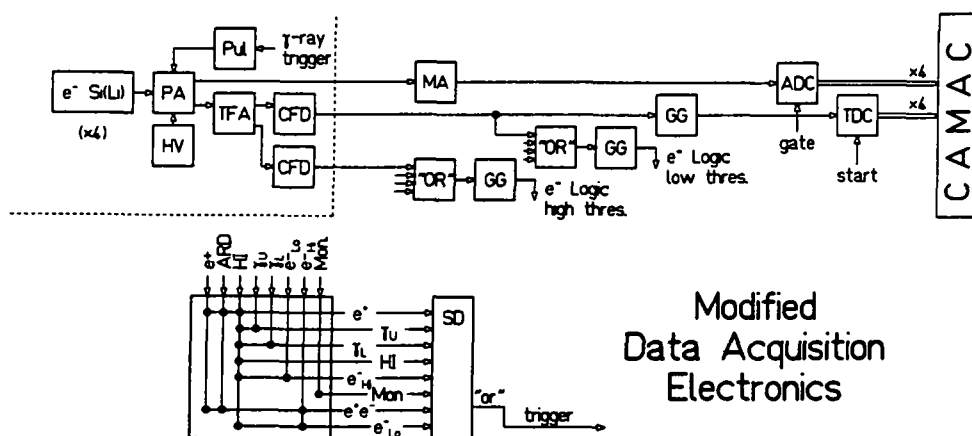


**Figure 5-11.** Data acquisition electronics for four-fold electron Si(Li) detectors, showing low and high energy logic thresholds which are included as separate event-types in the hardware trigger. (Compare Fig. 2-47.)

version lines. The HI-positron-electron coincidences were recorded as a subset of the HI-positron events and required no separate trigger.

A final positron-electron trigger alone, i.e., without the PPAC coincidence, was also included in order to obtain higher  $e^+/e^-$  statistics in case the heavy-ion coincidence proved to be unnecessary. A cursory analysis of this data indicated that while up to six times more data was accumulated than with the PPAC-coincident trigger (due to the solid-angle of the PPAC detectors), the coincidence positron-electron peak signals presented in Chap. 6 appeared with about the same intensity as with the PPAC trigger. Although this could be due to underlying physics (e.g., an azimuthal angular distribution, with respect to the scattering plane, of the source of the lines), it may simply be an effect of increased backgrounds. Without the PPAC trigger no time signal was available associated directly with the HI collision, so much of the chance background could not be subtracted. Perhaps additional contributions from small angle  $^{238}\text{U}$  beam  $\rightarrow$   $^{12}\text{C}$  target-backing scattering, or pair conversion from beam-induced radioactivity, increased the continuous backgrounds in this channel as well.

### Sec. 5.2.4 Data Reduction

Data reduction of the HI-electron coincidences was treated as described in Sec. 3.2 with the additional complication that each of the segmented electron counters was analyzed like the positron Si(Li) detector. As illustrated in Fig. 5-12a, time differences between the upper PPAC cathode and each segment were formed. The HI and electron flight-times were corrected for using Eqn. 3.5, and accidental background windows were taken symmetrically on either side of the prompt pulse and averaged for the background subtraction. The HI- $e^-$  chance rate amounted to  $\cong 10\%$ . When both the front and rear segments registered an event, their time difference was checked (Fig. 5-12b). If prompt, the sum of the signals was taken as  $E_{e^-}$ . The counting rate in the rear segments was  $\cong 10\%$  of that in the front segments, about 10% of which was due to scattering from the front segment into the rear detector.

Measurements with a  $^{113}\text{Sn}$  source indicated that no electrons scatter between the upstream and downstream detectors for  $E_{e^-} = 364$  keV. If both registered a hit, the energies were therefore *not* added. The event was discarded in order to avoid double counting of the associated positron, or piling up of the electron energies, both of which distort the coincident energy distributions. This partial software "pile-up rejection" (PUR) procedure reduced the total number of coincidence positron-electron events by 10-15% compared to the yield analyzed without discarding double electron hits, and therefore effectively reduced the coincidence detection efficiency.

The analysis of positrons with electrons included an extra coincidence condition which substantially cleaned up the positron channel compared to the normal HI-positron-ARD coincidence condition described in Sec. 3.3. In addition to the  $(t_{\text{HI}}-t_{e^+})$  plus  $(t_{e^+}-t_{\text{ARD}})$  analysis, a third condition, either a  $(t_{\text{HI}}-t_{e^-})$  or  $(t_{e^+}-t_{e^-})$  time difference, was included. The data were also analyzed with a  $(\text{HI}-e^-)-(e^-e^+)-(e^+-\text{ARD})$  combination. These two methods appear to be equivalent, although the  $(\text{HI}-e^-)$  time resolution of  $\cong 4$  ns was better than the  $(\text{HI}-e^+)$  resolution of  $\cong 7.5$  ns. In any case, the accidental background was subtracted by averaging more than one neighboring beam-pulse in each channel in order to ensure that the chance spectrum was statistically smooth and did not produce structure in the coincidence distributions. The weight given to each event was the product of the weights for each coincidence channel,

$$w_i = f_{\text{HI}/e^+} \cdot f_{e^+/\text{ARD}} \cdot f_{e^+/e^-} \cdot f_{\text{ARD}} \quad (5.11)$$

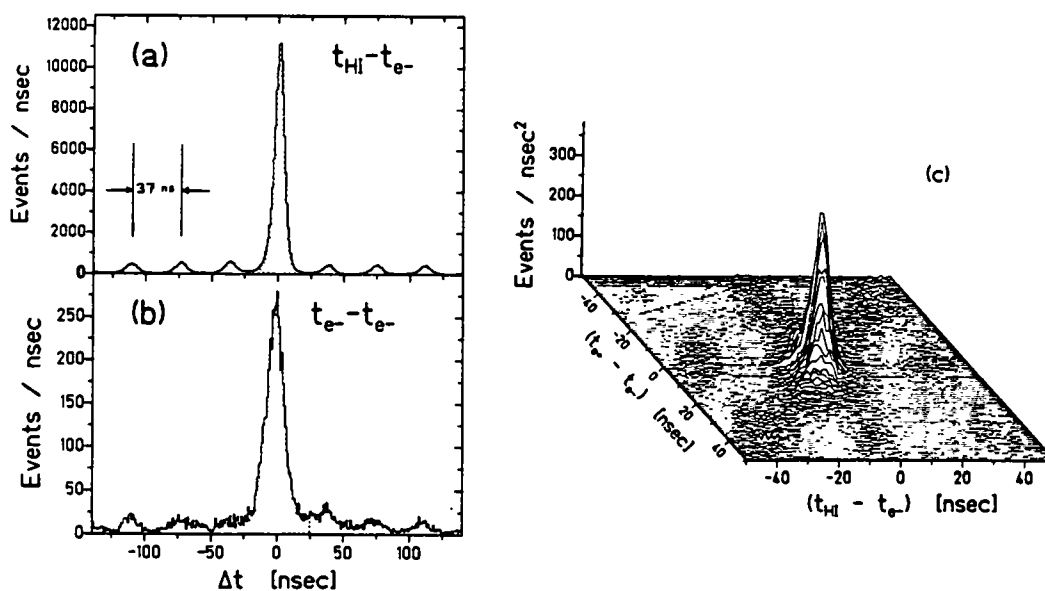


**Figure 5-12.** (A) Time difference spectrum for HI-electron coincidences, showing the 37 ns microstructure of the UNILAC, and (b) time spectrum for coincidences between forward and backward detector segments. Shaded regions denoted prompt analysis windows. (C) Two-dimensional distribution of HI-electron and positron-electron time differences for U+Th coincident events, after subtraction of chance backgrounds.

For prompt (or "true") events the weight,  $f_{\dots}$ , equaled 1. For chance events, the weight is  $f_{\dots} = -\Delta t_{tru}/\Delta t_{cha} = -1/2$ , which normalized the number of background events in the wider chance time window  $\Delta t_{cha}$  to the size of the expected accidental coincidence background in the narrower prompt time window  $\Delta t_{tru}$ . For computational simplicity, the ARD low-energy background was subtracted simultaneously. From a fit of the measured ARD sum-distribution to an exponential background plus the expected spectrum derived from  $\beta^+$  source data,  $f_{ARD}$  equals 1 or -0.24 for an event in the positron window (A) or the background window (B) of Fig. 3-4, respectively. Figure 5-12c presents the 2-dimensional  $\Delta t_{HI/e-}$  versus  $\Delta t_{e+e-}$  timing spectrum for  $\cong 3 \times 10^4$  coincidence events from U+Th collisions, after subtraction of the chance background. As desired, the chance background appears to be properly accounted for because the neighboring beam pulses are almost completely absent.

### Section 5.3 Detection Efficiency and Time-of-Flight

The EPOS detection efficiency is summarized for positrons and electrons as a function of emitted kinetic energy in Fig. 5-6a. The curves are calculated using an up-

dated version of the ray-tracing program ECPI described in App. C [Cow82b] which includes the modified detector geometry and magnetic field configuration. As mentioned above, the positron transport efficiency is reduced from the measurements presented in Part I of this dissertation by  $\sim 40\%$ , primarily because of the reduced magnetic mirror field. With the slightly improved ARD identification,  $\epsilon_{e^+}$  reaches 12% at  $E_{e^+} = 350$  keV. The electron efficiency curve exhibits a sharp cutoff, as desired, for energies below 300 keV, and high efficiency ( $\sim 15\%$ ) above 350 keV. The absolute magnitude and shape of both the positron and electron detection efficiencies are in good agreement with  $^{113}\text{Sn}$  conversion electron line source measurements shown by the data points.

Figure 5-13 presents the transport efficiency for positrons and electrons as a function of the energy and polar angle of emission. The oscillatory pattern in  $\epsilon_{e^+}$  corresponds to positron orbits returning to the solenoid axis at the spiral baffle where they are absorbed by the central hub, as explained in Sec. 2.2.5. A similar periodicity is observed in  $\epsilon_{e^-}$ , associated with electrons which, after an integral number of orbits, strike the casings of the electron detectors. The longer target-detector distance (112 cm compared to 34 cm for the spiral baffle) causes a more rapidly varying function versus  $E_{e^-}$  and  $\theta_{e^-}$ . The low energy electron cut-off from the detector displacement and the sheet-baffle are clearly evident, as is the reduction of high energy electrons which have sufficiently large orbital radii to strike the spectrometer chamber.

The fiducial detection volume sampled by the electron detectors is somewhat larger than that of the positron Si(Li), as shown in Fig. 5-6b. If electrons are emitted off-axis along the beam direction, the efficiency rises in the closer detector and falls in the further detector because of different ranges of orbital radii, and hence emission angles, which intercept the counters. Given sufficient statistical accuracy, long-lived sources which decay off-axis could therefore in principle be identified by the relative intensity of events in the forward versus the backward counter. As the source moves beyond the  $\ell = 9$  mm displacement of the detector from the axis, this counter then effectively shadows the other Si(Li), whose detection efficiency drops to nearly zero. The detection probability of positrons in the planar pair of Si(Li) detectors (measured with a  $^{113}\text{Sn}$  source but using the opposite magnetic field polarity to simulate positrons) shows a similar off-axis dependence, but is uniformly a factor  $\cong 3.8$  smaller than  $\epsilon_{e^-}$ . The steeply varying individual efficiencies at  $d_{\perp} = 0$  allows a continuous on-line check of the target alignment by comparing the  $\delta$ -electron counting

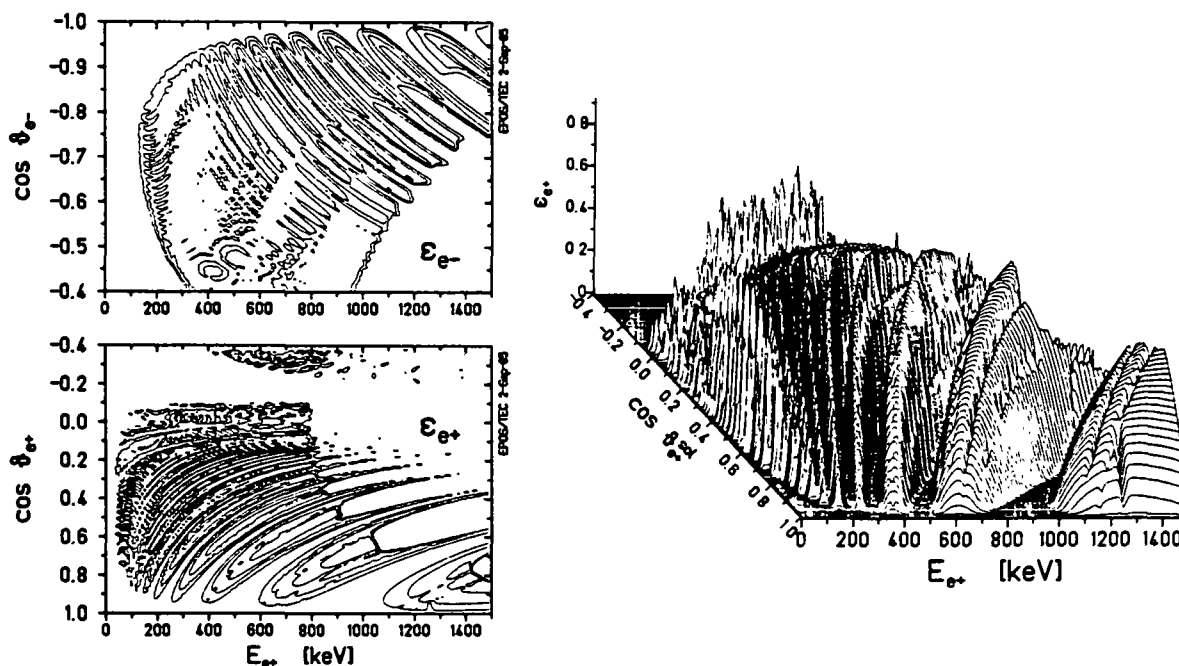


**Figure 5-13.** Contours of constant positron and electron detection efficiency (integrated over  $\phi$ ) plotted versus kinetic energy and solenoid emission angle (right), and an isomeric representation of the positron efficiency (left). Undulatory structures are produced by spiral baffle transmission, with finer structures from the target frame.

rates in the two planar Si(Li) detectors. A contribution from low-energy internal conversion electrons from long-lived transitions in the separated nuclei leads to an additional component in the electron spectrum measured in the downstream (along the beam direction) electron detector for  $E_{e-} \leq 200$  keV.

As described in Sec. 2.2.6, the time-of-flight of positrons from the target to the Si(Li) detector provides a rough measurement of the positron emission angle,  $\theta_{e+}$ . Figure 5-14 presents the positron and electron flight-times as a function of the emitted energy and polar angle with respect to the solenoid axis. As shown in Fig. 5-14b which presents the angular dependence for  $E_{e-} = E_{e+} = 350$  keV, throughout much of the angular range  $\text{TOF}_{e-}$  and  $\text{TOF}_{e+}$  increase monotonically with  $|\cos\theta_{e-,e+}|^{-1}$ , ranging from  $\sim 5$  to  $\sim 15$  ns. This contrasts the multi-valued behavior of  $\text{TOF}_{e+}$  shown in Fig. 2-24 for the arrangement used in Part I of this work. As opposed to that situation, here positrons emitted with  $\theta_{e+} \sim 90^\circ$  should be partially distinguished by their TOF from those emitted at flatter angles.

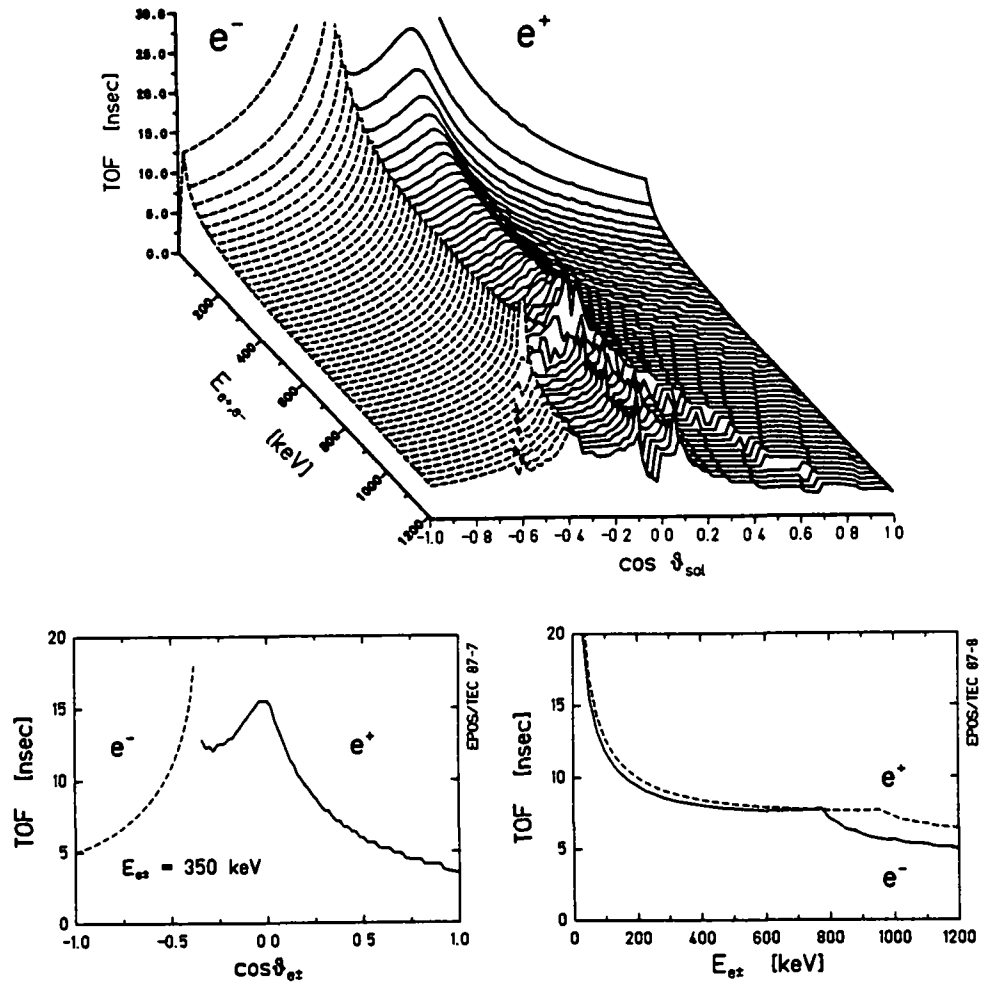


**Figure 5-14.** Time-of-Flight of positrons and electrons from the target to their respective detectors in the EPOS spectrometer, plotted as a function kinetic energy and solenoid emission angle (top). Emission angle dependence for  $E_{e^+}, E_{e^-} = 350$  keV (lower left), and mean TOF versus energy averaged over emission angle (lower right).

The average inverse dependence of the TOF on the momentum ( $1/P_{e^+, e^-}$  from Eqn. 2.53) is apparent in Fig. 5-14c where an isotropic emission angle distribution has been assumed for all energies. Both the mean transport time for electrons and positrons is  $\sim 8$  ns. The reduced range of emission angles transported, because of the spectrometer inner radius, is visible for energies above  $E_{e^+} \cong 800$  keV and  $E_{e^-} \cong 1000$  keV. As described above, the mean energy dependence of the TOF is corrected for in the data analysis.

$$E_{e^+,e^-} = 350 \text{ keV} \quad (1985)$$

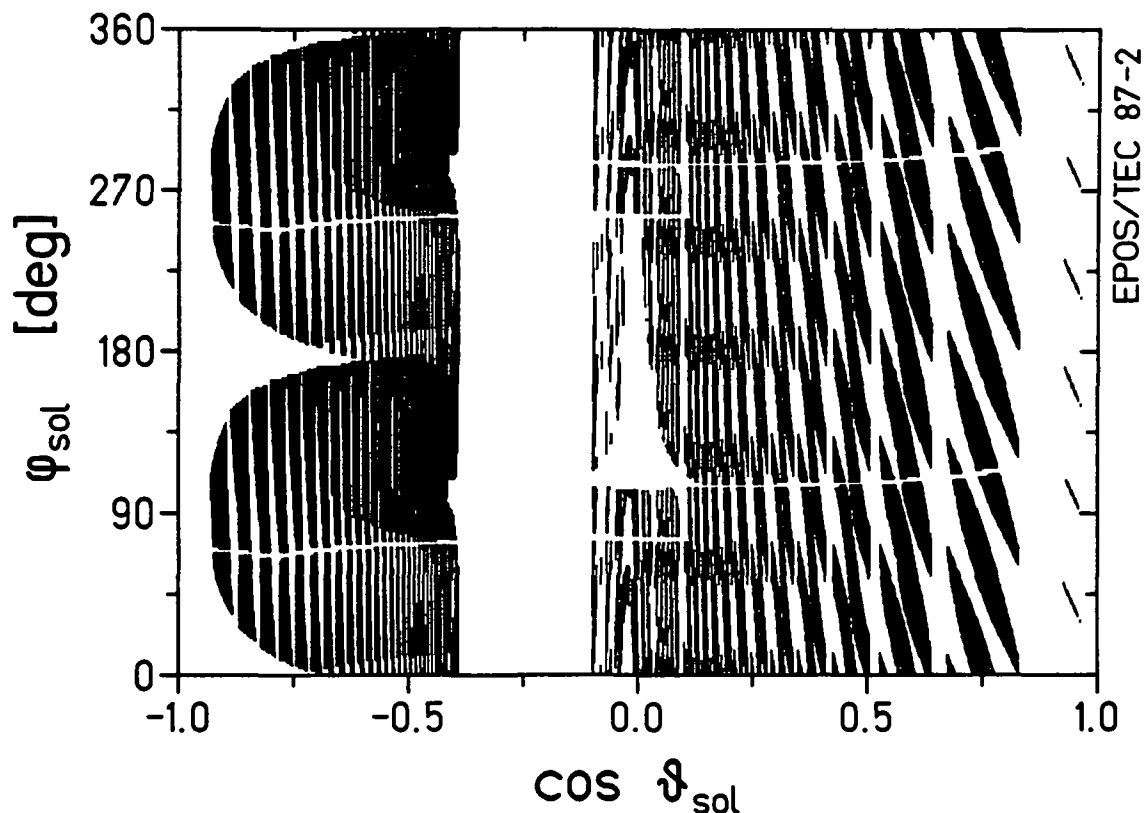


**Figure 5-15.** Transport efficiency for 350 keV positrons and electrons emitted from a point target with angles  $\theta$ ,  $\phi$  w.r.t. the solenoid axis. Dark (light) regions denote hits (misses) in corresponding detector. Evident features include the six-fold periodicity of  $e^+$  detection in  $\phi$  from the spiral baffle, gaps in efficiency at  $\cos\theta \cong 0$  and around  $\phi \cong 90^\circ$  and  $270^\circ$  from the target frame, and the oscillatory structure in  $\cos\theta$  when, after an integral number of orbits, the positron hits the central disk of the spiral baffle or an electron strikes the Si(Li) detector casing.

The oscillatory nature of the transport efficiency is more clearly seen in Fig. 5-15 which plots the  $\theta$ - $\phi$  emission angles for which a 350 keV positron or electron stops in its respective detector. As described in Fig. 2-17, several details of the EPOS positron transport system are readily apparent, such as the six-fold periodicity in  $\phi$  corresponding to the number of spiral baffle blades, the same  $\theta_{e^+}$  oscillations as seen in Fig. 5-13, and the destructive role of the target frame for  $\theta_{e^+} \sim 90^\circ$ . Electron detection ( $\cos\theta < -0.35$ ) exhibits similar features. As noted above, the  $\cos\theta_{e^-}$  oscillations in  $\epsilon_{e^-}$  correspond to electrons striking the Si(Li) detector casings. The horizontal bands at  $\phi_0 \cong 80^\circ$  and  $\phi_0 \cong 260^\circ$  correspond to elec-

trons emitted almost vertically which hit and are stopped in the target frame. The orbital trajectories of electrons emitted between  $90^\circ < \varphi_{e^-} < 180^\circ$  and  $270^\circ < \varphi_{e^-} < 360^\circ$ , with respect to the beam direction, overlap only one of the Si(Li) detectors, as is evident from Fig. 5-7c, and therefore have much less probability of striking a detector casing. The angular regions sampled by the two separate detectors is clearly evident. The upstream Si(Li) collects electrons emitted into the upward hemisphere ( $\sim 0^\circ < \varphi_{e^-} < \sim 180^\circ$ ), and the downstream Si(Li) collects electrons emitted downwards ( $\sim 180^\circ < \varphi_{e^-} < \sim 360^\circ$ ). Finally, the blank region in Fig. 5-15 between  $\cos\theta \cong -0.1$  and  $-0.38$  reflects the range of emission angles for which the electrons and positrons are stopped in the sheet baffle.

As described in Sec. 2.2.5, although the combination of magnetic transport system, baffles, and insensitive regions (e.g., Si(Li) housings) produces an efficiency response function having considerable fine-structure, these fluctuations do not lead to structure in the observed energy spectra of positrons and electrons emitted with broad distributions. The calculations of Figs. 5-13 and 5-15 overestimate the magnitude of the oscillatory pattern because they are performed assuming a point source and an idealized spectrometer with perfectly aligned elements. Scattering of leptons from the surfaces of the baffles, target frame and detectors is also not included. Section 2.2.5 showed that simply integrating over the size of the beam spot ( $\sim 5$  mm dia.) effectively integrates over a range of phases for the electron and positron trajectories, roughly equivalent to averaging over a  $\sim 60$  keV interval in emitted energy. This brings the calculated efficiency curves of Fig. 5-6, e.g., in better agreement with source measurements. Figure 5-16 presents polar plots of the detection efficiency as a function of  $\theta$  and  $\varphi$  for a mean positron or electron energy of 350 keV, averaged over  $300 < E_{e^+,e^-} < 400$  keV. The electron detection efficiency is very smooth between  $110^\circ < \theta_{e^-} < 160^\circ$ , and reflects as a function of  $\varphi_{e^-}$  the broad azimuthal variations which have a  $90^\circ$  period, as described above. The positron efficiency is similarly broad and smooth and almost uniform versus  $\varphi_{e^+}$ . Figure 5-17, shows the detected energy distribution of  $\beta$  decay electrons from a  $^{36}\text{Cl}$  source. The structureless spectrum provides a direct verification of the smooth response of the EPOS electron detection system.

Figure 5-16 also illustrates the back-to-back orientation of the detected positron and electron emission angle regions. To visualize the EPOS acceptance it is useful to picture these calculations in three dimensions. The regions of solid angle sampled resemble two thick hollow, coaxial cones, joined at their common vertex. While

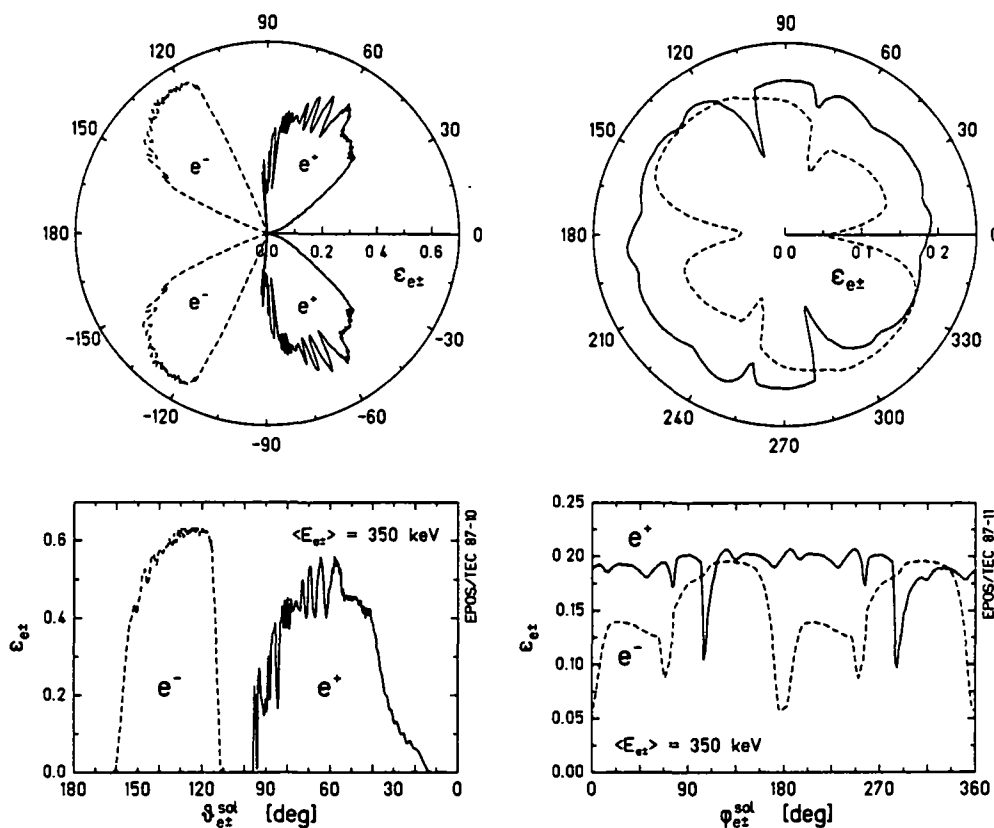


**Figure 5-16.** EPOS transport probability for  $E_{e^+}$  and  $E_{e^-}$  between 300 and 400 keV, shown as a function of: polar emission angle  $\theta$  (left) w.r.t. the solenoid axis (integrated over  $\phi$ ), and azimuthal angle  $\phi$  (right, integrated over  $\theta$ ).

obviously enhancing the measurement of back-to-back emitted positrons and electrons, a broad range of opening-angles is detected with substantial efficiency down to  $\theta_{e^+e^-} \sim 20^\circ$ . The observation of a monoenergetic electron peak in coincidence with a narrow positron line therefore does not necessarily require that they have spatially correlated emission angles. The design of the EPOS coincidence spectrometer, for what began as an exploratory experiment, is optimized for correlated efficiency by providing large solid angles for accepting positrons and electrons, at the expense of a stringent definition of the emission angles by the detector geometry. As mentioned in Sec. 5.1, a kinematic analysis of the positron and electron laboratory energies should, with sufficiently good detector energy resolution, be able to identify back-to-back emission from the two-body decay of a neutral object.

While verifying the smooth nature of the EPOS detection efficiency *individually* for positron and electron emission, the arguments presented here and

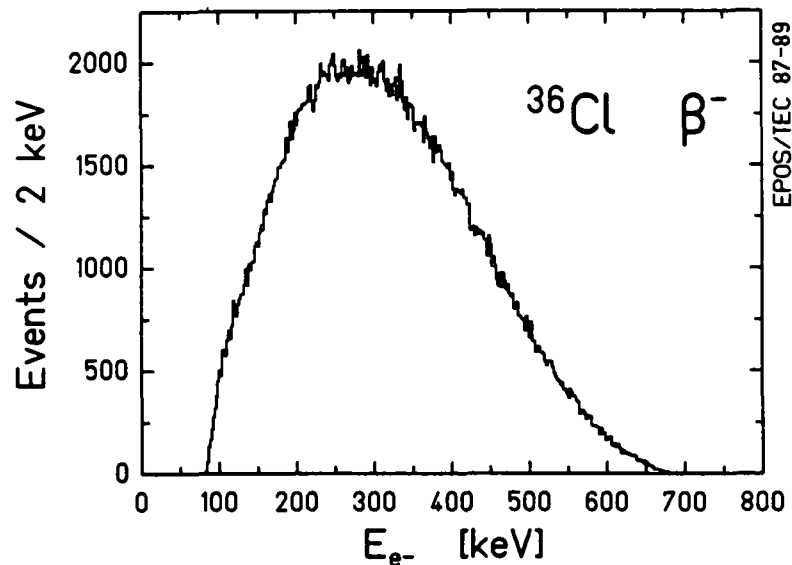


**Figure 5-17** Measured energy distribution of electrons from a  $^{36}\text{Cl}$   $\beta^-$  source illustrating smoothness of electron detection efficiency.

in Sec. 2.2.5 are not immediately applicable to coincident detection. Quantitative calculations of the detected energy distributions of coincident positrons and electrons are necessary to investigate the possibility that narrow lines may emerge from broad positron and electron distributions due to the overlap of their individual oscillating transport efficiencies. The detection efficiency of positrons and electrons emitted isotropically with no correlation between their momentum vectors is simply the product of the curves of Fig. 5-6 -  $\epsilon_{e^+e^-}(E_{e^+}, E_{e^-}) = \epsilon_{e^+}(E_{e^+}) \times \epsilon_{e^-}(E_{e^-})$ . For two-body decays, however, the laboratory positron-electron angular correlation depends on the velocity of the emitter. The coincidence detection efficiency can therefore only be calculated in a model-dependent way for a variety of source velocity distributions. Equal attention must also be paid to background processes and other spatially correlated emission mechanisms since their signature must be understood as obscuring backgrounds, as well as eventual explanations of structures observed in the coincidence spectra. These points have been addressed with a series of Monte-Carlo simulations described below.

## Section 5.4 Coincidence Detection

### Sec. 5.4.1 Monte-Carlo Simulations

The computer code MCSPEC (Monte-Carlo Simulation of Positron Electron Coincidences), described in App. C, was developed to generate a wide range of event scenarios and to model the response of the EPOS spectrometer in detecting positrons and coincident electrons. Several sources of coincident positrons and electrons are modeled, e.g., the production and two-body decay of neutral or charged objects, multi-body decays, various types of nuclear internal pair conversions, dynamic positron and  $\delta$ -electron emission, or any general source of positrons and electrons located near the target. The generated positrons and electrons are then transformed to the lab system, where they are tracked through the EPOS spectrometer to determine whether or not each is detected. The pulse-height responses of the Si(Li) counters are taken into account, pileup from the  $\delta$ -electron flux is added, and electronic pulse-shaping and trigger-logic efficiencies are simulated. Finally, the generated events are analyzed with a logical duplicate of the experimental data analysis program. Projections of the simulated events may then be compared with identical cuts applied to the experimental data. In addition to modeling complex emission processes, one important benefit of the Monte-Carlo studies has been to understand which aspects of the coincidence event yields are most important, and to decide how best to analyze the experimental data.

**Sec. 5.4.1.1 Event Generators:** Event generation for each specific scenario is flexible to allow a detailed study of various aspects of the simulated positron-electron source. For example, the production and decay of a neutral particle-like object includes its angular and momentum distributions with respect to the emitting frame (CM of the heavy-ion collision, the scattered nuclei, or the stationary laboratory frame). The positron and electron momentum vectors are constructed in the rest frame of the source, including the angular distribution with respect to the particle motion. They may be generated with an arbitrary distribution in  $e^+/e^-$  opening-angle in place of back-to-back emission. Similarly, studies of nuclear IPC include 1) determination of the scattering angle distribution for the detected heavy-ion (including the geometry of the PPAC's), 2) any nuclear charge or transition energy, 3) E0, E1, E2, or M1 conversion multipolarities, 4) angular distributions for the emitted positron, and 5) theoretical (Born approximation) or mutually isotropic opening-angle distributions for the positron-electron pair. In addition to IPC in the heavy-ion ejection

tiles, calculations of pair production from target contaminants, from nuclear clusters which might be emitted in the collision, and from external conversion of  $\gamma$ -rays in the target, its frame, or the sheet-baffle material, have been investigated.

**Sec. 5.4.1.2 Efficiency Determination:** Calculation of the large quantity of MCSPEC events necessary for studying a wide variety of production processes requires a computationally efficient evaluation of the EPOS Spectrometer response. The standard technique used here involved the interpolation of a look-up table of detection probabilities calculated for a large range of positron and electron emission with the ECPI ray-tracing code (see App. B). The mesh size (the pixel size in Fig. 5-15) is small compared to the periodicity of detection efficiency to ensure high accuracy (corresponding to steps of 10 keV in  $E_{e^+,e^-}$ ,  $1.5^\circ$  in  $\phi$ , and 0.002 in  $\cos\theta$ ). On the average, 60% of positron "hits" are assumed to be detected to account for the mean efficiency for detecting 511 keV annihilation quanta in the NaI ARD crystal array.

**Sec. 5.4.1.3 Detector Response:** Correction for the response of the solid state positron and electron detectors includes finite energy resolution, tailing due to energy-loss, pile-up due to the rescattering (with  $\cong 8\%$  probability) of an undetected 511 keV annihilation photon in the positron detector, the high multiplicity of  $\delta$ -electrons striking the electron detector ( $\cong 20\%$  probability), and the finite Si(Li) resolution for the fast TOF pickoff. The time-of-flight of the positrons and electrons to their respective detectors is evaluated by interpolating the smooth function of energy and polar emission angle shown in Fig. 5-14. Low-energy electronic discriminator thresholds are included separately for each detector. No attempt is made to evaluate the detector response in a "microscopic" Monte-Carlo fashion tracking the penetration of a positron or electron into the silicon crystal. To the extent that energy-loss, back-scattering, and time resolution are independent of the angle and position of incidence, or more realistically, that a broad range of Doppler-shifted emission momenta and incidence angles map onto closely spaced detected positron and electron energies, this pseudo-Monte-Carlo approach is extremely accurate.

**Sec. 5.4.1.4 Event Analysis:** The simulated positrons and electrons are finally analyzed by a logical duplicate of the experimental data analysis program, including adjustments for positron and electron flight-times and the software pileup rejection, as described in Secs. 5.2.2.3 and 5.3.

### Sec. 5.4.2 Two-Body Decay Coincidence Detection

The Monte-Carlo computations to evaluate the acceptance and response of the EPOS spectrometer have been used to quantitatively determine the efficiency for detection of back-to-back events, and in particular, the expected signature of the creation and two-body decay of neutral particle-like objects. Figure 5-18 presents expected coincident positron-electron yields for the decay of a neutral object, of mass  $1.8 \text{ MeV}/c^2$ , created at rest in the CMS of the HI collision ( $v_{\text{CM}} = .056c$ ). The energy spectrum of 250,000 detected positrons ( $2 \times 10^6$  generated  $X^0$ 's) is shown in Fig. 5-18a, taking into account all efficiencies and detector response. For clarity, the contributions from continuous atomic and nuclear processes are neglected, although  $\delta$ -ray pileup adding to the high energy electron tail to  $E_{e^-}$  is included. The electron energy resolution for the 1985 experiment is used. Since the velocity of the neutral object coincides with the CM motion, this spectrum gives the Doppler-broadened laboratory lineshape of a monoenergetic positron peak emitted from the CM (cf. Sec. 2.2.7). Although slight oscillatory structure remains in the emitted distribution, it is small compared to the Si(Li) energy resolution so that the observed peak is quite smooth.

Figure 5-18b plots the positron energy versus coincident electron energy, and Figs. 5-18c,d present the positron energy distribution when gating on the coincident electron peak ( $340 < E_{e^-} < 420 \text{ keV}$ ), and the electron distribution for  $340 < E_{e^+} < 420 \text{ keV}$ . These correspond to the events in the contours labeled C and D in Fig. 5-18b, projected onto the  $E_{e^+}$  and  $E_{e^-}$  axes, respectively. The diagonal orientation of the positron-electron energy correlation pattern illustrates the correlated cancellation of Doppler shifts characteristic of two-body decay. While the individual positron and electron lines exhibit the full Doppler broadening appropriate for the emitter velocity, their first-order Doppler shifts ( $\gamma\beta P_{e^+}^* \cos\theta_{e^+}^*$  and  $\gamma\beta P_{e^-}^* \cos\theta_{e^-}^*$ ) are equal and opposite, resulting in the diagonal correlation pattern.

**Sec. 5.4.2.1 Sum-Energy Distribution:** Adding the positron and electron laboratory energies leads to the narrow peak of Fig. 5-18e whose  $\cong 45 \text{ keV}$  width, due entirely to finite energy resolution of the Si(Li) detectors, is smaller than either the positron or electron peaks of Figs. 5-18c,d. As noted above, improvement of the electron energy resolution in later experiments reduced the minimum expected sum-energy peak width to  $\Delta E_{\Sigma} \cong 25 \text{ keV}$ .

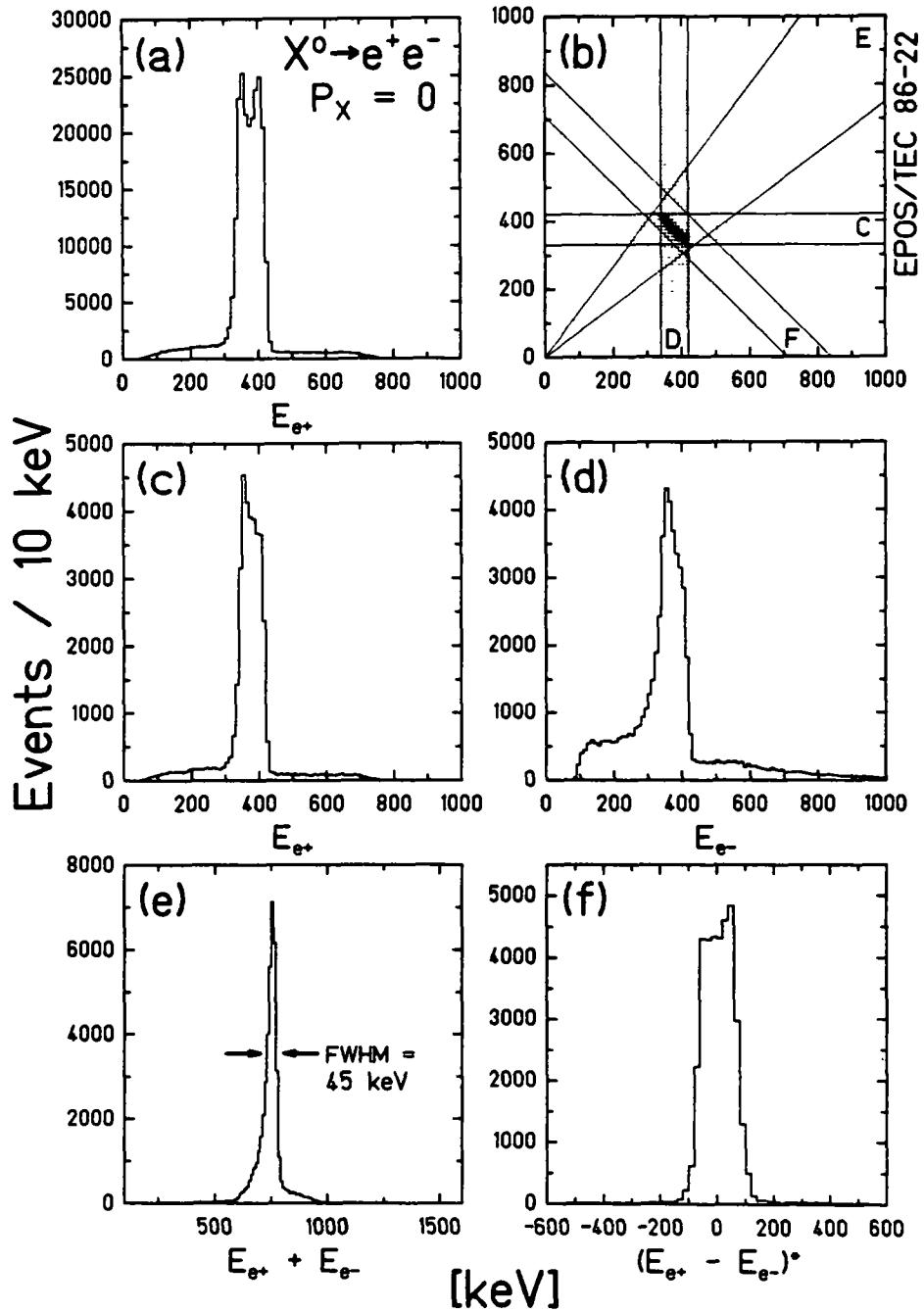


**Figure 5-18.** MCSPEC simulation of  $X^0 \rightarrow e^+e^-$  decays for a  $1.8 \text{ MeV}/c^2$  object created at rest in the CMS. (a) Total detected  $e^+$  distribution. (b) Plot of  $E_{e^+}$  vs.  $E_{e^-}$  illustrates the correlated cancellation of Doppler shifts. (c)-(f) Projections on the  $E_{e^+}$ ,  $E_{e^-}$ ,  $(E_{e^+} + E_{e^-})$ , and  $(E_{e^+} - E_{e^-})^2$  axes, respectively, for data within gates indicated in (b). The ratio of detected coincidence positron-electron peak events to total observed peak positrons is 16%. Sum-peak width of  $\sim 45 \text{ keV}$  reflects detector resolution (1985).

The rationale behind the wedge-shaped contour (labeled C in Fig. 5-18b) used to select the data included in the sum-energy projection of Fig. 5-18e is to account for the change in kinematic broadening of the individual positron and electron distributions as a function of energy. For example, the two-body decay of a  $2 \text{ MeV}/c^2$  object, created at rest in the CM, would lead to positron and electron lines centered at 490 keV, with a FWHM of about 96 keV, while a mass of  $1.4 \text{ MeV}/c^2$  would produce a mean  $e^+$  or  $e^-$  energy of 190 keV with a FWHM of only 53 keV. A wider range of positron and electron energies must therefore be added when searching for higher-energy structures, and a smaller range for low energy sum-lines. The wedge-shaped cut is parameterized by  $(E_{e^+} - E_{e^-}) / (E_{e^+} + E_{e^-}) = \text{constant}$ , and roughly follows the momentum dependence of the positron and electron linewidths. It effectively excludes as much background intensity (for which  $E_{e^+} \neq E_{e^-}$ ) as possible from the sum-energy projection.

It should be noted that the wedge-shaped contour was chosen specifically to search for correlated positron-electron emission from an object moving with low velocities in the CMS. As discussed below and in Chap. 7, completely different processes may also produce structure in the sum-energy spectrum, and complementary projections of the data must be considered to avoid misleading conclusions. Depending on the particular process under consideration, an entirely different cut in the  $E_{\Sigma}$  versus  $E_{\Delta}$  coincidence-event plane may be better suited for analyzing the data.

**Sec. 5.4.2.2 Difference-Energy Plot:** One important cut which complements the sum-energy projection is a plot of the the difference of the positron and electron energies, for events in a given interval of sum-energies. Figure 5-18f presents events within the diagonal contour labeled D in Fig. 5-18b, plotted against  $E_{\Delta} = E_{e^+} - E_{e^-}$ , for  $710 < (E_{e^+} + E_{e^-}) < 840$  keV. This projection provides information regarding the symmetry of the positron and electron peak energies and, for correlated (back-to-back) emission, is the best measure of the Doppler broadening and source velocity. Taking the difference of Eqns. 5.7a and 5.7b gives  $\Delta E_{\Delta} = 2\gamma\beta P^* \cos\theta^*$ , which attains a maximum FWHM of  $4\gamma\beta P^*$ . As discussed below, the shape of the difference-energy spectrum is central in discriminating against conventional origins of coincident positron-electron emission.

**Sec. 5.4.2.3 Detection Efficiency:** The detection efficiency for back-to-back emission of positrons and electrons from a source moving with the CM is directly given by the

yields of the simulated events. If detector response is neglected, the ratio of the observed number of coincident positron-electron pairs to the total number of detected positrons is  $N_{e^+e^-}/N_{e^+} = 0.32$ . Since the positron detection efficiency is approximately 12% (Fig. 5-6), the absolute coincidence detection efficiency is  $\epsilon_{e^+e^-} = 4\%$ , at  $E_{e^+,e^-} = 380$  keV. Lineshape tailing and pileup in the Si(Li) detectors reduce the fraction of total events which are identified in the positron, electron, or coincidence peaks. As noted previously, the lineshape peak-to-total ratio for positrons is  $(P/T)_{e^+} \cong 80\%$ , while for electrons  $(P/T)_{e^-} \cong 50\%$ . The relative detection ratio of coincident peak events is  $(N_{e^+e^-}/N_{e^+})_{pk} = 0.16$ . Including the software "pile-up rejection" of double electron hits, this falls to  $\cong 14\%$ . The absolute coincidence peak efficiency is therefore,

$$\epsilon_{e^+e^-}^{pk} = \epsilon_{e^+e^-} \cdot (P/T)_{e^+} \cdot (P/T)_{e^-} \cdot (PUR) = 1.4\%.$$

The larger low-energy tailing associated with electron detection not only decreases the coincidence peak detection efficiency, but also shifts the mean of the detected electron distribution to slightly lower energies than for positrons. In parts c,d of the Fig. 5-18, the mean observed positron energy is  $\langle E_{e^+} \rangle = 380$  keV while  $\langle E_{e^-} \rangle = 375$  keV. The difference-energy peak is similarly shifted to slightly positive values.

### Sec. 5.4.3 Non-Correlated Coincidence Detection

The enhancement of detection efficiency for back-to-back compared to spacially uncorrelated emission is demonstrated by the MCSPEC simulation shown in Fig. 5-19. Here it is assumed that the positron and electron are emitted isotropically with respect to each other from the CM system with equal energy  $E_{e^+} = E_{e^-} = 380$  keV. For comparison, the same number of total events is generated ( $2 \times 10^6$  X's,  $2.5 \times 10^5$  detected  $e^+$ 's), and the identical projections are plotted on the same absolute scale as those of Fig. 5-18. The detection efficiency for spacially uncorrelated events is much smaller than for back-to-back emission. The total  $N_{e^+e^-}/N_{e^+}$  ratio, excluding detector response, is 0.155 (compared to 0.32 in Fig. 5-18), and for peak events  $(N_{e^+e^-}/N_{e^+})_{pk} = 0.07$  (=6% including pile-up rejection), a factor of  $\cong 2.3$  smaller than for back-to-back emission.

As is apparent by the two-dimensional energy correlation plot in Fig. 5-19b, the pattern of events for isotropic emission differs substantially from the diagonal struc-

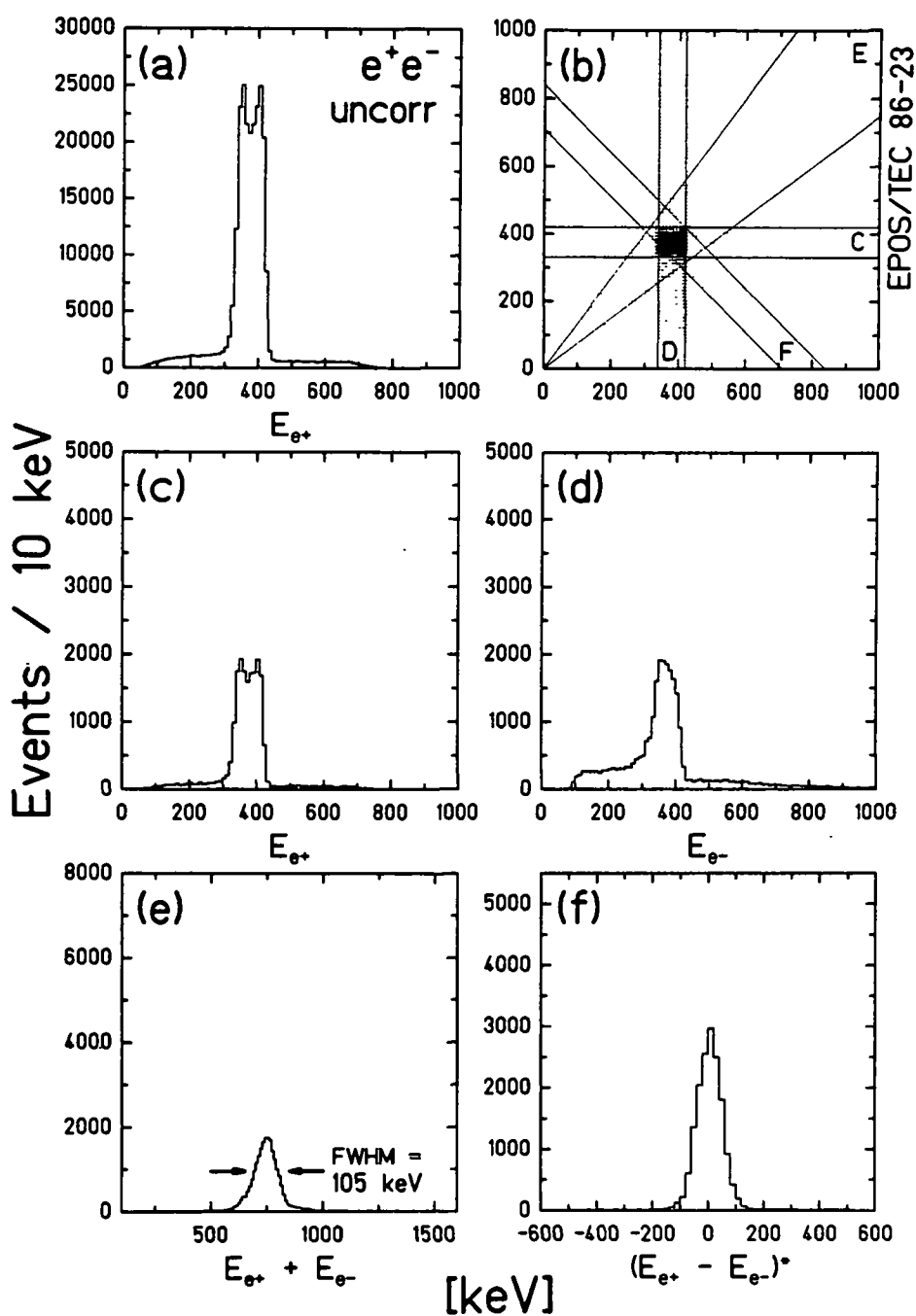


**Figure 5-19.** MCSPEC simulation of monoenergetic (380 keV)  $e^+$  and  $e^-$  isotropically emitted from the CM with no relative angular correlation. Parts (a)-(f) same as Fig. 5-18. (e) Sum-energy peak width,  $\sim 105$  keV, is approximately quadrature sum of individual  $e^+$  and  $e^-$  Doppler-broadened linewidths ( $v_{CM} = .056c$ ). The coincidence peak intensity relative to total observed  $e^+$  peak counts is 7%.

ture from two-body decay. Since the direction of the electron and positron are not relatively back-to-back, the Doppler shift of one lepton is unrelated to, and thus does

not cancel, the Doppler shift of the other. The sum-energy peak width for isotropic emission is approximately the quadrature sum of the individual positron or electron linewidths, about 105 keV (FWHM) for a mean source velocity of  $v_{CM}$  (Fig. 5-19e). The difference-energy peak (Fig. 5-19f) exhibits a similar width, as compared to back-to-back emission for which the Doppler correlation led to a width of 160 keV (Fig. 5-18f). For monoenergetic positron and electron lines having different energies, a similar rectangular pattern in the energy-energy plot can occur anywhere in the correlation plane, with suitably modified Doppler-broadened widths. The wedge-cut may not necessarily overlap such intensity patterns, complicating their identification, and the appropriate difference peak will not be centered near  $\langle E_{e+} - E_{e-} \rangle = 0$  keV.

#### **Sec. 5.4.4 Continuous Pair Creation Detection**

The preceding calculations show that detection of positrons and electrons resulting from a two-body decay is enhanced compared to uncorrelated, isotropically emitted monoenergetic lines and leads to a narrow peak in the sum-energy spectrum, identifying such events as candidates for representing the two-body decay of a neutral object. In addition, the positron Doppler-broadened lineshape remains intact when detected in coincidence with electrons (Fig. 5-18c). That is, no fragmenting of the positron distribution (which could resemble additional structure) occurs from the inclusion of the oscillating electron efficiency pattern. MCSPEC simulations of continuous dynamic positron and delta-electron emission similarly reveal no structure in the coincident intensity distributions. An important check that narrow peaks are not produced by instrumental effects entails simulating nuclear internal pair creation (IPC). This is the only conventional source of energy-correlated positron-electron pairs in HI collisions, and it accounts for  $\geq 20\%$  of the total detected positron yield in the U + Th system.

Figure 5-20 presents the expected energy distributions for internal pair creation of a 1.8 MeV electric monopole transition in one of the scattered nuclei ( $Z \cong 92$ ).  $2.5 \times 10^5$  detected positrons (from  $2.04 \times 10^6$  IPC decays) were generated using the IPC energy distribution of [Sof81] and assuming that the heavy nuclei were scattered uniformly over the solid-angle covered by the PPAC detectors ( $v_{nuc} \cong 2v_{CM} \cos\theta_{HI}$ ). In this three-body process, the heavy recoiling nucleus removes momentum but very little energy from the decay positrons and electrons, so that over their individually broad range, the positron and electron energies add to a constant sum-energy,

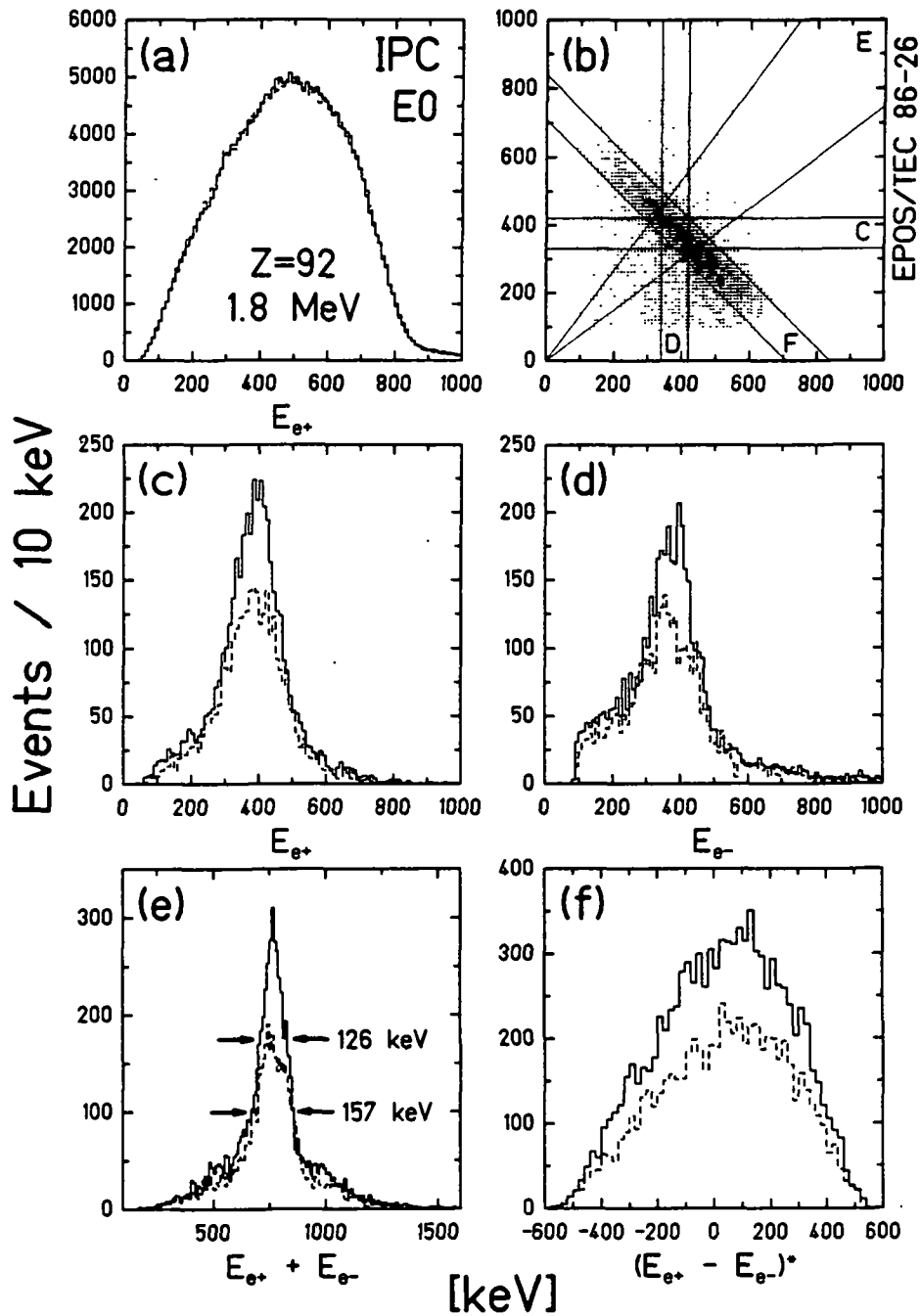


**Figure 5-20.** Simulation of IPC of a 1.8 MeV E0 transition in the scattered heavy-ions (Z=92). Parts (a)-(f) as in Fig. 5-18. Solid histograms assume relative isotropy between emitted  $e^+$  and  $e^-$ . The dashed curves include  $\omega(\cos\theta_{e^+e^-})$  calculated in Born approximation (Eqn. 5.12).

$E_{e^+} + E_{e^-} = W_0 - 2m_e c^2$ . The total positron distribution in Fig. 5-20a reflects the nearly triangular shape of  $d\beta/dE_{e^+}$  discussed in Sec. 4.2. A small fraction of the

total intensity falls within the windows C and D of Fig. 5-20b, leading to peak-like structure in the projections on the  $E_{e^+}$  and  $E_{e^-}$  axes (Fig. 5-20c,d). The dashed histogram is calculated assuming that the angle between the momentum vectors of the emitted positron and electron is given in the rest frame of the nucleus by the Born approximation (valid for  $Z \rightarrow 0$ ) [Ros35, Wil68],

$$dN_{E0}/d(\cos\theta_{e^+e^-}) \propto P_{e^+} P_{e^-} (E_{e^+} E_{e^-} - m_e^2 + P_{e^+} P_{e^-} \cos\theta_{e^+e^-}) \quad (5.12)$$

which exhibits a preference for the positron and electron to be emitted in the same direction, peaking at  $\theta_{e^+e^-} = 0^\circ$ . As shown in Fig. 5-21, maximum anisotropy occurs for  $E_{e^+} \cong E_{e^-}$  while as  $E_{e^+}$  or  $E_{e^-}$  approaches zero the distribution becomes more spherically symmetric. Since an exact calculation for  $Z \cong 92$  is not yet available, for comparison a very conservative limiting case assuming isotropy between the positron and electron emission directions is shown by the solid histogram.

The intensity of coincident positrons and electrons near 380 keV, relative to the total number of detected positrons, is small:  $\cong 0.82\%$  calculated in the Born approximation, or  $\cong 1.02\%$  assuming isotropy. These are reduced to  $\cong 0.72\%$  or  $\cong 0.89\%$ , respectively, when including pileup rejection. The broad angular distribution and rather large range of scattered heavy-ion velocities ( $.05 < v_{\text{NUC}} < .12c$ ) combine to form a wide sum-energy peak (FWHM = 126 or 157 keV) within the wedge-cut (Fig. 5-20e). The difference-energy distribution (Fig. 5-20f) reflects the broad range in positron and electron energy, in contrast to the well-defined peaks of two-body decay expected for monoenergetic positron electron emission (Fig. 5-18f). No fine-structure or narrow lines emerge in the sum-energy or difference-energy distribution from an interference pattern between the positron and electron detection efficiencies.

This very important result has been verified directly by measurements of IPC from the 1.76 MeV E0 transition in  $^{90}\text{Zr}$ . A  $^{90}\text{Sr}$  source was used which  $\beta^-$  decays to the ground-state of  $^{90}\text{Y}$ , which in turn  $\beta$ -decays with  $> 99.9\%$  probability to the  $0^+$  ground-state, and with 0.011% to the 1.76 MeV  $0^+$  first excited state of  $^{90}\text{Zr}$ . About 30% of  $0^+ \rightarrow 0^+$  transitions emit positron-electron pairs, and the remaining  $\cong 70\%$  internally convert atomic electrons. The only source of positrons in the decay scheme is the E0 transition. Its long transition lifetime (61 ns) distinguishes between  $\beta^-$  and IPC electrons. Only the correlated electrons from the created pairs are in prompt time coincidence, providing a very clean  $e^+e^-$  signal.  $\beta$ -decay electrons are

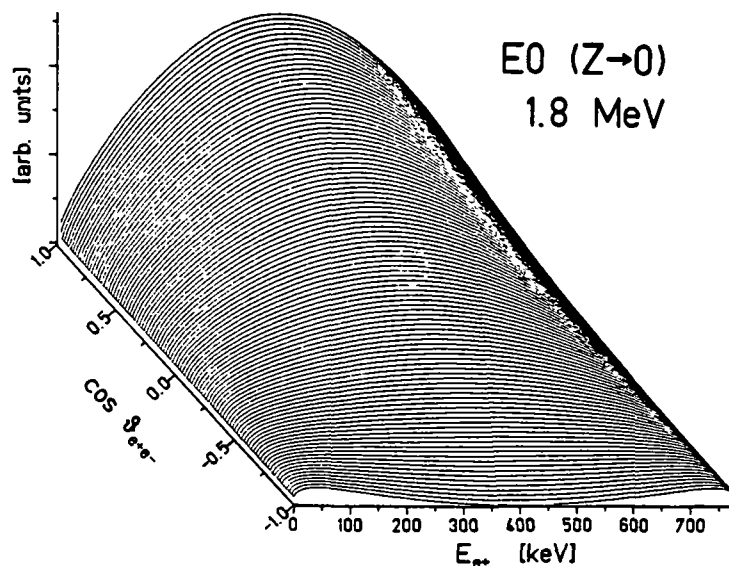


**Figure 5-21.** Emission probability of internally created electron-positron pairs plotted for a 1.8 MeV E0 transition as a function of positron kinetic energy and the angle between the  $e^+$  and  $e^-$  momentum vectors.

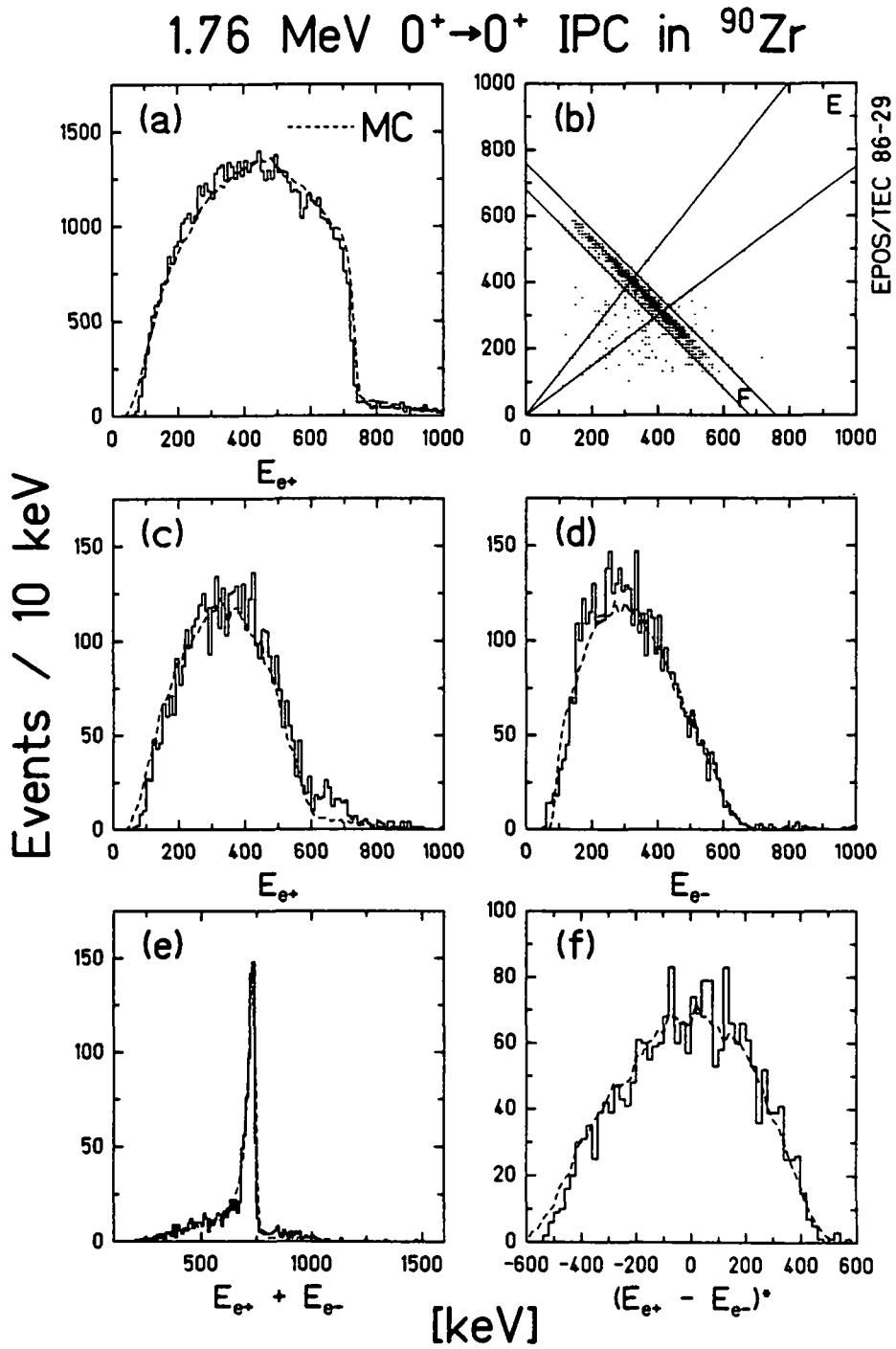
emitted a factor of  $6 \times 10^4$  more frequently, which simulates the adverse conditions of huge  $\delta$ -electron fluxes encountered experimentally in the heavy-ion collisions.

Figure 5-22 presents results of a two day measurement in which  $\sim 70,000$  total positrons and 4500 coincident pairs were detected. Parts (a) and (b) give the total positron energy distribution and the positron-electron energy correlation diagram of the coincidence events. Figures 5-22c,d present the total coincident positron and electron yields, respectively. For comparison, the dashed lines represent the results of an MCSPEC calculation (700,000 detected positrons generated) normalized to the total singles positron yield. The ratio of coincidence to positron singles events is not separately adjusted. The energy spectrum of the emitted positrons is adequately described for  $Z = 40$  by [Ros35, Wil68],

$$dN/dE_{e+} = P_{e^-} P_{e^+} \cdot F(-Z, E_{e+}) F(Z, E_{e^-}), \quad (5.13)$$

i.e., the phase space distribution times a product of Fermi functions

$$F(Z, E) = 2\pi n / (e^{2\pi n} - 1); \quad n = Z\alpha E/P, \quad (5.14)$$



**Figure 5-22.** IPC positrons and electrons from the 1.76 MeV  $0^+ \rightarrow 0^+$  transition in  $^{90}\text{Zr}$  ( $3 \times 10^{-5}$  branching ratio from a  $^{90}\text{Sr}$  decay). (a) Of 72,000 total  $e^+$ , (b)  $\sim 4500$  are in coincidence with  $e^-$ . (c)-(d) Total coincident  $e^+$  and  $e^-$  yields. (e)-(f) Projections onto  $(E_{e^+} + E_{e^-})$  and  $(E_{e^+} - E_{e^-})$  axes for events within the corresponding contours in (b). Dashed curves: MCSPEC simulation of 700,000 detected positrons (normalized to the detected yield). The narrow sum-energy peak width from the stationary source reflects Si(Li) resolution only ( $\cong 25$  keV, 1986).

which account for the suppression of low-energy positrons and high-energy electrons by the Coulomb field. The Born approximation result for the positron-electron opening-angle correlation has been assumed.

The good agreement within statistical uncertainty between the measured and calculated coincidence  $^{90}\text{Zr}$  E0 pair production yields demonstrates the accuracy with which the spectral shapes and coincidence efficiencies are calculated with MCSPEC. The experimental ratio of coincidence  $e^+/e^-$  events to total detected positrons is  $(N_{e^+e^-}/N_{e^+}) = (6.47 \pm 0.10)\%$ . The calculated rate is  $(6.12 \pm 0.03)\%$  -- a relative discrepancy of only  $(5.4 \pm 1.6)\%$ . Part of this is due to the difference between Eqn. 5.13 and relativistic theory. The shapes of the coincident energy distributions, in particular the sum- and difference-energy spectra, are well reproduced. It should be noted that the narrow sum-energy peak ( $\text{FWHM} \cong 25$  keV), which reflects the resolution of the improved electron Si(Li) detectors, is not Doppler broadened as in Fig. 5-20 because the  $^{90}\text{Sr}$  source is stationary.

This measurement also confirms the theoretical description of IPC for nuclear charges up to  $Z = 40$ . Theory successfully describes pair creation in  $^{206}\text{Pb}$  [Shl81] and other heavy nuclei. These calculations should therefore be applicable up to the region of interest around  $Z \cong 90$  (the relativistic calculations of [Shl81, Sof81] are employed in Fig. 5-20 for  $dN/dE_{e^+}$ ).

No significant fine-structure was observed in the  $^{90}\text{Zr}$  measurement, even though positrons and electrons are emitted with correlations over a range of energies and opening angles. For a given decay kinematic (fixed positron energy, electron energy, and opening angle), the broad acceptance of the EPOS spectrometer (resembling two back-to-back coaxial cones) requires an integration over a range of orientations of the emitted pair, which in turn averages over a large number of the rather finely spaced efficiency oscillations (Fig. 5-15). Unless emission of the positron and/or electron is extremely anisotropic, i.e., focussed in a small angular region comparable to the periodicity of the detection efficiency oscillations, no observable structure can arise. An MCSPEC study of anisotropic emission for two-body decay, IPC, and dynamic positron and  $\delta$ -electron emission revealed no significant efficiency-related structure for distributions of the form  $|Y_{\ell m}|^2$  for  $\ell \leq 2$ . The calculations and measurements presented here are valid for emission near ( $< \text{few mm}$ ) the solenoid axis, covering a source lifetime range of  $\leq 10^{-10}$  sec. Preliminary calculations and measurements of pair creation with a source positioned off-axis do not

indicate the formation of narrow structure. Calculations of nuclear IPC in which the direction of the scattered ion is exactly specified also produce no structure. It therefore appears to be very difficult to construct a situation in which the interplay between emission kinematics and positron and electron detection efficiencies quantitatively leads to narrow lines or a significant distortion of the expected coincident yields, especially when assuming smooth distributions in kinetic energy, or broad distributions in emission angle.

The absence of structure appearing due to instrumental effects in the energy distributions of positrons and electrons from  $\beta$ -decay sources, and more importantly, from coincident IPC positron-electron events, once again confirms our understanding of the EPOS transport system. The response of the spectrometer is clearly modelled to a degree which allows quantitative comparisons of various hypothetical sources for coincidence peaks to the experimental data. The preceding simulations also show that the sum-energy and difference-energy projections provide physically natural coordinates for characterizing both two-body decay and nuclear IPC, which is the major correlated positron-electron background. As discussed below, this helps in establishing meaningful criteria for searching for correlated positron-electron emission.

## **Section 5.5 Continuous Positron and Electron Backgrounds**

In order to search for structures in the experimental data and to quantitatively compare Monte-Carlo simulations of various processes to the results of the coincident positron-electron measurements, it is necessary to first understand the underlying backgrounds in the various projections introduced above. Continuous distributions of coincident positrons and electrons are produced by dynamic positron,  $\delta$ -electron, and nuclear pair production.

The dynamic and nuclear positron distributions were discussed in Sec. 3.3. As demonstrated earlier (Fig. 3-9), the shape and absolute magnitude of the total positron energy distribution is well described by the dynamic contribution (predicted by theory [Rei81]) plus the nuclear IPC component (calculated from the simultaneously measured  $\gamma$ -rays), corrected for the positron detection efficiency and lineshape response. This remains true for data collected with the coincidence spectrometer set-up, as shown by the total positron energy spectra plotted for U+Th and Th+Th collisions (July 1985) in Fig. 5-23a, and U+Th collisions (Feb./Mar. 1986) plotted in Fig. 5-24a. The dashed curves represent the calculated dynamic plus nuclear

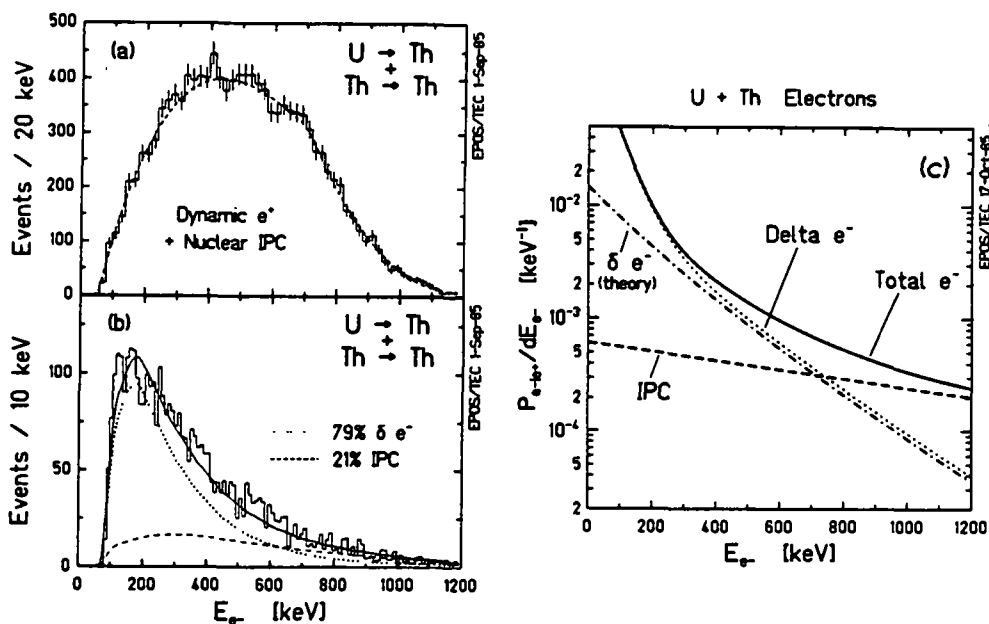


**Figure 5-23.** Continuous coincident positron (a) and electron (b) distributions measured for U+Th and Th+Th collisions in 1985. Dashed curve in (a) shows predicted dynamic positron distribution, plus nuclear IPC contribution calculated from simultaneously measured  $\gamma$ -rays, corrected for transport efficiency and detector response as described in text. Solid curve through coincident electron distribution in (b) consists of 79%  $\delta$ -electrons and 21% IPC electrons, corrected for efficiency and detector response. Shape of IPC distribution (dashed curve in C) taken from [Bac83], and  $\delta$ -electron spectrum (dotted) combines theoretical prediction (dot-dashed, [Rei81]) plus steep low energy contribution determined empirically, as described in text.

background, corrected as described in Sec. 3.3. We find empirically that the identical spectral shape also fits the energy distribution of positrons which are detected in coincidence with electrons, as indicated in Fig. 5-24c which presents the total coincident  $e^+$  yield for the 1986 U+Th data. This calculated positron background is therefore adequate for describing the energy distribution of coincidence positrons in the analyses presented in Chapters 6 and 7. Interestingly, we observe a slight  $\sim 5\%$  excess of events for energies between 200 and 400 keV, visible in Fig. 5-23a, which corresponds to the energy of the positron peaks observed in these data.

The continuous distribution of electrons, measured in coincidence with positrons from U+Th (5.75-5.85 MeV/u) and Th+Th (5.70-5.80 MeV/u) collisions, is shown in Fig. 5-23b. It consists mainly of  $\delta$ -electrons ejected from the quasi-atomic system, and electrons from internal pair creation decays of nuclear transitions. The  $\delta$ -energy distribution has a steep exponential shape which is theoretically understood

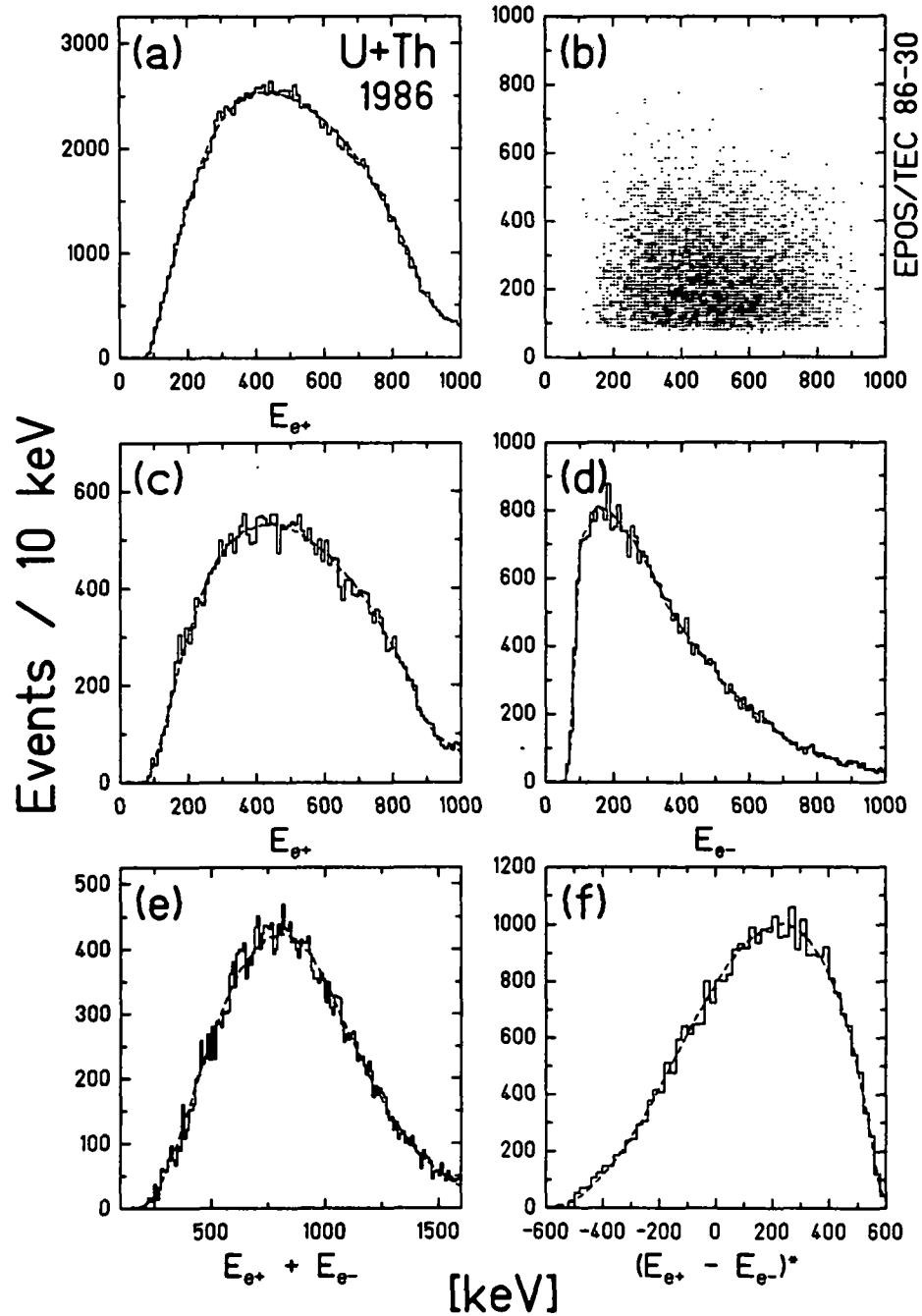


**Figure 5-24.** Total data for 5.81 to 5.90 MeV/u U+Th (Feb/Mar 1986): (a) 154,000 total detected  $e^+$ 's. (b) 32,500 coincidence events. (c-f) Projections of (b) onto the  $E_{e^+}$ ,  $E_{e^-}$ ,  $(E_{e^+} + E_{e^-})$ , and  $(E_{e^+} - E_{e^-})^*$  axes. Dashed lines are MCSPEC simulations of continuous dynamic and nuclear contributions expected from theory (see Fig. 5-23). (e) Sum- and (f) difference-energy spectra are well described assuming independent  $e^+$  and  $e^-$  energy distributions (Eqn. 5.15).

[Rei81, Reu87b] and experimentally well established [e.g., Koz81, Bac83], for energies above  $E_{e^-} \geq 200$  keV, As indicated by the dot-dashed line in Fig. 5-23c. For energies below  $\sim 200$  keV, the production probability increases very rapidly.

Electrons from IPC in the excited collision partners also have an exponential energy distribution, shown by the dashed curve in Fig. 5-23c whose slope is taken from the 5.9 MeV/u U + U positron-electron coincidence experiment of [Bac83]. The shape arises, despite the roughly triangular shaped distribution (peaking at  $E_{e^-} = 0$  keV for high Z nuclei) produced by single nuclear transition, from the exponential spectrum of nuclear  $\gamma$ -ray energies.

In order to construct a continuous electron background for comparison with the measured data of Fig. 5-23b, the energy distributions of  $\delta$ -electrons and IPC electrons were appropriately Doppler-shifted, multiplied by the electron transport efficiency, and folded with the detector lineshape (including 20% pileup calculated in Fig. 5-10). The resulting distributions are shown separately by the dashed and dotted lines in Fig. 5-23b for the IPC and  $\delta$ -electron components, respectively. The measured electron energy spectrum was then fit with a linear combination of these components (solid curve in Fig. 5-23b). Empirically we observe that  $\cong 80\%$  of the measured yield is from  $\delta$ -electrons, and  $\cong 20\%$  is from IPC, consistent with the previous measurements of [Bac83]. The solid and dotted curves in Fig. 5-23c show the total electron and  $\delta$ -electron production probabilities used to determine the continuous electron distribution in this analysis. In absolute terms, the measured  $\delta$ -electron yield is about 20% larger than that expected for 5.9 MeV/u U + U collisions [Rei81]. Taking into account the lower  $Z_U$  and beam energy of these data, this is consistent with the results of [Bac83] which found that the theoretical distribution had to be multiplied by a factor of 1.4. The shape and magnitude of the coincident electron spectrum are therefore also understood, and the calculated continuum distribution is suitable for use as a background curve in this analysis.

In order to investigate the shape of the continuous positron and coincident electron backgrounds in the various projections introduced above, we use the high statistics sample of  $\cong 150,000$  detected positrons and 32500 coincident pairs, presented in Fig. 5-24, measured in U+Th collisions between 5.8 and 5.9 MeV/u (February/March 1986). The dashed curves running through the total coincidence  $e^+$  and  $e^-$  spectra of Fig. 5-24c,d represent the expected yields calculated from the

theoretical shape of the dynamic and nuclear positron contributions, and the theoretical exponential slopes of the  $\delta^-$  and nuclear IPC electron yields, from Fig. 5-23.

The spectral shape of the electron distribution does not depend on the coincident positron energy, and vice versa, as illustrated in Fig. 5-25, which presents the coincident positron (electron) spectra when gating on different electron (positron) energy intervals (first and second columns, respectively). The bulk of the coincidence production is atomic in origin where an interdependence arises only indirectly via the HI impact parameter, whose effect on the *shape* of the positron and electron energy distributions is quite weak [Rei81]. A good approximation to the double-differential production probability is a simple product of the individual positron and electron production probabilities:

$$d^2P_{e^+e^-}/dE_{e^+}dE_{e^-} = (dP_{e^+}/dE_{e^+}) \cdot (dP_{e^-}/dE_{e^-}). \quad (5.15)$$

The dashed lines of Fig. 5-25 show a high statistics ( $10^7$  generated  $e^+$ ) MCSPEC simulation, which reflects Eqn. 5.15 by drawing on the calculated spectral forms for the positron and electron energy distributions. The simulated data are then normalized once to the entire event yield before cuts are taken. The total sum-energy and difference-energy distributions for all of the U+Th data are plotted in Figs. 5-24e and 5-24f (i.e., no wedge-shaped, or diagonal difference-energy cuts are applied). The dashed lines, projected out of the simulated coincidence yield, fit the measured data very well, indicating that Eqn. 5.15 accurately describes the observed positron-electron coincidence yield.

The third column of Fig. 5-25 extends this comparison by examining the sum-energy distributions for different wedge-shaped cuts denoted in Fig. 5-25a. The vertical scale for each is held constant to illustrate the fall-off of coincidence intensity as the wedge-shaped contour swings toward lower positron and higher electron energies. In the last column, the difference-energy spectra<sup>4</sup> are plotted for a variety of sum-energies. In both cases, the shape and magnitude of the expected continuum distributions (Eqn. 5.15) are in very good agreement with the observed data. As mentioned above, the simulated coincidence intensity is normalized once to the entire yield. No fits of the projected Monte-Carlo background shapes to the data within each cut were performed.

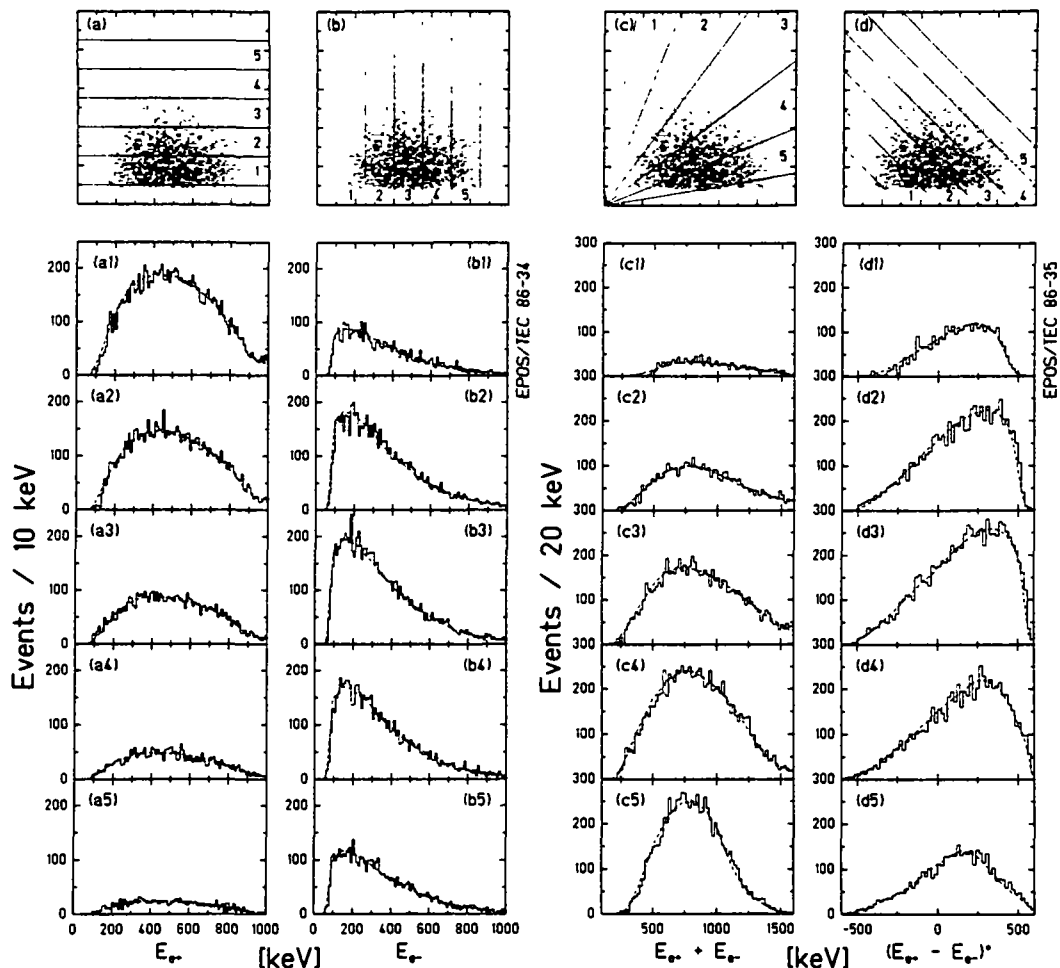


**Figure 5-25.** Projections of data of Fig. 5-24: (a) Positron energy distribution, gating on  $E_{e^-}$  as marked; (b)  $e^-$  spectra for various  $E_{e^+}$ ; (c)  $E_{e^+} + E_{e^-}$  distributions for various wedge cuts; and (d)  $E_{e^+} - E_{e^-}$  spectra vs. sum-energy. Positron and electron spectral shapes appear independent of one another. Dashed lines: identical cuts applied to MCSPEC calculation (Eqn. 5.15), normalized to total coincidence yield.

In the central region of the event correlation plane (i.e.,  $E_{e^+} \cong E_{e^-}$ ), the MCSPEC calculation over-estimates the measured data by  $\sim 1.5\%$ . Near the boundaries ( $E_{e^+}$  or  $E_{e^-} \cong 0$ ), the data is underestimated. This slight (but  $\sim 3\sigma$  statistically significant) redistribution of intensity from the central to outer regions of correlation energies indicates that, while for the bulk of coincidence events it is valid to assume an effective independence between coincident positron and

<sup>4</sup> To facilitate the comparison, these data are displayed as a function of  $E_{\Delta} = (E_{e^+} - E_{e^-}) / (E_{e^+} + E_{e^-}) \times 700$  keV. With this parameterization, the difference-energy spectral shape does not change substantially as a function of the sum-energy.

electron energies, some degree of positron-electron correlation remains. The  $\cong 20\%$  contribution of nuclear IPC coincidences may account for this effect since for  $E_{e+} \cong E_{e-}$ , the opening-angle distribution between positron and electron exhibits large anisotropy, hence reduced detection efficiency. On the other hand, for  $E_{e+} \neq E_{e-}$ ,  $\omega(\theta_{e+e-}^{\text{IPC}})$  approaches isotropy, which corresponds to relatively larger detection probability. Observation of IPC positrons and electrons should therefore be less probable in the central region of the event plane as compared to the outer regions.

The Frankfurt theory group has recently found that the dynamic positron and  $\delta$ -electron emission calculated in a full two-center potential exhibits an emission angle correlation of the form [Gra87],

$$\omega^*(\theta_{e+e-}^*) \propto (1 + \alpha \cos\theta_{e+e-}^*), \quad (5.16)$$

with  $\alpha$  independent of  $E_{e+}$  but rising from  $\alpha=0$  at  $E_{e-}=0$  to  $\alpha \cong 0.5$  for  $E_{e-} \geq 300$  keV. A MCSPEC simulation using this distribution provides a marginally better fit to the measured data.

## Section 5.6 Importance of Various Projections

As noted above, the sum-energy and difference-energy projections provide a natural parameterization by which to describe correlated positron-electron emission. To better know how to search for two-body decays, the relative sensitivity of the  $E_{e+}$ ,  $E_{e-}$ ,  $(E_{e+} + E_{e-})$ , and  $(E_{e+} - E_{e-})$  projections as indicators of back-to-back positron-electron emission has been quantitatively evaluated with a Monte-Carlo technique. Figure 5-26 presents a series of simulations in each of which 10,000 detected positrons ( $\sim 2000$   $e^+e^-$  coincidences) were generated. It was assumed that  $\sim 3\%$  of the total positron yield arises from the two-body decay of a  $1.8 \text{ MeV}/c^2$  neutral object,  $X^0$ , created at rest in the CM. The four projections of Fig. 5-18c-f are plotted for each run. It is apparent that the sum-energy and difference-energy spectra most clearly exhibit evidence for the coincidence peak. The positron energy distribution shows less evidence (statistically). The electron energy spectrum is the least sensitive indicator of the existence of structure, principally due to the steep exponential  $\delta$ -electron distribution which results for low statistics in an imbalanced clustering of events at low energies, making the identification of a coincident peak difficult. As per its design, the sum-energy peak has better energy resolution, having eliminated

the 1<sup>st</sup> order Doppler shifts, therefore leading to the emergence of more prominent structure. If a sum-energy peak is observed, then the difference spectrum is also very sensitive because by gating on sum-energies tightly around the peak, the maximum background, especially at energies near the positron and electron peaks, are excluded from the resulting projection.

The sensitivity of the sum-spectrum, and in combination, the difference-spectrum, suggests a new approach for analyzing experimental data, different from that previously used in searching for positron peak structures (Sec. 3.4). For the data of Fig. 3-16, the peaks were enhanced by cutting away the continuous dynamic and nuclear backgrounds by selecting heavy-ion scattering angle regions. This exploited the good PPAC resolution and apparent difference of the peak-related scattering events from the Rutherford elastic kinematics. It was accomplished, however, at the cost of total peak intensity. In the present EPOS configuration, the coincidence detection efficiency suggests that at most 14% of the intensity of a positron singles peak should appear in the corresponding coincident peaks. Instead of  $\sim 50-100 e^+$  peak counts, only  $\sim 7-14$  coincidence peak events should be accumulated in a typical experiment, insufficient for a meaningful statistical evaluation of the existence of structure. An alternate strategy could involve a direct search in the total data sample for structure in the sum-energy distribution. If corresponding difference-energy, positron, and electron peaks are found in conjunction with a sum-energy line, the increased intensity, by as much as a factor of two, should be advantageous in extracting valuable information, despite a somewhat smaller peak-to-background ratio.

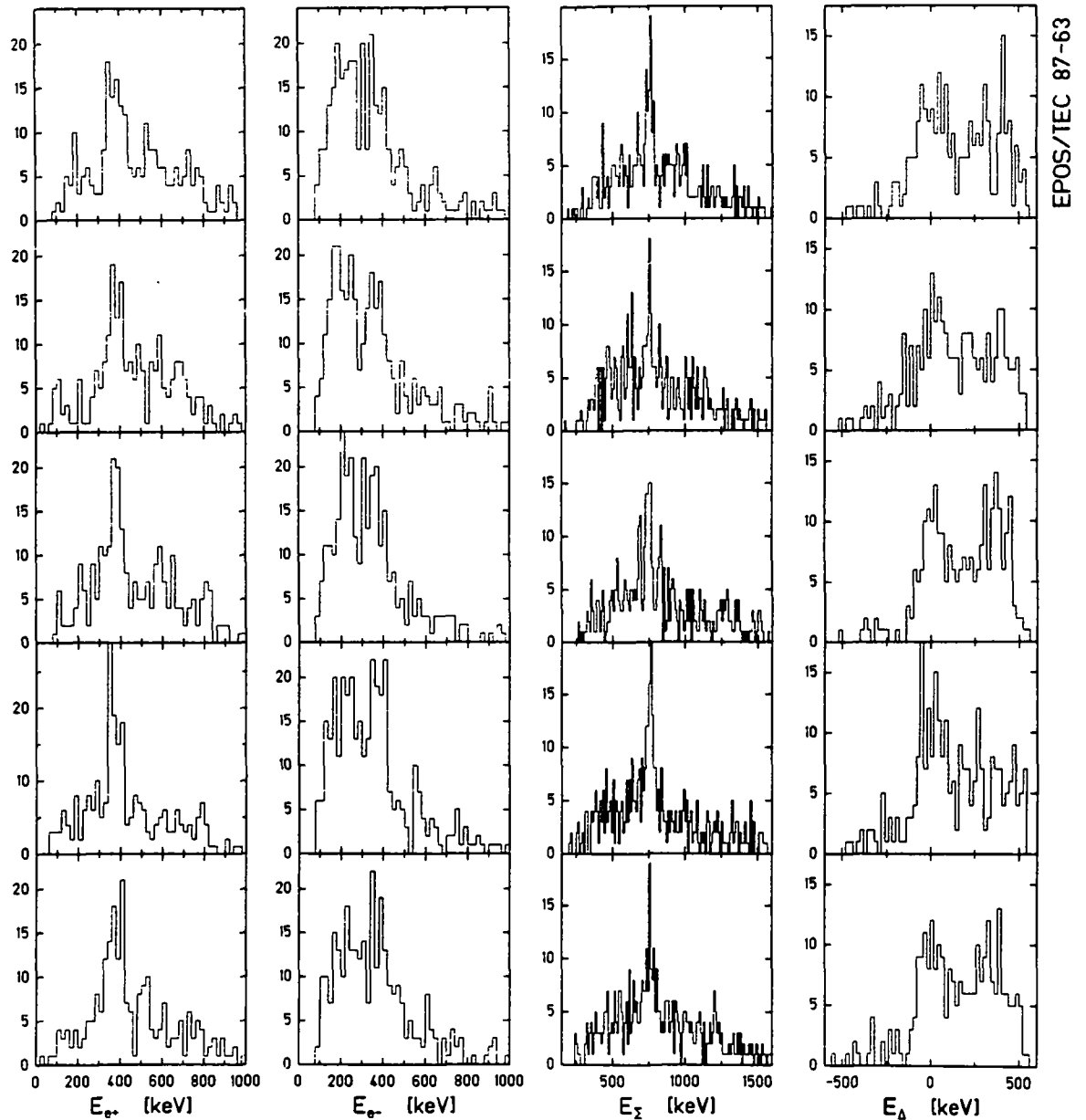


**Figure 5-26.** MCSPEC calculations of coincidence yields for  $10^4$  detected positrons (each row) assuming 3% of the yield is due to the decay of a 1.8 MeV neutral object created at rest in the CMS. Columns correspond to projections on the  $E_{e+}$ ,  $E_{e-}$ ,  $E_{\Sigma}$ , and  $E_{\Delta}$  axes, using the contours shown in Fig. 5-18b.

# Chapter 6 Data and Results

## Section 6.1 Measurements

The results of two experiments performed with the EPOS spectrometer described in Chapter 5 to search for coincident positron and electron emission are reported in Part II of this dissertation. In the first experiment of about two weeks in June and July, 1985, Th + Cm, U + Th, and Th + Th collisions were measured at beam energies ranging between 5.6 and 6.0 MeV/u. As mentioned in Sec. 2.6, because only a limited number of curium targets (fabricated at ORNL) were available, each was bombarded for very long times,  $\geq 24$  hours. Although some structure is present in these data, the peak to background is rather small and the proton backscattering analysis indicated very large deterioration (see Fig. 2-45). Most of the correlated positron-electron events mentioned in Chapter 1 were discovered in U + Th and Th + Th collisions, associated with two positron energies,  $E_{e^+} = 380$  and  $E_{e^+} = 300$  keV. These results were published in [Cow86].

After improving the electron energy resolution to  $\delta E_{e^-} \cong 10$  keV and increasing the solid angle of the HI PPAC detectors by a factor of  $\sim 3$ , we accumulated about ten times more data with the U + Th system in February and March 1986. Due to a UNILAC beam energy calibration error, however, during much of the experiment data were taken at lower beam energies than in the 1985 measurement. These showed little evidence for correlated emission. At slightly higher beam energy than that of 1985, in addition to reproducing the 750 keV  $E_{\Sigma}$  peak with similar statistical accuracy, and the  $E_{\Sigma} \cong 600$  keV peak with much higher accuracy, a third prominent sum-energy peak was discovered at  $\cong 815$  keV. For each of these, the improved energy resolution revealed that the  $E_{\Sigma}$  peak is much narrower ( $\sim 25$ -40 keV, FWHM) than the corresponding difference-energy structure.

Additional data on these lines were collected in a short run in July 1986. For some aspects of the analysis presented below, this was added to the preceding results. Most of the investigations of possible origins for the coincident positron-electron lines were originally performed for the 750 keV U + Th sum-energy peak measured in 1985, but they are equally relevant for the other structures as well.

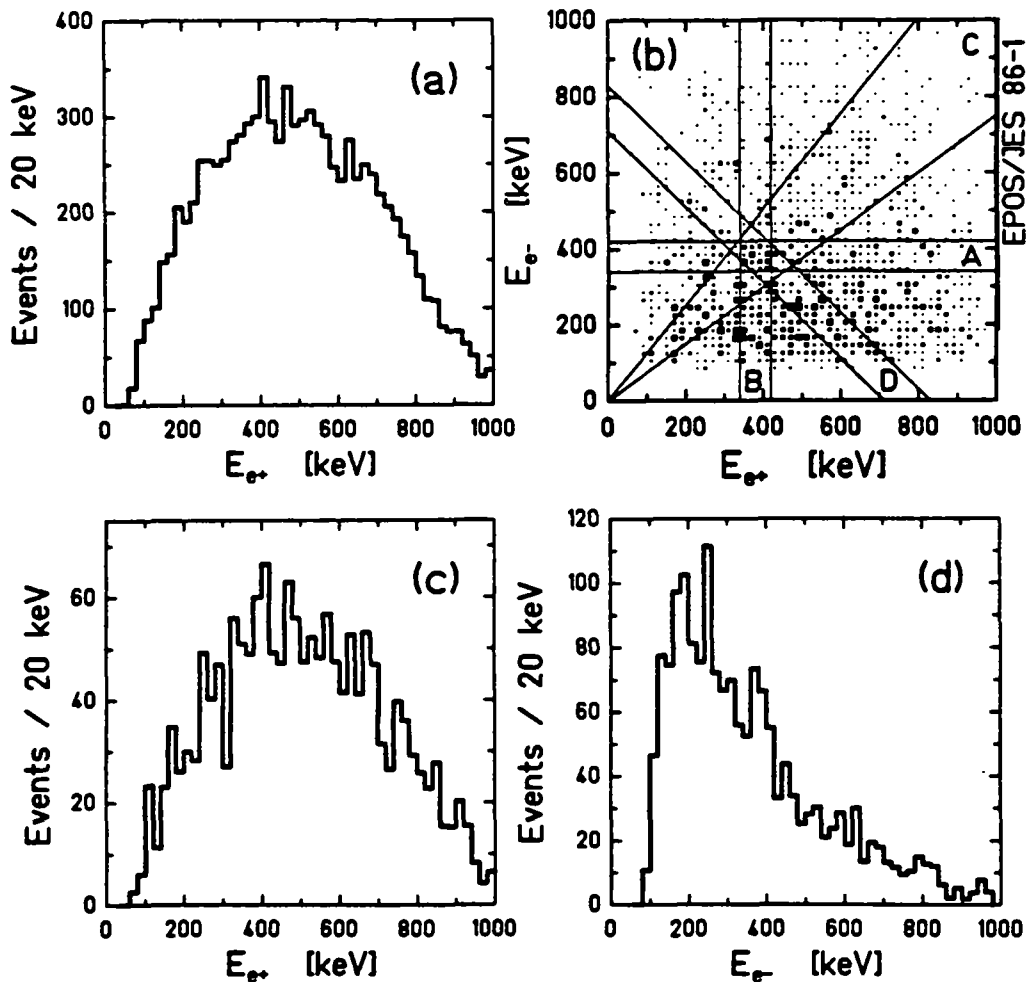


**Figure 6-1.** (a) Total energy distribution of positrons from 5.83 MeV/u U+Th collisions (July, 1985). (b) 2-dimensional  $E_{e^+}$  vs.  $E_{e^-}$  distribution of coincident  $e^+e^-$  events. Parts (c,d) present the total coincident positron and electron yields, respectively.

## Section 6.2 750 keV Structure in U+Th

Figure 6-1 presents a plot of the coincident positrons and electrons from U+Th collisions accumulated in the first series of coincidence experiments performed in June and July of 1985. The beam energy for the displayed data ranged from 5.80 to 5.85 with a mean of 5.83 MeV/u. Targets consisted of  $250 \mu\text{g}/\text{cm}^2$  layers of  $\text{ThF}_4$  evaporated on  $40 \mu\text{g}/\text{cm}^2$  carbon backings, covered with an additional  $20 \mu\text{g}/\text{cm}^2$  carbon covering foil. The entire scattering angle range of the PPAC's between  $20^\circ < \theta_{\text{HI}} < 70^\circ$  is included for a total of 9600 detected positrons (Fig. 6-1a), with 1690

coincident positron-electron events. The two-dimensional electron energy versus positron energy distribution is shown in Fig. 6-1b. The shapes of the individual coincident positron (6-1c) and electron (6-1d) energy spectra are in good agreement with those expected from the theoretical atomic and nuclear continua corrected for transport efficiency and detector response, as described in Sec. 5.5.

Although very little structure is readily apparent in the total coincident yields of Fig. 6-1, the sum-energy spectrum derived from plotting the events contained within the wedge-shaped contour (labeled C) versus  $E_{\Sigma} = (E_{e+} + E_{e-})$  reveals a narrow peak centered at  $760 \pm 20$  keV, shown in Fig. 6-2c, which has a width of  $80 \pm 20$  keV. Narrow lines in the positron and electron energy distributions are correlated with this peak. As shown in Fig. 6-2a, plotting the energy of positrons in coincidence with electrons having kinetic energy between 340 and 420 keV reveals a peak centered at  $380 \pm 15$  keV with a width of  $80 \pm 15$  keV. Gating on positrons between 340 and 420 keV yields an electron line at  $375 \pm 15$  keV with width  $75 \pm 15$  keV (Fig. 6-2c). Finally, by gating on the sum of positron and electron energies between  $710 < E_{\Sigma} < 830$  keV, the projection of the data on the difference-energy axis,  $E_{\Delta} = (E_{e+} - E_{e-}) \times [700 \text{ keV} / (E_{e+} + E_{e-})]$ , exhibits the structure shown in Fig. 6-2d. The difference peak is centered at a mean difference-energy of  $\langle E_{e+} - E_{e-} \rangle \cong 6$  keV, and has a width of  $\cong 100$  keV.

In each of the spectra in Fig 6-2a-d, the dashed curves represent the distribution expected assuming that the entire 1690 coincidence events are due to the continuous atomic and nuclear processes. An MCSPÉC simulation of  $5 \times 10^6$  detected coincidence events drawn from this smooth distribution (see Sec. 5.5) was normalized to the measured coincident event yield, after which the identical projections as taken for the experimental data were made (i.e., cuts A-D in Fig. 6-1). This provides a model-independent evaluation of the continuous background. The intensities of each of the individual projections of the continuum background distribution are not adjusted separately. Only a single overall normalization to the entire event yield was used.

Although the four projections of Fig. 6-2 are correlated, the experimentally observed intensity of the structure in each varies according to the extent that the different cuts exclude background events in the energy region surrounding the peak. For example, by fitting the background shapes described above (dashed curves) individually to each spectrum (excluding a region around the peak), the fol-

## U + Th 5.83 MeV/u

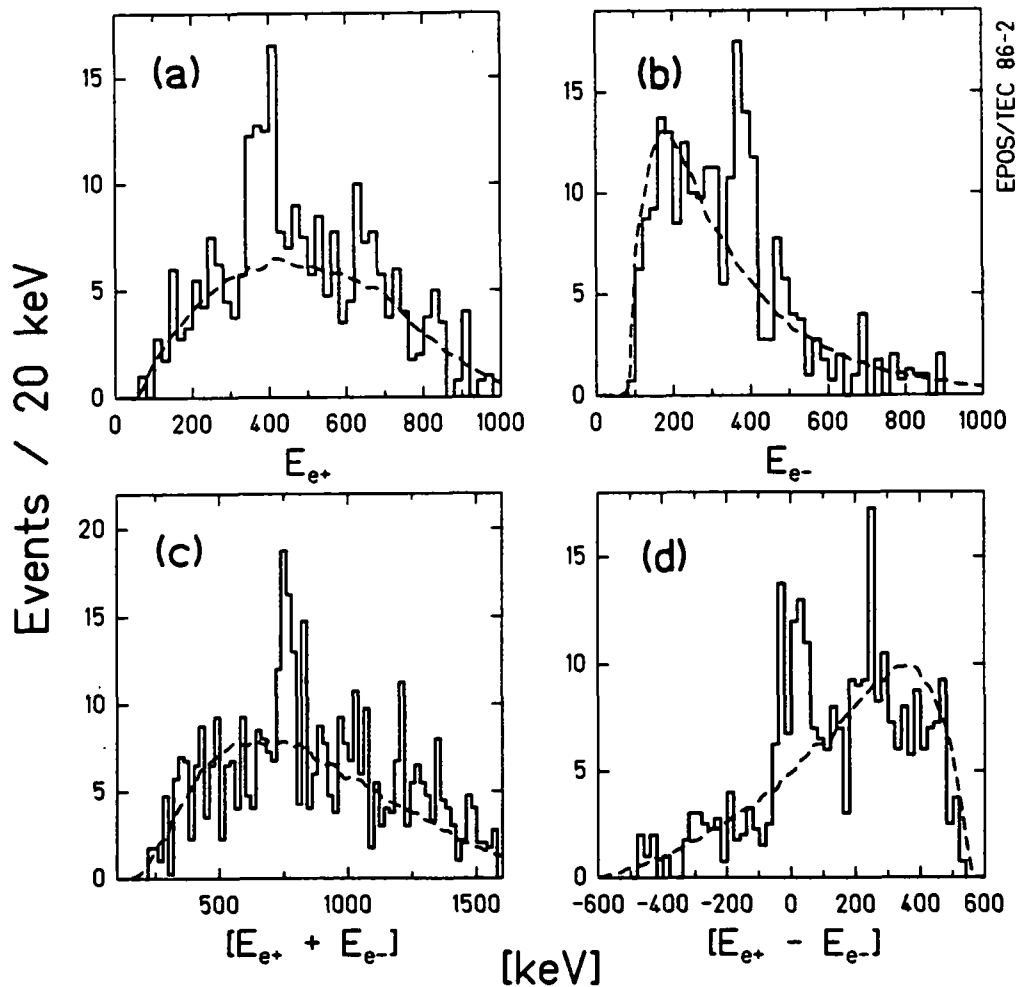


Figure 6-2. Projections onto the  $E_{e+}$ ,  $E_{e-}$ ,  $E_{\Sigma}$  and  $E_{\Delta}$  axes of the distribution of coincident positron-electron events contained in the windows labeled A-D in Fig. 6-1b, respectively.

lowing intensities for the coincidence peaks in each of the projections were obtained:  $N_{e+} = 26.7 \pm 7.7$ ,  $N_{e-} = 31.7 \pm 7.6$ ,  $N_{\Sigma} = 35.3 \pm 9.4$ , and  $N_{\Delta} = 38.5 \pm 9.7$  counts. As expected from Fig. 5-26, the  $E_{\Sigma}$  and  $E_{\Delta}$  projections exhibit the strongest indication of structure. To estimate the size of the signal, taking into account the energy-energy correlation, the intensity of the 2-dimensional continuum background distribution was fit as a whole (using a one-parameter maximum likelihood fit for normalization, see Eqn. 4.2) to the the measured coincident  $E_{e+} - E_{e-}$  data, excluding a region around the coincident line. In the energy interval containing the peak ( $340 \leq E_{e+} \leq 420$  keV,  $340 \leq E_{e-} \leq 420$  keV),  $N_{bk} = 21.8 \pm 0.53$  background counts

are expected, compared to 54 measured coincidence events. The net size of the correlated positron-electron signal is therefore  $N_{pk} = 32.2 \pm 7.4$  events.

Figure 6-3 compares these data to the results of an MCSPEC simulation of the production (at rest in the CM) and isotropic two-body decay of a neutral object (Fig. 6-3(i)-(j)). In order to reproduce the observed data, a mass of  $M_x = 1.8 \text{ MeV}/c^2$  and an intensity such that only 3% of the total detected positron yield arises from the decay of this object, were assumed. The shape and magnitudes of the positron, electron, sum-energy, and difference-energy peaks are remarkably well reproduced within this model. The sum-energy peak width of  $80 \pm 20 \text{ keV}$  is in agreement with that expected solely from detector resolution of  $\sim 50 \text{ keV}$ . Even the  $\sim 5 \text{ keV}$  lower mean electron peak energy is understood in terms of the larger low-energy tailing in the electron Si(Li) detector response (see Fig. 5-18f).

The coincidence peak intensity is confined to a small region centered around  $E_{e+} \cong E_{e-} = 380 \text{ keV}$ . Figure 6-4 shows the positron, electron, and difference-energy projections averaged for equal size gates taken on either side of the corresponding cuts in Fig. 6-1b. The sum-energy projections for events taken on either side of the wedge-shaped cut are shown in Fig. 6-5. (Figure 6-3e-h compares these adjacent cuts to the peak cuts of Figs. 6-2 and 6-3a-d.) The absence of significant structure in these spectra illustrates the correlated nature of the positron and electron peak events, and is in full agreement with the predictions from a two-body decay origin. Figures 6-3m-p compare the coincident structure to a simulation of nuclear IPC. As discussed in Sec. 7.2, IPC is not able to explain the data.

The relative intensity of the coincident sum-energy signal at 760 keV is obtained by comparing it to the peak in the total positron yield enhanced by heavy-ion kinematic cuts. For laboratory scattering angles between  $50^\circ < \theta_U < 70^\circ$ , a positron enhancement similar to those of Fig. 3-16 begins to emerge from the data with a mean energy of 380 keV (Fig. 6-6a). The associated coincident electron peak is enhanced accordingly over the continuous  $\delta$ -electron background (Fig. 6-6b). The ratio of coincidence electron peak counts to total positron peak events is  $19 \pm 8\%$ . This is consistent with 14% expected for the two-body decay of neutral objects produced at rest in the CM (see Fig. 5-18). Because of the rather weak statistical significance of this ratio due to the limited peak intensities available within this angular region, this comparison is not inconsistent with a ratio of 6% expected for spatially uncorrelated emission.

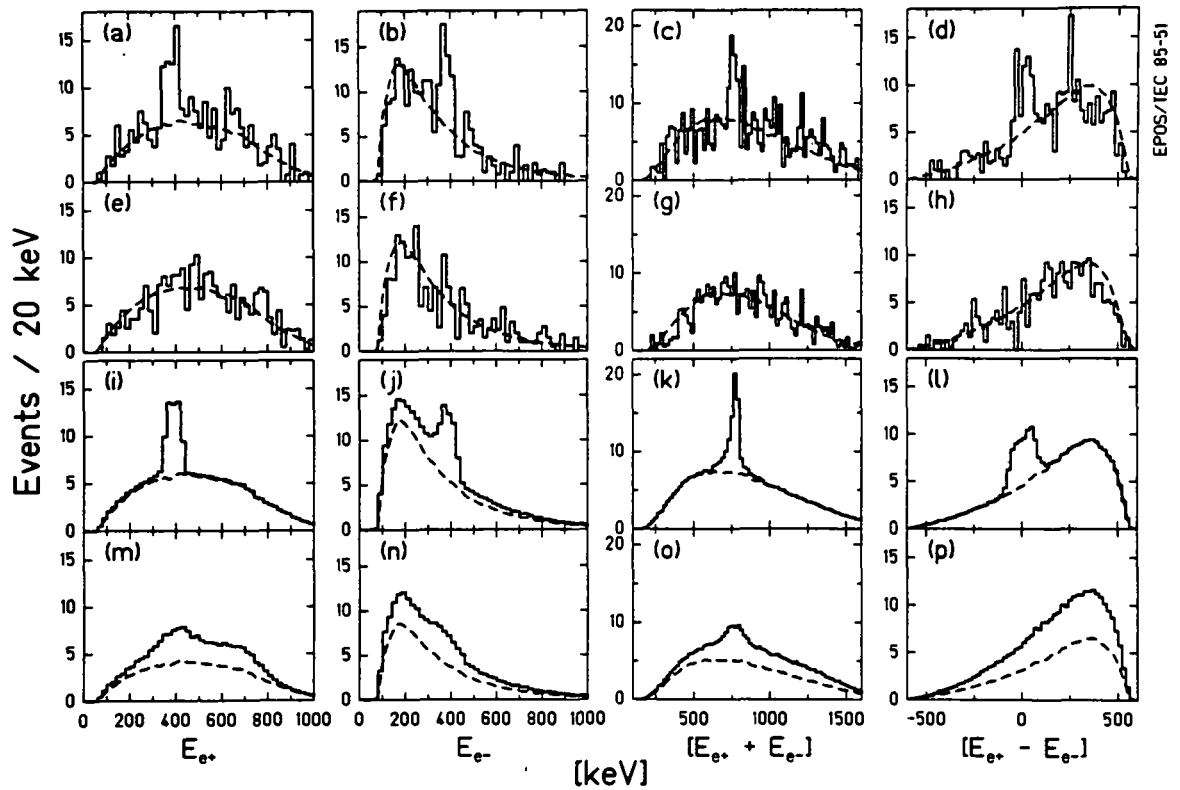


**Figure 6-3.** Projections of U+Th coincidence data from Fig. 6-2(a-d), and MCSPEC simulations of the two-body decay of a  $1.8 \text{ MeV}/c^2$  neutral object (i-l) and IPC of a  $1.8 \text{ MeV}$  E1 transition in the scattered nuclei (m-p). Columns correspond to projections onto the  $E_{e+}$ ,  $E_{e-}$ ,  $(E_{e+} + E_{e-})$ ,  $(E_{e+} - E_{e-})$  axes. Parts (e)-(h) are the average of similar gates adjacent to either side of the gates A-D of Fig. 6-1b. (Reproduced from [Cow86].)

As mentioned above, the peak has an estimated net intensity above background of  $32.2 \pm 7.4$  counts, which represents a  $4.3\sigma$  statistical significance. One may alternatively assess the probability that no correlated peak exists, i.e., that the entire coincident event yield is due to continuous atomic and nuclear processes (dashed curves in Fig. 6-2) from which the observed structure is merely a statistical fluctuation. In the region  $340 \leq E_{e+} \leq 420$  and  $340 \leq E_{e-} \leq 420$  keV,  $24 \pm 4.9$  counts are expected from continuous backgrounds. The observed 54 events in this interval therefore represents a 30 count,  $6\sigma$  excursion above the expected intensity [Ead71]. This strongly argues against the null-hypothesis that continuum production explains the data.

The data presented here were accumulated with targets identical to those employed in the Th+Th measurement shown in Fig. 3-16, and represent  $\cong 2/3$  of the

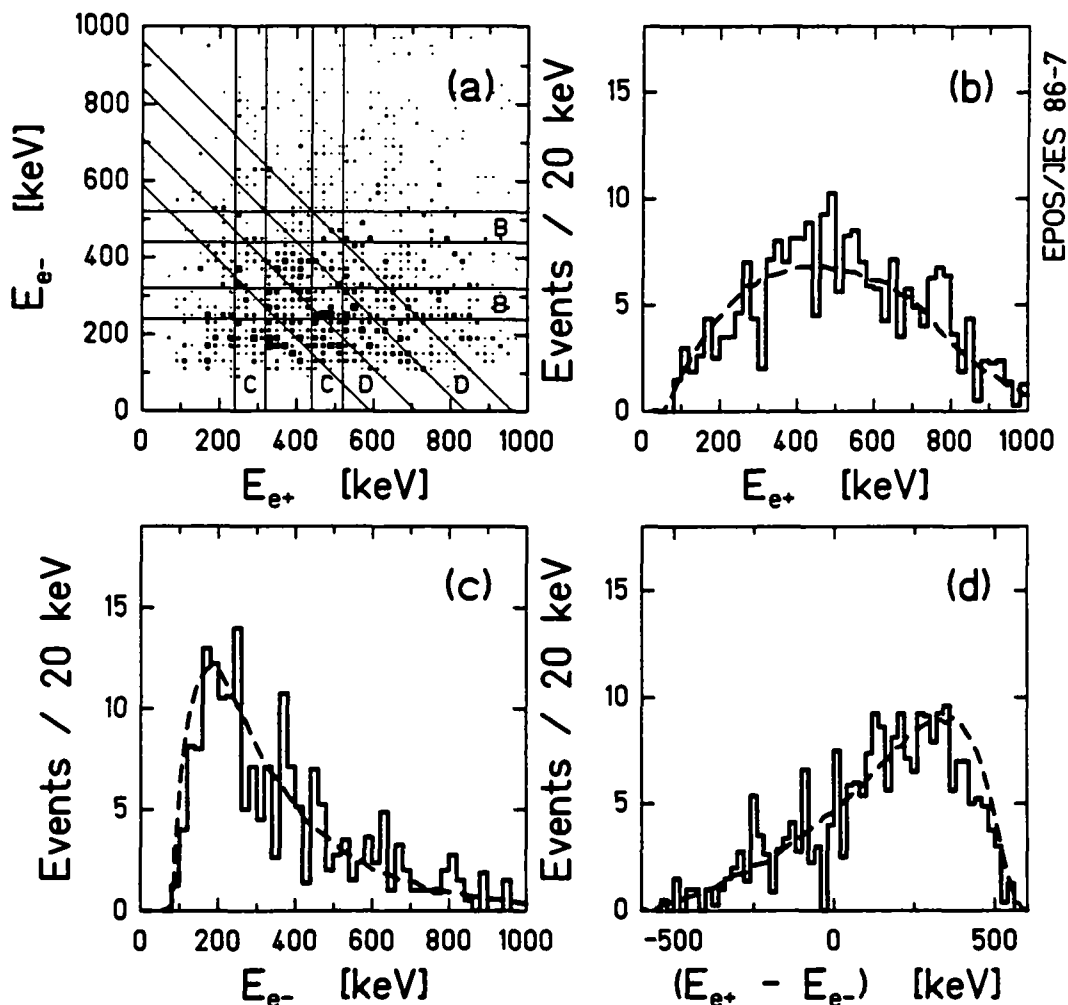


**Figure 6-4.** Projections of U+Th coincidence data on  $E_{e^+}$ ,  $E_{e^-}$ , and  $E_{\Delta}$  axes, averaged for gates (a) adjacent to either side of the gates A, B, and D in Fig. 6-1b.

total data collected on the U+Th system. An additional  $\sim 4500$  positrons were measured at somewhat lower beam energies (5.75 to 5.80 MeV/u) on targets fabricated with a different  $\text{ThF}_4$  evaporation procedure on different carbon backing foils [Fol85]. Viewed independently, these targets exhibit no statistical evidence for the appearance of the peak ( $N_{e^+e^-}^{\text{pk}} = 5 \pm 4$  counts). While this could reflect a reduced production cross-section at lower projectile energies, independent evidence alternatively suggests that these targets exhibited a rapid deterioration in the heavy-ion beam. If resonant processes contribute to the production of the sum-energy peak, then when non-uniformities set in, the thick portion of the target may lead to an overwhelming contribution of the continuous positron backgrounds which obscure the

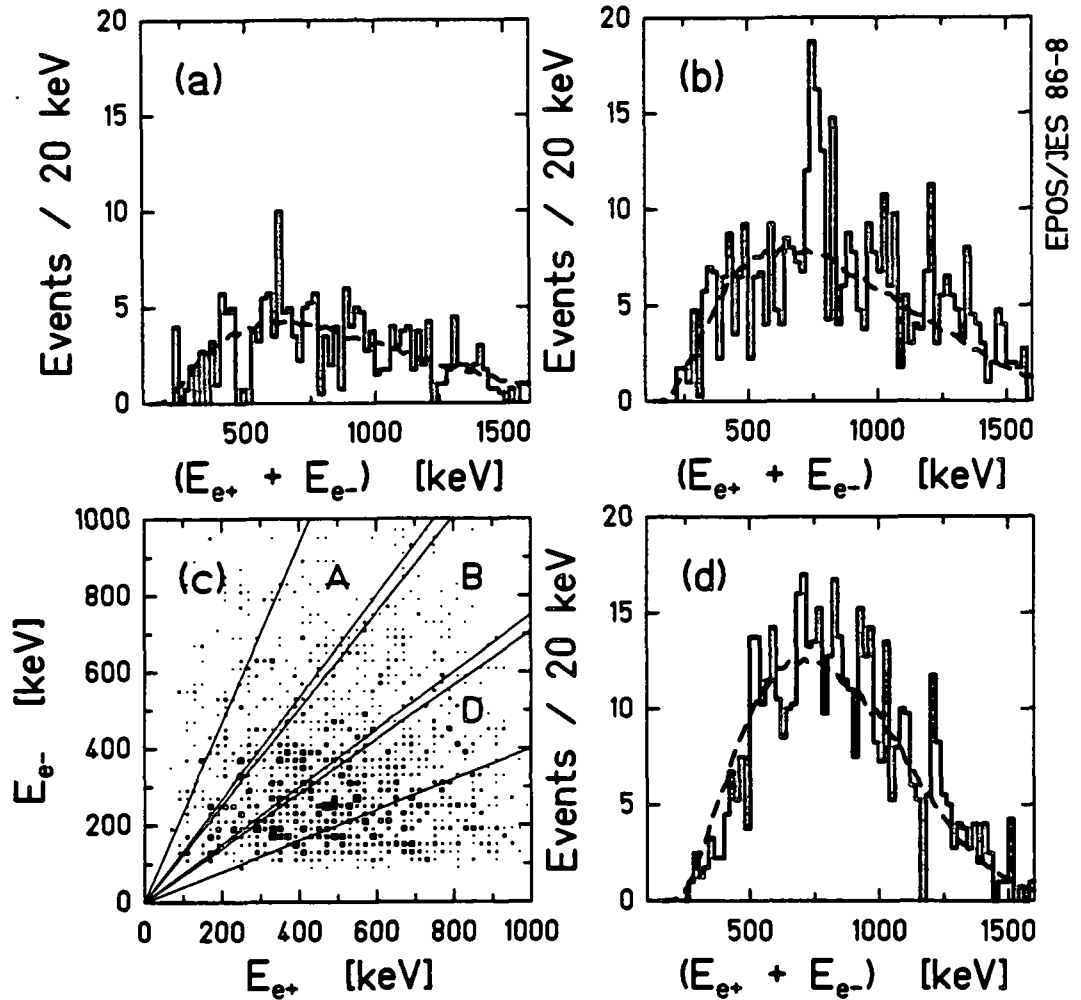


**Figure 6-5.** Projections of U + Th coincidence data on  $E_{\Sigma}$  axis for gates labelled A, B, and D in part (c).

peak. With this in mind, in a subsequent experiment using thorium beam we compared data collected for only short irradiation times ( $\leq 1$  hour) to that including longer heavy-ion bombardment of the targets (discussed in Sec. 3.4.4). Figure 3-28 showed that a peak in the total positron distribution emerges at  $\cong 325$  keV (using no kinematic selection), which seems to be correlated with "fresh" targets. In any case, adding the remaining 1/3 of the U + Th data measured in 1985 does not significantly dilute the results presented in Fig 6-3a-d. The coincidence structure remains a  $\sim 6\sigma$  deviation from the smooth background, and the net peak intensity is  $3.6\sigma$ .

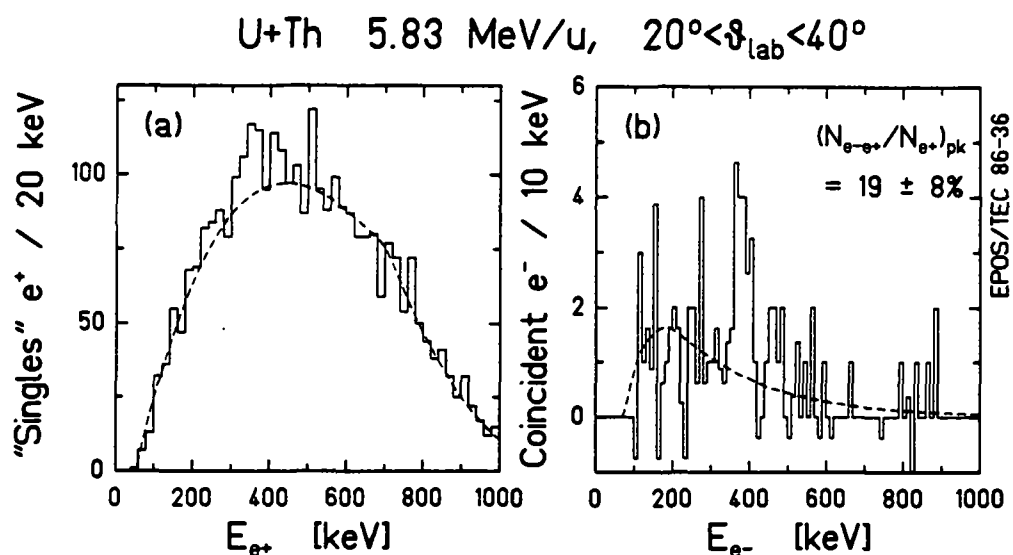


**Figure 6-6.** Total positron, and gated coincident electron ( $340 < E_{e^+} < 420$  keV) spectra for U+Th collisions (Fig. 6-1) with heavy-ions scattered between  $20^\circ$  and  $40^\circ$  in lab. The relative coincident  $e^-$  peak intensity to the  $e^+$  peak is  $19 \pm 8\%$ , consistent with 14% expected for back-to-back emission.

### Section 6.3 Additional Results

In addition to the U+Th data presented above, data were accumulated on the Th+Cm and Th+Th systems. In Th+Cm at 5.85 MeV/u, and in Th+Th at 5.75 MeV/u, the data indicate an excess of coincident positrons and electrons at  $E_{e^+} \cong E_{e^-} \cong 380$  keV. When added to the U+Th data, as shown in Fig. 6-7, the peak intensity is increased to  $\geq 40$  events. The positron, electron, and difference-energy peaks are comparable to those presented in Fig. 6-2. The increased statistical significance of the sum-energy spectrum suggests a narrower  $E_\Sigma$  line with a width of  $\Delta E_\Sigma = 50 \pm 10$  keV, centered at  $752 \pm 10$  keV. The width agrees with that expected from detector resolution alone and is clearly smaller than the  $\Delta E_{e^+} \cong 80$  keV,  $\Delta E_{e^-} \cong 70$  keV, and the  $\Delta E_\Delta \cong 100$  keV widths in the associated projections.

At lower beam energies, around 5.70 MeV/u in Th+Th and 5.75 MeV/u in U+Th, a second interesting feature in the coincidence positron-electron distribution was found. As shown in Fig. 6-8, a positron peak at 310 keV is observed in coincidence with an electron peak at  $\sim 295$  keV. Although the statistical evidence is weak here ( $N_{e^+e^-}^{\text{pk}} \cong 22 \pm 7$  counts), it indicates that more than one coincidence structure

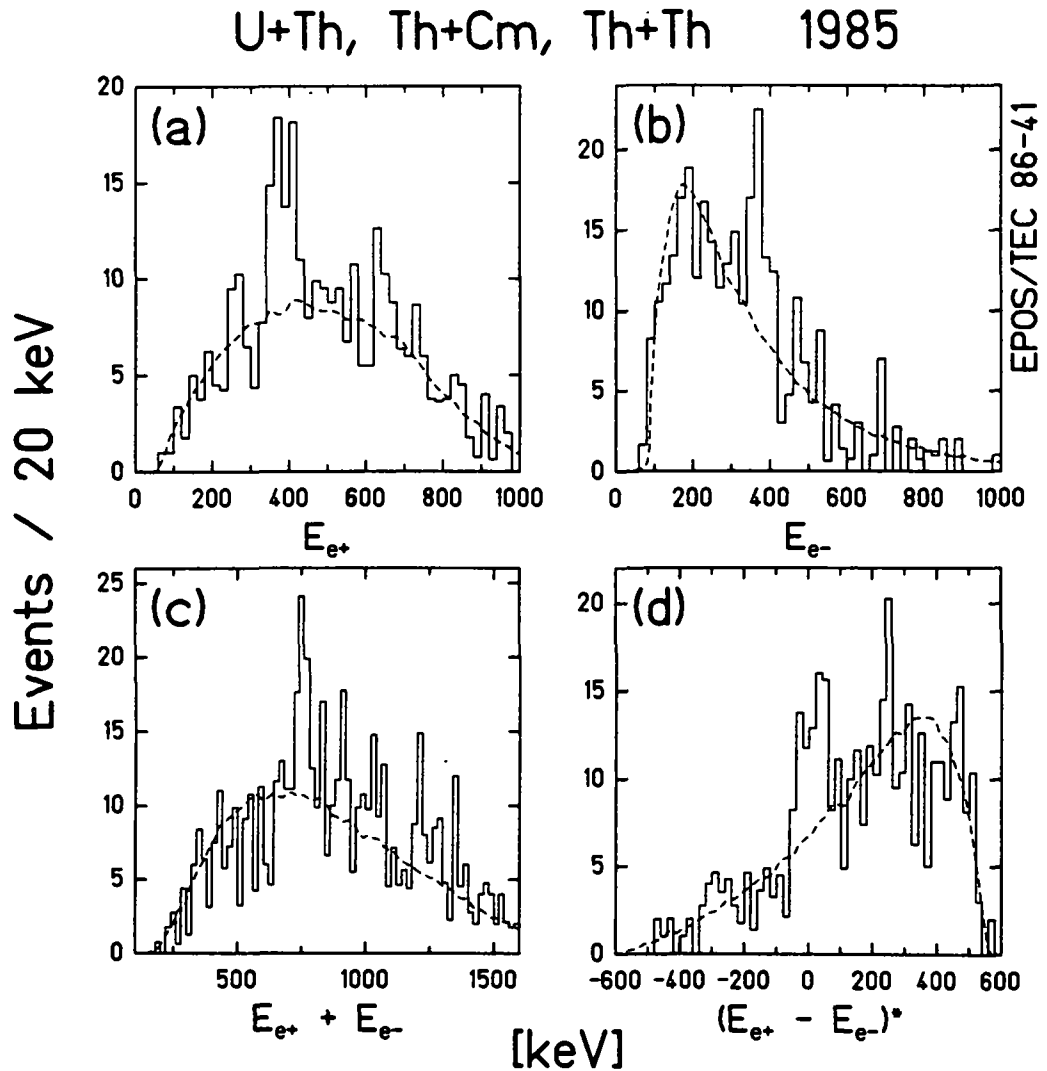


**Figure 6-7.** Data from 5.88 MeV/u Th+Cm and 5.75 MeV/u Th+Th collisions are shown added to those of Fig. 6-2. The coincident  $e^+/e^-$  peak intensity is increased to  $\cong 45$  counts, with a sum-line width of  $60 \pm 15$  keV.

may be associated with the positron peak energies between  $\sim 300$  and  $\sim 380$  keV discussed in Part I of this dissertation.

### Section 6.4 Follow-up Experiments

As mentioned above, the existence of correlated positron-electron structures was confirmed in a second series of coincidence measurements performed in February and March 1986. The electron energy resolution was improved to  $< 15$  keV, so that the minimum expected width of the sum-energy peak is  $\cong 25$  keV, if due entirely to

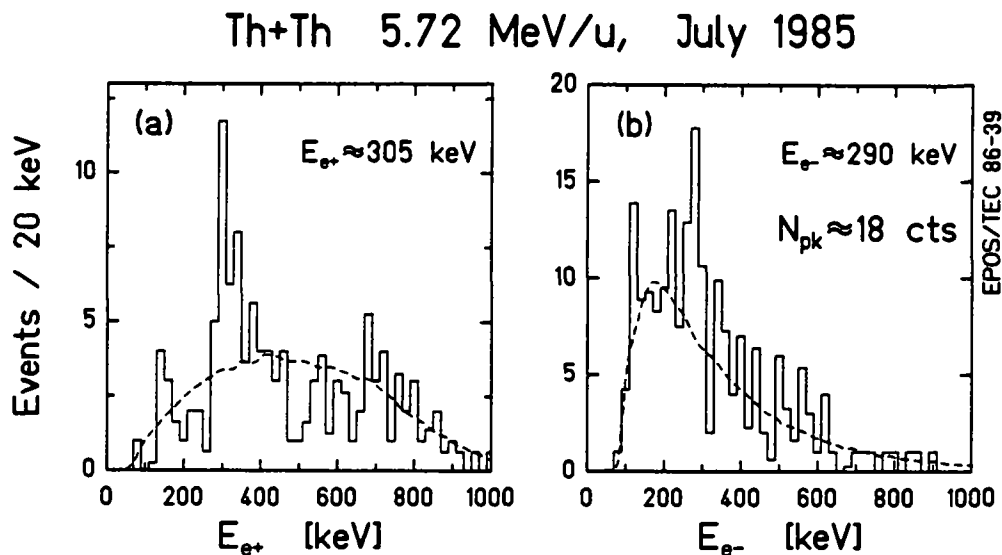


**Figure 6-8.** Th + Th collisions at 5.72 MeV/u. (a) Coincident peaks at  $E_{e^+} \cong 305$  keV and (b)  $E_{e^-} \cong 290$  keV suggest the presence of additional correlated structure.

detector response. New heavy-ion PPAC detectors with a factor three larger solid angle (at a cost of decreasing the scattering-angle resolution from  $0.5^\circ$  to  $\sim 1.2^\circ$ ) were employed in order to acquire greater statistical accuracy. This change seemed justified in light of the shift of the analysis approach away from exploiting heavy-ion scattering-angle correlations to suppress continuous backgrounds as discussed in Chap. 3, towards exploiting the sensitivity and selectivity of the EPOS coincidence spectrometer in detecting correlated positron-electron emission, as discussed in Sec. 5.6.

The study concentrated on the U + Th system at energies between 5.81 to 5.90 MeV/u. A 0.03 MeV/u recalibration of the UNILAC energy places the preceding U + Th measurement at  $\sim 5.86$  MeV/u. The targets were  $\sim 250 \mu\text{g}/\text{cm}^2$  ThF<sub>4</sub> evaporated on  $20 \mu\text{g}/\text{cm}^2$  carbon backings, covered with an evaporated carbon layer of  $5 \mu\text{g}/\text{cm}^2$ . Because of the apparent sensitivity of the quality of the data on target condition, as mentioned in regards to Fig. 3-28, we changed targets every  $1\frac{1}{2}$  hours, using a total of over 200 targets in the 20 days of beam time.

In addition to peak intensity near 750 keV, two very prominent narrow lines are present in these data at sum-energies of  $E_\Sigma \sim 610$  and  $\sim 815$  keV. The higher of these, already appearing at a  $3\sigma$  level in the total data of Fig. 5-25(c3), becomes

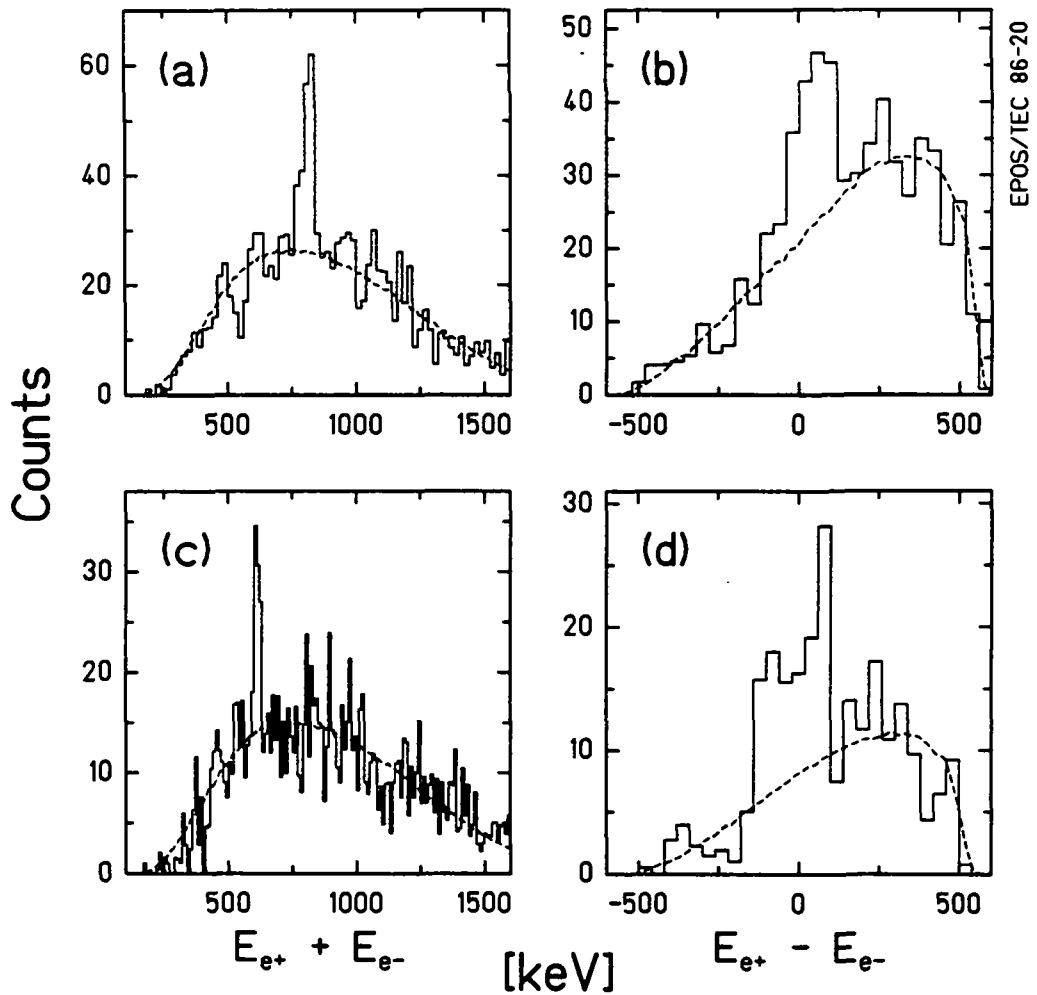


**Figure 6-9.** (a) Sum-energy and (b) Difference-energy projections for U+Th collisions between 5.87 and 5.90 MeV/u (Feb., 1986), selecting events for prompt  $e^+$  and  $e^-$  flight-times. The sum-energy line at  $\sim 815$  keV contains  $90 \pm 14$  counts, and has a width of  $40 \pm 4$  keV. Data of (c) and (d) are selected for 5.85 to 5.90 MeV/u collisions with prompt electron TOF but slightly delayed  $e^+$  TOF. The  $\cong 610$  keV sum-energy line has  $60 \pm 12$  counts with a width of  $23 \pm 3$  keV.

prominently visible by selecting beam energies higher than those employed in the measurements of Figs. 6-1 to 6-6. Figure 6-9a,b presents the sum-energy distribution and corresponding difference-energy spectrum for data accumulated for beam energies between 5.87 and 5.90 MeV/u. Events were selected which fall within a 7 ns wide window on the prompt HI- $e^-$  time-of-flight distribution (which exhibits a 7.7 ns FWHM). No HI scattering angle cut was made. The narrow sum-energy peak is centered at  $817 \pm 5$  keV, and is associated with narrow positron and electron lines, as shown in Fig. 6-10 for a subset of this data at 5.87 MeV/u. The intensity of the

$E_{\Sigma}$  peak in Fig. 6-9a is  $90 \pm 14$  counts which represents  $6.4\sigma$  level of confidence, and an  $8.6\sigma$  deviation from the underlying 90.5 count background. Fits of the smooth background curves to the  $E_{\Sigma}$  and  $E_{\Delta}$  distributions individually gives  $N_{\Sigma} = 90.0 \pm 13.5$  and  $N_{\Delta} = 90.3 \pm 14.8$  counts, respectively. Its narrow width of  $\Delta E_{\Sigma} = 39.5 \pm 3.6$  keV (FWHM) is clearly smaller than the individual positron and electron peak widths of  $\sim 80$  keV, and narrower than the  $E_{\Delta}$  structure whose width is  $\Delta E_{\Delta} = 158 \pm 21$  keV (FWHM).

Figure 6-9c,d presents the sum-energy and difference-energy spectra for data selected to isolate the lower energy structure ( $E_{\Sigma} = 612 \pm 4$  keV). Beam energies between 5.85 and 5.90 MeV/u were included, and positrons have been selected which arrived at the detector slightly delayed ( $\sim 3$  ns) with respect to the average TOF for the continuous dynamic distribution. This structure appears with an average intensity of  $N_{e^+e^-} \cong 60 \pm 12$  counts, deduced from fits of the background shapes to the sum-energy and difference-energy spectra individually ( $N_{\Sigma} = 54.1 \pm 10.5$ ,  $N_{\Delta} = 66.9 \pm 10.5$ ), which represents a  $\sim 5.5\sigma$  C.L. or a  $8.5\sigma$  deviation from the smooth underlying 50 count background. The narrow sum-energy peak width,  $\Delta E_{\Sigma} = 22.6 \pm 2.9$  keV (FWHM), is significantly smaller than the associated difference-energy structure whose width is  $\Delta E_{\Delta} = 153 \pm 9$  keV. (The structure in Fig. 6-9d appears wider than this because the plotted quantity is actually  $E_{\Delta} = (E_{e^+} - E_{e^-}) \times [700 \text{ keV} / (E_{e^+} + E_{e^-})]$ .) As with Fig. 6-9a,b, no HI angular cuts have been applied.

The 750 keV sum-energy peak appears, as in the previous measurement, for prompt HI- $e^+$  flight-times. Figure 6-11 presents an analysis by J. Schweppe of 5.85 MeV/u U+Th data. The  $E_{\Sigma}$  peak is centered at  $752 \pm 5$  keV. Additional data from 5.87 MeV/u yields a peak intensity of  $30 \pm 8$  counts. The narrow sum-energy peak width of  $25 \pm 5$  keV is, as for Fig. 6-7, consistent with the detector resolution. As noted in Sec. 6.6, the 750 keV sum-energy peak has also been recently observed in U+Ta collisions.

These structures were reproduced in a third U+Th measurement in July 1986. Upon adding all the available data together [Sal88], approximately 110 and 100 counts have been observed in each of the  $\sim 815$  keV and  $\sim 610$  keV sum-energy lines, respectively, and  $\geq 70$  counts in the  $\sim 750$  keV peak. The measured sum-energy linewidths are  $\cong 40$  keV for the  $\sim 815$  structure and  $\cong 25$  keV for the  $\sim 610$  and 750 lines.

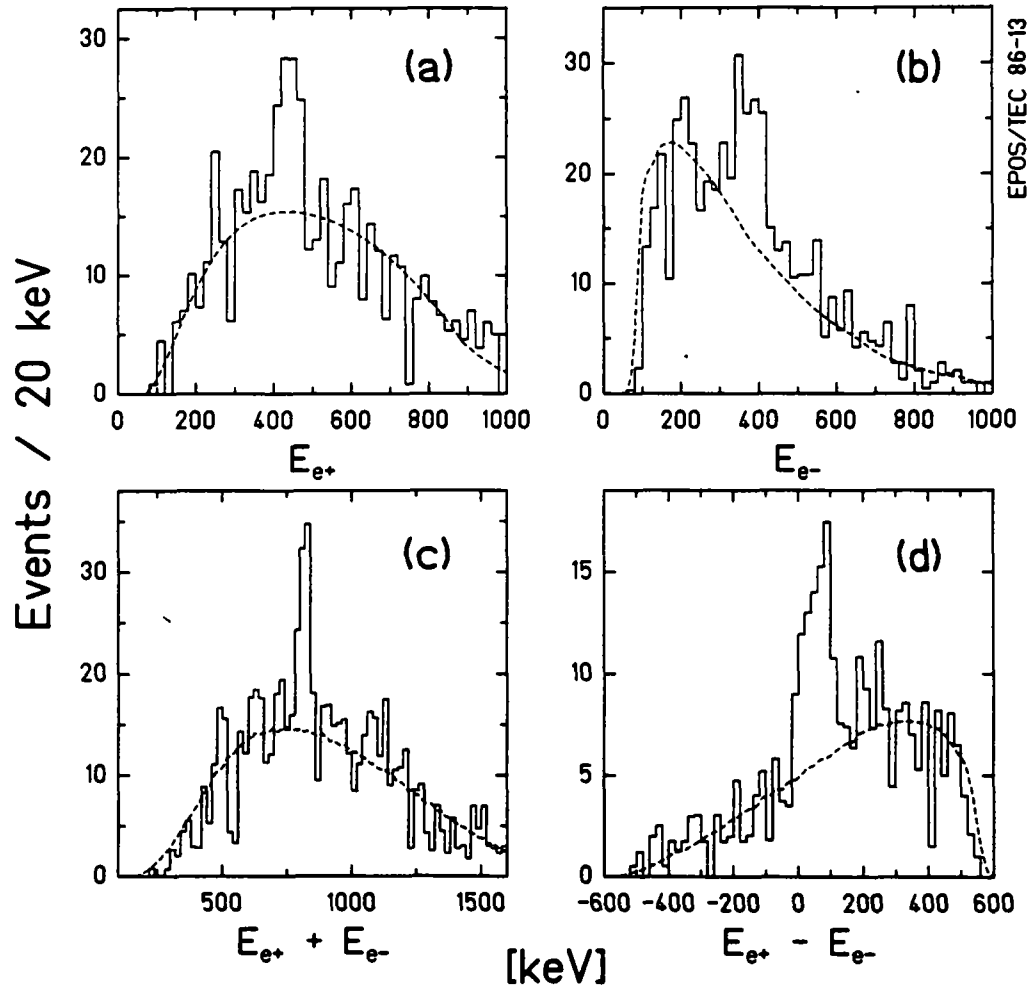


**Figure 6-10.** Projections onto the  $E_{e+}$ ,  $E_{e-}$ ,  $E_{\Sigma}$  and  $E_{\Delta}$  axes, as described in Fig. 6-2, for 5.87 MeV/u U+Th data which exhibits a sum-energy peak at  $\sim 815$  keV.

## Section 6.5 Correlations with Kinematic Parameters

The positions of the various sum-energy peaks overlap the positron peak energies observed in the previous experiments presented in Part I of this work. The 610 and 750 keV lines correspond to positron peaks at 310 keV (observed in Th+Th, U+Th, U+U, and U+Cm collisions) and 375 keV (observed in Th+Ta and U+Th collisions), respectively. The positron peak associated with the  $E_{\Sigma} = 815$  keV line appears to have a higher energy than the companion electron peak,  $E_{e+} \cong E_{e-} + 40$  keV, as suggested by the asymmetric  $E_{\Delta}$  peak in Figs. 6-9,10. Although this structure was not isolated in previous experiments, it did seem to appear in excess of the total dy-

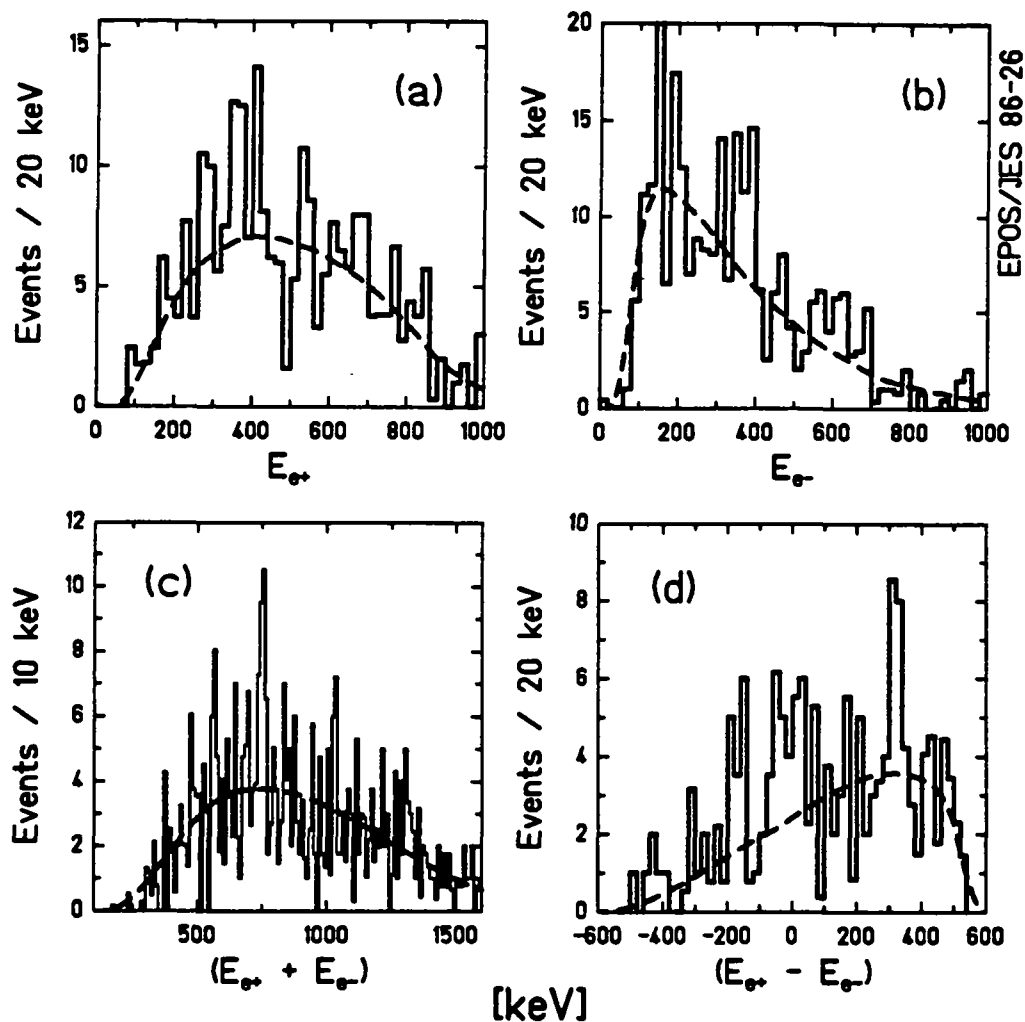


**Figure 6-11.** Same as Fig. 6-10 for 5.85 MeV/u U+Th data (1986) chosen for prompt electron and positron flight-times, which exhibits a sum-energy peak at  $\sim 750$  keV, in agreement with that of Fig. 6-2.

namic positron distribution. This is demonstrated in Fig. 6-12a which plots the sum of the peak cuts of Fig. 3-16, the sum of the total positron spectra out of which each of the positron "singles" peak cuts were projected (6-12b), and a positron distribution from the recent 5.87 MeV/u U+Th coincidence measurement (6-12c) projected for the HI scattering angle region of  $48^\circ < \theta_{HI} < 55^\circ$  [Sak88]. Spectrum (b) exhibits an excess of intensity at both  $\cong 336$  keV, which corresponds to the mean energy of the peaks presented in Fig. 3-16, and at  $E_{e^+} \cong 450$  keV, which agrees with the higher energy positron line associated with the  $\cong 815$  keV  $E_\Sigma$  peak.

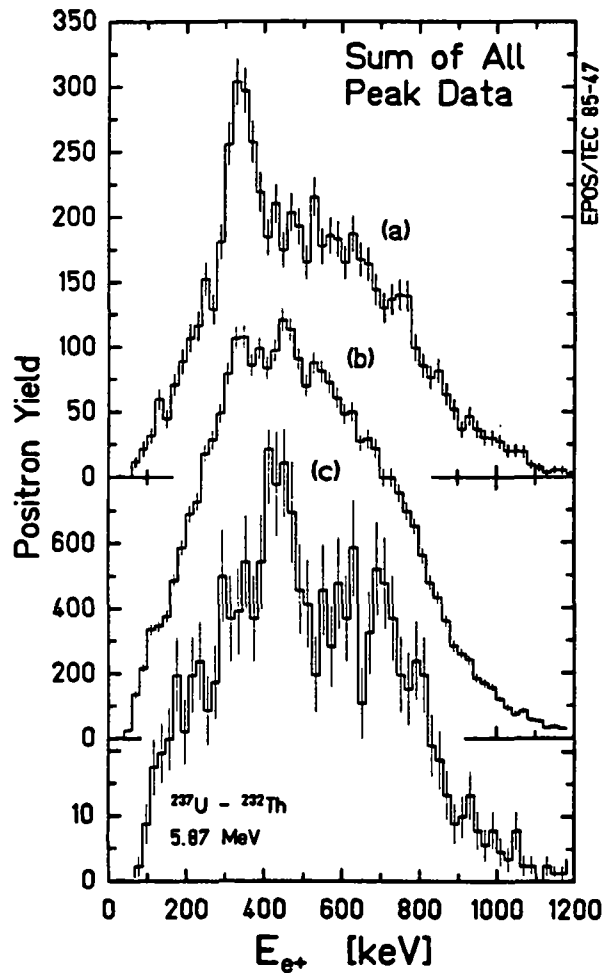


**Figure 6-12.** Comparison of  $\sim 430$  keV positron peak (c) projected from 5.87 MeV/u U + Th data containing  $E_{\gamma} \cong 815$  keV line, with the sum of total  $e^{+}$  distributions (b) out of which positron peaks of Fig. 3-16 were projected. Previous data exhibits evidence for  $\sim 440$  keV peak, in addition to  $\sim 336$  keV intensity consistent with sum of peak cuts (a) of Fig. 3-16.

The possibility of enhancing one of the several prominent sum-lines, to the exclusion of the others, also closely mirrors our experience with the "singles" positron peaks. The coincidence peak data of Figs. 6-9,10,11 were selected by projectile-energy and, for the 610 keV line, delayed positron arrival times. Similarly, the spectra of Fig. 3-16 were selected by beam-energy and scattering angle regions for which the positron line appeared most prominently above the background in each data sample. In addition to corroborating the correspondence between the previous and present experiments, this behavior seems to suggest that the peak production mechanism relies in some way on some particular aspect of the heavy-ion collision

environment. The experimental variables at our disposal are beam-energy, flight-time, and heavy-ion scattering angle.

### **Sec. 6.5.1 Projectile Energy**

Projectile energy and/or target condition seemed to play a role in the production of the positron peaks presented in Chap. 3. As mentioned above, as a result of the enhancement of the 320 keV peak for "fresh targets" in Fig. 3-28, each of the coincident structures presented here were accumulated with targets which were frequently changed. Deterioration of the ThF<sub>4</sub> targets was kept to a minimum as demonstrated in Fig. 2-45. The average energy-loss thickness was  $\cong 0.07$  MeV/u. The beam energy was also controlled to presumably within  $\sim 0.02$  MeV/u (determined by TOF measurements).

The 750 keV sum-energy peak emerged for beam energies of  $\sim 5.85$ - $5.86$  MeV/u (i.e.,  $5.83$  MeV/u +  $0.03$  MeV/u recalibration). As mentioned above, the 1/3 of the data accumulated at lower energies showed little evidence for a peak. In addition, the  $5.81$  MeV/u data from the 1986 run also exhibited little of the 750 keV or other sum-energy structures. This energy dependence is demonstrated in Fig. 6-13 for the 610 keV line. Identical time cuts that produce Fig. 6-9c,d are applied to all the data collected in both the February and July 1986 runs [Sal88], which are displayed for two beam energy intervals. In Fig. 6-13b, which includes  $5.81 \leq E_{\text{beam}} \leq 5.85$  MeV/u, there is little evidence for the peak, while Fig. 6-13a exhibits the presence of the line for  $5.86 \leq E_{\text{beam}} \leq 5.90$  MeV/u.

Figure 6-13c presents a similar analysis for the prompt time cut leading to the 815 keV  $E_{\Sigma}$  line, using a beam energy cutoff of  $E_{\text{beam}} \geq 5.87$  MeV/u. The low energy data of Fig. 6-13d,  $5.81 \leq E_{\text{beam}} < 5.87$ , exhibits little structure. If these data reflect a sharp threshold behavior, one interpretation is that the peaks are produced in a resonant scattering process. At beam energies slightly below  $E_{\text{res}}$ , no peak events are produced. For higher incident energies, the lines should emerge as long as  $E_{\text{res}}$  remains inside the target thickness. Including the beam energy resolution, one would expect a  $\sim 0.1$  MeV/u window of peak producing projectile energies (above the threshold,  $E_{\text{res}}$ ).

This interpretation of the data is challenged, however, by the observation that the peak production rate appears not to be constant for several runs at apparently identical beam energies. For example, Fig. 6-14 presents the sum-energy distribu-

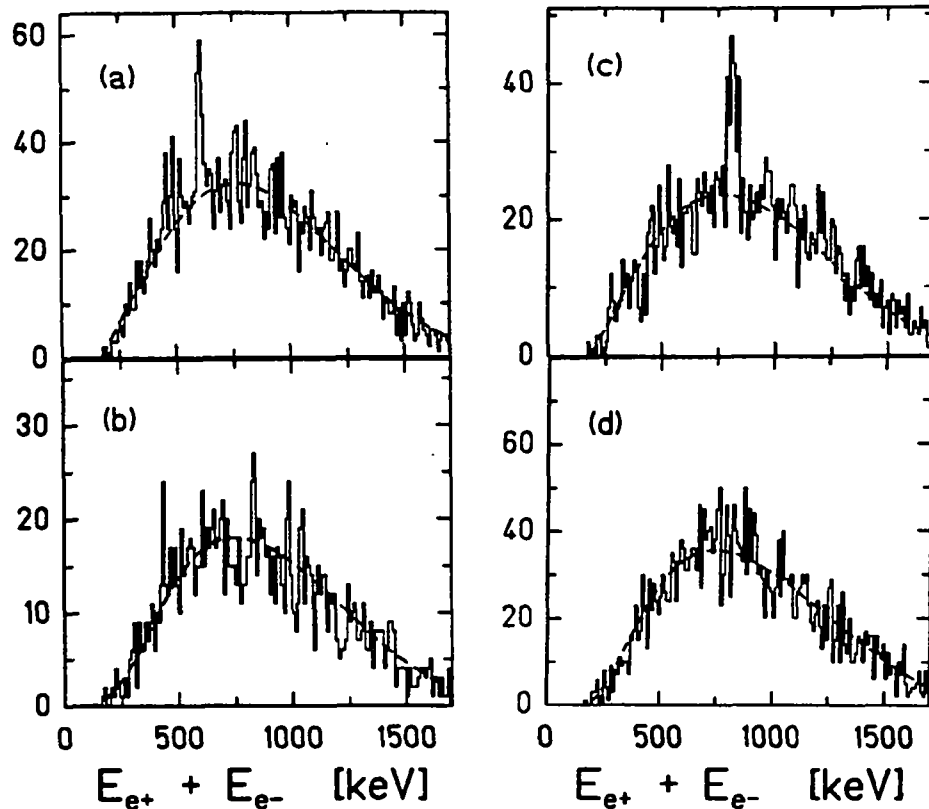


**Figure 6-13.** Sum-energy spectra for  $e^+/e^-$  flight-time conditions selected to emphasize the  $\sim 610$  keV (a,b) and  $\sim 815$  keV (c,d)  $E_\Sigma$  lines, each for two ranges of incident projectile energy. (a)  $5.85 < E_{\text{beam}} \leq 5.90$  MeV/u, versus (b)  $5.81 \leq E_{\text{beam}} < 5.85$  MeV/u. (c)  $5.87 \leq E_{\text{beam}} \leq 5.90$  MeV/u, versus (d)  $5.81 \leq E_{\text{beam}} < 5.86$  MeV/u. (Adapted from [Sal88].)

tion for data accumulated at 5.87 MeV/u in two runs. The data of 6-14a are included in the analysis of Fig. 6-9a and exhibit a large 815 keV  $E_\Sigma$  line. No HI angle cuts have been applied to the data. Figure 6-14b shows the  $E_\Sigma$  spectrum accumulated under apparently identical conditions two days after Fig. 6-14a. Between these two sets of data, the steering of the beam through the UNILAC was changed, but the average beam energy at the output of the accelerator was the same to within 0.003 MeV/u, as measured by the TOF probes.

Although each of the  $E_\Sigma$  lines has been reproduced in at least two or three pieces of data with a high statistical accuracy ( $\geq 4\sigma$ ), the details of the production mechanism remain unclear. In light of the possible target and UNILAC instabilities mentioned in Secs. 2.6 and 2.7, and the comparison of Fig. 6-14, it is possible that

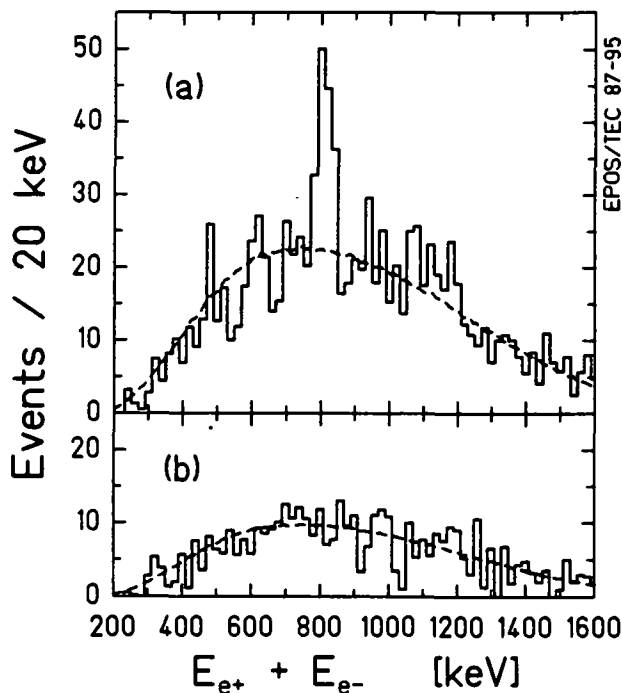


**Figure 6-14.** Sum-energy distributions for U+Th collisions at 5.87 MeV/u selected as in Fig. 6-9a. Data from first 3 days (a), and last 2 days (b) of a 5 day run. Between (a) and (b) the UNILAC beam was resteered.

the past and present attempts to measure a beam-energy dependence of the positron and correlated electron peak production reflect the influence of a sofar uncontrolled variable. A definitive result requires additional experimental measurements.

### Sec. 6.5.2 Flight Time

The next most important parameter in isolating the separate  $E_{\Sigma}$  peaks (after what was previously assumed to be projectile energy or target quality) appears to be the flight times of the positrons and electrons to their respective detectors. This rather new approach was originally motivated by the observation in July 1985 that the 320 keV positron peak in Th+Th collisions at 5.70 MeV/u is associated with longer flight times to the Si(Li) detector. As shown in Fig. 6-15a, the peak positrons are delayed with respect to the mean arrival time for the total continuous positron distribution,  $-5 < \Delta t_{e+} < -1$  ns, where  $\Delta t_{e+} = \langle \text{TOF}_{e+} \rangle - t_{e+}$ , corrected for  $\theta_{\text{HI}}$  and  $E_{e+}$  as described in Sec. 3.2. The corresponding spectrum for positrons gated on the "prompt" side of the time-of-flight distribution with  $+1 < \Delta t_{e+} < +5$  ns, exhibits no

## Th+Th 5.72 MeV/u, July 1985

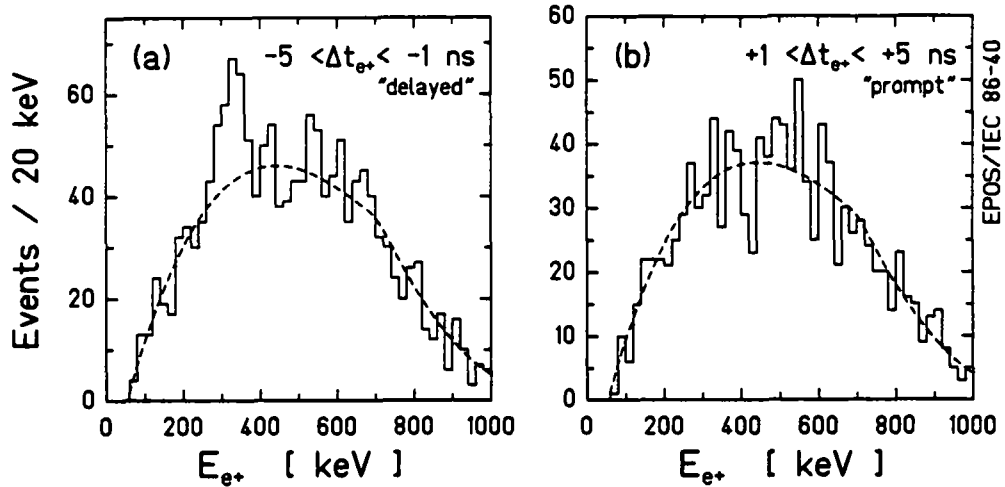


**Figure 6-15.** Energy spectrum of positrons collected in Th+Th collisions at 5.70-5.75 MeV/u ( $20^\circ < \theta_{HI} < 70^\circ$ ) which arrive at the Si(Li) detector either (a) slightly delayed, or (b) prompt, with respect to the mean positron TOF.

peak (Fig. 6-15b). This comparison is from total data with *no* HI scattering-angle cuts.

Exactly this behavior is observed for the 610 keV  $E_\Sigma$  line, again corroborating the correspondence between the coincidence data and the single positron peaks. The data of Fig. 6-9c,d were selected with an identical delayed cut on the HI-positron flight-time distribution. The peak is substantially smaller when the prompt positron events are selected. One possible interpretation of this delay is that the emitting source lives for  $\tau_x \sim 3$  ns and an appreciable delayed component is therefore observed in the data. Three observations argue against this interpretation. First, sources having an emitter velocity  $v_{em} \sim v_{CM}$  (i.e., 1.5 cm/ns) would frequently decay far off axis and would therefore tend to leave the  $\sim 1$ -2 cm fiducial volume of the EPOS spectrometer. Second, for prompt decays at time  $t \approx 0$ , the usual positron TOF distribution would be produced due to the range of  $e^+$  emission angles, so some prompt peak events should be observed. Third, a smaller delay ( $\sim 1$  ns) is observed for the electrons measured in coincidence with positrons in the 610 keV  $E_\Sigma$  peak [Sal88], even though a somewhat larger electron delay is expected from MCSPEC simulations. A different possibility is that the delayed flight-time reflects an emission angle distribution for the positrons. As described in Sec. 5.3 (see Fig. 5-14), longer

flight-times are associated with steep emission angles with respect to the solenoid axis. Figure 6-15 may therefore indicate that the peak events are emitted preferentially in the plane of the HI scattering. MCSPEC simulations indicate, however, that one should observe the back-to-back correlated electron with similar or longer time-delay. Perhaps a short source lifetime coupled with emission toward the electron detectors could accommodate both observations.

Following these investigations, the presence of such a delay was searched for in the positron peak data discussed in Chap. 3. A similar effect was not discovered. As discussed in Sec. 2.2.7, however, the positron collection geometry was unfavorable for the detection of a delay caused by steep emission angles, because positrons emitted at flatter angles toward the magnetic mirror were reflected and had longer flight paths and flight-times to the Si(Li) detector. An emission angular distribution would therefore have been largely obscured by the mixing of both steep and flat angles,  $\theta_{e+}$ .

The  $E_{\Sigma} \cong 750$  keV U+Th peak is associated with less delayed positron flight times. As shown in Fig. 6-16, however, it is enhanced slightly by selecting the central region of the positron TOF distribution. The total positron energy distribution (a,e) and the gated coincident positron (b,f) and electron (c,g) cuts are shown for the 1985 U+Th data. For  $-5 < \Delta t_{e+} < +2$  ns (e-h), the continuous backgrounds appear to be reduced in each spectrum. A peak begins to emerge in the total spectrum (no HI cut) and the coincident  $\sim 380$  keV positron and electron peaks are enhanced over the backgrounds. This time cut includes 40% of the data, and its centroid is delayed relative to the mean positron TOF by  $\cong 1$  ns.

The  $E_{\Sigma} \sim 815$  keV line appears to be associated with nearly prompt positron and electron events. One interesting feature, however, is a correlation between the mean energy of the  $E_{\Delta}$  peak and the arrival time of the associated positrons. This is illustrated in Fig. 6-17 for the 5.87 MeV/u U+Th data of Fig. 6-14a. Part (a) plots the  $E_{\Delta}$  spectrum from Fig. 6-10 for  $-2 < \Delta t_{e-} < +1.5$  ns, which is symmetric about the prompt portion of the electron TOF distribution. The width of the cut,  $\Delta t_{e-} \cong 3.5$  ns, is consistent with the 4 ns HI-electron TOF resolution. The associated coincident positrons have systematically larger energy than the electrons, i.e.,  $E_{\Delta} > 0$  implies  $E_{e+} > E_{e-}$ . The  $E_{\Delta}$  spectrum for an equal size cut on the prompt side of the TOF<sub>e-</sub> distribution  $1.5 < \Delta t_{e-} < 5.0$  ns, is shown in Fig. 6-17b. This selection seems to pick out the complementary half of the  $E_{\Delta}$  distribution,  $E_{e+} < E_{e-}$ .

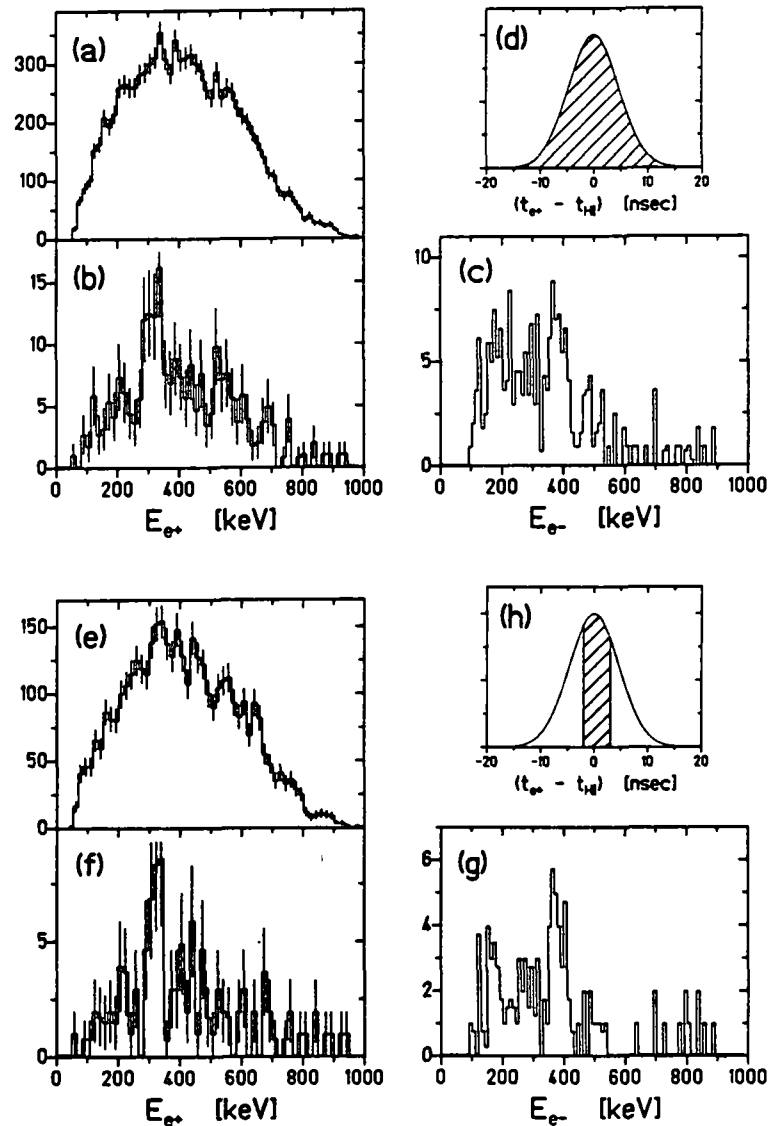


**Figure 6-16.** (a) Total positron, (b) coincident positron ( $340 \leq E_{e^+} \leq 420$  keV), and (c) coincident electron ( $340 \leq E_{e^+} \leq 420$  keV) energy distributions for 5.83 MeV/u U+Th data selected for entire range of HI-positron flight-times (a). Parts (e-g) present similar spectra selected for central portion of time distribution (h), for which a  $\sim 2\sigma$  enhancement of the peak signal w.r.t. the total continuous background is observed.

This odd behavior can be at least qualitatively understood within the context of the two-body decay of a moving source. Figure 6-17c presents an MCSPEC calculation of  $X^0$  decay assuming that the object is emitted isotropically in the CMS with a velocity of  $\langle v_X \rangle \sim 2v_{CM}$ . The difference-energy spectra for each of the time cuts in (a) and (b) are separated as observed in the data. Physically this arises from the interplay of emission angles, efficiency, and flight-time in such a way that the very

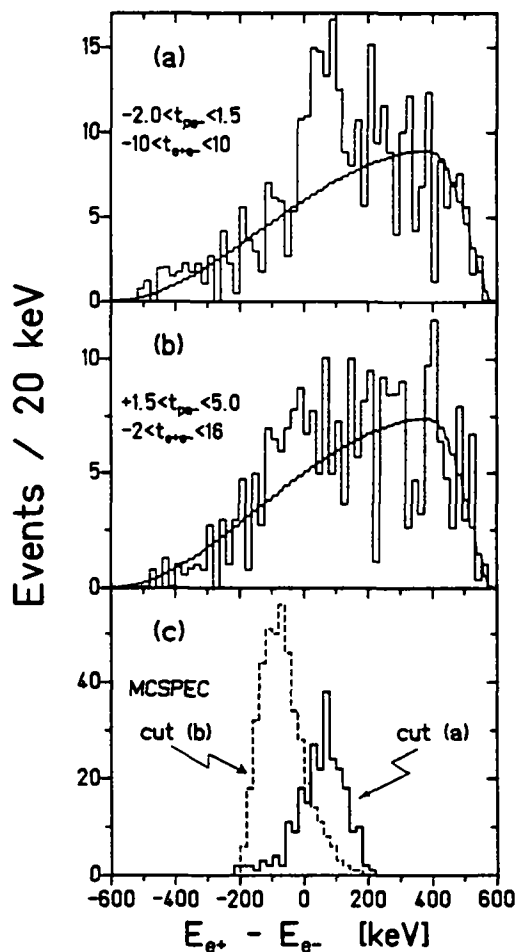


**Figure 6-17.** Difference-energy spectra gated on the  $\sim 815$  keV sum-energy peak in 5.87 MeV/u U+Th collisions, chosen for  $e^-$  flight-times in a 3.5 ns wide window centered about the mean electron flight-time (a), or prompt with respect to the mean flight-time (b). Part (c) presents an MCSPEC simulation of a 1.85 MeV neutral  $X^0$  emitted isotropically with a velocity  $\beta_X = 0.12c$  from the CMS, with identical time cuts applied as in (a) and (b).

prompt  $\text{TOF}_{e^-}$  values select  $X^0$ 's emitted preferentially toward the electron Si(Li) detectors. The detected electrons are therefore emitted forward with respect to the  $X^0$  motion and have positive Doppler-shifted kinetic energies. The gate of Fig. 6-17a selects those objects moving toward the positron detector, so  $E_{e^+}^{\text{obs}} > E_{e^-}^{\text{obs}}$ . Although very suggestive of a neutral-object origin, perhaps some other mechanism may eventually be found which explains these  $\text{TOF}_{e^-}$ - $E_{\Delta}$  correlations.

### Sec. 6.5.3 Heavy Ion Scattering Angle

The correlation of coincident positron-electron peak production with the heavy-ion scattering angle appears to be of secondary importance in isolating the structures. As described in Chap. 3, in the previous EPOS experiments ion-angle cuts were employed to "cut away" the continuous background of dynamic and nuclear positrons. In the present measurements, the added sensitivity and selectivity of the positron-electron coincidence condition, and the correlated cancellation of Doppler shifts in the  $E_{\Sigma}$  spectrum, already reveals the presence of  $E_{\Sigma}$  peaks in the total data sample. These are then most easily isolated by beam energy with TOF cuts, as discussed above. The remaining improvement gained in signal-to-noise by HI angle selection is rather small as was demonstrated in Fig. 6-6.

Figures 6-18 and 6-19 illustrate the improvement to the 610 keV and 815 keV  $E_{\Sigma}$  and  $E_{\Delta}$  peaks presented in Fig. 6-9 by selecting regions of  $\theta_{HI}$ . The 610 keV sum peak intensity is enhanced relative to the background by excluding data for  $41^{\circ} < \theta_U < 49^{\circ}$ , i.e., accepting  $25^{\circ} < \theta_U < 41^{\circ}$  plus  $49^{\circ} < \theta_U < 65^{\circ}$ , as shown in Fig. 6-18. The peak intensity is therefore roughly symmetric about  $\Delta\theta_{HI} = 0$  as expected. Figure 6-19 compares the data of 6-9a,b with no HI cut to that for  $37^{\circ} < \theta_U < 65^{\circ}$ . In both cases, the size of the peak is decreased slightly by the angular cut but the continuous backgrounds are reduced by a greater amount. Also, in both cases the windows are very broad in the  $\Delta\theta_{HI}$  coordinate, just as those leading to the positron spectra of Fig. 3-16. Unlike the positron peak data, however,  $\Sigma\theta_{HI}$  cuts do not significantly improve these data because of the attendant drop in statistical accuracy. Moreover, like the Th + Th, Th + Ta, and Th + U data of Fig. 3-16, the U + Th coincidence experiments used thin targets, and the peak-related scattering events do not appear to be rotated with respect to the angular correlation pattern of Rutherford scattering.

The correlation of the production of coincident positron-electron lines seems therefore to be weaker for the HI scattering angle than for the positron and electron TOF and the condition of the UNILAC beam and/or targets. The correlation in each of these parameters, insofar as has been determined, mirrors our experience with the positron peak data presented in Part I of this dissertation.

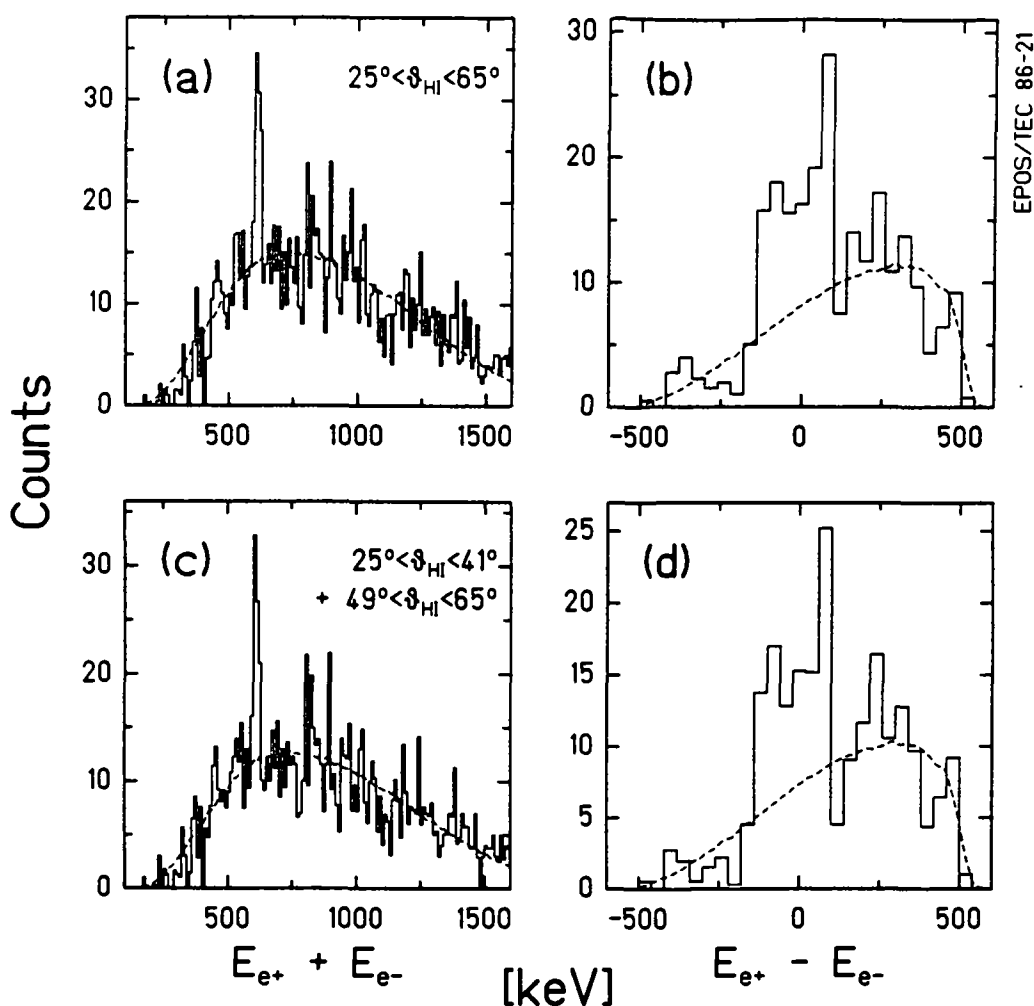


**Figure 6-18.** Sum-energy and difference energy spectra for the  $\sim 610$  keV  $E_\Sigma$  line observed in 5.85-5.90 MeV/u U + Th collisions, associated with heavy-ions scattered into the entire PPAC range (a,b), or into a region  $25^\circ < \theta_{HI} < 41^\circ$  plus  $49^\circ < \theta_{HI} < 65^\circ$  (c,d).

## Section 6.6 Other Structures

Before continuing in the next chapter with an analysis of the possible origins of these coincidence lines, it should be noted that there are suggestions of other structures in the data. For example, recent experiments by the Orange collaboration revealed positron singles peaks near 230 keV in low-Z U+Au, U+Ta, Pb+Pb collisions [Kön87]. Figure 6-20 presents evidence from the 1986 EPOS experiment for the existence of a corresponding sum-energy line at  $E_\Sigma = 460$  keV (6-20c), which appears at a  $3\sigma$  level of confidence in the total U + Th sum-energy distribution. It is correlated

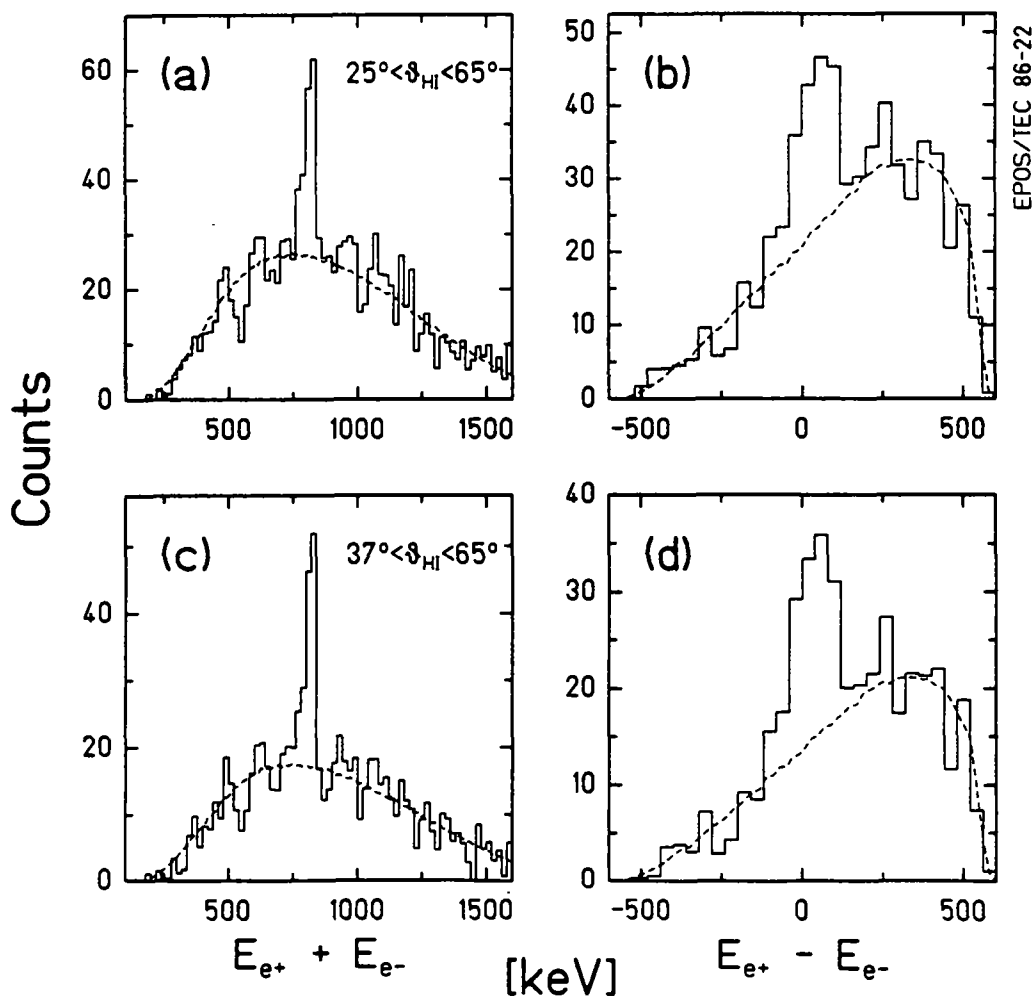


**Figure 6-19.** Same as Fig. 6-18 for the  $\sim 815$  keV  $E_{\Sigma}$  line observed in 5.87-5.90 MeV/u U+Th collisions, associated with heavy-ions scattered into the entire PPAC range (a,b), or into a region  $37^{\circ} < \theta_{HI} < 65^{\circ}$  (c,d).

with a broad enhancement in the  $E_{\Delta}$  spectrum, centered around  $E_{\Delta} = 0$  (Fig. 6-20d). On the basis of these data alone, it is difficult to unambiguously identify the structure because it is associated with electron energies (Fig. 6-20b) just at the threshold of the electron detection efficiency. Moreover, the associated coincident positron peak appears only as a shoulder on the low-energy side of the  $E_{e+}$  projection (Fig. 6-20a). It is nonetheless satisfying that this structure, observed in the positron singles experiments, also seems to be present in the coincidence data.

In a very recent experiment, we extended the coincidence measurements down to the U+Ta system ( $Z_U = 165$ ) in order to reproduce the low-Z Th+Ta peak pre-

sented in Fig. 3-15 and to check whether it is associated with a correlated monoenergetic electron. A  $^{238}\text{U}$  beam was chosen over  $^{232}\text{Th}$  for convenience. The data have not yet been completely analyzed. However, an preliminary "online" investigation [Sak88] revealed that at beam energies between 5.87 and 5.98 MeV/u, a narrow sum-energy peak emerges clearly over the continuum background, as shown in Fig. 6-21. The line has a mean energy of  $\langle E_{\Sigma} \rangle \cong 750 \pm 10$  keV and contains  $50 \pm 13$  counts. Analysis in progress [Sal88] suggests a larger intensity and a sum-energy peak width of  $\Delta E_{\Sigma} \cong 25$  keV, consistent with detector energy resolution. This result suggests that the identical positron and correlated electron lines emerge for several systems over a range of  $163 \leq Z_U \leq 188$ . Moreover, the size of each of the  $E_{\Sigma}$  peaks above the continuous background is comparable to those in Figs. 6-1

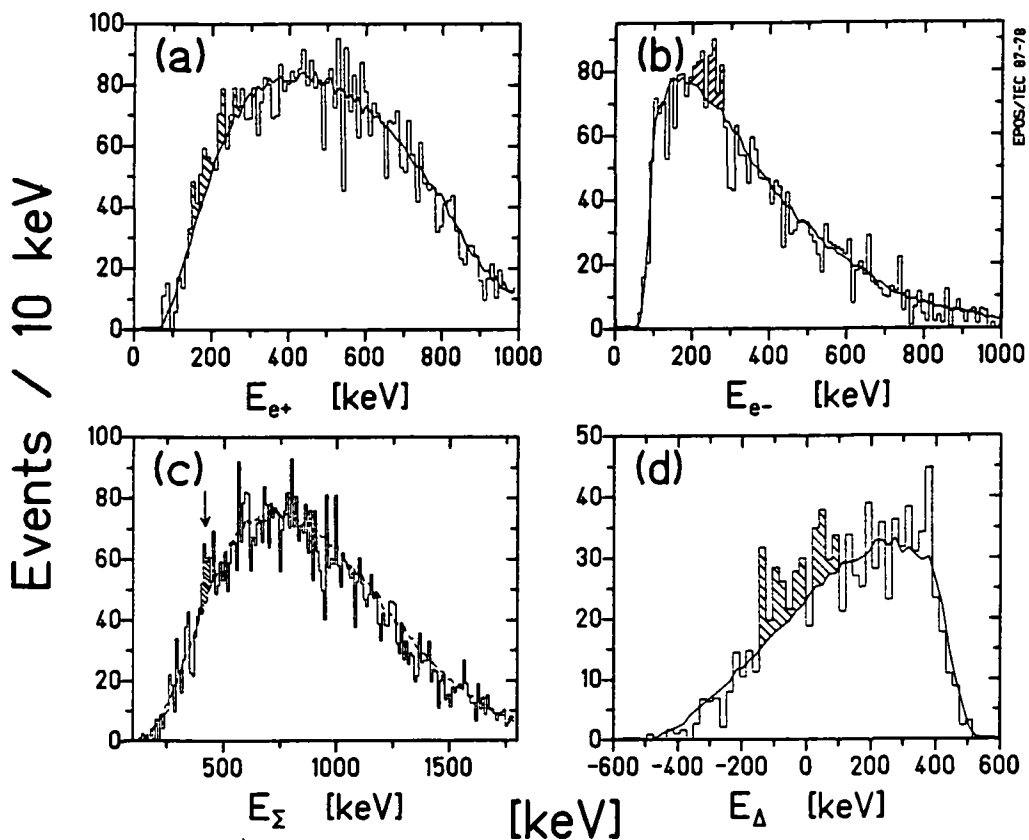


**Figure 6-20.** Projections of coincident positron-electron distribution for U+Th collisions at 5.81-5.90 MeV/u on (a)  $E_{e+}$  (for  $190 < E_{e-} < 280$  keV), (b)  $E_{e-}$  (for  $170 < E_{e+} < 260$  keV), (c)  $E_{\Sigma}$ , and (d)  $E_{\Delta}$  (for  $420 < E_{\Sigma} < 490$  keV) energy axes, which exhibit evidence for a  $\sim 3\sigma$  coincidence structure at  $E_{\Sigma} \cong 460$  keV (shaded regions).

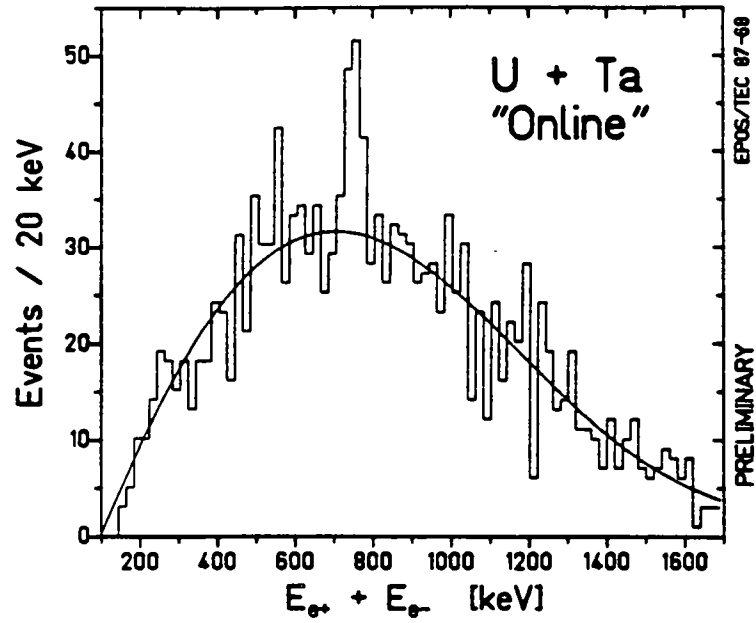


**Figure 6-21.** Preliminary sum-energy distribution for coincident positron-electron events observed in U + Ta collisions at 5.87-5.98 MeV/u. The peak at  $E_{\Sigma} \cong 750$  keV appears at a  $\sim 5\sigma$  level.

and 6-7, indicating, as discussed in Sec. 3.4.5, that when the coincidence structures appear, their production cross-sections are essentially independent of  $Z_U$ .

## Chapter 7 Discussion of Possible Origins

As noted above, the coincident positron-electron data associated with the sum-energy lines at  $E_{\Sigma} \cong 610, 750, \text{ and } 815 \text{ keV}$  bear a striking resemblance to the peak shapes expected for the two-body decay of neutral objects which are created with low velocity in the HI collision. Because of the obviously far-reaching consequences of such an interpretation, other possible origins for these structures must first be investigated. Several of those discussed in Chap. 4 as candidates for explaining the the positron peaks (e.g., spontaneous positron emission or monoenergetic positron creation) are immediately excluded because they do not involve the emission of monoenergetic electrons. Modified versions of these, and many additional sources of coincident positron-electron emission, including background radiations, a series of nuclear conversions, pair creation processes, and multi-body final states are discussed in the sections that follow. The final portion of this chapter discusses various aspects of a two-body final state and presents determinations of the positron-electron angular correlation and of the velocity distribution of the proposed neutral source created in the collisions.

### Section 7.1 Instrumental Backgrounds

Many of the arguments presented in Sec. 4.1 against an instrumental origin for the positron peaks apply as well to the coincident electron peaks discussed in Chap. 6. For example, the small geometric cross-section of the electron detectors precludes the possibility that the electron peaks are due to neutral radiation originating from the target or from the region around the positron detector. The planar Si(Li) crystals themselves subtend only  $1.3 \times 10^{-4} \text{ sr}$ . It is very unlikely that  $\gamma$ -rays scattered into the detectors produce this peak signal. Replacing the pair production cross-section in Eqn. 4.1 with the the  $\gamma$ -ray narrow-beam attenuation cross-section [Sto70], the probability that a  $\sim 500 \text{ keV}$   $\gamma$ -ray emitted from the target interacts in the Si(Li) detector and produces an observable energy signal is  $\sim 3 \times 10^{-6}$  (including solid angle and interaction cross-section). The detector casings, mounts, and cooling apparatus, together subtend a much larger solid-angle,  $\sim 1.5 \times 10^{-3}$  of  $4\pi \text{ sr}$ . A  $\sim 500 \text{ keV}$   $\gamma$ -ray has about a  $\sim 7 \times 10^{-6}$  chance producing an energy signal in the Si(Li) after scattering from the material surrounding the detectors. The exponential  $\gamma$ -ray energy spectrum leads to a broad continuum of energies in the electron detector, of which only  $\leq 10\%$  of the intensity is between 300 and 400 keV. Assuming an average multiplicity of  $\sim 10$   $\gamma$ -rays emitted per collision, the probability that  $\gamma$ -ray

scattering is mis-identified as an electron signal in those collisions which produce positron peak events is  $\sim 10^{-5}$ , and is therefore completely negligible.

Structure in the electron spectrum could, in principle, be produced by Compton scattering in the Si(Li) detectors of 511 keV photons from annihilation of positrons created by high energy  $\gamma$ -rays ( $E_\gamma > 2m_e c^2$ ) near the electron detectors. Using  $\sigma_{\text{pair}}$  from [Sto70] and 0.3  $\gamma$ -rays/collision with  $E_\gamma > 2m_e c^2$  (from Fig. 2-2), at most  $\sim 2 \times 10^{-6}$  pairs are created per collision. Including the approximate electron detector solid angle and Compton-scattering cross-section,  $< 4 \times 10^{-8}$  511 keV photons interact in the detector and  $\leq 25\%$  of these deposit  $\cong 300$  keV. It is *more* probable that a second positron is created in the collision ( $P_{e^+} \sim 10^{-4}$ ), which spirals through the mirror field and annihilates in the electron detector housings (prob.  $\sim 0.2$ ), after which the 511 keV photon Compton scatters in the Si(Li) (prob.  $\leq 0.05$ ), i.e.,  $P_{e^+/\text{Compton}} \sim 10^{-6}$ . Not only are these processes therefore infinitesimal, but measurements with sealed  $\gamma$ -ray sources placed at the target site revealed no "e<sup>-</sup>" events above the continuous energy distribution of low counting-rate room background.

The arrival time of the event in the electron detector further precludes similar scattering processes. A prompt  $\gamma$ -ray from the target has a  $\cong 4$  ns flight-time compared to the  $\sim 5$ -15 ns TOF's of electrons (Fig. 5-14). A  $\gamma$ -ray induced signal would therefore be readily identifiable. As noted in Sec. 4.1 for positron detection, neutron induced signals in the electron counter are also precluded based on an expected flight time of  $\sim 50$  ns. An electron detector signal would be more closely correlated to the positron event if one of its 511 keV annihilation photons were to travel two meters across the solenoid from the positron counter to scatter in the electron Si(Li)'s. Of course a direct process is ruled out both by the small geometric detector cross-section and the added  $\sim 7$  ns photon transit time which, together with the original positron target-detector TOF, would produce  $\text{TOF}_{e^-} \cong 12$ -22 ns, which would also be easily distinguishable. This time-of-flight argument similarly precludes processes in which the annihilation photon scatters in the spectrometer material, e.g., the spiral baffle, and emits a Compton electron with energy  $E_{e^-} \sim 340$  keV which could then be transported to the planar Si(Li) electron detectors.

All processes involving annihilation photons from the detected positron are ruled out by an inspection of the ARD sum spectrum gated on the measured sum-energy peaks, as shown in Fig. 7-1. Both the one and two 511 keV

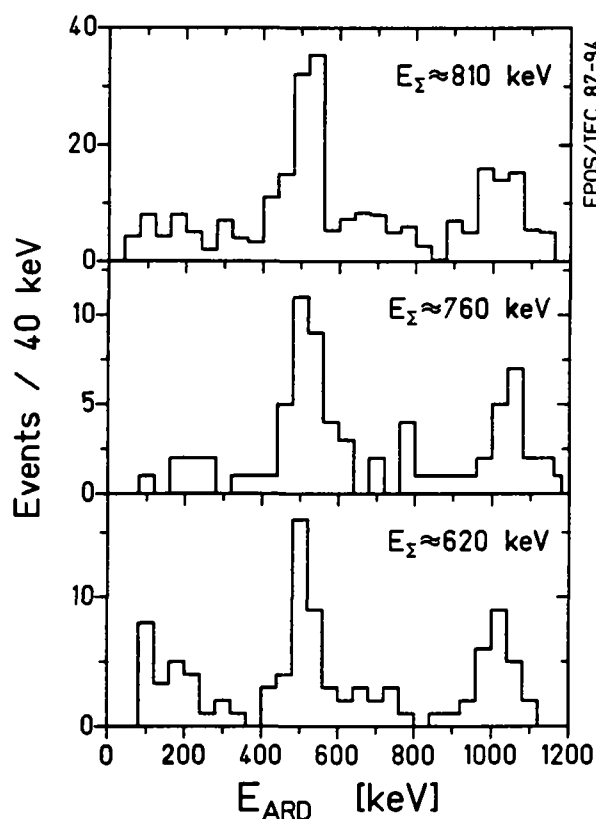


**Figure 7-1.** ARD sum-energy distributions gated on coincidence positron-electron events within the  $E_{\Sigma}$  peak energy intervals for the data of Figs. 6-2c and 6-9a,c.

$\gamma$ -ray photopeaks are readily apparent for each of the  $E_{\Sigma} \cong 610, 760,$  and  $815$  keV lines detected in U+Th collisions. This also unambiguously establishes the identity of the positron signal. The electron TOF identifies the event in the planar Si(Li) detectors as a lepton originating from or near the target in prompt ( $\sim ns$ ) coincidence with the HI collision.

It is very unlikely that the electron signal is a mis-identified monoenergetic positron incident in the counter, because the efficiency of detecting positrons in the planar-pair of Si(Li) crystals is a factor of  $\cong 4$  less than the electron detection efficiency (see Fig. 5-7). To achieve the relative back-to-back  $N_{e^+e^-}/N_{e^+}$  coincidence intensity, which is consistent with the observed coincidence peak yields, a high multiplicity of monoenergetic positrons of similar energy ( $E_{e^+} \cong 300-400$  keV) would have to be involved. Assuming that the monoenergetic positrons are emitted isotropically from the CMS, their relative detection efficiency in the electron detectors,  $\epsilon_{e^+}(e^- \text{ detector})/\epsilon_{e^+}(e^+ \text{ detector})$ , is approximately 0.25 times the uncorrelated

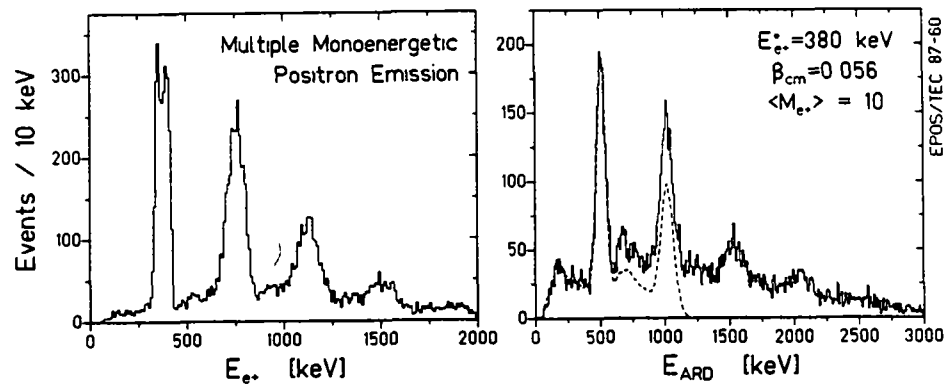


**Figure 7-2.** Positron energy distribution (left) and ARD sum spectrum (right) for MCSPEC simulation of the emission from the CMS of an average multiplicity of 10 monoenergetic 380 keV positrons per collision. Dashed curve presents the expected ARD energy distribution for the detection of single positrons.

electron detection efficiency of  $\cong 6\%$  from Sec. 5.4.3, or  $\sim 1.5\%$ . To match the  $\cong 14\%$  relative back-to-back detection efficiency from Sec. 5.4.2.3, an average multiplicity of about ten monoenergetic positrons ( $E_{e^+} \cong 380$  keV) emitted from the collision must be assumed. (A spontaneous positron "machine-gun" process along these lines was mentioned by [Sof86], in which conversions in the di-nuclear complex repeatedly empty the K-shell which is then filled by spontaneous vacuum decay.) Due to double and triple counting of the positrons in the  $e^+$  detector, peaks at 760 keV (two positrons) and 1140 keV (three positrons) would be observed in the positron energy spectrum, as shown by the MCSPEC simulation of Fig. 7-2a. In addition, for these multiple- $e^+$  emission structures, 25% to 40% of the annihilation radiation detector energy spectrum would exceed 1022 keV due to detection of more than two 511 keV photons (Fig. 7-2b). Neither of these effects are observed (compare Fig. 7-1), and scenarios based on emission of several monoenergetic positrons are therefore ruled out by the data.

Monte-Carlo simulations also rule out the trivial possibility that a peak-like structure in the electron spectrum at 300 keV could be produced by the summing of two  $\delta$ -electrons (whose detected energy distribution exhibits a maximum at  $\sim 150$  keV) [Cow86, Cow86b]. We therefore conclude that the observed signals in fact represent coincidences between monoenergetic positrons and electrons which are emitted from the target region within a few nanoseconds of a heavy-ion collision.

A recent measurement by Erb et al. ([Erb86], see also [Sak87]) suggested that the coincident electron lines may be recoiling atomic electrons from Bhabha scattering of positrons in the  $\text{ThF}_4$  target material. An extensive Monte-Carlo calculation by S. Henderson [Hen86], however, shows that the total number of coincident Bhabha-scattered positron-electron pairs (integrated over the dynamic positron energy distribution and  $\text{ThF}_4$  target thickness employed) which would be detected in the EPOS spectrometer per measured positron is  $2 \times 10^{-5}$ . The energy distribution of Bhabha electrons is very similar to the  $\delta$ -electron distribution, and only  $\sim 1.5\%$  of scattered pairs have final energies falling within any one of the measured sum-energy peaks. The calculation was directly verified by measurements in the EPOS spectrometer with a  $^{68}\text{Ge}/^{68}\text{Ga}$  source sandwiched between various target and carbon backing foils [Shw86]. For the  $2 \times 10^5$  positrons (and  $\sim 4 \times 10^4$  coincidences) detected in the 1986 U + Th experiments described in Chap. 6, this implies a total of about 4 Bhabha scattered electron-positron pairs. The Bhabha scattering background under each sum-energy peak is only 0.06 events. Recent measurements by [Pec87, Kli87, Wan87] improved upon the Erb et al. experiment and concluded that the "peak" structure observed by [Erb86] was due to secondary scattering of 511 keV annihilation photons (or possibly Compton electrons) between the positron and electron detectors. The unambiguous positron identification of the EPOS spectrometer, and the large separation (hence negligible "cross-talk") between the positron and electron detectors provides an exceptionally clean, nearly background free, environment for the positron-electron coincidence measurements presented here.

## Section 7.2 Uncorrelated, Independent Peaks

A next step in understanding these coincidence data is to determine whether the process which produces the monoenergetic positron is correlated with the process which emits the monoenergetic electron. It is possible, for example, that in addition to the narrow positron peaks, unrelated internal conversion electron lines from a particularly strong nuclear transition are detected in these collisions, leading to the coincidence signal.<sup>5</sup>

---

<sup>5</sup>

As noted in Chap. 4, however, no satisfactory explanation has been found for the narrow positron peaks. Hypothesizing an unrelated electron source does not address this fundamental issue.

## Emission of Independent $e^+$ and $e^-$ Structures

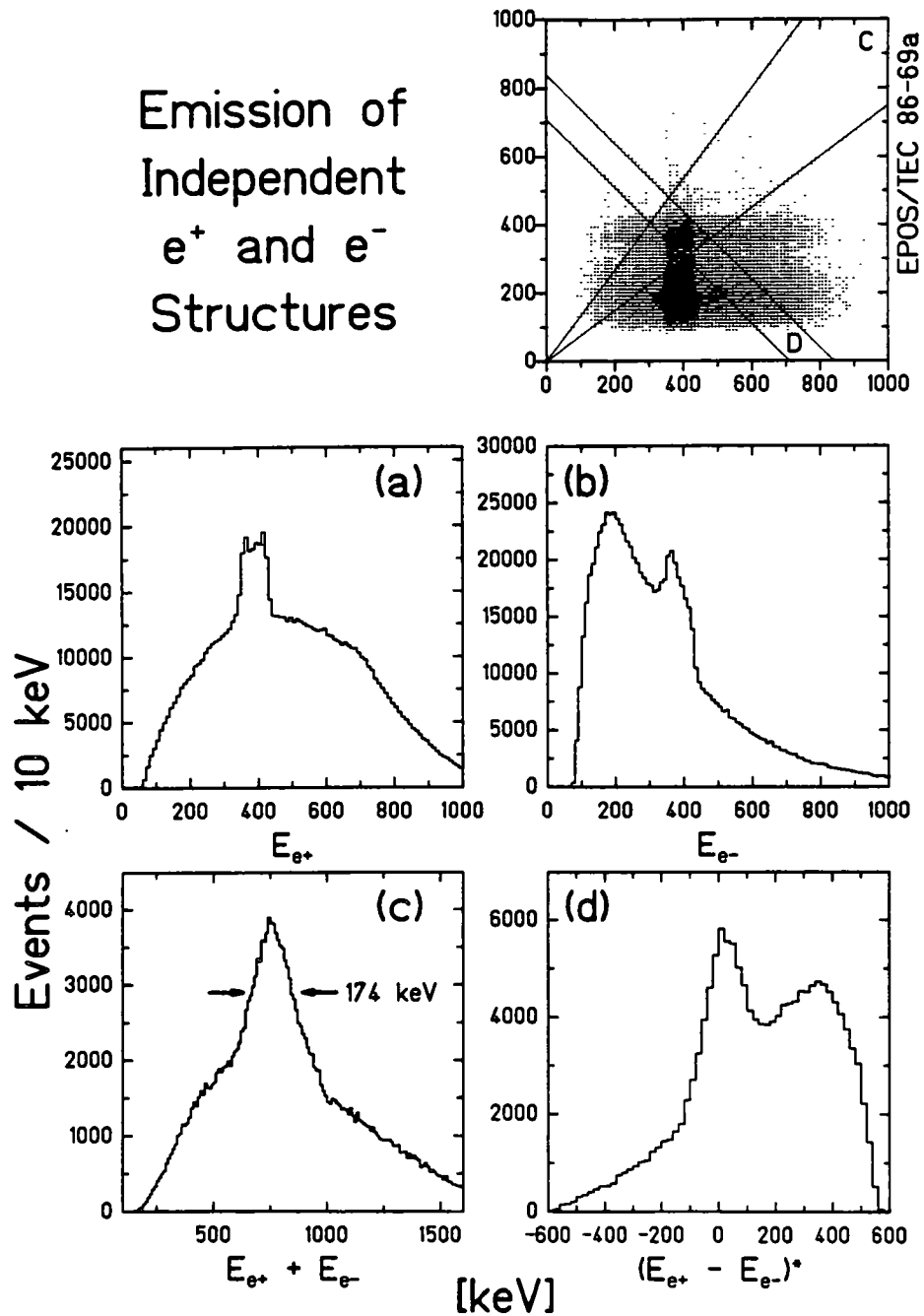


**Figure 7-3.** Simulation of independent emission of monoenergetic  $e^+$ 's and  $e^-$ 's (a,b). Energy correlation pattern (top) exhibits horizontal and vertical bands superimposed on continuous backgrounds. Projections onto  $E_{\Sigma}$  (c) and  $E_{\Delta}$  (d) axes as marked.

Figure 7-3 presents an MCSPEC simulation appropriate for this class of origins involving independent production of positron and electron peaks. Positron and electron lines at  $E_{e^+} \cong E_{e^-} \cong 380$  keV, emitted from the CMS, are assumed to account for

5.5% and 6.9% of the total positron and electron intensities, as shown in Fig. 7-3a,b respectively.  $5 \times 10^6$  detected positron events leading to  $8.76 \times 10^5$  coincidences were simulated. The vertical band in the 2-dimensional  $E_{e^+}$  vs.  $E_{e^-}$  distribution illustrates the presence of positron peak intensity for all electron energies, and the horizontal stripe indicates the electron line intensity independent of positron energy. In projections on either side of the positron peak, the electron line is clearly evident, and vice versa. In fact, the total coincident positron and electron yields (Fig. 7-3a,b) provide the best statistical indication of the presence of independent peaks. As mentioned in Sec. 6.2, the adjacent cuts presented in Figs. 6-4 and 6-5 revealed no statistically significant evidence for the  $\sim 380$  keV  $e^+$  and  $e^-$  peaks associated with the  $E_{\Sigma} = 760$  keV line, as would be required if the coincidence structure were due to independent positron and electron lines. The coincidence structures at  $E_{\Sigma} \cong 610, 760,$  and  $815$  keV measured in U+Th collisions all appear to be absent from these neighboring regions of the event plane.

Because the directions of emission of the peak positrons and electrons are uncorrelated, their Doppler shifts do not cancel and the sum-energy peak, shown in Fig. 7-3c for the wedge-shaped cut (C), is very wide,  $\Delta E_{\Sigma} \cong 174$  keV (FWHM). The difference-energy peak has a similar shape and width. These are wider than the  $\cong 105$  keV width expected for uncorrelated emission (see Fig. 5-19) because events along the horizontal and vertical bands outside of the  $340 < E_{e^+} < 420$  keV and  $340 < E_{e^-} < 420$  keV region add to the sum-energy and difference-energy projections. If the positron and electron lines are emitted from a source moving faster than  $v_{CM}$ , e.g., the positron produced by MPC and the electron by IC in the separated nuclei, these widths are correspondingly larger. Gating on either side of the wedge cut should similarly produce a sum-energy spectrum with two "peaks" (at  $E_{\Sigma} \sim 500$  and  $\sim 1000$  keV) where the cuts cross the banded contour. The difference-energy distribution for adjacent sum-energies would also exhibit two peaks, one on either side of  $E_{\Delta} = 0$ . Such features are absent in Fig. 6-4 and 6-5. Figure 7-4 expands this analysis, presenting positron and electron spectra for 100 keV wide gates on electron or positron energies around the 760 keV sum-line peak regions. In all cases, the dashed lines represent the expected distributions assuming that the entire coincident yield is attributable to the smooth dynamic and nuclear distributions. The absence of peak structure in regions adjacent to the coincident signal rules out the possibility that the positron and electron peaks are physically unrelated.

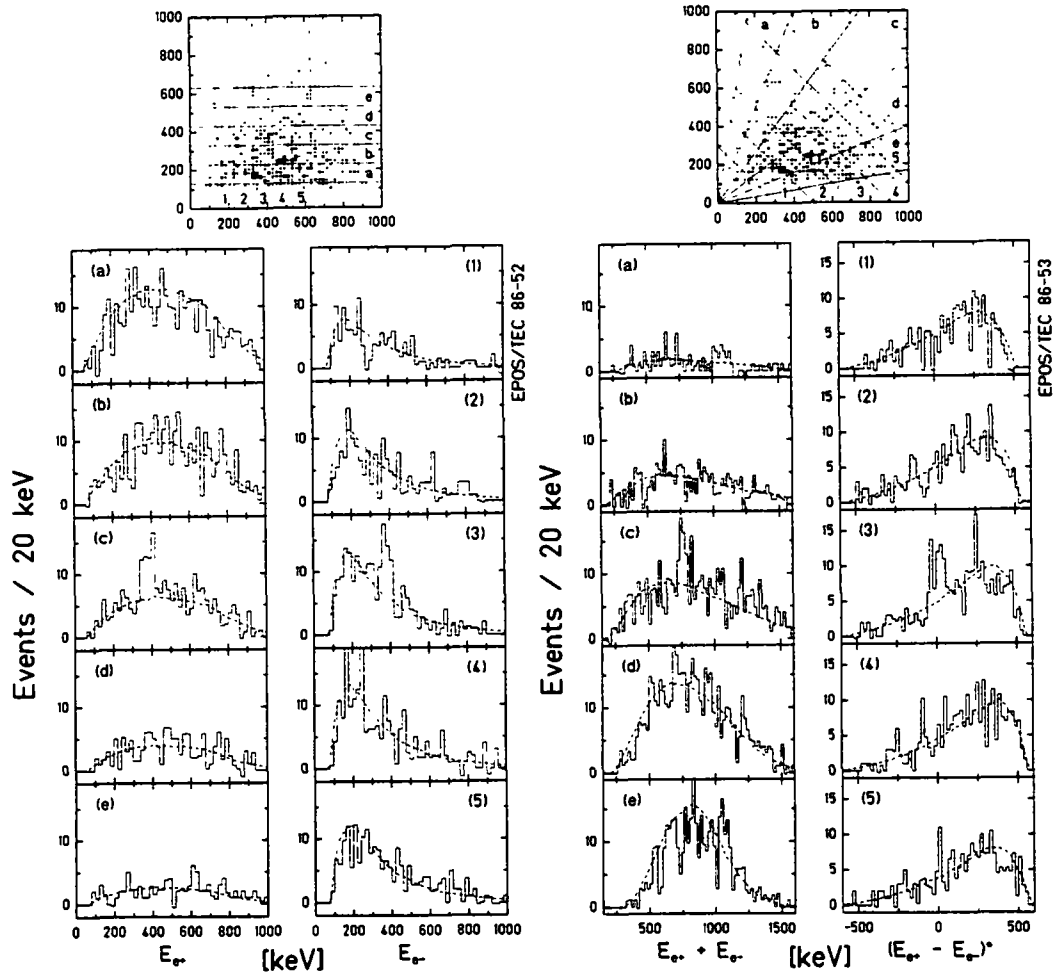


**Figure 7-4.** (Left) Coincident  $e^+$  and  $e^-$  spectra projected from the U + Th data of Fig. 6-1 for conditions as marked. (Right) Sum- and difference-energy distributions for gates as shown.

The energy correlation pattern of coincident positron and electron events from the "sudden rearrangement of atomic shells" process [Reu87] mentioned in Sec. 4.5 is similar to the kinematic distributions from independent monoenergetic emission in Fig. 7-3. An oscillatory interference pattern is superimposed on both the dynamic positron energy distribution and the  $\delta$ -electron spectrum. The resulting coincidence pattern resembles a mesh of narrow electron lines crossing several positron peaks, as shown in Fig. 7-5b. Structures are therefore produced in the sum-energy and difference-energy distributions which cut across this pattern (Figs. 7-5c,d). As noted in [Reu87b], however, electron ionization is more sensitive than positron production to the Coulomb potential at large inter-nuclear separations. The modified potential

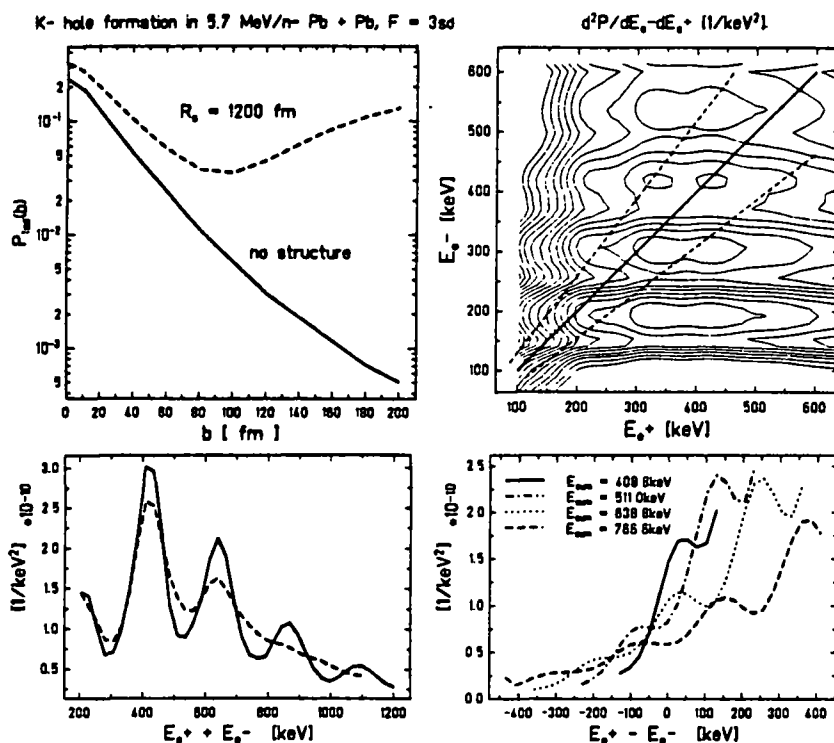


**Figure 7-5.** Positron-electron energy correlation pattern (upper right) and oscillatory structure in the  $E_\Sigma$  and  $E_\Delta$  spectra (lower panel) produced by the sudden rearrangement of atomic shells associated with a single potential step at 1200 fm [Reu87]. Upper left presents the calculated impact parameter dependence of the  $1\sigma$  ionization probability (dashed) which is inconsistent with the established behavior (solid line). (Reproduced from [Reu87b].)

used to produce Fig. 7-5 overestimates  $P_{1\sigma}(b)$ , for impact parameters  $b \geq 100$  fm, by a factor of  $\sim 10^2$  (Fig. 7-5a). A choice for  $V(R)$  which is in better agreement with the experimentally established  $1\sigma$  ionization rates, shown in Fig. 7-6, produces only very small oscillations [Reu87b] which fluctuate from the continuous positron and electron spectra by  $< 10\%$ . Almost no structure is then visible in the  $E_\Sigma$  and  $E_\Delta$  projections.

Moreover, after Doppler shifting the patterns of Figs. 7-5,6 to the lab system (assuming  $v_{em} = v_{CM}$ ) and correcting for efficiency and lineshape tailing, even these weak oscillations appear washed out and no  $E_\Sigma$  or  $E_\Delta$  structure is observed. Because of the uncorrelated nature of the positron and electron intensities and emission angles, this, and other processes characterized by independent mechanisms which

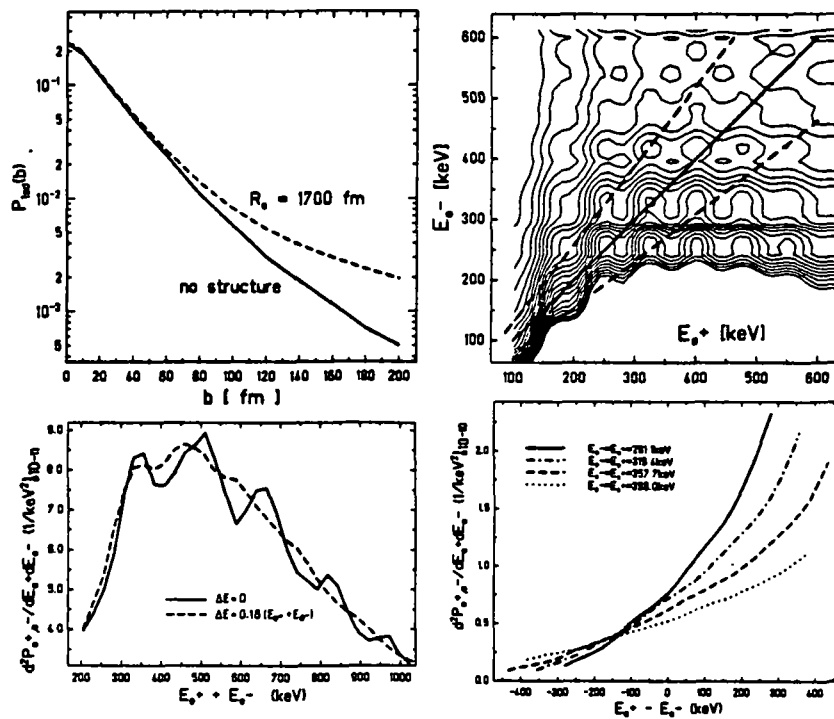


**Figure 7-6.** Same as Fig. 7-5 assuming two smaller potential steps at 1700 fm. Little or no  $E_{\Sigma}$  and  $E_{\Delta}$  structures are produced when model parameters are chosen to yield consistency with experimental  $P_{1S}$ . (Reproduced from [Reu87b].)

emitted monoenergetic positron and electron peaks, are ruled out as possible origins for the coincidence structures presented in Chap. 6.

## Section 7.3 Correlated Positron/Electron Pair Creation

### Sec. 7.3.1 Internal Pair Creation

The only conventional source of correlated positrons and electrons from heavy-ion collisions is internal pair creation from transitions in the final-state nuclei. As demonstrated in Fig. 5-20, cuts across the central region of the broad distribution of positron and electron energies for which  $E_{e+} + E_{e-} = W_0 - 2m_e c^2$ , i.e., for  $E_{e+} \sim E_{e-}$ , approximately simulate the observed coincidence signals.

Figure 7-7 presents an MCSPEC simulation of internal pair creation from a 1.8 MeV E1 transition in the U or Th nucleus ( $Z \cong 92$ ), scattered into the HI PPAC detec-

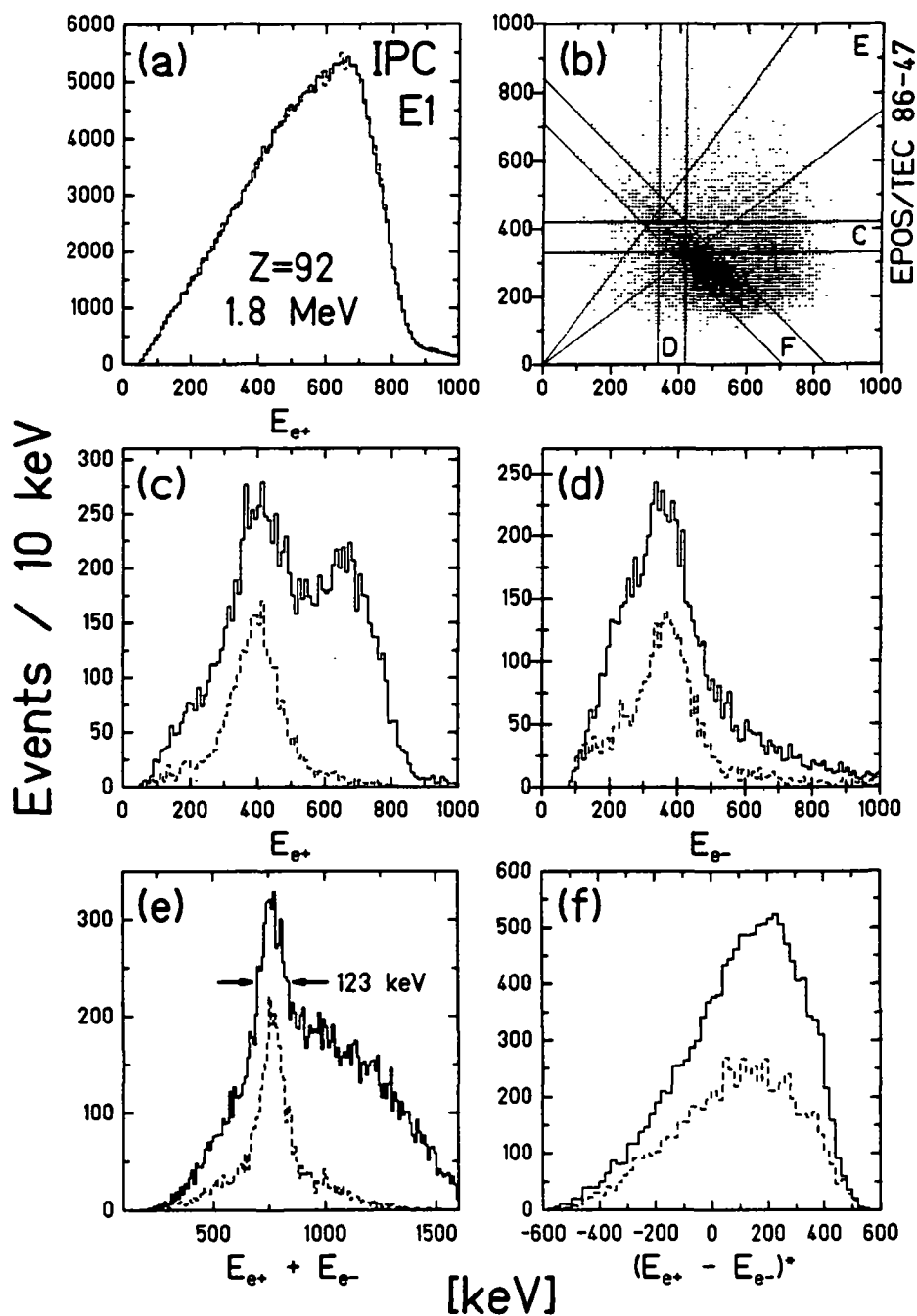


**Figure 7-7.** MCSPEC simulation of IPC of an 1.8 MeV E1 transition in the scattered heavy-ions ( $Z=92$ ). (a)-(f) Same as Fig. 5-20. Dashed histogram assumes isotropic  $\theta_{e^+e^-}$ . Born approximation angular distribution decreases the coincidence yield by  $\sim 20\%$ . Solid histogram includes detection of  $\delta$ -electrons with IPC positrons when correlated  $e^-$  partner is not observed. (e) Sum-energy peak intensity represents 0.75% of total  $e^+$  yield.

tors. As mentioned in Sec. 3.3, E1 multipolarity is typical for high energy ( $\hbar\omega > 1$  MeV) excitations. The dashed histograms present the expectations of mutually isotropic positron-electron emission. Unlike E0 conversions (Fig. 5-21), the E1 angular distribution given by the Born approximation [Ros35],  $P_{e^+e^-}$

$$\begin{aligned} dN_{E1}/d(\cos\theta_{e^+e^-}) &\propto P[1 + W_0^2 m/F^2 + (E_{e^+}^2 + E_{e^-}^2)/F], \\ F &= (m + E_{e^+}E_{e^-} - P_{e^+}P_{e^-}\cos\theta_{e^+e^-}), \end{aligned} \quad (7.1)$$

does not vanish for  $\theta_{e^+e^-} = 180^\circ$  emission, as shown in Fig. 7-8. When integrated over the EPOS acceptance, it leads to only a  $\cong 20\%$  reduction in detected intensity compared to relatively isotropic  $e^+e^-$  emission.

The solid histogram in Fig. 7-7 includes the distortion of the coincidence yields from the additional contribution of  $\delta$ -electrons coincident with 20% of the IPC positrons when the correlated IPC  $e^-$  is not detected. In addition to the  $e^+$  peak near 380 keV (when cutting across the two-dimensional contour with  $340 \leq E_{e^-} < 420$  keV), Fig. 7-7c reflects the shape of the total positron energy distribution.  $2.5 \times 10^5$  detected positrons ( $2.03 \times 10^6$  generated  $e^+$ 's) were simulated, with  $5.62 \times 10^4$  coincident positron-electron pairs. The sum-energy peak within projection (E) contains 1560 events.

This simulation is compared to the  $E_\Sigma = 760$  keV U+Th coincidence data in Fig. 6-3m-p. The expected IPC yield has been added to the continuous backgrounds assuming that 30% of all detected positrons are created from this single transition [Cow86]. The shape of the various coincidence spectra clearly argue against assigning the observed peaks to an IPC origin. A small sum-energy peak does appear in the IPC calculation but the broad lepton emission angle-correlation and the large emitter velocities ( $.05 < v_{nuc} < .12c$ ) lead to a very wide structure,  $\Delta E_\Sigma = 123 \pm 6$  keV (FWHM), compared to the observed width of  $80 \pm 20$  keV. The narrower 610 and 815 keV sum-energy peaks provide more stringent constraints against an IPC origin.

For IPC, the individual positron and electron spectra only exhibit peak structures when gating on the complementary lepton energy (e.g.,  $E_{e^+}^{pk} = [\hbar\omega - 2m_e c^2] - E_{e^-}^{gate}$ ). Figure 7-9 shows the array of adjacent positron (and electron) cuts calculated for IPC (solid histograms), and compared to the  $^{90}\text{Zr}$  source measurements (shaded regions), which illustrate the movement of the corresponding peak when changing the electron (or positron) window. Similar movement of the individual

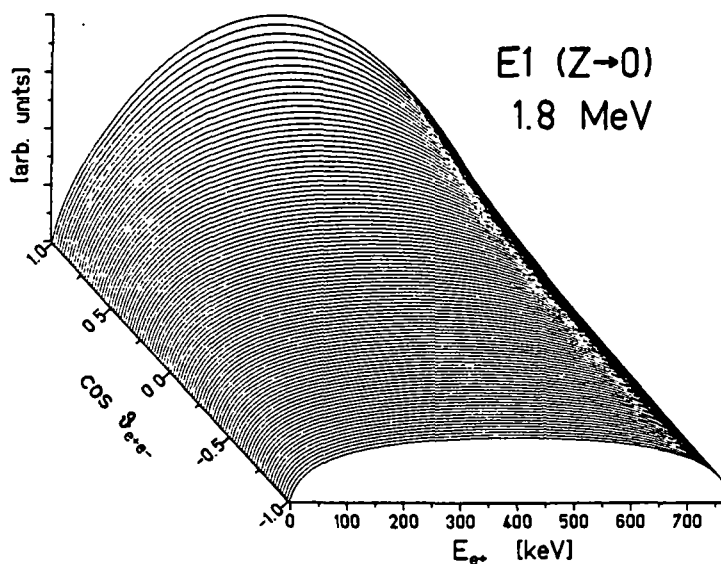


**Figure 7-8.** Emission probability of internally created electron-positron pairs plotted for a 1.8 MeV E1 transition in  $Z=92$ , as a function of positron kinetic energy and the angle between the  $e^+$  and  $e^-$  momentum vectors, in the rest frame of the emitting nucleus.

peaks is not observed in the coincidence data (Fig. 7-4), which exhibit very little structure in adjacent cuts (Fig. 6-3). In addition, the IPC sum-energy peak appears with high intensity in wedge-shaped contours on either side of the  $E_{e^+} \cong E_{e^-}$  projection. The difference-energy spectrum directly reflects this behavior based on the broad positron and electron energy distributions, and it does not exhibit a narrow peak for IPC processes as indicated in Fig. 7-7f. Each of these features contradicts the experimental observations. On the basis of the positron-electron energy correlations alone, IPC from the scattered heavy nuclei can be ruled out as an origin for the measured narrow coincidence peak structures.

A dominant feature of this analysis is the extremely low yield of coincidence peak events due to the large intensity for which the positron and electron energies are unequal. In order to obtain  $\cong 32$  count  $E_{\Sigma} = 760$  keV coincidence signal consistent with that presented in Fig. 6-2, one must assume that  $\cong 5000$  total positrons arising from this transition alone are detected among the 9600 observed positrons of Fig. 6-1. As discussed in Sec. 3.3, only about 30% of the *total* positron yield comes from the broad energy spectrum of all nuclear transitions, only a small fraction of which have  $\hbar\omega = 1.8$  MeV. The IPC transition strength necessary for explaining the coincidence peak counts can be translated by established conversion coefficients

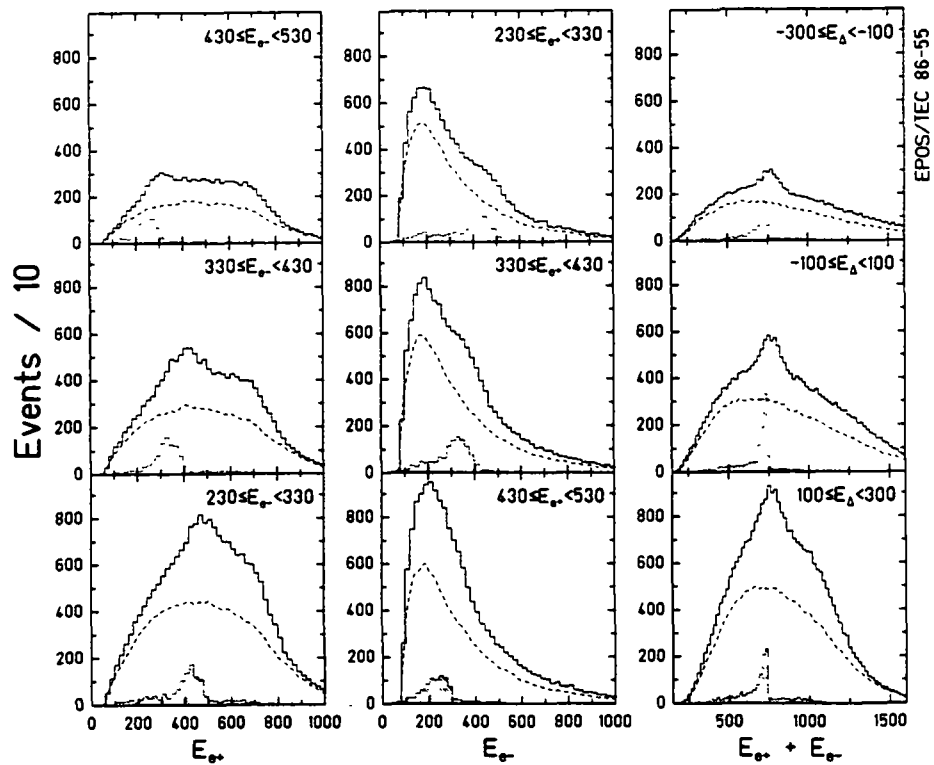
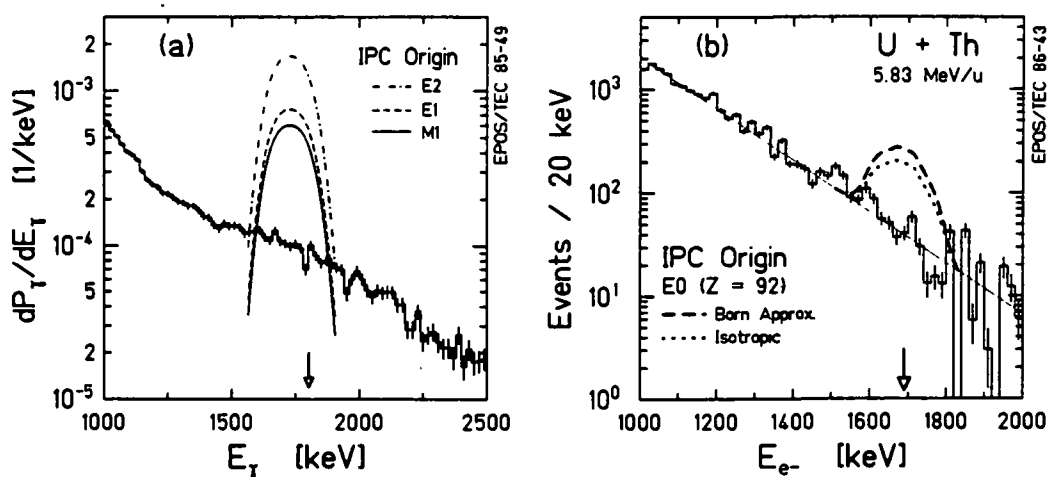
Adjacent Cuts: 30% IPC (E1) vs.  $^{90}\text{Zr}$ 

Figure 7-9. Adjacent cuts for the E1 simulation of Fig. 6-3m-p (solid curves; dashed lines denote continuous backgrounds), compared to  $^{90}\text{Zr}$  measurement (hatched). Projections onto  $E_{e^+}$ ,  $E_{e^-}$ , and  $(E_{e^+} + E_{e^-})$  axes identical to those of Fig. 7-4, as marked.

( $\beta \cong 10^{-4}$ ) into an intensity for the competing  $\gamma$ -ray line ( $\lambda \geq 1$ ) which must accompany nuclear IPC [see Sec. 4.2]. Figure 7-10a compares the expected  $\gamma$ -ray peak, for various IPC multiplicities, to the  $\gamma$ -ray yield measured simultaneously with the coincidence data presented in Figs. 6-1,2. An isotropic positron-electron emission correlation has been conservatively assumed. If the transition is electric monopole, the MCSPEC simulation of Fig. 5-20 is appropriate, which, to produce the necessary  $E_{\Sigma}$  peak intensity would require 3500 total detected positrons from this IPC transition alone. Figure 7-10b presents the expected size of the competing IC electron line, compared to the simultaneously measured high-energy electron spectrum. If the Born Approximation for the  $\theta_{e^+e^-}^*$  distribution is applicable (i.e., rather than isotropic  $\theta_{e^+e^-}^*$ ), the expected  $\gamma$ -ray and  $e^-$  peak intensities are increased by 20% (for E1) or by a factor of  $\sim 2$  (for E0 or E2 transitions). In either case, the measured  $\gamma$ -ray and electron yields are an order of magnitude smaller than the required peak

## Nuclear IPC Origin: 1.8 MeV



**Figure 7-10.** Required intensity of competing  $\gamma$ -ray and conversion electron lines, compared to the  $\gamma$  and  $e^-$  distributions measured simultaneously with data of Fig. 6-3. (1.8 MeV IPC in scattered nucleus assumed). (a) Expected  $\gamma$ -ray peaks for isotropic  $\theta_{e^+e^-}$  and various  $\gamma$ -ray multiplicities. Born-approximation  $\theta_{e^+e^-}$  dependence requires increased  $\gamma$ -ray peak intensity. (b) Expected IC electron line (for E0) is shown added to an exponential fit through the data.

intensities. Identical conclusions are reached for similar analyses of the  $\cong 610$  and 815 keV sum-energy peak data.

These intensity considerations, independent of arguments based on the broad energy distributions expected from IPC, rule out conventional internal pair creation in the separated nuclei as a source for the observed coincident positron-electron structures. MCSPEC simulations indicate that the coincidence distributions are not altered when the heavy-ions are scattered into a narrow angular range (e.g., to large angles with lower velocities, or to specific values of  $\theta$  and  $\phi$ ), nor do they appreciably change if anisotropic emission of the IPC positron is assumed with respect to the motion of the scattered nucleus. Even if a fragmenting of the broad IPC distribution by the overlap of the oscillatory positron and electron transport efficiencies were to occur through some exotic combination of kinematic variables, the theoretical conversion coefficients would have to be in error by an order of magnitude or more in order for IPC *not* to be excluded on intensity grounds alone.

### Sec. 7.3.2 IPC in Nuclear Fragments or Clusters

A further possibility is that a low mass ( $Z \sim 0$ ) nuclear fragment is formed in these collisions, in which IPC of an E0 transition leads to the observed coincidence structures. This consideration was motivated by the fact that the small nuclear charge leads to a more symmetric positron-electron energy distribution, determined almost purely by phase space ( $\propto P_{e^+} + E_{e^+} + P_{e^-} - E_{e^-}$ ). This could somewhat reduce the total singles positron yield which must accompany the coincident IPC signal. A cluster might furthermore be formed with no atomic electrons, removing the competing internal  $e^-$  conversion channel. In order to produce the transition, the cluster must obviously contain at least one proton, so the arguments against nucleon evaporation discussed in Sec. 4.4.4 (Figs. 4-27,29) are relevant. Schlüter et al. [Shl86b] suggest that in order to agree with our  $|Q| \leq 20$  MeV constraint for the HI collisions associated with the positron peak producing events, the cluster must be formed from the neck of the di-nuclear complex as the heavy ions separate. Its laboratory velocity would therefore equal  $v_{CM}$ .

An MCSPEC simulation of this scenario is shown in Fig. 7-11. The fragment was assumed to move with  $v_{CM}$ , and the distortion of the event yields caused by coincidences between IPC positrons and continuum  $\delta$ -electrons has been excluded for clarity. Of  $2.35 \times 10^6$  generated pairs,  $2.5 \times 10^5$  positrons were detected, of which  $2.43 \times 10^4$  were recorded in coincidence with correlated electrons. The intensity of the  $E_\Sigma$  peak in projection ( $E$ ) is 2382 counts. Its width is  $120 \pm 3$  keV (FWHM), much larger than the 25-50 keV widths of the measured U+Th sum-energy lines. Despite the more symmetric energy distribution, a very broad difference-energy spectrum emerges which is incompatible with the data. Adjacent cuts also exhibit significant structure in the positron, electron, and sum-energy spectra. Moreover, the singles positron intensity is only marginally reduced relative to the coincidence yield because for  $Z \cong 0$  the Born approximation result for  $dN/d(\cos\theta_{e^+e^-})$  definitely applies and the pairs are preferentially emitted with small positron-electron opening angles. One must still assume that  $\geq 35\%$  of the measured positron spectrum arises from this single transition to explain the 32 coincidence peak counts in Fig. 6-2, and similar portions,  $\geq 20\%$ , to explain the 610 and 815 keV sum-energy peaks of Fig. 6-9.

One attempt to accommodate the observed data within this model [Bac85b] assumed that the fragment converts several cm away from the target ( $\tau_{E0} > 10^{-9}$  sec, which is very long for excited states in light nuclei), perhaps leading to narrow

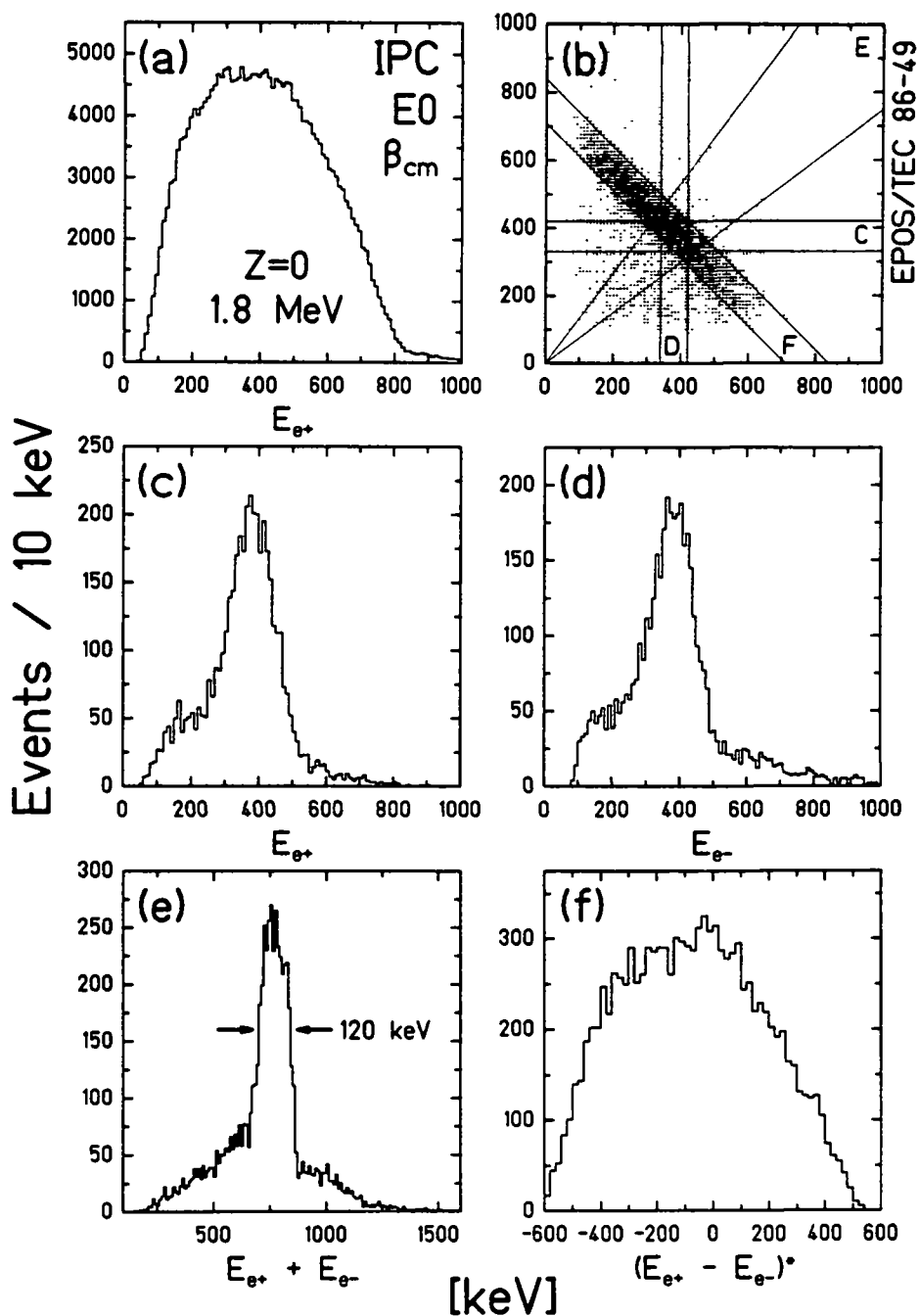


**Figure 7-11.** Simulation of 1.8 MeV E0 IPC in a nuclear fragment ( $Z \cong 0$ ) moving with  $v_{CM}$ : (a)-(f) As in Fig. 5-18.

structure by a suppression of some range of detected coincident positron and electron energies and opening angles. However, the positron detection efficiency decreases more slowly off-axis than the coincidence detection probability, so the ratio of positrons to coincidence events significantly increases. Considerably more than

20% of the detected positron yield must therefore arise from the particular E0 transition. This intensity argument holds for any other mechanisms involving pair production away from the target region, and has been verified with  $^{90}\text{Sr}$  source measurements off-axis.

### Sec. 7.3.3

#### $^{90}\text{Zr}$ IPC

The possibility that the U+Th coincidence data may be explained by the 1.76 MeV E0 transition in  $^{90}\text{Zr}$  (presumably formed as a fission product in the HI collisions) meets with similar difficulties. As was shown in Fig. 5-22, the energy distribution of positrons and electrons measured directly with a  $^{90}\text{Sr}$  ( $^{90}\text{Y}$ ) source is too broad to account for the narrow measured coincidence peaks. The sum-energy peak intensity requires a large ( $\cong 38\%$ ) portion of the total positron yield to be attributed to this transition. Detection of both scattered heavy-ions in these experiments reveals that the data are consistent with a nearly elastic binary exit channel, precluding the direct formation of a  $^{90}\text{Zr}$  nuclide in the collisions. Moreover, the long 1.76 MeV E0 transition lifetime (61 ns) in  $^{90}\text{Zr}$  contradicts the observed prompt time relationship between the sum-energy peak events and the HI collision. If formed with  $v_{em} > 0$ , the  $^{90}\text{Zr}$  nuclei exit the  $\cong 2$  cm fiducial volume of EPOS before decaying. If created at rest in the target, e.g., emission of  $^{90}\text{Zr}$  at  $\theta_{lab} = 90^\circ$  which is stopped in the backing foil, the coincident pair intensity would have been distributed over a broad range of times and then eliminated from the "prompt" data by subtraction of accidental coincidences. Examination of non-prompt ( $\Delta t > 10$  ns) events reveals no evidence for the coincidence peak.

### Sec. 7.3.4 External Pair Creation

External pair conversion (EPC) of nuclear  $\gamma$ -rays (i.e., multiplicities with  $\lambda \geq 1$ ) in the target or spectrometer material represents a final conventional source of correlated positron-electron emission. The spectral shapes resulting from EPC are comparable to those predicted for IPC, when using the Z of the converter material in place of the nuclear charge. Emission from a stationary converter leads to a narrow sum-energy peak if the incident  $\gamma$ -ray energy is not significantly Doppler-shifted by the subtended range of  $\gamma$ -ray emission angles with respect to the motion of the emitting nucleus. From the well-known EPC cross-sections [Sto70] and the geometry of the material near the target, Eqn. 4.1 gives the probability of producing a positron-electron

tron pair per emitted  $\gamma$ -ray.  $P_{\text{EPC}} \cong 5 \times 10^{-6}$  in a  $200 \mu\text{g}/\text{cm}^2$   $\text{ThF}_4$  target mounted on a  $50 \mu\text{g}/\text{cm}^2$  C backing, and  $P_{\text{EPC}} \cong 2 \times 10^{-5}$   $e^+e^-/\gamma$  from the aluminum material in the target frame and in both the spiral and sheet baffles. The total,  $P_{\text{EPC}} \cong 2.5 \times 10^{-5}$ , is about 20 times smaller than the comparable IPC coefficient of  $\beta_{\text{IPC}} \cong 5 \times 10^{-4}$   $e^+e^-/\gamma$  for a 1.8 MeV transition in  $Z \cong 92$ . The associated  $\gamma$ -ray line detected in the NaI counter would be correspondingly larger in Fig. 7-10, exceeding the measured  $\gamma$ -ray intensity by more than a factor of  $\sim 100$ .

Pair creation following neutron activation of the target material or aluminum target frame and baffles, which could produce correlated events, appears similarly unlikely. The positron-electron energy distributions would be very broad, and an implausibly large portion of the total positron yield must be accounted for by the decay. The required half-life of the decay,  $\tau \sim 10^{-9}$  sec, is much shorter than the usual scale of msec to minutes for beam-induced radioactivity.

It is apparent that no known internal or external pair creation processes lead to narrow peaks in the energy distributions of coincident positrons and electrons which could reproduce the measured U+Th data. Attempts to accommodate pair creation processes to the observed coincidence structure through a variety of unusual mechanisms have been modeled with MCSPEC simulations. These have included: 1) specifying the exact direction, or range of directions, for the scattered nucleus or for the emitted cluster; 2) assuming various broad or extremely narrow distributions for the positron-electron opening-angle; and 3) determining the direction of emission, or distribution of emission directions, of the positron with respect to the motion of the nuclide or fragment. No combination of the above leads to a significant change in the broad difference-energy distribution or in the relative intensity of detected pairs to total observed positrons. Over the normal range of nuclear velocities, the broad  $\theta_{e^+e^-}$  distribution leads to wide sum-energy peaks ( $\Delta E_{\Sigma}$  between 100 and 200 keV), in addition to the large spread in individual positron and electron energies. Greater than at least 20% to 50% of the total observed positron yield must arise from the single transition at 1.8 MeV, in order to explain the observed coincidence peak intensities alone. The large required positron yields and the absence of competing  $\gamma$ -ray and electron conversion lines appear, on intensity grounds alone, to rule out conventional and exotic IPC and EPC processes as possible explanations for the coincidence peak data.

## Section 7.4 Sequential Positron-Electron Emission

A third general class of models may contribute to the production of coincident positrons and electrons. Instead of the emission of both  $e^+$  and  $e^-$  from a single decay, monoenergetic positrons and electrons might be produced sequentially in a cascade-like process. If a monoenergetic electron is emitted every time that the positron is created, this would avoid the difficulties associated with independent  $e^+e^-$  emission (i.e., that the structures would have been easily observable in adjacent cuts), as well as the problems with pair conversion processes (i.e., the very broad distribution of positron and electron energies). One simple example is the sequential decay of a series of nuclear transitions in which a positron-creating conversion is uniquely preceded or followed by a separate internal electron conversion.

Figure 7-12 illustrates the coincidence yield expected if the peak positron were due to IPC of a 1.4 MeV transition in U or Th, followed, with a branching ratio of unity, by IC of an atomic K electron by a  $\sim 500$  keV transition.  $5 \times 10^4$  detected positrons have been simulated ( $4.54 \times 10^5$  generated cascades) of which 7433 are measured in coincidence with IC electrons. The coincident sum-energy peak in projection (E) contains 2136 counts and is very wide ( $\cong 203$  keV) because the emission angles of the positron and electron are assumed to be uncorrelated. The coincident detection of the IPC electron associated with the positron-producing transition adds an important background which has been neglected in this simulation. The IPC electron spectrum contributes mostly at low energies, but a 2nd sum-energy peak is produced at  $E_{\Sigma} \cong 380$  keV which distorts the projection of Fig. 7-12e. The coincident positron peak, which reflects the triangular IPC energy distribution, is  $\cong 200$  keV wide, incompatible with the observed widths,  $\Delta E_{e^+} \sim 80 \pm 15$  keV. As discussed in Secs. 4.2 and 4.3, this type of nuclear IPC is unable to account for the narrow positron peak widths or the required transition intensities for the data of Fig. 3-16. Figure 7-13 compares the expected competing  $\gamma$ -ray or IC electron line from the 1.4 MeV positron emitting transition (calculated using Eqns. 6.9 and 6.12) to the simultaneously measured yields of Fig. 7-10. The branching ratio for emitting the electron following the positron emission was assumed to be  $\cong 1$  for an E0 IC, or 0.65 for an M4 IC. (Other multipolarities have smaller IC conversion coefficients.)

The intensity and positron linewidth arguments could be mitigated if one assumed MPC of an E0 conversion as the origin of the coincidence positron peak, enhanced by the depletion of the K-shell by a preceding  $e^-$  IC, which could account for

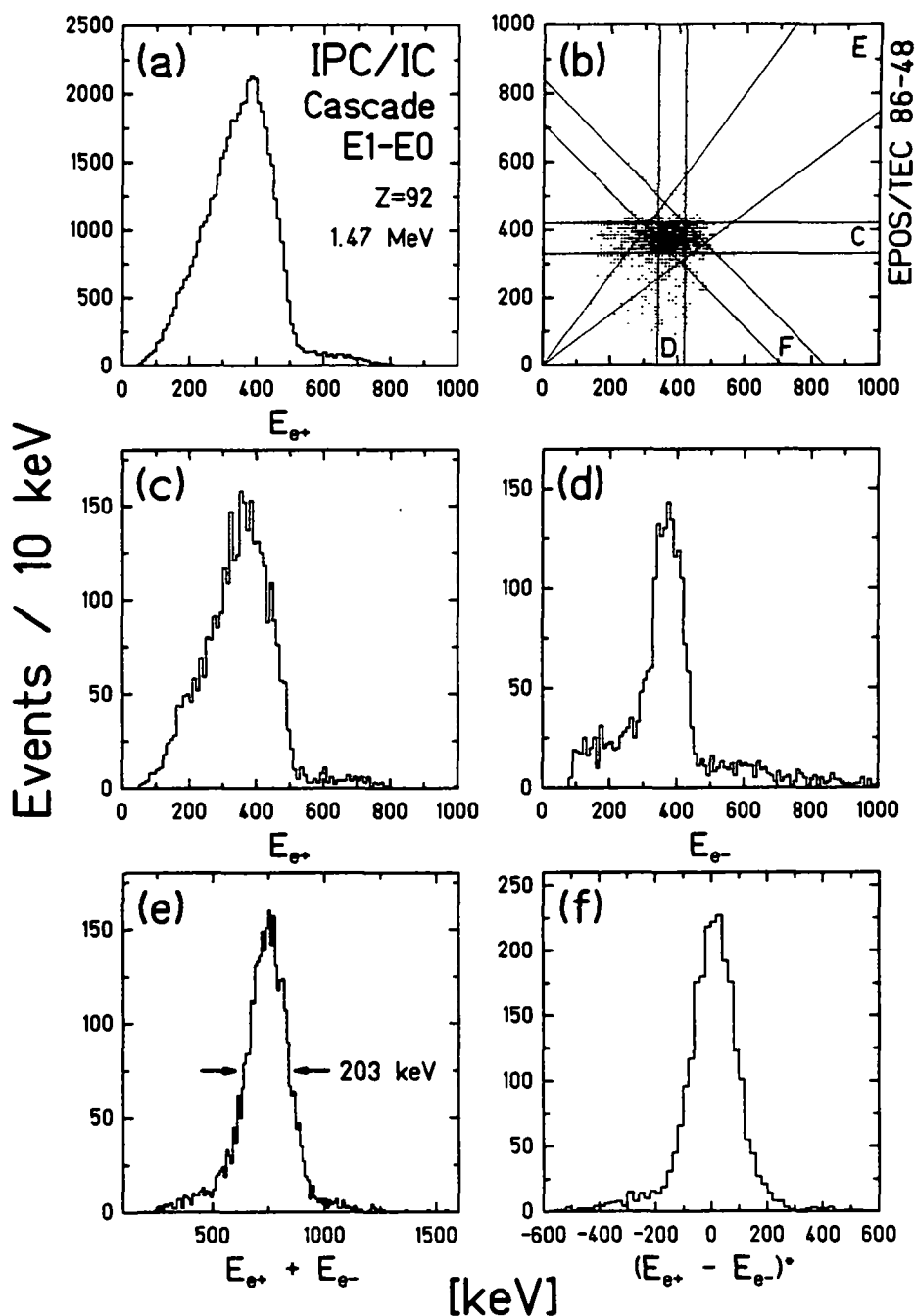


**Figure 7-12.** Simulation of a nuclear cascade process: (a) total, and (c) coincident positrons produced by 1.47 MeV IPC, and (d) coincident  $e^-$  from a 500 keV IC in the scattered nuclei. Positrons exhibit a triangular IPC energy distribution with width  $>180$  keV. Assuming an  $e^-/e^+$  branching ratio of unity,  $\cong 6\%$  of the  $e^+$  peak counts are associated with coincidence events in the very wide sum-peak (e).

the electron line. As discussed in Sec. 4.2, if the K-shell is empty at the moment of MPC conversion, no competing K-conversion  $e^-$  lines would be observed in

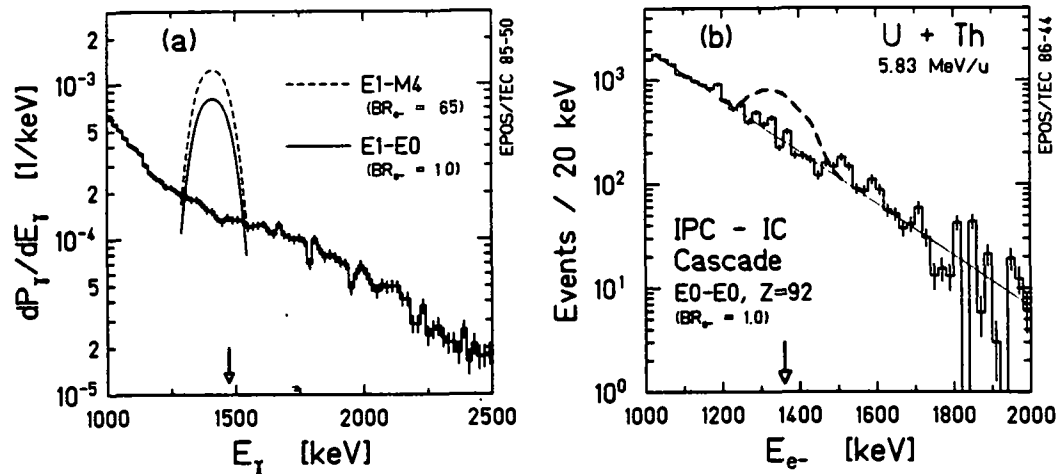
Nuclear Cascade: IPC(e<sup>+</sup>) - IC(e<sup>-</sup>)

Figure 7-13. Data of Fig. 7-10 compared to expected intensity of (a)  $\gamma$ -ray, and (b)  $e^-$  IC lines competing with the 1.47 MeV IPC branch of the nuclear cascade of Fig. 7-12.

Fig. 7-13b. Production of monoenergetic positron and electron lines which exhibit no angular correlation leads to an  $E_{e^+} - E_{e^-}$  diagram such as presented in Fig. 5-19. The widths of the individual positron and electron peaks depend on their mean energy and the nuclear velocity. This in turn leads to sum-energy peak widths ranging from 100 to 200 keV, depending on the HI scattering angle.

Cascade-like decays could also, in principle, occur for particularly fast transitions in a giant di-nuclear complex (see Sec. 4.5.4), where the strong localization of the electron wavefunctions increases the probability of MPC conversion. Assuming a branching ratio of unity and relatively isotropic emission of the positron and electron, Fig. 5-19 describes the expected coincidence yield appropriate for an emitter velocity of  $v_{CM}$ . Aside from questions based on nuclear physics concerning the plausibility of this scenario, the formation of intrinsically narrow positron and electron lines requires a long compound system lifetime ( $10^{-19}$  s), in which case spontaneous positron emission should occur with probability which dominates over MPC [Sh186]. Associating the coincidence positron line with spontaneous emission, rather than MPC, is difficult in light of the large measured peak energies ( $E_{e^+} = 300$  to 410 keV) compared to the QED predictions for U + Th ( $E_{e^+} \cong 140$  keV), as well as the near constancy of peak energies in Fig. 3-16 over a large range of combined charge ( $163 \leq Z_U \leq 188$ ).

The creation of monoenergetic positrons and electrons in cascade or sequential processes is not limited to nuclear conversions. As mentioned in Sec. 5.1, a neutral object could be produced which decays sequentially through an intermediate state, for example,  $X^0 \rightarrow e^- \chi^+$ , followed by  $\chi^+ \rightarrow e^+ \nu$ . A conjugate pair of charged objects formed directly in the collision, e.g.,  $\psi^+ \rightarrow e^+ \nu$  and  $\psi^- \rightarrow e^- \nu$  [Shä84], or  $(c^+ e^- e^+) \rightarrow e^+ \gamma$  and  $(e^- e^+ e^-) \rightarrow e^- \gamma$  [Won86, Chu86], could lead to coincident monoenergetic positrons and electrons.

The necessary feature of all these sequential processes is a one-to-one correspondence between monoenergetic positron and electron production. The absence of correlation between the  $e^+$  and  $e^-$  emission angles results in an intensity pattern typified by Fig. 5-19, exhibiting a wide sum-energy peak width (from 105 keV for  $v_{CM}$  to  $\sim 160$  keV for  $\langle v_{NUC} \rangle$ ), and a ratio of coincidence events to total detected positrons of  $\leq 6\%$ . In addition, the production of positrons and electrons with equal energy does not arise naturally in cascade models and must be assumed *ad hoc* by adjusting the nuclear transition energies or the masses of the  $X^0$  or  $\chi^+$  objects. While a pair of conjugate charged objects may naturally explain nearly equal positron and electron emission energies, their production must not occur close to the nuclear charge centers ( $r_{prod} \leq 10^4$  fm), otherwise the mean detected positron and electron energies are asymmetrically shifted by the Coulomb field,  $|E_{e^+} - E_{e^-}| \cong 2Ze^2/r_{prod}$ . Experimentally,  $\langle E_{e^+} - E_{e^-} \rangle_{obs} < 50$  keV. If such objects are produced with a distribution of momenta, the positron and electron would be Doppler-shifted by different source velocities. This would substantially smear out the energy correlations in the  $E_{e^+} - E_{e^-}$  event plane.

## Section 7.5 Two-Body Final States

### Sec. 7.5.1 Theoretical Motivation

With no suitable nuclear or atomic explanations for the data, we turn to a discussion of neutral particle-like objects, whose predicted two-body decay kinematics closely resemble the pattern of observed coincident positron and electron energies, as described in Chap. 6. Theoretical attempts to explain these data in terms of one or several new elementary particles<sup>6</sup> have met with difficulties in light of the negative results of recent experimental particle searches.<sup>7</sup> As mentioned in Sec. 5.1, early analyses of the possible existence of new light particles [Shä85, Bal85, Rei86, Cho86, Shä86a] favored a spin parity assignment of  $0^-$ . Assuming that they are produced

through interactions with the nucleons or atomic electrons [Shä85, Rei86, Shä86a, Kim87], or from the collisional electromagnetic fields [Bal85, Cho86, Lan86, Car86, Mü186b, Shä86b, Yam87], stringent limits were obtained on their possible couplings to electrons, photons, and quarks from a variety of low-energy experimental data. These include constraints from: electron and muon anomalous magnetic moment, the Lamb shift, muonic-atom transitions, and high-Z atomic binding energies [Shä85, Rei86]; positronium hyperfine splitting and Delbrück scattering [Shä86a, Shä86b];  $\pi^0 \rightarrow \gamma\gamma$  decay [Mas86]; and neutron-atom scattering [Shr86, Rei86]. Moreover, dynamic production of particles electromagnetically was found to be suppressed at low momenta [Bal85, Rei86, Cho86, Lan86], which led to suggestions that the particle could be emitted with discrete energies from the rotating [Cho86, Car86] or vibrating [Mü186c, Shä86b] di-nuclear complex.

Balantekin et al. interpreted the positron peak data as evidence for a short-lived axion [Bal85], which Mukhopadhyay and Zehnder [Muk86] pointed out could have evaded detection in previous search experiments [Cal79, Fai80, Edw82, and Zeh85]. The remaining window of possible masses and lifetimes for the standard axion was subsequently closed [Lan86] by experiments searching for particle production in nuclear decays in  $^{10}\text{B}$ ,  $^{12}\text{C}$ , and  $^{14}\text{N}$  [Sav86, Hal86, Boe86, Bab86], and in radiative  $\Upsilon(1S)$  decays [Mag86, Bow86, Alb86]. In order to get around these constraints, Peccei, Wu, and Yanagida [Pec86], and independently Krauss and Wilczek [Krs86a], proposed modifications which suppressed the axion coupling to heavy quarks. As summarized in [Bar86] and [Krs86c], these variant axions have also been excluded by limits from: nuclear transitions; rare  $\pi^+$ ,  $K^+$ , and  $\mu^+$  decays [Egl86, Eic86, Hof86, Bry86] (see also [Ma86, Suz86, Krs86b]);  $\pi^0 \rightarrow 2\gamma$  decays [Mas86]; and from proton [Ber85, Brn86] (see also [Eng87]) and electron [Kon86, Dav86, Rio87] beam-dump experiments (see also [Tsa86, Brd86]).

6

See [Shä84, Bal85, Shä85, Bar86, Bas86, Brd86, Car86, Cel86, Cho86, Chu86, Hof86, Krs86a, Krs86b, Krs86c, Lan86, Li86, Ma86, Mas86, Mü186, Mü186b, Mü186c, Mü186d, Muk86, Muk86b, Pec86, Rei86, Shä86, Shä86b, Shr86, Suz86, Tsa86, Zee86, Cal87, Gei87, Grb87, Kim87, Ng87, Rei87, Won87, Yam87, Ban87].

7

For a summary of experiments completed before the EPOS results see, e.g., [Cal79, Fai80, Edw82 and Zeh85], and references therein. For more recent work, see [Brg85, Alb86, Bab86, Boe86, Bow86, Brn86, Bry86, Cal86, Dav86, Eic86, Erb86, Hal86, Kon86, Mag86, Mey86, Sav86, Kli87, Mai87, Pek87, Wim87, Rio87, Mil87, Eng87, Dan87, Sak87].

Other  $J^\pi$  assignments for the particle were suggested by Zee who discussed limits on possible gauge bosons [Zee86], and Barshay who proposed a vector meson which couples to  $3\gamma$  [Bas86]. It was pointed out in [Zee86] and [Li86] that scalar ( $0^+$ ) and vector ( $1^-$ ) particles could be produced coherently by the collection of nucleons, leading to a possible enhancement of the production cross-section by a factor of up to  $(A_p + A_T)^2 \sim 2 \times 10^5$ . This would correspondingly lessen the constraints on the coupling of such particles derived from established experimental data [Shä85, Rei86, Shä86a,b]. Vector particles may also involve additional symmetries beyond the Standard Model [Zee86], with unusual couplings to the usual fermions. In light of the speculative nature of these latter possibilities, the reviews of Krauss and Zeller [Krs86c] and Reinhardt et al. [Rei86b] conclude that, within the Standard Model, an explanation for the EPOS positron-electron coincidence peaks by one or more elementary particles is unlikely unless they couple primarily to electrons and decay within the production target in the beam-dump experiments [Krs86c], or that they are produced by highly non-linear couplings, or are created in bound-states in the fields of the colliding heavy-ions [Rei86b].

In this connection it may be worthwhile to note that the environment in which these coincidence peaks are observed is very different than usually encountered in most other realms of physics. The heavy-ion quasimolecular collision is a unique "laboratory" characterized by large transient electric and magnetic fields, formed on the time scale of  $10^{-21}$  sec, with strengths exceeding  $|E| \sim 10^{16}$  V/cm and  $|B| \sim 10^{13}$  Gauss (measured at 100 fm from the di-nuclear center) [Raf76, Sof81, Rum87]. Because of the strong fields, non-linear effects may be important (see, e.g., [Bas86], [Shä84] and [Grb87], and [Ach79]). The presence of  $\sim 500$  nucleons and  $\sim 100$  electrons in a confined region of space may further complicate matters. In addition the the enhancement of particular production mechanisms by nuclear [Cho86, Mü186c, Shä86b, Car86, Kim87] and collective [Zee86, Li86] means already mentioned, it has been suggested that particles could be produced more easily in a bound state in the strong fields [Mü186b], or (if the binding energy exceeds the rest mass) copiously produced via a boson condensate [Mü186d, Krs86a, Shä86b].

Non-elementary objects having an internal structure, for example, bound states of positrons and electrons which eventually undergo a two-body decay, have also been proposed to explain these coincidence data. Müller et al. [Mü186] consider the formation of *tightly* bound "poly-positronium droplets," i.e.,  $n$  positron-electron pairs,  $(e^+e^-)^n$ , in analogy with the very loosely bound  $(e^+e^-e^+)$  and  $(e^+e^-e^+e^-)$  complexes

observed in atomic physics (see [Won86a] and refs. therein). Wong and Becker [Won86b] proposed a scalar magnetic ( $e^+e^-$ ) resonance, based on a short-range ( $\sim 10$  fm) interaction between the lepton magnetic moments (see also [Bat86]). It would presumably be formed by positron creation in the vicinity of the strongly localized quasi-atomic electrons. In the absence of a fully relativistic two-body theory, it is presently unclear whether such resonances exist [Jak87, Gei87, Won87]. The possible existence of a rich spectrum of positron-electron states has also recently been discussed within the context of modifications to QED in the strong collisional electric fields. Celenza et al. [Cel86] discussed quasi-positron and quasi-electron soliton solutions in the vacuum (see also [Hir87]), and Caldi and Chodos [Cal87], and Ng and Kikuchi [Ng87], suggest that we may be observing the transition to a confining phase of QED, in which an entirely new energy level scheme exists for positronium.

A more thorough discussion of these various theoretical ideas is beyond the scope of this dissertation. The present trend, however, seems to favor composite objects which can accommodate the multiplicity of observed positron-electron sum-energy peaks. One feature common to many of these models is the formation of the object in the very strong fields available in heavy-ion collisions. This might explain why the structures have not been observed in previous more traditional particle search experiments. As with the case of boson condensates, composite objects may be created in states bound to the heavy-ion collision partners. In addition to providing the perhaps necessary lepton localization and decreasing the effective mass-threshold which increases the production cross-section, this could also produce objects which, after the ions separate, are nearly at rest in the HI center-of-mass system.

The preceding sections have been largely concerned with ruling out classes of certain well-defined model-dependent origins for the coincidence peaks. This section attempts to experimentally determine, in an essentially model-independent way, whether the coincident positron and electron are actually emitted back-to-back. Within the context of a two-body decay, the distribution of source velocities and the appearance of multiple structures in the data are then addressed. Each of these studies requires a more detailed investigation of the kinematics of the emitted positron and electron.

### Sec. 7.5.2 Positron/Electron Lines from a Moving Source

The laboratory energies of monoenergetic positrons or electrons emitted at an angle  $\theta_{e+}^*$  from a system  $S^*$  moving in the lab with velocity  $\beta$ , are given by the Lorentz transformations of Eqns. 5.7 and 5.8. The individual positron (or electron) peak, when integrating over  $4\pi$  sr, can exhibit a full width of  $2\gamma\beta P_{e+}^*$  (corresponding to emission parallel and antiparallel to the emitter motion), centered at a lab energy of  $E_{e+} = E_{e+}^* + (\gamma-1)(E_{e+}^* + m_e c^2)$ . The sum-energy and difference-energy coordinates introduced previously are defined as:

$$E_{\Sigma} + 2m_e c^2 = \gamma(W_{e+}^* + W_{e-}^*) + \gamma\beta(P_{e+}^* \cos\theta_{e+}^* + P_{e-}^* \cos\theta_{e-}^*), \quad (7.3a)$$

$$E_{\Delta} = \gamma(W_{e+}^* - W_{e-}^*) + \gamma\beta(P_{e+}^* \cos\theta_{e+}^* - P_{e-}^* \cos\theta_{e-}^*). \quad (7.3b)$$

The positions and widths of the resulting sum-energy and difference-energy peaks depend both on the emitted energies and on the directions that the positron and electron are ejected.

For the special case where the electron and positron energies are equal ( $W_{e+}^* = W_{e-}^* \equiv W^*$ ), Eqns. 7.3a,b simplify to:

$$E_{\Sigma} = 2(\gamma W^* - m_e c^2) + \gamma\beta P^* (\cos\theta_{e+}^* + \cos\theta_{e-}^*), \quad (7.4a)$$

$$E_{\Delta} = \gamma\beta P^* (\cos\theta_{e+}^* - \cos\theta_{e-}^*). \quad (7.4b)$$

In this case, the relative widths of the  $E_{\Sigma}$  and  $E_{\Delta}$  peaks, determined by the bracketed expressions in Eqns. 7.4, depend only on the relative emission directions of the positron and electron. As mentioned in Sec. 5.1, if the positron and electron are emitted back-to-back, then  $\cos\theta_{e-}^* = -\cos\theta_{e+}^*$  and while the intrinsic  $E_{\Sigma}$  peak width is zero, the difference-energy structure reflects the maximum Doppler broadening with a full-width of  $\Delta E_{\Delta} = 4(\gamma\beta)_{em} P_{e+}^*$ . If, on the other hand, the positron and electron are emitted always in the same direction ( $\cos\theta_{e-}^* = \cos\theta_{e+}^*$ ), this situation is reversed yielding a narrow  $E_{\Delta}$  peak and a  $4\gamma\beta P_{e+}^*$  wide sum-energy structure. For uncorrelated emission directions (i.e., mutually isotropic  $\theta_{e+}^*$  and  $\theta_{e-}^*$ ), both the  $E_{\Sigma}$  and the  $E_{\Delta}$  peaks exhibit a width of  $\Delta E_{\Sigma,\Delta} \cong 2\sqrt{2}\gamma\beta P_{e+}^*$ ,  $\sqrt{2}$  larger than that of the individual positron or electron lines alone (see Figs. 6-2,6-10).

Figure 7-14 illustrates this point by presenting an MCSPEC calculation of the sum- and difference-energy peaks, assuming that monoenergetic positrons and

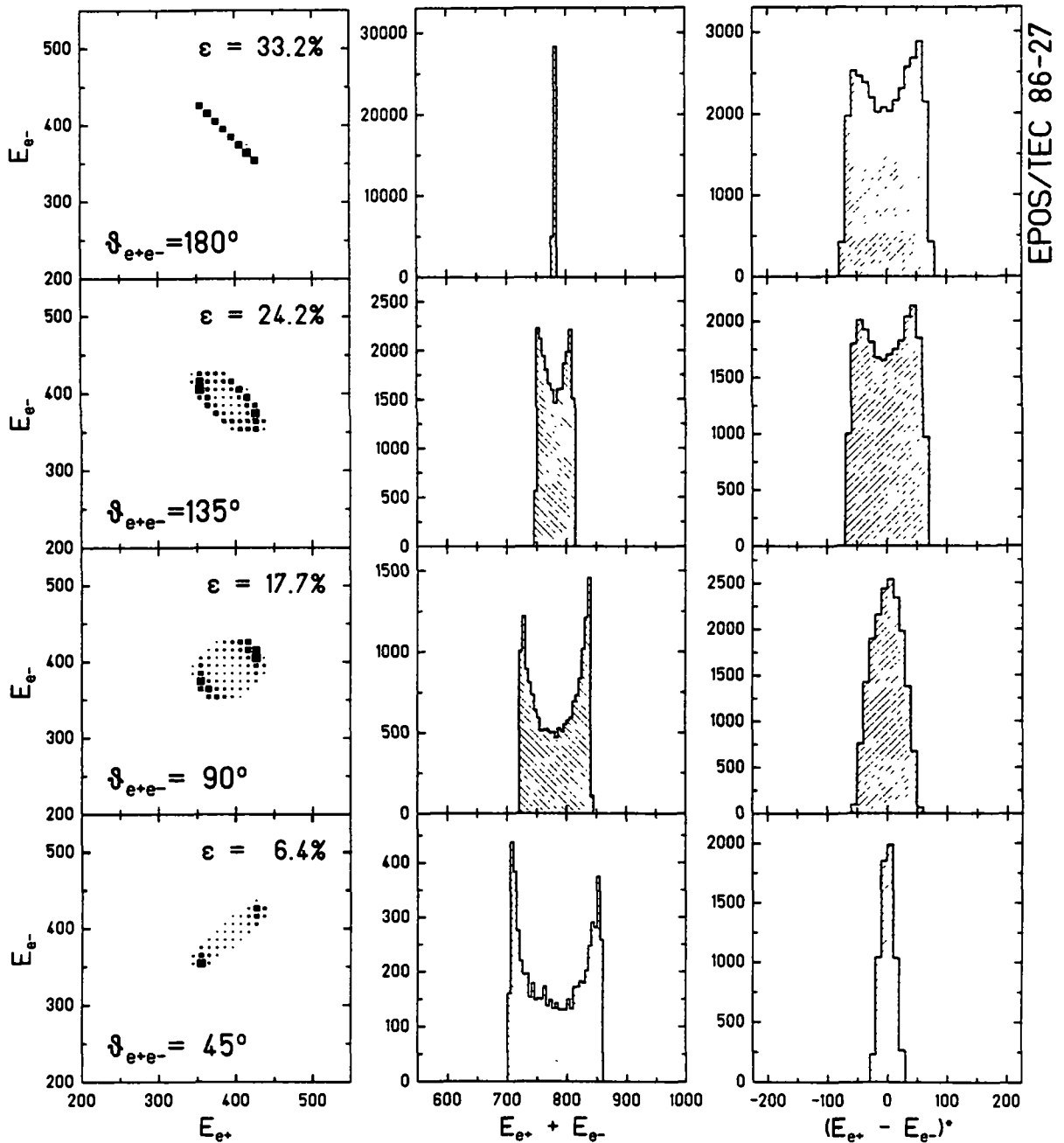


**Figure 7-14.** Monoenergetic  $e^+$  and  $e^-$  (380 keV) emitted isotropically from CMS with fixed relative opening angle. Energy correlation plot (left), and the widths of the sum-energy peak (center) and difference-energy peak (right) illustrate the effect of angular correlation on kinematic broadening. Detector response and backgrounds have been omitted for clarity.  $\epsilon$  denotes relative coincident/total  $e^+$  detection efficiency.

electrons are emitted with fixed opening angle  $\theta_{e^+e^-}^*$  from a source moving in the beam direction with  $v_{CM}$ . This could arise physically if the relative emission direc-

tion  $\theta_{e^+e^-}$  were highly constrained for one of the cascade or sequential processes of Sec. 7.4. Each simulation generated  $10^5$  detected positrons. The relative coincidence detection efficiency  $\varepsilon = (\varepsilon_{e^+e^-}/\varepsilon_{e^+})_{\text{total}}$  decreases with smaller opening angle as marked, because of the back-to-back orientations of the regions of  $e^+$  and  $e^-$  acceptance in the EPOS spectrometer (see Figs. 5-15,16). For clarity, detector resolution has been omitted.

The specific choice of  $v_{em} = v_{CM}$  used in Fig. 7-14 obviously influences the Doppler broadening of the positron and electron peaks, and hence the details of the  $E_{\Sigma}$  and  $E_{\Delta}$  lineshapes. For example for  $\theta_{e^+e^-}^* = 90^\circ$  (3<sub>rd</sub> panel in Fig. 7-14), the effect of the angular expressions for  $E_{\Delta}$  and  $E_{\Sigma}$  in Eqns. 7.4 are identical. The arrangement of acceptance regions symmetrically on either side of the beam direction, however, requires that the  $90^\circ$   $e^+/e^-$  vertex straddles the vertical plane (passing through the target, perpendicular to the solenoid axis). Events are then preferentially detected if the positron and electron are emitted in roughly the same direction with respect to the beam, and the  $E_{\Delta}$  peak is therefore somewhat narrower than the  $E_{\Sigma}$  peak.

The choice of velocity does not affect the salient feature that only for large opening angles —  $\theta_{e^+e^-}^* \gg 90^\circ$ , approaching back-to-back emission — do a narrow sum-energy and a wide difference-energy peak emerge which resemble the data. Moreover, it is clear that a quantitative analysis of the widths of the  $E_{\Sigma}$  and  $E_{\Delta}$  peaks should provide a measure of  $\theta_{e^+e^-}^*$ .

Before proceeding with a kinematic analysis of the experimentally observed positron/electron opening angle, the two general assumptions upon which this discussion will be based are addressed. First, it is assumed in the derivation of Eqn. 7.4 that two-body-like processes lead, at least separately, to monoenergetic positrons and electrons emitted in the rest frame of the source. The general features of three-body and multi-body ( $n \geq 4$ ) decays are therefore discussed. Second, it is assumed that the widths of the various lines reflect, in part, Doppler shifts of the laboratory positron and electron energies due to the motion of the source. The consequences of a stationary source are therefore also investigated.

### **Sec. 7.5.3 Multi-Body Final States**

As mentioned in Sec. 5.1, the emission of monoenergetic positrons and electrons which are confined to a small range of nearly equal energy arises most naturally in

the two-body decay of a neutral object. For a three-(or more)-body final state, each positron or electron takes on a range of energies from zero to some maximum, which is determined by the particular combination of decay-product masses. For 3-body decay,  $X \rightarrow e^+ e^- \xi$ , the maximum positron or electron kinetic energy is

$$E_{e^+,e^-}^{\max} = \frac{1}{2}(M_X c^2 - 2m_e c^2 - m_\xi c^2) \cdot (1 + m_\xi / M_X). \quad (7.5)$$

In general, the positron-electron energy correlation exhibits a broad oval pattern, several hundred keV wide. Figure 7-15a,b illustrates this for third body masses of  $m_\xi = 0$  and  $511 \text{ keV}/c^2$ , respectively. These distributions were calculated from kinematic considerations only, assuming a uniform phase space density for the 3-body final states,  $d^3N/dW_{e^+} dW_{e^-} dW_\xi = \text{constant}$ . Angular momentum and parity conservation for any given  $X$  particle quantum numbers are not included. Nuclear IPC represents a limiting case of 3-body final states in which the remaining participant has a much larger mass than the positron or electron. It removes very little kinetic energy from the decaying system and the positron-electron correlation pattern is then the familiar diagonal band for which  $E_{e^+} + E_{e^-} = \text{constant}$  (Fig. 7-15c).

As discussed in Sec. 7.3, the momentum taken up by the heavy partners in a multi-body final state (e.g., the recoiling nucleus in IPC) erases any back-to-back tendency for the remaining positron and electron. For a given positron and electron energy and momentum,  $P_{e^+}$ ,  $P_{e^-}$ , their opening angle in the rest frame of the emitter is

$$\cos \theta_{e^+e^-}^* = [P_\xi^2 - P_{e^+}^2 - P_{e^-}^2] / (2P_{e^+} P_{e^-}), \quad (7.6)$$

where,

$$P_\xi^2 c^2 = [M_X c^2 - 2m_e c^2 - E_{e^+} - E_{e^-}]^2 - m_\xi^2 c^4. \quad (7.7)$$

As shown in Fig. 7-16 for  $m_\xi = m_e$ , the opening angle is  $0^\circ$  along the inner perimeter of the phase space distribution in the event plane between the tangents to the  $E_{e^+}$  and  $E_{e^-}$  axes. Along the outer perimeter,  $\theta_{e^+e^-}^* = 180^\circ$ . The distribution of opening angles  $dN/d(\cos \theta_{e^+e^-}^*)$  is broad and peaked at  $\theta_{e^+e^-}^* = 180^\circ$  for small  $m_\xi$ , and it approaches isotropy for  $m_\xi \gg m_e$ .

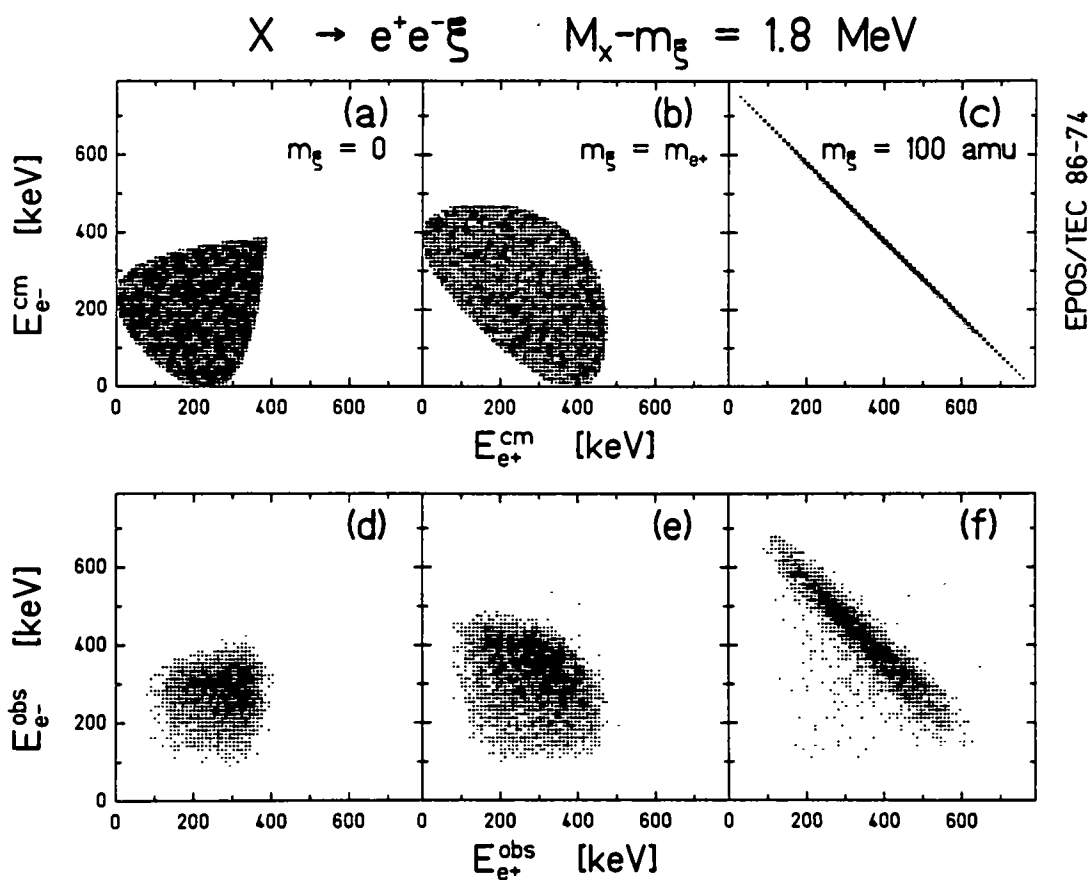


**Figure 7-15.** MCSPEC simulation of 3-body decay. (a-c)  $E_{e^+}$  vs.  $E_{e^-}$  in X object rest frame, given by phase space distributions only.  $m_\xi = 0$ ,  $m_{e^+}$ , and 100 amu, as marked. (d-f) Corresponding detected coincidence distributions assuming creation of the object at rest in heavy-ion CM system.

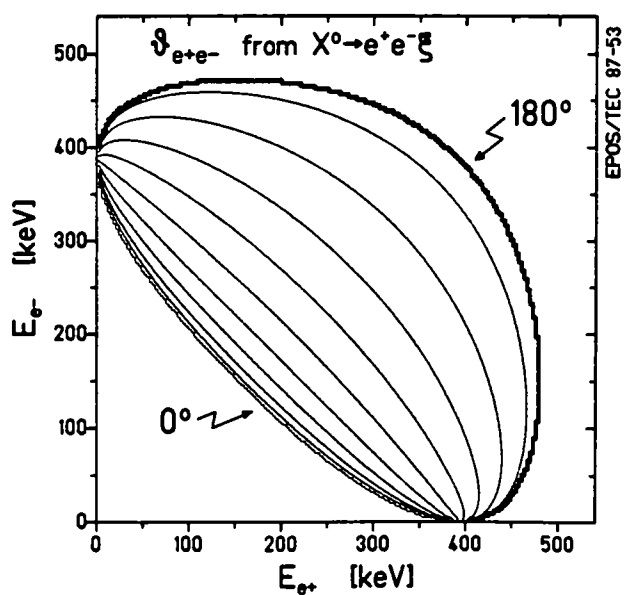


**Figure 7-16.** Contour plot (as a function of  $E_{e^+}$  and  $E_{e^-}$ ) of the angle between the emitted positron and electron in the rest frame of a 2.31 MeV object which decays into three bodies,  $e^+$ ,  $e^-$ , and  $\xi$ , with  $m_\xi = 511 \text{ keV}/c^2$ .

The particularly broad range of positron and electron energies expected from multi-body decays contradicts the pattern of the observed coincidence data. Even if the object decays at rest in the lab so that Doppler broadening is absent, the wide sum-energy and difference-energy distributions cannot be accommodated by the observed narrow  $E_{\Sigma}$  line, the well-defined difference-energy peak, or the absence of structure in adjacent cuts observed in the U+Th data. In order to fit the experimentally narrow  $E_{\Sigma}$  peak and the  $E_{\Delta}$  peak, the quantum numbers of the object must be such that only small, very specific regions of phase space are accessible to the decay products. Simple broad Dalitz patterns are, however, observed for most known mesons [Per82] suggesting that this is unlikely.

From very general considerations, it is clear that multi-body decays do not, in a natural way, describe the measured coincident structures. This conclusion is obviously reinforced by the preceding discussions of Sec. 7.3 which pointed out additional arguments against nuclear pair creation mechanisms, which are the most common multi-body processes in HI nuclear physics. Both the wide range of positron and electron energies and emission directions effectively rule out normal multi-body mechanisms as an explanation for the coincidence data.

#### **Sec. 7.5.4 Two-Body Decay from Rest in the Lab**

As is evident from Eqns. 7.3 and 7.4, the widths of the coincidence peaks are proportional to the laboratory velocity of the emitting system. No Doppler shifts or broadenings of the  $E_{\Sigma}$  and  $E_{\Delta}$  lines, or the individual positron and electron peaks occur if the source is at rest in the lab, i.e., if  $(\gamma\beta)_{em} = 0$ . Since multi-body final states lead to continuous distributions of positron and electron energy as indicated in Fig. 7-15, the narrow observed peaks therefore imply that the positron and electrons are, at least individually, each emitted monoenergetically in a two-body final state. The peak widths would therefore consist of intrinsic widths (from source lifetimes) folded with the detector lineshape response,

$$\Delta E_{e^+,e^-} = [ (N\tau_{e^+,e^-})^2 + (\delta E_{e^+,e^-})^2 ]^{1/2}. \quad (7.8)$$

If the positron and electron are emitted from different two-body processes, e.g.,  $X \rightarrow e^+\chi$  followed by  $\chi \rightarrow e^-\psi$ , the widths of the sum-energy and difference-energy peaks are nearly equal and are given by the quadrature sum of the individual positron

and electron linewidths,  $\Delta E_{\Sigma,\Delta} = [\Delta E_{e^+}^2 + \Delta E_{e^-}^2]^{1/2}$ . This clearly contradicts the narrow  $E_{\Sigma}$  and wide  $E_{\Delta}$  peak observed experimentally.

If on the other hand the positron and electron are decay products of the same two-body decay of a neutral object at rest in the lab, the intrinsic width of the parent is reflected in the sum-energy distribution,  $\Delta E_{\Sigma} = \hbar\tau_x$ . This energy, however, is divided equally between the emitted positron and electron. The individual positron and electron lines therefore exhibit only half the sum-energy peak width,  $\Delta E_{e^+} = \Delta E_{e^-} = \frac{1}{2}\Delta E_{\Sigma}$ , and the intrinsic difference-energy is identically zero. This pattern is evident in Fig. 7-17b which shows the detected positron-electron energy correlation diagram for a source lifetime of  $\tau_x \cong \hbar 100 \text{ keV} = 6.6 \times 10^{-21} \text{ sec}$ . It is the reverse of that predicted for a moving source (see Fig. 5-18), when the Doppler broadening dominates the intrinsic width of the state. If the source lives for longer than  $10^{-19} \text{ sec}$  ( $\delta E_{\Sigma} \leq 6.6 \text{ keV}$ ), the linewidths are determined by the detector resolution, as shown in Fig. 7-17a. The peak widths are  $\Delta E_{e^+,e^-} \sim 15 \text{ keV}$  for the positron and electron, and due to the convolution of both the positron and electron lineshapes,  $\Delta E_{\Sigma,\Delta} \sim 25 \text{ keV}$  for the sum- and difference-energy structures.

In each case, the width of the sum-energy line is at least as large as the individual positron and electron lines and the difference-energy structure,  $\Delta E_{\Sigma} \geq \Delta E_{e^+,e^-}$  and  $\Delta E_{\Sigma} \geq \Delta E_{\Delta}$ . The appearance of a narrow sum-energy peak in the data, accompanied by much wider positron, electron, and difference-energy peaks, therefore rules out the possibility that we are observing the two-body decay of an object at rest in the lab. Unless the observed patterns are due to a previously unknown mechanism which produces positrons and electrons correlated such that  $E_{e^+} + E_{e^-} = \text{constant}$  (similar to IPC or EPC), but limited to a small range about  $E_{e^+} \cong E_{e^-}$ , the widths of the coincidence peaks in the data must be due, in large part, to Doppler shifts associated with the emitter velocity.

### **Sec. 7.5.5 Emission Angle Correlation**

From these very general considerations, it is clear that the two-body decay of a neutral particle-like object provides the only simple explanation for the observed correlation of the peak widths. Moreover, the apparent equality of detected positron and electron energies arises naturally in this context. It should be noted, however, that the EPOS spectrometer does not allow a reconstruction of the decay in the CMS or a direct measurement of the invariant mass of the positron-electron pair. In fact, as described in Chaps. 2 and 5, the direct determination of the positron and electron

## Two-Body Decay of $X^0$ at Rest in Lab

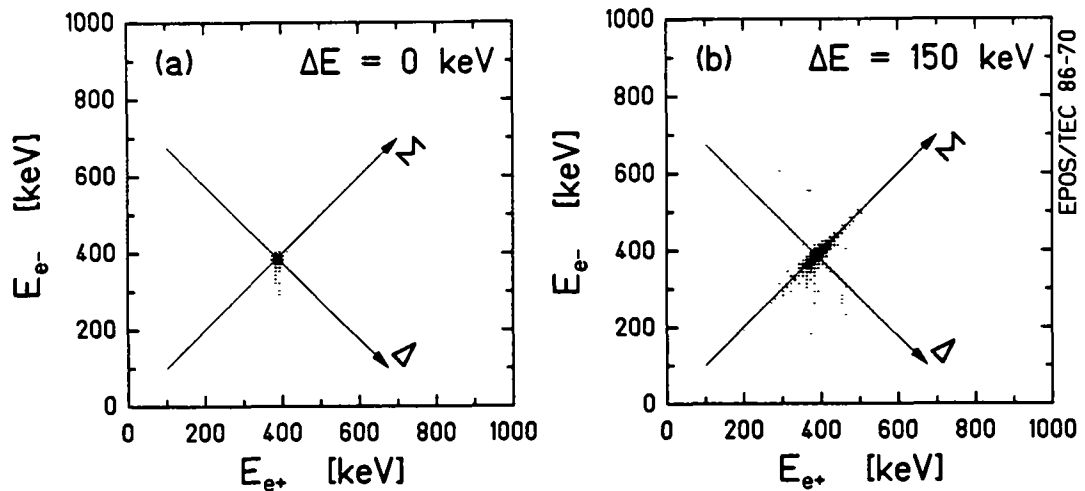


**Figure 7-17.** Expected pattern for two-body decay of an object at rest in lab, if (a) its intrinsic width is smaller than detector resolution (i.e.,  $\tau_X \geq 10^{-19}$  s), or (b)  $\Delta E_X = 150$  keV ( $\tau_X \cong 6.6 \times 10^{-21}$  s). Continuous background omitted for clarity.

laboratory emission angles is at best very coarse. From the discussion of Sec. 7.5.2 however, within the context of monoenergetic positron and electron emission (which is clearly indicated from the above discussion), the detected energies depend on the emission angle. As indicated in Eqns. 7.4, the widths of the  $E_\Sigma$  and  $E_\Delta$  peaks are linearly proportional to  $(\gamma\beta)_{em}$ , and under certain very general assumptions, taking the ratio of the widths cancels the source velocity dependence leaving only the emission angle information. As shown below, this provides a kinematic determination of  $\theta_{e^+e^-}^*$ .

**Sec. 7.5.5.1 Derivation:** From the discussion of Sec. 5.3, the FWHM's of the sum-energy and difference-energy peaks are quantitatively related to root mean square variations of the Doppler shifted laboratory energies.

$$\Delta E_{\Sigma,\Delta} \propto [ \langle (E_{\Sigma,\Delta} - \langle E_{\Sigma,\Delta} \rangle)^2 \rangle ]^{1/2}. \quad (7.9)$$

Assuming for illustration a nearly isotropic distribution of positron and electron emission angles (with a fixed relative  $\theta_{e^+e^-}^*$ ), the centroids of the  $E_\Sigma$  and  $E_\Delta$  peaks, from Eqn. 7.4, are  $\langle E_\Sigma \rangle = 2(\gamma_{em} W^* - m_e c^2)$  and  $\langle E_\Delta \rangle = 0$ , respectively. The

widths of the emitted laboratory sum-energy and difference-energy distributions are then given by,

$$\Delta E_{\Sigma, \Delta}^2 \propto [\int d\eta (2\gamma\beta_{em}P^*)^2 (\cos\theta_{e+}^* \pm \cos\theta_{e-}^*)^2] / [\int d\eta], \quad (7.10)$$

where

$$\int d\eta = \int \omega(\beta_{em}) d^3\beta_{em} \int \omega^*(\Omega_{e+}^*, \Omega_{e-}^*) d^2\Omega_{e+}^* d^2\Omega_{e-}^*$$

and +/- refers to  $E_{\Sigma}$  or  $E_{\Delta}$  respectively, as in Eqn. 7.4. Equation 7.10 provides for arbitrary source velocity and lepton emission-angle distributions.

The electron emission direction  $(\theta_{e-}^*, \varphi_{e-}^*)$  can be expressed in terms of the positron direction  $(\theta_{e+}^*, \varphi_{e+}^*)$  and the angle between the positron and electron momentum vectors  $(\theta_{e+e-}^*, \varphi_{e+e-}^*)$ . With  $\theta_{e+e-}^*$  and  $\varphi_{e+e-}^*$  expressed in a frame with the Z-axis aligned along the positron emission direction, the rotation transformation in Sec. 2.2.7 (Eqns. 2.62 with  $\theta_{em}$ ,  $\varphi_{em}$ ,  $\psi$ , and  $\Phi$  replaced by  $\theta_{e+}^*$ ,  $\varphi_{e+}^*$ ,  $\theta_{e+e-}^*$ , and  $\varphi_{e+e-}^*$ , respectively) gives

$$\cos\theta_{e-}^* = \cos\theta_{e+}^* \cdot \cos\theta_{e+e-}^* - \sin\theta_{e+}^* \cdot \sin\theta_{e+e-}^* \cdot \cos\varphi_{e+e-}^*$$

Thus,

$$[\cos\theta_{e+}^* \pm \cos\theta_{e-}^*] = [\cos\theta_{e+}^* (1 \pm \cos\theta_{e+e-}^*) \mp \sin\theta_{e+}^* \cdot \sin\theta_{e+e-}^* \cdot \cos\varphi_{e+e-}^*]. \quad (7.11)$$

With  $\theta_{e+e-}^*$  fixed, the angular integration in Eqn. 7.10 becomes

$$d^2\Omega_{e+}^* d^2\Omega_{e-}^* = d(\cos\theta_{e+}^*) d\varphi_{e+}^* d\varphi_{e+e-}^* \quad (7.12)$$

For a uniform distribution with  $\omega(\varphi_{e+e-}^*) = (2\pi)^{-1}$ , and  $\omega(\cos\theta_{e+}^*) = 1/2$ , integrating Eqn. 7.11 over solid angle yields zero, verifying that the simplification of using only the quadratic  $[\cos\theta_{e+}^* \pm \cos\theta_{e-}^*]^2$  term in Eqn. 7.10 is appropriate.

The solid angle integral of Eqn. 7.10 for isotropic positron emission gives,

$$\begin{aligned} (8\pi^2)^{-1} \int d(\cos\theta_{e^+e^-}^*) d\phi_{e^+e^-}^* [\cos\theta_{e^+}^* \pm \cos\theta_{e^-}^*]^2 \\ = 2/3 (1 \pm \cos\theta_{e^+e^-}^*). \end{aligned} \quad (7.13)$$

Equation 7.13 does not depend on source velocity and therefore factors out of the  $d^3\beta_{em}$  integral in Eqn. 7.10 leaving,

$$\Delta E_{\Sigma,\Delta} = 2\sqrt{2} P_{e^+,e^-}^* \langle (\gamma\beta)_{em}^2 \rangle^{1/2} (1 \pm \cos\theta_{e^+e^-}^*)^{1/2}. \quad (7.14)$$

For a fixed emitter velocity, e.g.,  $\beta_{em} = \beta_{cm}$ , the width takes on a maximum FWHM of  $4\gamma\beta P^*$  (for  $\cos\theta_{e^+e^-}^* = 0^\circ$  or  $180^\circ$  for  $E_\Sigma$  or  $E_\Delta$ , respectively) and a minimum of 0. Figure 7-18a illustrates the dependence of the  $E_\Sigma$  and  $E_\Delta$  peak widths on  $\theta_{e^+e^-}^*$  (solid and dashed curves). The identical momentum and velocity dependent factors in Eqn. 7.14 exactly cancel when the ratio of  $\Delta E_\Sigma/\Delta E_\Delta$  is formed,

$$R \equiv \Delta E_\Sigma/\Delta E_\Delta = [(1 + \cos\theta_{e^+e^-}^*)/(1 - \cos\theta_{e^+e^-}^*)]^{1/2} \quad (7.15)$$

Comparing this quantity, plotted in Fig. 7-18b for  $90^\circ < \theta_{e^+e^-}^* < 180^\circ$ , to the measured data provides a very direct determination of the relative positron-electron emission angle. A small ratio, such as appropriate for the narrow measured  $E_\Sigma$  peaks in light of the wide  $E_\Delta$  structures, sets a stringent limit on the minimum opening angle between the positron and electron in the rest frame of the source, and therefore represents a quantitative indication of back-to-back emission.

**Sec. 7.5.5.2 Finite Detector Resolution:** Two additional effects must be considered before deriving experimental limits on  $\theta_{e^+e^-}^*$  from the data. First, the finite detector energy resolution broadens both the  $E_\Sigma$  and  $E_\Delta$  peaks. Using  $\delta E_{\Sigma,\Delta} \cong 25$  keV (1986 arrangement), which adds in quadrature with Eqn. 7.15, the observed width is

$$\Delta E_{\Sigma,\Delta} \cong [(\delta E_{\Sigma,\Delta})^2 + 8P^{*2} \langle (\gamma\beta)_{em}^2 \rangle (1 \pm \cos\theta_{e^+e^-}^*)]^{1/2}, \quad (7.16a)$$

or,

$$\begin{aligned} R = \{[\varepsilon^2 + (1 + \cos\theta_{e^+e^-}^*)]/[\varepsilon^2 + (1 - \cos\theta_{e^+e^-}^*)]\}^{1/2}, \\ \varepsilon = \delta E_{\Sigma,\Delta}/[2\sqrt{2}P^* \langle (\gamma\beta)_{em}^2 \rangle^{1/2}]. \end{aligned} \quad (7.16b)$$

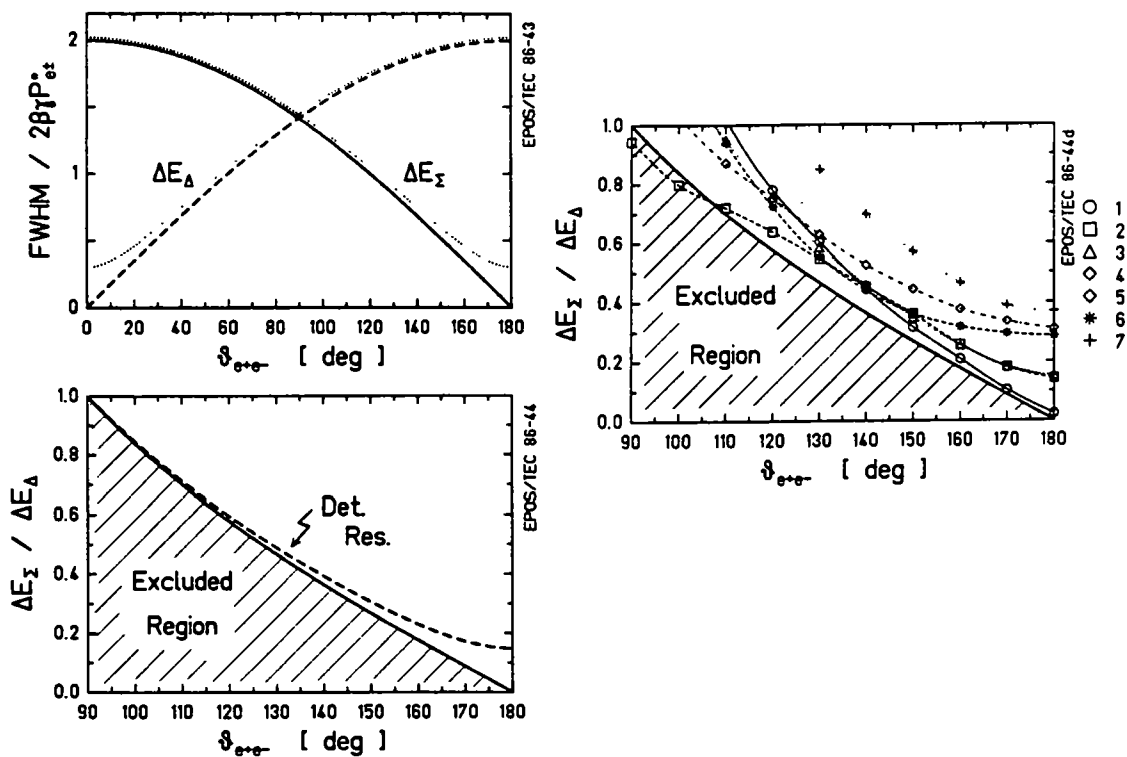


**Figure 7-18.** Calculated width of the  $E_{\Sigma}$  (solid curve) and  $E_{\Delta}$  (dashed line) structures as a function of the fixed angle between their momentum vectors in the rest frame of their mutual source (top left). Dotted lines include experimental energy resolution. Ratio of the sum-energy to difference-energy peak widths (lower left), plotted versus fixed opening angle, assuming uniform detection efficiency. Ratio calculated for several non-uniform emission distributions and detection efficiency (right), as described in text.

As indicated by the dotted curves in Figs. 7-18a,b, the minimum expected width is  $\delta E_{\Sigma,\Delta}$  and the minimum value of the ratio is  $R \geq (1 + 2/\epsilon^2)^{-1/2} \cong (\delta E_{\Sigma,\Delta} / \Delta E_{\Delta})$ , for  $\Delta E_{\Delta} \gg \delta E_{\Sigma,\Delta}$ . The ratio curve (Fig. 7-18b) flattens out for  $\theta_{e^+e^-} > 170^\circ$  due to the experimental resolution. In principle, this corresponds to an experimental kinematic opening-angle resolution of  $\delta\theta_{e^+e^-} \cong 10^\circ$ .

**Sec. 7.5.5.3 Non-Uniform Emission and Detection:** The second important consideration is the role of the EPOS detection efficiency and the emission distributions  $\omega(\beta_{em})$  and  $\omega(\Omega_{e^+}, \Omega_{e^-})$  on the ratio of  $E_{\Sigma}$  to  $E_{\Delta}$  widths. Transport and detection efficiencies enter the integrand  $\int d\eta$  of Eqn. 7.10, and the  $[\int d\eta]^{-1}$  normalization terms cancel when taking the ratio,

$$R = \frac{\int d\eta [2(\gamma\beta)_{em} P^*]^2 (\cos\theta_{e^+}^* + \cos\theta_{e^-}^*)^2}{\int d\eta [2(\gamma\beta)_{em} P^*]^2 (\cos\theta_{e^+}^* - \cos\theta_{e^-}^*)^2} \quad (7.17)$$

with,

$$\begin{aligned} \int d\eta \equiv & \int \omega(\beta_{em}) d^3\beta_{em} \\ & \times \int d^2\Omega_{e^+}^* d^2\Omega_{e^-}^* \omega^*(\Omega_{e^+}^*, \Omega_{e^-}^*) \cdot \epsilon_{e^+}(E_{e^+}, \Omega_{e^+}^*) \cdot \epsilon_{e^-}(E_{e^-}, \Omega_{e^-}^*). \end{aligned}$$

As is evident from Fig. 7-14 for isotropic emission from a source moving with  $\beta_{em} = v_{CM}/c$ , the difference-energy peak widths (for  $\theta_{e^+e^-}^* = \theta_0$ ) are consistently smaller than the corresponding  $E_\Sigma$  peaks for  $\theta_{e^+e^-}^* = 180^\circ - \theta_0$ . The ratio for CM emission therefore is larger (smaller  $\Delta E_\Delta$ ) for any given  $\theta_{e^+e^-}^*$ . As shown in Fig. 7-18c (circles), the opening angle between the positron and electron in the rest frame of the source must therefore be larger to achieve a given experimental ratio, than for the idealized case derived in Eqns. 7.15 and 7.16 (Fig. 7-18b).

Interestingly, the ratio of widths versus  $\theta_{e^+e^-}^*$  behaves in a very similar manner for any source velocity distribution or positron emission angle distribution. This is demonstrated in Fig. 7-18c, where  $R(\theta_{e^+e^-}^*)$  has been calculated by MCSPEC simulation for a variety of different assumptions concerning the emission distributions (curves labelled 1-7) including: (1)  $X^0$  created at rest in the CMS system; (2)  $X^0$  emitted isotropically from CMS with  $P_x^* = 0.2 \cdot M_{X^0} c$ ; (3)  $X^0$  travelling in beam direction with  $v_{em} = 2v_{CM}$ ; (4)  $X^0$  emitted isotropically in lab with  $v_x = v_{CM}$ ; (5)  $X^0$  emitted along the solenoid axis; (6) positron emitted with  $|Y_{10}|^2$  angular distribution; or (7) positron emitted with  $|Y_{11}|^2$  angular distribution. Several other scenarios have also been modelled, and for all of these situations, although the positron, electron,  $E_\Sigma$ , and  $E_\Delta$  peaks become narrow, or broad, or asymmetric, or almost washed out, the ratio  $\Delta E_\Sigma / \Delta E_\Delta$  consistently lies above the curve given by Eqn. 7.15. For whatever reason, it appears empirically that as soon as the acceptance of the detected events, or the emission distribution of the leptons or emitting source, is decreased the difference-energy peak becomes narrower more quickly than the sum-energy line. The idealized solid curve in Fig. 7-18b, which physically corresponds to the limit of isotropic emission with uniform detection in the lab, represents an essentially *model-independent* lower limit of the positron-electron opening angle for a given ratio of the widths.

**Sec. 7.5.5.4 Comparison to the Data.:** The empirical lower limit for  $\theta_{e^+e^-}^*$  given R (Eqn. 7.16) is the appropriate relation to compare to the measured data to obtain an experimental limit on the electron-positron opening angle. This is plotted in Fig. 7-19 as  $(\theta_{e^+e^-}^*)_{\min}$  versus  $R \equiv \Delta E_{\Sigma}/\Delta E_{\Delta}$ . The lower-left portion of the plot is excluded to the experimental data. The dashed curve includes the finite detector resolution,  $(\delta E_{\Sigma,\Delta})_{\min} \cong 25$  keV. Table 7-1 lists the sum- and difference-energy peak widths (gaussian FWHM, i.e.,  $2.548 \times$  St. Dev.) for the  $E_{\Sigma} \sim 610$  and  $\sim 815$  keV coincident structures.

The 95% Confidence Level on the ratio, i.e.,  $R_{\text{exp}} + 1.94\sigma_R$ , is plotted for each structure at the experimental lower limit for  $\theta_{e^+e^-}^*$  (dashed curve) in Fig. 7-19. The shaded regions indicate the allowed range of  $\theta_{e^+e^-}^*$  and R, given the widths of the measured peaks. The square and circle correspond respectively to the 610 and 815 keV sum-energy lines observed in U+Th collisions. Their upper limits on R translate into the following minimum opening angles:  $\theta_{e^+e^-}^* \geq 166^\circ$  ( $E_{\Sigma} = 612$  keV), and  $\theta_{e^+e^-}^* \geq 147^\circ$  ( $E_{\Sigma} = 817$  keV), at 95% C.L., respectively.

The data strongly suggest back-to-back positron-electron emission corresponding to the two-body decay of a neutral object. It should be noted that the 815 keV line in particular, whose sum-energy width is  $\cong 3\sigma$  larger than that expected for back-to-back emission,  $(\Delta E_{\Sigma})_{\text{exp}} \cong 25$  keV, may still be statistically consistent with  $\theta_{e^+e^-}^* = 180^\circ$ . If not simply a statistical fluctuation, this wider  $E_{\Sigma}$  peak could in principle reflect a larger mean emitter velocity (as discussed below), or possibly the presence of two very closely spaced lines.

**Sec. 7.5.5.5 Possible Difficulties:** It should be emphasized that despite the rather stringent limits set on  $\theta_{e^+e^-}^*$  by the kinematic analysis of Fig. 7-19, the emission angles are not directly measured in the EPOS spectrometer and the two-body decay of the source is not definitively proven. If the underlying assumptions leading to Eqn. 7.17 are false, the kinematic interpretation of the measured experimental peak widths could be mitigated. For instance, two basic points have been assumed in this derivation -- namely, that (1) the positron and electron are emitted with discrete energies, and (2) their correlated broadening is due to Doppler shifts. These in turn were based on the unsuitability of calculated 3-body final states and two-body decays at rest in the lab in describing the data.

Table 7-1 Opening Angle and Velocity Limits

$\langle E_{\Sigma} \rangle$	$\Delta E_{\Sigma}(\text{FWHM})$	$\Delta E_{\Delta}(\text{FWHM})$	$R_{\text{max}}$	$\sigma(E_{\Delta})_{\text{max}}$	$\alpha_{\text{max}}$
$612 \pm 4$ keV	$22.6 \pm 2.9$ keV	$153 \pm 9$ keV	0.187	78.2	0.037
$817 \pm 5$ keV	$39.5 \pm 3.6$ keV	$158 \pm 21$ keV	0.328	76.4	0.035

One example of a contrived mechanism which circumvents this analysis is a source of coincident positron and electrons such that, like IPC, their energies add to a constant  $E_{e^+} + E_{e^-} = E_{\Sigma}^{\text{em}}$ . This energy correlation would succeed in explaining a wide  $E_{\Delta}$  and narrow  $E_{\Sigma}$  peak, however the emission must further be limited to  $|E_{e^+} - E_{e^-}| \leq 100$  keV in order to agree with the measured  $\Delta E_{\Delta}$  peak width. Moreover, if the source is moving in the laboratory, the distribution of  $e^+$  and  $e^-$  emission angles must be constrained to maintain a narrow  $E_{\Sigma}$  peak. As described in Sec. 7.3, this cannot be related to external pair creation or any known IPC process both because of the known broad energy distributions and emission angle characteristics of pair creation mechanisms, and from straightforward intensity arguments.

If this hypothesized source is at rest in the lab, at least the narrow  $E_{\Sigma}$  peak could be trivially explained. However if moving, e.g., with  $\beta_{\text{em}} \sim \beta_{\text{cm}}$ , the possible emission angle distribution would be limited by the narrow  $E_{\Sigma}$  peak width of  $\Delta E_{\Sigma} \leq 25$  keV for the 610 keV  $E_{\Sigma}$  line. At a 95% confidence level,  $\Delta E_{\Sigma}^{\text{obs}} < 28.2$  keV. After correcting for detector resolution ( $\delta E_{\Sigma} \sim 20$  keV) the intrinsic sum-energy peak width must be  $\Delta E_{\Sigma}^{\text{exp}} < 20$  keV.

For uncorrelated emission, this would require that the positron and electron are each emitted in a narrow range of  $\theta_{e^+}^*$  and  $\theta_{e^-}^*$  with respect to the source motion so that  $\Delta E_{\Sigma} \cong [(\Delta E_{e^+})^2 + (\Delta E_{e^-})^2]^{1/2} \leq 20$  keV. The Doppler broadening of the individual positron and electron peaks for emission into a solid angle region  $\Delta(\cos\theta_{e^+}^*)$  about  $\theta_0^*$  is,

$$\Delta E_{e^+} = \langle (\gamma\beta)_{\text{em}}^2 \rangle^{1/2} P_{e^+}^* |\Delta \cos\theta_{e^+}^*|, \quad (7.18)$$

with a similar expression for  $\Delta E_{e^-}$ . At  $E_{e^+}^* \cong E_{e^-}^* \cong 380$  keV, and  $\beta_{\text{em}} \sim \beta_{\text{cm}}$ , to maintain  $\Delta E_{\Sigma} \leq 20$  keV requires,

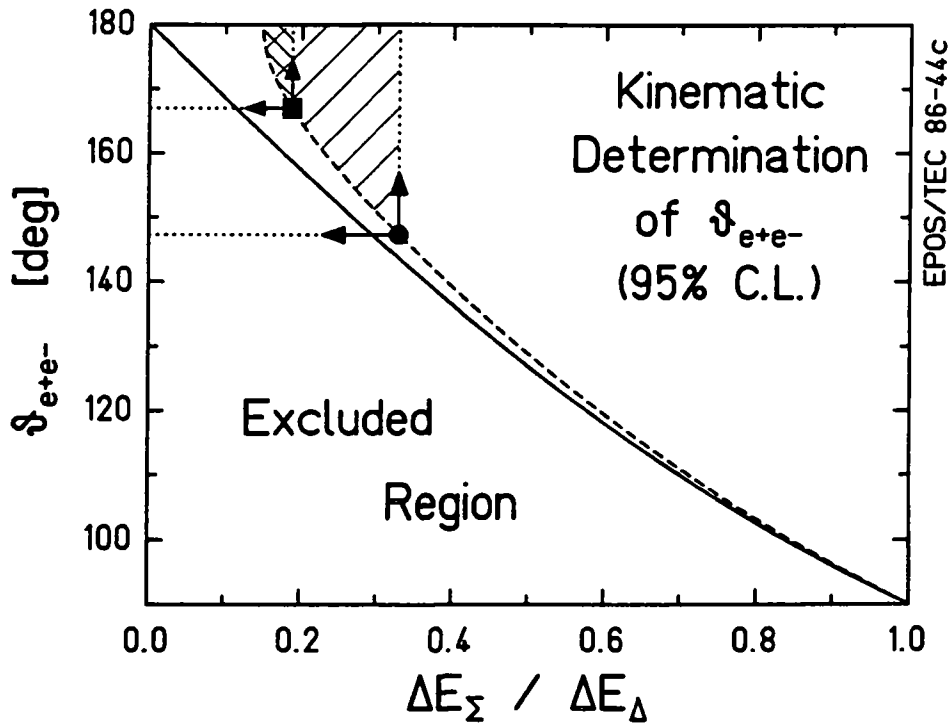


**Figure 7-19.** Ratio of sum- to difference-energy RMS peak widths as a function of fixed  $\theta_{e^+e^-}$ . The solid curve shows the kinematic broadening of emitted  $e^+$  and  $e^-$ ; dashed line plots the ratio of widths observed in EPOS for emission from the CMS (Fig. 7-14). Dotted lines include detector energy resolution.  $R \leq 0.328$  (95% C.L.) implies  $\theta_{e^+e^-} > 147^\circ$  for  $\sim 815$  keV line, and  $R \leq 0.187$  (95% C.L.) implying  $\theta_{e^+e^-} > 166^\circ$  for  $\sim 610$  keV peak.

$$\begin{aligned} \Delta E_\Sigma &= \langle (\gamma\beta)_{em}^2 \rangle^{1/2} P_{e^+,e^-} [(\Delta \cos \theta_{e^+}^*)^2 + (\Delta \cos \theta_{e^-}^*)^2]^{1/2} \\ &\cong (41 \text{ keV}) [(\Delta \cos \theta_{e^+}^*)^2 + (\Delta \cos \theta_{e^-}^*)^2]^{1/2} \leq 20 \text{ keV}. \end{aligned}$$

For  $|\Delta \cos \theta_{e^+}^*| \cong |\Delta \cos \theta_{e^-}^*|$ ,

$$|\Delta \cos \theta_{e^+}^*| \leq 0.35. \quad (7.19)$$

This would entail a very sharp angular distribution in  $\Delta \Omega_{e^+,e^-}^*$  of less than 18% of  $4\pi$  sr. The limiting maximum spread in  $\theta_{e^+}^*$  varies inversely with  $(\gamma\beta)_{em}$  so that for a source moving faster than  $v_{CM}$  a correspondingly smaller angular distribution would be required to fit the data. MCSPEC calculations indicate that  $|Y_{\ell m}|^2$  distri-

butions, for example, are not narrow enough to reproduce the narrow measured sum-energy peaks for  $\ell = 0, 1, \text{ or } 2$  (see Fig. 7-27).

The semi-classical limit on the positron (or electron) angular momentum presented in Chap. 4.3 further argues against an angular distribution as sharp as required by Eqn. 7.19 being produced in nuclear or inner shell atomic processes. As mentioned in Sec. 4.5, [Lic85] pointed out that, in principle, anisotropic positron emission might result from a large extended source, e.g., a di-nuclear configuration of  $\sim 500$  fm. Recently Lichten suggested that, since the amplitude of the electron ejected from a specific orbital adds coherently with the amplitude of the induced positron created by filling that vacancy, dynamic positrons and  $\delta$ -electrons could have correlated energies and emission angles which might conspire to produce the observed narrow sum-energy peaks. No model-calculations are presently available for comparison to the data. It should be stressed, however, that sharp distributions have been observed for electron emission only when the kinematics of the colliding ions are nearly exactly specified [Nie85]. The EPOS acceptance is large for both the positrons and electrons, and as noted in in Chap. 6, the coincidence structures are observed over a large range of HI scattering angles. The limit on the FWHM of the emission angle distribution for the coincident positron and electron extracted from the experimental data (Eqn. 7.19) provides a standard against which future hypothetical origins developed along these lines must be compared.

In summary, within the very general assumption that the coincident positron and electron are emitted with discrete energies from a moving source, the widths of the  $E_{\Sigma}$  and  $E_{\Delta}$  peaks provide a kinematic determination of their relative emission angle, in the rest frame of the emitter. For each of the measured sum-energy lines,  $\theta_{e^+e^-}^* \geq 145^\circ$  (95% C.L.), which is consistent with, and strongly argues for, back-to-back emission from the two-body decay of a neutral object.

### **Sec. 7.5.6 Emitter Velocity**

From the preceding kinematic arguments, it is clear that both the equal energy of the observed positron and electron signals, and their angular correlation, are best explained by a process that closely resembles the two-body final state of a decaying neutral object. Within this context, the pattern of positron-electron energy correlation becomes more complicated if that neutral object,  $X^0$ , is not created nearly at rest in the heavy-ion collision. Its total laboratory energy would then be kinematically shifted by its motion relative to the emitting frame. For example, a particle

emitted from the CMS with momentum  $P_x^*$  and total energy  $W_x^* = (P_x^{*2} + M_x^2)^{1/2}$  has a lab energy of

$$W_x = \gamma_{cm}[(P_x^{*2} + M_x^2)^{1/2} + \beta_{cm}P_x^* \cos\theta_x^*], \quad (7.20)$$

where  $\theta_x^*$  is the  $X^0$  emission angle in the CMS with respect to  $v_{CM}$ . The sum-energy line at  $E_\Sigma = (W_x - 2m_e c^2)$  is therefore also shifted from  $(M_x c^2 - 2m_e c^2)$  and will of course be broadened. For isotropic creation, the shift is  $\Delta E_\Sigma = (\gamma_{cm} W_x^* - M_x c^2)$ , which is just the additional mean laboratory kinetic energy of the object. The sum-energy peak width is  $\Delta E_\Sigma = 2(\gamma\beta)_{cm} P_x^*$ .

Figure 7-20 presents the positron-electron energy correlation pattern (left panel) for a neutral object of mass  $1.8 \text{ MeV}/c^2$  emitted isotropically from the CM system, with discrete kinetic energies  $T_x = 0, 10, 50, 200 \text{ keV}$ . For each  $T_x$ ,  $5 \times 10^4$  detected positrons were simulated. The coincidence detection efficiencies,  $\epsilon$ , are shown as marked. For clarity, the lineshape response of the detectors was omitted. Even for very small energies, Fig. 7-20 indicates that the width of the individual positron and electron peaks and the difference distribution (right panel) broaden very rapidly. Their mean positions, however, remain approximately constant. In contrast, the sum-energy peak centroid shifts linearly with  $T_x$  (center panel). The  $E_{e+}$ ,  $E_\Sigma$ , and  $E_\Delta$  peak widths are summarized as a function of the emitted  $X^0$  kinetic energy in Fig. 7-21b.

An important consequence of the motion of the  $e^+e^-$  source is the subsequent decrease in the laboratory of the opening angle between the positron and electron. As the velocity of the object increases, the back-to-back spatially correlated positron and electron are swept forward in the lab system. The positron lab angle is given by,

$$\theta_{e+}^{\text{lab}} = \tan^{-1}[\sin\theta_{e+} / \gamma_x (\cos\theta_{e+} + \beta_x / \beta_{e+}^*)], \quad (7.21)$$

with a similar expression for  $\theta_{e-}$ , where  $\gamma_x$  and  $\beta_x$  denote the  $X^0$  lab velocity and  $\beta_{e+}^*$  is the positron velocity in the  $X^0$  rest frame,

$$\beta_{e+}^* = P_{e+}^* / (E_{e+}^* + m_e c^2).$$

$$X^0 \rightarrow e^+e^- \quad M_X = 1.8 \text{ MeV}/c^2$$

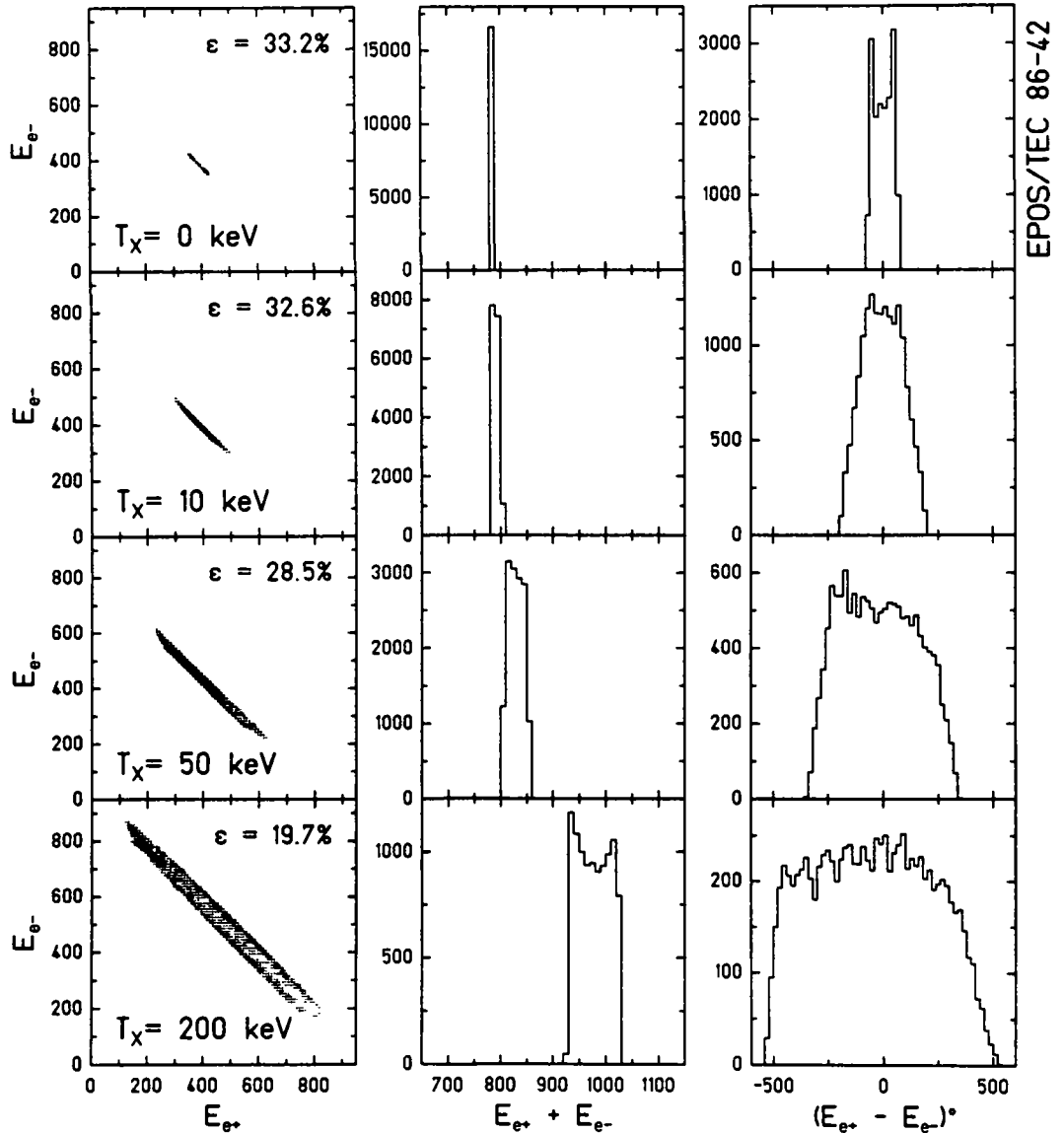


**Figure 7-20.** Simulation of  $1.8 \text{ MeV}/c^2$   $X^0$  created isotropically in CM with fixed kinetic energy  $T_X$  as explained in text (detector resolution omitted).

The opening angle, assuming back-to-back emission, is approximately  $\theta_{e^+e^-} \cong 2 \cdot \tan^{-1}(\beta_{e^+}/\beta_X \gamma_X)$ . Figure 7-21a presents an exact calculation of the mean laboratory opening angle as a function of the  $X^0$  kinetic energy in the CMS. Isotropic  $X^0$  emission in the CMS was assumed for masses of 1.6 and 1.8

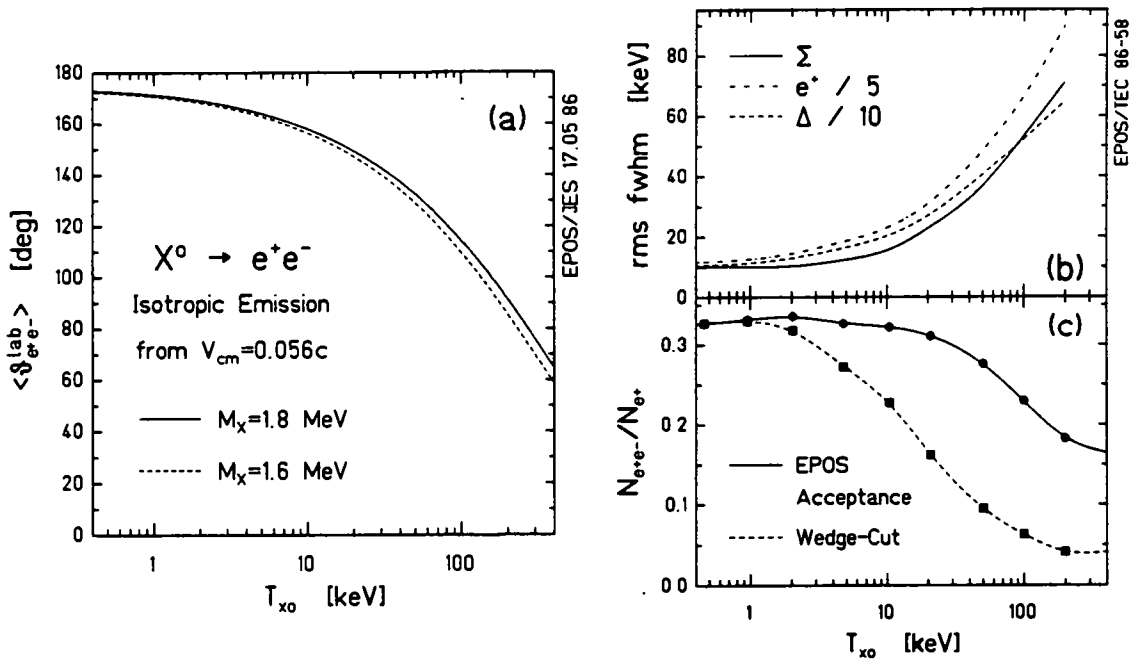


**Figure 7-21.** (a) Mean laboratory  $e^+/e^-$  opening angle for two-body decay of  $X^0$  emitted isotropically from CM system with fixed kinetic energy  $T_{x_0}$ . For creation at rest,  $\theta_{e^+e^-} = 172^\circ$  from CMS motion. (b) Widths of sum-energy, difference-energy ( $\div 10$ ), and individual positron peaks ( $\div 5$ ) vs.  $T_{x_0}$ . (c) Detection efficiency of coincidence relative to positron events. Solid-line indicates EPOS acceptance, dashed curve is portion of events in wedge-shaped contour.

$\text{MeV}/c^2$ . For creation at rest in the CMS,  $v_x = v_{\text{CM}}$ , the positron-electron opening angle is already reduced from  $180^\circ$  to  $\theta_{e^+e^-} \cong 172^\circ$ .

This decrease in opening angle naturally leads to a decrease in the detection efficiency as the mean laboratory positron-electron angular distribution deviates farther from a back-to-back orientation. The solid line in Fig. 7-21c plots the absolute acceptance of the EPOS spectrometer for the energetic neutral object. From the spreading of events in the energy correlation plane evident in Fig. 7-20, the portion of the coincident data within the wedge-shaped sum-energy projection also decreases with increasing energy. This therefore reduces the analysis efficiency as shown by the dashed line in Fig. 7-21c. In order to produce a given coincidence peak intensity, neutral objects emitted with higher energy must be created with larger cross-section to compensate for the drop in detection efficiency.

Those objects created with very large energies in the collision produce coincident positron-electron events which are detected with small probability and whose correlations are distributed over a wide area in the energy-energy plane. They therefore tend to merge with the bulk of continuous dynamic positron,  $\delta$ -electron, and nuclear IPC pair backgrounds. Only those  $X^0$ 's created with low velocities contribute substantially to intensity in the sum-energy peak. This parallels the discussion of Fig. 5-1 which showed that even the creation of a particle with a broad range of momenta can lead to the appearance of narrow positron structures.

To place this on a quantitative footing, Fig. 7-22 presents the expected coincidence yields for various distributions of  $X^0$  velocity. In order to include both the  $P^2$  phase space volume element, and the anticipated exponential decrease in production at large momentum, an  $X^0$  momentum distribution of the form

$$\omega(P_X) = P_X^2 \cdot \exp[-P_X/\alpha] \quad (7.22)$$

has been assumed. The four simulations for different values of  $\alpha = 0.02, 0.05, 0.1,$  and  $0.2 M_{Xc}$  correspond to average emitted particle kinetic energies of 4.2, 26, 99, and 352 keV, respectively (assuming  $M_X = 1.8$  MeV). In each case,  $5 \times 10^4$  detected positrons were simulated. The coincident positron-electron detection efficiency (including detector response) ranged from 29.9% ( $\alpha=0.02$ ) to 18.6% ( $\alpha=0.2$ ). The relative size and shape of the sum-energy peaks are shown to absolute scale in Fig. 7-22. (Note the expanded scale for the  $\alpha = 0.1$  and  $0.2 M_{Xc}$  simulations.) For increasingly broad distributions, the total positron energy spectra (parts (a) in Fig. 7-22) become quite wide over a range in which the sum-energy lines (parts (c)) remain fairly narrow.

The superposition of low momentum components, for which the sum-energy is kinematically shifted by small amounts, together with the distribution of larger  $X^0$  momenta, leads to peaks in the positron, electron, sum-energy, and difference-energy spectra which are centered at nearly the same position as expected for creation of  $X^0$ 's at rest in the CMS. The detected coincidence intensity is focussed within the region  $E_{e+} \cong E_{e-}$ , as suggested by the triangular shape of the difference-energy spectra, centered at  $E_{\Delta} = 0$  keV. Up to rather large mean  $X^0$  energies of  $T_X \sim 100$  keV, very little structure emerges in cuts adjacent to the positron and electron peak regions. This surprising result, in the context of the broad positron energy distribution, underlines the difference between kinematic correlations for this

$$\omega^*(P_X^*) = P_X^{*2} e^{-P_X^*/\alpha}$$

- (1)  $\alpha = 0.02 M_{Xc}$ ,  $\langle T_X \rangle = 4.2 \text{ keV}$   
 (2)  $\alpha = 0.05 M_{Xc}$ ,  $\langle T_X \rangle = 26 \text{ keV}$   
 (3)  $\alpha = 0.10 M_{Xc}$ ,  $\langle T_X \rangle = 99 \text{ keV}$   
 (4)  $\alpha = 0.20 M_{Xc}$ ,  $\langle T_X \rangle = 352 \text{ keV}$

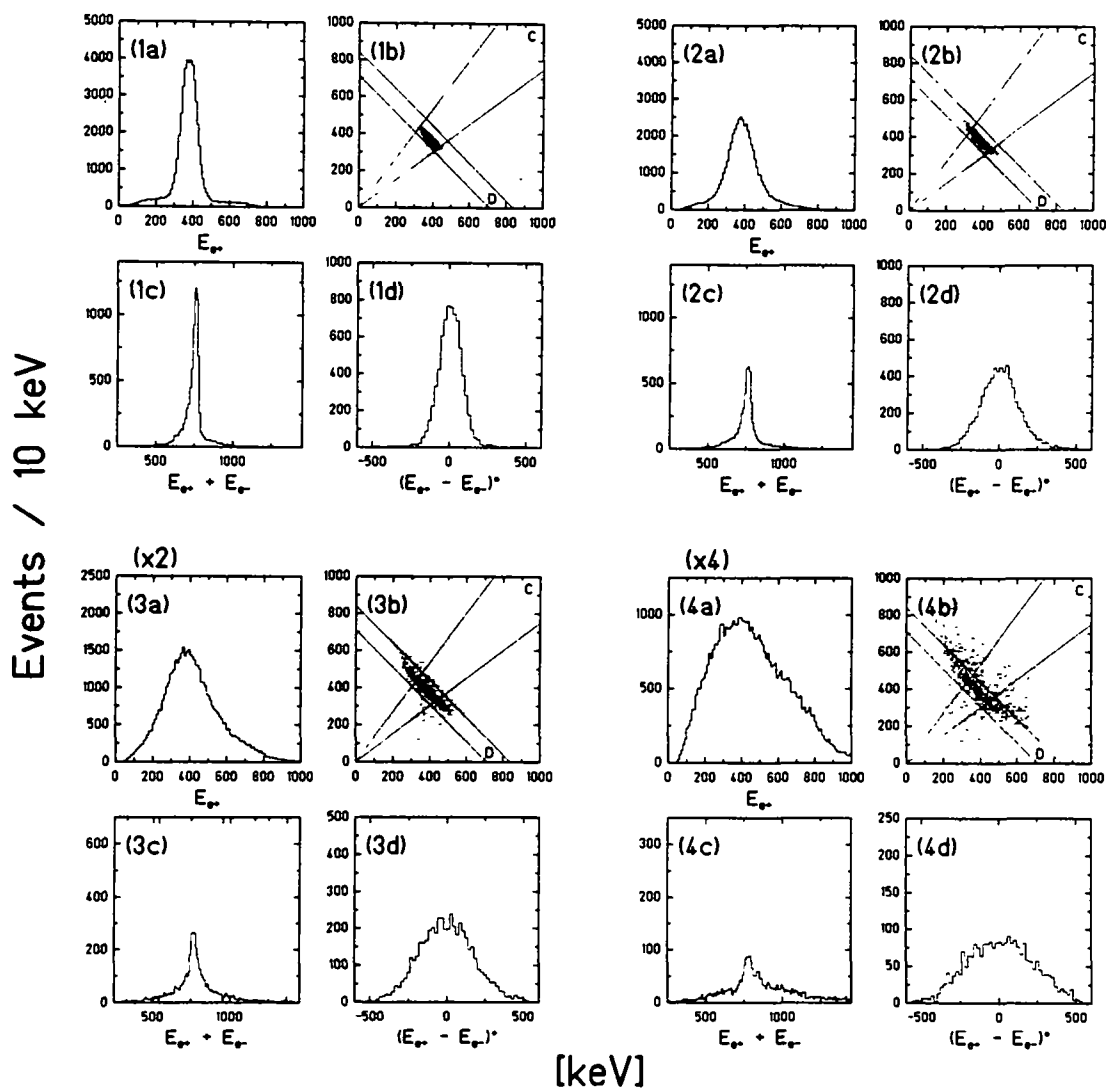
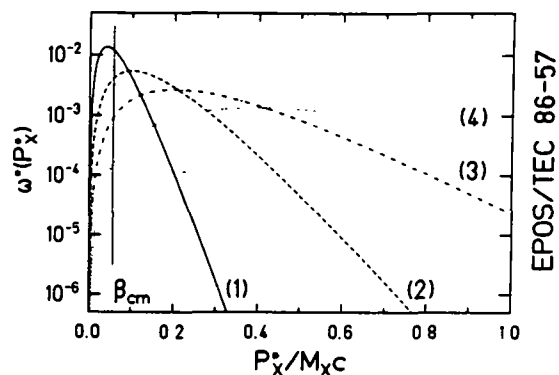


**Figure 7-22.** MCSPEC simulation of the two-body decay of  $1.8 \text{ MeV}/c^2$  objects created isotropically in the CM system with a distribution of momenta. (a) Total detected  $e^+$ , (b) coincident  $e^+/e^-$ , (c) sum-energy, and (d) difference-energy distributions. Quadrants correspond to  $w(P) = P^2 \exp(-P/\alpha)$ ,  $\alpha = 0.02, 0.05, 0.1$ , and  $0.2 M_{Xc}$ , as marked. 50000 detected  $e^+$  generated for each case. Note expanded scale for  $\alpha = 0.1, 0.2 M_{Xc}$ . (Detector response is included.)

case and those observed for IPC, where the much broader difference-energy spectrum and the presence of structure in adjacent cuts were sufficient to rule out a nuclear origin (Sec. 7.3). The angular correlation is also different. For  $\alpha \leq 0.1 M_{\chi}c$ , the positron and electron typically exhibit large laboratory opening angles,  $\theta_{e^+e^-} > 90^\circ$ . The detection efficiency of Lorentz boosted and energy broadened particle-decay products is therefore still much larger than for IPC, whose angular distribution peaks at  $\theta_{e^+e^-} = 0^\circ$  (see, e.g., Figs. 5-21 and 7-8). One requires only a moderate increase in the production cross-section (beyond the  $\cong 1-3\%$  of the total positron yield, as discussed in Chap. 6, appropriate for  $X^0$  creation at rest in the CMS) in order to adequately describe the observed data.

Figure 7-23 presents a determination of the limits on the possible  $X^0$  momentum distribution which could describe the measured data. For the simulations of Fig. 7-22, the  $E_{\Delta}$  spectrum best reflects the mean velocity  $\langle (\gamma\beta)_{em}^2 \rangle^{1/2}$  of the source, and its width,  $\Delta E_{\Delta}$  was therefore used in this analysis. Since the Doppler broadening is proportional to  $P_{e^+}^*$ , in order to compare structures have different sum-energies one must account for the dependence of the width on the positron momentum. As a reference value, an  $X^0$  mass of  $1.72 \text{ MeV}/c^2$  has been assumed in Fig. 7-23, which plots the expected width versus  $\alpha$ , assuming that the object is isotropically emitted from the CMS with a momentum distribution given by Eqn. 7.22 (solid curve). The  $E_{\Delta}$  peak widths from Table 7-1 must be adjusted to the Doppler-broadened width expected for the reference positron momentum by multiplying  $(\Delta E_{\Delta})_{obs}$  by  $(P_{e^+}^{ref}/P_{e^+}^{obs})$ . This yields "corrected"  $E_{\Delta}$  peak widths (standard deviations) of  $\sigma_{corr}(610) = 70.6 \pm 3.9 \text{ keV}$ , and  $\sigma_{corr}(815) = 60.7 \pm 8.0 \text{ keV}$  for the  $\sim 610$  and  $\sim 815 \text{ keV}$  sum-energy structures, respectively. At a 95% confidence level, each of these provides an upper limit of  $\sigma_{max} \cong 78 \text{ keV}$ , which is indicated by the shaded line in Fig. 7-23. The largest momentum distribution parameter which is consistent with the experimental data is  $\alpha \leq 0.035 \cdot M_{\chi}c$ , i.e.,  $\alpha \leq 60 \text{ keV}/c$  (or  $\langle T_{\chi} \rangle \cong 9.5 \text{ keV}$ ).

An MCSPEC simulation of  $X^0$ 's produced isotropically from the CMS with Eqn. 7.22 using  $\alpha = 0.035 \cdot M_{\chi}c$  is shown in Fig. 7-24. It has additionally been assumed that 4.2% of the total positron yield is due to these decays in order to explain the 32  $E_{\Sigma}$  peak counts out of  $\sim 10^4$  observed  $e^+$ 's for the  $E_{\Sigma} = 750 \text{ keV}$  peak. For the 610 and 815 keV lines, an  $X^0$  production cross-section amounting to about 1.5% to 3% of the total  $e^+$  yield is sufficient. These  $X^0$  production rates are easily consistent with the  $\sim 20\%$  uncertainty in the absolute magnitude of dynamic and nuclear

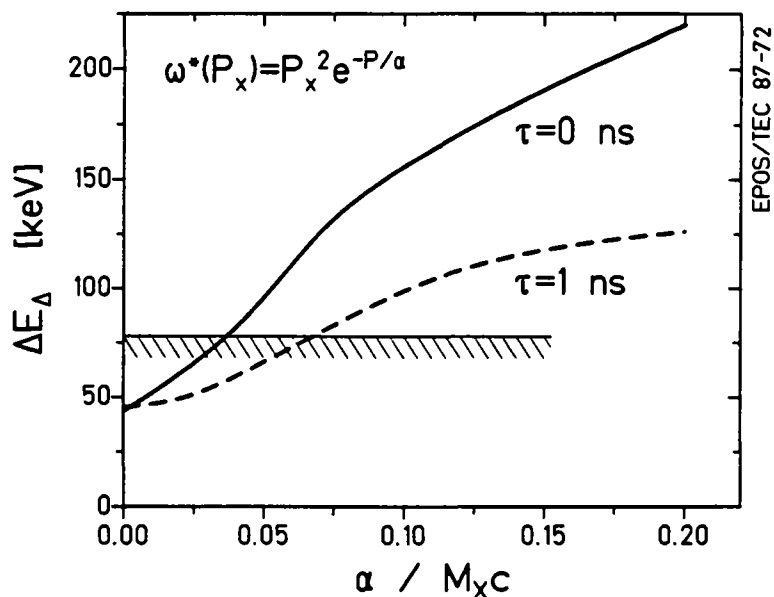


**Figure 7-23.** Width ( $1\sigma$  st. dev.) of the difference-energy structure calculated for  $X^0$  decay assuming a source momentum distribution of the form  $P^2 \exp(-P/\alpha)$ , plotted versus  $\alpha$  for decay near the solenoid axis (solid line). Dashed line includes the velocity filter effect assuming a source lifetime of  $10^{-9}$  s. Hatched region denotes the 95% C.L. upper limit on the measured  $E_\Delta$  peak width of the  $E_\Sigma = \sim 610$  and  $\sim 815$  keV structures.

positron production, discussed in Sec. 3.3. The broader positron energy spectrum associated with such a momentum distribution may also explain, in part, why the coincident  $e^+e^-$  peaks are more easily identified in the data than the corresponding positron "singles" lines. The high velocity  $X^0$ 's smear out the individual spectra much more quickly than the sum-energy distribution. Within this context, the HI scattering-angle cuts, or selected beam-energy intervals, discussed in Sec. 3.4 may be associated with a selection of neutral objects emitted with smaller than usual velocities.

The limiting value of  $\alpha \leq 0.035M_\chi c$  derived here leads to a momentum distribution which falls short of that predicted in most of the published theories involving the dynamic production of a neutral particle electromagnetically from the Coulomb field or by strong interactions from the assembly of quarks. References [Bal85, Cho86, Muk86, Rei86, Car86] predict a suppression of  $X^0$  creation at low-momenta beyond the  $P_x^2$  phase space volume, by an extra factor of  $P_x^3$  to  $P_x^5$ . From the above analysis it seems unlikely that these mechanisms can suitably describe the observed data. A necessary condition for understanding the narrow positron, elec-

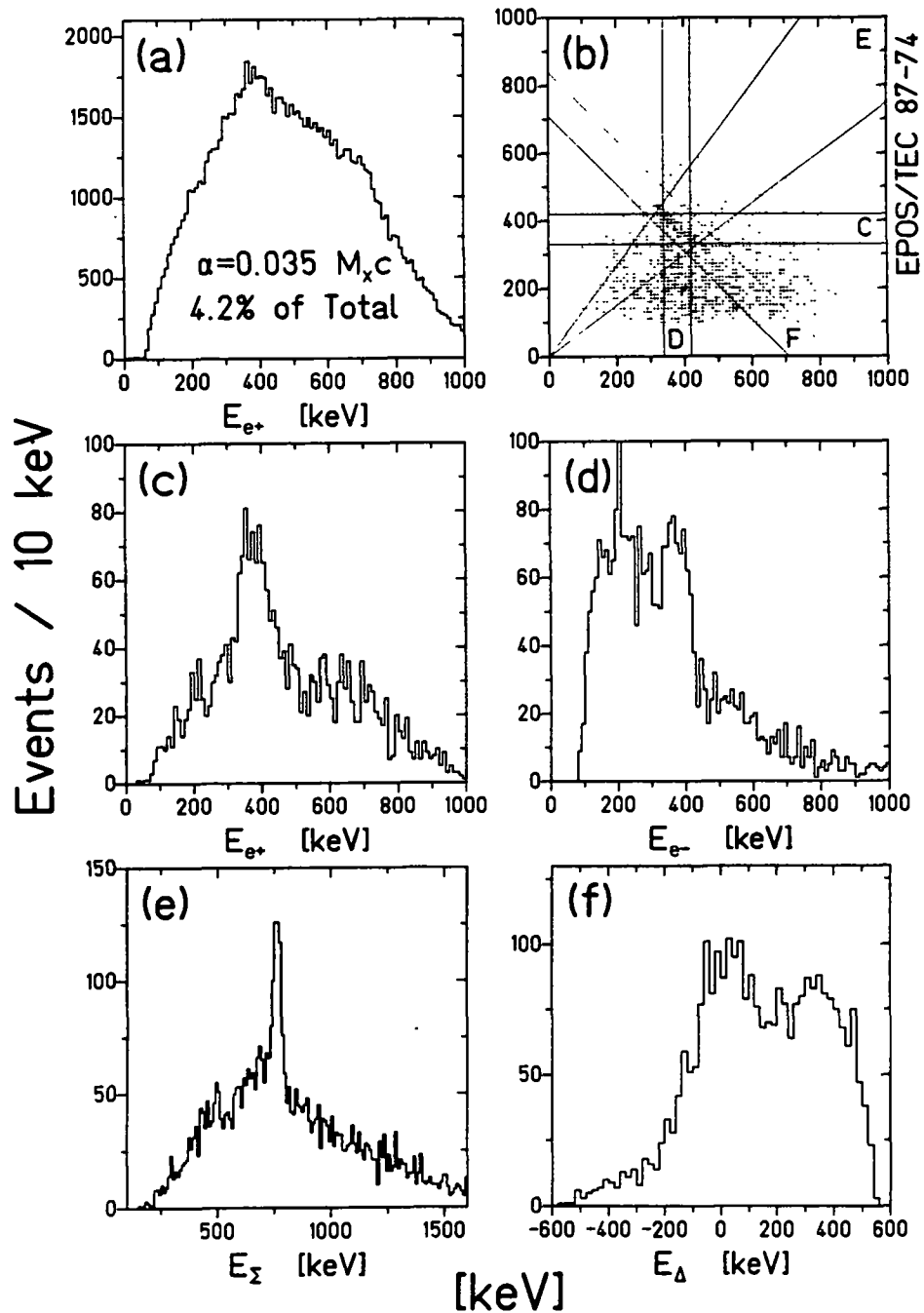


**Figure 7-24.** MCSPEC simulation of  $10^5$  detected positrons assuming the decay of a 1.8 MeV neutral object created isotropically in the CMS with a momentum distribution characterized by  $\alpha = 0.035$ , which accounts for 4.2% of total  $e^+$  yield. Part (a) presents total  $e^+$  distribution, and projections on the  $E_{e^+}$ ,  $E_{e^-}$ ,  $E_{\Sigma}$ , and  $E_{\Delta}$  axes (c-f) correspond to gates in (b).

tron, and difference-energy peak widths is the presence of a sufficient intensity of objects created with low momentum ( $P_x^*/M_{xc} < 0.1$ ). Although, as demonstrated in

Fig. 7-22, the high- $P_x$  components are smeared out and become indistinguishable from the continuous backgrounds, at some point, the intensity of the narrow sum-energy peak becomes so small that an unphysically large production rate must be assumed.

One theoretical momentum distribution predicted for created pseudoscalar particle production is not inconsistent with the model-dependent limit on  $\alpha$  presented here. Balantekin et al. [Bal85] suggest the empirical distribution

$$dN_x/dP_x^* = \sum \delta(P_x^* - \vec{k}_{e+}^* - \vec{k}_{e-}^*) (dN_{e+}/d\vec{k}_{e+}^*) (dN_{e-}/d\vec{k}_{e-}^*), \quad (7.23)$$

which has a mean of  $\langle P_x \rangle \cong 300$  keV/c. The experimental data clearly favor those theoretical explanations involving creation of the neutral object with low velocities, e.g., those which produce  $X^0$ 's at rest in the CMS [Cel86, Mül86d, Cal87, Ng87].

The broad momentum distribution expected for elementary particle creation could, however, be modified by the velocity filter effect mentioned in Sec. 5.1. Detection of positrons or electrons is suppressed if the neutral state has a long lifetime, so that the fast objects ( $v_x > 0.1c$ ) escape the EPOS fiducial volume ( $\sim 1$  cm for positrons,  $\sim 2$  cm for electrons). The coincidence detection efficiency, however, decreases even more quickly so even larger total  $X^0$  production cross-sections are required to explain a given observed peak intensity. The dashed curve in Fig. 7-23 plots the  $E_\Delta$  peak width versus  $\alpha$  assuming a  $10^{-9}$  sec emitter lifetime. The acceptable upper limit on  $\alpha$  is increased to  $\cong 0.07 \bullet M_x c$ . Figure 7-25 illustrates the effect of a source lifetime on the coincidence peaks using the momentum distribution given by Eqn. 7.22 with  $\alpha = 0.07 \bullet M_x c$ . For  $\tau_x \geq 1$  ns, the expected detected spectra are in good agreement with the data, *but*, the required  $X^0$  production cross-section is a factor of 8.3 times larger than that for the simulation presented in Fig. 7-24. A lifetime of only  $\tau_x \geq 5 \times 10^{-10}$  sec is required for the Balantekin et al. distribution (Eqn. 7.23) in order to provide a good fit to the coincidence data, as demonstrated in Fig. 7-26. In fact, there are certain indications in the experimental coincidence peak data that off-axis emission, associated with a source lifetime, may be involved.

The preceding analysis of the velocity of the source emitting the coincident positron-electron peaks indicates that a viable description of the data in terms of the two-body decay of a neutral state need not require creation of the object exactly at

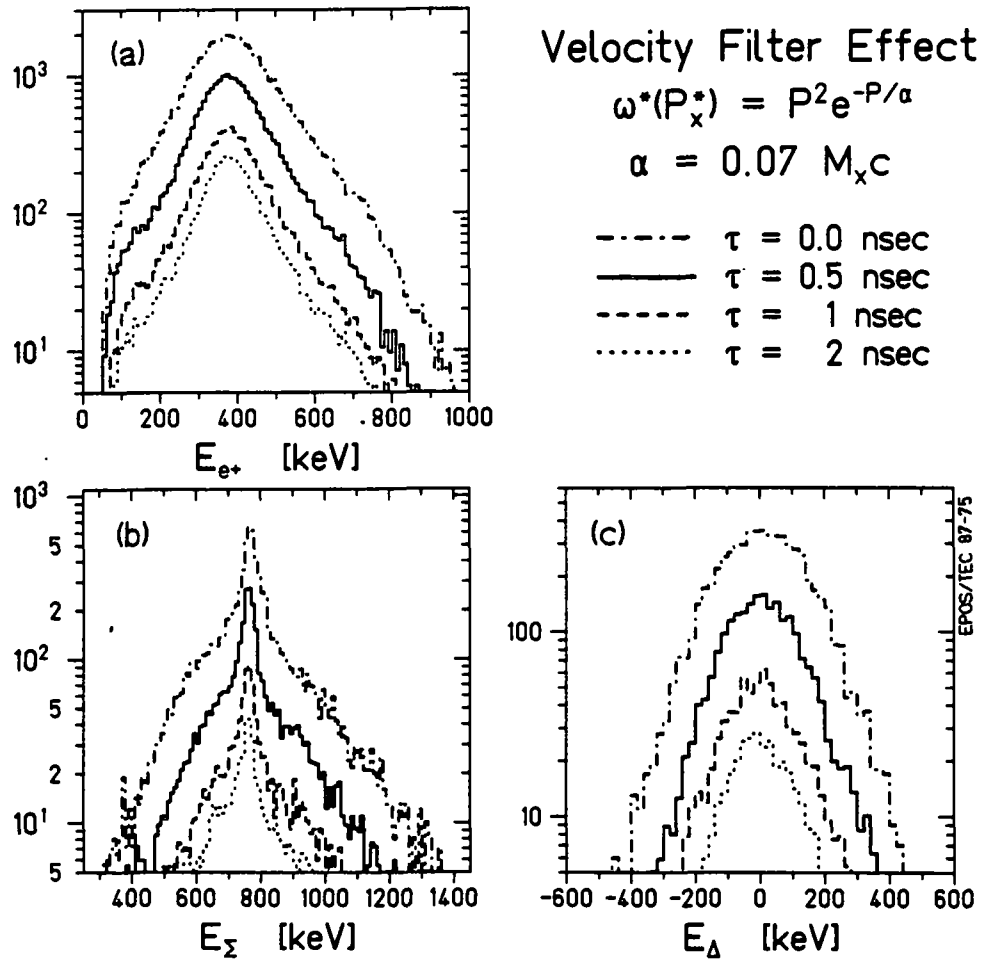


**Figure 7-25.** MCSPEC simulation of  $4.4 \times 10^5$   $1.8 \text{ MeV}/c^2$   $X^0$ 's created in the CMS with a momentum distribution characterized by  $\alpha=0.07$  and lifetimes of  $\tau_x = 0, 0.5, 1,$  and  $2 \text{ ns}$ . (A) Total positron spectrum. (B,C) Projections on  $E_\Sigma$  and  $E_\Delta$  axes.

rest in the CM system of the heavy-ion collision. The experimental observation that neutral particle-like objects must be formed with sufficient intensity at low velocities is consistent with creation with rather broad momentum distributions, due to the preferential detection of slowly moving objects in the EPOS spectrometer. In light of the larger required production cross-section for mechanisms involving long source lifetimes or substantial high-velocity  $X^0$  components, theoretical descriptions leading to emission with  $v_x \sim v_{CM}$  appear most likely.

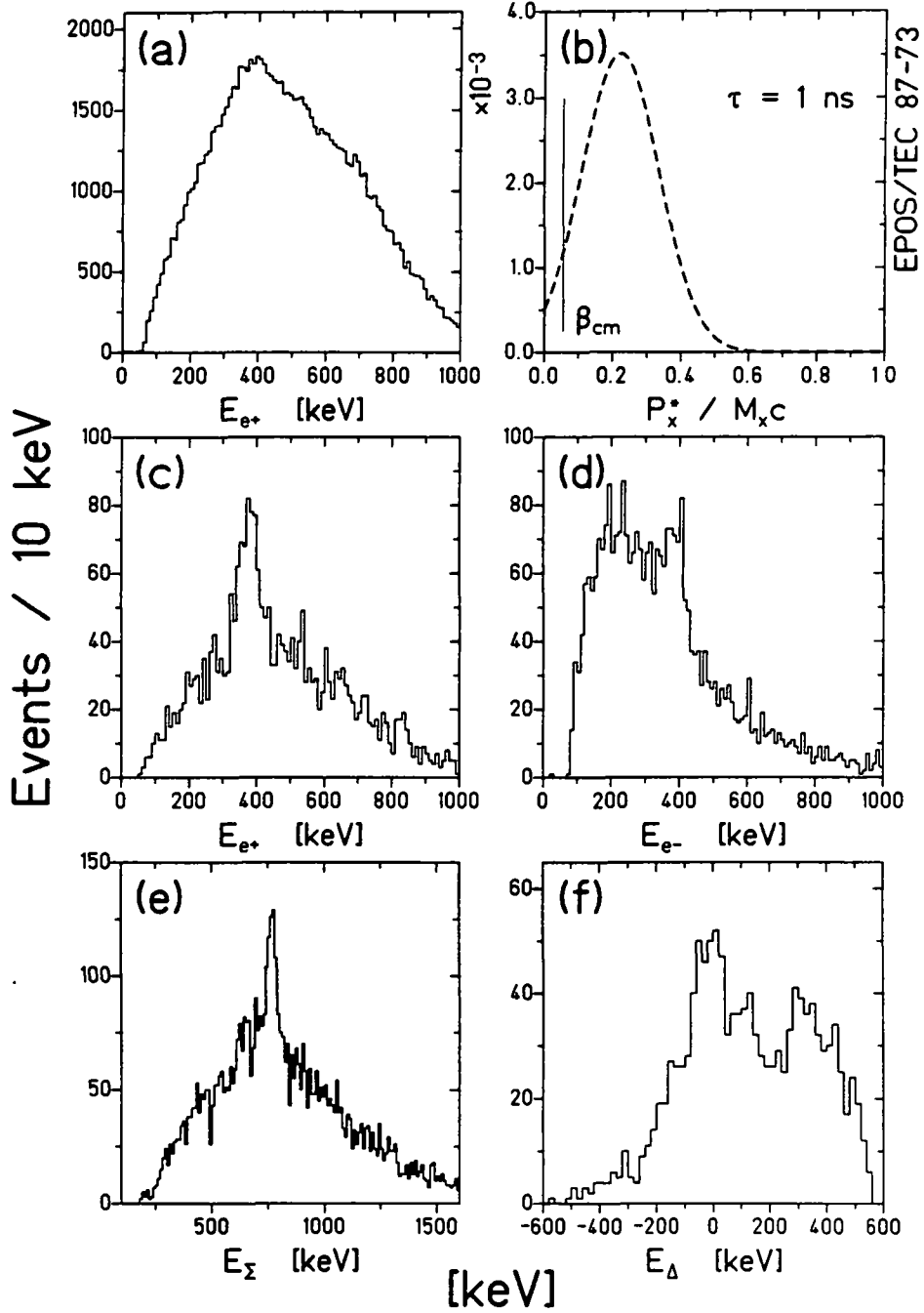


**Figure 7-26.** MCSPEC simulation of  $10^5$  detected positrons (a), assuming that 10% of the total yield is produced by decay of a 1.8 MeV neutral object created isotropically in the CMS with the momentum distribution given by [Bal85] (b), and which has a mean lifetime of 1 ns. Projections (c-f) as in Fig. 6-2.

### Sec. 7.5.7 Multiple Structure

Within the context of an elementary particle origin for the coincidence positron-electron peaks, the observation of at least three narrow sum-energy lines in U+Th collisions raises the unattractive prospect of hypothesizing a whole family of neutral objects instead of just one. An alternate possibility is that a single object is created with different discrete values of kinetic energy. As mentioned in Sec. 5.1, Chodos et al. [Cho86, see also Muk86, Shä86b, Car86] suggested a process in which the multiple positron peak energies arise from a single object receiving increments of kinetic energy from the nuclear complex. In order to retain a small Doppler-broadened linewidth, however, the velocity of the decay positron and electron in the rest frame of the source,  $v_{e^+,e^-}^*$ , must be small compared to  $v_{CM}$ . That implies  $T_{e^+,e^-} \leq 1$  keV. Only very small particle masses of  $M_x \leq 1023$  keV/c<sup>2</sup> can therefore be accommodated, and the small available lepton momentum implies that the positron and electron travel in nearly the same direction in the lab ( $\theta_{e^+,e^-} \leq 4^\circ$ ), and are not detected in coincidence in the EPOS spectrometer.

On the other hand, one may assume that a single object of mass  $\cong 1.65$  MeV/c<sup>2</sup>, explaining the lower observed sum-energy peak, is boosted by  $\sim 100$  to  $\sim 200$  keV in order to fit the higher lines. From Fig. 7-21b, however, the broadening of the positron and electron energy distributions is then very large which is inconsistent with the data. The observed narrow sum-energy peak widths of 25 to 40 keV set a limit on the maximum kinetic energy of the object, from Fig. 7-21b, of  $T_x < 60$  keV. This is not immediately inconsistent with describing the 815 keV peak as an accelerated 760 keV sum-energy line. A comparison of the 1st and 3rd panels of Fig. 7-20 indicates that this possibility is unlikely. The expected broad difference-energy distribution, in light of the measured narrow and well-defined  $E_\Delta$  peak associated with the  $E_\Sigma = 815$  keV line, argues against this interpretation.

Figure 7-27 presents an additional possibility for creating multiple  $E_\Sigma$  lines, based on the exotic scenario discussed in Sec. 7.5.5 in which energy correlated ( $E_{e^+} + E_{e^-} = \text{constant}$ ) positrons and electrons are emitted into specific angular regions. Assuming, for example, that both the positron and electron are emitted with a  $\cos^2\theta_{e^+,e^-}$  distribution with respect to the direction of motion of the source, each may have either a positive or negative Doppler shift of approximately,  $\delta E_{e^+,e^-} \sim (\gamma\beta)_{em} P_{e^+,e^-}^*$ . As indicated in Fig. 7-27a, three possible sum-energies are detected, corresponding to forward-forward, forward-backward, or backward-

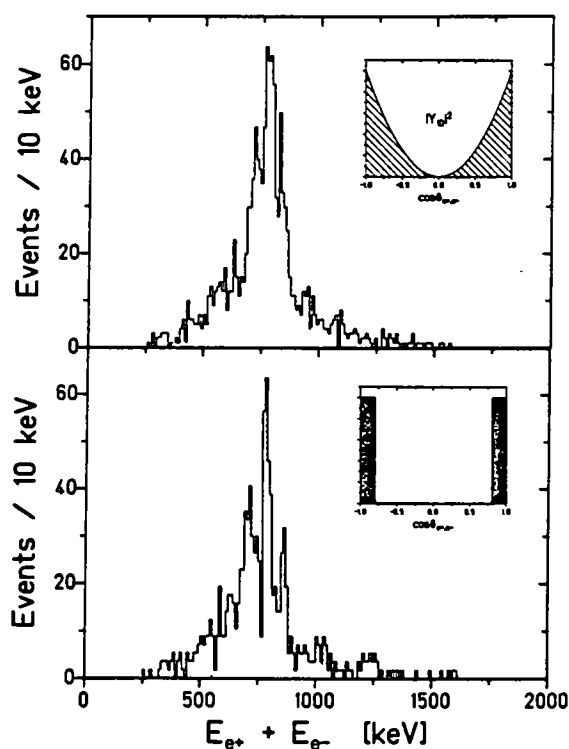


**Figure 7-27.** Sum-energy spectra generated for monoenergetic 380 keV positrons and electrons emitted from the CMS ( $\beta_{\text{CM}}=0.056$ ) with the angular distributions indicated. The wide structure expected for uncorrelated emission fragments into narrow, multiple  $E_{\Sigma}$  structures for very sharp angular distributions.

backward emission of the leptons. Narrow lines may result, as discussed in Sec. 7.5.5, for sufficiently narrow  $\omega^*(\Omega_{e^+}^*)$  and  $\omega^*(\Omega_{e^-}^*)$  distributions (Fig. 7-27b). Their spread in  $E_{\Sigma}$  depends on the velocity of the source. Apart from the unlikely required energy correlation, constrained to within  $\sim 100$  keV of  $E_{e^+}^* = E_{e^-}^*$ , it should be noted that all sum-energy "peaks" are expected to emerge simultaneously within this context, in contrast to the apparent separability of the individual structures evident in Figs. 6-2 and 6-9. A description of the multiple  $E_{\Sigma}$  lines by such a purely kinematic mechanism therefore appears implausible.

The data suggest that the different observed sum-energy peaks are not trivially related simply by the kinematic boost of a single object, or by kinematic shifts associated with a narrow lepton emission angle distribution. More than one, and possibly several objects, must be formed in the HI collision, with different values of total energy ranging from  $\sim 1.6$  to  $\sim 1.9$  MeV. As noted above, several recent theoretical models which avoid the necessity of hypothesizing a new family of elementary bo-

sons describe the multiple structures as various excited states of a single composite object. As mentioned in Sec. 7.2, an alternative explanation involving several structures from the interference pattern of atomic positron and electron emission fails to produce sharp  $E_{\Sigma}$  lines above the continuous dynamic backgrounds. Regardless of which mechanism produces the structures, the presence of several correlated coincidence peaks in the data is well established. The associated positron peak energies agree with the various "singles" positron lines which are presented in Part I of this dissertation and which have been discovered in more recent EPOS experiments.

In hindsight, the existence of several structures, often two or more of which are present in a single data sample, explains many of the difficulties in the earlier positron-peak search experiments. The MCSPEC simulation in Fig. 7-28, which assumes the production of three neutral objects ( $M_x = 1.65, 1.75, \text{ and } 1.85 \text{ MeV}/c^2$ ) each accounting for 1% of the total positron yield, helps to clarify this point. The multiple  $E_{\Sigma}$  peaks, separated by  $\cong 100 \text{ keV}$ , are easily resolved in the sum-energy spectrum because the correlated cancellation of the Doppler shifts produces an  $\cong 25 \text{ keV}$  experimental energy resolution. In the positron energy spectrum, however, the corresponding peaks are separated by only  $\sim 50 \text{ keV}$ , and the  $\cong 80 \text{ keV}$  Doppler broadening causes the lines to overlap. None of these three peaks is individually resolved. The resulting broad excess of positron intensity (between  $\sim 250$  and  $\sim 450 \text{ keV}$ ) above the continuous dynamic background resembles the typical total positron spectra measured in both Parts I and II of this dissertation. As mentioned in Sec. 3.4, the presence of such a shoulder in the positron singles spectrum served as a fairly reliable on-line indicator of the presence of peak events in the data.

Finally, it should be noted that the emergence of the narrow positron peaks in these [Shw83, Cow85] and other [Cle84, Tse85] experiments as a function of the kinematic parameters, such as the HI scattering angle and beam energy, may simply reflect changes in the relative intensity of the various structures (so that one dominates above the rest), rather than a selection of only a single structure to the complete exclusion of the others. Whether or not a positron peak is observed in a given experiment could therefore be coupled in a complex way to the details of the production mechanisms for each of the various coincidence lines. In light of this fact, caution is urged when attempting to interpret any systematic features of the positron peak data from Sec. 3.4 or the other positron experiments (e.g., [Cle84], [Tse85], or [Kön87]), or when comparing the results of the positron "singles" peak experiments with the much cleaner positron-electron coincidence data presented in this disserta-

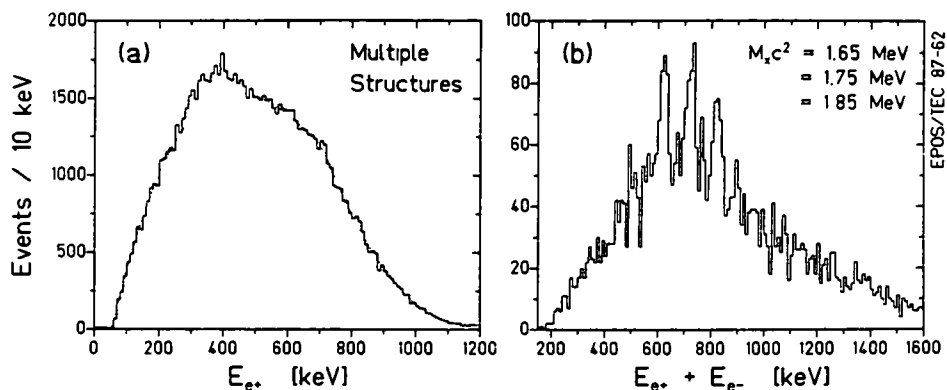


**Figure 7-28.** MCSPEC simulation of  $10^5$  detected positrons including the creation of three neutral objects of masses 1.65, 1.75, and 1.85 MeV/ $c^2$ , each accounting for 1% of the total  $e^+$  yield. Positron distribution (left) shows only broad enhancement over continuous dynamic plus nuclear background (dotted), while lines are individually resolved in sum-energy spectrum (right).

tion. By way of illustration, it is quite possible that the individual positron peaks published in [Cow85] or [Tse85] contain admixtures of more than one of the  $E_{\Sigma}$  structures presented in Chap. 6, which modifies the experimentally determined mean peak energies and cross-sections. Only with further coincidence measurements can the entire spectrum of positron peak structures, and the systematic dependence of their energy and production cross-section on  $Z_U$  and HI collision kinematics, be accurately determined.

# Chapter 8 Summary and Outlook

## Section 8.1 Positron Peak Data

Part I of this dissertation presented the results of a systematic investigation of the production of positron peaks in five supercritical and one subcritical collision system. Narrow peaks having mean energies between 300 and 380 keV were observed in U+Cm, Th+Cm, U+U, Th+U, Th+Th, and Th+Ta collisions, with values of the combined nuclear charge ranging from  $Z_U = 188$  to  $Z_U = 163$ . The peaks appear to be associated with heavy-ion collisions at the Coulomb barrier whose ion angle-angle correlations differ slightly from Rutherford elastic scattering. The narrow peak widths (all  $\sim 70$  keV) are dominated by Doppler broadening and imply that the emitting source lives for  $\tau \geq 10^{-19}$  sec, and that it travels with a mean laboratory velocity of  $\langle v_{em} \rangle \sim 0.05c$ . These structures are produced with similar cross-sections throughout the range of  $Z_U$  investigated,  $d\sigma_{e^+}/d\Omega_{HI} \sim 5-15 \mu\text{b/sr}$ , although for various combinations of beam energies and targets, the production rate does not appear to remain constant.

An extensive study of the EPOS spectrometer characteristics has shown that the peaks cannot be ascribed to instrumental origins or other trivial backgrounds. Moreover, the independence of the peak widths on  $\theta_{HI}$ , and the absence of competing lines in the simultaneously measured  $\gamma$ -ray and electron energy distributions, rule out origins involving nuclear transitions. Spontaneous positron emission is not able to explain the independence of the positron peak energies on  $Z_U$ , or the presence of structure in the subcritical Th+Ta system. Atomic processes involving interfering amplitudes for positron production concentrated at different locations along the Rutherford trajectory are similarly unable to describe the data.

## Section 8.2 Coincident Positron-Electron Peaks

The near degeneracy of the positron peak energies led us to investigate whether the monoenergetic positron lines signal the two-body decay of a previously undetected neutral object. As described in Part II of this dissertation, we discovered monoenergetic electron lines *in coincidence* with positron peaks in U+Th, Th+Th, Th+Cm (and most recently in U+Ta) collisions. The corresponding peaks in the distribution of the sum of the positron and electron energies are narrower ( $\Delta E_{\Sigma} \sim 25-40$  keV) than the individual lines ( $\Delta E_{e^+} \sim \Delta E_{e^-} \sim 75$  keV), suggesting the correlated can-

cellation of Doppler shifts expected for back-to-back positron-electron emission. The three most prominent coincidence peaks are observed at sum-energies of  $E_{\Sigma} \cong 610, 750, \text{ and } 815 \text{ keV}$ , although additional lines may be present in the data. The correlation of the peak intensities with kinematic variables such as the beam energy, heavy-ion scattering angle, and positron time-of-flight, mirror the behavior of the positron "singles" lines.

Origins involving instrumental backgrounds, external pair creation, uncorrelated emission of monoenergetic positron and electron peaks, nuclear internal pair creation, cascade or sequential processes, and multi-body decays all are unable to describe the several features of the coincidence data. These include the narrow width of the  $E_{\Sigma}$  peaks, the absence of peak intensity in adjacent cuts, the large size of the correlated peak signal compared to the total positron yield, and the absence of competing  $\gamma$ -ray or electron conversion lines. A kinematic analysis of the shapes of the coincident sum-energy and difference-energy peaks indicates that the positron and electron are most probably emitted back-to-back, with a relative opening angle in the rest frame of their source of  $\theta_{e^+e^-}^* > 165^\circ$ . The measured Doppler broadening also limits the possible velocity distribution of the hypothetical neutral source, implying a mean velocity of  $\sim 0.05 < v_x < 0.2c$ .

### Section 8.3 Open Questions

Our understanding of the nature of the positron peaks emitted from heavy-ion collisions has obviously evolved quite dramatically over the course of this dissertation research. For example, spontaneous positron emission, the search for which originally motivated this entire field, and nuclear decays were substantially precluded as possible origins by the  $Z_U$ -dependence and emitter velocity measurements. The pace was particularly accelerated by the advent of the electron-positron coincidence experiments which ruled out all other conventional, and most exotic processes as possible explanations for the data. Moreover, the excellent resolution afforded in the sum-energy spectrum by the coincidence technique has reliably established, for the first time, the presence of multiple structures in the data. This in turn clarified many unresolved questions from the earlier measurements.

However, some of the previous questions remain, and new ones have been raised by these experimental results. For example, if the two-body decay of a neutral object is involved, a mechanism must be found to produce this object with a suf-

ficient probability at low velocities. Although this general result can be mitigated if the source has a long lifetime ( $\tau \geq 10^{-10}$  sec), so that fast moving parents decay outside of the fiducial volume of the spectrometer, the data imply a velocity distribution slower than that predicted by most theories. Second, the angular distribution of the emitted positrons and electrons is not known, but could provide information about the quantum numbers of the source of the lines. The lifetime of the emitter (from the present data,  $10^{-19} \leq \tau \leq 10^{-9}$  sec) is important not only from a theoretical standpoint, but also to provide practical guidance for the design of other experiments. Next, the existence of several structures in the data obviously complicates any explanation in terms of elementary particles. The number of coincidence lines, their spectrum of energies, and the correspondence of the intensity of each with various kinematic variables are important parameters which remain to be determined. Despite the many indications of correlations with beam energy, scattering angle, and flight-time, very little is actually known about the mechanism producing the peaks in the HI collisions studied. A fifth relevant question is therefore whether nuclear contact is involved, for example, to produce strong electric fields for long times. A related point may concern the  $Z_U$  dependence of peak production. Measurements beyond the range of  $163 \leq Z_U \leq 188$  are required to test the several theories which rely on mechanisms involving strong field QED.

## **Section 8.4 Future Experiments**

### ***Sec. 8.4.1 Particle Experiments***

The compelling interpretation of the coincident positron-electron data presented in this dissertation in terms of a previously undetected neutral source has already motivated several searches for such an object in a variety of traditional particle physics experiments. As described in Sec. 7.5.1, no indication of a new particle-like object has yet been observed in heavy quarkonium decays, rare meson decays, beam-dump experiments, nuclear transitions, and several high-precision atomic physics measurements. Very stringent limits have been set for the coupling of this object to electrons, quarks, and photons. It may be, however, that the unique combination of strong fields and/or nuclear degrees of freedom available in HI collisions are important for producing this hypothetical object. In an experiment designed to search for the competing  $2\gamma$  decay of the 1.8 MeV coincidence structure in U+Th collisions, Meyerhof et al. [Mey86] observed no candidates, and they set a limit on the branching ratio of  $BR(X^0 \rightarrow 2\gamma)/BR(X^0 \rightarrow e^+e^-) < 1$ . A follow-up experiment has recently

suggested the presence of a peak at much lower sum-energies [Dan87] (see also [Shw87]).

Theoretically, the cleanest system for observing our effect should be through the time-reversed channel of the decay process, namely by resonant positron-electron scattering at CM kinetic energies of  $\sim 610$ - $815$  keV [Rei86, Rei87]. Several first generation fixed-target experiments have already been completed. No unambiguous structures have yet been reported down to the level of a few percent of the underlying continuous background from Bhabha scattering [Mai87, Wim87, Mil87, Kie87, Kli87], which corresponds to limits on the coupling to electrons of within an order of magnitude of those provided by precision (g-2) data [Rei87]. Improved experimental arrangements with better energy resolution and increased beam intensity [Gre87] promise to approach the (g-2) level in the near future.

#### **Sec. 8.4.2 Heavy-Ion Experiments**

Judging by the long list of unsolved questions, there are a considerable number of problems which must be addressed in the meantime using heavy-ion collisions. The most important experiment for the immediate future is to directly measure the emission angles of the positron and electron, in order to rule out the last of the exotic backgrounds, and to verify the kinematic result of  $\theta_{e^+} = 180^\circ$  emission. Obviously if the positrons and electrons prove not to be emitted back-to-back, much of the motivation for other experiments disappears. Ideally, one would like a  $4\pi$  detection system which simultaneously measures the  $e^+$  and  $e^-$  laboratory energies and angles with good precision in order to fully reconstruct the decay and measure the invariant mass. It presently appears very difficult to obtain sufficient angular resolution, while maintain good energy resolution, to improve on the invariant mass measurement afforded by the EPOS sum-energy spectrum. Even moderate angular resolution (e.g.,  $\delta\theta \sim 10^\circ$ ) should yield limited information regarding the emitter velocity and direction and the angular distribution of the decay products. Perhaps the most immediate advantage would be the reduction in background by gating on  $180^\circ$  emission, with a corresponding improvement in the sensitivity of the apparatus. Experiments along these lines are in progress by the EPOS collaboration, using sub-divided positron and electron detectors and time-of-flight techniques, and the Munich group, who have added a second Orange  $\beta$  spectrometer to measure positrons and electrons in coincidence.

With minor modifications to existing instruments, it should be possible to measure the source lifetime down to the  $\tau \geq 10^{-11}$  sec level with a well-designed recoil-shadow technique. A test measurement in the EPOS solenoid was limited only by secondary scattering backgrounds. Using a beam-dump production target, we also tried to determine whether the source is a penetrating neutral object. Although this too experienced large backgrounds (external pair conversion in the thick target-holder), there is ample room for improvement and both of these measurements should again be pursued.

In order to further study the processes which produce the peaks in heavy-ion collisions, systematic measurements are required of the beam-energy dependence for a variety of projectile and target nuclei. These should include non-deformed nuclides such as  $^{208}\text{Pb}$ , and beam energies well above and below the Coulomb barrier. If nuclear reactions appear to be important, we may need a more complex apparatus which incorporates a large solid-angle spectrometer for the scattered heavy-ions, which would provide better kinematic definition by high resolution identification of the charge and mass of the ejectiles. Heavy-ion experiments of this type will unfortunately be limited to the present rather slow data accumulation rates, and will require a considerable investment of accelerator time.

Finally, from a theoretical point of view it is also very important to search for correlated positron-electron emission in lower  $Z_U$  target-projectile combinations. The data presented in this dissertation indicate that the peak production cross-section remains fairly constant down to  $Z_U \cong 163$ . If we find that the peaks appear below this range, e.g., near  $Z_U \cong 100$ , then several difficult technical aspects of the high-Z experiments would be alleviated. In particular, there would be a wide choice of very stable self-supporting metallic targets, and the intense  $\delta$ -electron background would be reduced by an order of magnitude or more. Using the present EPOS detector geometry, much higher beam currents, and hence data accumulation rates could be tolerated. Finally, low- $Z_U$  experiments could be performed at a variety of different accelerators, many of which may be better suited than the UNILAC to investigate the nuclear physics aspects of the production process.

The data presented in this dissertation have had an unusually broad impact on the present physics community, from its original motivation in atomic physics, through many contributing nuclear processes, and finally reaching into the domain of elementary particle physics. Unfortunately, no theoretical model to date has been

wholly successful in describing all of the major experimental observations concerning the narrow positron and correlated electron peaks. The continuing search for a satisfactory explanation should prove very interesting for some time to come.

# Appendix A Heavy-Ion Kinematic Relations

Many of the heavy-ion kinematic relations used throughout this dissertation are collected in this appendix. Section 1 includes formulas for elastic heavy-ion scattering. Section 2 discusses inelastic collisions and outlines the effects of Q-loss, nucleon evaporation, and mass transfer. Section 3 deals with energy-loss of the beam ions penetrating the target material.

## Section A.1 Elastic Scattering

A non-relativistic treatment of elastic scattering in a repulsive Coulomb potential,

$$V(|\vec{r}_p - \vec{r}_t|) = Z_p Z_t e^2 / |\vec{r}_p - \vec{r}_t|, \quad (\text{A.1})$$

leads to hyperbolic trajectories for the nuclei. In polar coordinates  $(r, \theta, \phi)$  with the center-of-mass of the heavy-ion system taken as the origin, these are parameterized by

$$r = [2a(1 + \varepsilon \cos\Theta_{CM})]^{-1}, \quad (\text{A.2})$$

where  $\varepsilon$  is the eccentricity of the orbit, and  $2a$  is the center-to-center distance of closest approach of the nuclei for a head-on collision.

$$2a = Z_p Z_t e^2 / E_{cm}, \quad (\text{A.3})$$

where  $E_{cm}$  is the kinetic energy in the CMS,

$$E_{cm} = E_0 \cdot M_t / (M_p + M_t). \quad (\text{A.4})$$

and  $E_0$  is the laboratory energy (and  $\vec{v}_0$  the velocity) of the incoming projectile.  $Z_p$ ,  $Z_t$ ,  $M_p$ , and  $M_t$  are the charge and mass numbers of the projectile and target nuclei, respectively. The classical impact parameter,  $b$ , is related to the angle  $\Theta_{CM}$  through which the projectile is scattered, by

$$b = a \cdot \cot(\Theta_{CM}/2), \quad (\text{A.5})$$

and the distance of closest nuclear approach during a given collision is

$$R_{\min} = a \cdot [1 + 1/\sin(\Theta_{\text{CM}}/2)]. \quad (\text{A.6})$$

The laboratory angles of the scattered projectile and recoiling target nuclei,  $\theta_p^{\text{lab}}$ ,  $\theta_t^{\text{lab}}$ , are determined by conservation of energy and momentum, and do not depend on the form of the potential (A.1). Combining the CM velocity,

$$\vec{v}_{\text{cm}} = \vec{v}_o \cdot M_p / (M_p + M_t), \quad (\text{A.7})$$

with the asymptotic velocities of the projectile scattered through angle  $\Theta_{\text{CM}}$  having  $v_p^{\text{cm}} = (M_t/M_p)v_{\text{cm}}$ , and the target recoiling at an angle  $\pi - \Theta_{\text{CM}}$  with  $v_t^{\text{cm}} = -v_{\text{cm}}$ , yields the following relations.

$$\tan(\theta_p^{\text{lab}}) = \sin(\Theta_{\text{CM}}) [M_p/M_t + \cos(\Theta_{\text{CM}})]^{-1}, \quad (\text{A.8})$$

$$\theta_t^{\text{lab}} = (\pi - \Theta_{\text{CM}})/2. \quad (\text{A.9})$$

Eliminating  $\Theta_{\text{CM}}$  from Eqns. A.8 and A.9 gives

$$\cot(\theta_t^{\text{lab}}) = (\gamma - 1)^{-1} \{ \cot(\theta_p^{\text{lab}}) \pm [1 - \gamma^2 + \cot^2(\theta_p^{\text{lab}})]^{1/2} \}, \quad (\text{A.10})$$

where  $\gamma = M_p/M_t$ .

As discussed in Sec. 2.3, the heavy-ion data are analyzed using a rotated coordinate system,  $\Sigma\theta_{\text{HI}} = \theta_U + \theta_L$  versus  $\Delta\theta_{\text{HI}} = \theta_U - \theta_L$ . For collisions with  $M_p = M_t$ , the scattering angle correlations lie along the line  $\Sigma\theta_{\text{HI}} = 90^\circ$ . If  $M_p > M_t$ ,  $\Sigma\theta_{\text{HI}}$  is always less than  $90^\circ$ , and for  $M_p < M_t$ ,  $\Sigma\theta_{\text{HI}} > 90^\circ$ . The maximum projectile scattering angle for heavy-on-light collisions is

$$(\theta_p^{\text{lab}})_{\max} = \sin^{-1}(M_t/M_p). \quad (\text{A.11})$$

The kinematic branches cross at

$$\theta_p^{\text{lab}} = \theta_t^{\text{lab}} = \frac{1}{2} \{ \pi - \cos^{-1}[\frac{1}{2}(1 - M_p/M_t)] \}. \quad (\text{A.12})$$

The Rutherford scattering cross-section is given in CM coordinates by the usual expression,

$$d\sigma/d\Omega_{cm} = a^2 / [4 \sin^4(\Theta_{CM}/2)], \quad (\text{A.13})$$

or, in terms of the laboratory angles, by

$$d\sigma/d(\cos\theta_p^{lab}) = (d\sigma/d\Omega_{cm}) (1 + \gamma \cos\Theta_{CM})^{-1} [1 + \gamma^2 + 2\gamma \cos\Theta_{CM}]^{3/2}, \quad (\text{A.14})$$

$$d\sigma/d(\cos\theta_t^{lab}) = a^2/\cos^3(\theta_t^{lab}). \quad (\text{A.15})$$

Finally, the applicability of a non-relativistic treatment for heavy-ion scattering at the projectile energies of interest in these experiments ( $E_0/M_p \sim 6 \text{ MeV/u}$ ) is verified by comparing the above quantities with those calculated in a fully relativistic treatment. For example, for  $\Theta_{CM} = 90^\circ$  scattering of equal mass nuclei, Eqns. A.8,9 give  $\theta_p^{lab} = \theta_t^{lab} = \theta_{NR} = 45^\circ$ . Relativistically, however, for  $5.88 \text{ MeV/u } ^{238}\text{U} + ^{238}\text{U}$ ,

$$\beta_{cm} = [E_0^2 + 2E_0M_p c^2]^{1/2} / (M_t c^2 + M_p c^2 + E_0), \quad (\text{A.16})$$

and  $\theta_{REL} = \tan^{-1}[(1 - \beta_{cm}^2)^{1/2}] = 45.955^\circ$ . The  $0.045^\circ$  decrease in  $\theta_{REL}$  from the NR value ( $\delta\theta/\theta = 10^{-3}$ ) is much smaller than the  $\Delta\theta \cong 0.8^\circ$  experimental resolution, and is completely absorbed in the empirical HI angular calibration. Deviations from elastic scattering, e.g., a reaction Q-loss, calculated within the relativistic versus NR treatments also differ by only  $\sim 10^{-3}$ . The NR approximation is therefore completely appropriate for describing HI collisions at the Coulomb barrier.

## Section A.2 Inelastic Collisions

In order to deduce limits on the type of HI reactions which might be associated with the positron peak data, a general treatment of the inelastic scattering is required which includes nucleon evaporation, energy loss, and mass transfer. We consider collisions of a beam of particles of mass  $M_1$  and kinetic energy  $E_0$  incident on a target of mass  $M_2$ , with ejectile masses  $M_3$  and  $M_4$ .  $M_1 + M_2$  need not equal  $M_3 + M_4$ , and an energy,  $Q$ , may be dissipated from the available CM energy. In the CM frame, conservation of energy and momentum gives,

$$\frac{1}{2}[M_3(v_3^{cm})^2 + M_4(v_4^{cm})^2] = E_{cm} + Q, \quad (\text{A.17})$$

with

$$v_3^{cm} = \{2M_4(E_{cm} + Q)/[M_3(M_3 + M_4)]\}^{1/2}, \quad (\text{A.18a})$$

$$v_4^{cm} = \{2M_3(E_{cm} + Q)/[M_4(M_3 + M_4)]\}^{1/2}. \quad (\text{A.18b})$$

Transforming to the laboratory system gives the general expression for the laboratory angle,

$$\tan(\theta_i^{ab}) = \sin(\theta_i^{cm}) [v_{cm}/v_i^{cm} + \cos(\theta_i^{cm})]^{-1}, \quad (\text{A.19})$$

in analogy with Eqn. A.8, where

$$v_{cm}/v_i^{cm} = \{[M_1 M_i^2 (M_3 + M_4)]/[M_2 M_3 M_4 (M_1 + M_2)] \times E_{cm}/(E_{cm} + Q)\}^{1/2} \quad (\text{A.20})$$

for  $M_i = M_3, M_4$ .

For particular choices of  $M_3$ ,  $M_4$ , and  $Q$ , Eqns. A.19,20 reduce as follows.

**Case I.**  $M_3 = M_1$ ,  $M_4 = M_2$  For no mass transfer or nucleon evaporation, Eqn. A.20 gives,

$$v_{cm}/v_i^{cm} = (M_1/M_2) [E_{cm}/(E_{cm} + Q)]^{1/2}, \quad (\text{A.21})$$

with laboratory angles,

$$\tan(\theta_i^{ab}) = \sin(\theta_i^{cm}) \{(M_1/M_2)[E_{cm}/(E_{cm} + Q)]^{1/2} + \cos(\theta_i^{cm})\}^{-1}. \quad (\text{A.22})$$

For  $Q=0$ , the lab angles for elastic scattering (Eqn. A.8) are regained. Figure A-1a illustrates the effect of different  $Q$ -values on the angle-angle correlation pattern following  $^{232}\text{Th} + ^{248}\text{Cm}$  collisions at 6.02 MeV/u. At  $\Delta\theta_{HI} \sim 0^\circ$ , a  $Q$ -loss of 25 MeV translates into a shift in  $\Sigma\theta_{HI}$  of  $\delta(\Sigma\theta_{HI}) = 1.04^\circ$ .

**Case II.**  $(M_1 + M_2) = (M_3 + M_4)$ . Allowing for mass transfer without mass evaporation, Eqn. A.20 reduces to

$$v_{cm}/v_i^{cm} = \{[M_i^2 M_1/(M_2 M_3 M_4)] \times [E_{cm}/(E_{cm} + Q)]\}^{1/2}, \quad (\text{A.23})$$

with the lab angles given by Eqn. A.19. While the entrance channel mass ratio determines  $v_{cm}$  and  $E_{cm}$ , the exit state mass ratio almost completely determines the

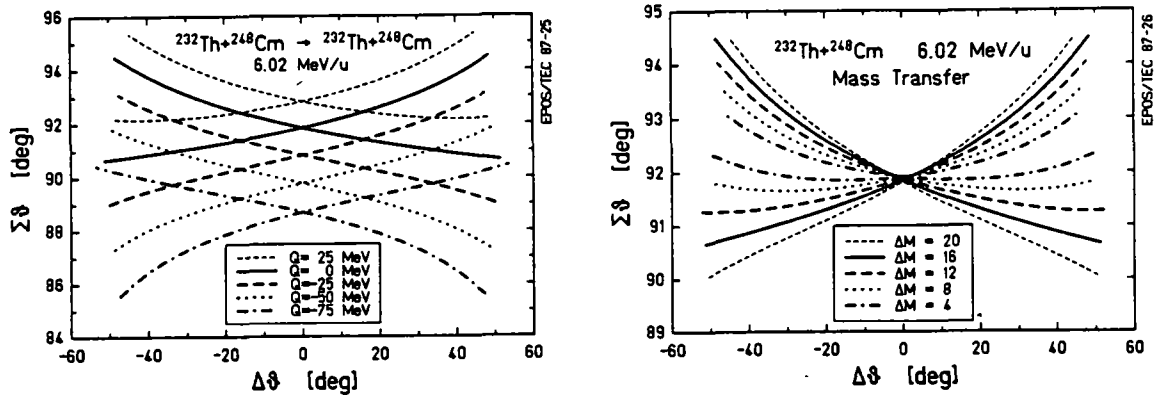


**Figure A-1.** *Figure A-1.*  $\Sigma\theta_{HI}-\Delta\theta_{HI}$  scattering angle correlations calculated for Th+Cm collisions with several values of  $Q$  (left) and exit channel masses (right).

angle-angle correlation pattern (as shown in Fig. A-1b for Th+Cm collisions). For heavy collisions, a mass asymmetry of 10 nucleons translates into a  $\Sigma\theta_{HI}$  separation between the kinematic branches of  $0.81^\circ$  at  $|\Delta\theta_{HI}| = 20^\circ$ .

For a given mass-drift between the colliding nuclei, the change in the nuclear binding energies enters as an effective  $Q$ -value (see Eqn. 4.46 in Sec. 4.4.4). Mass-excess tables [Mye77] indicate that for a broad range of nuclides from thorium to curium, the binding energy differences (given  $M_1 + M_2 = M_3 + M_4$ ) are typically smaller than  $\sim 2$  MeV.

**Case III.**  $(M_3 + M_4) < (M_1 + M_2)$ . If nucleons are evaporated isotropically from the CM system, then  $v_{CM}$  of the remaining heavy-ions remains, on the average, constant given by Eqn. A.7. Equations A. 19,20 then give the CM ejectile velocities and lab angles. The additional  $Q$ -value from the binding-energy lost from the evaporation of a neutron is  $\cong -8$  MeV. Normally, evaporation neutrons are emitted from the tails of a Maxwellian energy distribution, with mean kinetic energy  $E_n \sim 3$  MeV. Each ejected neutron therefore reduces the total available CM energy by  $Q \cong -11$  MeV. Charged particles require additional kinetic energy to overcome the Coulomb barrier. This amounts to  $E_p \cong 20$  MeV for proton emission from a  $^{238}\text{U}$  nucleus. Much of the mass-excess may be regained if nucleons are emitted in bound clusters, e.g., an  $\alpha$  particle has  $\Delta m \cong 2.4$  MeV/ $c^2$ . Figure A-2 illustrates the effect of nucleon evaporation from Th+Cm collisions with several combinations of ejected particles.

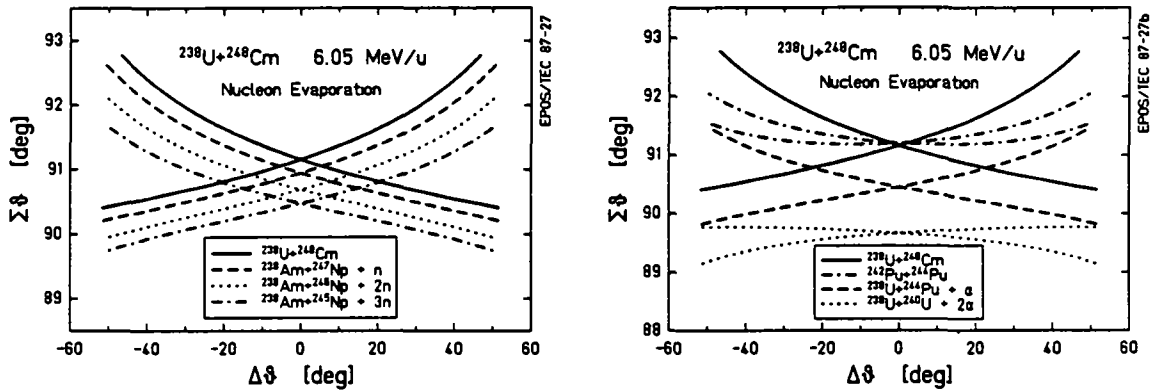


**Figure A-2.** Kinematic plots of the HI  $\Delta\theta_{\text{HI}} - \Sigma\theta_{\text{HI}}$  correlation patterns for neutron evaporation (left) or  $\alpha$  particle emission (right) following U + Cm collisions. Energetically most favorable exit channel nuclei are assumed.

If the evaporation products are emitted with an angular distribution with respect to the CM velocity,  $v_{\text{cm}}$  may decrease (if the nucleons are ejected forward), or increase (if backward). The lab angles of the heavy products will be consequently adjusted by the modified CM velocity,

$$\delta v_{\text{cm}} = \langle \cos(\theta_{\text{evap}}) \rangle \cdot [2 \cdot \Delta E_{\text{evap}} \cdot \Delta M_{\text{evap}}]^{1/2} / (M_1 + M_2), \quad (\text{A.24})$$

where  $\Delta E_{\text{evap}}$  is the kinetic energy of the evaporation nucleons in the CM frame. In the simplest example of 1 neutron emission, the  $\sim 0.5^\circ$  shift in  $\Sigma\theta_{\text{HI}}$ , assuming an average isotropic distribution, actually varies from  $\sim 0^\circ$  for forward emission, to  $\sim 1^\circ$  for backward emission. In general, isotropic emission therefore leads to a smearing of the  $\Sigma\theta_{\text{HI}}$  correlation pattern about the average  $\Delta(\Sigma\theta_{\text{HI}})$  shift with a width of,

$$\delta(\Sigma\theta_{\text{HI}}) \sim \Delta(\Sigma\theta_{\text{HI}})/3. \quad (\text{A.25})$$

### Section A.3 Heavy-Ion Energy-Loss

The ionization energy-loss of the projectile particles, while traversing the target material before scattering, is usually the limiting factor in maintaining constant CM collision energies. For a particular beam atomic number and incident energy, the stopping power varies with target the species approximately as [Hub80],

$$dE/dx = A + B/Z_{\text{tar}} \quad (\text{A.26})$$

For a uranium beam at 5.9 MeV/u, the constants are  $A \sim 40$  and  $B \sim 685$  in units of  $\text{MeV}/(\text{mg}/\text{cm}^2)$ . Over the range of projectile energies relevant to our experiments, the stopping power changes by only about 2% per 1.0 MeV/u change  $E_{\text{beam}}$ . The stopping power in a chemical compound (e.g.,  $\text{ThF}_4$ ) is the weighted average of  $dE/dx$  for each element, e.g.,

$$(dE/dx)_{\text{ThF}_4} = [232 \cdot (dE/dx)_{\text{Th}} + 4 \cdot 19 \cdot (dE/dx)_{\text{F}}] / (232 + 4 \cdot 19). \quad (\text{A.27})$$

Table A-1 lists the stopping power of Th and U projectiles in elements and compounds commonly encountered in the EPOS experiments.  $dE/dx$  is listed in units of both  $(\text{MeV})/(\text{mg}/\text{cm}^2)$  and  $(\text{MeV}/\text{u})/(\text{mg}/\text{cm}^2)$ .

Table A-1:  $dE/dx$  for Common EPOS Targets

Target	$^{232}\text{Th}$ 5.9 MeV/u		$^{238}\text{U}$ 5.9 MeV/u	
	MeV	MeV/u	MeV	MeV/u
C	158.49	0.6831	161.71	0.6795
O	143.60	0.6190	146.55	0.6157
F	138.48	0.5969	141.42	0.5942
Ta	48.48	0.2090	49.71	0.2089
Th	44.73	0.1928	45.88	0.1928
U	44.45	0.1916	45.59	0.1916
Cm	43.97	0.1895	45.08	0.1895
$\text{ThF}_4$	67.86	0.2925	69.45	0.2918
$\text{UF}_4$	67.21	0.2897	68.78	0.2890
$\text{CmF}_3$	61.63	0.2654	63.09	0.2651
$\text{Cm}_2\text{O}_3$	52.76	0.2274	54.04	0.2270

## Appendix B Ray-Tracing Calculations

Detailed calculations of the EPOS transport efficiency and its dependence on positron energy and emission angle are carried out with a ray-tracing program ECPI (Efficiency Calculation by Path Integration). ECPI numerically integrates the equations of motion of a positron (or electron) in an axial magnetic field, given the initial emitted energy and direction, tracing its path through the spectrometer to decide whether the positron strikes the Si(Li) detector or is stopped by some other element of the spectrometer system. The vector potential appearing in the 2<sup>nd</sup> order differential equations of motion is expanded from the magnetic field strength along the axis, which is calculated by superposition of Biot-Savat's law for the current loops produced by the pancake field coils. Next, a Runge-Kutta integration is used to calculate the first three points of the positron path with very high precision. The trajectory is then traced by a Milne Predictor-Corrector method, iteratively using the preceding four points to find the fifth. When any part of a trajectory interpolated between the calculated points passes through spectrometer material, the positron is assumed to be stopped. Positron and electron scattering are not considered.

ECPI is based on a ray-tracing code developed at Yale Univ. by E. Liarokapis [Lia82], which was adapted by R. Schule (Univ. Frankfurt) to incorporate the basic elements of the first version (pre 1981) of the EPOS spectrometer. From 1982 to the present, ECPI has been modified and updated by T. Cowan. Changes include: the actual magnetic field configuration used in each experiment; the present geometry of the vacuum chamber, positron detector, and spiral baffle; the electron detectors and baffles used in Parts I and II of this dissertation; and generalization of the program to calculate the full  $\phi$ -dependence of the EPOS transport efficiency. The transport efficiency calculated by ECPI is used as an input for the MCSPEC program described in Appendix C.

### *Section B.1 Equations of Motion*

The Lorentz force on a positron (or electron) moving in a magnetic field,  $B$ , is

$$dp/dt = (e/c)[v \times B]. \quad (B.1)$$

When separated in cylindrical coordinates, the equations of motion are [God44]

$$d^2z/dt^2 = -\partial M/\partial z, \quad (\text{B.2a})$$

$$d^2r/dt^2 = -\partial M/\partial r, \quad (\text{B.2b})$$

$$d\phi/dt = -C/r^2 - (e/\gamma mc)A/r, \quad (\text{B.2c})$$

where M and C (a constant of integration) are given by,

$$M = \frac{1}{2}\gamma m(C/r - eA_\phi/\gamma mc)^2, \quad (\text{B.3})$$

$$C = r_0\phi'_0 + (e/\gamma mc)r_0A_0. \quad (\text{B.4})$$

For emission of the positron from a point  $(r_0, z_0)$  along the solenoid axis, the constant is  $C \equiv 0$ , and the Eqns. B.2,3 reduce to the following set of uncoupled 2<sup>nd</sup> order differential equations in time t:

$$d^2z/dt^2 = -(e/\gamma mc)^2 A_\phi \partial A_\phi / \partial z, \quad (\text{B.5a})$$

$$d^2r/dt^2 = -(e/\gamma mc)^2 A_\phi \partial A_\phi / \partial r, \quad (\text{B.5b})$$

$$d\phi/dt = -(e/\gamma mc) A_\phi / r. \quad (\text{B.5c})$$

## Section B.2 Magnetic Field and Vector Potential

The vector potential,  $A_\phi$ , appearing in Eqns. B.5 is calculated from the magnetic field and its derivatives along the solenoid axis by the expression,

$$A_\phi = \sum_n \{(-1)^n [n!(n+1)!]^{-1} B_z^{(2n)} (r/2)^{2n+1}\}, \quad (\text{B.6})$$

where  $B_z^{(2n)}$  denotes  $(2n)$ -th derivative,  $d^{2n}B/dz^{2n}$ . As described in Sec. 2.2.1.3, the magnetic field on the axis is constructed by adding the field contributions from each of the 15 pancake coils. For a single coil,  $B(z)$  is calculated by superimposing the solutions of Biot-Savat's law for each current loop,

$$B(z;l,r,z_0) = (2\pi l/c) r^2 [r^2 + (z-z_0)^2]^{-3/2}, \quad (\text{B.7})$$

where  $l$  is the current and  $r$  is the radius of the given loop centered at  $z=z_0$ . The summation of Eqn. B.7 over a single coil includes the four planes of 18 windings, for each of which the current is assumed to be equally divided among eight points  $(r_k, z_k = \pm \frac{1}{2}, 0 \text{ cm})$  spaced around each of the  $1 \times 1 \text{ cm}^2$  copper channels. That is,

$$B(z) = \sum_{i=1}^4 \sum_{j=1}^{18} \sum_{k=1}^8 (1/8) B(z; l, r_{ijk}, z_{ijk}), \quad (\text{B.8})$$

with,

$$r_{ijk} = 12.95 + 1.1 \cdot j + r_k,$$

$$z_{ijk} = 1.1 \cdot i - 2.75 + z_k,$$

given in cm.

The vector potential and its derivatives are determined to order  $r^7$ , given explicitly by,

$$A_\phi = rB_z/2 - r^3B_z^{(2)}/16 + r^5B_z^{(4)}/384 - r^7B_z^{(6)}/18432, \quad (\text{B.9a})$$

$$\partial A_\phi / \partial r = B_z/2 - 3r^2B_z^{(2)}/16 + 5r^4B_z^{(4)}/384 - 7r^6B_z^{(6)}/18432, \quad (\text{B.9b})$$

$$\partial A_\phi / \partial z = rB_z^{(1)}/2 - r^3B_z^{(3)}/16 + r^5B_z^{(5)}/384 - r^7B_z^{(7)}/18432. \quad (\text{B.9c})$$

These are then stored in a  $1 \times 1 \text{ cm}^2$  mesh for  $0 \leq r \leq 10 \text{ cm}$ , and  $-150 \leq z \leq 150 \text{ cm}$ . For a given position  $(r, z)$ , the 1<sup>st</sup> and 2<sup>nd</sup> derivatives of  $r(t)$  and  $z(t)$  are determined from Eqns. B.5 and B.9, using the six-point interpolation scheme (Eqn. 25.2.67 in [Abr65]),

$$\begin{aligned} F(r_0 + p, z_0 + q) = & \frac{1}{2}q(q-1) \cdot F_{0,-1} + \frac{1}{2}p(p-1) \cdot F_{-1,0} \\ & + \frac{1}{2}p(p-2q+1) \cdot F_{1,0} + \frac{1}{2}q(q-2p+1) \cdot F_{0,1} \\ & + (1 + pq - p^2 - q^2) \cdot F_{0,0} + pq \cdot F_{1,1} \end{aligned} \quad (\text{B.10})$$

where  $p$  and  $q$  are in units of the  $\Delta r = \Delta z = 1 \text{ cm}$  mesh size, and  $F_{i,j}$  denotes  $A_\phi$  (or  $\partial A / \partial z$ ,  $\partial A / \partial r$ ) evaluated at  $(r_i, z_j)$ .

### Section B.3 Runge-Kutta Method

The first three points on the path are calculated by Runge-Kutta integration of Eqns. B.5 (see Sec. II.2 in [Col66], or 25.5 in [Abr65]). Starting with the origin,  $(r_0, z_0)$ , the first point is estimated from the derivatives ( $\dot{r}$ ,  $\dot{z}$ , etc.) at the origin,

$$r_1^e = r_0 + \tau \cdot r_0' + \tau^2 \cdot r_0''/2, \quad (\text{B.11a})$$

$$z_1^e = z_0 + \tau \cdot z_0' + \tau^2 \cdot z_0''/2, \quad (\text{B.11b})$$

for a time increment,  $\Delta t = \tau$ . Using the derivatives evaluated at the estimated point, a better estimate for the first point, and the following two points, are obtained using,

$$r_1 = r_1^e + \tau^2 \cdot (\ddot{r}_{1g} - \ddot{r}_0)/6, \quad (\text{B.12a})$$

$$r_2 = 2r_1 - r_0 + \tau^2 \cdot \ddot{r}_1, \quad (\text{B.12b})$$

$$r_3 = 2r_2 - r_1 + \tau^2 \cdot (12\ddot{r}_2 - 2\ddot{r}_1 + \ddot{r}_0)/12, \quad (\text{B.12c})$$

with similar equations for the  $z_i$ 's.

To improve the accuracy, the differential equations (B.5) are evaluated at the points given by Eqns. B.12, and the 2<sup>nd</sup> time derivatives are used to re-extrapolate "corrected" values for  $r_1$ ,  $r_2$ , and  $r_3$ ,

$$r_1^c = r_1^e + \tau^2 \cdot (\Delta_1 - \Delta_2/4)/6 + \Delta_3/45, \quad (\text{B.13a})$$

$$r_2^c = 2r_1 - r_0 + \tau^2 \cdot (\ddot{r}_1 + \Delta_2/12), \quad (\text{B.13b})$$

$$r_3^c = 2r_2 - r_1 + \tau^2 \cdot (\ddot{r}_2 + \Delta_3/12), \quad (\text{B.13c})$$

where,

$$\Delta_1 = \ddot{r}_1 - \ddot{r}_0, \quad (\text{B.14a})$$

$$\Delta_2 = \ddot{r}_2 - 2\ddot{r}_1 + \ddot{r}_0, \quad (\text{B.14b})$$

$$\Delta_3 = \ddot{r}_3 - 3\ddot{r}_2 + 3\ddot{r}_1 - \ddot{r}_0. \quad (\text{B.14c})$$

If the differences between the corrected points ( $r_i^c, z_i^c$ ) and the estimated points ( $r_i, z_i$ ) are larger than an acceptable error,  $\epsilon$ , the ( $r_i, z_i$ )'s of Eqn. B.12 are replaced by the corrected ( $r_i^c, z_i^c$ )'s of Eqn. B.13, and equations B.13 and B.14 are iterated until convergence is achieved,

$$|r_i^c - r_i| < \epsilon, \quad (\text{B.15})$$

for all  $i$ . Finally, the azimuthal angle  $\phi$  about the solenoid axis is calculated for each point using the radial velocity  $\dot{q}$  at each point ( $r_i, z_i$ ) computed from Eqn. B.5c,

$$\phi_1 = \phi_0 + \tau \cdot \dot{\phi}_1, \quad (\text{B.16a})$$

$$\phi_n = \phi_{n-1} + \tau \cdot \dot{\phi}_n. \quad (\text{B.16b})$$

### Section B.4 Milne Predictor-Corrector Method

At each step in the path integration, the preceding four points are used to calculate a fifth point by the Milne Predictor-Corrector method (see Sec. III.3.3.IV in [Col66], or Sec. 25.5.21 in [Abr65]). For the first iteration, the three Runge-Kutta points plus the origin are used. The next point  $(r_{4p}, z_{4p})$  is "predicted" by the interpolation,

$$r_{4p} = r_3 + r_2 - r_0 + \tau^2 \cdot (5\ddot{r}_3 + 2\ddot{r}_2 + 5\ddot{r}_1)/4, \quad (\text{B.17a})$$

$$z_{4p} = z_3 + z_2 - z_0 + \tau^2 \cdot (5\ddot{z}_3 + 2\ddot{z}_2 + 5\ddot{z}_1)/4. \quad (\text{B.17b})$$

The derivatives,  $\ddot{r}$ ,  $\ddot{z}$ , evaluated at this estimated position are used to more accurately extrapolate a "corrected" point,

$$r_4 = r_3 + r_1 - r_0 + \tau^2 \cdot [17(\ddot{r}_{4p} + \ddot{r}_0) + 232(\ddot{r}_3 + \ddot{r}_1) + 222\ddot{r}_2]/240, \quad (\text{B.18a})$$

$$z_4 = z_3 + z_1 - z_0 + \tau^2 \cdot [17(\ddot{z}_{4p} + \ddot{z}_0) + 232(\ddot{z}_3 + \ddot{z}_1) + 222\ddot{z}_2]/240. \quad (\text{B.18b})$$

If the difference between  $(r_{4p}, z_{4p})$  and  $(r_4, z_4)$  is larger than the allowable error  $\epsilon$ , the corrected point is used to determine  $\ddot{r}_{4p}$  and  $\ddot{z}_{4p}$ , and Eqns. (B.18) are iterated. After convergence is achieved, Eqn. (B.16) is used to calculate  $\phi_4$ . All the points are then shifted ( $r_i$  becomes  $r_{i-1}$ , etc.) and the Milne method is iterated to trace the trajectory through the spectrometer.

### Section B.5 Performance

The numerical technique presented above can provide a highly accurate integration of the positron trajectory with proper choice of the time increment,  $\tau$ . An unnecessarily small step size, however, increases the computational time of the ECPI calculation, while too large a step reduces the sensitivity to local variations in the vector potential, and increases errors in extrapolating the  $(i+1)^{\text{th}}$  point. We use  $\tau = 3.4 \times 10^{-12}$  sec, corresponding to a step size for a 350 keV positron of  $\Delta x \cong 0.82$  mm, or about 100 steps around a single circular orbit. It was optimized by constructing a shallow magnetic bottle around the target position,  $B_{\text{max}} = 1.01 \cdot B_{\text{tar}}$ , and determining critical reflection angle for various step sizes. For large values of  $\tau$  ( $\geq 10$  ps), steeply emitted positrons are not reflected by the pinch fields, while for decreasing step sizes ( $\tau < 3$  ps), the calculated reflection angle converges to the expected adiabatic value,  $\theta_{\text{mir}} = \sin^{-1}(B_{\text{tar}}/B_{\text{max}})^{1/2}$ .

The spacial accuracy of the ray-tracing path integration is better than  $\sim 0.1 \mu\text{m}$  for each iteration. Positrons propagate through the spectrometer to the Si(Li) detector in  $\sim 2.5 \times 10^3$  steps, implying an estimated final positional accuracy of better than  $\Delta x \sim 0.5 \text{ mm}$ . Running on the GSI IBM 3084 mainframe computer, each path requires on the average  $\sim 300$  msec of cpu time. Since the differential equations B.5 are independent of azimuth angle, the entire  $\varphi$  range is calculated simultaneously for a given emission energy and polar angle  $\theta$ , by rotating the trajectory through  $N$  values of  $\varphi$  (in increments of  $2\pi/N$ ) at each spectrometer element, and noting for which values of  $\varphi$  the positron is detected.

The transmission efficiencies calculated by ECPI for positrons and electrons are presented in Figs. 2-16 through 2-19, and 2-24, for the magnetic field configuration and detector geometry used in Part I of this dissertation, and in Figs. 5-13 through 5-16, for that used in Part II.

# Appendix C Monte-Carlo Simulations of Positron-Electron Coincidences

The computer code MCSPEC (Monte-Carlo Simulation of Positron Electron Coincidences) was developed to generate a wide range of event scenarios and to model the response of the EPOS spectrometer in detecting positrons and coincident electrons. Several sources of coincident positrons and electrons are modeled, e.g., the production and two-body decay of neutral or charged objects, multi-body decays, various types of nuclear internal pair conversions, dynamic positron and  $\delta$ -electron emission, or any generalized emission of positrons and electrons from the target. The generated positrons and electrons are then transformed to the lab system, where the positron and electron are tracked through the EPOS spectrometer to determine whether or not each is detected. The pulse-height responses of the Si(Li) counters are taken into account, pileup from the  $\delta$ -electron flux is added, and electronic pulse-shaping and trigger-logic efficiencies are simulated. Finally, the generated events are analyzed with a logical duplicate of the experimental data analysis program. Projections of the simulated events may then be compared with identical cuts applied to the experimental data.

## ***Section C.1 Event Generators***

Event generation for each specific scenario is flexible to allow a detailed study of various aspects of the simulated positron-electron source. For example, the production and decay of a neutral particle-like object includes its angular and momentum distributions with respect to the emitting frame (CM of the heavy-ion collision, the scattered nuclei, or the stationary laboratory frame). The positron and electron momentum vectors are constructed in the rest frame of the emitting source, including the angular distribution with respect to the particle motion. They may be generated with an arbitrary distribution in  $e^+/e^-$  opening-angle in place of back-to-back emission. Similarly, studies of nuclear internal pair conversion (IPC) include 1) determination of the scattering angle distribution for the detected heavy-ion (including the geometry of the EPOS PPAC's), 2) any nuclear charge or transition energy, 3) E0, E1, E2, or M1 conversion multipolarities, 4) angular distributions for the emitted positron, and 5) theoretical (Born approximation) or mutually isotropic opening-angle distributions for the positron-electron pair. In addition to IPC in the heavy-ion ejectiles, calculations of pair production from target contaminants, from nuclear clusters which

might be emitted in the collision, and from external conversion of  $\gamma$ -rays in the target, its frame, or the sheet-baffle material, have been investigated.

### **Section C.2 Efficiency Determination**

Calculation of the large quantity of MCSPEC events necessary for studying a wide variety of production processes requires a computationally efficient evaluation of the EPOS Spectrometer response. The standard technique employed involves the interpolation of a look-up table of detection probabilities calculated for a large range of positron and electron emission with the ECPI ray-tracing code (App. B). The mesh size (the pixel size in Fig. 5-15) is small compared to the periodicity of detection efficiency to ensure high accuracy (corresponding to steps of 10 keV in  $E_{e^+,e^-}$ ,  $1.5^\circ$  in  $\phi$ , and .002 in  $\cos\theta$ ). On the average, 60% of positron "hits" are assumed to be detected to account for the mean efficiency for detecting 511 keV annihilation quanta in the NaI crystal array.

### **Section C.3 Detector Response**

Correction for the response of the solid state positron and electron detectors includes finite energy resolution, tailing due to energy-loss, pile-up due to the rescattering ( $\cong 8\%$  probability) of an undetected 511 keV annihilation photon in the positron detector, the high multiplicity of  $\delta$ -electrons striking the electron detector ( $\cong 20\%$  probability), and the finite Si(Li) resolution for the fast TOF pickoff. Pulse-height corrections (i.e., energy resolution, tailing, and pileup) are made for positrons or electrons by the standard method of sampling at random the inverse,  $F^{-1}$ , of the cumulative probability of observing an energy  $E$ , given incident energy  $E_0$ ,

$$F(E, E_0) = \int_0^E R(E', E_0) dE' / \int_0^\infty R(E', E_0) dE', \quad (C.1)$$

where  $R(E, E_0)$  is the experimental response function determined from measurements with conversion electron line sources, by iterative unfolding of  $\beta$ -decay source spectra, or from measurements of pileup as described above.

The time-of-flight of the positrons and electrons to their respective detectors, which depends on their velocity parallel to the solenoid axis, is evaluated by interpolating a smooth function of energy and polar emission angle, calculated with ECPI. The fast timing resolution of the Si(Li) detectors is  $\cong 4$  ns FWHM for electrons and  $\cong 7.5$  ns FWHM for positrons, compared to average flight times to the counters

from 4 to 15 ns, with a mean of  $\sim 8$  ns. Low-energy electronic discriminator thresholds are measured separately for each detector. No attempt is made to evaluate the detector response in a "microscopic" Monte-Carlo fashion tracking the penetration of a positron or electron into the silicon crystal. To the extent that energy-loss, backscattering, and time resolution are independent of the angle and position of incidence, or more realistically, that a broad range of Doppler-shifted emission momenta and incidence angles map onto closely spaced detected positron and electron energies, this pseudo-Monte-Carlo approach is extremely accurate.

### **Section C.4 Event Analysis**

Detected positrons and electrons are analyzed by a logical duplicate of the experimental data analysis program, discussed in Sec. 5.3. Adjustments are made to the times-of-flight to correct, in an average way, for positron or electron energy and PPAC timing. (PPAC's provide the experimental "start" signal, which depends on heavy-ion TOF as a function of the scattering angles  $\theta$  and  $\phi$ ). Resulting time distributions reflect, in principle, only the positron or electron emission angle with respect to the solenoid axis, and real time delays (e.g., lifetimes). Positrons are experimentally identified by a clean three-fold coincidence signal: 1) prompt kinematic coincidence between both PPACs indicating a quasi-elastic binary heavy-ion scattering event, 2) prompt time and energy signal in the positron Si(Li) detector, and 3) coincident detection of  $\geq 1$  511 keV photon in the NaI(Tl) annihilation radiation detector array. As a subset of positrons, we look for a fourth condition, 4) a prompt time and energy signal in one of the electron detectors. If both electron counters register, the event is discarded to avoid double-counting of the positron, or piling-up of the electron signals which distort the positron-electron coincidence distributions. For each sequential pair of detector elements in the four-fold coincidence pattern, accidental background is evaluated by subtracting the event distributions averaged over several neighboring beam-pulses from the data of the prompt coincidence beam-pulse. The energies of the positron and electron signals are combined to give sum and difference energies as described below. Event sorting is performed first for detected positrons, of which coincidence events are a subset, thus retaining an absolute normalization for comparison to experiment.

## Appendix D Abbreviations

CFD	Constant Fraction Discriminator
CM	Center-of-Mass
CMS	Center-of-Mass System
ECPI	Efficiency Calculation by Path Integration
EPC	External Pair Creation
EPOS	Electron-Positron Solenoid Spectrometer
GSF	Gesellschaft für Schwerionenforschung
HI	Heavy-Ion
IC	Internal Conversion
IPC	Internal Pair Creation
LAM	Look-At-Me
MCSPEC	Monte-Carlo Simulation of Positron-Electron Coincidences
MPC	Monoenergetic Positron Creation
PPAC	Parallel-Plate Avalanche Counter
SATAN	System to Analyse Tremendous Amounts of Nuclear Data
SPE	Spontaneous Positron Emission
TOF	Time-of-Flight
UNILAC	Universal Linear Accelerator

## References

- [Abr65] M. Abramowitz and I.A. Stegun, eds., *Handbook of Mathematical Functions* (Dover, New York, 1965).
- [Ach79] P. Achuthan, T. Chandramohan, and K. Venkatesan, *J. Phys.* **A12**,2521 (1979).
- [Alb86] H. Albrecht, U. Binder, P. Böckmann, R. Gläser, G. Harder, I. Lembke-Koppitz, A. Philipp, W. Schmidt-Parzefall, H. Schröder, H.D. Schultz, R. Wurth, A. Yagil, J.P. Donker, A. Drescher, D. Kamp, U. Matthiesen, H. Scheck, B. Spaan, J. Spengler, D. Wegener, J.C. Gabriel, K.R. Schubert, J. Stiewe, K. Strahl, R. Waldi, S. Weseler, K.W. Edwards, W.R. Frisken, Ch. Fukunaga, D.J. Gilkinson, D.M. Gingrich, M. Goddard, H. Kapitza, P.C.H. Kim, R. Kutsche, D.B. MacFarlane, J.A. McKenna, K.W. McLean, A.W. Nilsson, R.S. Orr, P. Padley, P.M. Patel, J.D. Prentice, H.C.J. Seywerd, T.-S. Yoon, J.C. Yun, R. Ammar, D. Coppage, R. Davis, S. Kanekal, N. Kwak, G. Kernal, M. Plesko, L. Jönsson, A. Babaev, M. Danilov, A. Golutvin, I. Gorelov, V. Lubimov, V. Mateev, V. Nagovitsin, V. Ryltsov, A. Semenov, V. Shevchenko, V. Soloshenko, V. Tchistilin, I. Tichomirov, Yu. Zaitsev, R. Childers, C.W. Darden, Y. Oku, and H. Gennow, *Phys. Lett. B* **179**,403 (1986).
- [Ang77] N. Angert and C. Schmelzer, "UNILAC, the accelerator facility for heavy ions of the GSI," in: *Kerntechnik* **19**,57 (1977).
- [Anh75] R. Anholt and J.O. Rasmussen, *Phys. Rev. A* **9**,585 (1975).
- [Anh77] R. Anholt and W.E. Meyerhof, *Phys. Rev. A* **16**,190 (1977).
- [Anh78] R. Anholt, *Z. Phys.* **A288**,257 (1978).
- [Anh79] R. Anholt, W.E. Meyerhof, and Ch. Stoller, *Z. Phys.* **A291**,287 (1979).
- [Arm78] P. Armbruster, H.-H. Behnke, S. Hagmann, D. Liesen, F. Folkmann, and P.H. Mokler, *Z. Phys.* **A288**,277 (1978).
- [Bab86] C.V.K. Baba, D. Indumathi, A. Roy, and S.C. Vaidya, *Phys. Lett. B* **180**,406 (1986).
- [Bac78] H. Backe, L. Handschug, F. Hessberger, E. Kankeleit, L. Richter, F. Weik, R. Willwater, H. Bokemeyer, P. Vincent, Y. Nakayama, and J.S. Greenberg, *Phys. Rev. Lett.* **40**,1443 (1978).
- [Bac83] H. Backe, P. Senger, W. Bonin, E. Kankeleit, M. Krämer, R. Krieg, V. Metag, N. Trautmann, and J.B. Wilhelmy, *Phys. Rev. Lett.* **50**,1838 (1983).
- [Bac85] H. Backe and B. Müller, in: *Physics of Atoms and Molecules*, B. Crasemann, ed. (Plenum Press, New York, 1985), p. 627.
- [Bac85b] H. Backe, private communication (1985).

- [Bal85] A.B. Balantekin, C. Bottcher, M.R. Strayer, and S.J. Lee, *Phys. Rev. Lett.* **55**,461 (1985).
- [Ban79] J. Bang and J.M. Hansteen, *Phys. Lett. A* **72**,218 (1979).
- [Ban81] J. Bang and J.M. Hansteen, *Phys. Scripta* **22**,609 (1981).
- [Ban87] J.M. Bang, J.M. Hansteen, and L. Kocbach, "Anomalous Positron Production and its Dependence on the Heavy Ion Scattering Angle," Univ. Bergen preprint No. 181 (1987).
- [Bar86] W.A. Bardeen, R.D. Peccei, and T. Yanagida, preprint DESY 86-054.
- [Bas86] S. Barshay, *Mod. Phys. Lett. A* **1**,653 (1986).
- [Bat86] A.O. Barut, in: *Physics of Strong Fields*, W. Greiner, W. Greiner, ed. (Plenum Press, New York, 1987), p. 601.
- [Bec63] F. Beck, H. Steinwedel, and G. Süssmann, *Z. Phys.* **171**,189 (1963).
- [Beg83] M. Begemann and H. Backe were responsible for the design, operation, and calibration of the 500 mm<sup>2</sup> Si(Li) electron detector.
- [Beg87] M. Begemann-Blaich, Ph.D. Dissertation, Univ. Mainz, in progress.
- [Beh78] H.-H. Behnke, D. Liesen, S. Hagmann, P.H. Mokler, and P. Armbruster, *Z. Phys. A* **288**,35 (1978).
- [Beh79] H.-H. Behnke, P. Armbruster, F. Folkmann, S. Hagmann, J.R. MacDonald, and P.H. Mokler, *Z. Phys. A* **289**,333 (1979).
- [Bem73] C.E. Bemis, F.K. McGowan, J.L.C. Ford, W.T. Milner, P.H. Stelson, and R.L. Robinson, *Phys. Rev. C* **8**,1466 (1973).
- [Ber77] G. Bertsch, J. Borysowicz, H. McManus, and W.G. Love, *Nucl. Phys. A* **284**,399 (1977).
- [Ber85] F. Bergsma, J. Dorenbosch, J.V. Allaby, U. Amaldi, G. Barbiellini, C. Berger, W. Flegel, L. Lanceri, M. Metcalf, C. Nieuwenhuis, J. Panman, C. Santoni, K. Winter, I. Abt, J. Aspiazu, F.W. Büsser, H. Daumann, P.D. Gall, T. Hebbeker, F. Niebergall, P. Schütt, P. Stähelin, P. Gorbunov, E. Grigoriev, V. Kaftanov, V. Khovansky, A. Rosanov, A. Baroncelli, L. Barone, B. Borgia, C. Bosio, A. Capone, M. Diemoz, U. Dore, F. Ferroni, E. Longo, L. Luminari, P. Monacelli, F. De Notaristefani, P. Pistilli, R. Santacesaria, L. Tortora, and V. Valente, *Phys. Lett. B* **157**,458 (1985).
- [Ber86] A.M. van den Berg, W. Henning, L.L. Lee Jr., K.T. Lesko, K.E. Rehm, J.P. Schiffer, G.S.F. Stephens, and F.L.H. Wolfs, *Phys. Rev. Lett.* **56**,572 (1986).
- [Bet84] R.R. Betts, "Resonances in Collisions between S-D Shell Nuclei," in: *Proc. of 5th Adriatic International conference on Nuclear Physics*, (Hvar, Croatia, Yugoslavia, September 24-29, 1984); and Oxford Univ. preprint 76/84.

- [Bez76] W. Betz, G. Soff, B. Müller, and W. Greiner, *Phys. Rev. Lett.* **37**,1046 (1976).
- [Bie53] L.C. Biedenharn and M.E. Rose, *Rev. Mod. Phys.* **25**,729 (1953).
- [Boe86] F.W.N. de Boer, K. Abrahams, A. Balanda, H. Bokemeyer, R. Van Dantzig, J.F.W. Jansen, B. Kotlinski, M.J.A. De Voight, and J. Van Klinken, *Phys. Lett. B* **180**,178 (1986).
- [Bok81] H. Bokemeyer, H. Folger, H. Grein, S. Ito, D. Schwalm, P. Vincent, K. Bethge, A. Gruppe, R. Schule, M. Waldschmidt, J.S. Greenberg, J. Schweppe, and N. Trautmann, *GSI Scientific Report 1980*, **GSI-81-2**,127 (1981).
- [Bok83] H. Bokemeyer, K. Bethge, H. Folger, J.S. Greenberg, H. Grein, A. Gruppe, S. Ito, R. Schule, D. Schwalm, J. Schweppe, N. Trautmann, P. Vincent, M. Waldschmidt, in: *Quantum Electrodynamics of Strong Fields*, W. Greiner, ed. (Plenum Press, New York, 1983), p. 173.
- [Bok85] H. Bokemeyer, H. Folger, H. Grein, T. Cowan, J.S. Greenberg, J. Schweppe, A. Balanda, K. Bethge, A. Gruppe, K. Sakaguchi, K. Stiebing, D. Schwalm, P. Vincent, H. Backe, M. Begemann, M. Klüver, and N. Trautmann, *GSI Scientific Report 1984*, **GSI-85-1**,177 (1985).
- [Bok86] H. Bokemeyer, in: *Physics of Strong Fields*, W. Greiner, W. Greiner, ed. (Plenum Press, New York, 1987), p. 195.
- [Bos78] F. Bosch, H. Krimm, B. Martin, B. Povh, T. Walcher, and K. Traxel, *Phys. Lett. B* **78**,568 (1978).
- [Bos80] F. Bosch, D. Liesen, P. Armbruster, D. Maor, P.H. Mokler, H. Schmidt-Böcking, and R. Schuch, *Z. Phys.* **A296**,11 (1980).
- [Bos86] F. Bosch, and B. Müller, *Particle and Nuclear Physics*, Vol. 16, A. Faessler, ed., Pergamon Press, Oxford (1986), p. 195.
- [Bot85] C. Bottcher and M.R. Strayer, *Phys. Rev. Lett.* **54**,669 (1985).
- [Bow86] T. Bowcock, R.T. Giles, J. Hassard, K. Kinoshita, F.M. Pipkin, R. Wilson, T. Gentile, P. Haas, M. Hempstead, T. Jensen, H. Kagan, R. Kass, S. Behrends, Jan M. Guida, Joan M. Guida, F. Morrow, R. Poling, C. Rosenfeld, E.H. Thorndike, P. Tipton, J. Green, F. Sannes, R. Stone, M.S. Alam, N. Katayama, I.J. Kim, C.R. Sun, V. Tanikella, D. Bortoletto, A. Chen, L. Garren, M. Goldberg, N. Horowitz, A. Jawahery, P. Lubrano, G.C. Moneti, S.E. Csorna, M.D. Mestayer, R.S. Panvini, G.B. Word, A. Bean, G.J. Bobbink, I. Brock, A. Engler, T. Ferguson, R. Kraemer, C. Rippich, R. Sutton, H. Vogel, C. Bebek, K. Berkelman, E. Bulcher, D.G. Cassel, T. Copie, R. DeSalvo, J.W. DeWire, R. Ehrlich, R.S. Galik, M.G.D. Gilchriese, B. Gittelman, S.W. Gray, A.M. Halling, D.L. Hartill, B.K. Heltsley, S. Holzner, M. Ito, J. Kandaswamy, R. Kowaleski, D.L. Kreinick, Y. Kubota, N.B. Mistry, J. Mueller, R. Namjoshi, E. Nordberg, M. Ogg, D. Peterson, D. Pericone, M. Pisharody, K. Read,

- D. Riley, A. Silverman, P.C. Stein, S. Stone, Xia Yi, A.J. Sadoff, P. Avery, and D. Besson, *Phys. Rev. Lett.* **56**,2676 (1986).
- [Brd86] S.J. Brodsky, E. Mottola, I.J. Muzinich, and M. Soldate, *Phys. Rev. Lett.* **56**,1763 (1986).
- [Bro78] D.A. Bromley, in: *Nuclear Molecular Phenomena*, N. Cindro, ed. (North-Holland, New York, 1978), p. 3.
- [Bro78b] D.A. Bromley, "Nuclear Molecules," *Scientific American* **239**,58 (1978).
- [Bro82] D.A. Bromley, "Resonances in Heavy Ion Collisions," *Lecture Notes in Physics*, Vol. **156**, Springer-Verlag (1982).
- [Brn86] C.N. Brown, W.E. Cooper, D.A. Finley, A.M. Jonckheere, H. Jostlein, D.M. Kaplan, L.M. Lederman, R.S. Smith, K.B. Luk, R. Gray, R.E. Plaag, J.P. Rutherford, P.B. Straub, K.K. Young, Y. Hemmi, K. Imai, K. Miyake, Y. Sakai, N. Sasao, N. Tamura, T. Yoshida, A. Maki, J.A. Crittenden, Y.B. Hsiung, M.R. Adams, H.D. Glass, D.E. Jaffe, R.L. McCarthy, J.R. Hubbard, and Ph. Mangeot, *Phys. Rev. Lett.* **57**,2101 (1986).
- [Bru59] J.H. Brunner, H.J. Leisi, C.F. Perdrisat and P. Scherrer, *Phys. Rev. Lett.* **2**,207 (1959).
- [Bry86] D.A. Bryman and E.T.H. Clifford, *Phys. Rev. Lett.* **57**,2787 (1986).
- [Bur66] G.A. Burginyon and J.S. Greenberg, *Nucl. Inst. and Meth.* **41**,109 (1966).
- [Bus83] F. Busch, D. Croome, H. Göringer, V. Hartmann, J. Lowsky, D. Marinescu, M. Richter, and K. Winkelmann, EDAS Report 83-4, GSI, Darmstadt, Germany (1983).
- [Cal79] F.P. Calaprice, R.W. Dunford, R.T. Kouzes, M. Miller, A. Hallin, M. Schneider, and D. Schreiber, *Phys. Rev. D* **20**,2708 (1979).
- [Cal87] D.G. Caldi and A. Chodos, "Narrow  $e^+e^-$  Peaks in Heavy-Ion Collisions and a Possible New Phase of QED," Yale preprint YTP 87-10 (1987).
- [Car86] D. Carrier, A. Chodos, and L.C.R. Wijewardhana, *Phys. Rev. D* **34**,1332 (1986).
- [Cas50] K.M. Case, *Phys. Rev.* **80**,797 (1950).
- [Cel86] L.S. Celenza, V.K. Mishra, C.M. Shakin, and K.F. Liu, *Phys. Rev. Lett.* **57**,55 (1986).
- [Cel87] L.S. Celenza, V.K. Mishra, C.M. Shakin, and K.F. Liu, *Phys. Rev. Lett.* **57**,55 (1986).
- [Cho86] A. Chodos and L.C.R. Wijewardhana, *Phys. Rev. Lett.* **56**,302 (1986).
- [Chu64] E.L. Church, A. Schwarzschild, and J. Weneser, *Phys. Rev.* **133**,B35 (1964).

- [Chu86] M.-C. Chu and V. Pönisch, *Phys. Rev. C* **33**,2222 (1986).
- [Cle84b] M. Clemente, PhD Thesis, Tech. Univ. München (1984).
- [Coa34] W.M. Coates, *Phys. Rev.* **46**,542 (1934).
- [Col66] L. Collatz, *The Numerical Treatment of Differential Equations, 3rd ed.* (Springer Verlag, Berlin, 1966).
- [Cow82] T. Cowan, Adiabatic Efficiency and Doppler Lineshape Calculations, private notes and computer programs, unpublished (1982).
- [Cow82b] T. Cowan, Modifications to ECPI program [Lia82], unpublished (1982-1986).
- [Cow85] T. Cowan, H. Backe, M. Begemann, K. Bethge, H. Bokemeyer, H.Folger, J.S. Greenberg, H. Grein, Y. Kido, M. Klüver, D. Schwalm, J. Schweppe, K.E. Stiebing, N. Trautmann, and P. Vincent, *Phys. Rev. Lett.* **54**,1761 (1985).
- [Cow85b] T. Cowan, "Monte Carlo Simulations of Positron-Electron Coincidences," MCSPEC computer program and Yale Report, unpublished.
- [Cow86] T. Cowan, H. Backe, K. Bethge, H. Bokemeyer, H.Folger, J.S. Greenberg, K. Sakaguchi, D. Schwalm, J. Schweppe, K.E. Stiebing, and P. Vincent, *Phys. Rev. Lett.* **56**,444 (1986).
- [Cow86b] T.E. Cowan and J.S. Greenberg, in: *Physics of Strong Fields*, W. Greiner, W. Greiner, ed. (Plenum Press, New York, 1987), p. 111.
- [Cow87] T.E. Cowan, in: *Electronic and Atomic Collisions*, H.B. Gilbody, R.H. Read, W.R. Newell, and A.C.H. Smith, eds. (North-Holland, Amsterdam, 1987).
- [Dan87] K. Danzmann, W.E. Meyerhof, E.C. Montenegro, Xiang-Yuan Xu, E. Dillard, H.P. Hülskotter, F.S. Stephens, R.M. Diamond, M.A. Deleplanque, A.O. Macchiavelli, J. Schweppe, R.J. McDonald, B.S. Rude, and J.D. Molitoris, *Phys. Rev. Lett.* **59**,1885 (1987).
- [Dar28] C.G. Darwin, *Proc. Roy. Soc.* **A118**,654 (1928).
- [Dav74] C.K. Davis and J.S. Greenberg, *Phys. Rev. Lett.* **32**,1215 (1974).
- [Dav86] M. Davier, J. Jeanjean, and H.N. Ngoc, *Phys. Lett. B* **180**,295 (1986).
- [Dir28] P.A.M. Dirac, *Proc. Roy. Soc.* **A117**,610 (1928); *Proc. Roy. Soc.* **A118**,351 (1928).
- [Ead71] W.T. Eadie, D. Drijard, F.E. James, M. Roos, and B. Sadoulet, *Statistical Methods in Experimental Physics*, (North-Holland, Amsterdam, 1971), p. 272.
- [Edw82] C. Edwards, R. Partridge, C. Peck, F.C. Porter, D. Antreasyan, Y.F. Gu, W. Kollmann, M. Richardson, K. Strauch, A. Weinstein, D. Aschman, T. Burnett, M. Cavalli-Sforza, D. Coyne, C. Newman, H.F.W. Sadrozinski, D. Gelphman, R. Hofstadter, R. Horisberger, I. Kirkbride, H. Kolanoski, K. Königsmann, R. Lee, A. Liberman, J. O'Reilly, A. Osterheld,

- B. Pollack, J. Tompkins, E. Bloom, R. Bulos, R. Chestnut, J. Gaiser, G. Godfrey, C. Kiesling, W. Lockman, M. Oreglia, D.L. Scharre, and K. Wacker, *Phys. Rev. Lett.* **48**,903 (1982).
- [Egl86] S. Egli, R. Engfer, Ch. Grab, E.A. Hermes, H.S. Pruys, A. van der Schaaf, D. Vermeulen, R. Eichler, N. Kraus, C. Niebuhr, H.K. Walter, W. Bertl, N. Nordong, U. Bellgardt, G. Otter, and T. Kozlowski, *Phys. Lett. B* **175**,97 (1986).
- [Eic86] R. Eichler, L. Felawka, N. Kraus, C. Niebuhr, H.K. Walter, S. Egli, R. Engfer, Ch. Grab, E.A. Hermes, H.S. Pruys, A. van der Schaaf, D. Vermeulen, W. Bertl, N. Nordong, U. Bellgardt, G. Otter, T. Kozlowski, and J. Martino, *Phys. Lett. B* **175**,101 (1986).
- [Eng87] W. Enghardt, K.-H. Kaun, H. Prade, J. Blümlein, and K. Lanius, *Z. Phys. C* **35**,511 (1987).
- [Erb86] K.A. Erb, I.Y. Lee, and W.T. Milner, *Phys. Lett. B* **181**,52 (1986).
- [Fae87] A. Faessler, M. Ismail, N. Ohtsuka, M. Rashdan, and W. Wadia, *Z. Phys. A* **326**,501 (1987).
- [Fai80] H. Faissner, E. Frenzel, W. Heinrigs, A. Preussger, D. Sann, and U. Sann, *Phys. Lett. B* **96**,201 (1980).
- [Fan65] U. Fano and W. Lichten, *Phys. Rev. Lett.* **14**,627 (1965).
- [Fin86] J. Fink, U. Heinz, J.A. Maruhn, and W. Greiner, *Z. Phys. A* **323**,189 (1986).
- [Fol76] F. Folkmann, P. Armbruster, S. Hagmann, G. Kraft, P.H. Mokler, and H.J. Stein, *Z. Phys. A* **276**,15(1976).
- [Fol84] H. Folger, W. Hartmann, J. Klemm, and W. Thalheimer, "Special Aspects of Nuclear Targets for High-Energy Heavy-Ion Accelerator Experiments," in: *Proc. of 1983 Workshop of the International Nuclear Target Development Society*, (Argonne, Illinois, 1984); and GSI Preprint 84-49 (1984).
- [Fol85] H. Folger, private communication (1985).
- [For76] C. Forster, T.R. Hoogkammer, P. Woerlee, and F.W. Saris, *J. Phys. B* **9**,1943 (1976).
- [Fri74] J.H. Friedman, "Data Analysis Techniques for High Energy Particle Physics," SLAC preprint **SLAC-176** (1974).
- [Ful73] L.P. Fulcher and A. Klein, *Phys. Rev. D* **8**,2455 (1973).
- [Gei87] K. Geiger, J. Reinhardt, B. Müller, and W. Greiner, "Magnetic Moment Interactions in the  $e^-e^+$  System," UFTP preprint 200/1987.
- [Ger69] S.S. Gershtein and Ya.B. Zel'dovich, *ZETF* **57**,654 (1969) [*Sov. Phys. JETP* **30**,358 (1970)]; and *Lett. Nuovo Cimento* **1**,835 (1969).
- [Ger72] S.S. Gershtein and V.S. Popov, *Lett. Nuovo Cimento* **6**,593 (1973).

- [God44] L.S. Goddard, Proc. Phys. Soc. (London) **65**,372 (1944).
- [Gor28] W. Gordan, Z. Phys. **48**,11 (1928).
- [Göt72] U. Götz, H.C. Pauli, K. Adler, and K. Junker, Nucl. Phys. A **192**,1 (1972).
- [Gra87] O. Graf, J. Reinhardt, T. de Reus, B. Müller, and W. Greiner, Z. Phys. A **328**,81 (1987).
- [Grb87] M. Grabiak, G. Stadt, B. Müller, W. Greiner, and A. Schäfer, Phys. Lett. B **183**,259 (1987).
- [Gre56] J.S. Greenberg and M. Deutsch, Phys. Rev. **102**,415 (1956).
- [Gre74] J.S. Greenberg, C.K. Davis, and P. Vincent, Phys. Rev. Lett. **33**,473 (1974).
- [Gre77] J.S. Greenberg, H. Bokemeyer, H. Emling, E. Grosse, D. Schwalm, and F. Bosch, Phys. Rev. Lett. **39**,1404 (1977).
- [Gre77b] J.S. Greenberg, P. Vincent, and W. Lichten, Phys. Rev. A **16**,964 (1977).
- [Gre80] J.S. Greenberg, in: *Electronic and Atomic Collisions*, N. Oda and K. Takayanagi, eds. (North-Holland, Amsterdam, 1980), p.351.
- [Gre82] J.S. Greenberg, in: *X-Ray and Atomic Inner Shell Physics*, B. Crasemann, ed. (Plenum Press, New York, 1982), p. 173.
- [Gre83] J.S. Greenberg, in: *Quantum Electrodynamics of Strong Fields*, W. Greiner, ed. (Plenum Press, New York, 1983), p. 853.
- [Gre83b] J.S. Greenberg, in: *Nuclear Physics with Heavy Ions*, P. Braun-Munzinger, ed. (Harwood Academic Publishers, New York, 1983), p. 419.
- [Gre85] J.S. Greenberg and P. Vincent, in: *Treatise on Heavy-Ion Science, Vol. 5: High Energy Atomic Physics*, D.A. Bromley, ed. (Plenum Press, New York, 1985), p. 138..
- [Grn83] W. Greiner, ed., *Quantum Electrodynamics of Strong Fields* (Plenum Press, New York, 1983).
- [Grn83b] W. Greiner, in: *Proceedings of the International Conference on Nuclear Physics, Florence, 1983*, P. Blasi and R.A. Ricci, eds., (Topografia Compositori, Bologna, 1984).
- [Grn87] W. Greiner, ed., *Physics of Strong Fields*, W. Greiner, Proceedings of NATO Advanced Studies Institute Maratea/Italy, June 1-14, 1986.
- [Gru85] A. Gruppe, Ph.D. Dissertation, Univ. Frankfurt (1985).
- [Hal86] A.L. Hallin, F.P. Calaprice, R.W. Dunford, and A.B. McDonald, Phys. Rev. Lett. **57**,2105 (1986).
- [Hea64] R.L. Heath, "Scintillation Spectrometry," AEC report IDO-16880-1 (1964).

- [Hei83a] U. Heinz, J. Reinhardt, B. Müller, W. Greiner, and U. Müller, *Z. Phys.* **A314**,125 (1983).
- [Hei83b] U. Heinz, B. Müller, and W. Greiner, *Ann. Phys.* **151**,227 (1983).
- [Hei84a] U. Heinz, J. Reinhardt, B. Müller, W. Greiner, and W.T. Pinkston, *Z. Phys.* **A316**,341 (1984).
- [Hei84b] U. Heinz, U. Müller, J. Reinhardt, B. Müller, and W. Greiner, *Ann. Phys.* **158**,476 (1984).
- [Hen86] S. Henderson, unpublished notes (1986).
- [Hen87] W. Henning, F.L.H. Wolfs, J.P. Schiffer, and K.E. Rehm, *Phys. Rev. Lett.* **58**,318 (1987).
- [Hes84] P.O. Hess, W. Greiner, and W.T. Pinkston, *Phys. Rev. Lett.* **53**,1535 (1984).
- [Hir86] Y. Hirata and H. Minakata, *Phys. Rev. D* **34**,2493 (1986).
- [Hir87] Y. Hirata and H. Minakata, *Phys. Rev. D* **36**,652 (1987).
- [Hof86] C.M. Hoffman, *Phys. Rev. D* **34**,2167 (1986).
- [Hub80] F. Hubert, A. Fleury, R. Bimbot, D. Gardes, *Ann. Phys.*, Vol. 5 (1980).
- [Hun40] F. Hund, *Z. Phys.* **117**,1 (1940).
- [Ito81] S. Ito, unpublished notes (1981).
- [Jac75] J.D. Jackson, *Classical Electrodynamics, 2nd ed.* (J. Wiley & Sons, New York, 1975).
- [Jak87] D.H. Jakubassa-Amundsen, *Phys. Lett. A* **120**,407 (1987).
- [Jun74] F.C. Jundt, H. Kubo, and H.E. Grove, *Phys. Rev. A* **10**,1053 (1974).
- [Kat86] M.W. Katoot, V.E. Oberacker, and W.T. Pinston, *Phys. Lett. B* **172**,292 (1986).
- [Kid83] Y. Kido, private notes (1983).
- [Kie83] P. Kienle, in: *Quantum Electrodynamics of Strong Fields*, W. Greiner, ed. (Plenum Press, New York, 1983), p. 293.
- [Kie86] P. Kienle, *Ann. Rev. of Nuc. and Part. Sci.* **36**,605 (1986).
- [Kie87] P. Kienle, "Electron-Positron Pair Creation in Heavy-Ion Collisions and Bhabha Scattering in the MeV Range," GSI preprint **GSI-87-26** (1987).
- [Kim87] D.Y. Kim and S. Zahir, *Phys. Rev. D* **35**,886 (1987).
- [Kle29] O. Klein, *Z. Phys.* **53**,157 (1929); *Z. Phys.* **53**,11 (1928).

- [Kli87] J. van Klinken, W.J. Meiring, F.W.N. de Boer, H. Bokemeyer, T.R. Hageman, V.A. Wichers, S.Y. van der Werf, G.C.Th. Wierda, and H.W. Wilschut, Gronningen preprint (1987).
- [Klü84] M. Klüver, M. Begemann, K.E. Stiebing, "Untersuchung des Curium Targets," internal report, unpublished (1984).
- [Kno68] G. Knop and W. Paul, in:  *$\alpha$ -,  $\beta$ -, and  $\gamma$ -Ray Spectroscopy*, K. Siegbahn, ed. (North-Holland, Amsterdam, 1968), p. 1.
- [Kön87] W. König, F. Bosch, P. Kienle, C. Kozhuharov, H. Tsertos, E. Berdermann, S. Huchler, and W. Wagner, *Z. Phys. A* **328**,219 (1987).
- [Kon86] A. Konaka, K. Imai, H. Kobayashi, A. Masaïke, K. Miyake, T. Nakamura, N. Nagamine, N. Sasao, A. Enomoto, Y. Fukushima, E. Kikutani, H. Koiso, H. Matsumoto, K. Nakahara, S. Ohsawa, T. Taniguchi, I. Sato, and J. Urakawa, *Phys. Rev. Lett.* **57**,659 (1986).
- [Kot70] K. Kotajima and R. Beringer, *Rev. Sci. Instr.*, **41**,632 (1970).
- [Koz79] C. Kozhuharov, P. Kienle, E. Berdermann, H. Bokemeyer, J.S. Greenberg, Y. Nakayama, H. Backe, L. Handschug, and E. Kankeleit, *Phys. Rev. Lett.* **48**,376 (1979).
- [Koz81] C. Kozhuharov, in: *Quantum Electrodynamics of Strong Fields*, W. Greiner, ed. (Plenum Press, New York, 1983).
- [Koz82] C. Kozhuharov, in: *Electronic and Atomic Collisions*, S. Datz, ed. (North-Holland, Amsterdam, 1982), p. 179.
- [Kra87] D. Kraft, Diploma Thesis, Univ. Frankfurt, (1987).
- [Krs86a] L.M. Krauss and F. Wilczek, *Phys. Lett. B* **173**,189 (1986).
- [Krs86b] L.M. Krauss and M.B. Wise, *Phys. Lett. B* **176**,483 (1986).
- [Krs86c] L.M. Krauss and M. Zeller, *Phys. Rev. D* **34**,3385 (1986).
- [Lan86] K. Lane, *Phys. Lett. B* **169**,97 (1986).
- [Led78] C.M. Lederer and V.S. Shirley, eds., *Table of Isotopes, 7th Ed.*, (J.Wiley & Sons, New York, 1982).
- [Lei61] H.J. Leisi, J.H. Brunner, C.F. Perdrisat and P. Scherrer, *Helv. Phys. Acta* **34**,161 (1961).
- [Lem85] H. Lemmer and W. Greiner, *Phys. Lett. B* **162**,247 (1985).
- [Li86] Bing-An Li and H.T. Nieh, preprint ITP-SB-86-23 (1986).
- [Lia82] E. Liarokapis, R. Schule, and T. Cowan, "Efficiency Calculation by Path Integration," ECPI computer program, unpublished (1982-1986).
- [Lic67] W. Lichten, *Phys. Rev.* **164**,131 (1967).

- [Lic85] W. Lichten and A. Robatino, Phys. Rev. Lett. **54**,781 (1985).
- [Lic85b] W. Lichten and A. Robatino, Phys. Rev. Lett. **55**,135 (1985).
- [Lie78] D. Liesen, P. Armbruster, H.H. Behnke, and S. Hagmann, Z. Phys. **A288**,417 (1978).
- [Lie80] D. Liesen, P. Armbruster, F. Bosch, S. Hagmann, P.H. Mokler, H.J. Wollersheim, H. Schmidt-Böcking, R. Schuch, and J.B. Wilhelmy, Phys. Rev. Lett. **44**,983 (1980).
- [Ma86] E. Ma, Phys. Rev. D **34**,293 (1986).
- [Mac73] J.R. MacDonald, M.D. Brown, and T. Chiao, Phys. Rev. Lett. **33**,473 (1973).
- [Mac78] J.R. MacDonald, P. Armbruster, H.H. Behnke, F. Folkmann, S. Hagmann, D. Liesen, P.H. Mokler, and A. Warczak, Z. Phys. **A284**,57 (1978).
- [Mag86] G. Mageras, P. Franzini, P.M. Tuts, S. Youssef, T. Zhao, J. Lee-Franzini, and R.D. Schamberger, Phys. Rev. Lett. **56**,2672 (1986).
- [Mai87] K. Maier, W. Bauer, J. Briggmann, H.D. Carstanjen, W. Decker, J. Diehl, V. Heinemann, J. Major, H.E. Schaefer, A. Seeger, H. Stoll, P. Wesolowski, E. Widmann, F. Bosch, and W. Koenig, Z. Phys. A **326**,527 (1987).
- [Mal85] N. Malhotra and R.K. Gupta, Phys. Rev. C **31**,1179 (1985).
- [Man86] H.M.M. Mansour, M. Ismail, M. Osman, and K.A. Ramadan, Phys. Rev. C **34**,1278 (1986).
- [Mac82] D. Maor, P.H. Mokler, D. Schüll, and Z. Stachura, Nucl. Inst. and Meth. **194**,377 (1982).
- [Mas86] E. Masso, Phys. Lett. B **181**,388 (1986).
- [Met80] V. Metag, D. Habs, and H.J. Specht, Phys. Rep. **65**,1 (1980).
- [Mey73] W.E. Meyerhof, T.K. Saylor, S.M. Lazarus, W.A. Little, B.B. Triplett, and L.F. Chase Jr., Phys. Rev. Lett. **30**,1279 (1973).
- [Mey75] W.E. Meyerhof, T.K. Saylor, and R. Anholt, Phys. Rev. A **12**,2641 (1975).
- [Mey77] W.E. Meyerhof, R. Anholt, Y. El Masri, I.Y. Lee, D. Cline, F.S. Stephens, and R.M. Diamond, Phys. Lett. B **69**,41 (1977).
- [Mey79] W.E. Meyerhof, D.L. Clark, Ch. Stoller, E. Morenzoni, W. Wölfi, F. Folkmann, P. Vincent, P.J. Mokler, and P. Armbruster, Phys. Lett. **70A**,303 (1979).
- [Mey86] W.E. Meyerhof, J.D. Molitoris, K. Danzmann, D.W. Spooner, F.S. Stephens, R.M. Diamond, E.-M. Beck, A. Schäfer, and B. Müller, Phys. Rev. Lett. **57**,2139 (1986).
- [Mil87] A.P. Mills, Jr., and J. Levy, Phys. Rev. D **36**,707 (1987).

- [Mok72] P.H. Mokler, H.J. Stein, and P. Armbruster, *Phys. Rev. Lett.* **29**,827 (1972).
- [Mok87] P.H. Mokler, private communication (1987).
- [Mül72] B. Müller, H. Peitz, J. Rafelski, and W. Greiner, *Phys. Rev. Lett.* **28**,1235 (1972).
- [Mül72b] B. Müller, J. Rafelski, and W. Greiner, *Z. Phys.* **257**,62 (1972).
- [Mül73] B. Müller, J. Rafelski, and W. Greiner, *Phys. Lett. B* **47**,5 (1973).
- [Mül73b] B. Müller, J. Rafelski, and W. Greiner, *Nuovo Cimento* **A18**,551 (1973).
- [Mül74] B. Müller and W. Greiner, *Phys. Rev. Lett.* **33**,469 (1974).
- [Mül78] B. Müller, G. Soff, W. Greiner, and V. Ceausescu, *Z. Phys.* **A285**,27 (1978).
- [Mül83] B. Müller, J. Reinhardt, W. Greiner, and G. Soff, *Z. Phys.* **A311**,151 (1983).
- [Mül84] B. Müller, "Decay of the Vacuum in Heavy Ion Collisions," in: *Proc. of 1984 INS-RIKEN International Symposium on Heavy Ion Physics (Part 1: New Scope of Heavy Ion Physics), Tokyo, August 1984*, and GSI preprint GSI-84-62.
- [Mül86] B. Müller, J. Reinhardt, W. Greiner, and A. Schäfer, *J. Phys.* **G12**,L109 (1986).
- [Mül86b] B. Müller and J. Rafelski, *Phys. Rev. D* **34**,2896 (1986).
- [Mül86c] B. Müller and J. Reinhardt, *Phys. Rev. Lett.* **56**,2108 (1986).
- [Mül86d] B. Müller and J. Rafelski, preprint UFTP 170/1986.
- [MüU83] U. Müller, G. Soff, T. de Reus, J. Reinhardt, B. Müller, and W. Greiner, *Z. Phys.* **A313**,263 (1983).
- [MüU86] U. Müller, T. de Reus, J. Reinhardt, B. Müller, and W. Greiner, *Z. Phys.* **A323**,261 (1986).
- [Muk86] N. Mukhopadhyay and A. Zehnder, *Phys. Rev. Lett.* **56**,206 (1986).
- [Muk86b] N. Mukhopadhyay and A. Zehnder, preprint SIN-PR-86-02 (1986).
- [Mye77] W.D. Myers, *Droplet Model of Atomic Nuclei* (Plenum Press, New York, 1977).
- [Nee82] R.E. Neese and M.W. Guidry, *Phys. Rev. C* **25**,881 (1982).
- [Nei86] L.W. Neise, J.A. Maruhn, and W. Greiner, *Z. Phys.* **A323**,195 (1986).
- [Ng87] Y.J. Ng and Y. Kikuchi, "Narrow  $e^+e^-$  Peaks in Heavy-Ion Collisions as Possible Evidence of a Confining Phase of QED," UNC preprint IFP-289, Univ. North Carolina (1987).

- [Nie85] A. Niehaus, in: *Physics of Atoms and Molecules*, B. Crasemann, ed. (Plenum Press, New York, 1985), p. 377.
- [Nik68] V.S. Nikolaev and I.S. Dmitriev, *Phys. Lett.* **28A**,277 (1968).
- [Obe76] V. Oberacker, G. Soff, and W. Greiner, *Phys. Rev. Lett.* **36**,1024 (1976).
- [Obe76b] V. Oberacker, G. Soff, and W. Greiner, *Nucl. Phys.* **A259**,324 (1976).
- [Obe86] V.E. Oberacker, M.W. Katoot, and W.T. Pinkston; in: *Physics of Strong Fields*, W. Greiner, W. Greiner, ed. (Plenum Press, New York, 1987), p. 511.
- [Obr80] J.J. O'Brien, E. Liarokapis, and J.S. Greenberg, *Phys. Rev. Lett.* **44**,386 (1980).
- [Oer86] H. Oerschler, B. Blank, E. Bozek, U. Gollerthan, H. Jäger, E. Kankeleit, G. Klotz-Engmann, M. Krämer, R. Krieg, U. Meyer, C. Müntz, M. Rhein, and P. Senger, in: *Physics of Strong Fields*, W. Greiner, W. Greiner, ed. (Plenum Press, New York, 1987), p. 373.
- [Pec77] R.D. Peccei and H.R. Quinn, *Phys. Rev. Lett.* **38**,1440 (1977).
- [Pec86] R.D. Peccei, T.T. Wu, and T. Yanagida, *Phys. Lett.* **B 172**,435 (1986).
- [Pek87] R. Peckhaus, T.W. Elze, T. Happ, and T. Dresel, *Phys. Rev. C* **36**,83 (1987).
- [Pel82] D. Pelte and D. Schwalm, in: *Heavy Ion Collisions, Vol. 3*, R. Bock, ed. (North-Holland, Amsterdam, 1982), p. 1.
- [Per62a] C.F. Perdrisat, J.H. Brunner and H.J. Leisi, *Helv. Phys. Acta* **35**,175 (1962).
- [Per62b] C.F. Perdrisat, H.J. Leisi and J.H. Brunner, *Nucl. Phys.* **31**,157 (1962).
- [Per62c] C.F. Perdrisat, H.J. Leisi, J.H. Brunner and L. Plaggio, *Nucl. Phys.* **31**,160 (1962).
- [Pie69] W. Pieper and W. Greiner, *Z. Phys.* **A218**,327 (1969).
- [Pom45] I. Pomeranchuk and J. Smorodinsky, *J. Phys. USSR* **9**,97 (1945).
- [Raf71] J. Rafelski, L.P. Fulcher, and W. Greiner, *Phys. Rev. Lett.* **27**,958 (1971).
- [Raf72] J. Rafelski, B. Müller, and W. Greiner, *Lett. Nuovo Cimento* **4**,469 (1972).
- [Raf74] J. Rafelski, B. Müller, and W. Greiner, *Nucl. Phys.* **B38**,585 (1974).
- [Raf76] J. Rafelski and B. Müller, *Phys. Rev. Lett.* **36**,517 (1976).
- [Raf78] J. Rafelski, B. Müller, and W. Greiner, *Z. Phys.* **A285**,49 (1978).
- [Rch87] I. Reichstein, *Phys. Lett.* **B 192**,35 (1987).

- [Rei81] J. Reinhardt, B. Müller, and W. Greiner, *Phys. Rev. A* **24**,103 (1981).
- [Rei81b] J. Reinhardt, U. Müller, B. Müller, and W. Greiner, *Z. Phys. A* **303**,173 (1981).
- [Rei83] J. Reinhardt, B. Müller, W. Greiner, and U. Müller, *Phys. Rev. A* **28**,2558 (1983).
- [Rei85] J. Reinhardt and W. Greiner, in: *Treatise on Heavy-Ion Science, Vol. 5: High Energy Atomic Physics*, D.A. Bromley, ed. (Plenum Press, New York, 1985), p. 3.
- [Rei85b] J. Reinhardt, B. Müller, and W. Greiner, *Phys. Rev. Lett.* **55**,134 (1985).
- [Rei86] J. Reinhardt, A. Schäfer, B. Müller, and W. Greiner, *Phys. Rev. C* **33**,194 (1986).
- [Rei87] J. Reinhardt, A. Sherdin, B. Müller, and W. Greiner, *Z. Phys. A* **327**,367 (1987).
- [Reu81] T. de Reus, U. Müller, J. Reinhardt, P. Schlüter, K.H. Weitschorke, B. Müller, W. Greiner, and G. Soff, in: *Quantum Electrodynamics of Strong Fields*, W. Greiner, ed. (Plenum Press, New York, 1983).
- [Reu84] T. de Reus, J. Reinhardt, B. Müller, W. Greiner, G. Soff, and U. Müller, *J. Phys.* **B17**,615 (1984).
- [Reu86] T. de Reus, G. Soff, O. Graf, and W. Greiner, "The consequences of sudden rearrangements of electronic shells," GSI preprint GSI-86-49 (1986).
- [Reu87] T. de Reus, J. Reinhardt, U. Müller, B. Müller, W. Greiner, and G. Soff, *Phys. Scripta* **144C**,237 (1987).
- [Reu87b] T. de Reus, Ph.D. Dissertation, Univ. Frankfurt (1987).
- [Rho83] M.J. Rhoades-Brown, V.E. Oberacker, M. Seiwert, and W. Greiner, *Z. Phys. A* **310**,287 (1983).
- [Rio87] E.M. Riordan, M.W. Krasny, K. Lang, P. de Barbaro, A. Bodek, S. Dasu, N. Varelas, X. Wang, R. Arnold, D. Benton, P. Bosted, L. Colgher, A. Lung, S. Rock, Z. Szalata, B.W. Filippone, R.C. Walker, J.D. Bjorken, M. Crisler, A. Para, J. Lambert, J. Button-Shafer, B. Debebe, M. Frodyma, R.S. Hicks, G.A. Peterson, and R. Gearhart, *Phys. Rev. Lett.* **59**,755 (1987).
- [Ron81] R.M. Ronningen, R.C. Merlin, J.A. Nolan, G.M. Crawley, and C.E. Bemis, *Phys. Rev. Lett.* **47**,635 (1981).
- [Ros35] M.E. Rose and G.E. Uhlenbeck, *Phys. Rev.* **48**,211 (1935).
- [Sak87] M. Sakai, Y. Fujita, M. Imamura, K. Omata, S. Ohya, and T. Miura, "On the Mysterious Electron Peak in  $e^+ \rightarrow \text{Th}$  Interactions," Univ. Tokyo preprint, INS-Rep.-632 (May 1987).
- [Sak88] K. Sakaguchi, Ph.D. Thesis, Univ. Frankfurt (1988); and,

K. Sakaguchi, H. Backe, K. Bethge, H. Bokemeyer, T. Cowan, H. Folger, J.S. Greenberg, P. Salabura, D. Schwalm, J. Schweppe, and K.E. Stiebing, to be published.

- [Sal88] P. Salabura, Ph.D. Thesis, Univ. Frankfurt (1988); and, P. Salabura, H. Backe, K. Bethge, H. Bokemeyer, T. Cowan, H. Folger, J.S. Greenberg, K. Sakaguchi, D. Schwalm, J. Schweppe, and K.E. Stiebing, to be published.
- [Sar72] F.W. Saris, W.F. Van der Weg, H. Tawara, and R. Laubert, Phys. Rev. Lett. **28**,717 (1972).
- [Sat79] G.R. Satchler and W.G. Love, Phys. Rep. **55**,183 (1979).
- [Sau31] F. Sauter, Z. Phys. **69**,742 (1931); Z. Phys. **73**,547 (1931).
- [Sav86] M.J. Savage, R.D. McKeown, B.W. Filippone, and L.W. Mitchell, Phys. Rev. Lett. **57**,178 (1986).
- [Shä84] A. Schäfer, B. Müller, and W. Greiner, Phys. Lett. B **149**,455 (1984).
- [Shä85] A. Schäfer, J. Reinhardt, B. Müller, W. Greiner, and G. Soff, J. Phys. **G11**,L69 (1985).
- [Shä86a] A. Schäfer, J. Reinhardt, W. Greiner, and B. Müller, Mod. Phys. Lett. **A1**,1 (1986).
- [Shä86b] A. Schäfer, J. Reinhardt, B. Müller, and W. Greiner, Z. Phys. **A324**,243 (1986).
- [Sha86] G. Scharf, Phys. Lett. B **177**,429 (1986).
- [Shf40] L.I. Schiff, H. Snyder, and J. Weinberg, Phys. Rev. **57**,315 (1940).
- [Shl78] P. Schlüter, G. Soff, and W. Greiner, Z. Phys. **A286**,149 (1978).
- [Shl79] P. Schlüter and G. Soff, Atomic Data and Nuclear Data Tables **24**,509 (1979).
- [Shl81] P. Schlüter, G. Soff, and W. Greiner, Phys. Rep. **75**,327 (1981).
- [Shl83] P. Schlüter, T. deReus, J. Reinhardt, B. Müller and G. Soff, Z. Phys. **A314**,297 (1983).
- [Shl86] P. Schlüter, G. Soff, and W. Greiner, Phys. Rev. C **33**,1816 (1986).
- [Shl86b] P. Schlüter, U. Müller, G. Soff, T. de Reus, J. Reinhardt, and W. Greiner, Z. Phys. **A323**,139 (1986).
- [Shr86] U.E. Schröder, Mod. Phys. Lett. **A1**,157 (1986).
- [Shu80] R. Schule, private notes (1980).
- [Shü86] D. Schüll, private communication (1987).

- [Shm84] D. Schwalm, in: *Electronic and Atomic Collisions*, J. Eichler, I.V. Hertels, and N. Stolterfoht, eds. (North-Holland, Amsterdam, 1984), p. 295.
- [Shm86] S. Schramm, J. Reinhardt, U. Müller, B. Müller, and W. Greiner, *Z. Phys. A* **323**,275 (1986).
- [Shw83] J. Schweppe, A. Gruppe, K. Bethge, H. Bokemeyer, T. Cowan, H. Folger, J.S. Greenberg, H. Grein, S. Ito, R. Schule', D. Schwalm, K.E. Stiebing, N. Trautmann, P. Vincent, and M. Waldschmidt, *Phys. Rev. Lett.* **51**,2261 (1983).
- [Shw85] J. Schweppe, Ph.D. Dissertation, Yale University (1985).
- [Shw85b] J. Schweppe, program notes (1985).
- [Shw86] J. Schweppe, in: *Electronic and Atomic Collisions*, D.C. Lorents, W.E. Meyerhof, and J.R. Peterson, eds. (North-Holland, Amsterdam, 1986), p. 405.
- [Shw86b] J. Schweppe and S. Henderson, unpublished notes (1986).
- [Shw87] G.L. Shaw, "Spectrum of Narrow States Produced in Low-Energy Heavy-Ion Collisions," UCI Rep. No. 87-51.
- [Seg77] E. Segré, *Nuclei and Particles, 2nd ed.*, (Benjamin/Cummings Pub. Co., Reading Mass., 1979).
- [Sei79] G. Seiler-Clarc, D. Husar, R. Novotny, H. Gräf, and D. Pelte, *Phys. Lett. B* **80**,345 (1979).
- [Sei84] M. Seiwert, W. Greiner, V. Oberacker, and M.J. Rhoades-Brown, *Phys. Rev. C* **29**,477 (1984).
- [Sei85] M. Seiwert, W. Greiner, and W.T. Pinkston, *J. Phys. G***11**,L21 (1985).
- [Sei85b] M. Seiwert, J.A. Maruhn, W. Greiner, and J. Friedrich, *Z. Phys. A***321**,653 (1985).
- [Sen86] P. Senger, H. Backe, M. Begemann-Blaich, H. Bokemeyer, P. Glässel, D. v. Harrach, M. Klüver, W. Konen, K. Poppensieker, K. Stiebing, J. Stroth, and K. Wallenwein, in: *Physics of Strong Fields*, W. Greiner, W. Greiner, ed. (Plenum Press, New York, 1987), p. 423.
- [Shi64] S. Shimizu, Y. Nakayama, H. Hirata and H. Mazaki, *Nucl. Phys.* **54**,265 (1964).
- [Sli49] L.A. Sliv, *Dokl. Akad. Nauk SSSR* **64**,521(1949); *Sov. Phys. JETP* **25**,7 (1953); *J. Phys. et Rad.* **16**,589 (1959).
- [Smi74] K. Smith, H. Peitz, B. Müller, and W. Greiner, *Phys. Rev. Lett.* **32**,554 (1974).
- [Sof77] G. Soff, J. Reinhardt, B. Müller, and W. Greiner, *Phys. Rev. Lett.* **38**,417 (1977).

- [Sof78] G. Soff, J. Reinhardt, W. Betz, and J. Rafelski, *Phys. Scripta* **17**,417 (1978).
- [Sof79] G. Soff, W. Greiner, W. Betz, and B. Müller, *Phys. Rev. A* **20**,169 (1979).
- [Sof81] G. Soff, J. Reinhardt, and W. Greiner, *Phys. Rev. A* **26**,174 (1981).
- [Sof81b] G. Soff, P. Schlüter, and W. Greiner, *Z. Phys. A* **303**,189 (1981).
- [Sof81c] G. Soff, J. Reinhardt, and W. Greiner, *Phys. Rev. A* **23**,701 (1981).
- [Sof86] G. Soff, P. Schlüter, and W. Greiner, in: *Physics of Strong Fields*, W. Greiner, W. Greiner, ed. (Plenum Press, New York, 1987), p. 59.
- [Ste82] H. Stelzer, "Gas Filled Heavy Ion Detectors," in *Lecture Notes in Physics, Vol. 178, Detectors in Heavy-Ion Reactions* (Berlin, 1983).
- [Sti86] K.E. Stiebing, in: *Physics of Strong Fields*, W. Greiner, W. Greiner, ed. (Plenum Press, New York, 1987), p. 253.
- [Sto70] E. Storm and H.I. Israel, *Nuclear Data Tables* **A7**,565 (1970).
- [Str83] M.R. Strayer, R.Y. Cusson, H. Stöcker, and M.J. Rhoades-Brown, *Phys. Rev. C* **28**,228 (1983).
- [Str86] P. Strehl, "Beam Diagnostics," in: *Proc. CERN Accelerator School, Aarhus, Sept. 21-26, 1986*, and GSI preprint **GSI-86-39** (1986).
- [Suz86] M. Suzuki, *Phys. Lett. B* **175**,364 (1986).
- [Tom82] T. Tomoda and H.A. Weidenmüller, *Phys. Rev. A* **26**,162 (1982).
- [Tom82b] T. Tomoda, *Phys. Rev. A* **26**,174 (1982).
- [Tom83] T. Tomoda and H.A. Weidenmüller, *Phys. Rev. C* **28**,739 (1983).
- [Tra82] N. Trautmann, M. Weber, D. Gembalies-Datz, R. Heimann, H. Folger, and W. Hartmann, "Preparation of Actinide Targets by Molecular Plating for Experiments with Heavy-Ions," in: *Proc. of 13th World Conference of the International Nuclear Target Development Society, Seattle, Washington*; and GSI Preprint **GSI-82-40** (1982).
- [Tsa86] Y.S. Tsai, *Phys. Rev. D* **34**,1326 (1986).
- [Tse85] H. Tsertos, E. Berdermann, F. Bosch, M. Clemente, P. Kienle, W. König, C. Kozhuharov, and W. Wagner, *Phys. Lett. B* **162**,273 (1985).
- [Tse85b] H. Tsertos, PhD Thesis, Tech. Univ. München (1985).
- [Tse87] H. Tsertos, F. Bosch, P. Kienle, W. König, C. Kozhuharov, E. Berdermann, S. Huchler, and W. Wagner, *Z. Phys. A* **326**,235 (1987).
- [Vas60] S.S. Vasilenko, M.S. Kaganskii, D.L. Kaminskii and S.F. Koksharova, *JETP* **39**,970 (1960); *JETP (Soviet Physics)* **12**,672 (1961).

- [Vas85] D. Vasak, B. Müller, and W. Greiner, *J. Phys.* **G11**,1309 (1985);
- [Vin77] P. Vincent, Ph.D. Thesis, Yale University (1977).
- [Vin78] P. Vincent, C.K. Davis, and J.S. Greenberg, *Phys. Rev. A* **18**,1878 (1978).
- [Vin79] P. Vincent and J.S. Greenberg, *J. Phys. B* **12**,L641 (1979).
- [Vin83] P. Vincent, unpublished notes (1983).
- [Vor61] V.V. Voronkov and N.N. Kolesnikov, *Zh. Exsper. i Teor. Fiziki* **39**,189 (1960); in: *Sov. Phys. JETP* **12**,136 (1962).
- [Wan87] T.F. Wang, I. Ahmad, S.J. Freedman, R.V.F. Janssens, and J.P. Schiffer, "Search for Sharp Lines in  $e^+e^-$  Coincidences from Positrons on Th," Argonne preprint **PHY-5016-HI-87** (July, 1987).
- [Wei78] S. Weinberg, *Phys. Rev. Lett.* **40**,223 (1978).
- [Wie63] R. Wiener, C. Chasman, P. Harihar and C.S. Wu, *Phys. Rev.* **130**,1069 (1963).
- [Wie79] K.H. Wietschorke, B. Müller, W. Greiner, and G. Soff, *J. Phys.* **B12**,L31 (1979).
- [Wie87] K.H. Wietschorke, P. Schlüter, G. Soff, K. Rumrich, and W. Greiner, "The Relativistic Two-Centre Continuum," GSI preprint **GSI-87-5** (1987).
- [Wil68] R. Wilson, in:  *$\alpha$ -,  $\beta$ -, and  $\gamma$ -Ray Spectroscopy*, K. Siegbahn, ed. (North-Holland, Amsterdam, 1968), p. 1557.
- [Wil78] F. Wilczek, *Phys. Rev. Lett.* **40**,279 (1978).
- [Wil80] W.W. Wilcke, J.R. Birkelund, H.J. Wollersheim, A.D. Hoover, J.R. Huizenga, W.U. Schroeder, and L.E. Tubbs, *Atomic Data and Nuclear Data Tables* **25**,389 (1980).
- [Wim87] U. von Wimmersperg, S.H. Connell, R.F.A. Hoernle, and E. Sideras-Haddad, *Phys. Rev. Lett.* **59**,266 (1987).
- [Wir86] G. Wirth, W. Brüche, M. Brügger, Wo Fan, K. Sümmerer, F. Funke, V. Kratz, M. Lerch, and N. Trautmann, *Phys. Lett. B* **177**,282 (1986).
- [Won86] C.Y. Wong, *Phys. Rev. Lett.* **56**,1047 (1986).
- [Won86b] C.Y. Wong and R.L. Becker, *Phys. Lett. B* **182**,251 (1986).
- [Won87] C.Y. Wong, H.W. Crater, R.L. Becker, and P. Van Alstine, "Study of QED( $e^+e^-$ ) Resonances with Two-Body Dirac Equations from Constraint Dynamics," ORNL preprint (1987).
- [Yam87] Y. Yamaguchi and H. Sato, *Phys. Rev. C* **35**,2156 (1987).
- [Zee86] A. Zee, *Phys. Lett. B* **172**,377 (1986).

- [Zeh85] A. Zehnder, in: *Fundamental Interactions in Low-Energy Systems*, P. Dalpiaz, G. Fiorentine, and G. Torelli, eds. (Plenum Press, New York, 1985), p. 337.
- [Zel72] Ya.B. Zeldovich and V.S. Popov, *Sov. Phys. Usp.* **14**,673 (1972).
- [Zum84] J.D. Zumbro, E.B. Shera, Y. Tanaka, C.E. Bemis, R.A. Naumann, M.V. Hoehn, W. Reuter, and R.M. Steffen, *Phys. Rev. Lett.* **53**,1888 (1984).